The short-and long-term effects of genetically silencing deep-layer cortical glutamatergic projection neurons on GABAergic neurons



Florina Petra Szabó

St John's College

University of Oxford

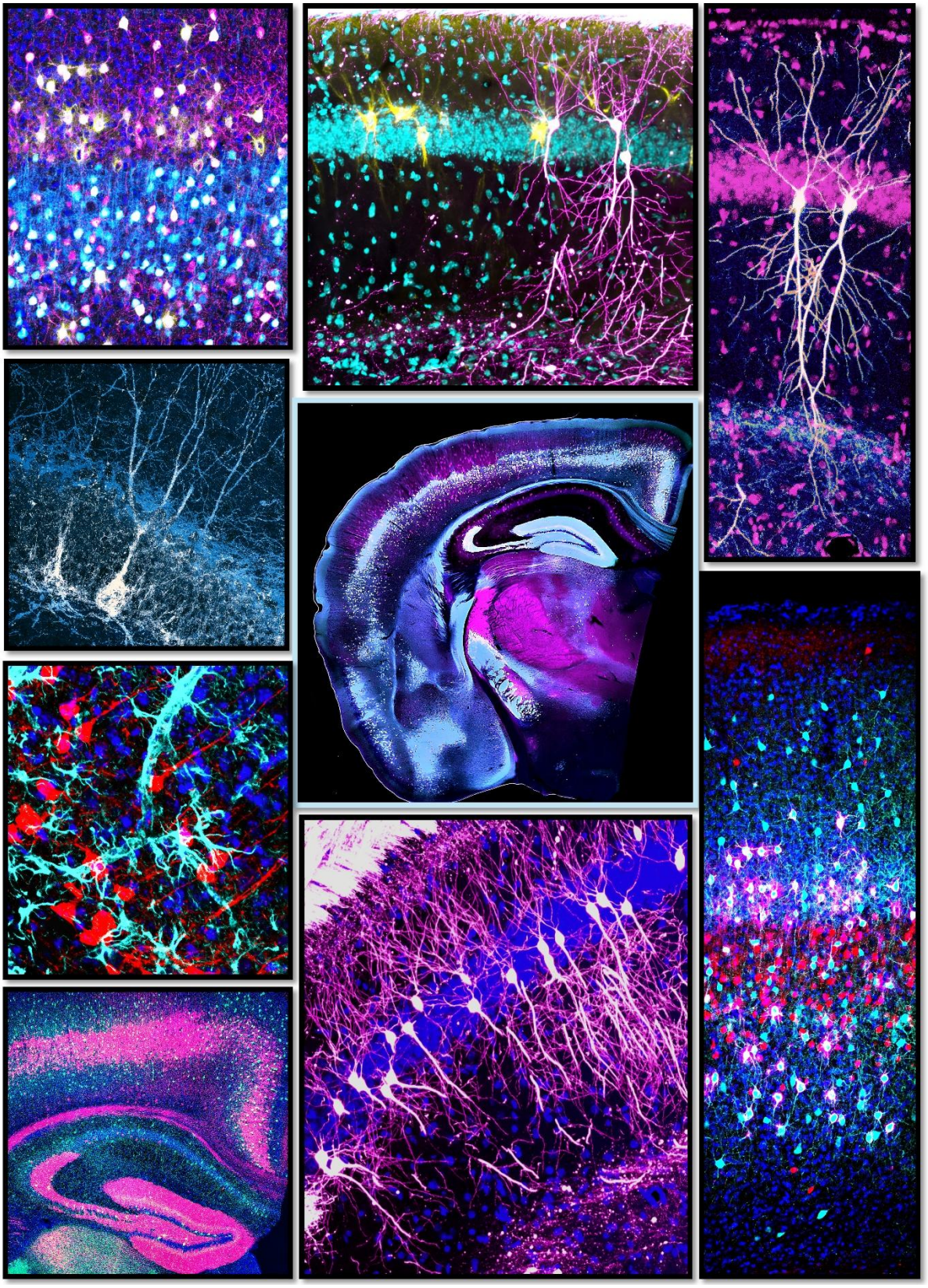
A thesis submitted for the degree of

Doctor of Philosophy

Michaelmas Term, 2025

"These are the principles for the development of a complete mind: Study the science of art. Study the art of science…"

Leonardo da Vinci



Abstract

The short-and long-term effects of genetically silencing deep-layer cortical glutamatergic projection neurons on GABAergic neurons

Florina Petra Szabó

St John's College

A thesis submitted for the degree of

Doctor of Philosophy

The intricate complexity of brain circuits stems from the morphologically and functionally distinct cell types present throughout the cerebral cortex. The formation of these finely tuned cortical networks relies on the precise connections between glutamatergic pyramidal neurons and GABAergic interneurons, which engage in dynamic interactions during the early stages of development. There has been significant research on how various subtypes of interneurons modulate the activity of pyramidal cells; however, the role of pyramidal neurons in instructing the spatial and laminar organisation of interneurons has received less attention. Addressing this gap is critical, as dysfunctional pyramidal neurons can lead to long-term impairments in inhibitory neurons, compromising the essential inhibitory control over excitatory neurons.

Employing three transgenic mouse strains, my DPhil thesis investigated the role of deep-layer cortical glutamatergic projection neurons in regulating inhibitory neuron number, laminar proportion, and morphology in *juvenile* and *adult* brains. To genetically 'silence' selected subtypes of glutamatergic layer 5 and layer 6 cortical projection neurons, I selectively deleted *Snap25* from Rbp4-Cre+ and Drd1a-Cre+ neurons, respectively. This led to the chronic abolition of action-potential-dependent neurotransmitter release from subsets of layer 5 and layer 6 projection neurons. By examining the interneurons near the cell bodies as well as the subcortical projection regions, I differentiated between the effects of silencing layer 5 and layer 6 neurons on cortical and subcortical GABAergic neurons. I have demonstrated that chronic silencing of Rbp4-Cre+ layer 5 projection neurons does not impede the development of cortical parvalbumin interneurons, but it has a delayed effect on their laminar distribution in layer 4 of the primary somatosensory cortex, which only manifests in adulthood. In contrast, chronic silencing of a subset of layer 6 projection neurons has a *long*-term impact on the laminar density of parvalbumin interneurons and the perineuronal nets in layer 5 of the primary motor cortex. Interestingly, silencing Drd1a-Cre+ neurons has a *short*-term effect on the laminar arrangement of neuropeptide-Y neurons in layer 6b, solely during development.

To chronically 'enhance' the same subset of layer 6 cortical projection neurons, I selectively ablated *Pten* from Drd1a-Cre+ neurons. Chronically enhancing the same subset of projection neurons in cortical layer 6 has yielded differential effects on the laminar distribution of adult parvalbumin and somatostatin interneurons, highlighting region and cell-type-specific dynamics. While it significantly decreased the density of somatostatin interneurons in layers 5 and 6b of the primary motor cortex, it significantly increased the density of parvalbumin interneurons in layer 2/3, without changing their total number. Therefore, the chronic deletion of *Pten* from Drd1a-Cre+ neurons suggests a redistribution of the density of MGE-derived interneurons in the primary motor cortex.

In conclusion, my doctoral research aims to enhance our understanding of the mechanisms that govern cell-type-specific connections between glutamatergic and GABAergic interneurons. Additionally, it seeks to clarify the role of pyramidal neurons in regulating the spatial and laminar arrangement of parvalbumin, somatostatin, and neuropeptide-Y interneurons.

Statement of Authorship

I hereby declare that all work presented throughout the thesis is my own, with the exceptions and collaborations listed below.

The first two sections of **Chapter 3**, titled "**Section 3.2**. *Local and Global Effects of the Chronic Abolition of Evoked Vesicle Release from Glutamatergic Layer 5 Projection Neurons on Parvalbumin Interneurons in the Juvenile Brain*" and "**Section 3.3.** *Local and Global Effects of the Chronic Silencing of Glutamatergic Layer 5 Projection Neurons on Parvalbumin Interneurons in the Adult Brain*," have been published as a research article. This publication fulfils the requirements of my PhD studentship granted by the Anatomical Society.

Szabó, F.P., Sigutova, V., Schneider, A.M., Hoerder-Suabedissen, A. & Molnár, Z. (2024) Chronic silencing of subsets of cortical layer 5 pyramidal neurons has a long-term influence on the laminar distribution of parvalbumin interneurons and the perineuronal nets. Journal of Anatomy, 00, 1–26. Available from: https://doi.org/10.1111/joa.14181

For **Chapter 3**, titled '*Chronic silencing of glutamatergic layer 5 cortical projection neurons*', the initial collection of brain samples from *Rbp4-Cre;Ai14;Snap25$^{fl/fl}$* transgenic mice (postnatal cohorts: P8, P14, and P21) was performed by my lead and co-supervisors, i.e., Professor Zoltán Molnár and Dr Anna Hoerder-Suabedissen, and my colleague, Dr Luana Campos-Soares. This assistance was provided during the period in which I was awaiting my Personal License (PIL), the issuance of which was significantly delayed as a result of the COVID-19 pandemic. Genotyping of the initial postnatal brains received (P8, P14, and P21) was performed by Dr Anna Hoerder-Suabedissen. After obtaining my PIL and completing competency measurements, I perfused and genotyped the remaining brain samples from both postnatal and adult cohorts (12 weeks).

For **Chapter 5**, entitled '*Chronic Augmentation of Subsets of Glutamatergic Drd1a-Cre+ Layer 6 Projection Neurons*', adult brain samples from *Drd1a-Cre;Ai9;Pten$^{fl/fl}$* transgenic mice (control: *Drd1a-Cre;Ai9;Pten$^{fl/+}$*, n=4; conditional homozygous knockout: *Drd1a-Cre;Ai9;Pten$^{fl/fl}$*, n=4) were generously provided by Professor Britta Eickholt and Dr. Timothy Zolnik. The mouse colony was maintained and bred at Charité University in Berlin, Germany; consequently, the procedures for perfusion, brain collection, and genotyping were all conducted in Berlin. I designed, performed, and analysed all experiments presented in **Chapter 5**.

For **Section 3.2.5.**, Figure 3.5., Panels A and B, anti-Vglut1 immunohistochemistry and confocal imaging were performed by Miss Veronika Sigutova. The cell density, morphometric analysis, and confocal imaging of parvalbumin interneurons at P14 and P21 were my own work.

For **Section 4.4.1** in Chapter 4 and **Sections 5.4.6. & 5.5.1.** in Chapter 5, spinning disk confocal imaging was conducted in collaboration with Dr James Bancroft and Edward Drydale at the Cellular Imaging Core of the Wellcome Centre for Human Genetics, University of Oxford. Confocal images were acquired by Ms. Marissa Mueller, and I assisted in setting and optimising the acquisition parameters. The preparation of brain samples for spinning disk imaging, which included brain perfusions, sectioning, and immunohistochemical staining, was conducted by me.

Acknowledgements

I would like to sincerely thank Professor Zoltán Molnár, my lead supervisor at the University of Oxford, for his unwavering support and years of mentoring since I first met him. Working with you and conducting scientific research in your laboratory has always been a real honour and privilege. I am extremely thankful for granting me such an amazing research opportunity and allowing me to contribute to one of your most cherished projects, the mysterious cortical layer 6b, which I have always found genuinely fascinating and full of opportunities for discoveries. I genuinely appreciate you igniting my interest in neuroscience and giving me a voracious appetite for science and research.

Additionally, I would like to express my gratitude to Dr Anna Hoerder-Suabedissen, my co-supervisor, for her guidance in the research conducted. I am incredibly appreciative of her support with the writing process, and her observations have greatly enhanced my academic writing and given me a more critical perspective. It has been my pleasure to have such a great research scientist as a supervisor.

I want to express my gratitude to Dr Eri Kawashita, a former Assistant Professor in the Molnár group, for helping me grow as a scientist. I appreciate you listening to my many vivid brainstorming sessions on interneurons and layer 5, and I have always liked having scientific conversations with you. I sincerely appreciate your advice and the time you always set aside to talk about so many journal papers and other subjects, even over lunch or dinner.

I also want to thank all lab members for being wonderful colleagues and friends, especially Dr Sara Bandiera, who has never failed to lift my spirits and rekindle my enthusiasm even in the face of difficulties. Even though she is now overseas, her enthusiasm, scientific curiosity, and exceptional research background inspire me to become an equally exceptional postdoc.

It would be impossible for me to complete my acknowledgements without sincerely thanking my former supervisor at the University of Szeged, Professor Károly Gulya, for always welcoming and supporting me. It was a great joy and honour to learn from him, and his constant enthusiasm for my research has motivated me to keep going. For his unwavering support throughout my undergraduate and doctoral studies, I am most grateful. Last but not least, he inspired me as a first-year biology student with his captivating lectures in Cell Biology and encouraged me to pursue academic research and become a neuroscientist. For this, I am incredibly thankful.

I am also immensely grateful to the Anatomical Society for awarding me their PhD scholarship and for funding my doctoral research.

I will always remember all the metal concerts and VIP Meet n' Greet experiences I attended during my PhD studies. Meeting my greatest guitar idols, including *Yngwie Malmsteen, Chris Broderick* from In Flames, and *Dave Mustaine* from Megadeth, who have inspired me since I first picked up the electric guitar at the age of 14, is a lifelong memory that I will always cherish. Thank you, Imi, for sharing this wonderful journey with me!

Finally, I want to express my sincere gratitude to my family for helping me with my education and believing in me to fulfil my greatest ambition of becoming a brain researcher. Without their unconditional love and support, I would never have been able to pursue my goals and realise my academic aspirations.

List of Figures

Chapter 1 Introduction

Figure 1.0. Heterogeneity of cortical pyramidal neurons

Figure 1.1. Schematic representation of the distinct subtypes of GABAergic interneurons in cortical layer 6

Figure 1.2. Assembling the laminar organisation of the mammalian cerebral cortex

Figure 1.3. Radial migration of glutamatergic cortical neurons

Figure 1.4. Tangential migration of cortical GABAergic interneurons

Figure 1.5. Birthdate of GABAergic interneurons

Figure 1.6. Translaminar L5b – L4 circuits dominate during early cortical development

Figure 1.7. Schematic illustrating the different methods used to manipulate pyramidal neurons

Figure 1.8. SNARE complex assembly and synaptic vesicle exocytosis

Figure 1.9. Action-potential-dependent neurotransmission and synaptic vesicle exocytosis in wild-type and Snap25-ablated mice

Figure 1.10. Tissue collection time points and the onset of Cre expression in *Rbp4-Cre;Ai14;Snap25*$^{fl/fl}$ mice

Figure 1.11. Overview of the effects of deep-layer pyramidal neuron manipulations on GABAergic interneurons examined in the thesis

Chapter 2 Methods

Figure 2.1. Breeding scheme of *Rbp4-Cre;Ai14;Snap25*$^{fl/fl}$ cKO mice

Figure 2.2. Representative fluorescent and confocal images of the regions of interest for all three conditional knockout strains

Figure 2.3. Finding the best image settings for VVA imaging by experimenting with pinhole diameters

Figure 2.4. 2D imaging of the VVA signal results in a significant loss of information

Figure 2.5. Representative images of full-coronal slices obtained with spinning disk SoRa confocal microscopes for mapping the projections of layer 6b projection neurons

Figure 2.6. Examples of cell segmentation of somatostatin and parvalbumin interneurons in the striatum

Figure 2.7. Examples of cell segmentation of parvalbumin interneurons in the primary somatosensory cortex

Chapter 3 Results

Figure 3.0. Overview of the structure of Chapter 3

Figure 3.1. Distribution of Rbp4-Cre-expressing neurons in layer 5 of the cortex and the dentate gyrus of the hippocampus in the *Snap25* cKO mice

Figure 3.2. Long-range axonal projections of the 'silenced' *Rbp4-Cre;Snap25$^{fl/fl}$* projection neurons in layer 5 of the cerebral cortex

Figure 3.3. Perturbing AP-dependent neurotransmitter release from Rbp4-Cre+ projection neurons does not affect cortical PV neuron development

Figure 3.4. Conditional silencing of Rbp4-Cre+ projection neurons in cortical layer 5 has no impact on the density and dynamics of subcortical PV neurons

Figure 3.5. Abolition of AP-dependent neurotransmitter release from layer 5 pyramidal neurons temporarily alters the morphology of striatal PV neurons in the juvenile brain

Figure 3.6. Striatal PV interneurons in the layer 5-silenced brains display an altered developmental trajectory of soma features between the early stages of development

Figure 3.7. Conditional silencing of Rbp4-Cre+ pyramidal neurons has no permanent impact on the morphology of striatal interneurons in the adult brain

Figure 3.8. VVA histochemical staining results in insufficient labelling of PNNs during the early stages of development in the primary motor and somatosensory cortex

Figure 3.9. VVA is not suitable for the precise detection of PNNs in the hippocampus and in subcortical regions during development

Figure 3.10. VVA sufficiently labels PNNs in the adult brain

Figure 3.11. Conditional silencing of subsets of layer 5 pyramidal neurons does not disrupt the laminar arrangement of PV interneurons in the juvenile cortex

Figure 3.12. Loss of Snap25 from layer 5 pyramidal neurons alters the correlation between PV interneurons and the perineuronal net in M1

Figure 3.13. Chronic silencing of layer 5 projection neurons rearranges the laminar distribution of PV and VVA cells in the adult primary motor and somatosensory cortex

Figure 3.14. Chronic silencing of layer 5 projection neurons unveils regional and layer-dependent differences in the correlation between PV interneurons and the perineuronal nets

Figure 3.15. Genetic silencing of Rbp4-Cre+ neurons has no long-term impact on the density of PV neurons in the subcortical projection regions of layer 5

Figure 3.16. Summary of the different regions of interest selected for parvalbumin and neuropeptide-Y interneurons

Figure 3.17. Long-term impact of the conditional silencing of subsets of layer 5 projection neurons on NPY+ interneurons in the ACA and M2

Figure 3.18. Loss of AP-dependent neurotransmitter release from layer 5 projection neurons influences the density and soma morphology of NPY+ neurons in the adult primary motor cortex

Figure 3.19. The genetic silencing of layer 5 projection neurons does not alter the density of NPY+ interneurons in the primary somatosensory cortex in the adult brain, but affects their soma morphology

Figure 3.20. Chronic silencing of layer 5 projection neurons rearranges the laminar distribution of cortical NPY+ interneurons in the adult primary motor cortex

Figure 3.21. Chronic silencing of subsets of layer 5 neurons leaves the laminar positioning of cortical NPY+ interneurons in the adult primary somatosensory cortex intact

Figure 3.22. Chronic silencing of Rbp4-Cre+ layer 5 projection neurons has no long-term impact on the density of NPY+ neurons in the striatum at 12 weeks of age

Figure 3.23. The density and developmental trajectories of parvalbumin interneurons are not affected by the chronic silencing of the mossy fibre pathway

Figure 3.24. Genetic silencing of granule cells does not have a long-term effect on parvalbumin neurons and the perineuronal nets within the hippocampus

Figure 3.25. From development to adulthood, the density of parvalbumin interneurons in the CA3 area of the hippocampus decreases considerably both in the ctrl and *Snap25* cKO mice

Figure 3.26. Neuropeptide-Y neurons in distinct regions of the hippocampus exhibit different responses to the deletion of Snap25 from the granule cells of the dentate gyrus

Figure 3.27. Genetic silencing of the mossy fibre pathway exclusively affects SST+ interneurons that are not encapsulated by perineuronal nets

Chapter 4 Results

Figure 4.1. Schematic drawing showing the structure of Chapter 4

Figure 4.2. a. Selected cortical regions of interest in *Drd1a-Cre;Ai14;Snap25$^{fl/fl}$* mice

Figure 4.2. b. Selected subcortical regions of interest in *Drd1a-Cre;Ai14;Snap25$^{fl/fl}$* mice

Figure 4.3. c. The selective innervation of the higher-order thalamic nuclei is retained in the Drd1a-Cre-silenced mice

Figure 4.3. d. Comparisons of the chosen cortical and subcortical regions of interest between layer 5 and layer 6-silenced mice

Figure 4.3. e. Overview of the cortical and subcortical regions of interest selected in layer 5 and layer 6-silenced mice.

Figure 4.4. tdTomato+ fibres are present in the stratum lacunosum-moleculare of CA1, CA2, and CA3 in the Drd1a-Cre;Ai14;Snap25fl/fl mice

Figure 4.5. *Drd1a-Cre;Snap25$^{fl/fl}$* projection neurons form VGluT1-positive synapses in the caudoputamen

Figure 4.6. Thalamus-projecting *Drd1a-Cre;Ai14;Snap25$^{fl/fl}$* neurons make excitatory synapses in the thalamic reticular nucleus

Figure 4.7. VGluT1-positive synapses are formed by *Drd1a-Cre;Ai14;Snap25$^{fl/fl}$* projection neurons in the external segment of the globus pallidus

Figure 4.8. Comparison of the excitatory synapses formed by *Drd1a-Cre;Ai14;Snap25$^{fl/fl}$* neurons in the selected subcortical regions of interest

Figure 4.9. Regional variations in the density of Drd1a-Cre+ neurons

Figure 4.10. The laminar positioning of parvalbumin interneurons following the chronic silencing of a subset of layer 6 projection neurons is altered in layer 5 of S1 at P21

Figure 4.11. Loss of AP-dependent neurotransmitter release from a subset of layer 6 pyramidal neurons leads to decreased soma size in striatal parvalbumin interneurons

Figure 4.12. GABA-B R1 receptors are significantly reduced in layer 5 of the primary motor and somatosensory cortices following the genetic silencing of layer 6 projection neurons

Figure 4.13. Loss of AP-dependent neurotransmitter release from cortical layer 6 neurons leaves the ionotropic GABA-A δ receptors in layer 6 intact during development

Figure 4.14. Neuropeptide-Y interneurons within distinct cortical regions demonstrate different susceptibility to the genetic silencing of Drd1a-Cre+ neurons

Figure 4.15. Striatal neuropeptide-Y interneurons react to the chronic silencing of layer 6 projection neurons during development

Figure 4.16. Silencing a subset of layer 6 projection neurons selectively affects neuropeptide-Y interneurons in the dentate gyrus, while leaving the CA1 and CA3 intact

Figure 4.17. Differential impact of the chronic silencing of a subset of layer 6 projection neurons on somatostatin and calretinin-expressing interneurons in the caudoputamen during development

Figure 4.18. Hippocampal calretinin and somatostatin-positive neurons in CA1 demonstrate notable changes in their density after silencing Drd1a-Cre+ neurons

Figure 4.19. Brain-wide mapping of the long-range projections of Drd1a-Cre+ corticothalamic neurons, as well as the distribution of parvalbumin interneurons and the perineuronal nets in the adult *Drd1a-Cre;Ai14;Snap25*$^{fl/fl}$ mice

Figure 4.20. Chronic silencing of subsets of layer 6 neurons does not cause cell death in Drd1a-Cre+ neurons, which exhibit regional variations across distinct fields of the primary somatosensory cortex

Figure 4.21. The genetic silencing of Drd1a-Cre+ neurons selectively affects the distribution of layer 5 PV+ interneurons in the primary motor cortex

Figure 4.22. Different subfields of S1 display changes in perineuronal net density in layer 4 following *Snap25* deletion from a subset of layer 6 neurons

Figure 4.23. Neuropeptide-Y interneurons in the anterior cingulate and secondary motor cortex are not dependent on AP-dependent neurotransmitter release from Drd1a-Cre+ neurons in the adult brain

Figure 4.24. Laminar maturation of neuropeptide-Y interneurons in layer 2/3 of the primary motor and somatosensory cortices is different in the cKO mice

Figure 4.25. Loss of AP-dependent neurotransmitter release from layer 6 neurons differentially affects the soma size of NPY+ interneurons in layer 2/3 and layer 6a in the primary motor and somatosensory cortex

Figure 4.26. Silencing Drd1a-Cre+ neurons does not lead to long-term changes in the soma area of striatal parvalbumin interneurons

Figure 4.27. The developmental trajectory of parvalbumin interneurons indicates notable changes in the TRN, both in control and layer 6-silenced mice, from development to adulthood

Figure 4.28. The density and soma characteristics of neuropeptide-Y interneurons in the adult striatum do not exhibit long-term changes in the cKO mice.

Figure 4.29. Silencing Drd1a-Cre+ neurons had no long-term effect on the density of neuropeptide-Y interneurons in the hippocampal regions

Figure 4.30. Somatostatin interneurons in the CA3 are enwrapped by perineuronal nets, and the

number of perineuronal net-bearing somatostatin neurons increases when layer 6 projection neurons are persistently silenced

Chapter 5 Results

Figure 5.1. Schematic of the PI3K/AKT/mTOR pathway along with the intracellular events it regulates

Figure 5.2. Schematic illustration of the breeding of the *Drd1a-Cre;Ai9,Pten*$^{fl/fl}$ conditional knockout mice

Figure 5.3. Schematic illustration of the central research questions addressed in Chapter 5

Figure 5.4. Elevated levels of phosphorylated ribosomal protein S6 in layer 6b of the *Pten* cKO mice indicate hyperactive mTOR signalling

Figure 5.5. Parvalbumin-positive interneurons comprise a subgroup of Drd1a-Cre-negative phospho-S6-expressing neurons in cortical layer 6

Figure 5.6. Conditional deletion of *Pten* from Drd1a-Cre+ neurons results in increased levels of c-Fos expression both in the supra-and infragranular layers

Figure 5.7. Differential activation of two activity-dependent immediate early genes, i.e., c-Fos and Npas4

Figure 5.8. Upregulation of Npas4 in the *Pten* cKO mice supports the transcriptional activation of immediate early genes and increased neuronal activation following the deletion of *Pten* from Dr1a-Cre+ neurons

Figure 5.9 Postnatal deletion of Pten from Drd1a-Cre+ projection neurons leads to neuronal hypertrophy and enlarged cell bodies in the adult cKO mice

Figure 5.10. The long-range axonal projections of Drd1a-Cre+ neurons are not misrouted in the *Pten* cKO mice

Figure 5.11. Without changing the overall amount of Drd1a-Cre+ neurons, the *Pten* cKO animals exhibit a change in the laminar distribution of these neurons in layer 6b of M1

Figure 5.12. Chronic deletion of *Pten* modifies the laminar distribution of Drd1a-Cre+ neurons in layer 6b in distinct subregions of S1, without affecting their total cell number

Figure 5.13. Mapping the brain-wide distribution of parvalbumin neurons and the perineuronal nets following the loss of *Pten* from Drd1a-Cre+ neurons

Figure 5.14. Deleting *Pten* from Drd1a-Cre+ neurons leads to enlarged soma size in parvalbumin interneurons in M1 in *Pten* cKO mice

Figure 5.15. Permanent loss of *Pten* from Drd1a-Cre+ neurons selectively affects the laminar distribution of PV+ VVA+ neurons and PNNs in layer 2/3 of the adult primary motor cortex

Figure 5.16. Parvalbumin interneurons in the lower limb of the primary somatosensory cortex remain unaffected by the loss of *Pten* from Drd1a-Cre+ projection neurons

Figure 5.17. *Pten* deletion from Drd1a-Cre+ neurons does not alter the soma shape of parvalbumin interneurons in S1LL

Figure 5.18. Layer 5 in S1UL/S1BF indicates a significant increase in PV+ VVA- density following the ablation of *Pten* from Drd1a-Cre+ projection neurons

Figure 5.19. The soma shape of striatal parvalbumin interneurons is significantly altered following the deletion of *Pten* from Drd1a-Cre+ neurons

Figure 5.20. Slight increase in the soma area of neuropeptide-Y interneuron in the secondary motor cortex following *Pten* deletion from Drd1a-Cre+ neurons

Figure 5.21. Deleting *Pten* from a subset of layer 6 projection neurons appears to result in somatic overgrowth in NPY+ interneurons in different areas of the cortex

Figure 5.22. Layer 2/3 and layer 6a neuropeptide-Y interneurons have enlarged somata and perimeter in the primary somatosensory cortex of *Pten* cKO mice

Figure 5.23. Conditional deletion of Pten from Drd1a-Cre+ projection neurons did not impact the overall density of NPY+ interneurons in the striatum and hippocampal areas

Figure 5.24. Loss of *Pten* from subsets of layer 6 neurons alters the distribution of somatostatin interneurons in layers 5 and 6b of the primary motor cortex

Figure 5.25. The soma area and shape of somatostatin interneurons are differentially affected by the long-term loss of *Pten* in the primary motor and somatosensory cortices

Figure 5.26. Drd1a-Cre+ neurons do not regulate the density and soma morphology of somatostatin interneurons in the adult caudoputamen

Figure 5.27. Perineuronal nets surround subsets of somatostatin interneurons in the hippocampus, but the loss of *Pten* from Drd1a-Cre+ neurons does not alter their density

Figure 5.28. Loss of *Pten* from Drd1a-Cre+ neurons has a region-specific influence on the soma morphology of somatostatin interneurons in the CA1

Figure 5.29. Summary of the anatomical, physiological, and behavioural phenotypes detected in our *Pten* cKO model

Figure 5.30. Schematic summarising the results of *Pten* deletion from Drd1a-Cre+ neurons on cortical and subcortical parvalbumin neurons in the adult brain

Figure 5.31. Overview of the results on somatostatin interneurons

Figure 5.32. Overview of the results on neuropeptide-Y interneurons

Chapter 6 Discussion

Figure 6.1. Overview of the developmental findings on the chronic silencing of Rbp4-Cre+ neurons on parvalbumin interneurons

Figure 6.2. Overview of the adult findings on the chronic silencing of Rbp4-Cre+ neurons on parvalbumin interneurons

Figure 6.3. Overview of the adult findings on the chronic silencing of Rbp4-Cre+ neurons on neuropeptide-Y interneurons

Figure 6.4. Overview of the developmental and adult findings on the chronic manipulation of the hippocampal mossy fibre pathway

Figure 6.5. Summary of the developmental results on the chronic ablation of *Snap25* from Drd1a-Cre+ neurons at P21

Figure 6.6. Overview of the adult findings on the effects of the chronic deletion of *Snap25* from Drd1a-Cre+ neurons on parvalbumin interneurons and the perineuronal nets

Figure 6.7. Overview of the adult findings on the effects of the chronic deletion of *Snap25* from Drd1a-Cre+ neurons on somatostatin and neuropeptide-Y interneurons

Figure 6.8. Overview of the adult findings on the effects of the chronic deletion of *Snap25* from Drd1a-Cre+ neurons on neuropeptide-Y interneurons in the striatum and the hippocampus

Figure 6.9. Overview of the results of the removal of *Pten* from Drd1a-Cre+ neurons on parvalbumin interneurons and perineuronal nets

Figure 6.10. Overview of the results of the removal of *Pten* from Drd1a-Cre+ neurons on somatostatin interneurons

Figure 6.11. Overview of the results of the removal of *Pten* from Drd1a-Cre+ neurons on neuropeptide-Y interneurons

List of Tables

Chapter 1 Introduction

Table 1.1. Summary of the molecular functions, tissue-specific expression (human), and associated disorders of syntaxin-1A.

Table 1.2. Overview of the main characteristics of animal models with specific SNARE protein deletions

Chapter 2 Methods

Table 2.1. Overview of the cell types, time points, and number of brains analysed for each Results chapter

Table 2.2. Overview of the cell types, time points, and number of sections analysed for each Results chapter

Table 2.3. Summary of the regions of interest selected for parvalbumin interneurons and *Vicia villosa* agglutinin cells

Table 2.4. Summary of the regions of interest selected for neuropeptide-Y and somatostatin interneurons

Table 2.5. Summary of the regions of interest selected for Drd1a-Cre+ projection neurons

Table 2.6. Summary of the different types of analyses conducted throughout the DPhil thesis

Table 2.7. PCR mix for Snap25 and Cre genotyping per reaction

Table 2.8. Forward and reverse primers for Snap25 and Cre genotyping

Table 2.9. PCR cycling conditions for Snap25 and Cre genotyping

Table 2.10. Overview of the primary and secondary antibodies used for immunohistochemistry experiments

Table 2.11. Summary of the main image acquisition parameters (ZEISS LSM710 confocal microscope)

Table 2.12. Overview of the cell detection parameters used to quantify each interneuron subtype

Table 2.13. Example of cell quantification of parvalbumin interneurons in the primary motor cortex

Table 2.14. Example of the quantification of the laminar density of parvalbumin interneurons across the different layers of the primary motor cortex

Table 2.15. Example of soma morphometric measurements of somatostatin interneurons in the striatum

Table 2.16. An overview of the datasets and statistical tests conducted

Chapter 5 Results

Table 5.1. Conditional deletion of *Pten* from select cell populations

Table 5.2. Half-lives of Pten mRNA and protein

Table 5.3. Overview of cortical and subcortical ROIs selected for distinct subtypes of interneurons investigated in Chapter 5

Table 5.4. Overview of cortical and subcortical ROIs selected for NPY+ interneurons.

List of Abbreviations

A

A1 ..... Primary auditory cortex

ACAd ..... Anterior cingulate area, dorsal part

ACAv..... Anterior cingulate area, ventral part

AEP..... Anterior entopeduncular area

AP..... Action potential

APN ..... Anterior pretectal nucleus

ASD..... Autism spectrum disorder

AUDd..... Auditory dorsal area

AUDv..... Auditory ventral area

B

BAC..... Bacterial Artificial Chromosome

Bdr..... Blind-drunk mouse

BF..... Brightfield

bHLH..... Basix helix-loop-helix

BLA..... Basolateral amygdala

C

CB..... Calbindin

CCN..... Cortico-collicular neurons

cDKO ..... Conditional double-knockout

CF ..... Confocal fusion

CGE..... Caudal ganglionic eminence

cKO ..... Conditional knockout

CL ..... Central lateral thalamic nucleus

CNS..... Central nervous system

CP ..... Cortical plate

CPu ..... Caudoputamen

CR..... Cajal-Retzius cells

CR..... Calretinin

CTGF ..... Connective Tissue Growth Factor

Cy5..... Cyanine 5

D

D1..... Dopamine 1 receptor

D2..... Dopamine 2 receptor

DAPI ..... 4,6-diamidine-2-phenylindole dihydrochloride

DNB ..... Diagonal band nucleus

dNTPs..... Deoxyribonucleotide triphosphate

DRD1A ..... Dopamine receptor D1A

DS..... Delayed-spiking (interneurons)

E

E/I..... Excitation/Inhibition

E11 ..... Embryonic Day 11

ECM ..... Extracellular matrix

ECT ..... Ectorhinal area

EDTA..... Ethylenediaminetetraacetic acid

EGF ..... Epidermal growth factor

ENTI ..... Entorhinal area

EPSCs..... Excitatory postsynaptic currents

ES ..... Embryonic stem cells

F

FS ..... Fast-spiking (interneurons)

G

GABA..... Gamma-aminobutyric acid

GABA-B R1 ..... GABA Type-B Receptor Subunit 1

GD ..... Gestational day

GPCRs..... G protein-coupled receptors

GPe..... Globus pallidus, external segment

Gsh2 ..... Genomic screened homeobox 2

H

HC ..... Histochemistry

I

i.c. ..... Internal capsule

i.p. ..... Intraperitoneal injection

IHC..... Immunohistochemistry

IL ..... Infralimbic area

IT ..... Intratelencephalic

IZ ..... Intermediate zone

K

KO ..... Knockout

L

LD..... Lateral dorsal nucleus

LGE ..... Lateral ganglionic eminence

Lhx6 ..... Lim homeobox 6

LP ..... Lateral posterior thalamic nucleus

LOF ..... Loss-of-function

L-VSCCs..... L-type voltage-sensitive calcium channels

M

M1 ..... Primary motor area

M2 ..... Secondary motor area

MBP ..... Myelin basic protein

MD ..... Mediodorsal thalamic nucleus

MGE ..... Medial ganglionic eminence

mGLUR ..... Metabotropic glutamatergic receptor signalling

Mgp ..... Matric Gla protein

mPFC ..... Medial prefrontal cortex

MS ..... Medial septal nucleus

mTOR ..... Mammalian target of rapamycin

MZ ..... Marginal zone

N

NCAM ..... Neural cell adhesion molecules

Nk6x.2 ..... Nk6 homeobox 2

NMDA ..... N-methyl-d-aspartic acid

NMJ ..... Neuromuscular junction

NPY ..... Neuropeptide-Y

NSF ..... N-ethylmaleimide sensitive factor

O

OB ..... Olfactory bulb

P

P14 ..... Postnatal day 14

PBS ..... Phosphate-buffered saline

PBSA ..... Phosphate-buffered saline with sodium azide

PCR ..... Polymerase Chain Reaction

PDK1 ..... Phosphoinositide-dependent protein kinase-1

PERI ..... Perirhinal area

PFA ..... Paraformaldehyde

PFC ..... Prefrontal cortex

PH ..... Pleckstrin-homology

PI3K ..... Phosphatidylinositol-3-OH kinase

PIP_2..... Phosphatidylinositol (3,4)-bisphosphate

PIP_3..... Phosphatidylinositol (3,4,5)-trisphosphate

PL ..... Prelimbic area

PNS ..... Peripheral nervous system

PO..... Posterior nucleus of the thalamus

PP ..... Preplate

PRAS40 ..... 40 kDa proline-rich AKT substrate

$pS6^{235/236}$ ..... ribosomal protein S6 phosphorylated at serine residues 235 and 236

PT ..... Pyramidal tract

PTEN..... Phosphatase and tensin homologue deleted on chromosome 10

PTLp..... Posterior parietal association area

PV..... Parvalbumin

R

Rbp4 ..... Retinol binding protein 4

Rheb..... Ras enriched in brain

Rgs12..... Regulator of G-protein signalling 12 gene

RMS ..... Rostral migratory stream

RMTW ..... Rostromedial telencephalic wall

ROI..... Regions of interest

RSNP ..... Regular spiking nonpyramidal

RSPd..... Retrosplenial area, dorsal part

RSPv..... Retrosplenial area, ventral part

RT..... Room temperature

RTKs..... Receptor tyrosine kinases

S

S6 ..... Ribosomal protein S6

S6K1..... Ribosomal protein S6 kinase

S1 ..... Primary somatosensory cortex

S1bf ..... Primary somatosensory cortex barrel field

SC ..... Superior colliculus

SDS ..... Sodium dodecyl sulfate

Ser473..... Serine 473

Sla1..... Scr-like adaptor

s.l.m. ..... Stratum lacunosum moleculare

SM proteins..... Sec1/Munc18-like proteins

Snap25..... Synaptosomal-associated protein of 25 kDA

SNAPs..... Soluble NSF-attachment proteins

SNARE..... Soluble NSF attachment receptor proteins

SP ..... Subplate

SSN ..... Spiny stellate neuron

SST..... Somatostatin

SSt..... Supplemental somatosensory area

SVZ..... Subventricular zone

T

tdTomato..... Tandem-dimer tomato

TEa ..... Temporal association area

Thr308..... Threonine 308

TRN ..... Thalamic reticular nucleus

TSC..... Tuberous sclerosis complex

U

UV ..... Ultraviolet

V

V1 ..... Primary visual area

VAL ..... Ventral anterior lateral nucleus

VAMP ..... Vesicle-associated membrane protein

VB..... Ventrobasal

VGCCs ..... Voltage-gated calcium channels

VGluT1 ..... Vesicular glutamate transporter 1

VGluT2 ..... Vesicular glutamate transporter 2

VIP ..... Vasoactive intestinal peptide

VISal..... Anterolateral visual area

VISam ..... Anteromedial visual area

VM..... Ventral medial nucleus

VPm..... Ventral posteromedial nucleus

VVA..... *Vicia villosa* agglutinin

VZ..... Ventricular zone

W

WFA..... *Wisteria floribunda* agglutinin

WGA-HRP..... Wheat germ lectin horseradish-peroxidase complex

WM ..... White matter

Z

ZI ..... Zona incerta

Table of Contents

Chapter 1 Introduction 1

1.1. The laminar organisation of the neocortex 1

1.1.1. The cytoarchitecture of the cerebral cortex 1

1.1.2. Infragranular pyramidal neurons: why are they important? 1

1.1.3. Neural heterogeneity of cortical layer 6 3

1.1.3.1. Layer 6b and the transient lamina, the subplate 3

1.1.3.2. Which cell types reside in neocortical layer 6? 4

1.1.3.3. What is the GABAergic and glutamatergic neuron ratio in the cerebral cortex? 7

1.2. Pyramidal neurons instruct the development, density, and distribution of GABAergic interneurons 9

1.2.1. Birthdates, origins, and migration of pyramidal neurons and cortical GABAergic interneurons 9

1.2.2. Fate-changing the identity of pyramidal neurons 20

1.2.3. Activity-dependent mechanisms orchestrating the assembly of cortical circuits 21

1.2.4. Transient circuits involving glutamatergic and GABAergic neurons during development 22

1.2.5. The role of pyramidal neurons in instructing interneuron development 26

1.2.6. Excitatory inputs and glutamatergic transmission modulate interneuron development 28

1.3. Synaptic transmission 30

1.3.1. SNARE proteins and their role in intracellular membrane fusion 30

1.3.2. Molecular machinery of Ca^{2+}-evoked synaptic vesicle release 31

1.3.3. Knockout models of SNARE proteins with special attention to Snap25 33

1.3.3.1. Synaptobrevins/VAMPs 33

1.3.3.2. Syntaxins 33

1.3.3.3. Munc18-1 and Munc13-1 35

1.3.3.4. Synaptosomal-associated protein of 25 kDa 36

1.4. Aims of the thesis 46

1.4.1. Aims and Objectives of Chapter 3 47

1.4.2. Aims and Objectives of Chapter 4 48

1.4.3. Aims and Objectives of Chapter 5 49

Chapter 2 Methods 52

2.1. Breeding and maintenance of transgenic mice 52

2.2. Cell-type specific deletion of *Snap25* from subsets of deep-layer glutamatergic projection neurons 52

2.3. Perfusion fixation and vibratome sectioning 59

2.4. Genotyping 59

2.4.1. DNA extraction 59

2.4.2. Polymerase Chain Reaction (PCR) 59

2.4.3. Gel electrophoresis and gel imaging 61

2.7. Histology 62

2.7.1. General immunohistochemical staining protocol for GABAergic interneurons and GABA receptors 62

2.7.2. Double-labelling parvalbumin interneurons and the perineuronal nets 62

2.8. Image acquisition 66

2.8.1. Epifluorescence imaging 66

2.8.2. Confocal laser-scanning microscopy 70

2.8.2.1. Confocal imaging of perineuronal nets – Optimising the pinhole diameter for *Vicia villosa* agglutinin cells 70

2.8.3. Spinning disk confocal imaging 73

2.9. Image analysis 75

2.9.1. Cell quantification of GABAergic interneurons 75

2.9.2. Cell quantification of VVA+ cells 86

2.9.3. Quantification of GABA receptors and Drd1a-Cre+ neurons 87

2.10. Morphometric analysis of GABAergic interneurons 89

2.10.1. The relationship between roundness and circularity – why to measure both? 89

2.11. Statistics 90

Chapter 3 Results 92

Chronic silencing of glutamatergic layer 5 cortical projection neurons 92

3.1 Aims and Objectives 92

3.2 The effects of genetically silencing layer 5 projection neurons on parvalbumin neurons in the juvenile brain 93

3.2.1 The *Rbp4-Cre;Ai14;Snap25$^{fl/fl}$* mice genetically label two types of cells – cortical layer 5 projection neurons and hippocampal granule cells 93

3.2.2 Genetically 'silenced' Rbp4-Cre+ neurons in layer 5 exhibit similar corticothalamic and corticofugal projections as Rbp4-Cre+ neurons 96

3.2.3 Conditional deletion of Snap25 from layer 5 projection neurons does not interfere with the development of PV neurons 98

3.2.4 Loss of AP-dependent neurotransmitter release from layer 5 projection neurons leaves subcortical PV neurons intact during the early stages of development 100

3.2.5 The absence of AP-dependent neurotransmitter release from Rbp4-Cre+ layer 5 pyramidal neurons causes alterations in the morphology of striatal PV+ neurons at P21 105

3.2.6 Striatal PV interneurons in layer 5-silenced brains show an altered developmental trajectory of soma features throughout postnatal development 106

3.2.7 Genetically silencing subsets of layer 5 projection neurons has no long-term impact on the morphology of striatal interneurons in the adult brain 108

3.2.8 VVA is not a suitable non-activity-dependent marker during development 110

3.2.8.1 VVA produces non-specific staining in the postnatal murine cortex 110

3.2.8.2. VVA staining within the hippocampus and subcortical areas leads to inadequate perineuronal net detection at different developmental stages 112

3.2.8.3. *Vicia villosa* agglutinin is an efficient marker for the visualisation of perineuronal nets in the adult brain 113

3.2.9 The absence of AP-dependent neurotransmitter release from Rbp4-Cre+ layer 5 does not alter the laminar organisation of PV interneurons in the juvenile brain 116

3.3 The effects of chronically silencing layer 5 projection neurons on parvalbumin neurons in the adult brain 120

3.3.1. Chronic silencing of L5 projection neurons does not influence the density of PV neurons in the adult cortex but disrupts the correlation between PV interneurons and the perineuronal net in M1 120

3.3.2. Chronic silencing of subsets of layer 5 projection neurons has a delayed effect on the laminar organisation of PV interneurons and the perineuronal nets 125

3.3.3. The correlation between PV and the perineuronal net is cortical layer-dependent 129

3.3.4. Silencing layer 5 does not lead to long-term changes in the density of subcortical PV neurons in the projection regions of layer 5 131

3.4. The effects of chronically silencing layer 5 projection neurons on neuropeptide-Y interneurons in the adult brain 135

3.4.1. Loss of AP-dependent neurotransmitter release from layer 5 projection neurons affects the density of NPY-expressing neurons in the primary and secondary motor cortices 136

3.4.2. Silencing layer 5 projection neurons alters the density of NPY+ interneurons in the primary motor cortex 139

3.4.3. The conditional deletion of *Snap25* from subsets of layer 5 projection neurons affects the laminar distribution of NPY+ interneurons in L1 and L2/3 of the primary motor cortex 142

3.4.4. The soma shape of NPY+ neurons in layer 5 of the somatosensory cortex is altered by the chronic silencing of layer 5 projection neurons, but their laminar positioning remains unchanged 142

3.4.5. The density of striatal NPY+ neurons remains unchanged following the deletion of Snap25 from Rbp4-Cre+ neurons 146

3.6. The effects of genetically silencing the hippocampal mossy fibre pathway on GABAergic interneurons 149

3.6.1. Genetic silencing of dentate gyrus granule cells does not affect the density of parvalbumin interneurons during development 150

3.6.2. The conditional silencing of hippocampal granule cells does not impact perineuronal nets in the adult hippocampus 153

3.6.3. The density of parvalbumin interneurons significantly declines in the CA3 of the hippocampus from development to adulthood, both under normal and chronic conditions 155

3.6.4. Chronic silencing of the hippocampal mossy fibre pathway does not uniformly affect the density of neuropeptide-Y interneurons within the hippocampus 157

3.6.5. The genetic silencing of hippocampal granule cells alters the density of somatostatin neurons in the dentate gyrus 158

3.6.6. Perineuronal nets surround SST neurons in the hippocampus and are not exclusively present around PV interneurons 159

3.6.7. Somatostatin neurons with perineuronal nets are unaffected by the genetic silencing of the mossy fibre pathway 160

3.7. Discussion 163

3.7.1. The effects of chronically silencing layer 5 projection neurons on parvalbumin interneurons in the *juvenile* brain 163

3.7.2. The effects of chronically silencing layer 5 projection neurons on distinct subtypes of GABAergic interneurons in the adult brain 166

3.7.3. The effects of manipulating the hippocampal mossy fibre pathway on different subtypes of GABAergic interneurons in the adult brain 168

3.8. OVERVIEW OF RESULTS 170

3.9. Summary 175

Chapter 4 Results 176

Chronic silencing of a subgroup of glutamatergic layer 6 cortical projection neurons 176

4.1. Introduction 176

4.2. Aims and Objectives 176

4.3. The effects of chronically silencing a subset of layer 6 projection neurons on GABAergic neurons in the juvenile brain 178

4.3.1. Targeting layer 6b neurons (Drd1a-Cre lines) 178

4.3.2. Selecting my regions of interest 179

4.3.3. *Drd1a-Cre+ tdTomato+* fibres are present in the stratum lacunosum-moleculare of CA1, CA2, and CA3 186

4.3.4. *Drd1a-Cre;Ai14;Snap25*$^{fl/fl}$ neurons form excitatory synapses in subregions of the basal ganglia and the thalamic reticular nucleus 189

4.3.5. Regional variations in the density of *Drd1a-Cre+;Ai14;Snap25*$^{fl/fl}$ neurons 195

4.3.6. The effects of silencing Drd1a-Cre+ neurons on cortical parvalbumin interneurons during development 197

4.3.6.1. Genetically silencing Drd1a-Cre+ neurons reorganises the laminar distribution of parvalbumin neurons in S1 at P21 197

4.3.7. The effects of silencing Drd1a-Cre+ neurons on subcortical parvalbumin neurons during development 199

4.3.7.1. The soma morphology of striatal parvalbumin interneurons is altered at P21, without corresponding changes in their density 199

4.3.8. The effects of silencing Drd1a-Cre+ neurons on GABA-$_B$ receptors in the juvenile cortex 201

4.3.8.1. The density of GABA-$_B$ receptors decreased in the primary motor and somatosensory regions in the layer 6-silenced mice during development 201

4.3.9. The effects of silencing Drd1a-Cre+ neurons on GABA-$_A$ receptors in the juvenile cortex 205

4.3.9.1. Ionotropic GABA-$_A$ receptors in the juvenile neocortex remained unaffected by the chronic abolition of evoked vesicle release from Drd1a-Ce+ neurons 205

4.3.10. The effects of silencing Drd1a-Cre+ neurons on cortical neuropeptide-Y interneurons during development 208

4.3.10.1. Neuropeptide-Y interneurons significantly increased in layer 6b of the primary somatosensory cortex in the Snap25 cKO mice during development 208

4.3.11. The effects of silencing Drd1a-Cre+ neurons on subcortical neuropeptide-Y neurons during development 211

4.3.11.1. Neuropeptide-Y interneurons significantly increased in layer 6b of the primary somatosensory cortex in the Snap25 cKO mice during development 211

4.3.11.2. Upregulation of NPY+ interneuron expression in the dentate gyrus at P21 following the conditional deletion of Snap25 from Drd1a-Cre+ neurons 213

4.3.12. The effects of silencing Drd1a-Cre+ neurons on somatostatin and calretinin-positive neurons during development 216

4.3.12.1. Chronic silencing of glutamatergic layer 6 projection neurons selectively affects the soma size of calretinin-positive interneurons in the striatum 216

4.3.12.2. Hippocampal calretinin and somatostatin-positive neurons exhibit significant alterations in their density upon the abolition of evoked vesicle release from layer 6 neurons 206

4.4. The effects of chronically silencing a subset of layer 6 projection neurons on GABAergic interneurons in the adult brain 220

4.4.1. Mapping the brain-wide distribution of Drd1a-Cre+ neurons, PV interneurons, and the perineuronal nets in the *Snap25* cKO mice 220

4.4.2. Regional and laminar differences in the number of Drd1a-Cre+ projection neurons in different subdivisions of the primary somatosensory cortex 224

4.4.3. The effects of silencing Drd1a-Cre+ neurons on parvalbumin interneurons and the perineuronal nets in the adult neocortex 227

4.4.3.1. The genetic silencing of Drd1a-Cre+ neurons alters the density of those parvalbumin interneurons which are surrounded by perineuronal nets in layer 5 of M1 227

4.4.3.2. Distinct subdivisions of the adult S1 exhibit changes in perineuronal net density exclusively in layer 4 upon the chronic silencing of layer 6 neurons 230

4.4.4. The effects of silencing Drd1a-Cre+ neurons on neuropeptide-Y interneurons in the adult neocortex 235

4.4.4.1. The genetic silencing of Drd1a-Cre+ neurons does not have a long-term effect on neuropeptide-Y neurons in the adult prefrontal and secondary motor cortex 235

4.4.4.2. Neuropeptide-Y interneurons display density and laminar changes in layer 2/3 of the primary motor and somatosensory cortices from development to adulthood 238

4.4.4.3. Conditional deletion of *Snap25* from Drd1a-Cre+ neurons leads to morphological alterations in the soma area of NPY+ neurons in layer 2/3 of the adult primary motor cortex 241

4.4.5. The effects of silencing Drd1a-Cre+ neurons on subcortical parvalbumin neurons in the adult brain 244

4.4.5.1. Conditional deletion of *Snap25* from a subset of Drd1a-Cre+ neurons has no long-term influence on the density and morphology of striatal PV interneurons 244

4.4.5.2. The density of parvalbumin neurons substantially decreases in the thalamic reticular nucleus both in control and *Snap25* cKO mice from development to adulthood 247

4.4.6. The effects of silencing Drd1a-Cre+ neurons on NPY+ neurons in the adult striatum and hippocampus 249

4.4.6.1. Silencing Drd1a-Cre+ neurons does not cause long-term alterations in the density and soma parameters of neuropeptide-Y interneurons in the adult striatum 249

4.4.6.2. The density of neuropeptide-Y interneurons in the adult hippocampal regions is not altered by silencing Drd1a-Cre+ neurons 251

4.4.7. The effects of silencing Drd1a-Cre+ neurons on somatostatin interneurons in adult striatum and hippocampus 253

4.4.7.1. Somatostatin interneurons in the dentate gyrus are selectively affected by the long-term absence of Ca2+-dependent neurotransmission from Drd1a-Cre+ neurons in the adult hippocampus 253

4.4.8. Discussion 257

Overview 257

Excitatory synaptic contacts formed by *Drd1a-Cre+;Ai14;Snap25$^{fl/fl}$* neurons in subcortical regions 257

Drd1a-Cre+ fibres are present in the stratum lacunosum moleculare of the hippocampus .259

The effects of silencing Drd1a-Cre+ neurons on cortical parvalbumin interneurons during and after development 259

The effects of silencing Drd1a-Cre+ neurons on the perineuronal nets after development ..261

The effects of silencing Drd1a-Cre+ neurons on subcortical parvalbumin neurons during and after development 263

The effects of silencing Drd1a-Cre+ neurons on somatostatin interneurons during and after development 265

The effects of silencing Drd1a-Cre+ neurons on neuropeptide-Y interneurons during and after development 267

Summary of results – PARVALBUMIN INTERNEURONS 270

Summary of results – NEUROPEPTIDE-Y INTERNEURONS 273

Summary of results – SOMATOSTATIN INTERNEURONS 274

Summary of results – GABA RECEPTORS 275

Chapter 5 Results 276

Chronic augmentation of a subset of glutamatergic Drd1a-Cre+ layer 6 projection neurons 276

5.1. Introduction 276

5.1.1. The PI3K/AKT/mTOR pathway 276

5.1.2. Germline mutations of *PTEN* and its associated diseases 279

5.1.3. Conditional deletion of *Pten* from select cell populations 279

5.2. Selective deletion of *Pten* from subsets of cortical Drd1a-Cre+ projection neurons in layer 6 287

5.3. Aims and objectives 292

5.4. Characterisation of the novel *Pten* conditional knockout mice 294

5.4.1. Elevated levels of phospho-S6 in subsets of cortical layer 6b neurons after *Pten* deletion 294

5.4.2. A subset of phospho-S6-expressing Drd1a-Cre-negative neurons are parvalbumin-positive GABAergic interneurons 297

5.4.3. *Pten* cKO mice display immediate early gene activation in cortical regions 300

5.4.4. Activation of Npas4 expression in the *Pten* cKO mice supports increased neuronal activation following *Pten* deletion 301

5.4.5. Constitutive activation of mTOR signalling causes neuronal hypertrophy in *Pten*-deleted Drd1a-Cre+ neurons 305

5.4.6. Loss of *Pten* from subsets of Drd1a-Cre+ projection neurons does not cause ectopic projections or misrouted axonal tracts 308

5.4.7. Selective loss of *Pten* from Drd1a-Cre+ neurons modifies their laminar distribution but does not increase their overall number 311

5.4.8. The total number of Drd1a-Cre+ neurons does not change in different subregions of the primary somatosensory cortex following the loss of Pten 314

5.5. Elucidating the long-term consequences of conditionally deleting *Pten* from Drd1a-Cre+ projection neurons on GABAergic interneurons 319

5.5. CORTICAL PARVALBUMIN INTERNEURONS 320

5.5.1. The brain-wide distribution of parvalbumin interneurons and the perineuronal nets in the *Pten* cKO mice does not differ from control mice 320

5.5.2. *Pten* deletion from Drd1a-Cre+ neurons slightly increases the soma area of PV+ interneurons in M1 without affecting their density 323

5.5.3. The laminar density of PV+ neurons bearing perineuronal nets is significantly increased in layer 2/3 of M1 following the loss of *Pten* from Drd1a-Cre+ neurons 326

5.5.4. Dysregulated mTORC1 signalling in layer 6b neurons does not have a lasting influence on the density and laminar distribution of PV neurons in the lower limb of S1 329

5.5.5. No soma hypertrophy was detected in PV+ interneurons in S1 dense following the deletion of *Pten* from Drd1a-Cre+ neurons 331

5.5.6. PV+ interneurons without perineuronal nets are elevated in layer 5 of the upper limb/barrel cortex of S1 when *Pten* from Drd1a-Cre+ neurons is deleted.....332

5.6. SUBCORTICAL PARVALBUMIN NEURONS..... 335

5.6.1. *Pten* deletion from Drd1a-Cre+ neurons results in altered soma shape in striatal PV+ interneurons.....316

5.7. NEUROPEPTIDE-Y INTERNEURONS – Neocortex..... 338

5.7.1. Loss of *Pten* from Drd1a-Cre+ neurons alters the soma area of NPY+ interneurons in the adult M2 without affecting their density.....338

5.7.2. NPY+ interneurons in M1 and S1 of *Pten*-deleted mice exhibit morphological changes but no laminar changes.....340

5.7.3. NPY+ interneurons in layer 2/3 and layer 6 of S1 exhibit increased soma area and perimeter 342

5.8. NEUROPEPTIDE-Y INTERNEURONS – CPu and hippocampus 344

5.8.1. Subtle changes in soma morphology with no alteration in cell number observed in NPY+ interneurons in the striatum and CA3 region after Pten deletion.....344

5.9. SOMATOSTATIN INTERNEURONS – Neocortex..... 347

5.9.1. Permanent loss of *Pten* from subsets of layer 6 neurons rearranges the laminar distribution of SST+ interneurons in layer 5 and layer 6b of M1 347

5.9.2. Morphological alterations in SST+ interneurons in the adult primary motor and somatosensory cortices after *Pten* deletion 349

5.10. SOMATOSTATIN INTERNEURONS – CPu and hippocampus 353

5.10.1. SST+ interneurons in the striatum are unaffected by the permanent loss of *Pten* from Drd1a-Cre+ neurons.....353

5.10.2. Subsets of SST+ interneurons are enwrapped by perineuronal nets in the hippocampus and remain unaffected by *Pten* deletion from Drd1a-Cre+ neurons 354

5.10.3. Permanent deletion of Pten from Drd1a-Cre+ neurons selectively alters the soma area and shape of CA1 SST+ interneurons.....356

5.11. Discussion..... 358

5.11.1. Generating a novel conditional knockout mouse strain where Pten is selectively deleted from Drd1a-Cre+ projection neurons....358

5.11.2. The long-term effects of *Pten* deletion from Drd1a-Cre+ neurons on parvalbumin interneurons....360

5.11.3. The long-term effects of Pten deletion from Drd1a-Cre+ neurons on somatostatin and neuropeptide-Y interneurons....364

5.12. Conclusion....368

Chapter 6 General Discussion....369

6.1. Chronic manipulation of different subsets of glutamatergic deep-layer cortical projection neurons....369

6.1.1. Overview....369

6.1.2. What is the significance of this DPhil research? Why study how projection neurons affect GABAergic neuron development?....369

6.1.3. The importance of the cell-type-specific targeting of pyramidal neurons....370

6.1.4. What were the *expected* outcomes?....370

6.1.5. What were the *actual* outcomes?....371

6.1.5.1. Chronic deletion of *Snap25* from subsets of Rbp4-Cre+ pyramidal neurons....371

6.1.5.2. What can we learn from 'silencing' Rbp4-Cre+ pyramidal neurons?....372

6.1.5.3. Chronic deletion of *Snap25* from subsets of Drd1a-Cre+ pyramidal neurons....377

6.1.5.4. What can we learn from 'silencing' Drd1a-Cre+ pyramidal neurons?....377

6.1.5.5. Chronic deletion of *Pten* from subsets of Drd1a-Cre+ pyramidal neurons....382

6.1.5.6. What can we learn from 'overexciting' Drd1a-Cre+ pyramidal neurons?....383

6.1.6. Investigating other SNARE proteins beyond Snap25....387

6.1.7. Does synaptic transmission play a role in interneuron development?....388

6.1.8. Clinical implications of research....389

6.1.8.1. The link between SNAP25 and neuropsychiatric diseases....389

6.1.8.2. Deep-layer pyramidal neurons in mental disorders 389

6.1.9. Unresolved questions 390

6.1.9.1. Pyramidal neuron identity and/or activity driving interneuron distribution? 390

6.1.9.2. Loss of cell number or downregulation of protein expression? 390

6.1.9.3. PV regulating PNNs or PNNs regulating PV neurons? 391

6.1.9.4. Why do deep-layer projection neurons have different susceptibility to Snap25 ablation? 391

6.1.10. Limitations of the DPhil thesis 392

6.1.11. Conclusion 392

7.1. References 393

7.2. Appendices .....

Chapter 1 ..... Introduction

1.1. The laminar organisation of the neocortex

1.1.1. The cytoarchitecture of the cerebral cortex

Given the exceptionally varied cell populations in the mammalian neocortex, one must inevitably question how distinct cortical neurons combine to form functional networks**.** That great degree of variation potentially explains the wide array of sensory, motor, and higher-order cognitive functions the cerebral cortex performs. Even though research into the neural underpinnings of many prime cortical functions, such as attention, cognition, memory, and learning, has increased, there is still a lot to discover regarding how distinct subsets of glutamatergic and GABAergic neurons wire together to form these elaborately linked cortical circuits.

1.1.2. Infragranular pyramidal neurons: why are they important?

The synaptic arrangements of infragranular projection neurons demand special focus among the six layers. Cortical layers 5 and 6 receive many afferent inputs from subcortical locations, especially the thalamus (Briggs 2010; Baker et al. 2018; Haley and Maffei 2018). Every single cortical area has a thalamic input and returns projections to the respective thalamic nucleus, and every dorsal thalamic nucleus has a subcortical input and sends projections back to the cerebral cortex (Jones 2009; Deschênes et al. 1998). Although layer 4 is the primary thalamo-recipient layer where thalamocortical axons terminate upon entering (Stratford et al. 1996; Guillery and Sherman 2002; Sherman 2005; Binzegger et al. 2004), thalamocortical afferents also preferentially target layer 6. Besides innervating thalamic relay cells, layer 6 is considered to be in a key laminar position to receive, transmit, and modulate incoming signals from the thalamus. Not only does this cortical layer have long-range projections descending to thalamic nuclei (Bourassa et al. 1995; Zhang and Deschênes 1998; Killackey and Sherman 2003; Viswanathan et al. 2017; Hoerder-Suabedissen et al. 2018), but it

also comprises a variety of corticothalamic and corticocortical pyramidal neurons. They can play a pivotal role in fine-tuning and integrating incoming subcortical inputs, regulating cortical excitability, or maintaining synchrony within the thalamo-cortico-thalamic networks (Jones 1998; Jones 2001; Jones 2009; Contreras and Steriade 1997; Haley and Maffei 2018). The heterogeneity of cortical pyramidal neurons is illustrated in Figure 1.0.

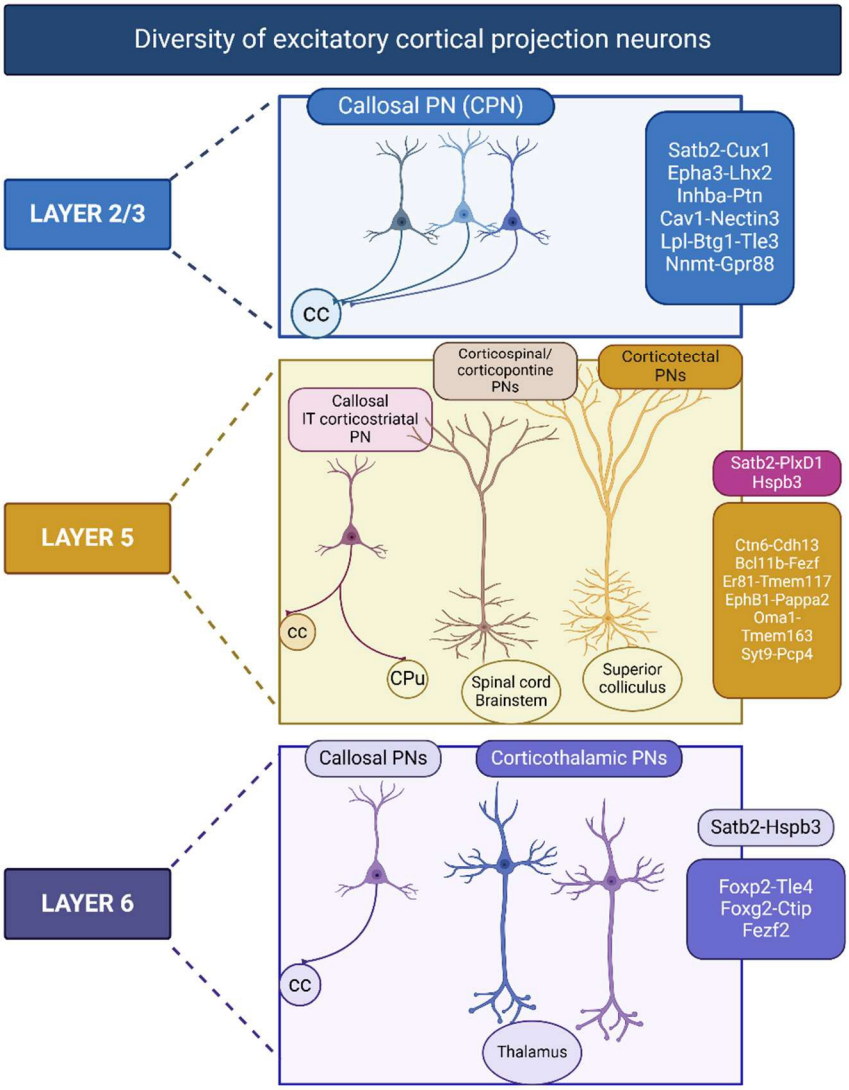


Figure 1.0. Heterogeneity of cortical pyramidal neurons. Commissural neurons reside in layer 2/3, whereas intratelencephalic corticostriatal pyramidal neurons and corticofugal pyramidal neurons are located in layer 5. Layer 6 contains callosal projection neurons as well as thalamic-projecting corticothalamic pyramidal neurons. Each class can be identified by distinct gene profiles expressed by pyramidal neurons (right column). Figure was created with BioRender based on (Lodato and Arlotta 2015).

1.1.3. Neural heterogeneity of cortical layer 6

1.1.3.1. Layer 6b and the transient lamina, the subplate

The murine cortical layer 6 is divided into two sublayers, upper layer 6a and lower layer 6b, that can be distinguished by the differential expression of specific marker genes identified by single-cell transcriptomics (Hoerder-Suabedissen et al. 2009; Chevée et al. 2018; Belgard et al. 2011; Loo et al. 2019; Tasic et al. 2016; Lodato and Arlotta 2015). Both layer 6a and layer 6b, which are transcriptomically two different laminae, harbour different types of corticothalamic neurons. For example, glutamatergic layer 6a cells are identified by the Matrix Gla protein (*L6a-Mgp*) or the Scr-like adaptor (*L6a-Sla*) gene, while glutamatergic layer 6b cells are identified by Serpinb11 (*L6b-Serpinb11*) or the Regulator of G-protein signalling 12 gene (*L6b-Rgs12*) (Tasic et al. 2016). Layer 6b, also known as the subgriseal layer or layer 7 (Bayer & Altman, 1991; (Woo et al. 1991; Marx and Feldmeyer 2013) is generally thought to consist of neurons being the remnants of the subplate (Kostovic and Rakic 1980; Kostovic and Rakic 1990; Wahle et al. 1987; Kanold et al. 2003; Feldmeyer 2023). The subplate is a transient lamina between the white matter and the cortical plate that has a crucial role in brain development, including directing axonal pathfinding, regulating the evolution of cortical inhibition, and creating thalamocortical connections (Rakić 1977; Kostović and Rakić 1980; Judaš et al. 2013; Ghosh et al. 1990; Molnár 1998; Kanold and Shatz 2006; Marx et al. 2017).

The origin of the subplate remains controversial, with debates focused on whether subplate neurons are ancient or newly evolved cell populations that developed to support cortical development in mammals. There are three distinct hypotheses regarding the phylogenetic origin of subplate neurons: the ancestral hypothesis, the derived hypothesis, and the dual origin hypothesis (Montiel et al. 2011; Wang et al. 2011; Judaš et al. 2013). The ancestral hypothesis posits that subplate neurons have an ancient origin, having evolved before the divergence of mammals and sauropsids, and were present in the common ancestor of both groups (Marin-Padilla 1971; Marin-Padilla 1978; Goffinet 1983; Aboitiz et al. 2005). In contrast, the derived hypothesis suggests that the subplate is a

phylogenetically novel structure that emerged in mammals (Aboitiz et al. 2005; Wang et al. 2011). This hypothesis views the subplate as an embryonic adaptation that has no homologue in the reptilian cortex (Kostovic and Rakic 1990; Molnár et al. 2006; Supèr and Uylings 2001). The dual origin hypothesis suggests that subplate neurons comprise both ancestral and newly derived cell populations. According to this theory, the subplate was first developed from the dorsal pallium and then expanded with more cell populations in the synapsids to accommodate the increasing complexity of the brains of mammals (Aboitiz et al. 2005; Wang et al. 2011; Montiel et al. 2011).

Although it has been known that subplate neurons originate from the ventricular zone (VZ) of the cortical neuroepithelium, there is also a population of subplate cells that derive from the rostromedial telencephalic wall (RMTW) (Pedraza et al. 2014). This indicates that subplate neurons have both cortical and extracortical origins, highlighting their developmental diversity.

1.1.3.2. Which cell types reside in neocortical layer 6?

The remarkable heterogeneity within cortical layer 6 can partially be explained by the varied neural populations of layer 6b, including polymorphic, inverted, tripolar, and fusiform multipolar neurons (Kostović and Rakić 1980; Kostović and Rakić 1990; Wahle et al. 1987; Marx and Feldmeyer 2013). Excitatory pyramidal neurons in layer 6 can also be classified based on the targets of their descending projections. According to this classification, 2 major classes of corticothalamic pyramidal neurons are differentiated in layer 6: 1) primary sensory pyramidal cells projecting solely to primary sensory thalamic nuclei, e.g., the somatosensory thalamic relay ventral posteromedial nucleus (VPm) that send collaterals to the thalamic reticular nucleus (TRN); 2) non-primary corticothalamic pyramidal neurons projecting to both sensory and association thalamic nuclei, without innervating the TRN (Bourassa et al. 1995; Fitzpatrick 1996; Jones 2001). A third subtype of pyramidal neurons, namely corticocortical layer 6 pyramidal neurons, does not project to subcortical areas. Claustrum-

projecting pyramidal neurons, which have horizontal projections limited to layers 6 and 5b, constitute the fourth major category of pyramidal layer 6 neurons (Katz 1987; Thomson 2010).

Besides the subgroups of corticothalamic and corticocortical pyramidal cells, layer 6 includes several other non-pyramidal excitatory and inhibitory neurons. Spiny stellate neurons, classified as non-pyramidal excitatory neurons, reside in upper layer 6a with vertical fusiform neurons (Zhang and Deschênes 1998). Horizontal fusiform neurons and bipolar neurons are restricted to layer 6b (Prieto and Winer 1999; Andjelic et al. 2009). It is estimated that approximately 10% of neurons in layer 6 are GABAergic interneurons, though their precise numbers may differ by cortical regions and species (Arzt et al. 2018; Briggs 2010). A sparse number of long-range GABAergic interneurons in the subplate has also been discovered that project to the internal capsule or callosum (Boon et al. 2019). The inhibitory neurons that have been identified thus far based on morphological criteria in layer 6 include multiple types of basket and basket-like cells, double-bouquet cells, chandelier cells, and Martinotti cells (Thomson and Bannister 2003; Prieto et al. 1994; Kumar and Ohana 2008).

Classifying GABAergic interneurons based on the laminar profiles of their axon projections has revealed a mixture of local (*intralaminar*) and translaminar (*interlaminar*)-projecting inhibitory cells in the rat medial prefrontal cortex (mPFC). Of the translaminar-projecting subtypes, layer 1 and layer 2/3-projecting interneurons in layer 6 are Martinotti-like cells, whereas layer 5-projecting interneurons resemble large basket cells and exhibit the electrophysiological phenotype of fast-spiking (FS) interneurons (Ding et al. 2021). The latter subtype, positive for parvalbumin, has also been identified in the visual cortex and receives innervation from corticothalamic layer 6 pyramidal neurons (West et al. 2006). Layer 6a harbours a distinct population of interlaminar-projecting FS parvalbumin (PV) interneurons in the mouse barrel cortex (Frandolig et al. 2019). Driven by inputs from the VPm, these subgroups of PV+ interneurons only exist in the upper lamina of layer 6a (Frandolig et al. 2019). The intralaminar-projecting layer 6 interneurons comprise non-Martinotti FS interneurons and non-FS interneurons (Ding et al. 2021). These basket cell-like GABAergic neurons

inhibit the dendrites of various types of pyramidal neurons in layer 6 (Ding et al. 2021). Although the majority of GABAergic neurons in layer 6 are composed of PV-expressing basket cells, the non-FS subtypes of layer 6 interneurons primarily consist of GABAergic neurons that express somatostatin (SST), neuropeptide-Y (NPY), and vasoactive intestinal peptide (VIP) (Kumar and Ohana 2008; Ding et al. 2021). For a summary of the distinct subtypes of inhibitory neurons in cortical layer 6, please refer to Figure 1.1.

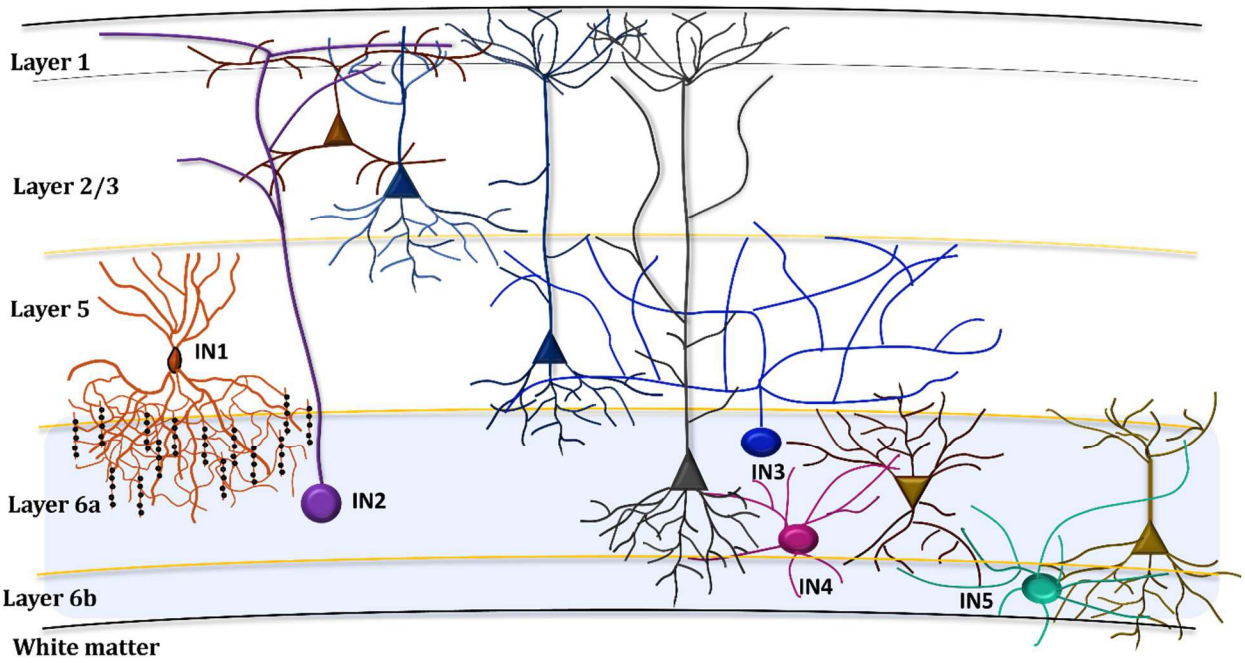


Figure 1.1. Schematic representation of the distinct subtypes of GABAergic interneurons in cortical layer 6. The rat medial prefrontal cortex is used to illustrate the subgroups of inhibitory cells in layer 6. IN1 (interneuron subtype 1) depicts chandelier cells known to inhibit the axon initial segment of pyramidal neurons and are mainly concentrated in cortical layer 5 and layer 6. IN2 depicts the superficial-projecting Martinotti cell-like interneurons. IN3 illustrates basket cell-like, fast-spiking interneurons targeting layer 5 pyramidal cells in layer 6. IN4 indicates fast-spiking and non-fast-spiking interneurons with basket cell-like morphologies inhibiting the dendrites of layer 6 pyramidal neurons. IN5 shows a restricted subset of interneurons in layer 6b, which project to the white matter. Figure was created based on the following article: (Ding et al., 2021)

1.1.3.3. What is the GABAergic and glutamatergic neuron ratio in the cerebral cortex?

The regulation of the proportions of GABAergic and glutamatergic neurons is essential for maintaining a balanced excitation-inhibition (E/I) ratio in cortical networks. Therefore, research dating back to 1987 has been concerned with the exact numbers of inhibitory to excitatory neurons across a variety of species and cortical areas. Hendry et al (1987) investigated the primate cerebral cortex and reported that the proportion of GABA-immunoreactive neurons was consistent throughout cortical regions. He estimated the GABAergic neurons to be 25-30% of the total neuronal population, except for the primary visual area, where this number was 20% (Hendry et al. 1987). In the adult cat auditory cortex, Prieto et al. (1994) determined that the fraction of GABAergic neurons was approximately the same, reporting a value of 24.6% (Prieto et al. 1994). Estimates of the laminar proportion of GABAergic and glutamatergic neurons showed that GABAergic cells comprise 94% of layer 1 neurons, whereas they only constitute 27% and 16% of total cell populations in layers 5 and 6, respectively (Prieto et al. 1994). In the rat cerebral cortex, GABA-immunoreactive neurons have been reported to be present in lower percentages within the adult primary visual (V1), primary somatosensory (barrel cortex) (S1bf), and primary motor areas (M1) (Beaulieu 1993). In all three cortical regions, inhibitory cells were estimated to comprise 15% of the total cell population. This implies that the percentage of GABAergic neurons does not vary substantially between cortical areas. Between V1 and S1bf, the laminar proportion of GABA-immunoreactive neurons remained constant, with layer 1 and layer 5 encompassing the largest amount of GABAergic neurons (87%–92% and 18%–22%, respectively) (Beaulieu 1993). Since layer 4 is absent in M1, more GABAergic cells are concentrated in the supragranular layers, which results in a higher percentage of GABAergic neurons in layer 2/3 (18%) and a lower percentage in layer 5 (10%) in M1 when compared to V1 and S1 (Beaulieu 1993).

The ratio of GABAergic to glutamatergic neurons is set and maintained at 1:5 in the adult cerebral cortex, which is established during early corticogenesis (Sahara et al. 2012). An elegant study

by Sahara et al (2012) revealed that a 1:5 GABAergic cell fraction is formed as early as embryonic day 14.5, and it continues to be maintained during postnatal development and in adulthood (Sahara et al. 2012). Surprisingly, this ratio is achieved when most GABAergic interneurons are still migrating from the ganglionic eminences and have not yet settled into their designated laminar positions (Sahara et al. 2012).

1.2. Pyramidal neurons instruct the development, density, and distribution of GABAergic interneurons

1.2.1. Birthdates, origins, and migration of pyramidal neurons and cortical GABAergic interneurons

1.2.1.1. Assembling the cytoarchitecture of the cerebral cortex

The assembly of the six-layered structure of the mammalian cerebral cortex begins early during embryonic development. Approximately on embryonic day 11 (E11), the first cohort of neurons migrates outward from the ventricular zone (VZ), forming a transient layer known as the preplate (PP) or the primordial plexiform layer between E11 and E13 (Ayala et al., 2007; Marin-Padilla, 1971). Subsequently, the migration of later-born neurons along radial glial fibres gives rise to a new set of layers referred to as the cortical plate (CP), at around E14 (Xie et al., 2002), which divides the PP into two layers: the superficial marginal zone (MZ) and a lower layer named the subplate (SP). The MZ and the SP are unique structures since 1) they constitute the earliest-born neurons, 2) form in an 'outside-in' sequence, and 3) house transient cell populations (Marin-Padilla & Marin-Padilla, 1982). Specifically, Cajal-Retzius (CR) cells reside in MZ (destined to become layer 1), while the remaining primordial cells constitute the SP (Ayala et al., 2007). The intermediate zone (IZ) separates the SP from the VZ, which ultimately forms the white matter (WM) tract (Parnavelas, 2002). Cortical development progresses further with additional waves of neuronal migration. As subsequent waves of migrating neurons enter the CP, they circumvent the earlier-generated neurons and establish the future neocortical layers 6 to 2 in an 'inside-out' progression (Angevine & Sidman, 1961; Bystron et al., 2008; Luhmann et al., 2014). This sequence ensures that the deep cortical layers are formed first, whereas the superficial layers are established last (Figure 1.2.).

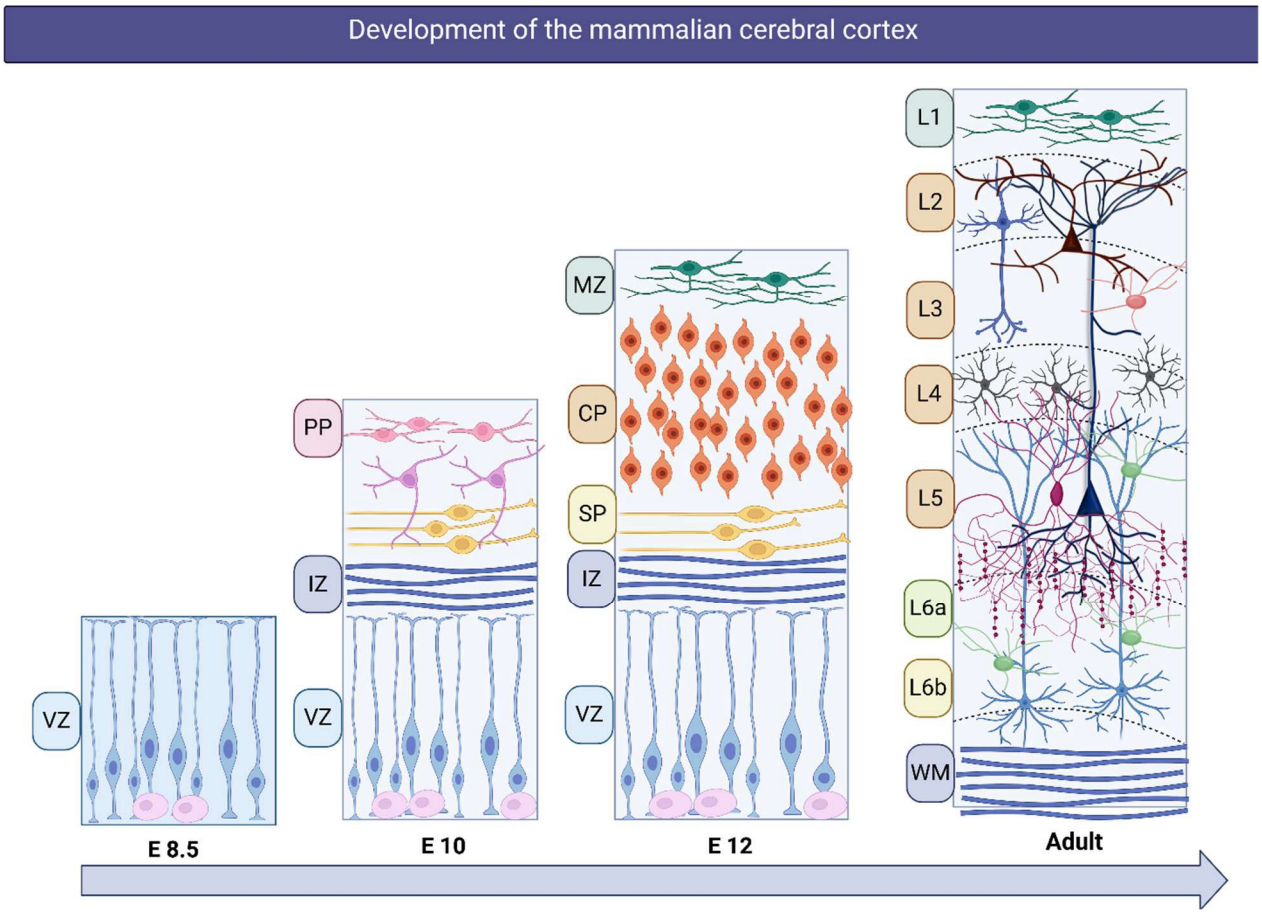


Figure 1.2. Assembling the laminar organisation of the mammalian cerebral cortex. Glia and neuron progenitors reside in the embryonic ventricular zone (VZ). The earliest generated neurons establish the preplate (PP), while the intermediate zone (IZ) is formed by the axons of these initial neurons and axons sprouting from the thalamus. The next round of migrating neurons forms the cortical plate (CP), dividing the PP into the subplate (SP) and the marginal zone (MZ), where transient neuronal populations are located. Following neuronal migration and differentiation, the subplate has mostly vanished, and the typical laminar organisation of the cerebral cortex is formed. Created with BioRender based on (Bronner & Hatten, 2013).

1.2.1.2. Origin and migration of pyramidal neurons

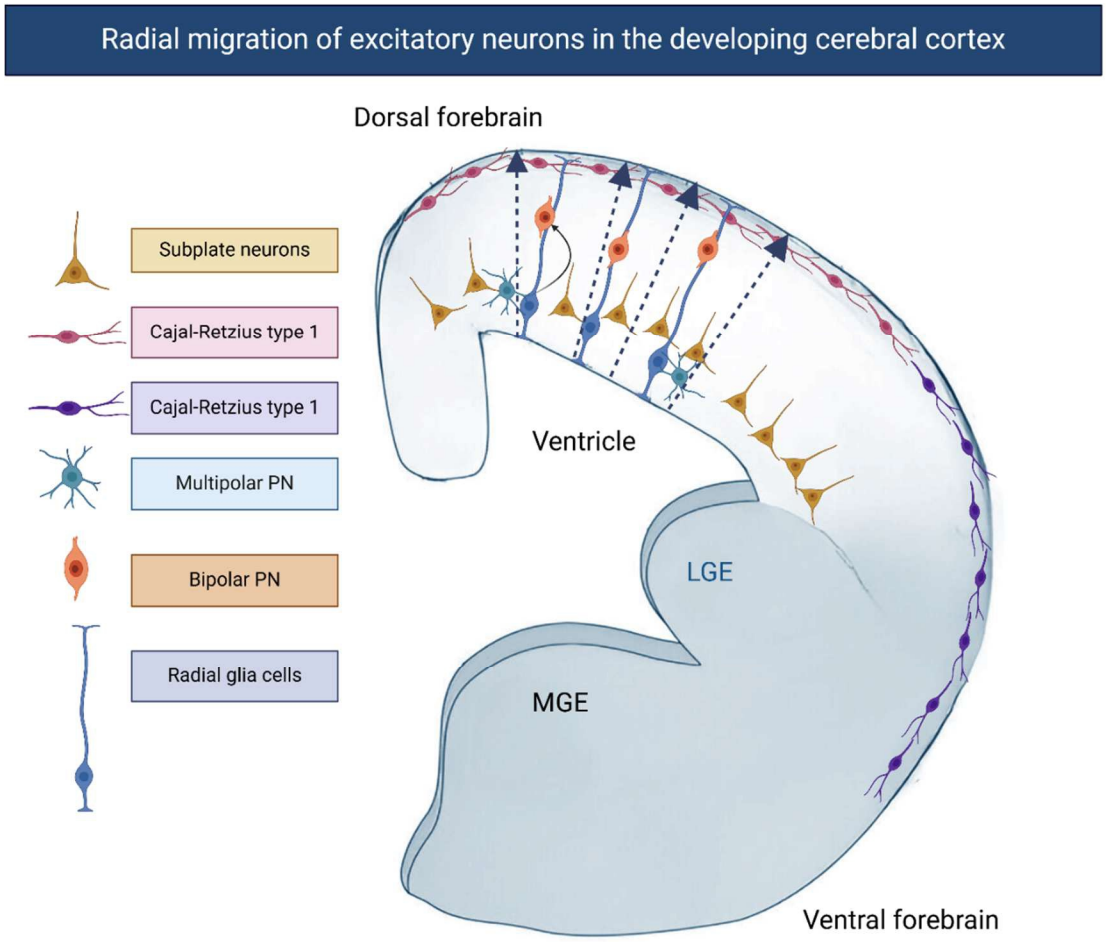
Cortical pyramidal neurons derive from the germinal/proliferative zones of the dorsal telencephalon (Hatanaka & Murakami, 2002; Kriegstein & Noctor, 2004), i.e., the ventricular zone of the embryonic cerebral cortex, which is the first to appear during cortical development and lines the walls of the lateral ventricles (Martínez-Cerdeño & Noctor, 2018). It was initially believed that cortical neurogenesis was primarily the reserve of the VZ, and the subventricular zone (SVZ) served to

generate glial cells (S C Noctor et al., 2001; Privat, 1975; Takahashi et al., 1995). This conventional view has been challenged by studies demonstrating that SV can give rise to neurons indirectly from radial glial cells that generate intermediate progenitor cells, also termed basal progenitor cells (Haubensak et al., 2004; Stephen C Noctor et al., 2004). These intermediate progenitors were generated in the VZ and subsequently migrated to the SVZ, where they underwent symmetric divisions and produced two daughter cells that migrated to the CP (Stephen C Noctor et al., 2004). In light of this evidence, the SVZ is not a gliogenic compartment *per se*. Wu et al (2005) demonstrated *in vivo* that a proportion of the excitatory neurons in the upper cortical layers are generated by a distinct set of neuronal progenitors in the SVZ, which are created by VZ cells, migrate into the SVZ, and go through several symmetrical and asymmetrical cell divisions (S.-X. Wu et al., 2005). These SVZ progenitor cells that differentiate into glutamatergic neurons have been molecularly defined as being positive for the neuronal basic helix-loop-helix (bHLH) transcription factor gene (NEX) (S.-X. Wu et al., 2005). Tarabykin et al (2001) were the first to identify SVZ-specific molecular markers. They not only discovered that *Svet1* was exclusively expressed by proliferating cells residing in the SVZ but also showed that *Svet1* was a cell-type-specific marker for a subset of superficial cortical neurons (Tarabykin et al., 2001). Another important finding of the study was the discovery of the *Otx1* gene, which selectively marks deep cortical neurons and its expression is restricted to the VZ (Tarabykin et al., 2001).

The birthdates of cortical projection neurons have been determined by employing tritiated thymidine autoradiography in conjunction with the retrograde labelling of wheat germ lectin horseradish-peroxidase complex (WGA-HRP) in the rat visual area (Miller, 1985). Projection neurons are born between gestational day (GD) 14 and GD 20, with GD 14 being the birthdate of cortico-cortical projection neurons destined to inhabit layer 6b. Layers 6a, 5, 3, and 2 are occupied by neurons born on the following days, GD 15, 17, 19, and 20, respectively (Miller, 1985).

The neurogenesis of a subset of superior colliculus-targeting layer 5 projection neurons, namely the cortico-collicular neurons (CCN), falls between GD 15 and 17 (Contamina & Boada, 1992). Compared to the CCNs in the upper third sublamina of layer V, the population of CCNs in the lower two-thirds of layer V was generated earlier at GD 15 and in greater proportions in the rat visual area (Contamina & Boada, 1992). These studies have demonstrated unequivocally that the laminar allocation of cortical neurons is birthdate-dependent.

Pyramidal neurons follow the neural tube's radial arrangement as they migrate radially from the proliferative zones of the dorsal telencephalon to the cortical plate (Figure 1.3.). The migration process is guided by the processes of the radial glial cells (S C Noctor et al., 2001; Rakic, 1972), acting as a scaffold for the migrating cortical neurons. This glial-guided migration is a conventional example of locomotion, which consists of brief, fast-forward motions interspersed with comparatively lengthy immobile phases. These freely migrating cells contain a short, unbranched leading process that is not connected to the pial surface (Oscar Marín & Rubenstein, 2003; Nadarajah et al., 2001). Perikaryal or somal translocation is another type of migratory behaviour displayed by radially migrating cortical neurons. Characterised by continuous movements, cells moving via somal translocation extend a long leading process upon departing from the VZ, which is anchored to the pial surface (Oscar Marín & Rubenstein, 2003). During early corticogenesis, this radial migratory mechanism appears to predominate, indicating that the earliest-born deep-layer neurons use this mode of migration to reach their destination (Kriegstein & Noctor, 2004).


Radial migration of excitatory neurons in the developing cerebral cortex
Dorsal forebrain
Subplate neurons
Cajal-Retzius type 1
Cajal-Retzius type 1
Multipolar PN
Bipolar PN
Radial glia cells
Ventricle
LGE
MGE
Ventral forebrain

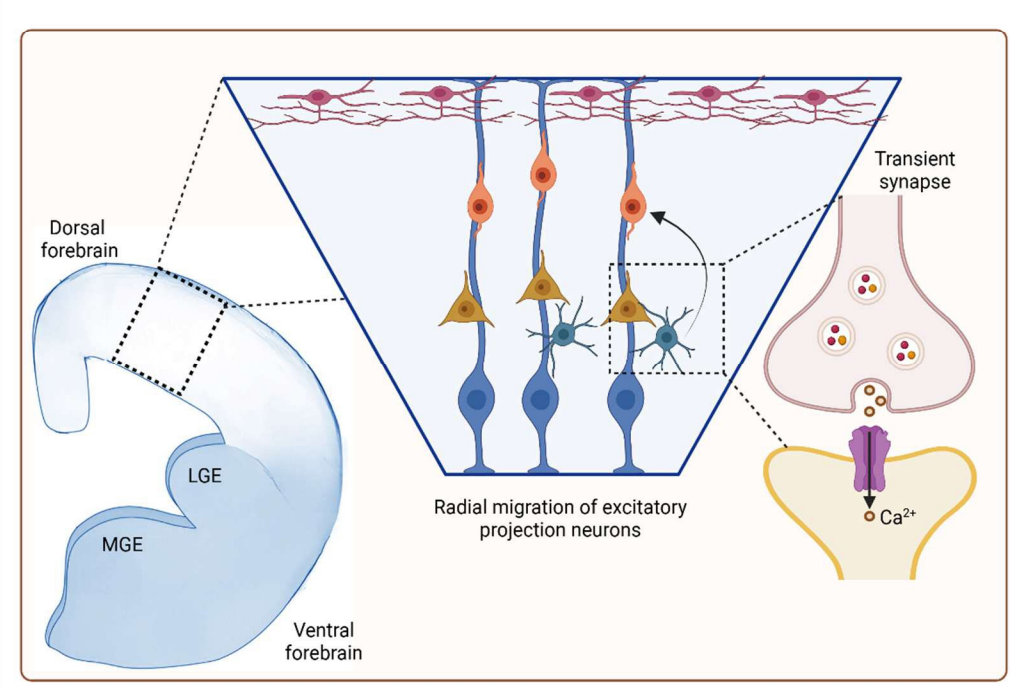

Dorsal forebrain
LGE
MGE
Ventral forebrain
Radial migration of excitatory projection neurons
Transient synapse
Ca2+

Figure 1.3. Radial migration of glutamatergic cortical neurons. The upper panel shows two transient cell populations, subplate neurons and Cajal-Retzius cells, that start migrating at the beginning of cortical development and reside below the cortical plate and the marginal zone. Different colours are used to distinguish between the different subsets of Cajal-Retzius cells generated through corticogenesis. Multipolar neurons generated by radial glia cells transform into bipolar neurons to traverse along radial glia fibres and use somal translocation to migrate to their respective cortical destination. The lower panel depicts the transient excitatory synapses formed between multipolar projection neurons and subplate neurons. The morphological transformation of multipolar to bipolar neurons is facilitated by calcium entry triggered by NMDA receptors. Modified from (Silva et al., 2019) and Created with BioRender.

1.2.1.3. Origin and migration of cortical GABAergic interneurons

While radial migration is recognised as the primary method of cell migration for neurons in the mammalian cerebral cortex, an equally significant mode is seen in cells originating from the embryonic subpallium. These neurons migrate along non-radial or tangential pathways, primarily comprising GABAergic interneurons (Figure 1.4.) and a smaller number of oligodendrocyte progenitors (OLPs) originating from the ventral forebrain (Kessaris et al., 2006). During embryonic development, olfactory bulb (OB) interneurons derive from the lateral ganglionic eminences (LGE) of the subpallium, whereas after birth, they arise from the anterior subventricular zone of the lateral ventricle (Lois & Alvarez-Buylla, 1994; Lois et al., 1996). Neuronal precursors form chains while tangentially migrating from the SVZ to the OB via a unique migratory pathway known as the rostral migratory stream (RMS) (Lois et al., 1996). Radial glial fibres do not facilitate the chain migration of neuroblasts, which appears to be regulated by a wide array of factors, including extracellular matrix (ECM) and neural cell adhesion molecules (NCAMs) (Oscar Marín & Rubenstein, 2003). New GABAergic neurons are continuously being added to the olfactory bulb by the migration of olfactory interneuron precursors throughout adulthood, and OB neurogenesis has been reported to be present in the human OB (Bédard & Parent, 2004; Sun et al., 2010).

Most interneurons fated to the cortex derive from the proliferative zones of the ventral telencephalon, namely the medial and caudal ganglionic eminences (MGE and CGE, respectively) (Fishell & Rudy, 2011; Fogarty et al., 2007; Hanganu-Opatz et al., 2021; Kessaris & Denaxa, 2023;

Kessaris et al., 2014; Kessaris, 2022; Lavdas et al., 1999; Oscar Marín & Rubenstein, 2003; Tamamaki et al., 1997). The majority of cortical interneurons (60%) originate in the MGE (Kessaris et al., 2014), including the parvalbumin (PV) and the somatostatin (SST)-expressing subtypes (S. J. Butt et al., 2017; S. J. B. Butt et al., 2007); however, the anterior entopeduncular area (AEP), the retrobulbar area (Meyer et al., 1998), and even the VZ/SVZ of the dorsal telencephalon may also serve as origins for GABAergic neocortical neurons (Kriegstein & Noctor, 2004; O Marín & Rubenstein, 2001). The latter appears to constitute an uncommon subtype of Mash1-positive GABAergic neurons detected in the human neocortex (Letinic et al., 2002).

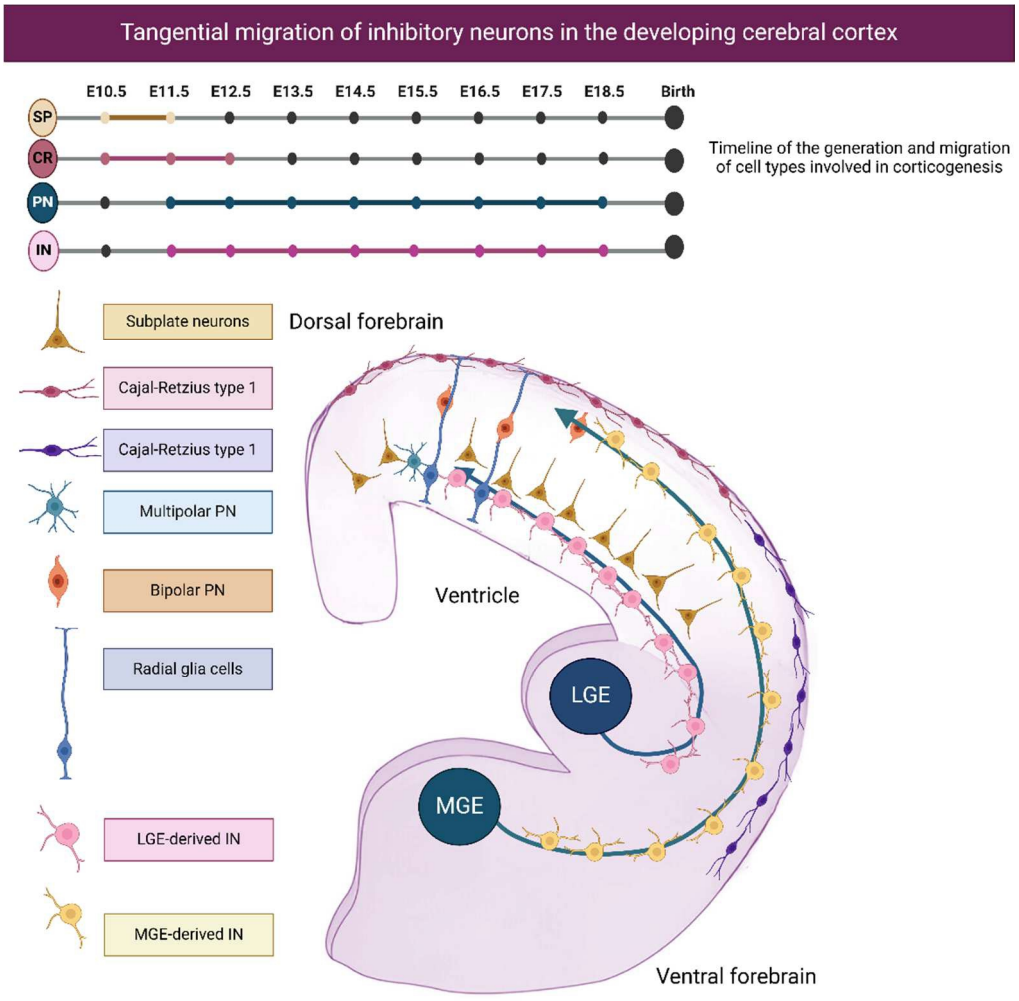


Figure 1.4. Tangential migration of cortical GABAergic interneurons. The panel illustrates the two migratory streams employed by cortical interneurons. Early-migrating interneurons born before

E12.5 (yellow) enter the cortical plate through the marginal zone and take a superficial path. Late-migrating interneurons (pink) travel tangentially across the subventricular zone (SVZ) and lower intermediate zone (IZ), following a deep-layer path. Following the tangential migration, interneurons move radially within the cortical plate to allocate their designated laminar position. Modified from (Silva et al., 2019; Sultan et al., 2013) and created with BioRender.

Three phases can be distinguished in the migration of interneurons according to the progenitor domains from which they originate (Anderson et al., 2001). In the early phases of embryonic development, the first stream of interneurons originating from the MGE and AEP begins migrating in mice at approximately E11.5. (O Marín & Rubenstein, 2001). This stream of cells circumvents the cortical plate and travels superficially to the developing striatum before entering the marginal zone and the subplate (Marín and Rubenstein 2003; Lavdas et al. 1999). For interneurons destined to the cortex, chemorepulsive signals composed of class 3 semaphorins and their receptors ensure that cortical interneurons migrating to the cortex steer clear of the striatum (Marín et al., 2001).

MGE-derived cells predominate the second phase of migration, occurring between E12.5 and E14.5 (mid-embryonic stage), and take either the superficial or the deep migratory pathway to travel to the developing striatum (Marín & Rubenstein, 2001). Upon reaching the cortex, migrating neurons occupy the SVZ/lower IZ from which they expand into the PP (Marín & Rubenstein, 2001). Numerous streams allow interneurons to enter the cortex, primarily through the SVZ and lower IZ, in addition to the migratory streams in the marginal zone (MZ) and subplate.

The third stream of migrating interneurons, present during the late gestation stage at E15.5, is mainly composed of cells derived from the CGE. These late-born cells take a distinct migratory path, initially moving caudally toward the posterior end of the telencephalon before turning to reach the posterior cerebral cortex (Yozu et al., 2005). To enter the developing cortex, CGE-derived interneurons utilise the IZ/SVZ first and only later in development take the superficial migratory

stream (Miyoshi & Fishell, 2011). The molecular guidance cues that facilitate their migration include intrinsic genetic factors, particularly the high expression of COUP-TFII, as well as extrinsic cues such as chemokines (notably CXCL12/SDF-1) and growth factors (including HGF/SF, BDNF, and GDNF) (Guo & Anton, 2014; Kanatani et al., 2008; Llorca & Deogracias, 2022; Miyoshi et al., 2010). Unlike MGE- and CGE-derived interneurons, the majority of cells that originate from the LGE during early neurogenesis (E13.5) do not migrate into the cortex; instead, they occupy the striatum, the nucleus accumbens, and the olfactory bulbs (Wichterle et al. 2001; Anderson et al. 2001). Tangential migration of certain LGE-derived cells occurs later in neurogenesis, with these cells entering the cortex via the SVZ and utilising the deep migratory stream (Anderson et al., 2001).

The distinct origins of the three migratory streams have been unveiled by genetic perturbations of the transcription factors required for the regional specification in the ventral telencephalon. Differential expression of *Nkx2.1*, *Pax6*, and *Gsh2* delineates the anatomical boundaries of distinct progenitor domains, with *Nkx2.1* homeobox gene defining the specification of the MGE and AEP, and *Gsh2* being required for specification of the dorsal LGE (S. J. B. Butt et al., 2008; Corbin et al., 2000; Flames et al., 2007; Sussel et al., 1999; Yun et al., 2001). *Nkx2.1*-deficient mutants not only fail to form the pallidum but also exhibit a drastic reduction in the GABA-expressing cortical and striatal interneurons, while leaving OB interneurons intact (Marin et al., 2000; Sussel et al., 1999). *Gsh2*-deleted mutants displayed cortical-related molecular marker genes in dorsal LGE progenitor neurons and diminished OB interneurons during mid-gestation (Yun et al., 2001).

Research elucidating the temporal origin of GABAergic neurons has shown a strong correlation between the birthdate of interneuron progenitors and their laminar allocation. Early birthdating studies relying on timed [3^{H}]thymidine injections with GABA immunocytochemistry have demonstrated that the generation of cortical interneurons falls between GD 14 and 20 in the rat visual cortex, with interneurons residing in deep cortical layers being born first (Miller, 1985). Similar findings in the mouse somatosensory cortex showed that GAD-immunoreactive neurons were formed

in two stages. The first phase (E12–14) saw the birth of layer 6 and layer 5 interneurons, while the second phase (E13–E17) saw the generation of layer 4 and layer 1 interneurons (Fairén et al., 1986). Except for layer 1 GAD-neurons, which were continuously created during the embryonic stage of neurogenesis, the generation of interneurons thus occurs in an "inside-out" gradient (Fairén et al., 1986; Miller, 1985). It was subsequently revealed that the calretinin (CR)-positive subtype of interneurons occupies cortical layers with an “outside-in” sequence, and contrary to PV neurons, their dates of birth differ from those of the projection neurons within the same layer (Rymar & Sadikot, 2007). Miyoshi et al (2010) demonstrated that the commencement and peak of CGE-derived interneuron generation happen three days after the MGE-originated populations, and their allocation to the supragranular cortical layers is irrespective of their time of origin (Miyoshi et al., 2010).

Genetic fate-mapping studies and *in vivo* transplantation of MGE or CGE-derived progenitors have provided further proof that the birthdate (time) and the location of interneuron progenitors (place) are major factors in determining the subtype produced. E13.5 MGE transplants comprised different subclasses of cortical interneurons, including fast-spiking (FS), regular spiking nonpyramidal (RSNP), and delayed-spiking (DS) interneurons, which corresponded to PV-positive basket cells, and somatostatin (SST)-positive Martinotti cells, respectively (S. J. B. Butt et al., 2005). However, a diverse population of RSNP neurons with bitufted, bipolar (CR+), and double bouquet RSNP neurons was derived from early (E13.5) and late (E15.5) CGE transplants (S. J. B. Butt et al., 2005). This has established that the MGE and CGE generate distinct subtypes of interneurons, and the time and place of interneuron progenitors forecast the subtype generated (S. J. Butt et al., 2017; S. J. B. Butt et al., 2007; Kessaris et al., 2014). It can be broadly stated that the PV+ and SST+ subtypes originate in the ventral and dorsal MGE (S. J. Butt et al., 2017), respectively, whereas the CR+ and VIP-expressing subsets derive from the CGE and mainly inhabit the upper cortical layers (S. J. Butt et al., 2017; S. J. B. Butt et al., 2005; López-Bendito et al., 2004; Miyoshi et al., 2007; Xu et al., 2004; Yozu et al., 2004). The temporal and spatial segregation of interneuron production entails that MGE-

derived interneurons are generated at the early phase of neurogenesis, while CGE-derived interneurons are born during later embryonic time points (S. J. Butt et al., 2017; S. J. B. Butt et al., 2007). During the time window for neurogenesis, PV+ interneurons are born continuously (E9.5 – E15.5), while SST+ cells preferentially arise at early stages of embryonic development (E9.5 – E13.5) (S. J. B. Butt et al., 2007) (Figure 1.5.). CGE-derived CR and VIP-expressing cells are born between E12.5 and E15.5 (S. J. Butt et al., 2017; S. J. B. Butt et al., 2007).

In vivo Cre–lox-based fate-mapping has further refined the subtypes of classes derived from the different subpallial progenitor domains. While the CR+ SST+ Martinotti cells originate in the dorsal MGE precursors expressing *Nkx6.2* (Nk6 homeobox 2), the PV+, SST+, and calbindin (CB)-positive subgroups are derived from *Lhx6* (Lim homeobox 6)-expressing precursors (Fogarty et al., 2007). Neuropeptide-Y (NPY+) interneurons are produced by genomic screened homeobox 2 (*Gsh2*) precursors in the LGE/CGE (Fogarty et al., 2007). Now that the various progenitor zones in the mouse subpallium have been molecularly identified, they can be described using the discrete expression gradient of several transcription factors (Flames et al., 2007; Kessaris & Denaxa, 2023; Kessaris et al., 2014). With the advent of single-cell transcriptomics, it has also become evident that even before the interneurons migrate and arrive at their final cortical destination, the transcriptomes of embryonic interneurons disclose their fate (Mi et al., 2018).

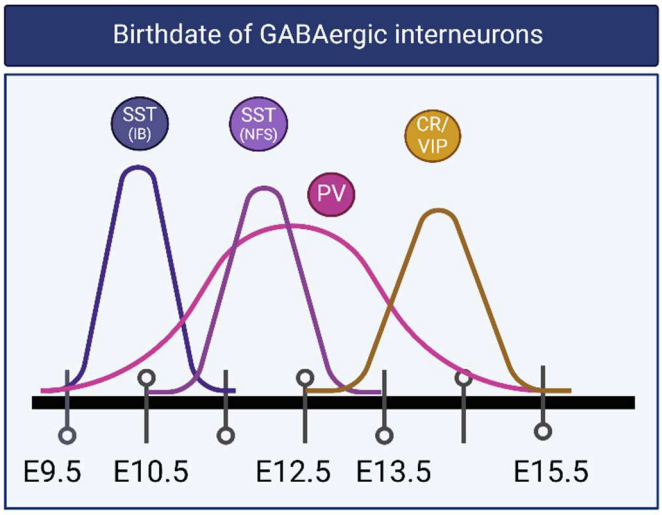


Figure 1.5. Birthdate of GABAergic interneurons. Between E9.5 and E15.5, different kinds of interneurons emerge during embryonic development; parvalbumin interneurons derived from MGE are produced earlier, while CGE-derived interneurons are produced later. While nonfast-spiking interneurons that express somatostatin and burst-spiking (IB) interneurons are born between E9.5 and E11.5 and E9.5 and E13.5, the neurogenesis of parvalbumin-interneurons occurs between E9.5 and E15.5. Subclasses of interneurons that express CR and VIP only begin to form between E12.5 and E15.5. Figure created with BioRender based on (S. J. Butt et al., 2017; S. J. B. Butt et al., 2007)

1.2.2. Fate-changing the identity of pyramidal neurons

Molecularly unique subtypes of interneurons are crucial in defining circuit functions, regulating information transfer to the cerebral cortex, and coordinating the activity of neural assemblies within oscillatory neuronal networks (McBain and Fisahn, 2001; Somogyi and Klausberger, 2004; Gupta et al., 2000). In rodents, GABAergic and glutamatergic neurons originate in distinct areas of the neuroepithelium, driven by various combinatorial transcriptional codes (Butt et al., 2008; Marín and Rubenstein, 2011; Price et al., 1992; Sultan et al., 2013; Lodato and Arlotta, 2015; (S. J. B. Butt et al., 2005). Pioneering studies have demonstrated that the transcriptional and laminar identity of pyramidal neurons form an essential part of the cortical cytoarchitecture and may instruct the integration of GABAergic neurons into cortical circuits (Lodato et al., 2011; Wester et al., 2019). Disrupting the transcriptional identity of intratelencephalic (IT) projection neurons by knocking out the transcription factor *Satb2* from pyramidal neurons not only converted the IT-type excitatory

neurons to pyramidal-tract (PT) type neurons but also caused aberrations in the cortical lamination of CGE-derived interneurons (Wester et al., 2019). The absence of the transcription factor *Fezf2*, which determines the fate of subcerebral projection neurons, resulted in an abnormal distribution of parvalbumin and somatostatin interneurons across layers, along with significant impairments in GABAergic inhibition (Lodato et al., 2011). Although the specification, development, and differentiation of pyramidal neurons are tightly controlled by essential transcription factors, including *Fezf2*, *Satb2*, and *Ctip2* (Alcamo et al., 2008; Arlotta et al., 2005; Britanova et al., 2008; Molyneaux et al., 2005, 2007), the fate specification of pyramidal neuron identity can be altered in the developing cortex through genetic modifications.

1.2.3. Activity-dependent mechanisms orchestrating the assembly of cortical circuits

The temporal coincidence of the emergence of GABAergic oscillations produced by pyramidal cell activity and the onset of interneuron cell death has provided evidence for the link between network activity and increased interneuron survival (Duan et al., 2020). This contradicts the general notion that the critical size of the interneuron pool is exclusively dictated by programmed cell death. N-methyl-D-aspartate (NMDA) receptor-mediated synaptic currents have been shown to control the degree of neuronal cell death and the number of cortical interneurons in the developing mammalian cortex (Denaxa et al., 2018; Roux et al., 2015). When pharmacological blockade of NMDA receptors deprives migrating GABAergic interneurons of glutamatergic inputs, suppression of excitatory neurotransmission negatively impacts immature interneurons and encourages apoptosis (Ikonomidou et al., 1999; Roux et al., 2015).

The findings that *Lhx6* mutations result in a sharp decline in SST+ and PV+ interneuron density and that *Lhx6* expression is essential for the survival of MGE-derived interneurons led to the hypothesis that elevated network activity might be associated with an upregulation of activity-dependent genes in cortices lacking *Lhx6* (Denaxa et al., 2018). These experiments have

demonstrated that neural activity markers such as *Bdnf*, *Npas4*, *Npy*, and *cfos* are indeed upregulated following the ablation of *Lhx6*. Since the deep cortical layers exhibit the highest overexpression of activity-associated genes, which indicates higher network activity in Lhx6 mutants, they are the most responsive to alterations in the density of MGE-derived interneurons (Bloodgood et al., 2013; Denaxa et al., 2018; Gall et al., 1990; Hartmann et al., 2001). Likewise, the compensatory processes for the decrease in MGE-derived interneurons have been shown to occur within the infragranular layers.

1.2.4. Transient circuits involving glutamatergic and GABAergic neurons during development

Prior to the establishment of mature cortical circuits, transient neuronal networks emerge in the developing brain. These networks consist of excitatory and inhibitory neuron populations, which are influenced by spontaneous activity before they begin to process signals from the sensory periphery (Kanold & Shatz, 2006; Katz & Shatz, 1996; Luhmann & Khazipov, 2018; Luhmann et al., 2016; Zoltán Molnár et al., 2020; Ohtaka-Maruyama et al., 2018). Subplate neurons are likely the most noticeable elements of these transitory cortical networks. They function as conductors in the cortico-thalamo-cortical circuits, directing the development of thalamocortical connections and coordinating the growth of corticothalamic projections (Kanold & Luhmann, 2010; Z Molnár et al., 1998; Zoltán Molnár et al., 2020). During the first postnatal week, GABAergic interneurons integrate into the cerebral cortex and form synapses with transient neuron populations, such as Cajal-Retzius cells (Luhmann et al., 2014), suggesting that local inhibitory neurons are integral to the transient cortical networks.

SST+ interneurons play a crucial role in the formation of early thalamocortical networks (Anastasiades et al., 2016; Baruchin et al., 2022; Marques-Smith et al., 2016). A specific subset of non-fast spiking SST+ interneurons located in layer 5b has been identified to receive thalamic input, as well as transient translaminar excitatory input from layer 4 during the early stages of cortical development (Marques-Smith et al., 2016). Concurrently, the spiny stellate neurons (SSNs) found in

layer 4 of the somatosensory barrel field (S1BF) also receive similar transient translaminar innervation from GABAergic interneurons in layer 5b (Marques-Smith et al., 2016). However, these transient connections diminish with the closure of critical period plasticity, marking a developmental shift from early translaminar GABAergic inhibition originating in layer 5b to localised inhibition onto SSNs within layer 4 (Marques-Smith et al., 2016). Moreover, the chronic ablation of *Snap25* from SST+ interneurons resulted in the loss of transient translaminar inputs to SSNs (Marques-Smith et al., 2016) (Figure 1.6.).

These findings have significantly contributed to our understanding of the transient cortical circuitry between layer 5b SST+ interneurons and L4 SSN neurons in the S1BF during early cortical development (Figure 1.6.). Additionally, Anastasiades et al. (2016) demonstrated that *Nkx2-1*-derived interneurons and pyramidal neurons establish transient, translaminar synaptic connections at critical stages of cortical network formation and plasticity (Anastasiades et al., 2016). Progressive weakening of the translaminar glutamatergic inputs to layer 4 FS neurons from layer 2/3 pyramidal neurons coincided with a concurrent increase in inputs from layer 4 SSN, indicating the gradual pruning of superficial connections to layer 4 FS neurons (Anastasiades et al., 2016). There were similar translaminar connections to NFS interneurons that were transient and derived from layer 2/3 pyramidal neurons, which were eliminated by P13 (Anastasiades et al., 2016). Therefore, distinct yet transient connections characterised by layer-specific patterns are present in the early neuronal circuits of the developing cerebral cortex, which are fundamentally different from those observed in the mature brain.

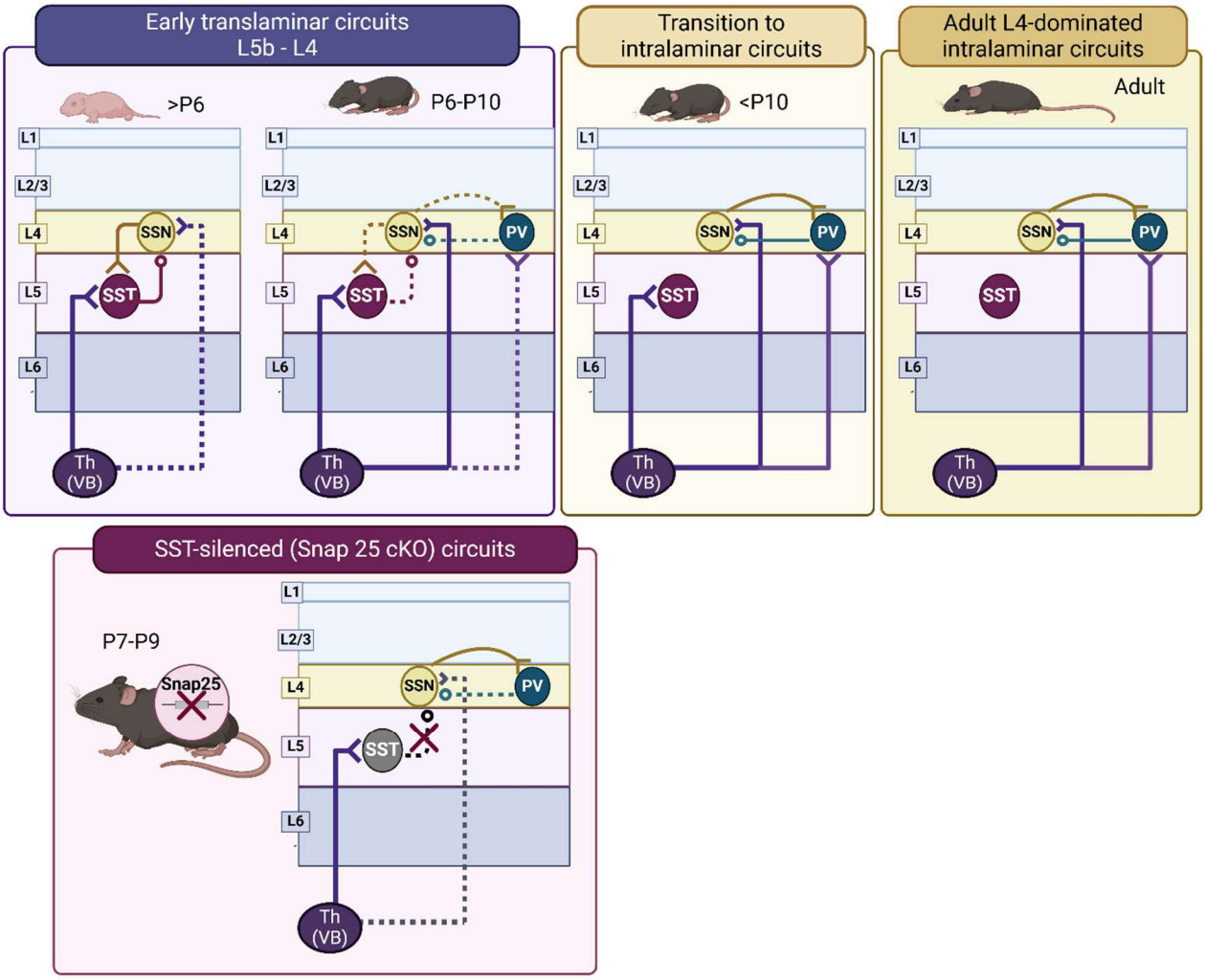


Figure 1.6. Translaminar L5b – L4 circuits dominate during early cortical development. Schematic representation illustrates the early postnatal cortical circuits, highlighting the reciprocal connections between somatostatin interneurons in layer 5b and spiny stellate neurons (SSN) in layer 4 of the barrel cortex. These transient translaminar connections are prominent during the period from postnatal day 4 to 9 (P4-P9), prior to the establishment of thalamic innervation of layer 4 parvalbumin neurons and thalamic input to layer 4 SSNs. As the development shifts from translaminar (L5b-L4) to intralaminar (L4-dominated) circuits, the reciprocal connectivity between SST interneurons and SSNs in layer 4 is diminished by postnatal day 10 (<P10) (Marques-Smith et al., 2016). Additionally, the early thalamic input to layer 5 SST interneurons is absent in the adult brain. The chronic removal of *Snap25* from SST neurons results in not only the loss of layer 5 GABAergic input to layer 4 SSNs but also a delay in the maturation of thalamic connectivity onto SSNs (Marques-Smith et al., 2016). The dotted lines in the figures represent maturing synaptic connectivity. Created with BioRender based on (Marques-Smith et al., 2016), (Anastasiades et al., 2016),(Tuncdemir et al., 2016) and (Zoltán Molnár et al., 2020).

Substantial evidence indicates that various cohorts of GABAergic neurons play a crucial role in establishing early afferent and efferent connections, which are subsequently refined and regulated through sensory experience, thalamocortical inputs, and activity-dependent mechanisms (Zoltán Molnár et al., 2020). These immature synaptic connections are essential for the integration of GABAergic interneurons into adult cortical networks. Disruptions in the early formation of somatostatin networks can hinder the proper development of thalamocortical inputs to parvalbumin neurons (Tuncdemir et al., 2016). The formation of these early SST networks is initiated when immature SST interneurons in cortical layers 5 and 6 receive extensive thalamocortical innervation from the ventrobasal (VB) and posterior medial thalamic nuclei (Tuncdemir et al., 2016). Notably, the strength of the monosynaptic thalamocortical inputs targeting deep-layer SST neurons progressively diminishes by the end of the first postnatal week in the developing primary somatosensory cortex, suggesting a significant reduction in thalamocortical excitation of SST neurons over this period (Tuncdemir et al., 2016). During the early stages of postnatal development, layer 5/6 SST neurons begin to establish synaptic connections with local pyramidal neurons in the infragranular cortical layers, while PV interneurons experience an increase in thalamic drive (Tuncdemir et al., 2016). Importantly, the ablation of SST interneurons has been shown to impair the formation of thalamocortical inputs to PV neurons (Marques-Smith et al., 2016), thereby demonstrating that early-born SST neurons are vital for the maturation of thalamocortical synapses on PV neurons (Tuncdemir et al., 2016). This also underscores the interdependent relationship between SST and PV interneurons within the immature cortical circuits. Dwivedi et al (2024) have unveiled that metabotropic glutamatergic receptor signalling (mGlur1) is non-conventionally responsible for eradicating transient VB thalamocortical inputs to SST interneurons during the maturation of cortical circuits (Dwivedi et al., 2024). Moreover, failure to eliminate these early thalamic inputs to SST interneurons interferes with adult exploratory behaviour (Dwivedi et al., 2024).

Recent evidence suggests that the developmental reorganisation of synaptic connections in immature cortical circuits is not exclusive to the somatosensory cortex. The primary auditory cortex (A1) similarly undergoes a remodelling of glutamatergic and GABAergic intracortical connections during the critical period in mouse development (Meng et al., 2020). Subgranular inputs from layer 4 and particularly from layer 5/6 dominate the cortical inputs that layer 2/3 neurons receive in A1 during P12 and P16; however, the infragranular inputs from layer 5/6 recede over the late postnatal developmental stages (Meng et al., 2020). This observation indicates that the hyperconnectivity between supra-and infragranular layers is a transient phenomenon, present only during the critical period (Meng et al., 2020). Collectively, these findings have enhanced our understanding of the functional maturation of early cortical circuits and highlighted the importance of the transitory, layer-specific synaptic connections that predominate throughout early cortical development.

1.2.5. The role of pyramidal neurons in instructing interneuron development

The ability of various GABAergic interneuron subtypes to modulate pyramidal cell activity has long been researched. Still, the part pyramidal neurons play in forming inhibitory circuits has received less attention. Numerous research studies have reported that the number, laminar allocation, and survival of GABAergic interneurons have all been directly impacted by perturbations in pyramidal cell function, identity or activity (Duan et al., 2020; Fazel Darbandi et al., 2018; Kroon et al., 2024; Lodato et al., 2011; Sreenivasan et al., 2022; Wester et al., 2019; Wong et al., 2018, 2022; S. J. Wu et al., 2024; Ye et al., 2015; Yook et al., 2019). The survival of interneurons in the developing cerebral cortex relies on the activity of pyramidal neurons, which protect them from apoptosis by enhancing their connections to GABAergic neurons prior to cell death (Denaxa et al., 2018; Priya et al., 2018; Sreenivasan et al., 2022; Wong et al., 2018, 2022). The intrinsically programmed process of interneuron apoptosis itself can be modulated by chemogenetically activating pyramidal neurons and/or inhibiting PTEN signalling in pyramidal cells during the critical window of interneuron cell death in mice (Southwell et al., 2012; Wong et al., 2018, 2022). When pyramidal neurons are

temporarily activated chemogenetically, parvalbumin and somatostatin interneuron density rises; conversely, when pyramidal neuron activity is manipulated during crucial stages of postnatal development, it decreases with transient inhibition (Wong et al., 2018). New evidence suggests that PV interneuron survival in subcortical projection regions of cortical pyramidal neurons depends on the presence of glutamatergic inputs. When excitatory inputs from corticostriatal layer 5 projection neurons were absent, the number of striatal interneurons declined (Sreenivasan et al., 2022). This further supports the role of glutamatergic transmission and cortical control over the spatial distribution of cortical and subcortical subtypes of interneurons.

The regulatory role of pyramidal neurons in the formation of inhibitory circuits has recently been evidenced by the genetic deletion of *Fezf2*. *Fezf2* KO mice have been known to exhibit loss of PT projection neurons in cortical layer 5 along with an elevation in IT neurons in layer 6 (Stogsdill et al., 2022); however, it was only recently discovered that different interneuron subtypes respond differently to the alterations in pyramidal neurons (S. J. Wu et al., 2024). Due to the inherent variations in their developmental trajectories, late-developing PV+ interneurons experience a fate change, whereas early-born SST+ neurons depend on apoptosis to align with the modified number of pyramidal neurons within the cortical network (S. J. Wu et al., 2024). The reduction of interneuron cell counts in layer 5b alongside an increase in layer 6b in the *Fezf2* KO cortex (S. J. Wu et al., 2024) reinforces the idea that cortical microcircuits must maintain a highly regulated ratio of excitatory to inhibitory neurons to sustain E/I balance. The many methods for manipulating pyramidal neuron identity, function, and number are summarised in Figure 1.7.

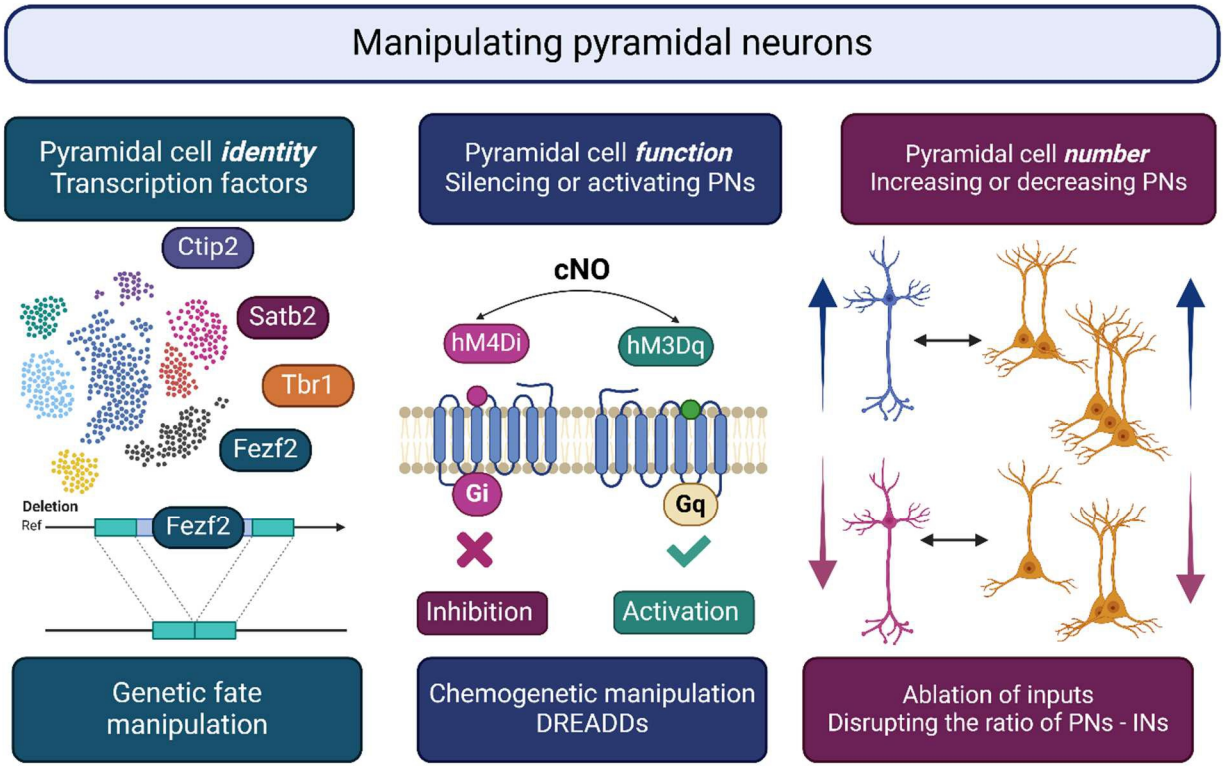


Figure 1.7. Schematics illustrating the different methods used to manipulate pyramidal neurons. Deleting certain transcription factors expressed in select populations of pyramidal neurons and converting them from subcerebral (*Fezf2*) to callosal-projecting neurons (*Satb2*) leads to a fate change in pyramidal neurons. Chemogenetic inhibition or excitation of pyramidal neurons changes the activity of pyramidal cells. Ablating subsets of pyramidal neurons leads to alterations in the number of excitatory and inhibitory neurons that may lead to E/I imbalance within cortical networks.

1.2.6. Excitatory inputs and glutamatergic transmission modulate interneuron development

Ablating the vesicular glutamate transporters *Vglut1* and *Vglut2* to eliminate glutamate release from pyramidal neurons has been demonstrated to differently affect the population of GABAergic interneurons. While the abolition of excitatory transmission from pyramidal neurons has caused a marked decrease in the density of neurogliaform and basket cells, it has not altered the density of bipolar neurons (Wong et al., 2022). These findings indicate that glutamatergic transmission and excitatory pyramidal neuron inputs govern the survival of inhibitory cells in the nascent brain. Tetanus toxin injections to ablate excitatory inputs in the somatosensory cortex at postnatal day 0 (P0) caused a notable reduction in the number of somatostatin interneurons in the

infragranular cortical layers at P9 (Duan et al., 2020). Intriguingly, the lack of elimination of the excess number of GABAergic interneurons during development results in permanent disruptions that only surface in adulthood (Magno et al., 2021). Considering that the removal of excitatory synaptic inputs during neonatal development drastically affects interneuron survival in deep cortical layers (Duan et al., 2020), it seems that pyramidal cells may act as key regulators of the formation of GABAergic circuits.

1.3. Synaptic transmission

1.3.1. SNARE proteins and their role in intracellular membrane fusion

Synaptic transmission is an essential form of interneuronal communication which requires precise spatial and temporal control over neurotransmitter release. At the core of synaptic vesicle release lies the *s*oluble *N*SF *a*ttachment *re*ceptor proteins (SNARE) complex, a piece of presynaptic fusion machinery, which comprises SNARE proteins crucial to intracellular membrane fusion and trafficking (Rizo and Südhof 2002; Rizo 2022). The discovery of the subcellular localisation of SNARE proteins to specific membrane compartments (Söllner et al. 1993) has enabled the classification of SNAREs into two distinct classes of membrane protein superfamilies depending on whether the SNAP receptors are present on the target membrane (t-SNARE) or the transport vesicle (v-SNARE). Synaptosomal-associated protein of 25 kDA (SNAP-25) and syntaxins are transmembrane proteins that are part of the t-SNARE superfamily. They are implicated in intracellular membrane trafficking and fusion events while enhancing the specificity of transport vesicle docking and fusion (Duman and Forte 2003; Yoon and Munson 2018). SNAP-25 is retained in the membrane by palmitoylation on many cysteine sites, but syntaxin and synaptobrevin (also known as vesicle-associated membrane protein or VAMP) have carboxy-terminal transmembrane regions (Rizo 2022; Lin and Scheller 2000). The SNARE proteins have been demonstrated to undergo differential cleavage by clostridial botulinum and tetanus neurotoxins (Schiavo et al. 1992; Link et al. 1992; Blasi et al. 1993). The neurotoxin-mediated inhibition of synaptic transmission selectively impairs presynaptic vesicle fusion but does not interfere with vesicle docking (Broadie et al. 1995; Rizo and Südhof 2002).

The three SNARE proteins assemble into a stable four-helical bundle named the core or SNARE complex (Poirier et al. 1998; Sutton et al. 1998). It consists of four α-helices (syntaxin H3 domain, VAMP coiled-coil domain, SNAP-25 amino-terminal helix, and SNAP-25 carboxy-terminal helix) where the coiled-coil domains of the synaptic proteins are oriented in a parallel fashion (Lin and Scheller 2000). The parallel configuration of the α-helices draws synaptobrevin close to the SNARE proteins

on the target membrane, inducing the fusion of the vesicle and the plasma membrane (Rizo and Rosenmund 2008). Upon the assembly of the *trans*-SNARE complex (refers to the ternary core complex prior to membrane fusion), energy is released, and a thermodynamically spontaneous mechanism of protein folding propels membrane fusion (Südhof and Rothman 2009).

1.3.2. Molecular machinery of Ca^{2+}-evoked synaptic vesicle release

The synaptic SNARE and SM proteins (for "*S*ec1/*M*unc18-like proteins")-mediated membrane fusion entails an ATP-dependent cycle of association and dissociation, with N-ethylmaleimide sensitive factor (NSF) and soluble NSF-attachment proteins (SNAPs) executing the disassembly of the complex (Rizo and Südhof 2002). When SNAREs are recycled after synaptic vesicle exocytosis, the synaptic proteins become accessible for the subsequent membrane fusion cycle (Südhof and Rizo 2011). Syntaxin-1, existing initially in a closed state and thereby inhibiting the assembly initiation of the SNARE complex, needs to be opened for the core complex to form. This nucleation is the first step in the series of events leading to membrane fusion (Lin and Scheller 2000). At the closed configuration, the SM protein Munc18-1 is attached to syntaxin-1. However, with the opening of syntaxin-1, Munc18-1 changes the way it binds to syntaxin-1 by attaching to form trans-SNARE complexes through its interaction with the N-terminal sequence of syntaxin-1 (i.e., H_{abc} domain) (Dulubova et al. 2007). When the four α-helices are partially 'zippered' toward the carboxyl terminus during the first phase of priming, the plasma and synaptic vesicle membranes are drawn to proximity (Rizo and Südhof 2002). Complexin then attaches to the partially assembled *trans*-SNARE complex to enhance its priming after they are halfway formed (priming II) (Südhof 2013). The binding of complexin serves to activate the SNARE/SM protein complex prior to membrane fusion. The membranes are then drawn apart upon the completion of the full SNARE-complex assembly, creating the fusion pore (Südhof and Rizo 2011). Since neuronal SNARE proteins are not directly engaged in Ca^{2+} sensing, Ca^{2+} binding to synaptotagmin, which functions as a Ca^{2+} sensor, is another significant

event in the opening of the fusion pore (Chen et al. 2005). The expansion of the fusion pore then triggers the merging of the vesicle membrane with the target membrane, leading to the conversion of the *trans*-SNARE-complex to *cis*-SNARE-complex (Südhof 2013). The binding of NSF to the cis-SNARE-complex through its α/β/γ-SNAP adaptor proteins dissociates the complex and facilitates the termination of the association-disassociation cycle, permitting the recycling of proteins for the subsequent fusion cycle (Südhof and Rizo 2011). It is important to note that the SNAP proteins are unrelated to the t-SNARE SNAP-25 protein. For a schematic illustration of the assembly and disassembly of the SNARE complex, please refer to Figure 1.8.

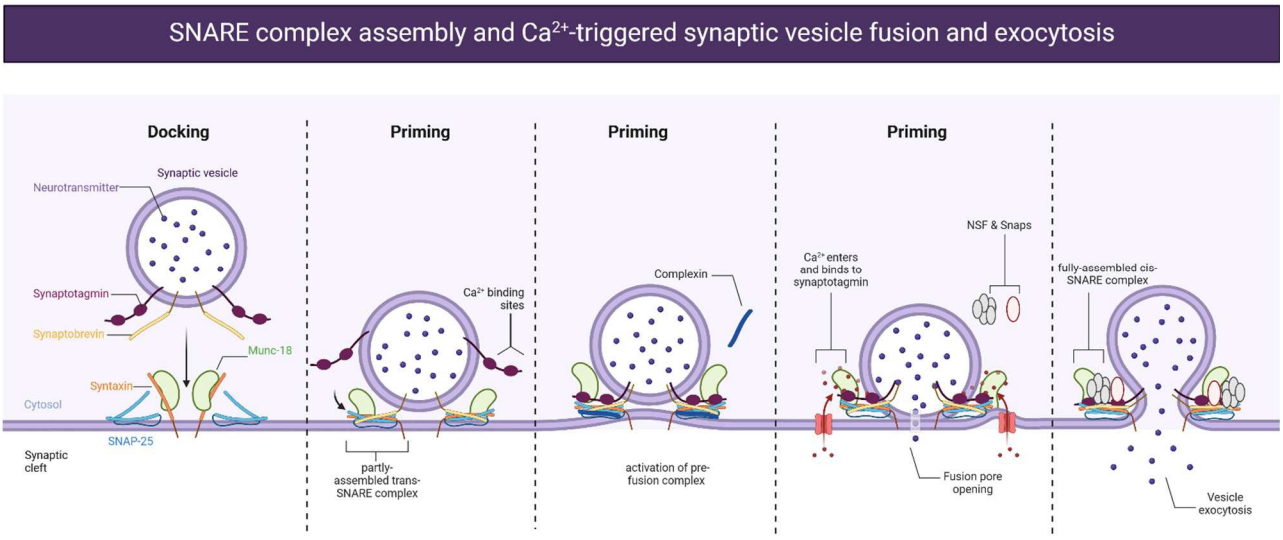


Figure 1.8. SNARE complex assembly and synaptic vesicle exocytosis. The vesicular SNARE protein synaptobrevin plays a crucial role in forming a trans-SNARE complex with the plasma membrane SNARE proteins (syntaxin-1 and SNAP-25) during the priming phase of neurotransmitter release. The closed conformation of syntaxin-1, characterized by its H_{abc} domain being concealed within the SNARE motif, inhibits SNARE assembly. This assembly is only facilitated when syntaxin-1 adopts an open conformation. Munc18-1 alters its binding interaction with syntaxin-1 as it transitions into the open state during the formation of the SNARE complex by engaging with the syntaxin-1 N-peptide within the assembling trans-SNARE complexes. Following the establishment of the trans-SNARE complex, complexin further enhances the priming process. The opening of the fusion pore is mediated by calcium ions, which bind to synaptotagmin, allowing it to subsequently interact with the SNARE proteins. Upon the opening of the fusion pore, the NSF and SNAP ATPases disassemble the resulting cis-SNARE complexes. This process enables the recycling of vesicles, which are then replenished with neurotransmitters for subsequent vesicle release. Created with BioRender based on (Südhof, 2013).

1.3.3. Knockout models of SNARE proteins with special attention to Snap25

1.3.3.1. Synaptobrevins/VAMPs

The consequences of interfering with synaptic vesicle fusion and neuroexocytosis have been examined using various animal models targeting canonical elements of the presynaptic machinery. Homozygous deletion of the synaptobrevin-2/VAMP2 gene led to perinatal mortality in mice, with mutants exhibiting a distinctly altered body shape. Defects in exocytic processes in endocrine cells and adipocytes may underlie the marked body alterations (Schoch et al. 2001). The widespread presence of the two isoforms of synaptobrevins in the murine central and peripheral nervous systems (Raptis et al. 2005) predicts severe developmental defects in VAMP2 mutants; however, VAMP2-deficiency did not result in neurodegeneration, and the formation of brain structures remained intact (Schoch et al. 2001). While the VAMP2 knockouts exhibited attenuated spontaneous vesicle and sucrose-mediated fusion, fast Ca^{2+}-triggered vesicle release was impaired the most (Schoch et al. 2001).

1.3.3.2. Syntaxins

Of the 15 mammalian syntaxins identified to date, syntaxins 1A, 1B, 2, 3, and 4 are found on the plasma membrane, while the spliced isoforms of syntaxin 1 are primarily restricted to the presynaptic membrane (Teng et al. 2001). The chromosomal location of HCP-1/ Syntaxin-1A gene (7q11.23) corresponds to the region typically deleted in Williams-Beuren syndrome. Loss-of-function (LOF) experiments in *Drosophila* have proven that syntaxin-1 is critical for embryonic viability, as mutants are not viable due to severe defects in the secretory system and the complete cessation of evoked vesicle release (Schulze et al. 1995). Contrary to the invertebrate null mutants, homozygous syntaxin-1 KO mice are viable, develop normally, and are indistinguishable from the control littermates (Fujiwara et al. 2006). Mishima et al (2012) showed that the secretion of catecholamines in the hippocampus in syntaxin-1A mice was disrupted owing to the perturbation in synaptic vesicle

exocytosis (Mishima et al. 2012). This emphasises the function of syntaxin-1A in catecholaminergic neurotransmission and synaptic plasticity besides exocytosis.

Stx1A/1B conditional double-knockout (cDKO) neuron cultures revealed the complete abolition of both spontaneous and evoked neurotransmitter release in the absence of syntaxin-1, demonstrating that synaptic vesicle priming and fusion are entirely dependent on syntaxin-1 (Vardar et al. 2016). For an overview of the molecular functions of syntaxin-1A and associated disorders, please refer to Table 1.1.

SPLICED ISOFORM	GENE INTER-ACTIONS	MOLECULAR FUNCTIONS	TISSUE-SPECIFIC EXPRESSION (mRNA expression, human)	TISSUE-SPECIFIC EXPRESSION (PROTEIN expression, human)	ASSOCIATED DISORDERS	References
HPC-1/ Syntaxin 1A	STXBPI KCNB1 SYTL4 SLC6A4 SYT6 SYT8 VAMP8 SNAP23 SNAP25	Ca^{2+}-dependent exocytosis and endocytosis; regulation of neurotransmitter release; docking and fusion of vesicles with the presynaptic plasma membrane, may be required for neural survival and development; hormone exocytosis (insulin and glucagon-like peptide)	multiple areas of the central nervous system (cortex, olfactory bulb, hippocampal formation, caudate putamen, thalamus, white matter tracts, brainstem, cerebellum, spinal cord, pituitary gland), neuroendocrine cells, sensory organs, intestine, pancreas	frontal cortex, immune cells, including NK cells, B-lymphocytes CD8 T cells, spinal cord, retina, colon, pancreas, Islet of Langerhans prostate	STX1A gene hemizygously deleted in patients with William-Beuren syndrome, abnormal neuropsychological features, sensory perturbations disruptions in serotonergic and dopaminergic systems exhibited by STX1A KO mice seen in autistic and schizophrenic patients	(Fujiwara et al., 2010) (Fujiwara et al., 2006) (Mishima et al., 2012) (Ruiz-Montasell et al., 1996) (Gerber et al., 2008) GeneCards

Table 1.1. Summary of the molecular functions, tissue-specific expression (human), and associated disorders of syntaxin-1A.

1.3.3.3. Munc18-1 and Munc13-1

Munc18-1, a member of the SM protein family that includes Sec1/Munc18, Sly1, Vps33, and Vps45, was first believed to be an upstream negative regulator of neurotransmission that prevented the ternary complex from assembling by modulating the closed confirmation of syntaxin-1 (Jahn 2000; Archbold et al. 2014). However, it has become clear that Munc18-1 is an indispensable element of the SNARE fusion machinery. It has a vital role in the secretion of neurotransmitters from presynaptic nerve terminals as well as the release of large dense-core vesicles from neuroendocrine cells, thereby regulating vesicle fusion and docking (Rizo and Südhof 2012; Voets et al. 2001; Toonen et al. 2006). Regarding the three mammalian Munc18 isoforms (Munc18-1, Munc18-2, and Munc18-3), Munc18-1 is the predominant form in the brain and neuroendocrine tissue (Toonen and Verhage 2007). Deletion of Munc18-1 leads to the complete 'silencing' of the brain, where all forms of neurotransmitter secretion are abolished; however, the constitutive non-vesicular release is still potentially present. While the assembly of the neocortex and the formation of synapses proceed without perturbations at embryonic stages, null mutants fail to survive after birth (Verhage et al. 2000). Massive neurodegeneration of multiple brain structures and extensive cell death indicated that the maintenance of synaptic connections absolutely requires neurotransmitter secretion (Verhage et al. 2000). The knockdown of Munc18-1 was found to significantly hinder vesicle transport from the Golgi apparatus to the plasma membrane, as well as impede subsequent membrane fusion both *in vitro* and *in vivo* (Hamada et al. 2017). Similar to Munc18-1 KO mice, mice lacking Munc13-1 are entirely paralysed at birth and die instantly. The synapses at the neuromuscular junction (NMJ) demonstrated a reduced quantity of fusion-competent vesicles in the absence of Munc13-1. Additionally, there was an observed increase in spontaneous quantal acetylcholine release, along with notable morphological irregularities (Varoqueaux et al. 2005).

1.3.3.4. Synaptosomal-associated protein of 25 kDa

1.3.3.4.1. Alternative splicing of Snap25 results in two isoforms

The sole component of the SNARE machinery without transmembrane domains is the soluble Snap-25 protein, which is bound to the presynaptic membrane by palmitoylation of centrally located cysteine residues (Veit et al. 1996). Snap-25a and Snap-25b originate from the same gene, *Snap-25*, through alternative splicing of exon 5, with only nine amino acids out of 206 amino acids being distinct between the two isoforms (Bark and Wilson 1994). The differing amino acid sequences and the different configurations of the cysteine residues may endow the two Snap-25 isoforms with distinct functional properties. This is supported by overexpression studies of the two splice variants, where Snap25-b overexpression in adrenal chromaffin cells not only rescued Ca^{2+}-triggered exocytosis, but also increased the pool size of the releasable vesicles greater than Snap25-a rescue experiments (Sørensen et al. 2003). The generation of *Snap25*-b deficient mice, in which a second Snap-25a copy was introduced to replace the SNAP-25b segment within the *Snap25* gene, resulted in developmental anomalies and the occurrence of spontaneous seizures (Johansson et al. 2008). These findings have shown that the two variants are not functionally redundant and may have distinct roles in mediating vesicle fusion events. Snap-25a and Snap-25b display unique regional and age-related expression patterns. Snap25-a is the predominant splice variant during embryonic and early postnatal development; however, Snap25-b becomes the predominantly expressed isoform beyond the first week of development in the mouse brain (Bark et al. 1995). Interestingly, deep cortical layers still expressed low but measurable levels of Snap-25a mRNA in the adult brain (Bark et al. 1995). The shift in the expression of Snap-25 isoforms from development to adulthood has also been established in the human brain (Prescott and Chamberlain 2011).

1.3.3.4.2. Global deletions of Snap25 are perinatally lethal

The generation of *Snap25* mutant mice demonstrated that while fetal development appears to remain unaffected and action potential (AP)-independent vesicle release persists in the absence of *Snap25*, homozygous deletion of this gene is perinatally lethal and *Snap25*-deficient mice ultimately die of respiratory failure at birth (Washbourne et al. 2002). The *Snap25* null mutants did not exhibit compensatory alterations in the levels of other presynaptic proteins or an increase in the non-neuronal homologous protein Snap-23 (Washbourne et al. 2002). This work has been crucial in demonstrating that spontaneous quantal release can happen even when evoked release completely ceases and that Snap25 is pivotal for AP-dependent synaptic transmission both at CNS synapses and NJMs (Washbourne et al. 2002).

The *in vitro* and *in vivo* deletion of Snap25 reflected the phenotype of animals deficient in Munc18-1. In both mutants, fetal development itself occurs without aberrations; however, apparent normal brain development is followed by severe neurodegeneration and neuromuscular defects (Delgado-Martínez et al. 2007; Verhage et al. 2000). Hippocampal and striatal neuron cultures obtained from *Snap25* null mutants have shown that the elimination of evoked vesicle release impedes neuronal survival and axonal branching, without affecting synapse formation (Delgado-Martínez et al. 2007). Interestingly, decreased neurite branching, survival, and the cessation of AP-triggered neurotransmitter release in *Snap-25*$^{-/-}$ neurons were restored by not only the two splice variants of Snap25 but also by Snap23 (Delgado-Martínez et al. 2007). Snap25 seems to be dispensable for synaptogenesis and axonal outgrowth, given that the topography of thalamocortical projections, their conduction of APs, and the invasion of the cortical plate, were found to be intact in *Snap25*-deficient embryonic brains (Molnár et al. 2002).

1.3.3.4.3. Conditional deletions of Snap25 from deep-layer projection neurons

Conditional silencing of various subsets of excitatory cortical projection neurons has revealed that eliminating AP-dependent vesicle release can influence various functions ranging from myelination to synapse maturation. The *Rbp4-Cre;Ai14;Snap25*$^{fl/fl}$ and the *Ntsr1-Cre;Ai14;Snap25*$^{fl/fl}$ conditional knockout mice (cKO) selectively disrupt Ca^{2+}-dependent neurotransmission in subsets of layer 5 and layer 6 neurons (Figure 1.9), respectively, while leaving spontaneous vesicle release intact (Hoerder-Suabedissen et al. 2019; Washbourne et al. 2002). The validation of the *Snap25* cKO models and the absence of regulated vesicular release using synaptophysin-pHluorin fluorescence have been previously described in Supplementary Figure 2. in (Hoerder-Suabedissen et al. 2019).

The genetic silencing of Ntsr1-Cre+ and Rbp4-Cre+ neurons did not influence the initiation of myelination. However, in the absence of *Snap25*, layer 6 neurons exhibited reduced levels of myelination, and the mutant M1 region contained a diminished number of mature oligodendrocytes (Korrell et al. 2019). Since alterations in myelin basic protein (MBP) levels were exclusive to Ntsr1-Cre+-silenced neurons, the abolition of regulated vesicle release has differing effects on subtypes of layer 5 vs layer 6 projection neurons. Silencing subsets of Rbp4-Cre+ neurons also revealed that the presence of regulated vesicle release is fundamental to the maturation of the specialised synapses of L5 corticothalamic projection neurons in the posterior thalamic nucleus (PO) (Hayashi et al. 2021). In the absence of *Snap25*, the giant boutons of layer 5 neurons are devoid of the excrescences of Po dendrites (Hayashi et al. 2021). Remarkably, layer 5 seems to play an important part in the regulation of sleep-wake cycles. *Snap25*-ablated mice exhibit atypical sleep architecture, characterised by extended periods of wakefulness and diminished slow-wave activity following sleep deprivation (Krone et al. 2021). Recent evidence indicates that chemogenetic and reversible silencing of Rbp4-Cre+ neurons resulted in an increase in synaptic density and a decrease in microglial reactivity while maintaining parvalbumin interneuron density (Vadisiute et al. 2024). Loss of synaptic transmission from subsets of layer 5 neurons seems to be dispensable for interneuron development, but ablation

of *Snap25* redistributes the laminar arrangement of PV+ neurons within S1 in the adult brain (Szabó et al. 2024). Please see Table 1.2. for a summary of the molecular, electrophysiological, and behavioural phenotypes of the *Snap25*, *VAMP2*, and *syntaxin-1A* knockout mice.

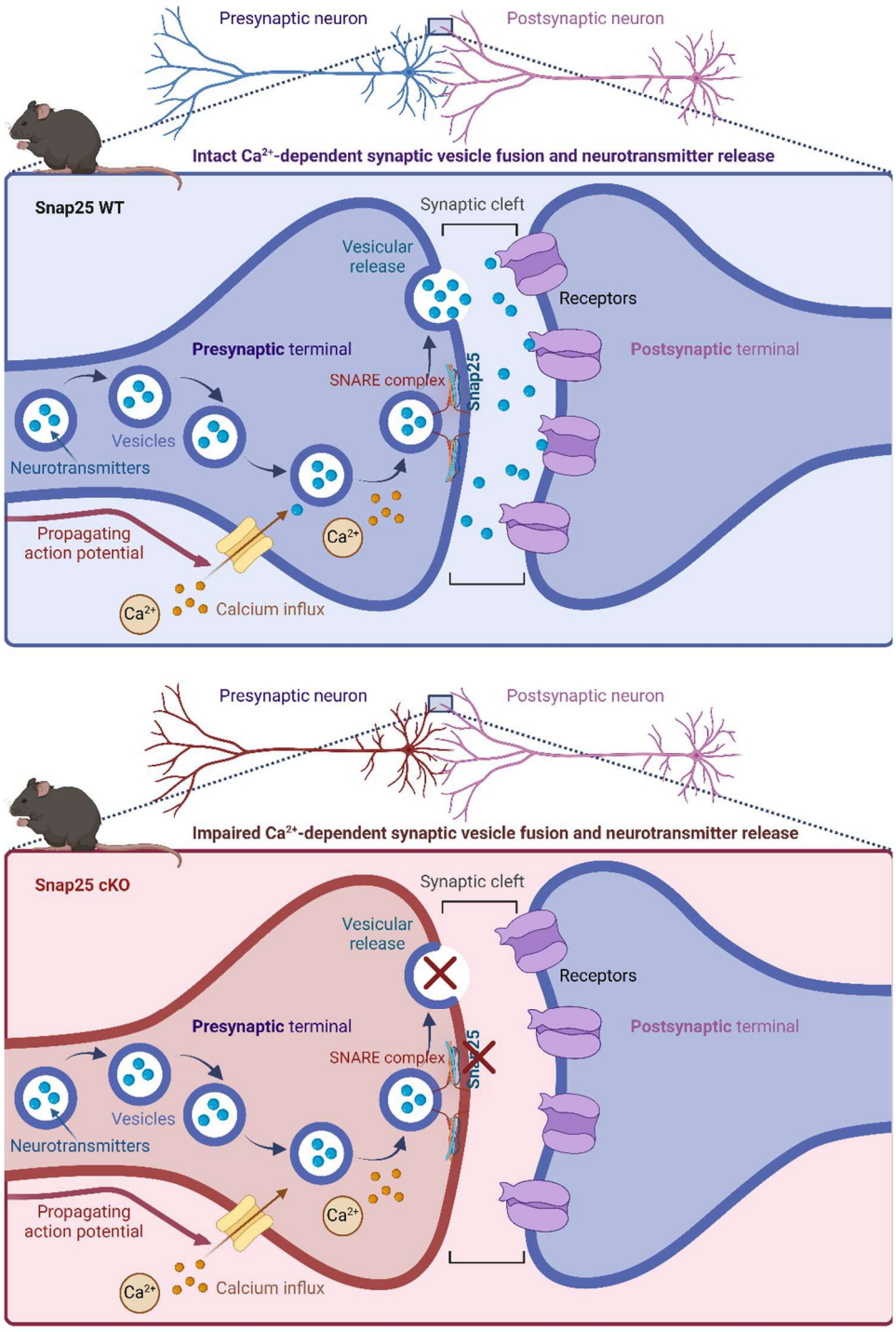


Figure 1.9. Action-potential-dependent neurotransmission and synaptic vesicle exocytosis in wild-type and *Snap25*-ablated mice. Genetic ablation of *Snap25* impairs action potential-dependent neurotransmission and abolishes regulated vesicle release, thereby impeding synaptic transmission between the pre-and postsynaptic neurons. Using the Cre-loxP system, conditional ablation of *Snap25* can be achieved in selected populations of neurons, which allows for the selective 'silencing' of the cells of interest. Created with BioRender.

KO animal models	SNAP25 KO	SNAP25 cKO (Rbp4-Cre;Snap25$^{fl/fl}$)	VAMP2/ Synaptobrevin-2	Syntaxin-1A
Protein cleaved by clostridial neurotoxins	Yes	Yes	Yes	Yes
Neurotoxin type and subtype	BoNT/A BoNT/C & BoNTC/D BoNT/E	BoNT/A BoNT/C & BoNTC/D BoNT/E	BoNT/F_5, FA BoNT/D BoNT/DC BoNT/G BoNT/B_1 TeNT	BoNT/C & BoNTC/D
Mechanisms of synaptic transmission affected	AP-independent, spontaneous NT release intact. AP-dependent, Ca2+-evoked NT release was completely abolished	spontaneous synaptic vesicular release remains intact, AP-evoked NT release is abolished, but residual NT release is detected.	low level of spontaneous NT sustained, AP-dependent regulated NT release abolished	both spontaneous and evoked neurotransmitter release remain intact, normal basal synaptic transmission
Homozygous mutant phenotype	embryonic lethal (possibly due to respiratory failure)	Offspring are viable	perinatal lethal, VAMP2-/- die immediately after birth	null mutant HPC-1/syntaxin 1A KO mice are viable and fertile

Gross morphological changes	Snap25$^{-/-}$ fetuses are smaller in size, lack of sensorimotor reflexes, vascular skin abnormality (hyperemic blotches)	overt differences in body weight in adult SNAP25-cKO animals, hindlimb claps observed in cKO mice over 30 weeks of age	newborn KO mutants have a characteristic rounded appearance with a shoulder hump and brown fat accumulation in upper back	no differences measured in body weight gain between KO and WT mice, mutants have similar appearance to the wild type, normal body growth in KO animals
Levels of synaptic proteins	No major differences observed in SNAP23 levels and levels of other presynaptic proteins in Snap25−/− embryos	no data available	no signal for synaptobrevin-1 and cellubrevin in immunoblots, no noticeable changes in the expression of other synaptic proteins	protein expression of other plasma membrane localising syntaxins (syntaxin 2, syntaxin 3, or syntaxin 4) remains unchanged, syntaxin 1B and protein levels of SNAP-25, VAMP-2 synaptotagmin e, and Munc-18/nSec-1 are unaffected
Brain development	normal brain development (neocortex, hippocampus, thalamus, midbrain develops normally), normal developmental trajectories of cortical and thalamic	normal development of axonal projection pathways and innervation density in silenced cKO brains until P21, signs of axonal fragmentation in mutants appear over 3 weeks of age	No developmental changes or brain abnormalities were detected in knockout mice	brain development intact in KO mice, with normal morphological appearance of the hippocampus and the cerebral cortex; neither synaptic structure nor the number of

	axons in null mutants			synaptic vesicles in presynaptic terminals was affected in mutants
Signs of degeneration	accumulation of vesicles in null mutants, immature synapses observed in Snap25 KO mice in vitro and in vivo, similar cell density in KO and WT fetal brains, no cell loss reported	axon disintegration detected from P21, axonal degeneration affecting other deep-layer cortical cell populations, neurodegeneration not followed by apoptosis, and accumulations of autophagosome/lysosome-like vacuoles in Rbp4-Cre;SNAP25-cKO mutants	no signs of neurodegeneration or axonal fragmentation, but increased dendritic branching and synaptic density were recently reported along with an increase in immature spines in mutants	No signs of neurite degeneration documented, synaptic structures syntaxin- 1A KO mice are unaffected, mutant hippocampus has the same number of docked vesicles and shows similar distribution of presynaptic vesicles and postsynaptic densities when compared to ctrl
Electro-physiological phenotype	mEPSCs detected in SNAP-25-deficient hippocampal neurons, amplitude of mEPSCs normal, but a decrease in frequency in cell cultures	no reduction in the amplitude of excitatory and inhibitory spontaneous synaptic events, but reduced frequency of mEPSCs and mIPSCs	impaired hypertonic sucrose-mediated and spontaneous synaptic vesicle fusion, only rare and erratic spontaneous events recorded in mutant hippocampal neurons, fast Ca2+-evoked fusion was	unaltered glutamatergic and GABAergic fast synaptic transmission, but impaired long-term potentiation

	of mutant neurons		significantly impaired in synaptobrevin knockouts	
Behavioural phenotype	SNARE mutants are neonathal lethal, Blind-drunk mice (Bdr) with a missense mutation in SNAP25 are viable, But exhibits signs of ataxia and deficits in sensorimotor gating. Coloboma mice display locomotor hyperactivity	no overt behavioural impairments, but sleep disruptions, increased wakefulness and reduced slow-wave sleep activity documented in layer 5-silenced Rbp4-Cre;SNAP25-cKO mutants	reduced sleep phenotype, deficits in state switching, severe reductions in wake-to-REM phase transitions, no impairments in sensory functions, but impaired working memory	attenuation of latent inhibition, impaired memory consolidation after weak training, decreased performance in novel object exploration, reduced glutamate-induced 5-HT release, and disruption in serotonergic systems
References	(Hess et al., 1992; Jeans et al., 2007; Zoltán Molnár et al., 2002; Washbourne et al., 2002)	(Hoerder-Suabedissen et al., 2019; Krone et al., 2021)	(Banks et al., 2020; Schoch et al., 2001)	(Fujiwara et al., 2006, 2010; Kofuji et al., 2014; Mishima et al., 2012)

Table 1.2. Overview of the main characteristics of animal models with specific SNARE protein deletions. *Snap25*, *VAMP2*, and *syntaxin-1A* knockout mice exhibit distinct molecular, electrophysiological, and behavioural phenotypes.

1.3.3.4.4. Perturbations in Snap25 are associated with symptoms of psychiatric disorders

Contrary to global deletions, cell-specific ablations of *Snap25* have allowed for the investigation of stimulus-dependent neurotransmitter release beyond fetal development *in vivo*. Loss of *Snap25* from forebrain excitatory neurons leads to stereotypical movements, enhanced locomotion, and increased concentration of extracellular glutamate. It not only recapitulated symptoms analogous to schizophrenia but also established a positive correlation between the dysfunction of *Snap25* and neuropsychiatric disorders (Yang et al. 2017). The blind-drunk mouse (Bdr), harbouring a missense mutation in Snap25b in a highly conserved domain, also exhibits a schizophrenic behavioural phenotype characterised by defective sensorimotor gating, perturbed sensory processing, and ataxia (Jeans et al. 2007). This further supports the notion that perturbed exocytosis and germ-line SNARE mutations contribute to the emergence of psychiatric disorders. The presynaptic roles of Snap25, such as regulating synaptic transmission and inhibiting voltage-gated calcium channels (VGCCs), have traditionally been viewed as contributing factors to the development of synaptopathies associated with Snap25. However, it is becoming increasingly clear that Snap25 may also play a role in neuropsychiatric disorders by influencing postsynaptic receptor trafficking, dendritic spine formation, and synaptic plasticity (Antonucci et al. 2016; Pozzi et al. 2008; Fossati et al. 2015). Snap25 could have a dual role: one as a presynaptic SNARE protein that regulates action potential-dependent vesicle release, and the other as a postsynaptic molecule that governs functions independent of exocytosis, including receptor trafficking (Antonucci et al. 2016).

1.3.3.4.5. Does Snap25 control evoked synaptic vesicle exocytosis in GABAergic neurons?

Studies have presented conflicting evidence regarding the localisation of Snap25 within GABAergic synapses and suggested that inhibitory neurons may not utilise Snap25 for stimulus-driven exocytosis. This raised the possibility that distinct molecular mechanisms may regulate synaptic transmission at glutamatergic and GABAergic synapses. The lack of Snap25 colocalisation

with GABAergic markers in the adult rat and mouse hippocampal regions contributed to some of the confusion, showing that mature hippocampal GABAergic synapses appeared to be *Snap25*-deficient. (Verderio et al. 2004; Frassoni et al. 2005). While these studies have acknowledged that a fraction of GABAergic neurons exhibited immunoreactivity for Snap25 in the developing rat hippocampus, the expression of Snap25 diminished as GABAergic neurons matured (Frassoni et al. 2005). However, Tafoya et al (2006) showed evidence for the co-localisation between Snap25 and the presynaptic terminals of mature GABAergic neurons in multiple brain regions, including the cortex, the thalamus, the hippocampus, and the striatum (Tafoya et al. 2006). These findings also revealed that GABAergic neurons, primarily interneurons, in the growing and mature neocortex express the same relative amounts of SNAP-25 isoforms as most cortical excitatory neurons in the adult brain, which express SNAP-25b primarily (Tafoya et al. 2008). Despite the functional GABA-A receptors, no evoked inhibitory postsynaptic responses could be elicited from fetal brain slices derived from *Snap25*-deleted mutants (Tafoya et al. 2006). Evoked GABAergic neurotransmission was observed to be absent in hippocampal cultures with ablated *Snap25* (Bronk et al. 2007). This absence was further associated with significant impairments in vesicular fusion and vesicle recycling at both inhibitory and excitatory nerve terminals (Tafoya et al. 2006; Matteoli et al. 2009). Collectively, these investigations have proven that stimulus-evoked neurotransmitter release is Snap25-dependent both at GABAergic and glutamatergic synapses. This indicates that Snap25 has a ubiquitous role in modulating vesicle trafficking and intracellular membrane fusion.

1.4. Aims of the thesis

Previous studies have demonstrated that perturbations in pyramidal neuron function and number during the critical window of developmental programmed cell death have directly affected the number of GABAergic interneurons, proving that interneuron survival is dependent on pyramidal neuron activity. Similarly, genetic manipulation of the fate of pyramidal neurons has been shown to alter the predetermined projection patterns of principal neurons and redistribute interneuron inputs. (Duan et al., 2020; Fazel Darbandi et al., 2018; Hsu et al., 2012; Kroon et al., 2024; Lodato et al., 2011; Magno et al., 2021; Molyneaux et al., 2005; Sreenivasan et al., 2022; Wester et al., 2019; Wong et al., 2018, 2022; S. J. Wu et al., 2024; Ye et al., 2015; Yook et al., 2019). The development, maturation, and synaptic connections of neurons cannot therefore be solely driven by genetically predetermined mechanisms, and pyramidal neural activity may play an indispensable role in regulating the correct ratio of cortical interneurons in the cerebral cortex.

Drawing upon previous studies, I hypothesised that pyramidal neurons instruct the spatial and laminar distribution of GABAergic interneurons and influence the formation of inhibitory circuits through activity-dependent mechanisms. To test my hypothesis, I genetically manipulated distinct subtypes of deep-layer cortical projection neurons using three different conditional knockout mouse lines. To determine whether infragranular projection neurons regulate the density and distribution of GABAergic interneurons, I selectively deleted *Snap25* from subsets of Rbp4-Cre+ or Drd1a-Cre+ glutamatergic cortical projection neurons in layer 5 and layer 6, respectively. The genetic ablation of *Snap25* abolished evoked neurotransmitter release from subsets of layer 5 and layer 6 neurons and, therefore, chronically silenced these cells. Through the use of Cre driver lines specific to anatomically and functionally diverse subtypes of glutamatergic projection neurons, I was able to clarify how infragranular pyramidal neurons are involved in the layer-specific regulation of interneuron survival and maintenance.

1.4.1. Aims and Objectives of Chapter 3

My primary aim was to assess how GABAergic interneurons were affected by the absence of synaptic transmission from layer 5 projection neurons, both in the vicinity of the somata of the 'silenced' layer 5 neurons as well as in their output regions. Therefore, I differentiated between the *local* and *global* effects of chronically silencing layer 5 projection neurons on GABAergic interneurons. In the first sections of Chapter 3, I investigated the *short*-term effects on parvalbumin interneurons during the early stages of development, followed by the *long*-term effects on parvalbumin neurons and the perineuronal nets (PNNs) in the adult brain. I aimed to elucidate whether the chronic abolition of neurotransmitter release from layer 5 projection neurons altered the laminar distribution of mature parvalbumin neurons and their PNNs. Next, I examined how a different subtype of GABAergic interneuron, i.e., neuropeptide-Y (NPY)-expressing subtype, responded to the chronic cessation of regulated vesicle release from layer 5 pyramidal neurons. This helped me determine whether interneurons originating from the MGE versus the CGE were differentially affected by the absence of synaptic transmission from layer 5. In Figure 1.10., I illustrated the developmental and adult time points when I chose to assess the density and distribution of PV interneurons in layer 5-silenced mice.

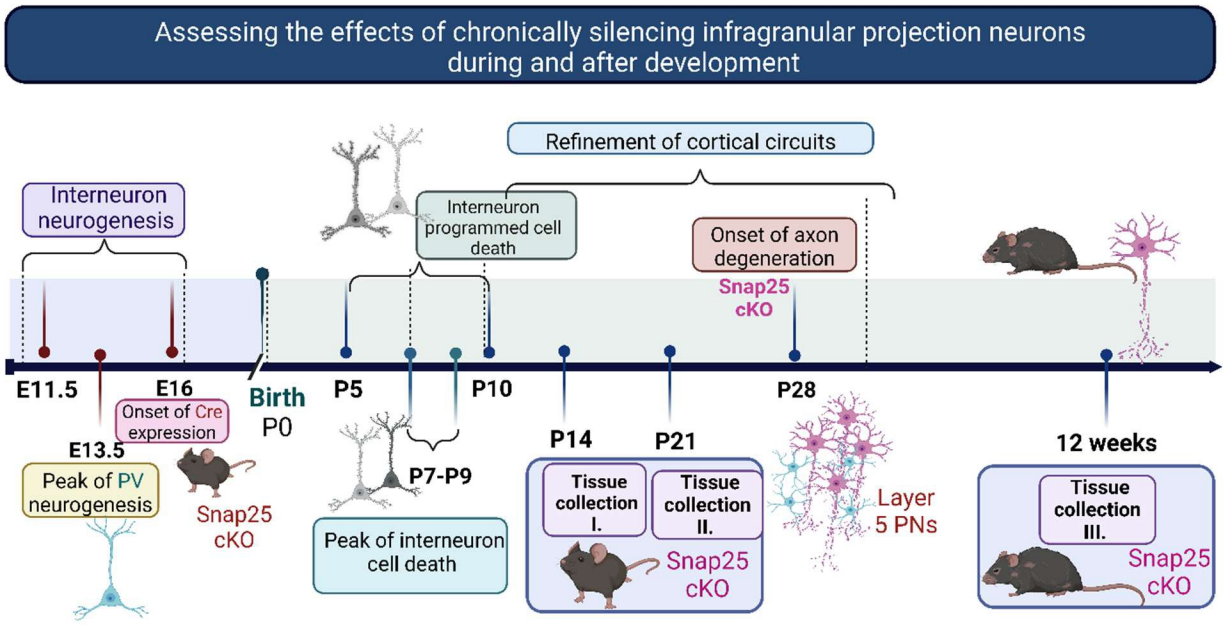


Figure 1.10. Tissue collection time points and the onset of Cre expression in *Rbp4-Cre;Ai14;Snap25$^{fl/fl}$* mice. The effects of silencing Rbp4-Cre+ pyramidal neurons on GABAergic interneurons were investigated both during and after development. Brain tissues were collected at three distinct time points, i.e., postnatal (P) day 14, 21, and 12 weeks of age. First Cre-expressing cells can be detected at E16 in the embryonic cortex (Hoerder-Suabedissen et al. 2019). P28 marks the onset of axon degeneration in *Rbp4-Cre;Ai14;Snap25$^{fl/fl}$* mice. Degenerative events are apparent in multiple brain regions by 3 months. Coloured boxes highlight significant moments in the development of cortical GABAergic neurons during the early embryonic and postnatal stages (e.g., neurogenesis and programmed cell death). Created with BioRender based on (Lim et al. 2018).

1.4.2. Aims and Objectives of Chapter 4

In Chapter 4, I chose to manipulate a distinct subset of deep-layer projection neurons, the Drd1a-expressing corticothalamic projection neurons of layer 6. This enabled me to further investigate how perturbations in anatomically and functionally distinct types of infragranular pyramidal neurons influenced GABAergic interneurons. First, I continued to investigate the MGE-derived interneuron populations and assessed the *short*-term effects on parvalbumin interneurons following the chronic silencing of Drd1a-Cre+ neurons. Specifically, I sought to examine how the density, laminar distribution, developmental trajectory, and morphology of GABAergic neurons were altered in the absence of Ca^{2+}-dependent transmission from layer 6. After examining PV neurons, I shifted my focus to the SST and NPY interneurons. I aimed to ascertain whether distinct interneuron subtypes were more vulnerable to long-term disruptions in deep-layer excitatory neurons.

Previous research has demonstrated that abnormal lamination of MGE-derived interneurons after pyramidal neuron fate transition elicited changes in GABAergic inhibition (Lodato et al. 2011). Therefore, I sought to investigate the ionotropic and metabotropic GABA receptors in the layer 6-silenced mice. In particular, how chronic cessation of evoked vesicle release from *Drd1a-Cre+;Snap25$^{fl/fl}$* neurons influenced the distribution of GABA-A and GABA-B type 1 receptors. I chose to examine a specific subunit of the GABA-A receptor, namely GABA-A δ, that has been shown to be enriched in PV interneurons (Huang et al. 2023). To complement the developmental results, the adult findings were covered in the last section of Chapter 4, where my goal was to determine whether

chronic silencing of a subset of layer 6 cortical projection neurons led to *region*-, *age*-, and *layer*-specific differences in the spatial and laminar distribution of NPY and SST interneurons.

1.4.3. Aims and Objectives of Chapter 5

My major goals in the preceding chapter were to demonstrate the *local* and *global* effects on the MGE- and CGE-derived interneurons in the juvenile and adult brains of *Snap25* cKO mice, where Ca^{2+}-dependent neurotransmission was abolished from subsets of layer 6 projection neurons. However, Chapter 5 does a reverse manipulation of Drd1a-Cre+ neurons. Instead of chronically 'silencing', I chronically 'augmented' Drd1a-Cre+ neurons by deleting the master regulator of the PI3K/AKT pathway. I postulated that the genetic ablation of *Pten* from Drd1a-Cre+ neurons led to a chronic increase in pyramidal cell number, size, and activity. Therefore, it enabled me to investigate the long-term consequences of a defective PI3K/AKT signalling pathway and the impact of *Pten*-deficient Drd1a-Cre+ neurons on GABAergic interneurons. Drawing upon previous findings that pyramidal cells non-autonomously regulate the number and survival of GABAergic interneurons through *Pten* in the developing neocortex (Wong et al. 2018), I set out to examine the following questions:

1) How does the conditional deletion of *Pten* from subsets of Drd1a-Cre+ neurons during postnatal development affect mTOR signalling?

2) Does the loss of *Pten* from Drd1a-Cre+ neurons lead to increased neuronal activity and induce the transcription of immediate early genes in layer 6b?

3) Does the conditional deletion of *Pten* from subsets of Drd1a-Cre+ neurons alter the number, distribution, and projectome of Drd1a-Cre+ neurons in layer 6b?

4) How do distinct subtypes of GABAergic interneurons respond to the deletion of *Pten* from Drd1a-Cre+ neurons?

5) What are the long-term local and global consequences of the loss of *Pten* from Drd1a-Cre+ neurons on PV+, SST+, and NPY+ interneurons?

Hypotheses

Considering the role of *Pten* in inhibiting the PI3K/AKT/mTOR pathway and regulating cell survival, I hypothesized that the conditional deletion of *Pten* from Drd1a-Cre+ neurons would lead to the constitutive activation of the PI3K/AKT/mTOR pathway. This would further result in abnormal growth, neuronal hypertrophy, and an aberrant number of Drd1a-Cre+ pyramidal neurons in layer 6b. If the genetic removal of *Pten* perturbs subplate cell death and leads to an altered number of Drd1a-Cre+ neurons in the neocortex, then interneurons are expected to be altered as well to match the number of excitatory neurons. Otherwise, an improper ratio of glutamatergic and GABAergic neurons would lead to an imbalance in excitation and inhibition, which is critical to the proper functioning of neuronal networks in the cortex. Therefore, I postulated that the loss of *Pten* from subsets of pyramidal neurons in layer 6b and layer 6a would have permanent consequences on the number and morphology of Drd1a-Cre+ neurons as well as the distribution of cortical interneurons in the cerebral cortex.

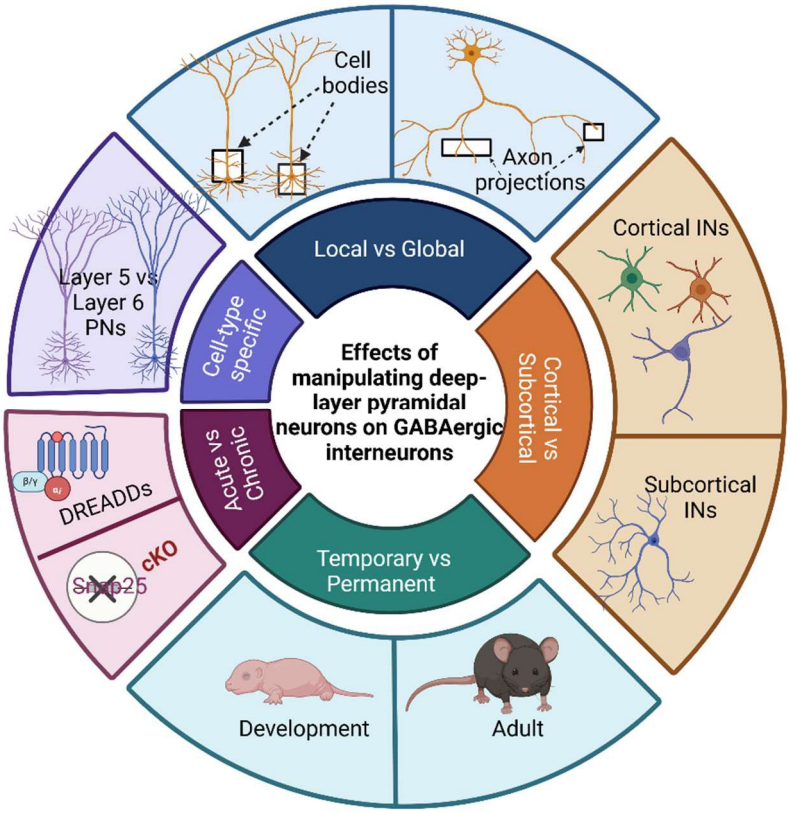


Figure 1.11. Overview of the effects of deep-layer pyramidal neuron manipulations on GABAergic interneurons examined in the thesis. *Local* versus *global* effects refer to examining interneurons near the cell bodies versus in the long-range projection regions of glutamatergic neurons. *Cortical* versus *subcortical* refers to distinct subtypes of interneurons within the neocortex versus outside the neocortex. *Temporary* versus *permanent* effects distinguish between interneurons investigated during development versus adulthood. *Acute* versus *chronic* manipulation distinguishes between short-term versus long-term effects using DREADDs or genetic deletions. *Cell-type specific* effects differentiate between silencing layer 5 versus layer 6 glutamatergic projection neurons.

Chapter 2 .....Methods

2.1. Breeding and maintenance of transgenic mice

All experimental procedures were conducted under project and personal license authority in compliance with the Animals (Scientific Procedures) Act 1986 in the Biomedical Services (BMS, University of Oxford), following local animal care and welfare regulations. Animals were kept on a 12-hr light/12-hr dark cycle, and food and water were available *ad libitum*. Transgenic mice with a genetic ablation in the synaptosomal-associated protein 25 kDa (SNAP25) gene (*B6-Snap25tm3mcw* (*Snap25*-flox)) were used to engineer cell-type-specific conditional knockout strains enabling the selective abolition of Ca^{2+}-dependent neurotransmitter release from subsets of infragranular projection neurons. The generation and characterisation of the *Rbp4-Cre+;Ai14;Snap25$^{fl/fl}$* mice and the validation of the absence of regulated vesicle release have previously been described (Welch et al., 2000; Marques-Smith et al., 2016; Gustus et al., 2018; Hoerder-Suabedissen et al., 2019; Korrell et al., 2019, Hayashi et al., 2021; Krone et al., 2021).

2.2. Cell-type specific deletion of *Snap25* from subsets of deep-layer glutamatergic projection neurons

To abolish regulated synaptic vesicle release from subsets of deep-layer glutamatergic projection neurons, homozygous B6-Snap25tm3mcw (*Snap25$^{fl/fl}$*) mice were first crossed to *B6;129S6-Gt(ROSA)26Sortm14(CAG-tdTomato)Hze/J*(Ai14) reporter mice. The homozygous *Snap25$^{fl/fl}$;Ai14* mice were then crossed to bacterial artificial chromosome (BAC) Cre-recombinase driver lines, *Tg(Rbp4-cre)KL100Gsat/Mmucd* (Rbp4-Cre; Jackson Laboratories) or *Tg(Drd1a-cre)FK164Gsat/Mmucd* (Drd1a-Cre), suitable for the cell-type-specific targeting of layer 5 or layer 6b pyramidal neurons, respectively. For the layer 5-silenced studies, *Rbp4-Cre/+;Snap25$^{fl/+}$;Ai14* female mice were crossed to *Snap25$^{fl/fl}$;Ai14* males to generate conditional homozygous *Rbp4-*

Cre+;Ai14;Snap25$^{fl/fl}$, *Rbp4-Cre-;Ai14;Snap25*$^{fl/+}$, and *Rbp4-Cre-;Ai14;Snap25*$^{fl/fl}$ mice (Figure 2.1.) For the layer 6-silenced studies, *Drd1a-Cre/+;Snap25*$^{fl/fl}$*;Ai14* female mice were crossed to *Snap25*$^{fl/fl}$*;Ai14* males to generate conditional homozygous (*Drd1a-Cre+;Ai14;Snap25*$^{fl/fl}$) mice. *Drd1a-Cre-;Ai14;Snap25*$^{fl/fl}$ were used as control animals. Note that the control mice lack tdTomato expression; therefore, no red fibres are visible in the layer 5 and layer 6 control animals. Both male and female mice were used throughout the thesis. The breeding strategy is illustrated in Figure 2.1.

DPhil thesis				CHAPTER 3		CHAPTER 4		CHAPTER 5	
Data summary				Layer 5-silenced (*Rbp4-Cre;Ai14;Snap25*$^{fl/fl}$)		Layer 6b-silenced (*Drd1a-Cre;Ai14;Snap25*$^{fl/fl}$)		Layer 6b-enhanced (*Drd1a-Cre;Ai9;PTEN*$^{fl/fl}$)	
Theme	Cells of interest	Cohort	Age	Number of brains					
				ctrl	cKO	ctrl	cKO	ctrl	cKO
INTER NEURONS	PV VVA	Developmental	P14	3	3	N.A.		N.A.	
			P21	4	4	5	5		
		Adult	12 wks	5	5	5	5	4	4
	SST	Developmental	P21	N.A.		5	5	N.A.	
		Adult	12 wks	5	5	5	5	4	4
	NPY	Developmental	P21	N.A.		5	5	N.A.	
		Adult	12 wks	5	5	5	5	4	4
GABA receptors	GABA-B R1	Developmental	P21	N.A.		5	5	N.A.	
	GABA-A δ					5	5		
PYRAMIDAL NEURONS	Drd1a	Developmental	P21	N.A.		5	5	N.A.	
		Adult	12 wks			5	5	4	4

Table 2.1. Overview of the cell types, time points, and number of *brains* analysed for each Results chapter.

DPhil thesis				CHAPTER 3		CHAPTER 4		CHAPTER 5	
Data summary				Layer 5-silenced (*Rbp4-Cre;Ai14;Snap25$^{fl/fl}$*)		Layer 6b-silenced (*Drd1a-Cre;Ai14;Snap25$^{fl/fl}$*)		Layer 6b-enhanced (*Drd1a-Cre;Ai9;PTEN$^{fl/fl}$*)	
Theme	**Cells of interest**	**Cohort**	**Age**	**Number of slices**					
				ctrl	**cKO**	**ctrl**	**cKO**	**ctrl**	**cKO**
INTER NEURONS	**PV VVA**	Developmental	P14	4	4	N.A.		N.A.	
			P21	4	4	4	4		
		Adult	12 wks	3-4	3-4	3	3	3	3
	SST	Developmental	P21	N.A.		3	3	N.A.	
		Adult	12 wks	3	3	3	3	3	3
	NPY	Developmental	P21	N.A.		3	3	N.A.	
		Adult	12 wks	3	3	3	3	3	3
GABA receptors	**GABA-B R1**	Developmental	P21	N.A.		3	3	N.A.	
	GABA-A δ					3	3		
PYRAMIDAL NEURONS	**Drd1a**	Developmental	P21	N.A.		3	3	N.A.	
		Adult	12 wks			3	3	3	3

Table 2.2. Overview of the cell types, time points, and number of *sections* analysed for each Results chapter.

	CHAPTER 3		CHAPTER 4		CHAPTER 5
	Regions of interest (ROIs)				
Strain	**Layer 5-silenced** *(Rbp4-Cre;Ai14; Snap25$^{fl/fl}$)*		**Layer 6b-silenced** *(Drd1a-Cre;Ai14; Snap25$^{fl/fl}$)*		**Layer 6b-enhanced** *(Drd1a-Cre;Ai9; Pten$^{fl/fl}$)*
Cohort	**Develop mental**	**Adult**	**Develop mental**	**Adult**	**Adult**
Parvalbumin	M1 S1 Striatum GPe MD LP SC Dentate gyrus CA3	M1 S1 Striatum GPe MD LP SC TRN Dentate gyrus CA3	M1 S1 PFC (ACAd, ACAv) Striatum GPe TRN	M1 S1 dense S1 sparse PFC (ACAd, ACAv) Striatum GPe TRN	M1 S1 dense S1 sparse PFC (ACAd, ACAv) Striatum GPe TRN

	CHAPTER 3	CHAPTER 4	CHAPTER 5
	Regions of interest (ROIs)		
Strain	**Layer 5-silenced** *(Rbp4-Cre;Ai14; Snap25$^{fl/fl}$)*	**Layer 6b-silenced** *(Drd1a-Cre;Ai14; Snap25$^{fl/fl}$)*	**Layer 6b-enhanced** *(Drd1a-Cre;Ai9; Pten$^{fl/fl}$)*
Cohort	**Adult**	**Adult**	**Adult**
***Vicia villosa* agglutinin**	M1 S1 Striatum CA3 Dentate gyrus	M1 S1 dense PFC (ACAd, ACAv)	M1 S1 dense PFC (ACAd, ACAv) Striatum

Table 2.3. Summary of the regions of interest selected for parvalbumin interneurons and *Vicia villosa* agglutinin cells. Columns indicate the regions of interest where parvalbumin and *Vicia villosa* agglutinin were analysed in each strain and each time point.

	CHAPTER 3	CHAPTER 4		CHAPTER 5
	Regions of interest (ROIs)			
Strain	**Layer 5-silenced** *(Rbp4-Cre;Ai14; Snap25$^{fl/fl}$)*	**Layer 6b-silenced** *(Drd1a-Cre;Ai14; Snap25$^{fl/fl}$)*		**Layer 6b-enhanced** *(Drd1a-Cre;Ai9; Pten$^{fl/fl}$)*
Cohort	**Adult**	**Developmental**	**Adult**	**Adult**
Neuropeptide-Y	M2 M1 S1 PFC (ACAd, ACAv) Striatum CA1 CA3 Dentate gyrus	M2 M1 S1 PFC (ACAd, ACAv) Striatum CA1 CA3 Dentate gyrus	M2 M1 S1 PFC (ACAd, ACAv) Striatum CA1 CA3 Dentate gyrus	M2 M1 S1 PFC (ACAd, ACAv) Striatum CA1 CA3 Dentate gyrus

	CHAPTER 3	CHAPTER 4		CHAPTER 5
	Regions of interest (ROIs)			
Strain	**Layer 5-silenced** *(Rbp4-Cre;Ai14; Snap25$^{fl/fl}$)*	**Layer 6b-silenced** *(Drd1a-Cre;Ai14; Snap25$^{fl/fl}$)*		**Layer 6b-enhanced** *(Drd1a-Cre;Ai9; Pten$^{fl/fl}$)*
Cohort	**Adult**	**Develop mental**	**Adult**	**Adult**
Somatostatin	CA1 CA3 Dentate gyrus	Striatum CA1	Striatum CA1 CA3 Dentate gyrus	M1 S1 PFC (ACAd, ACAv) Striatum CA1 CA3 Dentate gyrus

Table 2.4. Summary of the regions of interest selected for neuropeptide-Y and somatostatin interneurons. Columns indicate the regions of interest where neuropeptide-Y and somatostatin interneurons were analysed in each strain and each time point.

	CHAPTER 4		CHAPTER 5
	Regions of interest (ROIs)		
Strain	**Layer 6b-silenced** *(Drd1a-Cre;Ai14;Snap25$^{fl/fl}$)*		**Layer 6b-enhanced** *(Drd1a-Cre;Ai9;Pten$^{fl/fl}$)*
Cohort	**Developmental**	**Adult**	**Adult**
Drd1a	M1 S1	M1 S1 dense S1 sparse	M1 S1 dense S1 sparse

Table 2.5. Summary of the regions of interest selected for Drd1a-Cre+ projection neurons. Columns indicate the regions of interest where Drd1a-Cre+ neurons were analysed in each strain and each time point.

Effects of manipulating pyramidal neurons on GABAergic interneurons			
Areas of investigation	**Variables**	**Timepoint(s)**	**Effect**
Genotype	cKO vs ctrl	P14 P21 3 months	*Cell density*
Age	Development vs Adult	P14 to P21 P21 to 3 months	*Cell development/trajectory*
Layers	L1 - L6b	P21 3 months	*Laminar density & distribution*
Regions	Cell body vs Projection site	P14 vs P21	*Local vs global effect*
Strains	Projection neuron subtype (L5 vs L6b)	P21 3 months	*Cell-type specific effects*

Table 2.6. Summary of the different types of analyses conducted throughout the DPhil thesis.

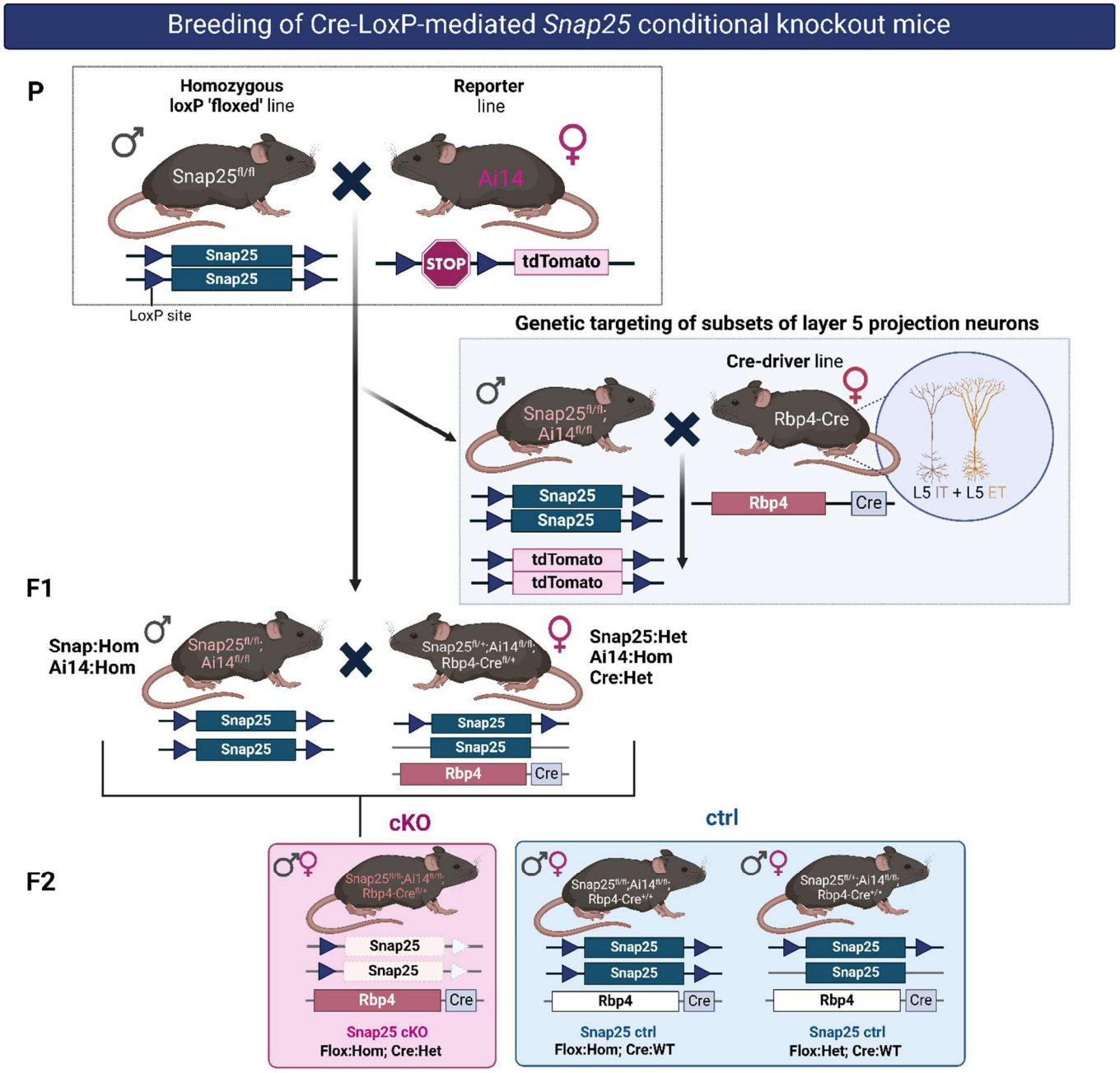


Figure 2.1. Breeding scheme of *Rbp4-Cre;Ai14;Snap25* cKO mice. The first step in the generation of *Rbp4-Cre;Ai14;Snap25* cKO mice was crossing homozygous *Snap25*$^{fl/fl}$ mice with the Ai14 reporter mice. Homozygous *Snap25*$^{fl/fl}$*;Ai14* mice were then crossed to the *Tg(Rbp4-cre)KL100Gsat/Mmucd* driver line. Conditional homozygous (*Rbp4-Cre+;Ai14;Snap25*$^{fl/fl}$) and heterozygous knockout (*Rbp4-Cre+;Ai14;Snap25*$^{fl/+}$) mice were created by crossing *Rbp4-Cre/+;Snap25*$^{fl/+}$*;Ai14* female mice to *Snap25*$^{fl/fl}$*;Ai14* males. Control animals included both *Rbp4-Cre-;Ai14;Snap25*$^{fl/+}$ and *Rbp4-Cre-;Ai14;Snap25*$^{fl/fl}$ mice. Created with BioRender.

2.3. Perfusion fixation and vibratome sectioning

Mice aged P14, P21, and 3 months of age were anaesthetised with an overdose of sodium pentobarbital (60 mg/kg, intraperitoneal injection (i.p.)) and were trans-cardially perfused using ice-cold saline (0.9% NaCl) solution followed by 4% paraformaldehyde (PFA, F8775; Sigma-Aldrich) diluted in 0.1 M phosphate-buffered saline (PBS, pH 7.4). Brains were dissected and postfixed in 4% PFA for 24 hours at 4 ◦C. Following post-fixation, brains were transferred to 0.1 M PBS containing 0.05% sodium azide (PBSA) (Sodium azide ReagentPlus®, S2002-5G, Sigma Aldrich, CAS number: 26628-22-8) and kept at 4 ◦C for long-term storage. Coronal slices of 50 µm thickness were cut from 4.5% agarose-embedded brains using a vibrating microtome (Leica VT1000S; Leica Microsystems, Wetzlar, Germany), and hemisections were collected in 0.1M PBSA in 24-well cell culture plates (CLS3526, Corning® Costar®).

2.4. Genotyping

2.4.1. DNA extraction

The initial step in DNA extraction involved digesting ear clips obtained from mouse pups (P14 and P21) in 200 µl of tissue lysis solution, followed by a three-hour incubation at 55˚C. The tissue lysis buffer consisted of the following reagents: 100 mM Tris-HCl, 5 mM EDTA, 200 mM NaCl, and 0.2% Sodium dodecyl sulfate (SDS). Prior to starting DNA extraction, 100 µg/ml Proteinase K (3115879001, from *Titrirachium album*, expressed in *Pichia pastoris*, lyophilisate, Roche Diagnostics Limited, West Sussex, UK) was added to the tissue lysis buffer to deactivate endogenous RNases and DNases rapidly. Proteinase K was deactivated after tissue digestion by heating the crude extract to 99˚C for 20 minutes.

2.4.2. Polymerase Chain Reaction (PCR)

Following the dilution of 2 µl extracted DNA in 1:10 with nanoH_2O, 1 µl diluted DNA was added to 19 µl PCR mix for Snap25 genotyping. For Cre genotyping, 19.25 µl PCR mix and 0.75 µl crude (undiluted) DNA extract were used per PCR reaction. The PCR mix used for *Snap25* and *Cre* genotyping

per reaction, as well as the reverse and forward primers, is indicated in Table 2.7. and Table 2.8, respectively.

PCR mix for *Snap25* genotyping	
Components	**Amount**
nH_2O	17.3 µl
10x buffer (*without* $MgCl_2$)	2.5 µl
$MgCl_2$	1.5 µl
10 mM dNTPs (deoxyribonucleotide triphosphate)	0.5 µl
20 µM Forward primer	1.0 µl
20 µM Reverse primer	1.0 µl
Platinum™Taq DNA polymerase (ThermoFisher)	0.2 µl
PCR mix for *Cre* genotyping	
Components	**Amount**
nH_2O	17.25 µl
Cre2 Forward primer	1.0 µl
Cre2 Reverse primer	1.0 µl
NEB OneTaq® buffer	10 µl

Table 2.7. PCR mix for Snap25 and Cre genotyping per reaction

Primers for Snap25 genotyping	
LoxP E5a Forward primer	5' CCC TGG GGA ACC ACG GCA GA 3'
LoxP E5a Reverse primer	5' TCC CAG GAA ACA GCA CAG CGT 3'
Primers for Cre genotyping	
Cre2 Forward primer	5' TGG AAA ATG CTT CTG TCC GT 3'
Cre2 Reverse primer	5' CAT CGC TCG ACC AGT TTA GT 3'

Table 2.8. Forward and reverse primers for *Snap25* and *Cre* genotyping

Negative controls were employed for every genotyping to ensure the genotyped samples were free of contamination of the reagents. The cycling conditions for Snap25 and Cre genotyping are illustrated in Table 2.9.

Polymerase Chain Reaction for Snap25 and Cre genotyping			
Steps	**Temperature**	**Length of cycles**	**Repeat**
Initial denaturing	95 ˚C	3 minutes	N.A.
Denaturing	95 ˚C	20 sec	40x cycles
Primer annealing	62 ˚C for Snap25 54 ˚C for Cre	30 sec	
Elongation	72 ˚C	45 sec	
Final elongation	72 ˚C	10 minutes	N.A.

Table 2.9. PCR cycling conditions for Snap25 and Cre genotyping

2.4.3. Gel electrophoresis and gel imaging

Following the amplification of DNA sequences, an agarose gel was made for subsequent gel electrophoresis to separate DNA fragments of varying sizes based on their molecular weight. 1.0 g agarose powder (Sigma-Aldrich) was mixed with TAE buffer containing a mixture of Tris base, acetic acid and EDTA. After the polymerisation of the agarose gel, 4 µl of 6x gel loading dye was added to the PCR mix for Snap25 genotyping. This step was omitted for Cre genotyping, given that the loading dye was already present in the MasterMix solution. Prior to loading the PCR samples (10 µl/well), a molecular weight ladder (100 bp) was loaded into the first well of the agarose gel. Gel electrophoresis was typically conducted at 125 V for around 25 minutes, but running time and voltage varied depending on the number of samples and gel concentration. DNA segments were visualised using a

BioRad Gel Doc Imaging system equipped with an ultraviolet (UV) transilluminator suitable for imaging nucleic acids.

2.7. Histology

2.7.1. General immunohistochemical staining protocol for GABAergic interneurons and GABA receptors

Postnatal and adult brain samples were collected from *Rbp4-Cre;Ai14;Snap25*$^{fl/fl}$ and *Drd1a-Cre;Ai14;Snap25*$^{fl/fl}$ mice at P21 and 3 months of age. For all PTEN-related experiments (Chapter 5), only adult brain samples were available (~3-4 months). Brains that were postfixed for only two hours were also collected for SST immunohistochemistry; however, regular, 24-hour postfixed brains were used after the staining protocol was optimised and an appropriate antibody was found. The postnatal and 3-month-old *Rbp4-Cre;Ai14;Snap25*$^{fl/fl}$ and *Drd1a-Cre;Ai14;Snap25*$^{fl/fl}$ brains were perfused well before performing the SST immunostaining experiments; therefore, only selected subcortical areas with adequate signal and antibody penetration were analysed. For *Drd1a-Cre;Ai9;Pten25*$^{fl/fl}$ brains, all areas were quantified.

For free-floating immunohistochemical staining of GABAergic interneurons and GABA receptors, selected coronal control and knockout sections (3 per ROI) were first washed in 0.1M PBS three times prior to permeabilisation with blocking solution for 2 hours and incubation with primary antibodies overnight at 4˚C. Following that, slices were rinsed in 0.1M PBS three times for ten minutes, incubated for two hours at room temperature (RT) in the dark with Alexa-conjugated fluorescent secondary antibodies, and then washed again in 0.1M PBS before being counterstained with 4,6-diamidine-2-phenylindole dihydrochloride (DAPI). The components and exact concentration of the blocking solution, as well as the primary and secondary antibodies used, are listed in Table 2.10.

2.7.2. Double-labelling parvalbumin interneurons and the perineuronal nets

To study how the abolition of Ca^{2+}-dependent neurotransmission from subsets of layer 5 pyramidal neurons affected interneurons, double histochemistry (HC) was performed to label parvalbumin (PV) interneurons and the perineuronal nets (PNNs) using the *Vicia villosa* agglutinin (VVA) plant lectin. For free-floating PV & VVA double histochemistry, sections were washed three times in 0.1M PBS for 10 minutes. Sections were then permeabilised with a blocking solution containing 2% donkey serum (D9663, Sigma-Aldrich) and 0.2% Triton-X100 (X-100, CAS number: 9002-93-1, Sigma-Aldrich) diluted in VVA buffer for 2 hours at RT before overnight incubation with primary antibody at 4 ◦ C. For Vglut1 staining, 5% goat serum and 0.3% Triton-X100 were used. VVA buffer consisted of 0.01 M PBS, 0.15 M NaCl, and 0.1 mM CaCl2 to reach the minimum Ca^{2+} level required for optimal lectin binding. Rabbit anti-PV (Cat# PV27, RRID:AB_2631173, Swant, Marly, Switzerland) was diluted at 1:5000 for postnatal and 1:500 for adult brains, and the biotinylated VVA lectin (B-1235-2, Vector Laboratories, Burlingame, US) was used at 2 µg/ml concentration and diluted in a blocking solution consisting of 2% donkey serum and 0.2% Triton-X100 diluted in VVA buffer. To ascertain whether Rbp4 or Drd1a/tdTomato-expressing axonal processes and Vglut1-positive synapses colocalise in the striatum, slices were incubated with guinea pig anti-Vglut1 (1:500, EMD Millipore AB5905, lot: 3258729). After rinsing sections three times in 0.1M PBS, slices were incubated with the following secondary antibodies: goat anti-guinea pig Alexa Fluor™ 633 (Invitrogen, A-21105), donkey anti-rabbit Alexa Fluor™ 488 (Invitrogen, A-21206, Thermo Fisher, Waltham, MA USA 02451) at 1:500 and Streptavidin-conjugated Cy5 (Invitrogen, SA1011) at 1:200 for 2 hours at RT. Sections were rinsed twice in 0.1M PBS for 10 minutes and counterstained with DAPI (1:1000 in 0.1M PBS, overnight). Postnatal coronal sections were coverslipped with 0.1M PBS, while adult sections were coverslipped using Prolong™ Gold antifade mountant (P36930, Molecular Probes, Eugene, OR USA 97402). To determine the specificity of the antibody used, control sections were processed following the same steps of histochemistry, but they were incubated only with secondary antibodies. Non-

specific staining was not observed in any samples. When performing single immunofluorescence staining for PV, no VVA buffer was used, and sections were permeabilised with a blocking solution containing 2% donkey serum and 0.2% Triton-X100 diluted in 0.1M PBS for 2 hours.

Strain(s)	Primary antibody	Supplier	Host	Blocking solution	Primary block	Primary dilution	Secondary antibody and dilution
Rbp4-Cre; Ai14; Snap25$^{fl/fl}$ *Drd1a-Cre; Ai14; Snap25$^{fl/fl}$* *Drd1a-Cre; Ai9; Pten$^{fl/fl}$*	anti-**PV** (VVA, Biotinylated)	PV: Swant (PV 27) VVA: Vector Laboratories (B-1235-2)	PV: rabbit VVA: N/A	2% normal donkey serum 0.2% Triton X-100 in VVA buffer	2% normal donkey serum 0.2% Triton X-100 in VVA buffer	PV: (1:5000) P14, P21 PV: (1:500) Adult VVA: 2µg/ml	donkey anti-rabbit Alexa Fluor™ 488 (1:500) (Invitrogen, #A-21206) + VVA Streptavidin Cy5 (1:200) (Molecular Probes, SA1011)
Drd1a-Cre; Ai9;Pten$^{fl/fl}$	anti-**PV** anti-**pS6** Ser235/236	PV: Swant (PV 235) pS6: Cell Signalling (#2211)	PV: mouse pS6: rabbit	5% normal donkey serum 0.3% Triton X-100 in 0.1M PBS	2% normal donkey serum 0.1% Triton X-100 in 0.1M PBS	PV: (1:400) pS6: (1:200)	donkey anti-mouse Alexa Fluor™ 647 (1:200) (Invitrogen, #A-31571) donkey anti-rabbit Alexa Fluor™ 488 (1:500) (Invitrogen, #A-21206)
Rbp4-Cre; Ai14;Snap25$^{fl/fl}$ *Drd1a-Cre; Ai14;Snap25$^{fl/fl}$* *Drd1a-Cre; Ai9;Pten$^{fl/fl}$*	anti-**NPY**	Abcam (ab221145, recombinant)	rabbit	5% normal donkey serum 0.3% Triton X-100 in 0.1M PBS	2% normal donkey serum 0.1% Triton X-100 in 0.1M PBS	(1:2000)	donkey anti-rabbit Alexa Fluor™ 488 (1:500) (Invitrogen, #A-21206)
Rbp4-Cre; Ai14;Snap25$^{fl/fl}$ *Drd1a-Cre; Ai14;Snap25$^{fl/fl}$* *Drd1a-Cre; Ai9;Pten$^{fl/fl}$*	anti-**SST**	Invitrogen Thermofisher, (PA5-82678)	rabbit	5% normal donkey serum 1% Triton X-100 in 0.1M PBS	2% normal donkey serum 0.3% Triton X-100 in 0.1M PBS	1:500 (P21) 1:1000 (Adult)	donkey anti-rabbit Alexa Fluor™ 488 (1:500) (Invitrogen, #A-21206)
Drd1a-Cre; Ai14;Snap25$^{fl/fl}$	anti-**CR**	Swant (6B3)	mouse	5% normal	2% normal	(1:2000)	donkey anti-mouse Alexa Fluor™ 488 (1:500)

				donkey serum 1% Triton X-100 in 0.1M PBS	donkey serum 0.3% Triton X-100 in 0.1M PBS		(Invitrogen, #A-21202)
Drd1a-Cre; Ai14;Snap25$^{fl/fl}$	anti-**GABA-$_A$ δ**	Alomone Labs (AGA-014)	rabbit	5% normal donkey serum 0.5% Triton X-100 in 0.01M PBS	2% normal donkey serum 0.3% Triton X-100 in 0.01M PBS	(1:100)	donkey anti-rabbit Alexa Fluor™ 488 (1:500) (Invitrogen, #A-21206)
Drd1a-Cre; Ai14;Snap25$^{fl/fl}$	anti-**GABA-$_B$ R1**	Merck (AB2256)	guinea pig	10% normal goat serum 0.3% Triton X-100 in 0.1M PBS	5% normal goat serum 0.1% Triton X-100 in 0.1M PBS	(1:200)	goat anti-guinea pig Alexa Fluor™ 488 (1:500) (Invitrogen, #A-11073)
Drd1a-Cre; Ai9;Pten$^{fl/fl}$	anti-**Npas4**	Activity Signaling (NP41-2)	rabbit	5% normal donkey serum 0.3% Triton X-100 in 0.1M PBS	2% normal donkey serum 0.2% Triton X-100 0.1M PBS	(1:250)	donkey anti-rabbit Alexa Fluor™ 488 (1:500) (Invitrogen, #A-21206)
Drd1a-Cre; Ai9;Pten$^{fl/fl}$	anti-**c-Fos**	Synaptic Systems (226 009)	chicken	5% normal donkey 0.3% Triton X-100 in 0.1M PBS	2% normal donkey serum 0.2% Triton X-100 in 0.1M PBS	(1:500)	donkey anti-chicken Alexa Fluor™ 488 (Jackson ImmunoResearch, AB 2340375)
Rbp4-Cre; Ai14;Snap25$^{fl/fl}$	anti-**VGlut1**	EMD Millipore (AB5905)	guinea pig	2% normal donkey	2% normal donkey	(1:500)	goat anti-guinea pig Alexa Fluor™ 633 (Invitrogen, #A-21105)

				0.2% Triton X-100 in 0.1M PBS	0.2% Triton X-100 in 0.1M PBS		
Drd1a-Cre; Ai14;Snap25$^{fl/fl}$	anti-**VGlut1**	Synaptic Systems (135 303)	rabbit	2% normal donkey 0.2% Triton X-100 in 0.1M PBS *72 hrs primary incubation	2% normal donkey 0.2% Triton X-100 in 0.1M PBS	(1:1000)	donkey anti-rabbit Alexa Fluor™ 488 (1:500) (Invitrogen, #A-21206)

Table 2.10. Overview of the primary and secondary antibodies used for immunohistochemistry experiments.

2.8. Image acquisition

2.8.1. Epifluorescence imaging

Low-power photomicrographs (1.6x and 2.5x) representing the location of high-power confocal images (20x) were obtained with an upright widefield Leica fluorescence microscope equipped with a colour camera for brightfield and fluorescence imaging (Leica DMR, DFC 280, HC PL FLUOTAR 2.5x / 0.07). Exposure time was adjusted for each channel. No fluorescent microscope images were used for cell quantification.

2.8.2. Confocal laser-scanning microscopy

Images containing the cortical and subcortical projection regions of Rbp4-Cre+ layer 5 and Drd1a-Cre+ layer 6b projection neurons were acquired with an inverted laser-scanning confocal microscope (Zeiss LSM 710, Germany) equipped with the following laser lines: Diode (405 nm), Argon laser (458, 488, 514 nm), Diode-Pumped Solid-State (DPSS, 561nm), Helium-Neon (633nm). High-resolution confocal images for interneuron quantification (PV, NPY, SST, CR) were acquired

using an EC Epiplan-Apochromat 20x (0.80 NA) dry objective at 1x optical zoom (Figure 2.2). For the density and laminar distribution analyses of GABAergic interneurons and Drd1a-Cre+ projection neurons, 1x4 tile scans combined with z-stack imaging (3.5 µm z-step size) spanning the whole depth of M1 and S1 were acquired using sequential (best signal) mode scanning (Figure 2.2). For subcortical region and soma morphometric analyses, 20x confocal image stacks (Nyquist sampling interval) were obtained for PV, NPY, SST, and CR quantification (Figure 2.2). Z-projection images using the maximum intensity function in Fiji (ImageJ) were produced for subsequent cell quantification. For each channel, the optimal laser power, digital gain, offset, and pinhole settings were identified and kept constant throughout image acquisition for all three strains. The acquisition parameters are summarised in Table 2.11.

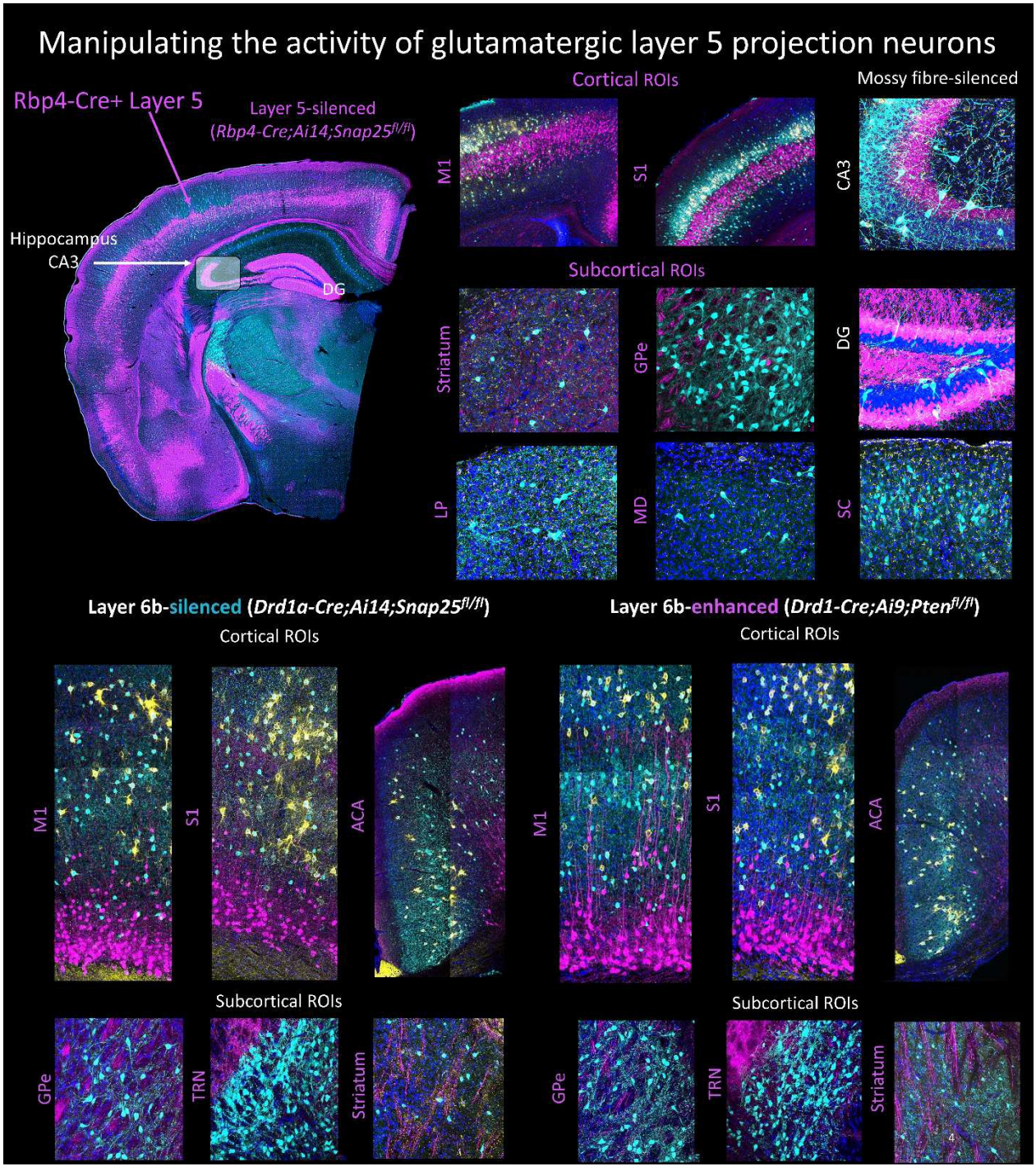


Figure 2.2. Representative fluorescent and confocal images of the regions of interest for all three conditional knockout strains. Upper panel showing subsets of *Rbp4-Cre+* projection neurons in magenta, parvalbumin-immunoreactive neurons in cyan, and VVA-labelled perineuronal nets in yellow. Lower panels depicting subsets of *Drd1a-Cre+* projection neurons in magenta, parvalbumin-immunoreactive neurons in cyan, and VVA-labelled perineuronal nets in yellow in the *Drd1a-Cre;Ai14;Snap25*$^{fl/fl}$ and *Drd1a-Cre;Ai9;Snap25*$^{fl/fl}$ mice. Cortical and subcortical regions of interest for cell quantification were selected based on the output areas of layer 5 and layer 6b projection neurons.

Acquisition parameters	
Confocal imaging (ZEISS LSM 710)	
Objective	EC Epiplan Apochromat 20x/0.6x HD DIC
Dataset 1	Cell density (subcortical regions) and morphometrics (soma analysis)
Frame size	1024 x 1024
Individual image size (scan area)	424.7 µm x 424.7 µm
Dataset 2	Laminar distribution (cortical regions)
Frame size	1024 x 4096
Individual image size (scan area)	425.10 µm x 1700.37 µm (1x4 tile-scan)
Pixel size	0.42 µm
Imaging mode	Sequential (best signal, channel by channel)
Imaging speed	9
Pixel dwell	0.79 sec
Averaging number	4
Bit depth	8
Mode	Line
Z-stack	First to last
Step size	subcortical regions: optimal interval (Nyquist sampling) cortical regions: 3.5 µm
Pinholes and optical slice thickness	
405 nm (DAPI)	1.34 AU = 3.1 µm, pinhole: 39.6 µm
488 nm (Alexa488)	1.30 AU = 3.4 µm, pinhole: 44.2 µm
568 nm (tdTomato)	1.00 AU = 3.3 µm, pinhole: 39.4 µm
633 nm (Cy5)	1.01 AU = 3.8 µm, pinhole: 45.7 µm

Table 2.11. Summary of the main image acquisition parameters (ZEISS LSM710 confocal microscope).

2.8.2.1. Confocal imaging of perineuronal nets – Optimising the pinhole diameter for *Vicia villosa* agglutinin cells

The lattice-like morphology of VVA+ cells required careful optimisation of the image acquisition parameters to ensure that no positive cells are lost, and the web-like structure is captured across the 3D plane. Different pinhole diameters were tested to determine which setting gives optimal results for subsequent cell quantification. Note that the transgenic mice's genetically encoded red fluorophore always occupied the red channel, and the blue channel was utilised to examine the DAPI signal; the VVA signal could only be imaged using the green and far-red channels. GABAergic interneurons were often imaged using the green channel; therefore, the far-red channel was left open for VVA imaging. Following the imaging principles of confocal microscopy, the pinhole was first set to 1 AU, which gives optimal optical thickness. This prevented out-of-focus light from being captured, but it also reduced signal intensity, making detection less effective and less accurate for quantification despite the crispy images obtained. When opening the pinhole to aid cell detection, the VVA signal looked dim and patchy, which would also give inaccurate cell counts (Figure 2.3.). Therefore, the optimal detection for VVA cells was achieved by setting the pinhole slightly above 1 AU unit and combining tile-scans with 3D z-stack imaging, which decreased the chances of uncaptured cells (Figure 2.3.). Due to the inability to fully capture the lattice-like net surrounding the cells, 2D imaging was found to be inadequate for correctly and consistently quantifying the VVA+ signal. This made it challenging to identify whether or not the signal was coming from a cell out of focus or a fuzzy background. 2D imaging would also result in undersampling as illustrated in Figure 2.4., biasing cell counts to lower numbers. Note that using a relatively high master gain (Master gain – 871) when imaging the VVA signal was justified, as the Zeiss LSM 710 is equipped with traditional HeNe gas lasers, and the quantum efficiency of fluorophores is always worse in the far-red channel.

Summary of the different pinhole settings and their conclusions

1) **<u>1 AU unit -> Optical section thickness = 3.8 µm. Pinhole diameter = 46 µm</u>**

The original setting used to image VVA cells -> images noisy, hard-to-count VVA cells reliably and accurately.

2) <u>Opened pinhole (above 1 AU unit) -> Optical section thickness = 4.4 µm. Pinhole diameter = 56 µm</u>

A larger pinhole diameter was used (increased from 46 µm to 56 µm). The signal intensity increased as expected due to more light being used to create the confocal image, but the image is noisier because of the extra focal signals reaching the detector that blur the sharp focal information -> hard-to-count VVA cells accurately.

3) <u>Closed pinhole (below 1 AU unit) -> Optical section thickness = 3.2 µm. Pinhole diameter = 36 µm</u>

A smaller pinhole was used to increase resolution. The signal-to-noise ratio slightly improved, yet a significant loss of information occurred -> the image is not suitable for quantification.

4) <u>Optical section thickness (1 AU), z-stack imaging</u>

*The optimal 1 AU setting was selected, but **combined tile scans with z-stacking** to see if 3D imaging increased detection efficiency. Cell detection improved significantly – Some cells that were out of focus and appeared as a patch on the 2D image can now be seen, easily identified, and checked in the z-axis in the 3D image stack -> Optimal setting to reliably quantify VVA.*

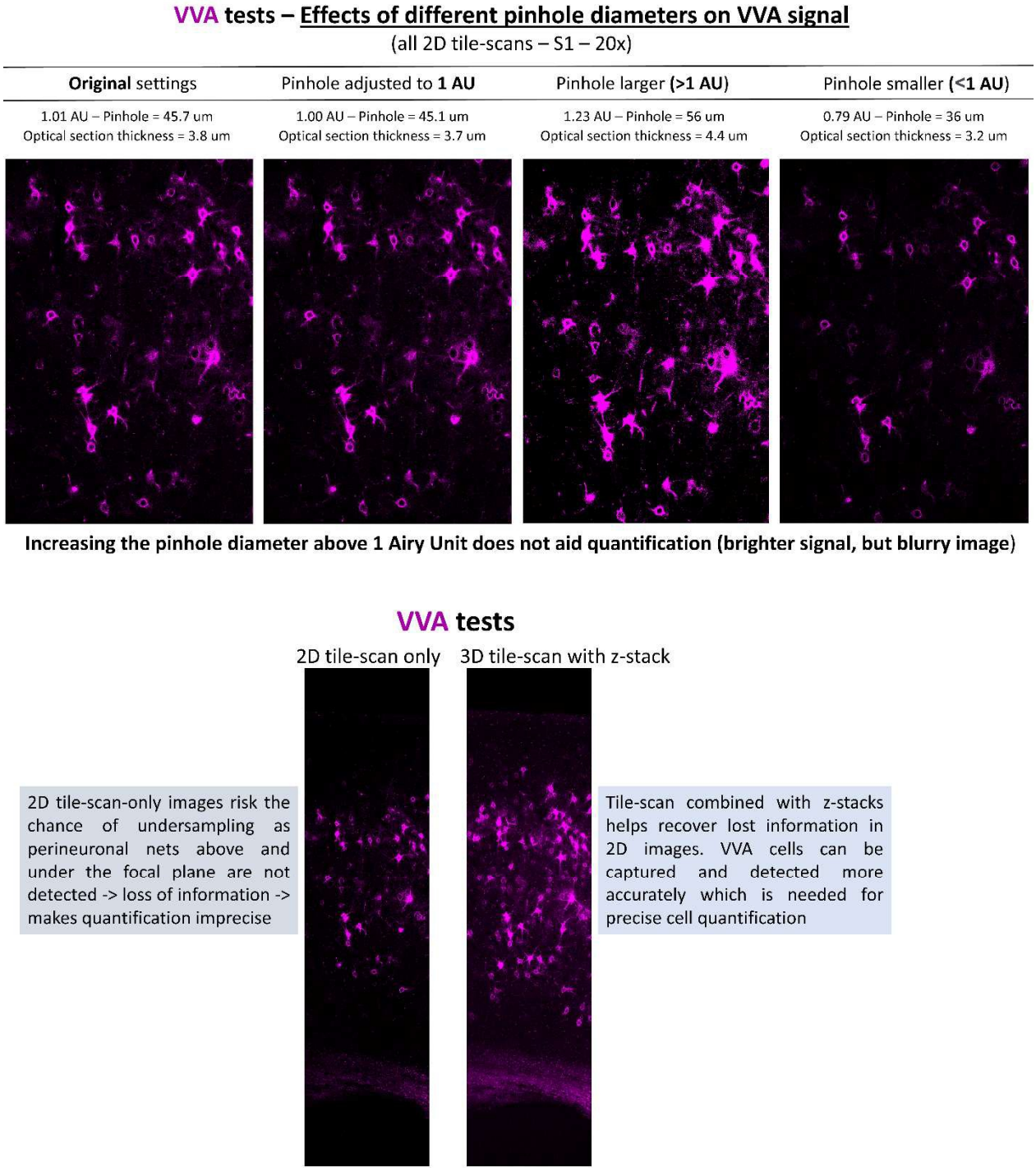


Figure 2.3. Finding the best image settings for VVA imaging by experimenting with pinhole diameters (upper panel)**.** Disparities between 2D and 3D imaging in terms of image quality and cell density (lower panel).

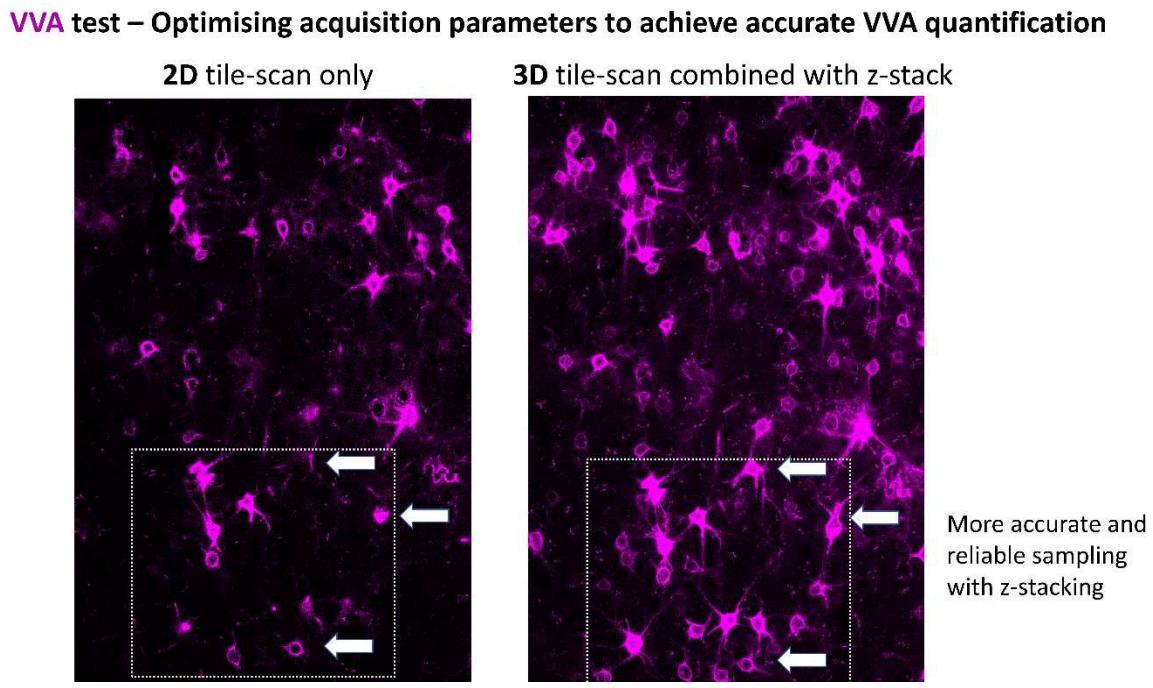


Figure 2.4. 2D imaging of the VVA signal results in a significant loss of information. One region of the image where 2D imaging causes VVA+ cells to be undersampled is indicated by a white box. White arrows point to the location of the VVA+ neurons that can only be captured with 3D imaging.

2.8.3. Spinning disk confocal imaging

Whole coronal slices for mapping the axonal projections of *Drd1a-Cre;Ai14;Snap25*$^{fl/fl}$ and *Drd1a-Cre;Ai9;Snap25*$^{fl/fl}$ neurons at 3 months of age were obtained using a spinning disk confocal microscope (Olympus SpinSR SoRa, Yokogawa CSU-W1 SoRa unit) at the Core Imaging Facility of the Wellcome Centre for Human Genetics, University of Oxford, Headington (Figure 2.5.). 20 control and 20 knockout images per transgenic strain were acquired with a 20×/0.8 air objective and a pixel size of 0.325 µm. First, using the stage navigator of the cellSens software, a quick tiled overview of the entire glass side was captured at 4x magnification using the brightfield (BF) observation mode with no shutter option. The subarray size defining the image being captured was set to its maximum size (2300 x 2300), and the IX3 halogen lamp was adjusted to 4 V when obtaining an overview of the

sections. After setting the exposure time to 50 ms, the regions of interest were defined by tracing the anatomical contours of each coronal slice using the Polygon tool. Next, under the observation methods, Confocal Fusion (CF) was selected to prevent spectral overlaps across the four different fluorophores. The laser lines utilised were as follows, with exposure time and laser power tailored to each channel: 1) F405, 5%, t=50 ms; 2) F488, 10%, t=100 ms; 3) F561, 5%, t=100 ms; 4) F647, 10%, t=100 ms.

After the acquisition settings have been set, the disk speed was synchronised with the exposure time selected, the pixel clock was set to 480 MHz, and the subarray size was cropped to 1500 x 1500. Next, the range for the z-stack loop was defined based on the top and bottom positions (30 µm range, 5 µm step size) and high-density focus maps were assigned to set the focus positions across the tissue. Besides the automatically assigned focus points, eight extra points were set up (bilaterally at S1, the hippocampus, the striatum, and the globus pallidus) for each coronal section to enhance focus maps in regions of interest further to prevent potential focus drift.

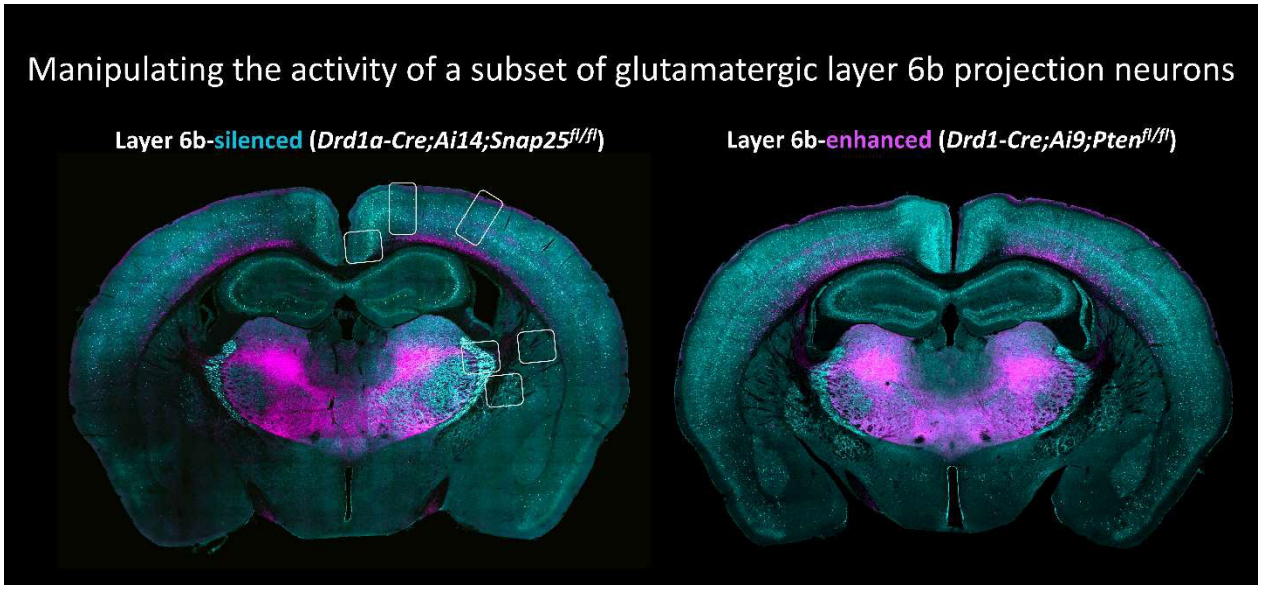


Figure 2.5. Representative images of full-coronal slices obtained with spinning disk SoRa confocal microscopes for mapping the projections of layer 6b projection neurons. Cyan channel illustrates parvalbumin-immunoreactive neurons, while magenta shows the distribution of the axonal projections of the 'silenced' (*Drd1a-Cre;Snap25*$^{fl/fl}$) and 'augmented' (*Drd1a-Cre;Pten*$^{fl/fl}$) layer 6b neurons. White boxes denote cortical and subcortical regions of interest

2.9. Image analysis

2.9.1. Cell quantification of GABAergic interneurons

Confocal image files of ".lsm" extensions were processed in Fiji (ImageJ). For the quantification of cortical GABAergic interneurons in M1 and S1, a semi-automated custom-designed macro written in Fiji (NIH) was used to assess the density and laminar distribution of GABAergic interneurons both in the postnatal and adult brains. Due to the varying nature of cell morphology in subcortical brain regions, most non-cortical PV-immunoreactive cells were quantified manually using the Cell Counter plugin of Fiji (ImageJ) in the globus pallidus and the superior colliculus. Please see Table 2.12. for a detailed summary of the quantification of each interneuron cell type (PV, NPY, SST, CR) and the quantification method applied (*semi-automatic* vs *manual*). The accuracy of the semi-automated cell quantification method was confirmed by manual recounting of cells. In the case of SST+ and NPY+ neurons, false positive cell counts were manually excluded from the analysis when dendritic segments or axonal fragments were detected. For all laminar density analyses, confocal tile scans spanning the entire depth of M1 and S1 were captured at 20x magnification, and DAPI nuclear counterstain was used to delineate cortical boundaries (Figure 2.7.). All quantification was performed on maximum-intensity z-stack projected confocal images (Figure 2.6.). Cell counts were averaged to give a mean cell number per brain. For all density measurements, raw cell numbers were normalised by the counting area. For all laminar distribution measurements, raw cell numbers were normalised by the area of the layers. No raw cell numbers are reported throughout the thesis except for the cell measurements of Drd1a-Cre+ neurons in Chapter 5 (Pten), where both cell counts and cell density are provided.

The workflow of the custom-designed pipeline for semi-automatic quantification of GABAergic interneurons is as follows. In brief, multichannel confocal images were first duplicated and split into individual channels using the Fiji *Color -> Split* Channels function. Pre-processing of images was then conducted using the rolling ball algorithm to correct uneven backgrounds, and a linear Gaussian blur filter with a sigma value of 1 was applied to reduce noise. After filtering and noise

correction, segmentation of foreground (objects of interest) from background objects was performed using the *Otsu* thresholding method. Following segmentation, a *Watershed* binary process was applied to separate touching or merged objects. Finally, the *Analyse particle > Set measurements* function was used to set the size and circularity of objects. Objects falling outside the preset range were excluded from the cell measurements. Double-positive cells (PV+ VVA+ and subpopulations, SST+ VVA+, PV+ GABA-B R1) were identified based on the co-localisation of the two channels of interest, and quantification was manually performed. The thresholding method, value, particle size, and circularity parameters were all adjusted for the cell type, age, and region being quantified (Table 2.12.). Examples of raw cell counts and normalised density values are provided in Table 2.13. and Table 2.14.

Overview of cell quantification	
Semi-automated	Parvalbumin (PV)
	Somatostatin (SST) *
	Neuropeptide-Y (NPY)
	Calretinin (CR)
Manual 1 (*Single cell counts*)	*Vicia villosa* agglutinin (VVA)
	Drd1a-Cre neurons
	GABA-A δ
	GABA-B R1
Manual 2 (*Co-localisation*)	Interneuron subpopulations (PV+ VVA+, PV+ VVA-, PV- VVA+) (SST+ VVA+) (PV+ GABA-B R1+)

**Quantified semi-automatically in the layer 6b-augmented strain (Pten cKO), where all cortical and subcortical regions were examined and newer brains were immunostained, whereas manually in the layer 5- and layer 6b-silenced strains (Snap25 cKO), where only the CPu and the hippocampus were examined, and older brains were immunostained.*

Cell quantification	
Parvalbumin	
Layer 5-silenced strain (Chapter 3)	
Semi-automated quantification	Primary motor cortex (M1)
	Primary sensory cortex (S1)
	Striatum (CPu)
	Mediodorsal thalamic nucleus (MD)
	Lateral posterior thalamic nucleus (LP)
	Dentate gyrus
	CA3
Manual cell quantification	Globus pallidus, external segment (GPe)

	Superior colliculus (SC)
Pre-processing	Yes
Background subtraction	Yes
Subtraction method and value	Rolling ball, rolling=30
Filters	Yes
Filters applied	Gaussian blur
Sigma radius (Gaussian blur)	1
Noise reduction	Yes
	Despeckle
Segmentation	
Thresholding mode	Otsu (minimising intra-class variance, defined as a weighted sum of variances of the two classes)
Thresholding value	196, 255 (all regions except CPu)
Thresholding value	106, 255 (CPu)
Cell detection	
Analyse particles	
Size (pixel^2)	40-infinity
Circularity	0.1 – 1.00
Include holes	No
Exclude edges	No
Area quantified (subcortical regions, z-stacks)	424.7 µm
Area quantified (cortical regions, tile scan & z-stack)	1,698.8 µm x 424.7 µm (1 cortical column: 4 vertical x 1 horizontal tile)

Cell quantification	
Parvalbumin	
Layer 6b-*silenced* (Chapter 4) + Layer 6b-*enhanced* (Chapter 5)	
Semi-automated quantification	Primary motor cortex (M1)
	Primary sensory cortex (S1)
	Anterior cingulate area (ACA)
Manual cell quantification	Globus pallidus, external segment (GPe)
	Thalamic reticular nucleus (TRN)
Pre-processing	Yes
Background subtraction	Yes
Subtraction method and value	Rolling ball, rolling=30
Filters	Yes
Filters applied	Gaussian blur
Sigma radius (Gaussian blur)	1
Noise reduction	Yes
	Despeckle
Segmentation	
Thresholding mode	Otsu (minimising intra-class variance, defined as a weighted sum of variances of the two classes)
Thresholding value	196, 255 (all regions, *adult* brains)
Thresholding value	118, 255 (all regions, *developmental* brains)

Cell detection	
Analyse particles	
Size (pixel^2)	40-infinity
Circularity	0.1 – 1.00
Include holes	No
Exclude edges	No
Area quantified (subcortical regions, z-stacks)	424.7 µm
Area quantified (cortical regions, tile scan & z-stack)	1,698.8 µm x 424.7 µm (1 cortical column: 4 vertical x 1 horizontal tile)

Cell quantification	
Somatostatin	
Layer 6b-*enhanced* (Chapter 5)	
Semi-automated quantification	Primary motor cortex (M1)
	Primary sensory cortex (S1)
	Striatum (CPu)
	CA1
	CA3
	Dentate gyrus
Manual cell quantification	Anterior cingulate area (ACA)
Pre-processing	Yes
Background subtraction	Yes
Subtraction method and value	Rolling ball, rolling=50
Filters	Yes
Filters applied	Gaussian blur
Sigma radius (Gaussian blur)	1
Noise reduction	Yes
	Despeckle
Segmentation	
Thresholding mode	Otsu
Thresholding value	110, 255 (all cortical regions)
Thresholding mode	Yen
Thresholding value	110, 255 (CPu and hippocampal regions)
Cell detection	
Analyse particles	
Size (pixel^2)	10-infinity (cortical regions)
Circularity	0.10 – 1.00 (cortical regions)
Size (pixel^2)	20-infinity (CPu and hippocampal regions)
Circularity	0.20 – 1.00 (CPu and hippocampal regions)
Include holes	No
Exclude edges	No
Area quantified (subcortical regions, z-stacks)	424.7 µm
Area quantified (cortical regions, tile scan & z-stack)	1,698.8 µm x 424.7 µm (1 cortical column: 4 vertical x 1 horizontal tile)

Cell quantification	
Neuropeptide-Y	
Layer 6b-*enhanced* (Chapter 5)	
Semi-automated quantification	Primary motor cortex (M1)
	Secondary motor cortex (M2)
	Primary sensory cortex (S1)
	Anterior cingulate area (ACA)
	Striatum (CPu)
	CA1
	CA3
	Dentate gyrus
Pre-processing	Yes
Background subtraction	Yes
Subtraction method and value	Rolling ball, rolling=50
Filters	Yes
Filters applied	Gaussian blur
Sigma radius (Gaussian blur)	1
Noise reduction	Yes
	Despeckle
Segmentation	
Thresholding mode	Yen
Thresholding value	105, 255 (ACA)
Thresholding mode	Yen
Thresholding value	100, 255 (cortex, CPu and hippocampal regions)
Cell detection	
Analyse particles	
Size (pixel^2)	12-200 (ACA)
Circularity	0.10 – 1.00 (ACA)
Size (pixel^2)	20-300 (CPu)
Circularity	0.10 – 1.00 (CPu)
Size (pixel^2)	15-300 (cortex and hippocampal regions)
Circularity	0.10 – 1.00 (cortex and hippocampal regions)
Include holes	No
Exclude edges	No
Area quantified (subcortical regions, z-stacks)	424.7 µm
Area quantified (cortical regions, tile scan & z-stack)	1,698.8 µm x 424.7 µm (1 cortical column: 4 vertical x 1 horizontal tile)

Cell quantification	
Neuropeptide-Y	
Layer 5-*silenced* (Chapter 3) + Layer 6b-*silenced* (Chapter 4)	
Semi-automated quantification	Primary motor cortex (M1)
	Secondary motor cortex (M2)
	Primary sensory cortex (S1)

	Anterior cingulate area (ACA)
	Striatum (CPu)
	CA1
	CA3
	Dentate gyrus
Pre-processing	Yes
Background subtraction	Yes
Subtraction method and value	Rolling ball, rolling=50
Filters	Yes
Filters applied	Gaussian blur
Sigma radius (Gaussian blur)	1
Noise reduction	Yes
	Despeckle
Segmentation	
Thresholding mode	Yen
Thresholding value	100, 255 (ACA)
Thresholding mode	Yen
Thresholding value	100, 255 (cortex, CPu and hippocampal regions)
Cell detection	
Analyse particles	
Size (pixel^2)	20-200 (ACA) (adult and developmental)
Circularity	0.10 – 1.00 (ACA)
Size (pixel^2)	20-300 (CPu) (adult)
	25-300 (CPu) (developmental)
Circularity	0.10 – 1.00 (CPu)
Size (pixel^2)	25-300 (cortex and hippocampal regions, adult and developmental brains)
Circularity	0.10 – 1.00 (cortex and hippocampal regions)
Include holes	No
Exclude edges	No
Area quantified (subcortical regions, z-stacks)	424.7 µm
Area quantified (cortical regions, tile scan & z-stack)	1,698.8 µm x 424.7 µm (1 cortical column: 4 vertical x 1 horizontal tile)

Cell quantification	
Calretinin	
Layer 6b-*silenced* (Chapter 4)	
Semi-automated quantification	Striatum (CPu)
	CA1
Pre-processing	Yes
Background subtraction	Yes
Subtraction method and value	Rolling ball, rolling=50
Filters	Yes
Filters applied	Gaussian blur
Sigma radius (Gaussian blur)	1

Noise reduction	Yes
	Despeckle
Segmentation	
Thresholding mode	Yen
Thresholding value	100, 255
Cell detection	
Analyse particles	
Size (pixel^2)	20-200 (developmental)
Circularity	0.10 – 1.00
Include holes	No
Exclude edges	No
Area quantified (subcortical regions, z-stacks)	424.7 µm

Table 2.12. Overview of the cell detection parameters used to quantify each interneuron subtype.

Cell quantification		PV raw number					
Genotype	Region	Layer 1	Layer 2/3	Layer 5	Layer 6a	Layer 6b	Total
Drd1a-Cre;Ai9;PTEN$^{fl/fl}$ (blind)	M1	0	41	34	37	7	119
Drd1a-Cre;Ai9;PTEN$^{fl/fl}$ (blind)	M1	0	30	28	27	0	85
Drd1a-Cre;Ai9;PTEN$^{fl/fl}$ (blind)	M1	0	39	40	42	0	121
	MEAN	**0**	**36.666667**	**34**	**35.333333**	**2.33333333**	**108.33333 33**
Drd1a-Cre;Ai9;PTEN$^{fl/fl}$ (blind)	M1	0	19	24	25	1	69
Drd1a-Cre;Ai9;PTEN$^{fl/fl}$ (blind)	M1	0	17	20	17	1	55
Drd1a-Cre;Ai9;PTEN$^{fl/fl}$ (blind)	M1	0	33	30	27	0	90
	MEAN	**0**	**23**	**24.666667**	**23**	**0.66666667**	**71.333333 33**
Drd1a-Cre;Ai9;PTEN$^{fl/fl}$ (blind)	M1	0	50	25	20	0	95
Drd1a-Cre;Ai9;PTEN$^{fl/fl}$ (blind)	M1	0	38	28	23	0	89
Drd1a-Cre;Ai9;PTEN$^{fl/fl}$ (blind)	M1	0	31	36	34	1	102
	MEAN	**0**	**39.666667**	**29.666667**	**25.666667**	**0.33333333**	**95.333333 33**
Drd1a-Cre;Ai9;PTEN$^{fl/fl}$ (blind)	M1	0	34	24	14	1	73
Drd1a-Cre;Ai9;PTEN$^{fl/fl}$ (blind)	M1	0	30	20	24	2	76
Drd1a-Cre;Ai9;PTEN$^{fl/fl}$ (blind)	M1	2	36	25	21	1	85
	MEAN	**0.666666667**	**33.333333**	**23**	**19.666667**	**1.33333333**	**78**

Table 2.13. Example of cell quantification of parvalbumin interneurons in the primary motor cortex. The table shows raw cell counts.

Area measurements					
Layer 1	**Layer 2/3**	**Layer 5**	**Layer 6a**	**Layer 6b**	**Total**
52337.209	150316.915	146728.032	159064.657	34424.846	542369.302
46100.048	164114.944	145722.455	161411.003	27636.04	542038.935
48642.856	151769.53	126539.809	155957.279	27060.957	508141.608
46168.982	137655.093	109409.331	137989.252	29046.432	457097.603
51662.516	127193.994	112545.145	125377.579	28842.043	445970.255
47517.851	152931.07	130620.882	132193.614	33284.848	498980.261
37651.997	144824.761	116055.443	123503.26	22360.338	440206.844
43740.088	164113.91	100457.544	140959.451	25571.118	482792.286
46556.392	154471.231	130418.732	127954.337	27857.663	478863.729
50817.039	165264.421	155587.964	125435.484	28848.936	535379.725
47865.796	169020.642	124736.664	153667.976	25093.749	522323.083
49972.596	160430.76	118864.682	162309.387	30576.598	528780.143

PV cell density					PV density (cells/mm²)
Layer 1	Layer 2/3	Layer 5	Layer 6a	Layer 6b	Total
0	272.7570613	231.7212297	232.6098122	203.341505	219.407698
0	182.7987097	192.1460903	167.2748419	0	156.8153033
0	256.968576	316.1060564	269.304519	0	238.1225983
0	**237.5081156**	**246.6577921**	**223.0630577**	**67.7805017**	**204.7818665**
0	138.0261317	219.359718	181.1735308	34.4276364	150.9524433
0	133.6541095	177.7064661	135.5904312	34.6716077	123.3266107
0	215.7834899	229.6723123	204.2458723	0	180.3678563
0	**162.4879104**	**208.9128322**	**173.6699448**	**23.0330814**	**151.5489701**
0	345.2448301	215.4142826	161.9390452	0	215.8076397
0	231.5464911	278.7247118	163.1674913	0	184.3442876
0	200.6846181	276.0339673	265.7197935	35.8967656	213.0042303
0	**259.1586464**	**256.7243206**	**196.94211**	**11.9655885**	**204.3853859**
0	205.7309117	154.2535771	111.611161	34.6633235	136.3518202
0	177.4931135	160.3377817	156.1808818	79.701124	145.5038126
40.0219352	224.3958702	210.3231976	129.3825353	32.7047502	160.7473373
13.3406451	**202.5399651**	**174.9715188**	**132.3915261**	**49.0230659**	**147.5343234**

Table 2.14. Example of the quantification of the laminar density of parvalbumin interneurons across the different layers of the primary motor cortex. Cell counts were normalised for counting area.

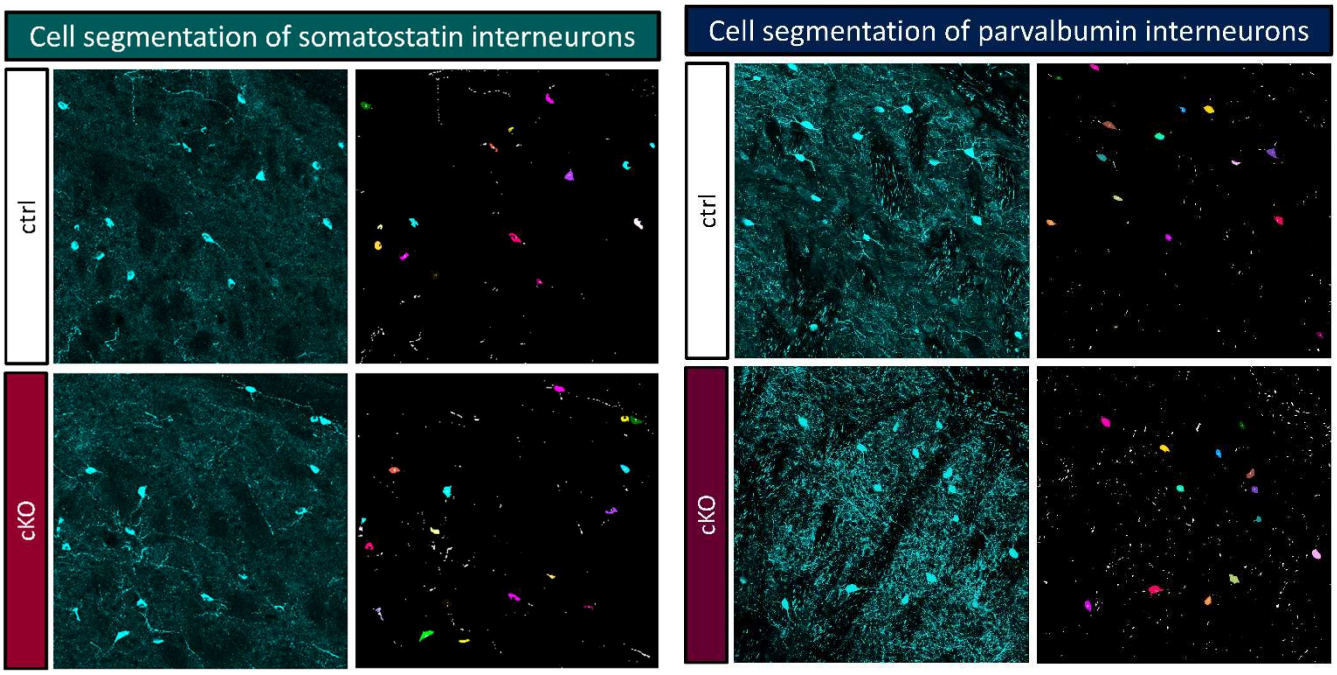
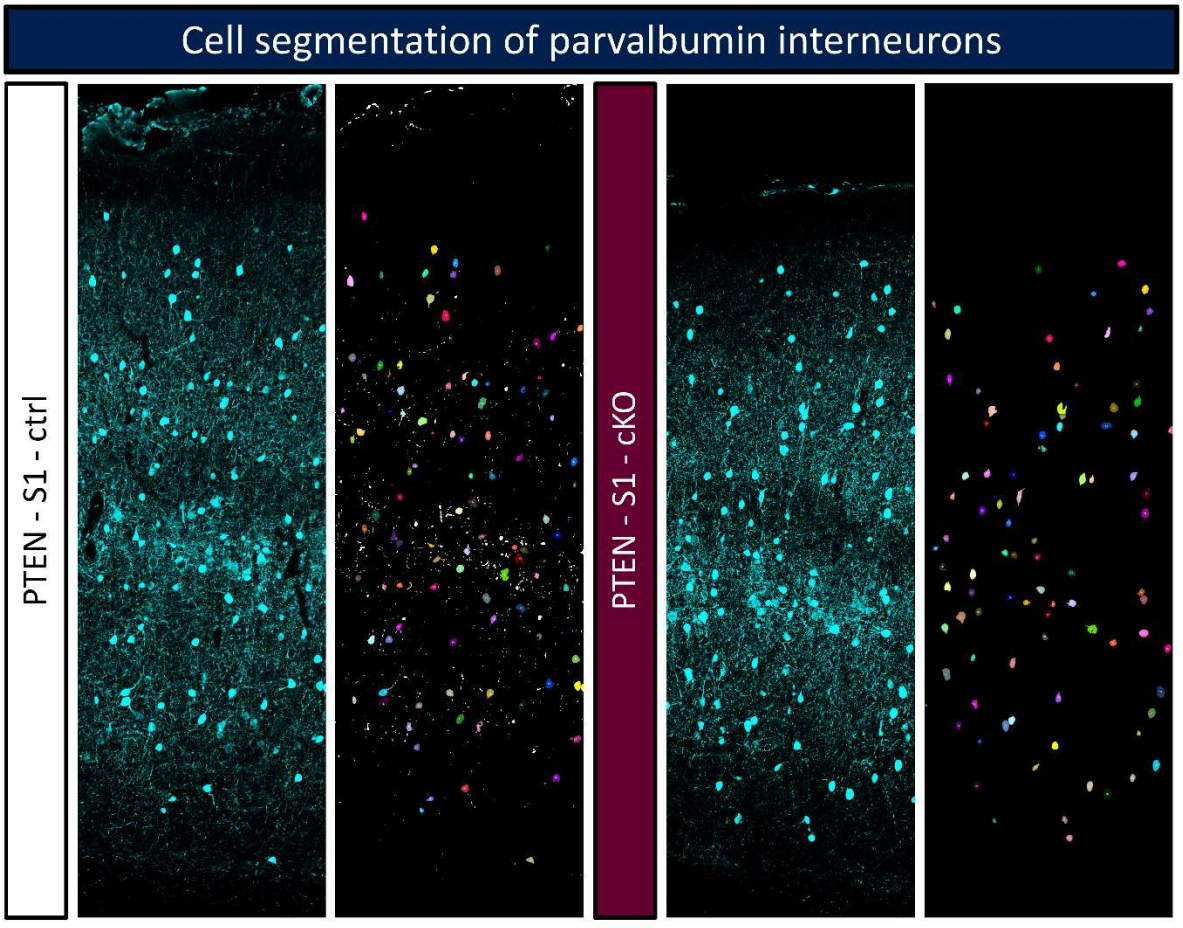


Figure 2.6. Examples of cell segmentation of somatostatin and parvalbumin interneurons in the striatum.



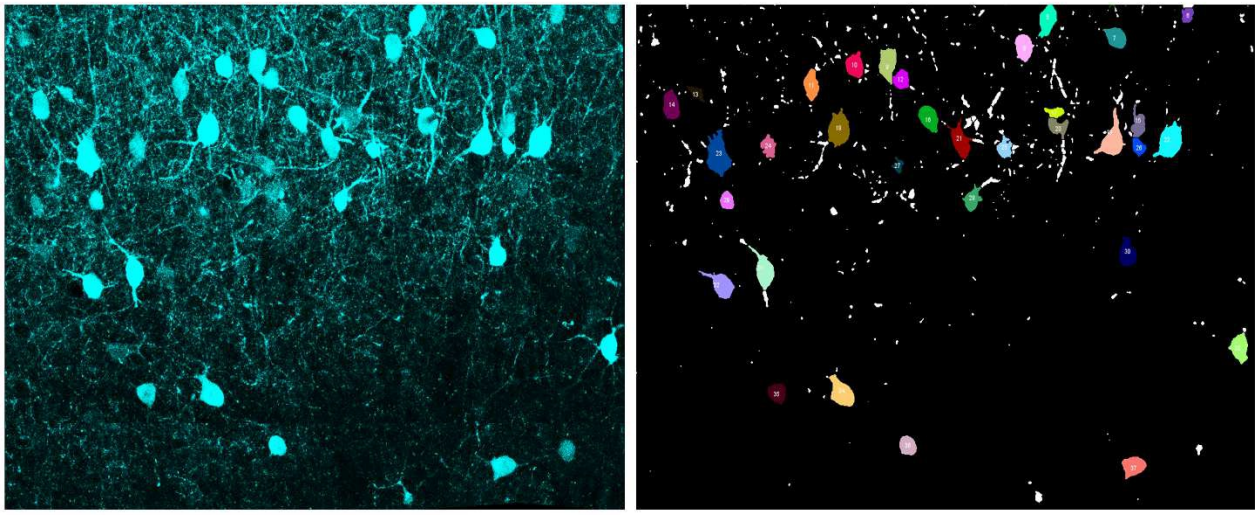


Figure 2.7. Examples of cell segmentation of parvalbumin interneurons in the primary somatosensory cortex. Bottom panel shows parvalbumin interneurons in cortical layer 5 of the primary somatosensory cortex.

2.9.2. Cell quantification of VVA+ cells

For the density and laminar distribution analysis of VVA+ cells in the adult brain, manual cell counting was selected over semi-automated quantification as the segmentation of the lattice-like morphology of PNNs proved to be unreliable. The atypical cell structure would have required a relatively high threshold, which would have resulted in lower cell counts because of the loss of information. Manual quantification of VVA+ cells was performed using the Cell Counter plugin of Fiji (NIH). Z-stack images were maximum-intensity projected in ImageJ, and collated confocal images were used for cell quantification. Only VVA+ cells that 1) exhibited a typical web-or lattice-like morphology, and 2) co-localised with the nuclear counterstain DAPI signal were counted as positive.

Histochemical staining of PNNs in the developing brains yielded varied results, and therefore, the VVA+ cells were only quantified in the adult brain at 3 months of age. In the postnatal brains, the visualisation of PNNs was either insufficient due to low staining intensity or the staining produced diffuse non-specific labelling in subcortical structures. The typical web or lattice-like structure of PNNs was not detectable in all postnatal brains. To quantify the density of VVA+ cells in postnatal

brains, P14 and P21 brains were deemed inappropriate. Considering the condensation of proteoglycans into PPNs is not yet complete at such early developmental ages, the detection of PNNs and the quantification of VVA+ cells might not be feasible with plant lectins during early brain development.

2.9.3. Quantification of GABA receptors and Drd1a-Cre+ neurons

Similar to VVA+ cells, cell density and laminar distribution of the GABA receptors (GABA-$_A$ δ and GABA-$_B$ R1 in layer 5) and Drd1a-Cre+ neurons were performed in ImageJ (Fiji) using the Cell Counter plug-in. Drd1a-Cre+ neurons were double-counted, i.e., manually and semi-automatically, giving similar cell counts. However, because of the high abundance of tdTomato+ neurons in cortical layer 6b in M1 and S1, especially in the *Pten* cKO mice, I chose to report the results of manual cell quantification and preferred manual quantification over semi-automatic measurements. The biggest challenge in quantifying Drd1a-Cre+ neurons in layer 6b stems from the high number of overlapping cells that cannot be separated accurately using the *Watershed* function. Therefore, running a fully automated macro on the cKO slices can easily result in oversampling. Cells were quantified on maximum-intensity projected confocal images in selected cortical regions. Tracing the cells of interest in the z-plane using the z-stack assisted in distinguishing between overlapping neurons when three of the four tdTomato+ neurons in layer 6b were closely positioned and had overlapping somata. Pre-processing, including background subtraction and filtering, was applied to images prior to cell quantification. The size of each individual image for Drd1a-Cre+ quantification was one cortical column, measuring 1,698.8 µm by 424.7 µm. Four brains were processed per genotype, and three slices per ROI were measured for all cell measurements. The cell counts of three slices were averaged to determine the total number of cells in each brain. First, raw cell counts were determined, and then cell density was calculated for each ROI by dividing cell counts per counting area, which was multiplied by 1000000.

2.10. Morphometric analysis of GABAergic interneurons

Point-scanning confocal z-stack images of the regions of interest were obtained using a 20x objective (Epiplan-Apochromat 20x (0.80 NA) dry) and then maximum-intensity projected in Fiji to construct 2D images for morphometric analysis of GABAergic neurons (PV, NPY, SST, and CR). The analysis pipeline was identical to that of the density and laminar distribution analyses. The *Analyse > Set measurements* function was used to select the parameters to be investigated, i.e., *soma area, soma circularity, soma perimeter, soma roundness, and soma solidity*. Following the semi-automated quantification of GABAergic interneurons, the results of density counts and morphometric measurements were stored in ".csv" files (Table 2.15.) and exported to Prism 10 (GraphPad) for plotting and statistical analysis. The number of animals and cells analysed for each group and region is presented in the Appendices. The number of animals used for morphological analyses matched the number used for cell measurements. Scatter plots of morphometric analyses of inhibitory neurons represent individual cell measurements.

The shape descriptors and definitions for each measured parameter are provided below. The definitions provided here are from *Shape Analysis & Measurement*, Michael A. Wirth, Ph.D., University of Guelph, Computing and Information Science, Image Processing Group, 2004, and from the ImageJ documentation, which can be accessed at https://imagej.net/ij/docs/menus/analyze.html#set.

a. ***Area*** - Area of selection in square pixels. *Analyze>Set Scale* was used to spatially calibrate the image; thus, the soma area is given in calibrated units (μm^2).

b. ***Perimeter*** [length] - the number of pixels in the boundary of the object (Wirth, 2004).

   If x1,...,xN is a boundary list, the perimeter is given by:

$$\text{perimeter} = \sum_{i=1}^{N-1} d_i = \sum_{i=1}^{N-1} |x_i - x_{i+1}|$$

c. ***Circularity*** - (area-to-perimeter-ratio) - the ratio of the area of an object to the area of a circle with the same convex perimeter. This statistic equals 1 for a circular object and less than 1 for

an object that departs from circularity, except that it is relatively insensitive to irregular boundaries (Wirth, 2004). As the value approaches 0.0, it indicates an increasingly elongated shape.(https://imagej.net/ij/docs/menus/analyze.html#set)

$$\frac{x = 4\pi \cdot \text{area}}{(\pi \cdot perimeter^2)}$$

d. ***Roundness*** - the inverse of the aspect ratio (major_axis/minor_axis). (https://imagej.net/ij/docs/menus/analyze.html#set)

$$\frac{x = 4 \cdot \text{area}}{(\pi \cdot major\ axis^2)}$$

e. ***Solidity*** - measures the density of an object (Wirth, 2004). A measure of solidity can be obtained as the ratio of the area of an object to the area of a convex hull of the object:

$$\frac{area}{convex\ area}$$

	Label	Area	X	Y	XM	YM	Perim.	Circ.	Round	Solidity
1	MAX_PTEN	99.782	170.031	67.912	170.031	67.912	62.825	0.318	0.439	0.755
2	MAX_PTEN	82.204	121.106	116.091	121.106	116.091	44.299	0.526	0.475	0.816
3	MAX_PTEN	63.764	239.194	123.232	239.194	123.232	41.121	0.474	0.604	0.686
4	MAX_PTEN	92.027	155.768	191.29	155.768	191.29	61.592	0.305	0.278	0.638
5	MAX_PTEN	34.122	35.735	303.793	35.735	303.793	26.301	0.62	0.54	0.834
6	MAX_PTEN	64.453	275.662	348.159	275.662	348.159	49.969	0.324	0.419	0.564
7	MAX_PTEN	73.07	221.491	398.968	221.491	398.968	44.341	0.467	0.392	0.71

Table 2.15. Example of soma morphometric measurements of somatostatin interneurons in the striatum.

2.10.1. The relationship between roundness and circularity – why measuring both?

According to the ImageJ Analyse Particles documentation (https://imagej.net/ij/docs/menus/analyze.html#set), ***roundness*** is defined as 4*area/(π*major_axis^2), whereas ***circularity*** is defined as 4π*area/perimeter^2. Roundness, therefore, measures the ratio of area to the major axis, while circularity is the ratio of area to perimeter. Hence, they are sensitive to different descriptors of shape. If we consider a circle versus an ellipse (similar areas and major axes), they will have a similar roundness value but have a different

circularity. Since circularity is dependent on the perimeter of the object and is independent of the major axis, an ellipse ('skewed circle') will have a lower circularity because the perimeter of the object is different from that of the circle (Takashimizu and Iiyoshi 2016). Therefore, roundness is not sensitive to changes in perimeter length and does not detect differences between two objects of the same area that have a high or similar degree of roundness but have different perimeters. If only the perimeter increases, but the area remains the same, the circularity decreases (Takashimizu and Iiyoshi 2016). Hence, the roundness and circularity values will be different. This justified the need to distinguish between roundness and circularity in my morphometric measurements to detect irregular shapes and/or cell boundaries.

2.11. Statistics

For a detailed overview of the number of sections and the number of brains analysed, please refer to Table 2.2. In brief, adult cell density and laminar distribution analyses of GABAergic interneurons were performed on data obtained from n=4 brains per genotype for the *Pten* cKO experiments, and n=5 brains for the *Snap25* cKO adult studies. All data are reported as mean ± standard error of the mean (SEM). Shapiro-Wilk tests were computed to determine normality. When comparing two groups that were normally distributed (*cell density)*, a two-tailed unpaired t-test with Welch's correction was applied. For *morphometric* measurements, where the data did not follow a normal distribution, a two-tailed unpaired Mann-Whitney test was computed. A two-way ANOVA using Šidák's multiple comparisons test was employed when comparing more than two groups that have a normal distribution (*density, distribution,* and *developmental dynamics* of *GABAergic interneurons*). For *morphometric layer* analysis, a one-way ANOVA Kruskal-Wallis test (non-parametric) with Dunn's multiple comparisons was selected. Scatter plots of morphometric analyses of PV+ cells represent individual cell measurements. Heatmaps present the Pearson correlation between PV and VVA in different cortical regions and different cortical layers (PV, n=5 per genotype;

VVA, n=4 per genotype). Statistical tests were computed in Prism 10.2.1 (GraphPad Software, San Diego, CA, USA). For an overview of the different tests computed, please refer to Table 2.16.

	2 groups		>2 groups	
Distribution	**Normal**	**Not normal**	**Normal**	**Not normal**
Statistical test performed	unpaired two-tailed Student's t-test with Welch's correction	unpaired two-tailed Mann-Whitney	unpaired 2-way ANOVA with Sidak's multiple comparisons	unpaired one-way ANOVA, Kruskal-Wallis test with Dunn's multiple comparisons
Dataset	*cell density*	*morphometrics (cell analysis)*	*laminar distribution*	*morphometrics (layer analysis)*

Table 2.16. An overview of the datasets and statistical tests conducted.

Chapter 3 ..... Results

Chronic silencing of glutamatergic layer 5 cortical projection neurons

3.1 Aims and Objectives

In this chapter, I have outlined the following research goals.

1) Elucidate the role of AP-dependent neurotransmitter release in the development of parvalbumin neurons
2) Explore the effects of genetically silencing Rbp4-Cre+ glutamatergic projection neurons on the laminar and spatial distribution of parvalbumin neurons
3) Examine the effects of genetically silencing layer 5 projection neurons on distinct subtypes of GABAergic neurons in the adult brain
4) Compare how silencing glutamatergic layer 5 projection neurons versus hippocampal granule cells influences the density and distribution of GABAergic neurons in the adult brain

3.2 The effects of genetically silencing layer 5 projection neurons on parvalbumin neurons in the juvenile brain

3.2.1 The *Rbp4-Cre;Ai14;Snap25$^{fl/fl}$* mice genetically label two types of cells – cortical layer 5 projection neurons and hippocampal granule cells

To elucidate the role of glutamatergic layer 5 cortical projection neurons in the development and spatial organisation of GABAergic PV+ neurons, I conditionally deleted *SNAP25* from Rbp4-Cre+ neurons in L5 of the cortex and thus, selectively abolished AP-dependent neurotransmitter release from specific subsets of L5 neurons. I selected my regions of interest (ROI) based on the location of the cell bodies (*cortical/columnar effect*) and the long-range axonal projections of the genetically silenced L5 *Snap25* cKO neurons (*subcortical effect*). The primary motor (M1) and the primary somatosensory cortices are densely populated with Rbp4-Cre+ cortical projection neurons (Figure 3.1. A2, A6, A10) and PV interneurons (Figure 3.1. A3, A7, A11); therefore, I selected M1 and S1 as my cortical ROIs. In the *Rbp4-Cre+;Ai14;Snap25$^{fl/fl}$* mice, Cre expression is mostly detected in the pyramidal tract (PT) and intratelencephalic (IT) subgroups of L5 projection neurons throughout the neocortex. The *Rbp4-Cre;Ai14* mice capture 15% of PT and IT neurons in L5 at P6 (Hoerder-Suabedissen et al. 2019). There are six available Bac Cre-driver lines for selectively targeting the IT and PT-type of L5 pyramidal neurons (i.e., *Rbp4, Dbp, Grm2, Colgalt2, Sema3e, and Gpr26*). Of the 6 Cre lines, the Rbp4-Cre (KL100) strain has the largest percentage of PT/IT subtypes labelled with the most selectivity (see Table 1 in (Gerfen et al. 2013), 10.1016/j.neuron.2013.10.016). Therefore, I chose to use a pan layer 5 line that gave me the highest genetic labelling of IT and PT layer 5 neurons.

Regarding layer specificity, both anatomical and molecular evidence confirm that the Rbp4-Cre mice specifically target glutamatergic pyramidal neurons in L5a of the neocortex and the entorhinal area (Tsoi et al. 2022). The somata of Rbp4-Cre-labelled neurons are primarily located in the upper sublamina of layer 5. Their gene expression profiles align with the L5a transcriptomic

subtypes (Munz et al. 2023; Whitesell et al. 2021). Notably, Rbp4-Cre+ neurons exhibit robust expression of L5a-enriched markers, including Etv1 (Tsoi et al. 2022), an ETS-binding transcription factor also known as ER81.

Cre-expressing tdTomato+ neurons were also observed in the dentate gyrus of *Rbp4-Cre;Ai14;Snap25*$^{fl/fl}$ mice(Figure 3.1. B2, B4, B6, B8, B10, B12), indicating that AP-dependent neurotransmitter release was ablated in the granule cells in addition to the Rbp4-Cre+ L5 neurons. The *Snap25* cKO mice can thus be used not only for studying the effects of conditionally silencing L5 projection neurons but also for the effects of genetically silencing the mossy fibre pathway (Figure 3.1. B3, B7, B11).

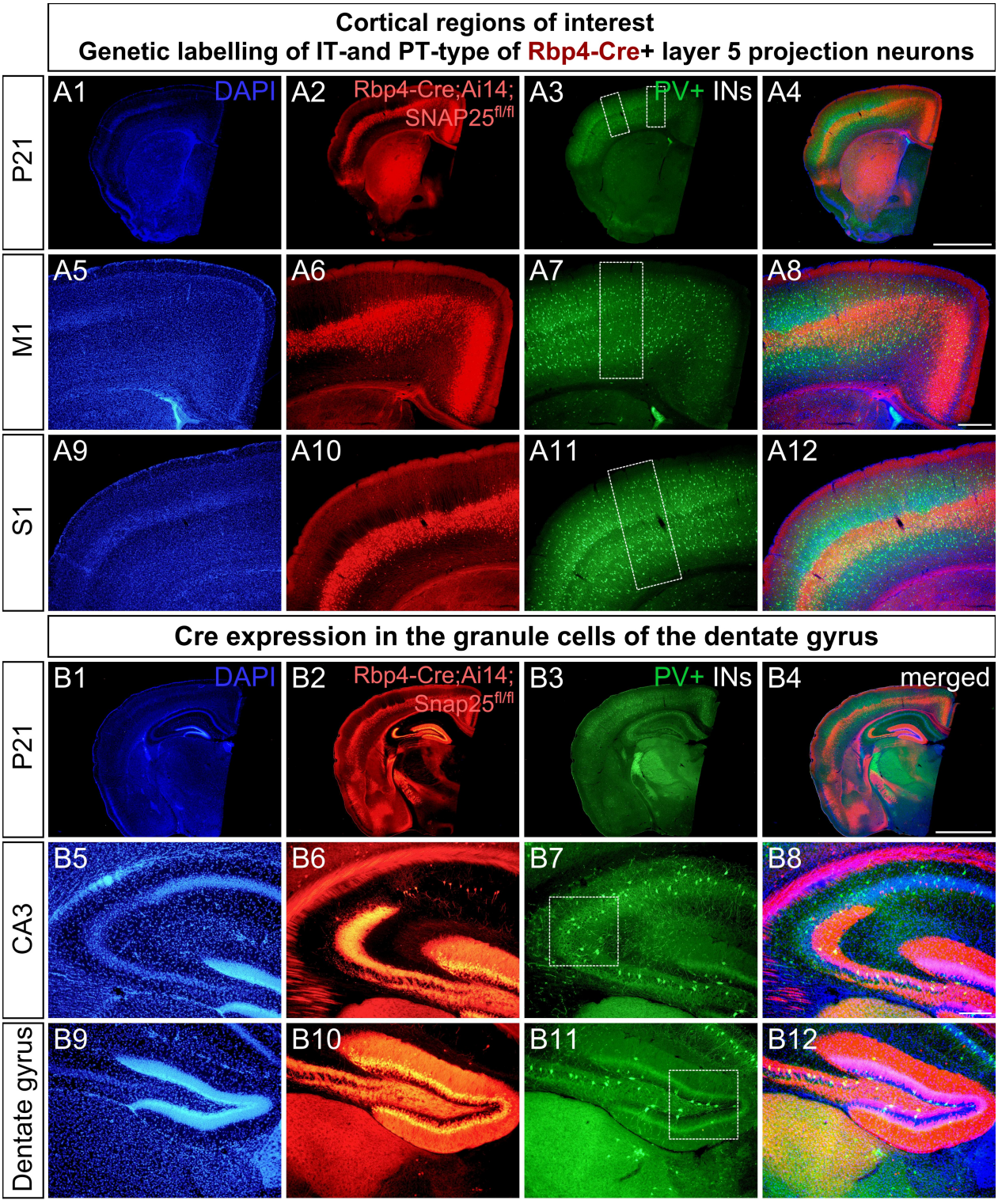


Figure 3.1. Distribution of Rbp4-Cre-expressing neurons in layer 5 of the cortex and the dentate gyrus of the hippocampus in the *Snap25* cKO mice. Low-magnification epifluorescence photomicrographs of *Snap25* cKO brains at P21 (A1-A4, B1-B4) counterstained with DAPI (blue) and immunostained for parvalbumin neurons (green) (A3, B3). Epifluorescence images illustrating the distribution of silenced Rbp4-Cre+ projection neurons in the primary motor and somatosensory

cortices (A6, A10). Note that the Rbp4-Cre driver line labels mixed subpopulations of intratelencephalic and extratelencephalic projection neurons in L5 of the cortex (A2, B2). Merging *Rbp4-Cre;Ai14; Snap25*$^{fl/fl}$ and PV epifluorescence micrographs reveal the presence of PV-immunoreactive neurons in the vicinity of the cell bodies of L5 projection neurons in the primary motor and somatosensory cortices (A8, A12). Cortical regions of interest are marked by white boxes (A7, A11). Nuclear counterstains of cortical and hippocampal ROIs (A5, A9, B5, B9). Epifluorescence images depicting the distribution of Cre expression in the developing *Snap25* cKO brains in L5 across the cortical mantle and the hippocampus (B2, B4). Note the robust Cre expression in the granule cells of the dentate gyrus, indicating the chronic silencing of the mossy fibre pathway (B6, B10). White boxes denote hippocampal ROIs (B7, B11). Fluorescence micrographs of Cre-expressing granule cells superimposed on PV+ interneurons in the *Snap25* cKO mice (B4, B8, B12). Scale bars: 1000 µm (A4, B4), 200 µm (A8), 100 µm (B8).

3.2.2 Genetically 'silenced' Rbp4-Cre+ neurons in layer 5 exhibit similar corticothalamic and corticofugal projections as Rbp4-Cre+ neurons

To investigate the effects of genetically silencing subsets of L5 pyramidal neurons on subcortical PV-expressing neurons, I selected those output regions of tdTomato+ L5 neurons where PV-immunoreactive cells were present (Figure 3.2. A3, A7, A11, A15, A19, A23). *Rbp4-Cre;Snap25*$^{fl/fl}$ L5 neurons project to the contralateral caudoputamen (CPu) (Hoerder-Suabedissen et al. 2019) (Figure 3.2. A2, A4), the globus pallidus external segment (GPe) (Figure 3.2. A6, A8), the higher-order thalamic nuclei, including the lateral posterior nucleus (LP) (Figure 3.2. A10, A12) and the mediodorsal nucleus of the thalamus (MD (Figure 3.2. A14, A16). Collaterals of the silenced Rbp4-Cre+ L5 axons also target midbrain areas such as the pontine nuclei (Figure 3.2. A22, A24) and the superior colliculus (SC) (Figure 3.2. A18, A20), and they extend to the spinal cord through the pyramidal tract. Of the output regions of L5 *Rbp4-Cre;Snap25*$^{fl/fl}$ neurons, the following innervation sites, where the projections of layer 5 and the distribution of PV interneurons overlap, were selected as my subcortical ROIs: CPu, LP, MD, GPe, and SC. These subcortical regions are of great importance as the silenced pyramidal cells of layer 5 could exert considerable effects on the number and distribution of PV+ cells through their corticofugal projections.

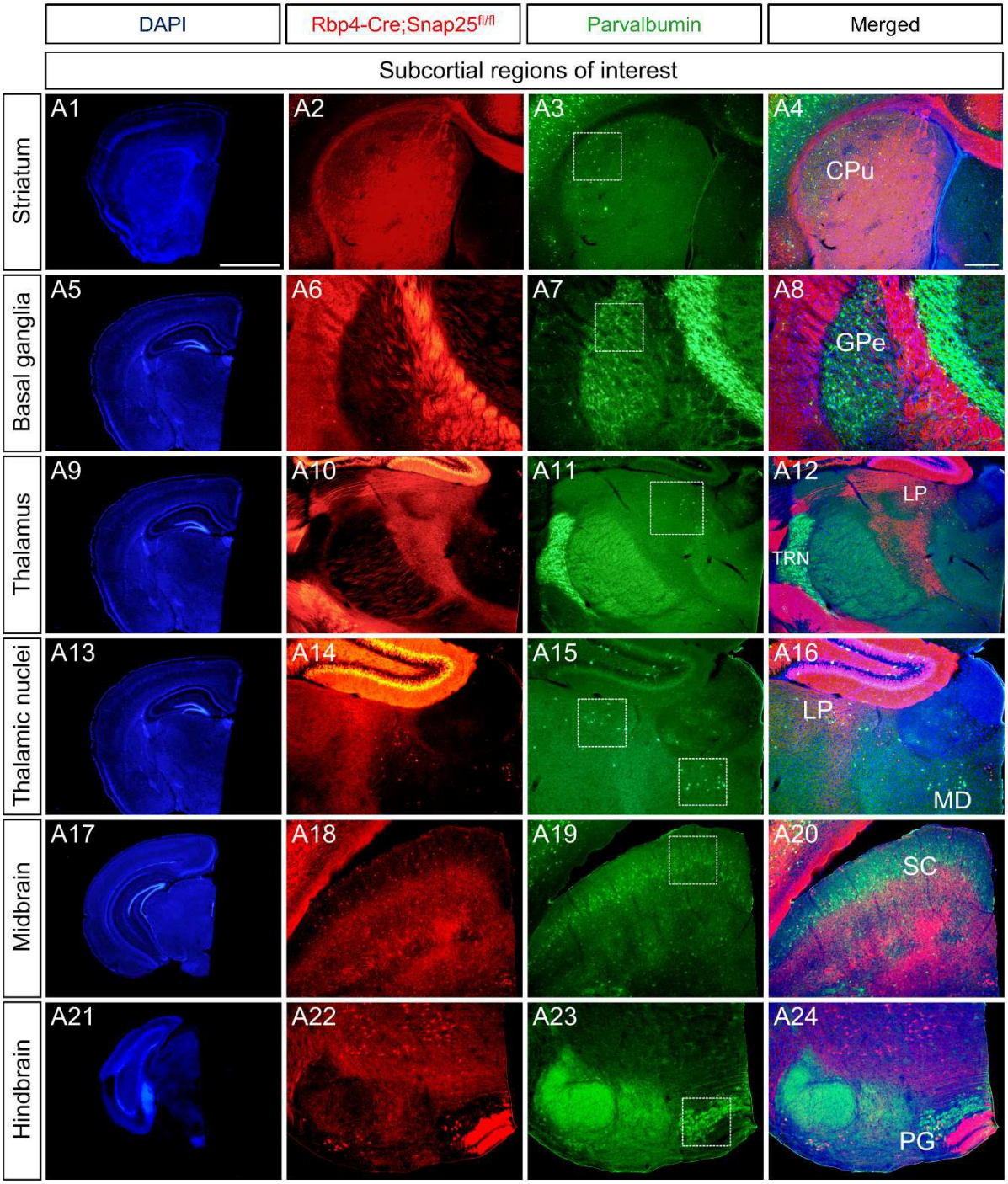

DAPI
Rbp4-Cre;Snap25fl/fl
Parvalbumin
Merged
Subcortial regions of interest
Striatum
Basal ganglia
Thalamus
Thalamic nuclei
Midbrain
Hindbrain
A1
A2
A3
A4
CPu
A5
A6
A7
A8
GPe
A9
A10
A11
A12
LP
TRN
A13
A14
A15
A16
LP
MD
A17
A18
A19
A20
SC
A21
A22
A23
A24
PG

Figure 3.2. Long-range axonal projections of the 'silenced' *Rbp4-Cre;Snap25$^{fl/fl}$* projection neurons in layer 5 of the cerebral cortex. Epifluorescence micrographs of P21 *Snap25* cKO mice obtained at different rostrocaudal levels and counterstained with DAPI (A1, A5, A9, A13, A17, A21). Long-range corticothalamic and subcortical projections of *Rbp4-Cre;Ai14;Snap25$^{fl/fl}$* neurons innervate the basal ganglia (A2, A6), the higher-order thalamic nuclei (A10, A14), and the superior colliculus (A18). Collaterals of the descending corticofugal fibres of Rbp4-Cre+ L5 projection neurons target the brainstem motor regions, including the pontine grey (A22), before reaching the spinal cord. White boxes define subcortical regions of interest: the caudoputamen (A2-A4), the external segment of the globus pallidus (A6-A8), the lateral posterior nucleus of the thalamus (A10-A12, A15-16), the mediodorsal thalamic nucleus (A15-A16), the superior colliculus (A18-A20), and the pontine grey (A22-A24). Subcortical projection sites of Rbp4-Cre+ L5 neurons were carefully selected to explore the global effects of abolishing Ca^{2+}-dependent neurotransmission from L5 projection neurons. Note that the distribution of subcortical PV neurons overlaps with the output regions of silenced L5 cortical projection neurons (A4, A8, A12, A16, A20, A24). Scale bars: 1000 µm (A1), 200 µm (A4).

3.2.3 Conditional deletion of Snap25 from layer 5 projection neurons does not interfere with the development of PV neurons

To ascertain whether AP-dependent neurotransmitter release from L5 is required for the development of PV interneurons, I assessed the effects of silencing Rbp4-Cre+ neurons on the density of cortical PV neurons at postnatal day 14 (P14) and postnatal day 21 (P21). No changes were detected in the density of PV-immunoreactive cells in M1 at P14 and P21 (Figure 3.3. A1-A1', B1-B1', E1, E1', E3, E3', f; two-way ANOVA with Šídák's multiple comparisons test, p= 0.3679 (P14), p= 0.6323 (P21)). At both P14 and P21, the density of cortical PV neurons in S1 remained unaffected, indicating that AP-dependent neurotransmitter release from L5 pyramidal neurons is dispensable for the development of cortical PV+ cells (Figure 3.3. C1-C1', D1-D1', E2, E2', E4, E4', g; two-way ANOVA with Šídák's multiple comparisons test, p=0.5806 (P14), p=0.8327 (P21)). After confirming that there were no changes in the density of PV neurons in M1 and S1, I investigated the developmental trajectory of cortical PV interneurons between P14 and P21. Neither M1 nor S1 showed a change in PV cell density in the control brains, suggesting that there is no significant decrease in the number of PV interneurons following developmentally programmed cell death (Figure 3.3. h, two-way ANOVA with Šídák's multiple comparisons test, p= 0.7467 (M1 ctrl), p= 0.8398 (S1 ctrl)). The developmental trajectory of cortical PV+ interneurons in the mutant brains was identical to the trajectory observed in the control

brains (Figure 3.3. i), two-way ANOVA with Šídák's multiple comparisons test, p= 0.9868 (M1 cKO), p= 0.9671 (S1 cKO). These results indicate that the development of cortical PV neurons is not affected by the genetic silencing of L5 projection neurons during the early stages of development. However, it is important to consider where PV cells in the neocortex receive their input. L5 pyramidal neurons establish highly convergent glutamatergic excitatory synapses onto L5 PV interneurons (Naka and Adesnik 2016). The significance of this synaptic connection is found in the reciprocal feedback loop between L5 pyramidal neurons and local PV neurons. This loop forms a potent inhibitory feedback circuit that is crucial for regulating the activity and timing of L5 outputs with high temporal precision (Naka and Adesnik 2016). The loss of excitatory inputs from Rbp4-Cre+ pyramidal neurons is probably compensated for by other pyramidal cell populations in L5.

Neocortical PV neurons primarily receive local excitatory inputs from pyramidal neurons located within the same cortical layer or from adjacent layers (Hafner et al. 2019). Specifically, layer 4 serves as the primary and most significant source of glutamatergic input in sensory areas, such as the barrel cortex (Hafner et al. 2019; Staiger et al. 2009). Excitatory drive to PV cells predominantly arises from pyramidal and spiny stellate neurons in layer 4 (Staiger et al. 2009). However, the source of glutamatergic input to fast-spiking interneurons in layer 4 undergoes significant changes during early development, with a developmental shift in input distribution after the end of the layer 4 critical period of plasticity (Anastasiades et al. 2016). FS interneurons in layer 4 S1BF received translaminar inputs from supragranular layers during the peak critical period (P5-P8), but these afferent inputs from L2-4 decreased post-critical period and eventually disappeared (Anastasiades et al. 2016). Concomitantly, local excitatory inputs from L4 spiny stellate neurons began to emerge later during development, signalling a shift in the origin of inputs and a change from translaminar to local excitation (Anastasiades et al. 2016).

3.2.4 Loss of AP-dependent neurotransmitter release from layer 5 projection neurons leaves subcortical PV neurons intact during the early stages of development

Next, I assessed the effect of genetically silencing subsets of L5 pyramidal neurons on subcortical PV cells. At P14, none of the subcortical regions displayed a difference in the density of PV-immunoreactive cells between the control and *Snap25* cKO brains (Figure 3.4. a, b, d) (LP, p=0.999; MD, p= >0.9999; CPu, p=0.9998; GPe, p= 0.9813; SC, p= 0.4308; two-way ANOVA with Šídák's multiple comparisons test). Similarly, no alterations were found in the density of subcortical PV cells at P21 (LP, p= >0.9999; MD, p= >0.9999; CPu, p= >0.9999; GPe, p= 0.7598; SC, p= 0.9992; two-way ANOVA with Šídák's multiple comparisons test, implicating the chronic cessation of layer 5 activity since birth does influence the development of PV neurons (Figure 3.4. c, e).

Since the maturation of subcortical PV+ neurons may follow a different trajectory than that of the cortical PV+ cells, I established the developmental profile of subcortical PV neurons. Of the output regions of L5 projection neurons, there was a significant increase in the density of PV+ cells in the superior colliculus between P14 and P21 in the control brains (Figure 3.4. f) (p= 0.0217, two-way ANOVA with Šídák's multiple comparisons test). No changes were observed in the control thalamic nuclei and the basal ganglia between P14 and P21 (Figure 3.4. f) (LP, p= >0.9999; MD, p= >0.9999; CPu, p= >0.9999; GPe, p= 0.9997, two-way ANOVA with Šídák's multiple comparisons test). Contrary to the significant rise noted in the superior colliculus of the control brains, PV cell density did not follow the same trend in the *Snap25* cKO mice between P14 and P21 (p= 0.9605) (Figure 3.4. g), indicating an altered developmental trajectory of PV neurons in the superior colliculus after L5 was silenced. There were no developmental alterations in PV cell density in the thalamic nuclei and the basal ganglia, either in the layer 5-silenced brains (Figure 3.4. g) (LP, p= >0.9999; MD, p= >0.9999; CPu, p= >0.9999; GPe, p= 0.9474; two-way ANOVA with Šídák's multiple comparisons test).

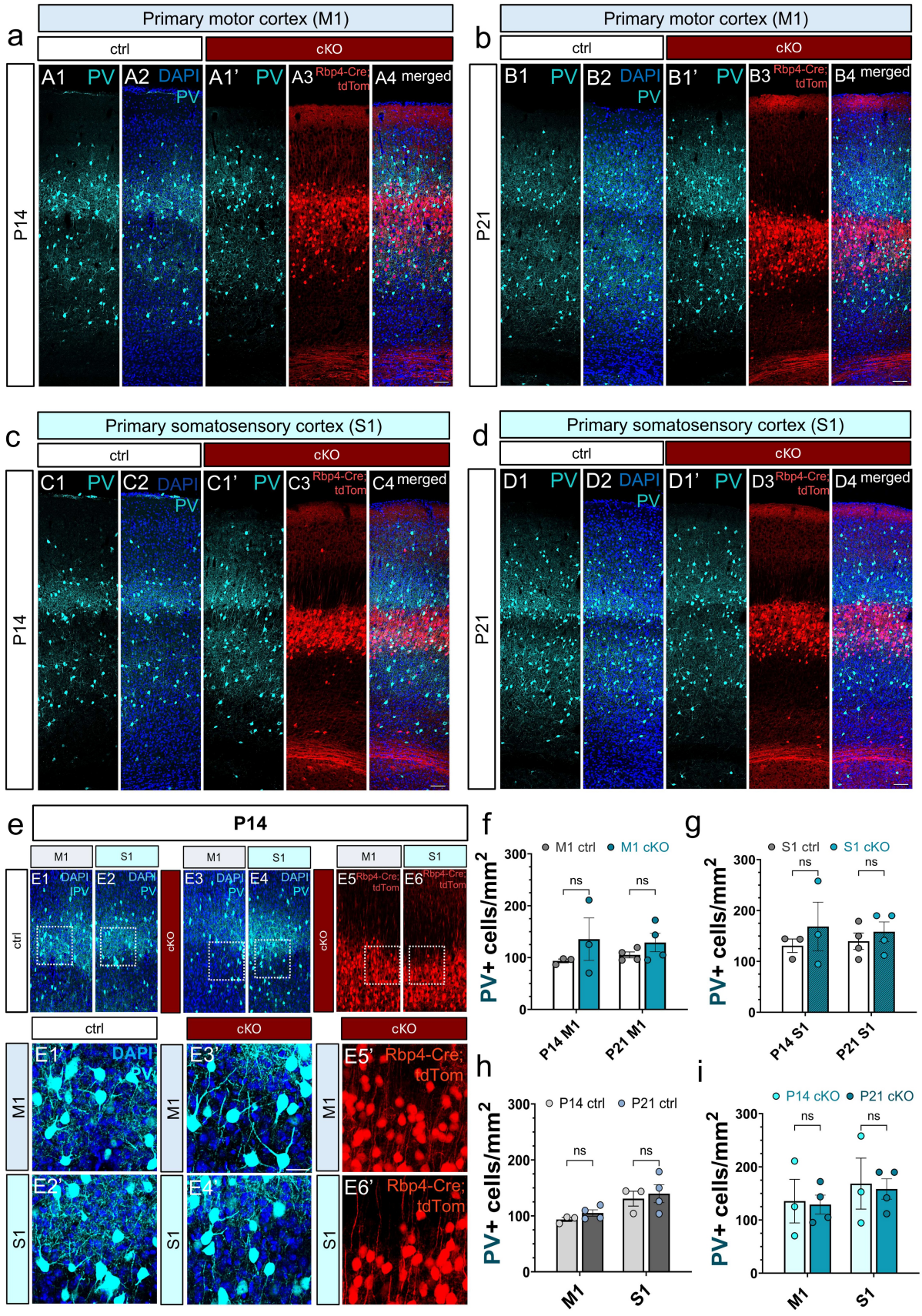

a
Primary motor cortex (M1)
ctrl
cKO
P14
A1 PV
A2 DAPI PV
A1' PV
A3 Rbp4-Cre; tdTom
A4 merged
b
Primary motor cortex (M1)
ctrl
cKO
P21
B1 PV
B2 DAPI PV
B1' PV
B3 Rbp4-Cre; tdTom
B4 merged
c
Primary somatosensory cortex (S1)
ctrl
cKO
P14
C1 PV
C2 DAPI PV
C1' PV
C3 Rbp4-Cre; tdTom
C4 merged
d
Primary somatosensory cortex (S1)
ctrl
cKO
P21
D1 PV
D2 DAPI PV
D1' PV
D3 Rbp4-Cre; tdTom
D4 merged
e
P14
M1
S1
ctrl
cKO
E1 DAPI PV
E2 DAPI PV
E3 DAPI PV
E4 DAPI PV
E5 Rbp4-Cre; tdTom
E6 Rbp4-Cre; tdTom
E1' DAPI PV
E3'
E5' Rbp4-Cre; tdTom
E2'
E4'
E6' Rbp4-Cre; tdTom
f
M1 ctrl
M1 cKO
PV+ cells/mm2
ns
P14 M1
P21 M1
g
S1 ctrl
S1 cKO
PV+ cells/mm2
ns
P14 S1
P21 S1
h
P14 ctrl
P21 ctrl
PV+ cells/mm2
ns
M1
S1
i
P14 cKO
P21 cKO
PV+ cells/mm2
ns
M1
S1

Figure 3.3. Perturbing AP-dependent neurotransmitter release from Rbp4-Cre+ projection neurons does not affect cortical PV neuron development. 2D tile scans of the primary motor cortex during the second and third weeks of postnatal development. PV-immunoreactive neurons (A1-A1', B1-B1') and *Rbp4-Cre;Snap25*$^{fl/fl}$ projection neurons in the *Snap25* cKO brains in M1 at P14 (A3-A4) and P21 (B3-B4). Confocal tile-scans of the primary somatosensory cortex depicting PV-positive neurons and *Rbp4-Cre;Snap25*$^{fl/fl}$ projection neurons (C3-C4, D3-D4) in S1 in the ctrl and *Snap25* cKO brains at P14 (C1-C1') and P21 (D1-D1'). High-magnification confocal images of PV interneurons in M1 and S1 in the ctrl (E1, E2, E1', E2') and L5-silenced brains at P14 (E3, E4, E3',E4'). *Snap25*-deleted projection neurons in layer 5 of M1 and S1 at P14 (E5, E6, E5', E6'). The regions of high-magnification images are delineated by white boxes. Quantification of PV cells in M1 in the second and third postnatal weeks revealed no significant differences in the density of PV neurons between the control and the silenced L5 brains (f). No changes were detected in the density of PV neurons in S1 at P14 and P21 either (g). The developmental trajectory of cortical PV interneurons in the control brains revealed no significant changes in their density between P14 and P21 (h). Loss of AP-dependent neurotransmitter release from Rbp4-Cre+ neurons did not alter the developmental trajectory of PV neurons (i). Scale bars: 100 μm (all panels). Data is represented as mean ± SEM. M1: primary motor cortex; S1: primary somatosensory cortex.

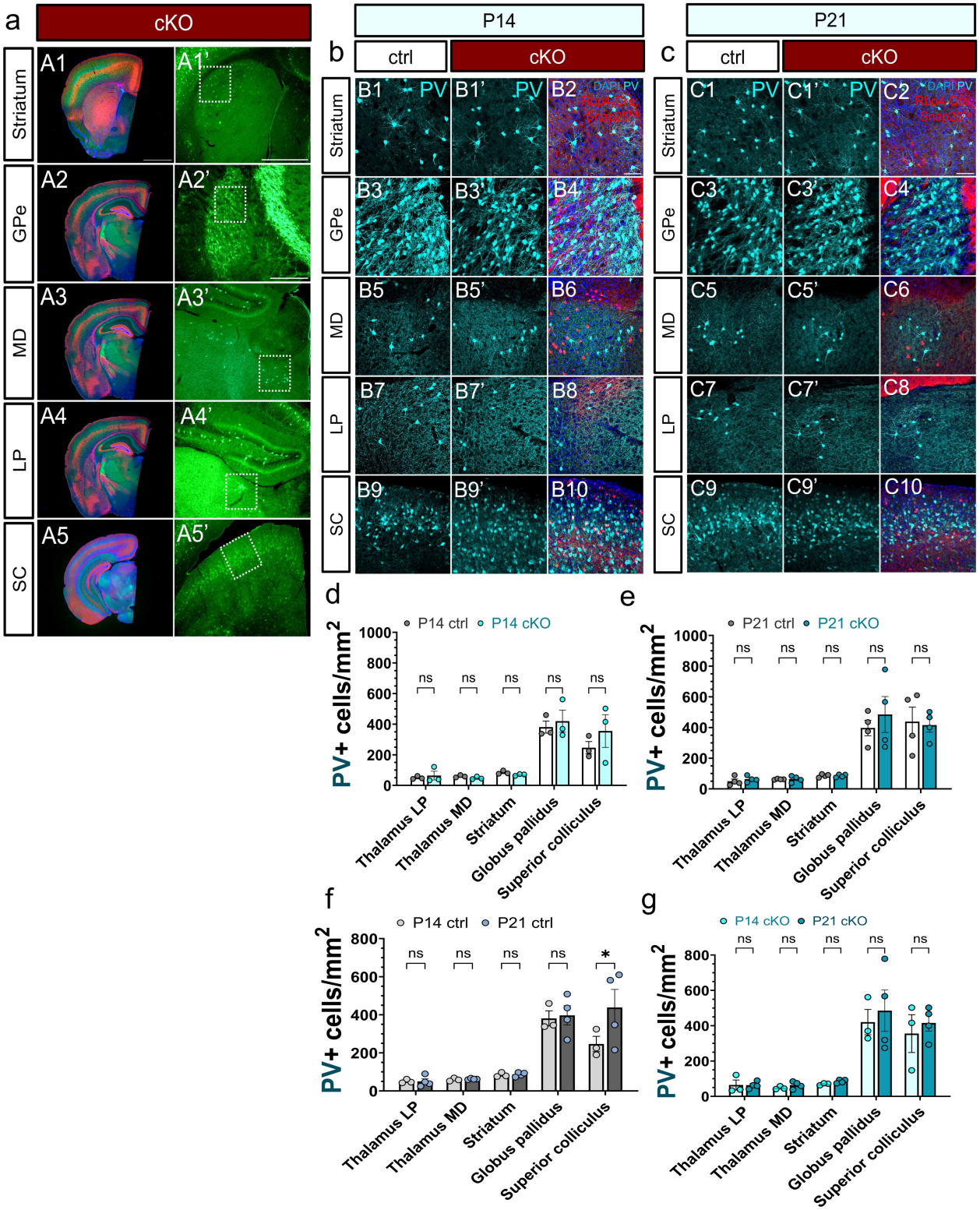


Figure 3.4. Conditional silencing of Rbp4-Cre+ projection neurons in cortical layer 5 has no impact on the density and dynamics of subcortical PV neurons. Low-magnification

epifluorescence images showing the level of sections selected for density analyses (A1, A2, A3, A4, A5). Epifluorescence micrographs illustrating subcortical regions of interest. The white dotted squares highlight the location of images in panels b and c (A1', A2', A3', A4', A5'). Maximum intensity projected z-stack images representing the projection regions of Rbp4-Cre+ L5 neurons at various rostrocaudal levels in the *Snap25* control and cKO brains at P14 (B2, B4, B6, B8, B10) and P21 (C2, C4, C6, C8, C10). The red signal indicates the axonal fibres of the 'silenced' layer 5 projection neurons. Parvalbumin-immunoreactive neurons (cyan) in the caudoputamen (B1, B1', C1, C1') and the external segment of the globus pallidus (B3, B3', C3, C3') in the control and cKO brains at P14 (B1-B4) and P21 (C1-C4). PV+ neurons in the lateral posterior and mediodorsal nuclei of the thalamus at P14 (B5-B8) and P21 (C5-C8). Maximum-intensity projected z-stack image showing PV-immunoreactive neurons in the superior colliculus at P14 (B9-B10) and P21 (C9-C10). Quantification of PV+ cell density in the subcortical projection regions of *Rbp4-Cre;Ai14;Snap25*$^{fl/fl}$ cortical neurons at P14 (d) and P21 (e). Developmental dynamics of subcortical PV neurons in the output regions of L5 neurons between P14 and P21 in the control (f) and cKO (g) brains. Scale bars: 100 µm (A1), 500 µm (A1'), 200 µm (A2'). All data are represented as mean ± SEM. *p < 0.05, SC, P14-P21, ctrl, p = 0.0217. 2-way ANOVA with Šídák's multiple comparisons test.

3.2.5 The absence of AP-dependent neurotransmitter release from Rbp4-Cre+ layer 5 pyramidal neurons causes alterations in the morphology of striatal PV+ neurons at P21

I next investigated whether the disruption of L5 affects the morphology of PV cells in the striatum. This output region of L5 receives dense synaptic innervation as shown by the presence of Vglut1+ tdTomato+ punctae in the dorsal striatum (Figure 3.5. a, b). No differences were detected between the ctrl and the cKO brains at P14 in the soma parameters of striatal PV+ neurons (Figure 3.5. c, d) (soma area, p= 0.8085; perimeter, p= 0.5071; circularity, p= 0.7071; roundness, p= 0.2717; solidity, p= 0.2479, two-tailed Student's t-test with Welch's correction). However, at P21, I noticed a significant decrease in the soma area and roundness of striatal PV+ neurons in the L5-silenced brains (Figure 3.5. e, f) (soma area, p= 0.0192; perimeter, p= 0.2311; circularity, p= 0.9626; roundness, p= 0.0035; solidity, p= 0.7592; two-tailed Student's t-test with Welch's correction). Chronic silencing of subsets of L5 neurons, therefore, did not influence the density or developmental trajectory of striatal PV+ neurons at P21, but it did alter their morphology. Striatal PV+ interneurons appeared to be more elongated, with less rounded and smaller somata in the *Snap25* cKO mice.

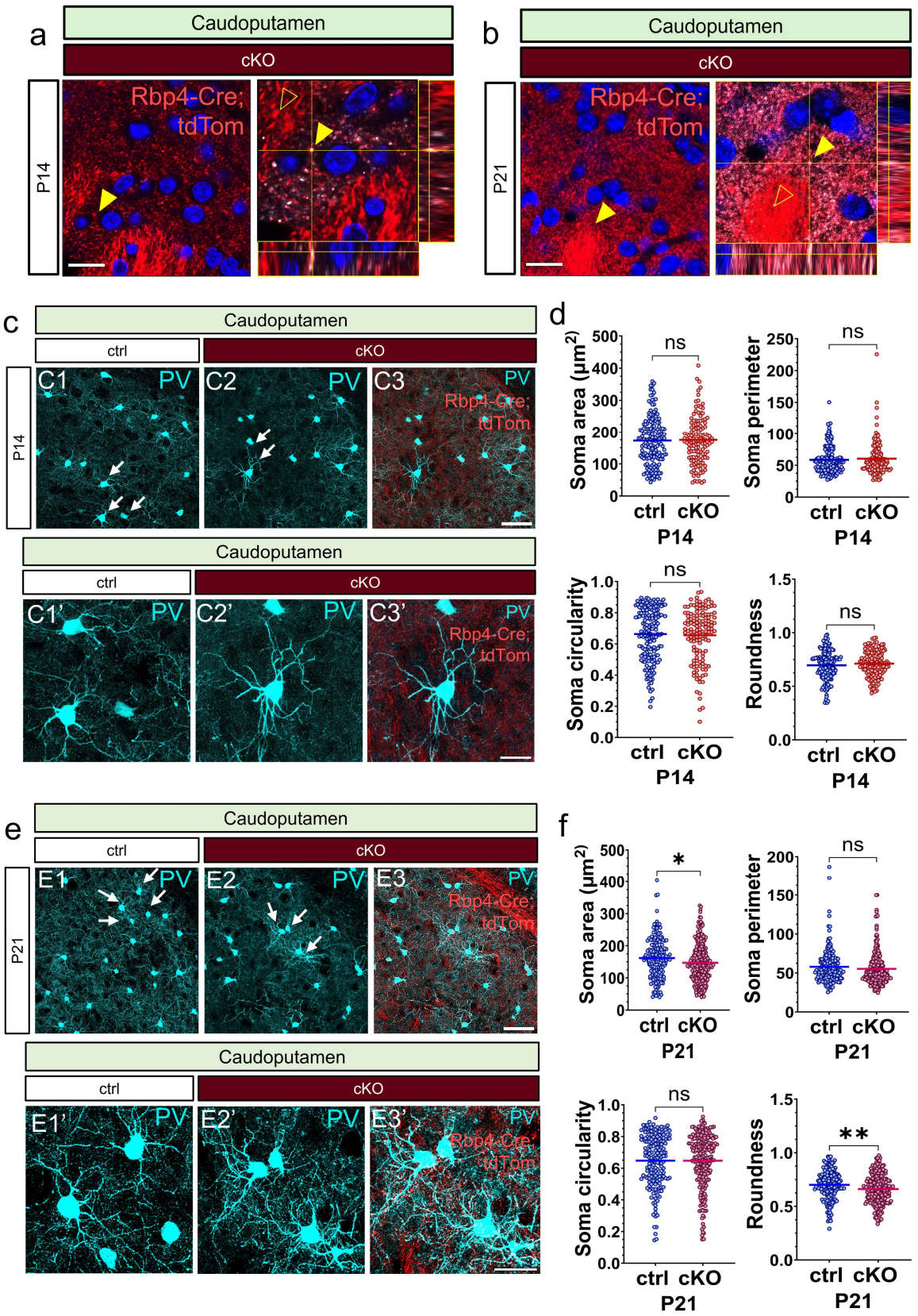

a
Caudoputamen
cKO
P14
Rbp4-Cre; tdTom
b
Caudoputamen
cKO
P21
Rbp4-Cre; tdTom
c
Caudoputamen
ctrl
cKO
P14
C1
PV
C2
PV
C3
PV
Rbp4-Cre; tdTom
Caudoputamen
ctrl
cKO
C1'
PV
C2'
PV
C3'
PV
Rbp4-Cre; tdTom
d
Soma area (µm2)
ns
ctrl cKO
P14
Soma perimeter
ns
ctrl cKO
P14
Soma circularity
ns
ctrl cKO
P14
Roundness
ns
ctrl cKO
P14
e
Caudoputamen
ctrl
cKO
P21
E1
PV
E2
PV
E3
PV
Rbp4-Cre; tdTom
Caudoputamen
ctrl
cKO
E1'
PV
E2'
PV
E3'
PV
Rbp4-Cre; tdTom
f
Soma area (µm2)
*
ctrl cKO
P21
Soma perimeter
ns
ctrl cKO
P21
Soma circularity
ns
ctrl cKO
P21
Roundness
**
ctrl cKO
P21

Figure 3.5. Abolition of AP-dependent neurotransmitter release from layer 5 pyramidal neurons temporarily alters the morphology of striatal PV neurons in the juvenile brain. Glutamatergic synapses are formed in the striatum by Rbp4-tdTomato+ neurons (a, b). Confocal images of P14 and P21 *Rbp4-Cre;Ai14;Snap25*$^{fl/fl}$ brains, along with orthogonal views through image stacks displaying puncta of VGluT1+ and tdTomato+ in the dorsal striatum. Fluorescence colocalisation is evident at both ages (yellow arrowheads), with more punctae noted at P21 (white arrowheads). The tdTom+ fibre bundles (empty yellow arrowheads) are negative for VGluT1 staining (a, b). Z-stack images of PV-immunoreactive neurons in the caudoputamen at P14 and P21 in the ctrl (C1, C1', E1, E1') and L5-silenced brains (C2, C2', E2, E2'). Merged confocal images demonstrating the presence of tdTomato+ fibres in the caudoputamen in the vicinity of PV+ neurons (C3, C3', E3, E3'). There were no significant alterations in the soma features of PV+ neurons at P14 (d). Significant reductions in the soma area and roundness of striatal PV+ neurons were detected at P21 in the *Snap25* cKO mice (f) (soma area, p= 0.0192; roundness, p= 0.0035, ctrl, n=180; cKO, n=236 cells). Unpaired t-test with Welch's correction. Scale bars: 50 μm (C3, E3, E3'), 20 μm (a, b, C3').

3.2.6 Striatal PV neurons in layer 5-silenced brains show an altered developmental trajectory of soma features throughout postnatal development

Having shown that the conditional silencing of Rbp4-Cre+ neurons causes alterations in the soma features of striatal PV+ neurons at P21, I next assessed the course of striatal PV+ morphology between P14 and P21 in the ctrl brains. No significant changes in the morphology of PV neurons in the striatum were observed between P14 and P21 in control brains (Figure 3.6. a, b). In the layer 5-silenced brains; however, I detected a significant reduction in the striatal PV+ neurons' soma area and roundness between 14 and P21 (Figure 3.6. c, d) (soma area, p= 0.0003; perimeter, p= 0.0558; circularity, p= 0.6464; roundness, p= 0.0003; solidity, p= 0.9262; two-tailed Student's t-test with Welch's correction). The somata of PV+ cells in the *Snap25* cKO mice became more compressed and less rounded due to the considerable decrease in their soma area and roundness values. While PV morphology was indistinguishable between ctrl and cKO at P14, measures were significantly different by P21, suggesting a maturational effect of *Snap25* cKO on PV interneuron morphology in the striatum.

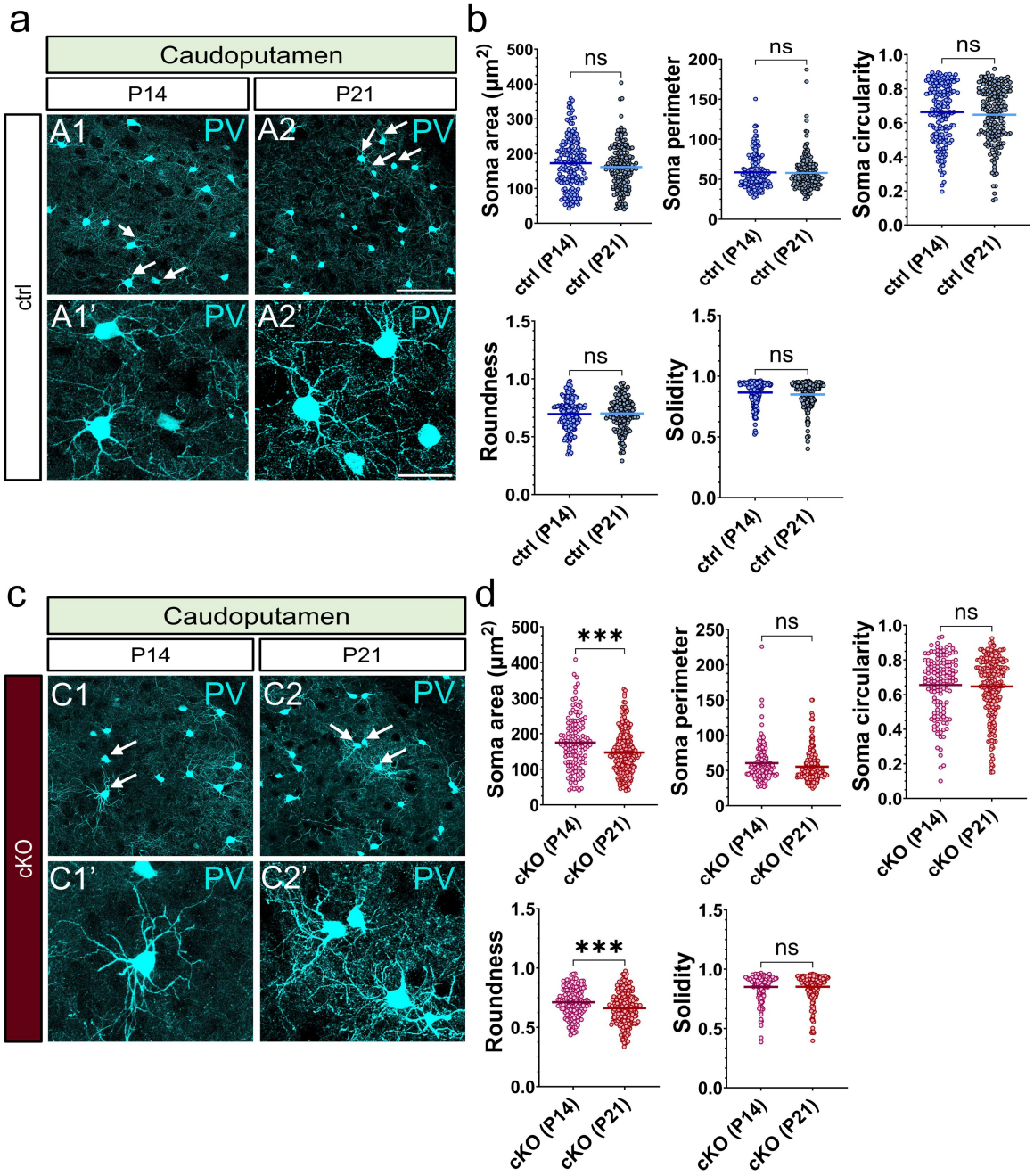


Figure 3.6. Striatal PV interneurons in the layer 5-silenced brains display an altered developmental trajectory of soma features between the early stages of development. Maximum-intensity projected z-stacks of PV-immunoreactive neurons in the caudoputamen in the control mice at P14 (A1, A1') and P21 (A2, A2'). The trajectory of PV neuron morphology in the caudoputamen of control mice did not exhibit significant alterations in the soma characteristics of PV+ neurons between P14 and P21 (b). Confocal z-stacks of PV-immunoreactive neurons in the caudoputamen in the *Snap25* cKO mice at P14 (C1, C1') and P21 (C2, C2'). In the L5-silenced animals, there was a considerable reduction in the soma area and roundness of striatal PV+ interneurons between P14 and P21 (d) (soma area, p= 0.0003, roundness, p= 0.0003. Unpaired t test with Welch's

correction. P14, n=136, P21, n=236). Arrows denote PV+ neurons shown in high-magnification images. Scale bars: 100 µm (A2), 20 µm (A2').

3.2.7 Genetically silencing subsets of layer 5 projection neurons has no long-term impact on the morphology of striatal interneurons in the adult brain

To further investigate whether the changes in the morphology of PV interneurons at P21 persist into adulthood, I conducted the same morphometric analyses on striatal PV neurons in the adult brain. Interestingly, none of the observed differences in PV morphology was observed at three months of age in the L5-silenced brains (Figure 3.7. a, b) (soma area, p= 0.2301; perimeter, p= 0.9398; circularity, p= 0.1721; roundness, p= 0.4804; solidity, p= 0.3412; two-tailed Student's t-test with Welch's correction). I next assessed how the trajectory of PV morphology changed from development to adulthood. The striatal PV neurons in the control brains exhibited distinct alterations in soma area, circularity, roundness, and solidity. By three months of age, all these characteristics had significantly decreased (Figure 3.7. C1-C2, d) (soma area, p= <0.0001; perimeter, p= 0.6702; circularity, p= <0.0001; roundness, p= 0.0050; solidity, p= <0.0001, two-tailed Student's t-test with Welch's correction). Similar reductions in soma area, circularity, and solidity values were observed in the *Snap25* cKO brains (Figure 3.7. C3-C4'', e) (soma area, p= 0.0028; perimeter, p= 0.6048; circularity, p= 0.0020; roundness, p= 0.6391; solidity, p= <0.0001, two-tailed Student's t-test correction). These results suggest that chronic silencing of L5 neurons may modify or accelerate the morphological trajectory of striatal PV neurons while leaving their density intact. It seems that the chronic loss of AP-dependent neurotransmitter release in L5 has a transient effect on striatal PV+ neurons since the observed variations in striatal PV morphology were no longer detectable at twelve weeks of age.

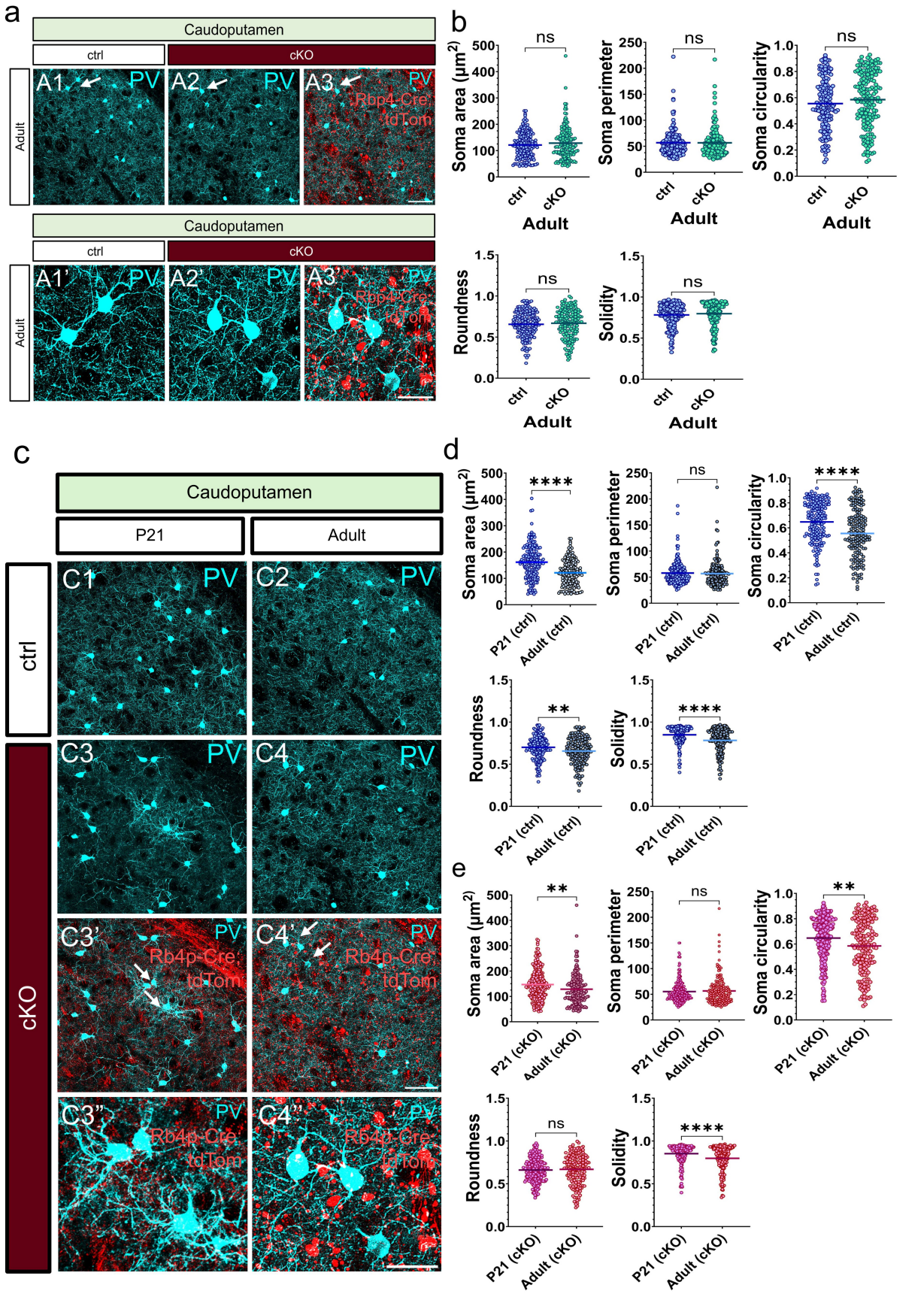

a
Caudoputamen
ctrl
cKO
Adult
A1
A2
A3
PV
Rbp4-Cre
tdTom
A1'
A2'
A3'
b
Soma area (µm2)
Soma perimeter
Soma circularity
Roundness
Solidity
ns
ctrl
cKO
Adult
c
P21
Adult
C1
C2
C3
C4
C3'
C4'
C3''
C4''
d
****
**
e
P21 (ctrl)
Adult (ctrl)
P21 (cKO)
Adult (cKO)

Figure 3.7. Conditional silencing of Rbp4-Cre+ pyramidal neurons has no permanent impact on the morphology of striatal interneurons in the adult brain. Maximum-intensity projected images of PV+ interneurons in the caudoputamen in the ctrl (A1, A1') and L5-silenced mice at 3 months of age (A2, A2'). Z-stack images of PV+ neurons and *Rbp4-Cre;Ai14;Snap25*$^{fl/fl}$ neurons in the striatum of adult *Snap25* cKO mice (A3, A3'). White arrows mark the location of striatal PV+ neurons depicted in higher magnification (A1-A3'). No significant differences were observed in the soma parameters of PV+ neurons in the striatum of L5-silenced mice compared to control mice at 12 weeks of age (b). PV+ interneurons in the caudoputamen of ctrl mice at P21 (C1) vs 12 weeks of age (C2). PV+ interneurons in the caudoputamen of *Snap25* cKO mice at P21 (C3) and 12 weeks of age (C4). Axonal projections of *Rbp4-Cre;Ai14;Snap25*$^{fl/fl}$ neurons in the caudoputamen in the L5-silenced mice at P21 (C3', C3'') and 12 weeks of age (C4', C4"). Note the stark contrast in the axonal fibres of L5 projection neurons between the developing versus the adult *Snap25* cKO mice. Quantitative analysis of the trajectory of PV neuron morphology from P21 to 12 weeks of age in the ctrl brains (d) (P21, n=180; 12 wks, n=168 cells, **** p<0.0001, unpaired t-test with Welch's correction) and L5-silenced mice (e) (P21, n=236; 12 wks, n=171 cells). Scale bars: 50 µm (A3, C4'), 20 µm (A3', C4'').

3.2.8 VVA is not a suitable non-activity-dependent marker during development

3.2.8.1 VVA produces non-specific staining in the postnatal murine cortex

To determine whether VVA can be used as an activity-independent marker in the developing brain to detect the presence of PNNs around PV+ interneurons, I performed histochemical experiments at P8, P14, and P21, which yielded varied results. Either the staining resulted in widespread non-specific labelling, or the inadequate labelling made the visualisation of PNNs insufficient. The lattice-like structure of PNNs was only detected in a few slices. While the labelling of VVA+ cells using freshly perfused brain tissues did seem to improve the staining quality, the diffuse non-specific pattern observed in the VVA channel remained an issue. That made these sections unsuitable for the precise quantification of VVA+ cell density in postnatal brains. While the developmental maturation of PV+ interneurons and the condensation of proteoglycans into PNNs are not yet complete at early developmental ages, samples collected at P21 did not yield significantly better detection of VVA+ cells than samples collected at P8 and P14. Both the *Snap25* cKO and control brains exhibited the weakest histochemical signal at P8, as expected from the developmental

trajectory of the formation of PNNs and the maturation of PV+ interneurons. Representative confocal images of VVA+ cells in M1 (Figure 3.8. A-C, A'-C') and S1 are shown in Figure 3.8. D-F, D'-F'.

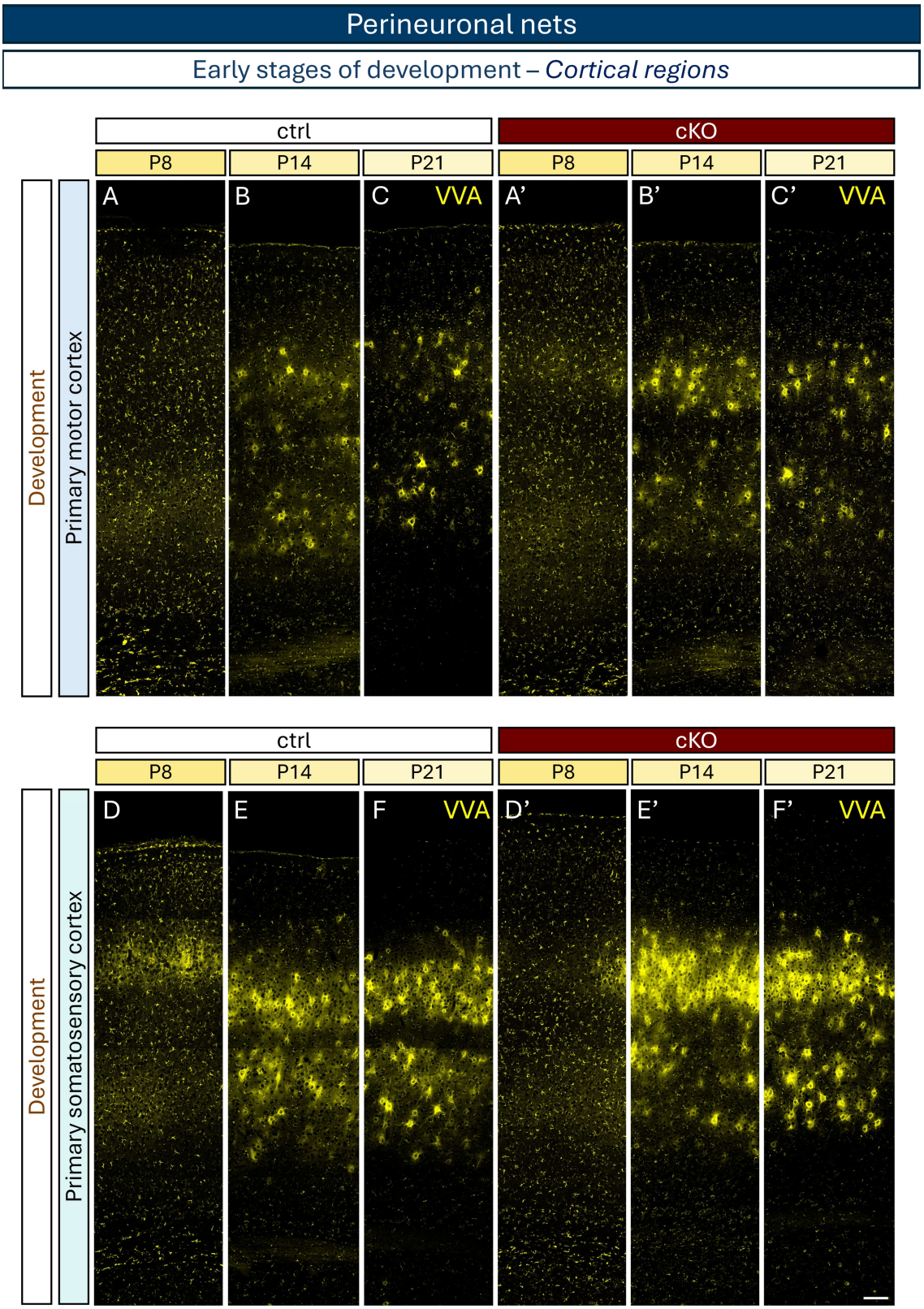


Figure 3.8. VVA histochemical staining results in insufficient labelling of PNNs during the early stages of development in the primary motor and somatosensory cortex. (A, B, C) Confocal images illustrating the detection of VVA-positive cells at three different developmental time points (P8, P14, and P21) in the control (A, B, C) and layer 5-silenced mice (A', B', C') in M1. Confocal images showing a gradual increase in the expression of PNNs around VVA+ cells in control mice in S1, but non-specific staining is still observed at P8 and P14. (D, E, F). Confocal images depicting VVA+ cells in M1 in the *Snap25* cKO brains at P8, P14, and P21. (D', E', F') Scale bars = 100 µm.

3.2.8.2. VVA staining within the hippocampus and subcortical areas leads to inadequate perineuronal net detection at different developmental stages

When comparing the results of VVA+ labelling in cortical versus subcortical areas, I observed the same diffuse non-specific staining in the striatum, the thalamus, and the superior colliculus. The thalamic nuclei showed a dotty pattern of non-specific labelling. No lattice-like morphology was observed for VVA+ cells in the *Snap25* cKO and control brains at P8, P14, and P21. Regarding the hippocampal areas, the CA3 and the dentate gyrus revealed the presence of VVA+ cells at P14 and P21; however, the detection of VVA+ cells remained unfeasible due to the poor visualisation of PNNs in most of the brains. These findings point to either the inadequate detection limit of the experimental procedure utilised to label VVA+ cells during the first two weeks of postnatal development or the unsuitability of the VVA lectin as a marker for developing brains. Representative images of VVA+ labelling within the hippocampus and subcortical regions of interest are presented in Figure 3.9.

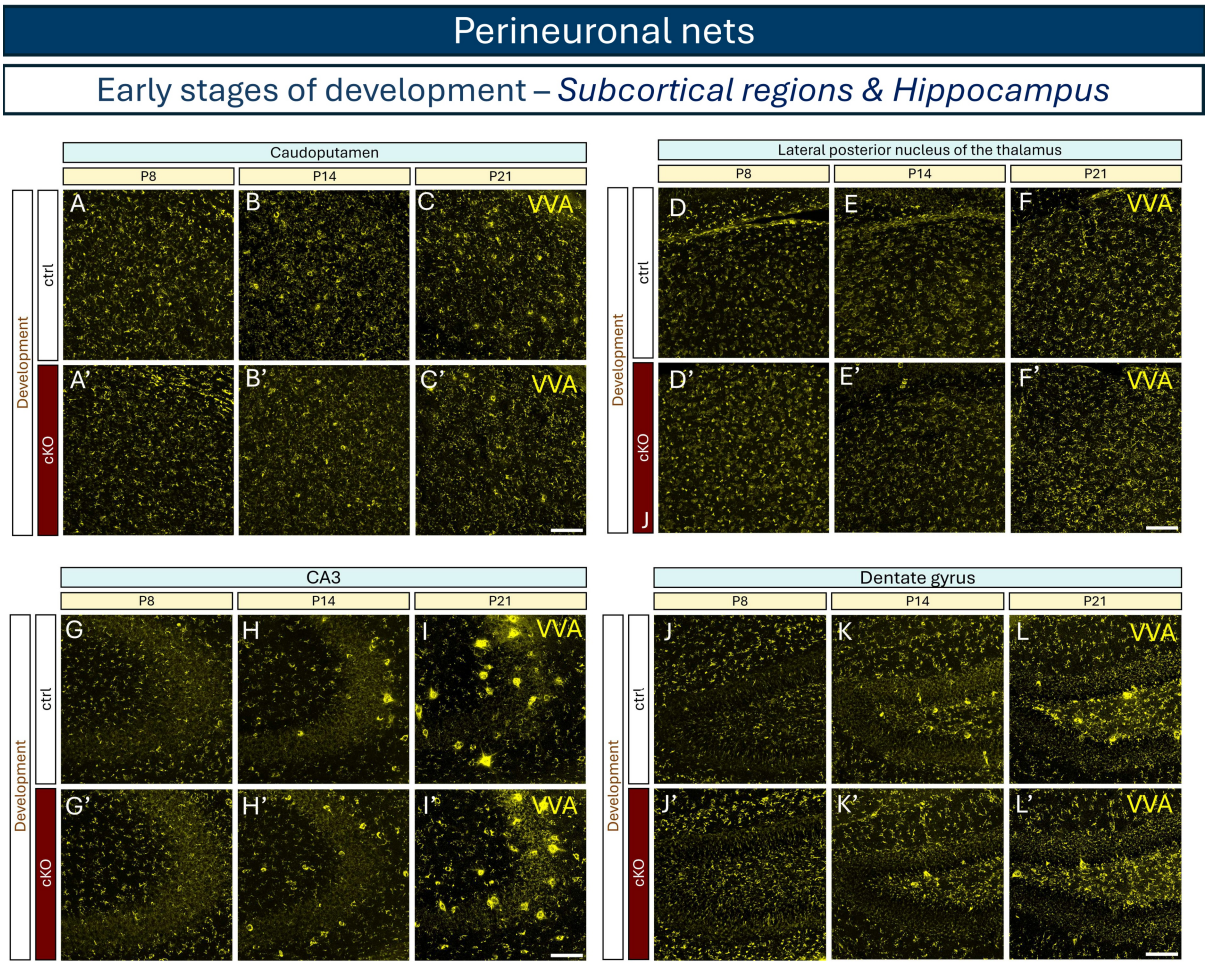


Figure 3.9. VVA is not suitable for the precise detection of PNNs in the hippocampus and in subcortical regions during development. Z-stack images of the striatum and the lateral posterior nucleus show extensive non-specific staining at P8, P14, and P21 in the control (A, B, C, D, E, F) and *Snap25* cKO brains (A', B', C', D', E', F'). The CA3 of the hippocampus in the layer 5-silenced and ctrl brains revealed the lattice-like morphology for VVA-positive cells at P14 and P21 (ctrl, G, H, I; cKO, G', H', I';), but the visualisation of PNNs remained poor in the dentate gyrus as seen in the ctrl (J, K, L) and *Snap25* cKO (J', K', L') brains. Scale bars = 100 µm (all panels).

3.2.8.3. Vicia villosa agglutinin is an efficient marker for the visualisation of perineuronal nets in the adult brain

Histochemical staining of VVA+ cells in the adult *Snap25* cKO and control brains produced efficient labelling of PNNs. The detection of VVA+ cells in Figure 3.10. is shown at 12 weeks of age when the PNNs have fully matured and reached the adult-like stage (Pizzorusso et al. 2002). The precision of detection was deemed sufficient for further cell quantification. These results indicate that

VVA is suitable for the efficient detection of PNNs in cortical, subcortical, and hippocampal regions in the adult brain when the maturation of PV+ interneurons and the formation of PNNs are complete.

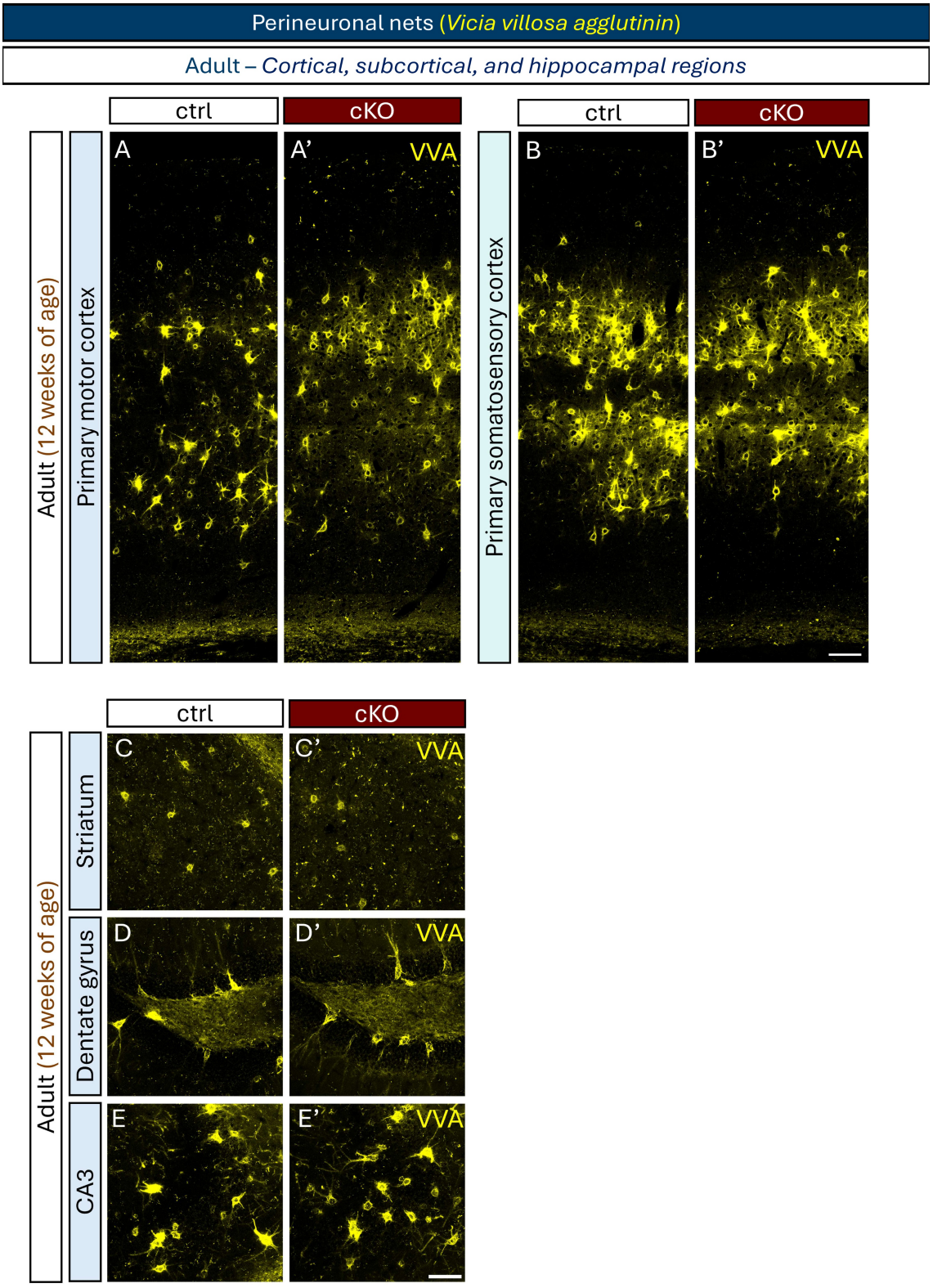


Figure 3.10. VVA sufficiently labels PNNs in the adult brain. (A, A') Tile scans of coronal sections from the primary motor cortex of adult control and Snap25 mutant mice showing sufficient detection of PNNs. (B, B') Tiled images depicting PNNs in the primary somatosensory cortex. (C, C') Z-projection confocal images of striatal and hippocampal PNNs in the control and layer 5-silenced brains. (D, D', E, E'). Specific labelling of PNNs in the dentate gyrus in the adult *Snap25* cKO and control mice. Scale bars = 100 μm (all panels).

3.2.9 The absence of AP-dependent neurotransmitter release from Rbp4-Cre+ layer 5 does not alter the laminar organisation of PV interneurons in the juvenile brain

After confirming that the chronic silencing of Rbp4-Cre+ neurons did not affect the density of cortical and subcortical PV neurons during development, I investigated whether it influenced their laminar distribution at P14 and P21. Two-way ANOVA tests only revealed a significant *layer* but no *genotype* effect on the distribution of PV neurons in M1 and S1 at P14 and P21 ($p<0.0001$). No differences were detected by post-hoc tests in the laminar positioning of PV cells in M1 at P14 (Figure 3.11. A1-A3, c) (L1, p= >0.9999; L2/3, p= 0.5340; L5, p= 0.7345; L6, p= 0.9370) and P21 (Figure 3.11. B1-B3, d) (L1, p= >0.9999; L2/3, p= 0.6876; L5, p= 0.6454; L6, p= 0.4757). The absence of regulated vesicle release from L5 projection neurons did not alter the distribution of PV across the cortical layers in S1 at P14 (Figure 3.11. G1-G3, i) (L1, p= >0.9999; L2/3, p= >0.9999; L4, p= 0.9541; L5, p= 0.9434; L6, p= 0.9824) and P21 (Figure 3.11. H1-H3, j) (L1, p= >0.9999; L2/3, p= >0.9999; L4, p= 0.6483; L5, p= 0.9640; L6, p= 0.9024; two-way ANOVA with Šídák's multiple comparisons test).

Since *genotype* did not influence the laminar arrangement of immature PV interneurons, I then investigated their developmental dynamics. Between P14 and P21, I did not observe a significant change in the laminar distribution of PV neurons in the ctrl brains in M1 (Figure 3.11. e) (L1, p=>0.9999; L2/3, p=0.3337; L5, p=0.5500; L6,p=0.3260; two-way ANOVA with Šídák's multiple comparisons test). The developmental trajectory of PV neurons in M1 in the L5-silenced brains was identical to that of the control brain (Figure 3.11. f) (L1, p= >0.9999; L2/3, p=0.9939; L5, p=>0.9999; L6, p=0.9849; two-way ANOVA with Šídák's multiple comparisons test). Similar to M1, I observed no alterations in the laminar positioning of PV interneurons in S1 across the cortical layers in the ctrl brains between P14 and P21 (Figure 3.11. k) (L1, p=>0.9999; L2/3, p=0.9706; L4, p=0.9964; L5, p=>0.9999; L6, p=>0.9999; two-way ANOVA with Šídák's multiple comparisons test). Silencing layer 5 had no impact on the trajectory of the laminar distribution of PV in S1, either in the *Snap25* cKO mice (Figure 3.11. l). These findings suggest that long-term L5 neuron manipulation does not change

the spatial arrangement of PV+ neurons in the cortex during development and preserves the trajectory of PV distribution. Considering that the conditional deletion of *Snap25* and the subsequent loss of AP-dependent neurotransmitter release from L5 pyramidal neurons do not appear to impact the laminar positioning of PV cells during early development, it raises the question of what determines the laminar location of PV cells in the neocortex. Key factors defining their laminar allocation include their origin's time and place, intrinsic genetic programs such as transcription factors *Lhx6* and *Sox6*, extracellular cues that guide migration, network activity, and cell-cell interactions (Lim et al. 2018). Despite the lack of effect on PV distribution in our model, pyramidal neurons still appear to play a significant role in determining the laminar positioning of GABAergic interneurons. This is supported by evidence showing that interneurons do not establish their specific laminar position until the corresponding pyramidal neurons begin to occupy their respective layers in the cortex (Lim et al. 2018; Miyoshi and Fishell 2011). Lodato et al (2011) have shown that the loss of *Fezf2* leads to abnormally distributed GABAergic neurons in the *Fezf2* mutants, with significantly decreased inhibitory neurons in layer 5 and increased GABAergic neuron numbers in the superficial layers. Since the genetic manipulation I performed 1) did not target a key transcription factor determining the fate of the cell and 2) only affected a subset of L5 neurons (15%), it might be that activity from other L5 cells was sufficient to maintain the correct positioning of PV cells. Interestingly, chemogenetic studies manipulating pyramidal neuron activity have only found a significant effect on the density of PV+ and SST+ neurons, without altering their laminar distribution (Wong et al. 2018). My results similarly had no impact on PV+ laminar allocation at P21, indicating potential compensatory effects occurring in the cortex during early development.

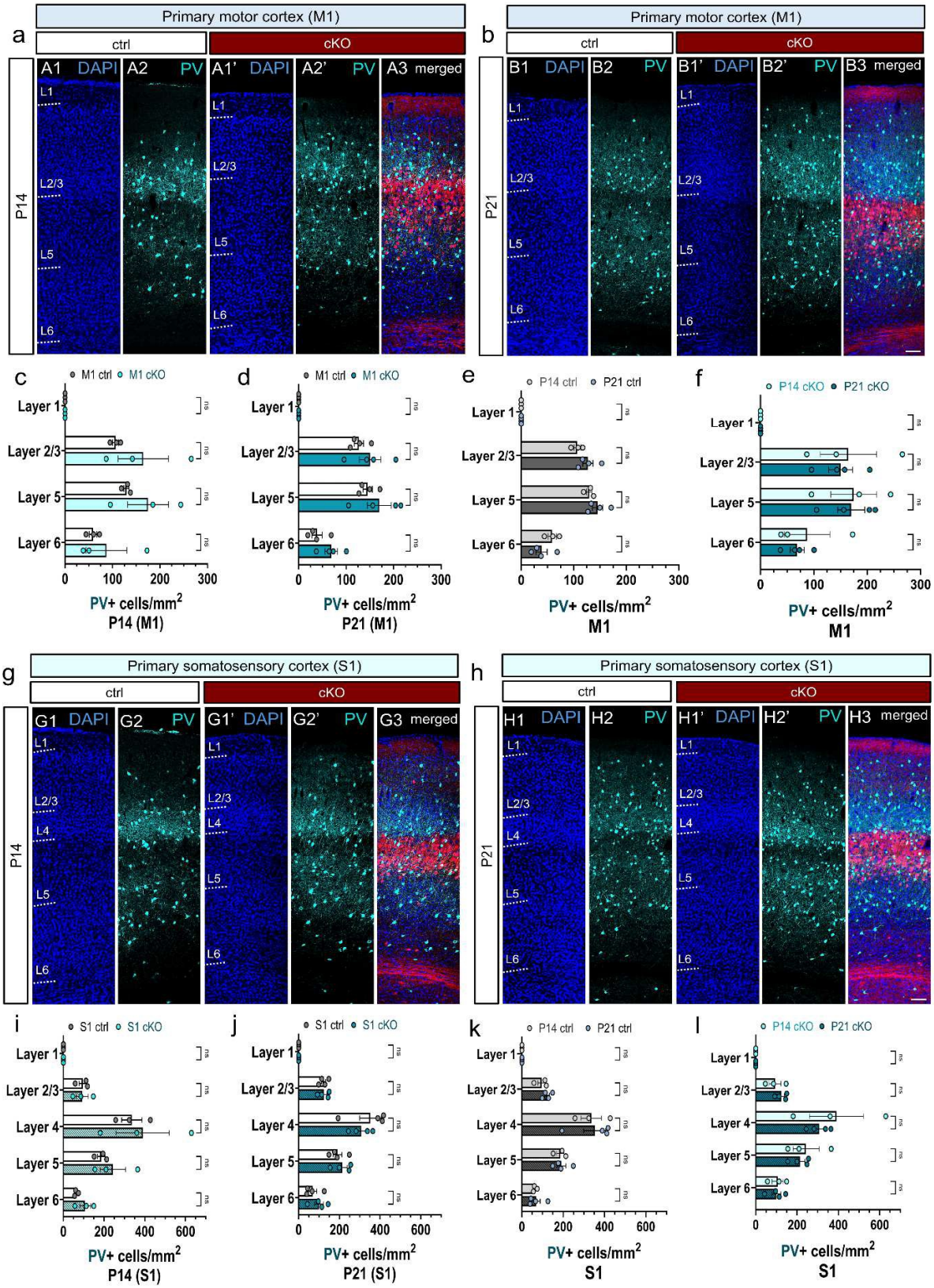


Figure 3.11. Conditional silencing of subsets of layer 5 pyramidal neurons does not disrupt the laminar arrangement of PV interneurons in the juvenile cortex. Confocal tile scan images of PV+

immunostaining in ctrl and cKO brains at P14 and P21. DAPI nuclear counterstaining was performed to define the boundaries of cortical layers in M1 (A1, A1', B1, B1') and S1 (G1, G1', H1, H1'). Tile scans showing the distribution of PV+ neurons across the cortical layers in M1 at P14 (A2, A2') and P21 (B2, B2'). Tile scans depicting the distribution of PV+ neurons across the cortical layers in S1 at P14 (G2, G2') and P21 (H2, H2'). Merged images displaying *Rbp4-Cre;Ai14;Snap25*$^{fl/fl}$ neurons in red and PV-immunoreactive neurons in cyan in M1 (A3, B3) and S1 (G3, H3). Quantification of the laminar distribution of PV+ neurons in M1 at P14 and P21 (c, d). Developmental trajectory of the distribution of PV neurons in M1 in the ctrl brains (e). Developmental trajectory of the laminar distribution of PV neurons in M1 in the mutant brains (f). Laminar distribution of PV neurons across the cortical layers in S1 at P14 (g, i) and P21 (h, j). Developmental trajectory of the laminar distribution of PV+ neurons between P14 and P21 in the S1 ctrl and the L5-silenced brains (k, l). Scale bars: 100 μm. All data are represented as mean ± SEM.

3.3. The effects of chronically silencing layer 5 projection neurons on parvalbumin neurons in the adult brain

3.3.1. Conditional silencing of L5 projection neurons does not influence the density of PV neurons in the adult cortex but disrupts the correlation between PV interneurons and the perineuronal net in M1

My next aim was to determine whether chronically silencing L5 had a delayed impact on PV interneurons in the adult brain. I postulated that the removal of *Snap25* from L5 might affect PV neurons differently, whether or not PNNs encapsulated them. I used the *Vicia villosa* agglutinin (VVA) to visualise the perineuronal net and distinguished between PV neurons with PNN (PV+ VVA+) and PV neurons without PNN (PV+ VVA-). No differences were observed in the density of PV cells in M1 and S1 between the ctrl and cKO brains despite the *Rbp4-Cre;Snap25* cKO L5 neurons displaying clear signs of neurodegeneration and neuroinflammation by 3 months of age (Figure 3.12. A2, A2', B4', C2, C2', D4') (please see Hoerder-Suabedissen et al., 2019). Considering the drastic impairments of the silenced L5 projections, it is intriguing that cortical PV interneurons in M1 and S1 remain unaffected by the ongoing neurodegenerative events in the adult *Snap25* cKO brains (Figure 3.12. A1, A1', B1, B1', C1, C1', D1, D1', e) (M1, p= 0.9700; S1, p= 0.2887; two-way ANOVA with Šídák's multiple comparisons test). The initial signs of neurodegeneration and axon disintegration could first be detected in the spinal cord, followed by the fragmentation of distal axons of L5 neurons in the striatum and the dorsal lateral geniculate nucleus (dLGN) (Hoerder-Suabedissen et al. 2019). By 8 months of age, the long-range axonal projections of Rbp4-Cre+ neurons had completely disappeared in the thalamus, which was accompanied by a significant reduction in the number of L5 cells in the *Snap25* cKO cortex (Hoerder-Suabedissen et al. 2019). The Rbp4-Cre+ neurites exhibited altered ultrastructure, characterised by numerous vacuoles containing structures resembling autophagosomes and lysosomes (Hoerder-Suabedissen et al. 2019). Additionally, the presence of

microglia and lipofuscin in the mutant cortex suggested signs of inflammation (Hoerder-Suabedissen et al. 2019).

To determine whether silencing L5 alters the PNN, I assessed the density of VVA+ cells in the adult cortex. There were no differences in the density of VVA+ cells in M1 and S1 between the control and the cKO brains (Figure 3.12. A3, B2, B2', C3, D2, D2', f) (M1, p= 0.0544; S1, p= 0.1044; two-way ANOVA with Šídák's multiple comparisons test).

While the density of PV and VVA cells remained unchanged in the adult cortex, I did notice an alteration in their co-expression. Three groups were distinguished based on the presence of PNN: 1) PV neuron with PNN or the double positives (PV+ VVA+); 2) PV neuron without PNN (PV+ VVA-); and 3) PNN around non-PV neuron (PV- VVA+). There was a significant decline in the density of PV- VVA+ cells in M1 in the *Snap25* cKO brains (Figure 3.12. h) (PV+ VVA+, p= 0.3793; PV+ VVA-, p= 0.7926; PV- VVA+, p= 0.0263; two-way ANOVA with Šídák's multiple comparisons test). Remarkably, the decrease in the density of PV- VVA+ cells is happening without a change in the density of PV+ neurons, indicating that the PNN is still plastic and capable of dynamic changes in the adult brain. I also noted a significant decrease in the percentage of the double-positive cells in M1 in the layer 5-silenced mice (Figure 3.12. g) (M1, p= 0.0081; S1, p= 0.1479; two-way ANOVA with Šídák's multiple comparisons test). Contrary to M1, the density of PV+ VVA+, PV+ VVA-, and PV- VVA+ cells did not differ significantly in S1 between the control and mutant brains (Figure 3.12. i) (PV+ VVA+, p=0.2707; PV+ VVA-, p= 0.9978; PV- VVA+, p= 0.9343; two-way ANOVA with Šídák's multiple comparisons test).

Next, I explored how the genetic silencing of subsets of L5 pyramidal neurons influenced the correlation between PV and VVA in different cortical regions. The PNN is thought to be predominantly surrounding PV interneurons; therefore, the positive association between PV and VVA in ctrl M1 and S1 is not an unanticipated result (Figure 3.12. j, l). However, this correlation was altered in the motor cortex of L5-silenced mice (Figure 3.12. k) (M1: r= 0.6 (ctrl), p=0.449; r= -0.8 (cKO), p=0.172). It is

noteworthy that the effect of L5 appears to vary depending on the cortical region, as, although decreasing, the correlation between PV and VVA in S1 did not alter (Figure 3.12. m) (S1: r=0.4 (ctrl), p=0.578; r=0.1 (cKO), p=0.923).

The differential impact on M1 and S1 may indicate a variable degree of plasticity in the adult cortex. The greater adaptability of M1 compared to S1 can be attributed to their distinct functional demands, synaptic plasticity, and different circuit organisation. When considering the functional requirements of cortical circuits, M1 must quickly respond to changes in the environment and adjust motor outputs accordingly. This necessitates rapid remodelling and structural plasticity (Feldman 2009). Similar to M1, S1 exhibits plasticity, but it is more difficult to activate. For discernible changes to occur, significant and sustained changes in sensory input are usually needed (Castro-Alamancos et al. 1995; Buonomano and Merzenich 1998; Mohammed and Hollis 2018). Therefore, S1 may not be substantially changed by less robust changes in input. Moreover, M1 and S1 display unique organisational characteristics in L5 that correspond to their respective functions in motor control and sensory processing. While both M1and S1 harbour IT and PT types of L5 pyramidal neurons, PT neurons in L5 of M1 are the dominant subtypes with long-range projections to the brainstem, subcortical motor regions, and the spinal cord and control motor commands (Kawaguchi 2017; Molnár and Cheung 2006). L5 of S1, due to its sensory processing needs, is populated by a mixture of PT and IT neurons, including corticocortical and corticothalamic neurons (Kim et al. 2015; Moberg and Takahashi 2022).

Another key difference between M1 and S1 L5 is their synaptic input characteristics. L5 M1 pyramidal neurons receive a strong descending excitatory input from L2/3 neurons, and this L2/3 to L5 pathway plays a crucial role in motor output, movement control, and sensory input integration (Quiquempoix et al. 2018; Pluta et al. 2019). L5 S1 neurons receive a variety of inputs, integrating synaptic input from layers 2/3, 4, 5, and 6, with a significant contribution from layers 2/3 and 4 for sensory and local processing (Naka and Adesnik 2016). It is also worth noting that M1 and S1 have

distinct maturational profiles, and therefore, the onset and closure of critical periods (CPs) differ between the two regions. Beginning around birth and lasting until the third postnatal week, the CP of S1 operates on a shorter timescale than M1 and is heavily influenced by sensory experience, as well as by both extrinsic and intrinsic factors, including GABAergic circuit maturation (Pedrosa et al. 2022; Erzurumlu and Gaspar 2012; Larsen et al. 2023). Following the establishment of sensory maps, the closure of CP S1 is followed by the opening of the CP of M1 (~P14-P21 in rodents), which has a prolonged time window and is shaped by motor activity, skill learning, and the maturation of GABAergic inhibition (Larsen et al. 2023; Patton et al. 2019). Therefore, the differences in the duration of CPs in M1 and S1 endow these regions with a different degree of neuroplasticity and sensitivity to adapt to changes after the closure of CPs.

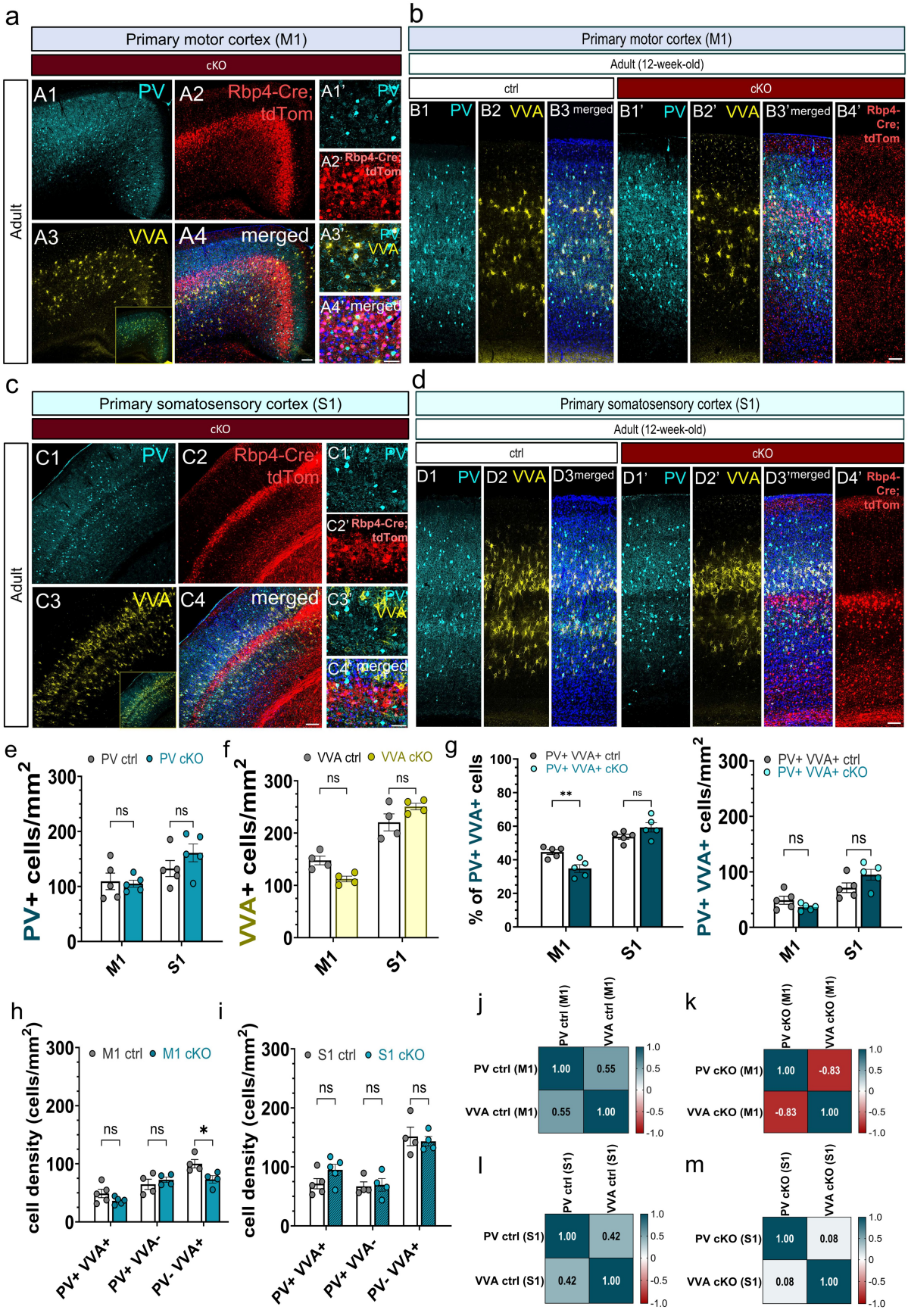

a
Primary motor cortex (M1)
cKO
Adult
A1 PV
A2 Rbp4-Cre; tdTom
A3 VVA
A4 merged
b
Primary motor cortex (M1)
Adult (12-week-old)
ctrl
cKO
B1 PV
B2 VVA
B3 merged
B4' Rbp4-Cre; tdTom
c
Primary somatosensory cortex (S1)
cKO
Adult
C1 PV
C2 Rbp4-Cre; tdTom
C3 VVA
C4 merged
d
Primary somatosensory cortex (S1)
Adult (12-week-old)
ctrl
cKO
D1 PV
D2 VVA
D3 merged
D4' Rbp4-Cre; tdTom
e
PV ctrl
PV cKO
PV+ cells/mm2
M1
S1
f
VVA ctrl
VVA cKO
VVA+ cells/mm2
g
PV+ VVA+ ctrl
PV+ VVA+ cKO
% of PV+ VVA+ cells
PV+ VVA+ cells/mm2
h
M1 ctrl
M1 cKO
cell density (cells/mm2)
PV+ VVA+
PV+ VVA-
PV- VVA+
i
S1 ctrl
S1 cKO
j
PV ctrl (M1)
VVA ctrl (M1)
1.00
0.55
k
PV cKO (M1)
VVA cKO (M1)
-0.83
l
PV ctrl (S1)
VVA ctrl (S1)
0.42
m
PV cKO (S1)
VVA cKO (S1)
0.08

Figure 3.12. Loss of *Snap25* from layer 5 pyramidal neurons alters the correlation between PV interneurons and the perineuronal net in M1. Low-magnification images of the primary motor cortex in the *Snap25* cKO brains showing PV-immunoreactive neurons in cyan (A1, A1') and *Rbp4-Cre;Snap25$^{fl/fl}$* projection neurons in red (A2, A2'). Examples of co-localisation of PV and VVA in M1 in *Snap25* cKO brains (A3, A3'). PV+ and VVA+ cells are highly concentrated near the cell bodies of *Rbp4-Cre;Snap25$^{fl/fl}$* neurons (A4, A4'). Z-stack and tile-scan images of M1 depicting PV-immunostained neurons (B1, B1') and PNN labelling in the ctrl (B2) and L5-silenced brains at 12 weeks of age (B2', B3). *Rbp4-Cre;Snap25$^{fl/fl}$* neurons in the adult motor cortex showing signs of degeneration and fragmentation (B4'). Single-scan images of PV+ neurons (C1, C1') and VVA+ cells in the primary somatosensory cortex of *Snap25* cKO brains at 3 months of age (C3, C3'). Ongoing degenerative processes and heightened inflammation in the *Snap25* cKO mice (C2, C2'). PV+ and VVA+ signals superimposed on *Rbp4-Cre,Ai14;Snap25$^{fl/fl}$* neurons (C4, C4'). Combined tile-scan and z-stack images of PV-immunostained neurons (D1, D1') and VVA-labelled PNNs in the ctrl and L5-silenced brains at 12 weeks of age (D2, D3, D2', D3'). Accumulation of tdTomato+ punctae throughout the cortex (D4'). Quantification of PV+ and VVA+ cells in M1 and S1 at 3 months of age (e, f). Percentage and density calculations of PV+ VVA+ cells in M1 at 3 months of age (g). Significant decrease in the density of PV-VVA+ neurons in the adult motor cortex in the *Snap25* cKO mice (h) (p= 0.0263, 2-way ANOVA with Šídák's multiple comparisons test). Total density of PV+ VVA+, PV+ VVA-, PV- VVA+ cells in the adult S1 (i). Pearson correlation between PV and VVA cells in M1 (j-k) and S1 (l-m). *p < 0.05, **p< 0.01.*p < 0.05, **p< 0.01. Scale bars: 100 µm (A4, C4), 50 µM (A4', C4', B3, D4). M1: primary motor cortex, S1: primary somatosensory cortex.

3.3.2. Chronic silencing of subsets of layer 5 projection neurons has a delayed effect on the laminar organisation of PV interneurons and the perineuronal nets

Next, I explored whether the chronic silencing of L5 neurons had long-lasting effects on the laminar arrangement of PV+ interneurons that may only emerge in the adult brain, months after the genetic deletion of *Snap25*. The distribution of VVA+ cells in M1 was, in fact, significantly impacted by both *genotype* and *layer*, with a notable interaction between the two variables (genotype, p=0.0003; layer, p<0.0001; interaction, p=0.0084). Two-way ANOVA with Šídák's multiple comparisons test revealed a significant reduction in the density of VVA+ cells in L5 and L2/3 of M1 in the L5-silenced mice (Figure 3.13. b, g) (L2/3, p= 0.0028; L5, p= 0.0011). A similar trend was noted for PV- VVA+ cells as two-way ANOVA tests indicated a significant *genotype* and *layer* effect, albeit with no interaction (genotype, p=0.0170; layer, p<0.0001). Post-hoc tests showed a significant decrease in PV- VVA+ cell density in L5 of M1 in the *Snap25* cKO mice (Figure 3.13. f) (L5, p= 0.0119).

When investigating PV+ cells without PNNs, there was a significant *layer* effect and significant *interaction* with *genotype* on the distribution of the PV+ VVA- cells in M1 (layer, $p<0.0001$, interaction, $p=0.0256$). L5 of the *Snap25* cKO brains showed a markedly higher PV+ VVA- cell density, according to post-hoc experiments (Figure 3.13. e). No *genotype* effect observed on the PV+ only and PV+ VVA+ cells ($p=0.8158$ and $p=0.1781$) (Figure 3.13. a, b, c, d). These results suggest that PV+ neurons devoid of PNNs might re-enter a plastic phase by continuing to be able to react to shifts in network activity even after the network has consolidated and critical developmental windows have closed.

Similar to M1, two-way ANOVA tests indicated a significant *layer* effect on the distribution of all cells investigated in S1 ($p<0.0001$); however, a significant *genotype* effect was only noted on the distribution of PV+ and PV+ VVA+ cells ($p=0.0050$ and $p=0.0115$). The density of PV+ and PV+ VVA+ neurons rose significantly in L4 of S1 in the *Snap25* cKO brains as revealed by Šídák's multiple comparisons tests (Figure 3.13. j, k, l, m) (S1 L4, PV+, $p= 0.0063$; PV+ VVA+, $p= 0.0023$), but no interaction between *layer* and *genotype* was found in any instances. After the chronic silencing of L5 projection neurons, the laminar distribution of PV+ and VVA+ cells has changed solely in the adult cortex, leading one to assume that this is a delayed effect that does not emerge until adulthood. In the adult brain, chronic L5 silencing does not result in interneuron cell death or loss of PNNs because the overall density of PV and VVA cells was constant. Nonetheless, changes in PV and VVA distribution in different cortical layers point to a rearrangement of their laminar positions, possibly to compensate for the lack of excitatory inputs from L5.

Despite PV being a canonical marker for labelling the fast-spiking (FS) cortical interneuron subtype, it has to be acknowledged that the PV expression may not be the best tool to mark FS interneurons. As expression of the parvalbumin protein itself is activity-dependent and tightly linked to neuronal activity (Patz et al. 2004; Selten et al. 2023), one has to be cautious about relying on PV expression when quantifying PV cell numbers. Observing a decrease in PV numbers can be related to fluctuations in PV expression based on network circuit state, and the detected decrease can rather be a

downregulation of the parvalbumin protein itself than a true loss of PV cells (Filice et al. 2016). Another caveat of using PV as an interneuron marker is that PV expression is not exclusive to cortical interneurons, and a substantial fraction of pyramidal cells located in L5 of S1 and L6 of M1 of the rat neocortex have been documented to be PV-immunoreactive (van Brederode et al. 1991). The distal subiculum has also been found to contain PV-expressing glutamatergic principal neurons (Baccini et al. 2025). Additionally, single-cell RNA sequencing has further verified the presence of two clusters of excitatory PV+ neurons within the subiculum (Ding et al. 2020).

Even though PV is a well-known marker for fast-spiking GABAergic interneurons, activity-independent markers or genetic/lineage-based markers like *Lhx6* can be used to identify PV cortical neurons with greater accuracy. One promising alternative is synaptotagmin-2, a synaptic vesicle protein that is highly colocalised with PV and can accurately identify PV cells even when they are weakly expressed and in low-state conditions (Sommeijer and Levelt 2012).

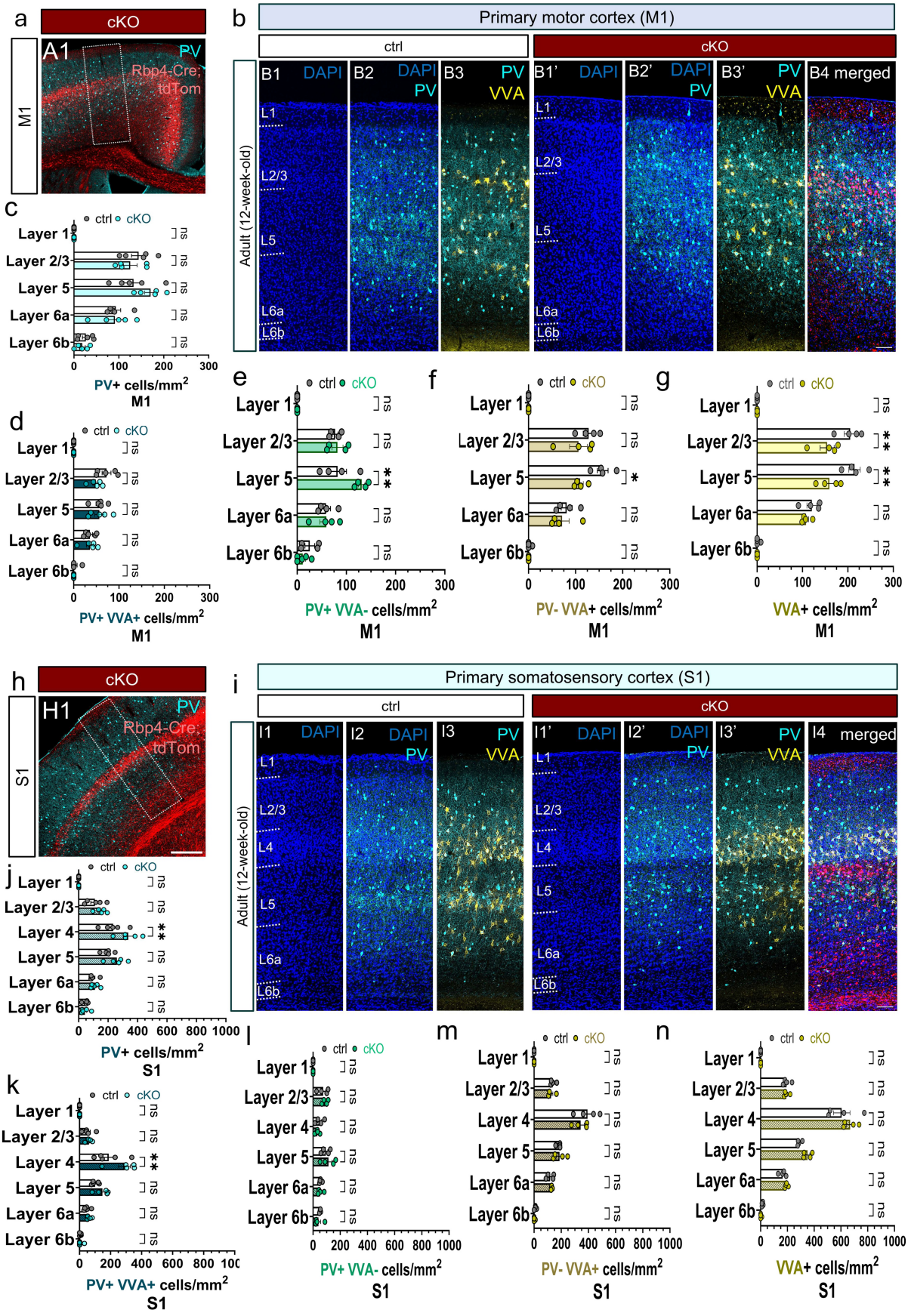

a
cKO
A1
PV
Rbp4-Cre;
tdTom
M1
b
Primary motor cortex (M1)
ctrl
cKO
Adult (12-week-old)
B1 DAPI
B2 DAPI PV
B3 PV VVA
B1' DAPI
B2' DAPI PV
B3' PV VVA
B4 merged
L1
L2/3
L5
L6a
L6b
c
ctrl cKO
Layer 1
Layer 2/3
Layer 5
Layer 6a
Layer 6b
ns
0 100 200 300
PV+ cells/mm2
M1
d
PV+ VVA+ cells/mm2
M1
e
PV+ VVA- cells/mm2
M1
f
PV- VVA+ cells/mm2
M1
g
VVA+ cells/mm2
M1
h
cKO
H1
PV
Rbp4-Cre;
tdTom
S1
i
Primary somatosensory cortex (S1)
ctrl
cKO
Adult (12-week-old)
I1 DAPI
I2 DAPI PV
I3 PV VVA
I1' DAPI
I2' DAPI PV
I3' PV VVA
I4 merged
L1
L2/3
L4
L5
L6a
L6b
j
Layer 4
0 200 400 600 800 1000
PV+ cells/mm2
S1
k
PV+ VVA+ cells/mm2
S1
l
PV+ VVA- cells/mm2
S1
m
PV- VVA+ cells/mm2
S1
n
VVA+ cells/mm2
S1

Figure 3.13. Chronic silencing of layer 5 projection neurons rearranges the laminar distribution of PV and VVA cells in the adult primary motor and somatosensory cortex. Low-magnification image of the primary motor cortex (a) at 3 months of age, illustrating PV interneurons (cyan) and L5-silenced neurons (red) (A1). The imaging site is outlined by a white rectangle. Combined tile-scan and z-stack images representing the laminar distribution of PV+ and VVA+ cells in the control and *Snap25* cKO mice in M1 (B1-B4). White dotted lines delineate cortical layer boundaries. (c, d) Laminar distribution analysis of the density of PV+ and PV+ VVA+ cells in M1 at 12 weeks of age between the control and L5-silenced brains. (e, f, g) Laminar distribution analysis of the density of PV+ VVA-, PV- VVA+, and VVA+ cells in M1. (h) Low-magnification confocal image of the primary somatosensory cortex at 3 months of age. Combined tile-scan and z-stack images showing the laminar distribution of PV+ and VVA+ cells in the control and *Snap25* cKO mice in S1 (I1-I4). Quantifying the laminar distribution of PV+, PV+ VVA+, and PV+ VVA- in S1 at 3 months of age between control and mutant mice (j, k, l). Quantification of the laminar distribution of PV- VVA+ and VVA+ cells in S1 (m, n). Scale bars: 200 µm (H1), 50 µm (B4, I4). M1: primary motor cortex, S1: primary somatosensory cortex, PV: parvalbumin, VVA: *Vicia villosa* agglutinin.

3.3.3. The correlation between PV and the perineuronal net is cortical layer-dependent

I previously demonstrated that the degree of correlation between PV and VVA neurons differed depending on the cortical area investigated. Considering that the correlation between PV and VVA may also be influenced by their laminar positions, I examined the Pearson correlation between PV+ and VVA+ in different cortical layers of M1 and S1. Additionally, I aimed to determine whether the correlation between PV and VVA varied between the upper and lower cortical layers. In M1, the *Snap25* cKO brains displayed a negative correlation between PV and VVA in L2/3 and L6a, in contrast to the ctrl brains' positive correlation in L2/3 and L6a (Figure 3.14. c) (M1 L2/3: r= 0.3 (ctrl), r= -0.4 (cKO), L6a: r=0.0 (ctrl), r= -0.4 (cKO). In the L5-silenced brains, the correlation between PV and VVA in L2/3 and L4 of S1 was reversed (Figure 3.14. d) (S1 L2/3: r= 0.0 (ctrl), r= -0.7 (cKO), L4: r= 0.0 (ctrl), r= -0.5 (cKO). The negative correlation between PV and VVA in the *Snap25* cKO mice suggests that not all PV+ cells are surrounded by PNNs, and there are PNNs around neurons that are PV-. My density results indicating that VVA rarely occurs in L6b are supported by the negative correlation in L6b shown in the control and cKO brains. Taken together, these findings imply that the correlation between PV and VVA changes in degree throughout cortical layers and cortical regions. Establishing that PV-VVA correlation is both region and layer dependent further highlights how dynamically PV and PNNs interact, and how their link is more nuanced than previously believed (Lupori et al. 2023;

Xia et al. 2021; Ueno et al. 2018; Carceller et al. 2020; Santos-Silva, Colodete, al.2024; Santos-Silva, Souza, et al. 2024).

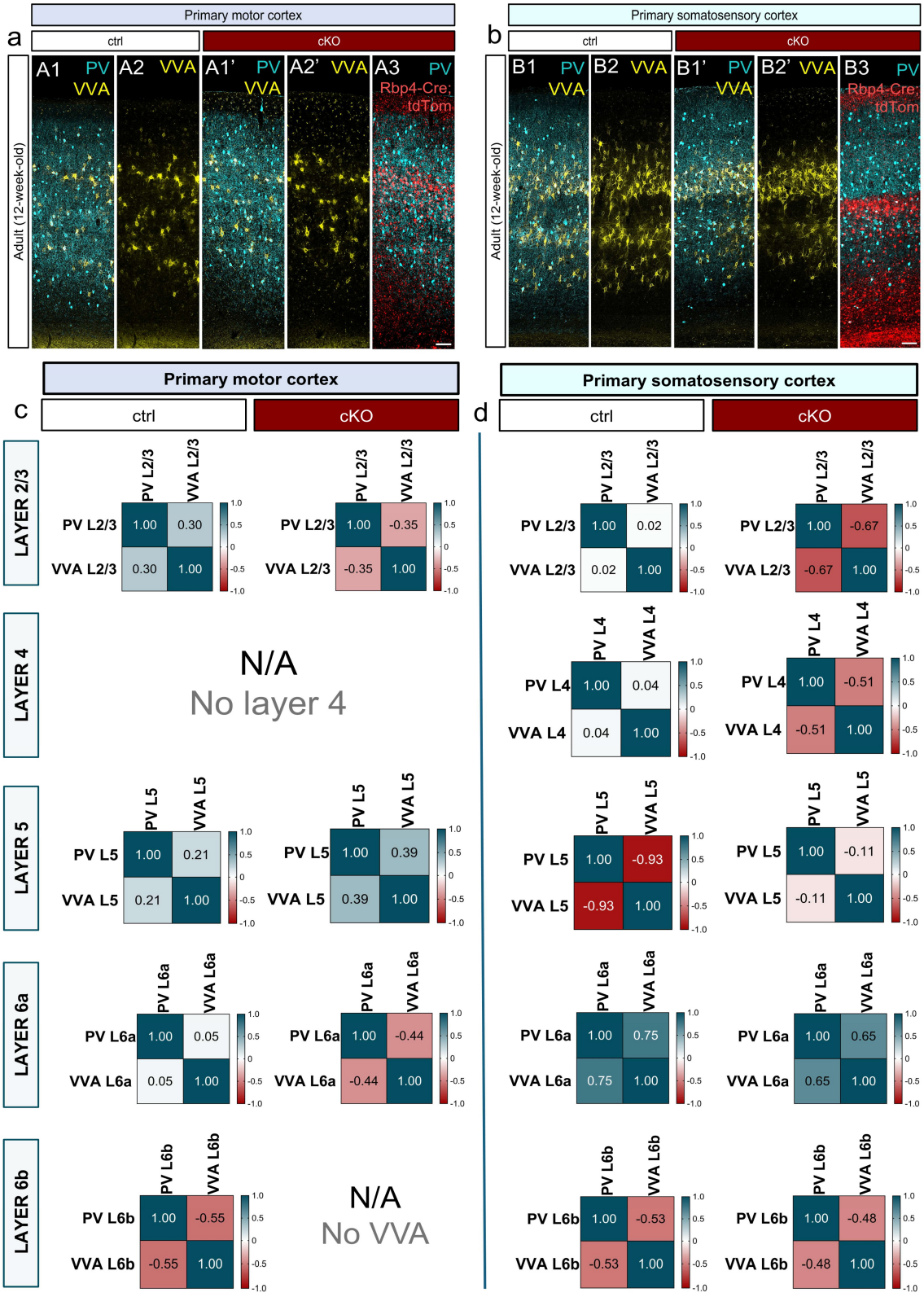


Figure 3.14. Chronic silencing of layer 5 projection neurons unveils regional and layer-dependent differences in the correlation between PV interneurons and the perineuronal nets. Tile-scan and z-stack confocal images depicting PV-immunostained neurons, VVA-labelled PNNs, and *Rbp4-Cre;Ai14;Snap25*$^{fl/fl}$ neurons in M1 and S1 in the control (A1, A2, B1, B2) and *Snap25* cKO brains at 12 weeks of age (A1'-A3, B1'-B3). Heatmaps illustrating the Pearson correlation between PV+ and VVA+ cells in all cortical layers in M1 (c). In the Snap25 cKO brains, there were no VVA+ cells in L6b in M1. Heatmaps illustrating the Pearson correlation between PV+ and VVA+ cells in all cortical layers in S1 (d). Numbers in heatmaps represent r-values of Pearson correlation. Scale bars: 50 µm (A3, B3).

3.3.4. Silencing layer 5 does not lead to long-term changes in the density of subcortical PV neurons in the projection regions of layer 5

To investigate the long-term influence of the loss of *Snap25* on subcortical PV cells, I analysed their density in the output regions of L5 at three months of age. It is important to note that by this age, most subcortical axons from the silenced L5 projection neurons had degenerated. Surprisingly, the layer 5-silenced brains did not reveal significant alterations in the density of subcortical PV neurons in the projection regions of L5 investigated (Figure 3.15. a, c) (CPu, p= >0.9999; GPe, p= 0.9989; LP, p= >0.9999; MD, p= >0.9999; TRN, p= 0.9966; SC, p= 0.9989; two-way ANOVA with Šídák's multiple comparisons test). In the striatum, neither the density of the PNN nor the density of PV- VVA+ cells changed in the adult *Snap25* cKO brains (Figure 3.15. b, f, g) (VVA+, p= 0.2743; PV- VVA+, p=0.8362; PV+ VVA+, p=0.5326; two-way ANOVA with Šídák's multiple comparisons test).

I next examined the trajectory of subcortical PV neurons from development to adulthood. First, I analysed the course of maturation of subcortical PV neurons between P21 and 3 months of age in the ctrl brains, where I noted a significant decrease in PV cell density in the GPe (Figure 3.15. d) (p= <0.0001, two-way ANOVA with Šídák's multiple comparisons test). I noticed the same trend in the layer 5-silenced brains where the density of PV neurons was only altered in the GPe, whilst the rest of the projection sites remained unchanged (Figure 3.15. e) (GPe, p= <0.0001; two-way ANOVA with Šídák's multiple comparisons test). These findings are consistent with the notion that the first week of development marks the most significant milestones in the maturation of PV neurons, and when these neurons undergo developmental apoptosis, their populations appear to stabilise and hold

steady into adulthood (Southwell et al., 2012; Denaxa et al., 2018; Wong et al., 2018, 2022; Magno et al; 2021). There is evidence that programmed cell death occurs in MGE/POA-derived interneurons in the striatum during postnatal development, with a peak of apoptosis at around P10 (Sreenivasan et al. 2022). In the GPe, a progressive decrease in PV+ cell density has been seen between P21 and P42 in addition to the striatum, suggesting that the distribution of PV+ is considerably changed during post-weaning periods and that the alterations are region-specific (Kon et al. 2024).

Finally, I examined the correlation between PV and VVA in subcortical regions. The striatum of the layer 5-silenced mice showed a positive PV-VVA correlation compared to control mice (Figure 3.15. h), although the level of correlation was not as great as that of the control brains (CPu: r=0.8 (ctrl), p=0.075; r=0.1 (cKO), p=0.879). These results suggest that the chronic loss of AP-dependent neurotransmitter release from L5 does not alter the correlation between PV and VVA, which may exhibit variation between cortical and subcortical regions.

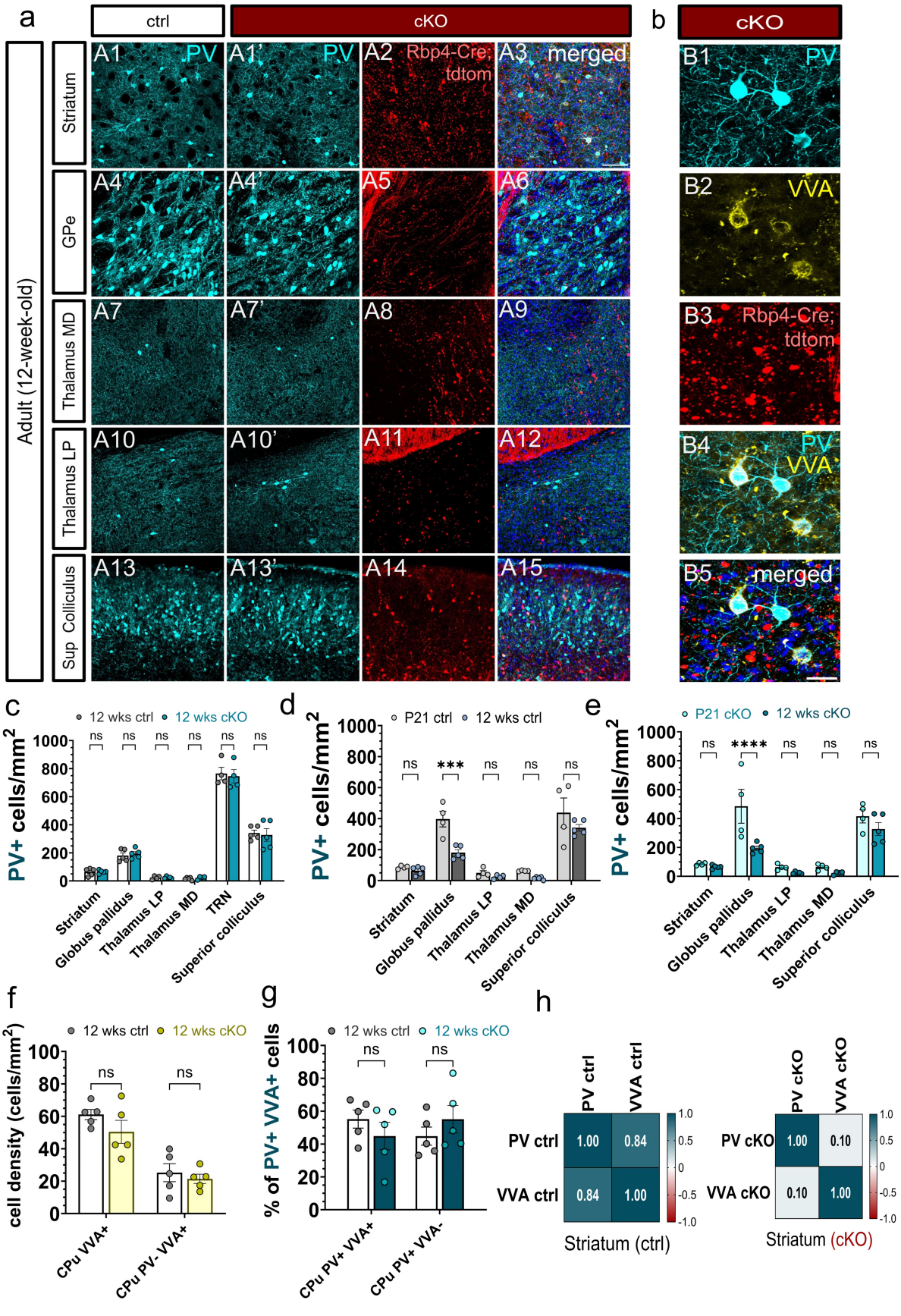

a
ctrl
cKO
Adult (12-week-old)
Striatum
GPe
Thalamus MD
Thalamus LP
Sup Colliculus
A1 PV
A1' PV
A2 Rbp4-Cre; tdtom
A3 merged
A4' A4'
A5
A6
A7 A7'
A8
A9
A10 A10'
A11
A12
A13 A13'
A14
A15
b
cKO
B1 PV
B2 VVA
B3 Rbp4-Cre; tdtom
B4 PV VVA
B5 merged
c
12 wks ctrl
12 wks cKO
PV+ cells/mm2
ns
Striatum
Globus pallidus
Thalamus LP
Thalamus MD
TRN
Superior colliculus
d
P21 ctrl
12 wks ctrl
***
e
P21 cKO
12 wks cKO
****
f
cell density (cells/mm2)
CPu VVA+
CPu PV- VVA+
g
% of PV+ VVA+ cells
CPu PV+ VVA+
CPu PV+ VVA-
h
PV ctrl
VVA ctrl
1.00
0.84
0.10
Striatum (ctrl)
PV cKO
VVA cKO
Striatum (cKO)

Figure 3.15. Genetic silencing of Rbp4-Cre+ neurons has no long-term impact on the density of PV neurons in the subcortical projection regions of layer 5. Maximum-intensity projected z-stacks demonstrating the selected output regions of the silenced Rbp4-Cre projection neurons at 3 months of age. Subcortical PV+ neurons are shown in cyan, while *Rbp4-Cre;Ai14;Snap25*$^{fl/fl}$ neurons are in red. PV-immunopositive neurons in the caudoputamen and the external segment of the globus pallidus in the control (A1, A4) and *Snap25* cKO mice (A1', A4'). PV+ neurons in the lateral posterior and mediodorsal thalamic nuclei in the ctrl (A7, A10) and *Snap25* cKO mice (A7', A10'). PV-immunoreactive neurons in the superior colliculus at 12 weeks of age in the ctrl (A13) and L5-silenced mice (A13'). Long-range corticofugal projections of *Rbp4-Cre;Ai14;Snap25*$^{fl/fl}$ neurons in the adult *Snap25* cKO mice in the basal ganglia (A2-A6), the higher-order thalamic nuclei (A8-A12), and the midbrain (A14-A15). Maximum-intensity projected z-stacks of striatal PV+ neurons and VVA-labelled PNNs at 12 weeks of age in the *Snap25* cKO mice (B1, B2). Disintegrating axonal fibres of the silenced L5 projection neurons in the caudoputamen (B3). Presence of perineuronal nets surrounding striatal PV+ neurons in adult L5-silenced mice (B4, B5). Quantification of PV+ neurons in the output regions of *Rbp4-Cre;Ai14;Snap25*$^{fl/fl}$ neurons at 12 weeks of age (c). Analysis of the dynamics of PV+ neurons between P21 and 3 months of age in control and mutant mice (d, e). Total cell density of VVA+ and PV- VVA+ cells in the adult striatum (f). Percentage of PV+ VVA+ and PV- VVA+ neurons in the striatum (g). Pearson correlation computed for PV and VVA correlation (h). Scale bars: 50 μm.

3.4. The effects of chronically silencing layer 5 projection neurons on neuropeptide-Y interneurons in the adult brain

In the first part of Chapter 3, I demonstrated that the conditional deletion of *Snap25* from Rbp4-Cre+ neurons had a delayed effect on PV interneurons and the PNNs, leading to alterations in their laminar distribution in the adult cortex. These results raised the questions of whether this effect was exclusive to PV interneurons and if subtype-specific changes in GABAergic neuron density and distribution could be detected following *Snap25* deletion. Therefore, I investigated the effects of chronically silencing L5 projection neurons on cortical NPY-expressing interneurons. I hypothesised that the native distribution, or laminar position, of a cortical interneuron subtype influences its response to the removal of excitatory inputs and changes in network activity. NPY+ neurons are concentrated in the superficial and deep layers of the murine neocortex (Hendry et al. 1984; Karagiannis et al. 2009), while PV+ neurons have a more diffuse laminar distribution and are found across nearly all cortical layers, except for layer 1 (Xu et al. 2010). The laminar position of an interneuron subtype defines the synaptic inputs it receives (Pouchelon et al. 2021; Dantzker and Callaway 2000); therefore, the diversity of sources that converge onto an interneuron—determined by its distribution—may also affect its responsiveness. With their unique native distributions in the cortex, I expected that various interneuron subtypes—like PV and NPY—would react differently to modifications in pyramidal neurons.

Since the distribution of NPY+ neurons differs from PV+ neurons, I selected new cortical, subcortical, and hippocampal ROIs based on 1) the distribution of NPY+ interneurons, and 2) the overlap between the projections of *Rbp4-Cre+;Snap25*$^{fl/fl}$ neurons and NPY+ cells. Figure 3.16. summarises the ROIs selected for PV and NPY interneurons.

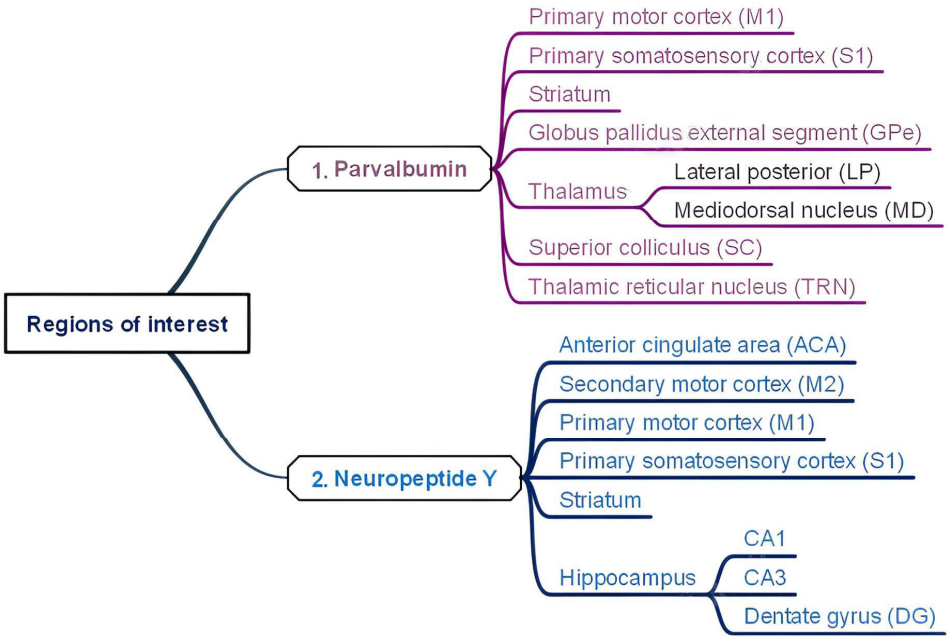
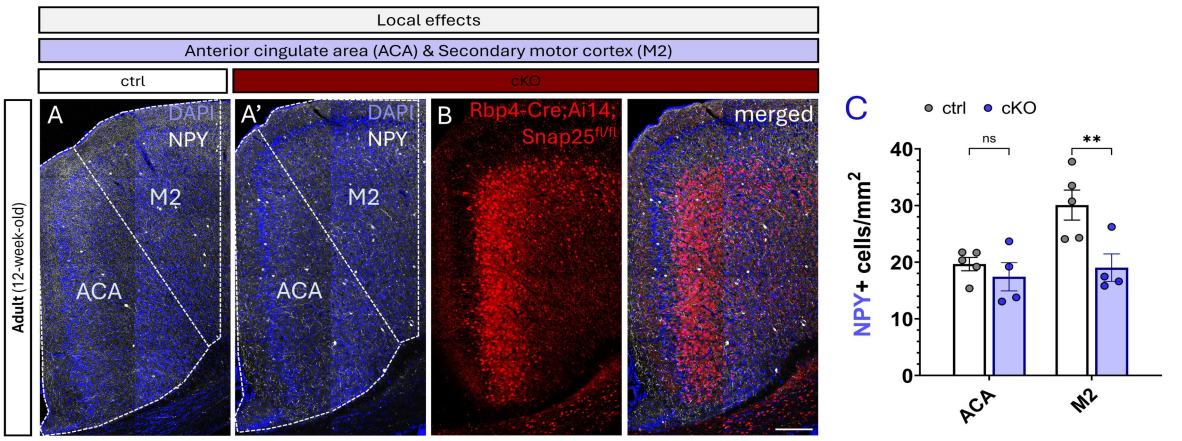


Figure 3.16. Summary of the different regions of interest selected for parvalbumin and neuropeptide-Y interneurons.

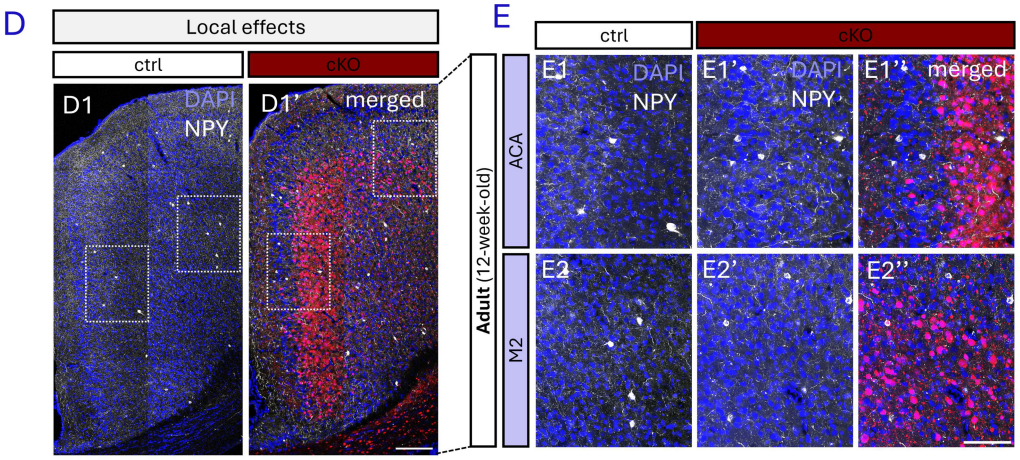
3.4.1. Loss of AP-dependent neurotransmitter release from layer 5 projection neurons affects the density of NPY-expressing neurons in the primary and secondary motor cortices

First, I assessed the density of NPY+ cells in the vicinity of the somata of the 'silenced' L5 neurons in the anterior cingulate area (ACA) and the secondary motor cortex (M2) (Figure 3.17. A-B). There was a significant *genotype* and *region* effect, with no interaction (genotype, p=0.0103; region, p=0.0179). Whilst no significant differences in the density of NPY+ neurons were detected in the ACA in the layer 5-silenced mice relative to the ctrl mice (Figure 3.17. C), there was a significant decrease of ~37% in the density of NPY+ cells in M2 at 12 weeks of age as shown by Šídák's multiple comparisons test (ACA, p=0.7420; M2, p=0.0073) (Figure 3.17. C). Although the density analysis of NPY+ neurons in the ACA did not identify changes in their number, analysis of soma morphology discovered a robust increase in their soma area and perimeter in the layer 5-silenced mice compared to ctrl mice (p=<0.0001; two-tailed Mann-Whitney test) (Figure 3.17. D, E1-E1", F). In contrast to ACA, reductions in the density of NPY+ neurons in M2 were accompanied by a significant decrease in the

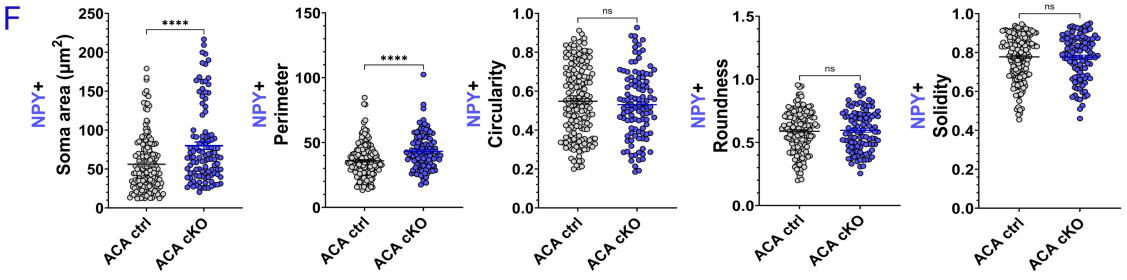
soma circularity and solidity in the *Snap25* cKO mice compared to controls (circularity, p=0.0147; solidity, p=0.0315; two-tailed Mann-Whitney test) (Figure 3.17. D, E2-E2", G). The genetic silencing of subsets of L5 projection neurons seems to have varying impacts on NPY+ neurons. It leads to significant reductions in the density and soma parameters of NPY+ neurons in M2, while it results in no changes in the density of ACA NPY+ neurons. The reason for the contrasting changes in NPY+ neurons in the ACA and M2 following the ablation of *Snap25* from Rbp4-Cre+ neurons is yet to be determined.



Local effects



Anterior cingulate area (ACA)



Secondary motor cortex (M2)

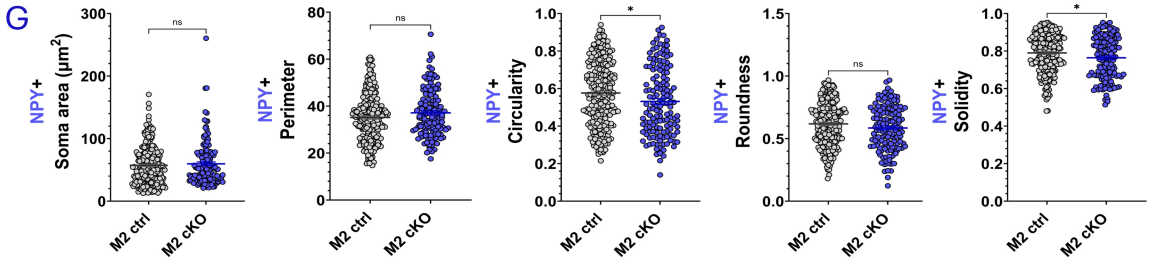


Figure 3.17. Long-term impact of the conditional silencing of subsets of layer 5 projection neurons on NPY+ interneurons in the ACA and M2. (A-A') Confocal tile-scan image of the anterior cingulate area and the secondary motor cortex in the control (A) and the layer 5-silenced mice (A') at 12 weeks of age. NPY-immunostained neurons are shown in grey. (B) Subsets of Rbp4-Cre-expressing layer 5 projection neurons in which AP-dependent neurotransmitter release was abolished at 12 weeks of age. (C) Quantification of the density of NPY-immunoreactive neurons in the anterior cingulate area and the secondary motor cortex. (D) Tile-scan image of the anterior cingulate area in the control (D1) and the layer 5-silenced mice (D1'). White dotted square boxes indicate the location of NPY-expressing neurons depicted in panels E1-E1" (ctrl) and E2-E2" (mutant). (F) Morphometric analyses of soma features of NPY+ cells in the anterior cingulate area. (G) Morphometric analyses of NPY+ cells in the secondary motor cortex. Scale bars=100 µm.

3.4.2. Silencing layer 5 projection neurons alters the density of NPY+ interneurons in the primary motor cortex

Similar to the findings on M2, the genetic silencing of Rbp4-Cre+ L5 pyramidal neurons led to a significant decrease of ~20% in the density of NPY+ interneurons at 3 months of age in M1 (p=0.0178, unpaired t-test with Welch's correction) (Figure 3.18. A, A', B, D). The morphometric analyses of NPY+ neurons in M1 revealed further alterations in the perimeter, circularity, and solidity values of NPY+ cells (Figure 3.18. C, C', E) (perimeter, p=0.0053; circularity, p=0.0029; solidity, p=0.0056; unpaired two-tailed Mann-Whitney test). The considerable increase in soma perimeter, accompanied by a significant reduction in soma circularity and solidity, may imply more elongated and irregularly shaped neuronal somata.

When assessing the local effects on NPY+ interneurons in S1, I observed no significant reduction in the density of NPY+ cells (Figure 3.19. A, A', D). However, the soma area, circularity, and solidity were significantly decreased in the layer 5-silenced mice relative to control mice (area, p=0.0003; circularity, p=0.004; solidity, p=0.0008; two-tailed Mann-Whitney test) (Figure 3.19. C, C', E). It is noteworthy that significant changes in the density of NPY-expressing neurons were only noted in the primary and secondary motor cortices. Considering that other cortical regions remained unaffected, it remains to be elucidated what makes the motor cortices more vulnerable to changes in synaptic transmission in layer 5.

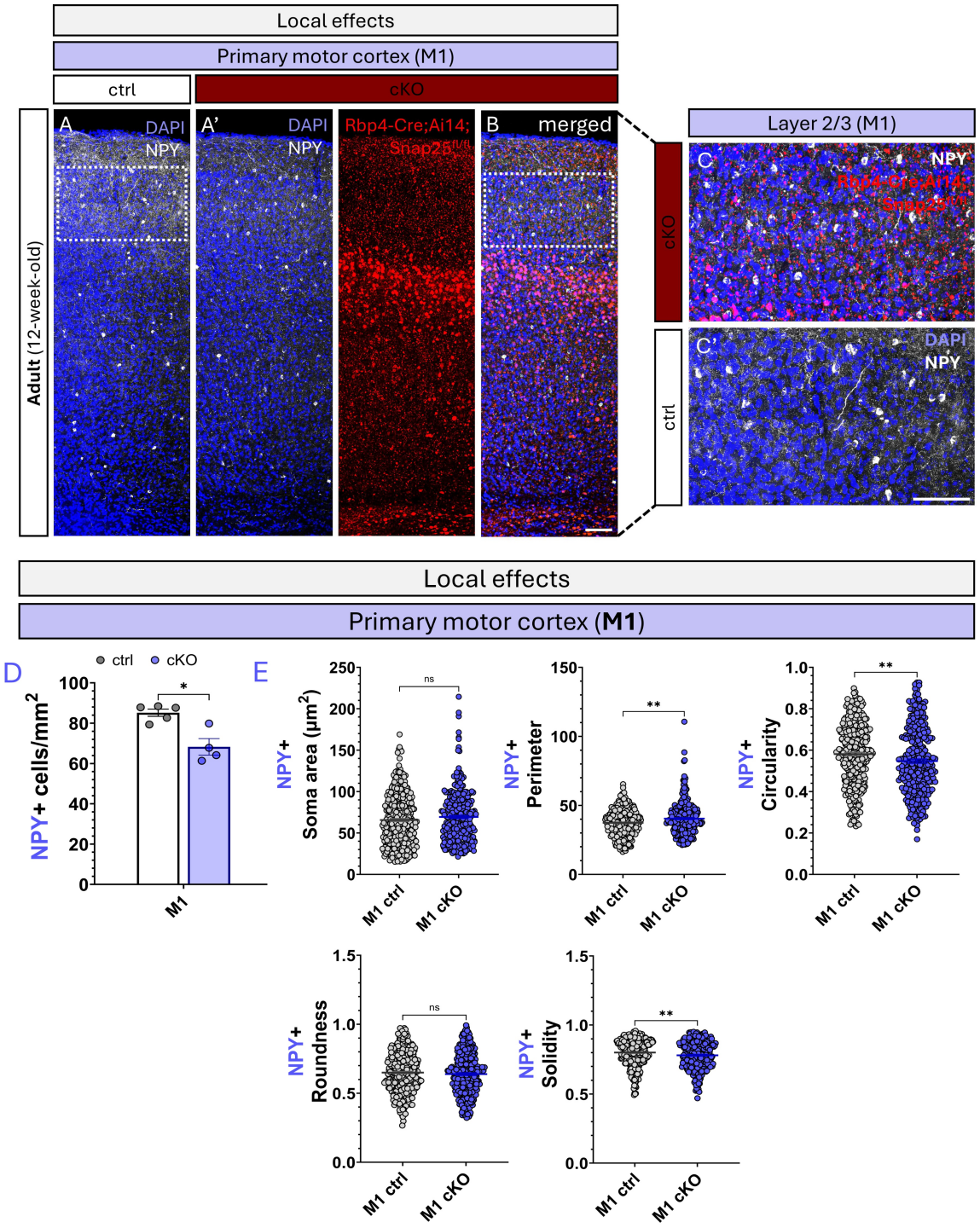


Figure 3.18. Loss of AP-dependent neurotransmitter release from layer 5 projection neurons influences the density and soma morphology of NPY+ neurons in the adult primary motor cortex. (A-A') Tiled maximum-intensity projection z-stack image of NPY-positive interneurons at 12 weeks of age in the primary motor cortex of control and cKO brains. (B) Merged images of NPY+ neurons and Rbp4-Cre+ 'silenced' projection neurons in layer 5 of the primary motor cortex. Note the advanced neurodegeneration and disintegration of chronically silenced layer 5 cell bodies, as well as the accumulation of tdTomato-positive punctae throughout the brain. (C-C') Confocal images illustrating NPY-immunostained neurons in layer 2/3 of the primary motor cortex at 3 months of age

in the Snap25 cKO (C) and ctrl mice (C'). Cell locations on tile-scan pictures are shown by white rectangular boxes. (D) Quantification of NPY-immunoreactive cell density at 12 weeks of age in the primary motor cortex. (E) Soma features selected for morphometric analysis of NPY+ neurons in the primary motor cortex. Scale bars = 100 µm (B), 200 µm (C').

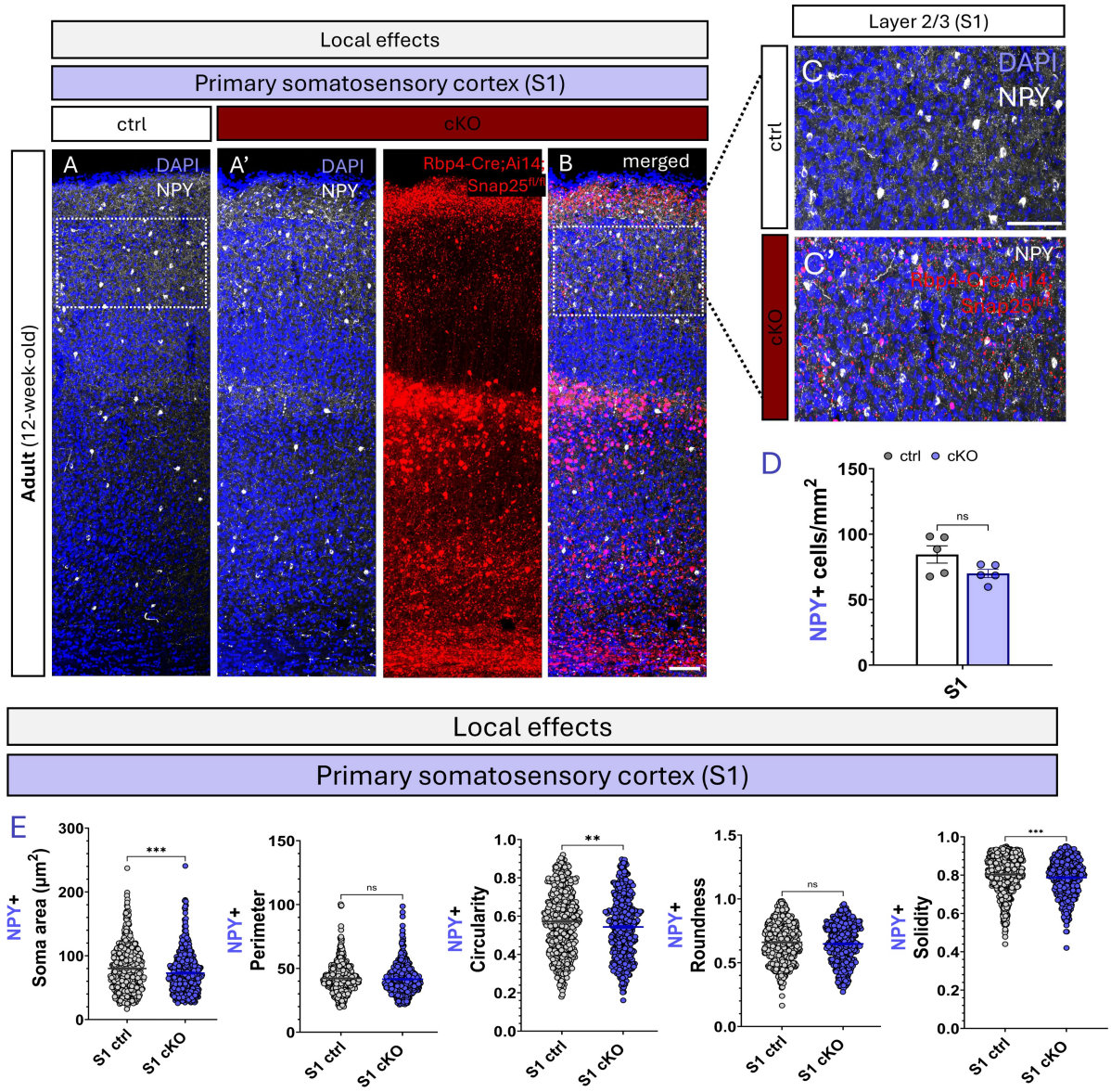


Figure 3.19. The genetic silencing of layer 5 projection neurons does not alter the density of NPY+ interneurons in the primary somatosensory cortex in the adult brain but affects their soma morphology. (A-A') Tiled maximum-intensity projected z-stack image of the primary somatosensory cortex depicting NPY-immunopositive neurons at 3 months of age. (B) 'Silenced' Rbp4-Cre+ layer 5 neurons that are unable to secrete synaptic vesicles in a regulated fashion. (C-C') Confocal images of NPY-immunostained neurons in layer 2/3 of the primary somatosensory cortex in the control (C) and layer 5-silenced mice (C'). (D) Quantification of the cell density of NPY-immunopositive neurons at 12 weeks of age. (E) Measurements of select soma features of NPY+ neurons in the primary somatosensory cortex. Scale bars = 100 µm (B), 200 µm (C).

3.4.3. The conditional deletion of Snap25 from subsets of layer 5 projection neurons affects the laminar distribution of NPY+ interneurons in L1 and L2/3 of the primary motor cortex

The previous results have shown that genetically silencing Rbp4-Cre+ neurons affected the density and soma morphology of NPY+ interneurons in the motor cortices. Next, I sought to examine whether the observed changes were accompanied by alterations in their laminar distribution. I discovered that the *Snap25* cKO mice had a significantly lower density of NPY+ neurons in the superficial cortical layers of M1 compared to control mice. Two-way ANOVA tests revealed a significant *layer* and *genotype* effect ($p<0.0001$), with significant *interaction* between the two variables ($p=0.0030$). Šídák's multiple comparisons test indicated a significant decrease of ~53% in the density of NPY+ cells in layer 1 of M1 in the *Snap25* cKO mice ($p=0.0004$), and a more moderate decrease of ~26% in the density of NPY+ cells in layer 2/3 ($p=0.003$) (Figure 3.20. A-B', C).

Since the laminar positioning of cortical interneurons is an important indicator of their input connectivity and distinct interneuron subtypes occupy different cortical layers, I investigated the soma characteristics of NPY+ neurons in a layer-specific manner. In particular, I aimed to know whether layer-specific morphological alterations can be detected following the chronic silencing of L5 projection neurons. Interestingly, the soma features of NPY+ neurons in L2/3 and L1 in M1 did not differ significantly between the control and *Snap25* cKO mice at 3 months of age (Figure 3.20. D). Similarly, no significant alterations were noted in any other cortical layers in M1.

3.4.4. The soma shape of NPY+ neurons in layer 5 of the somatosensory cortex is altered by the chronic silencing of layer 5 projection neurons, but their laminar positioning remains unchanged

Next, I sought to determine whether the laminar distribution of NPY+ interneurons was similarly impacted in S1. There was a significant *layer* and *region* effect ($p<0.0001$ and $p=0.0050$; two-way ANOVA with Šídák's multiple comparisons test); however, *post*-hoc tests did not identify

significant changes in the laminar positioning of NPY+ neurons between the ctrl and cKO mice (Figure 3.21. A-B', C). The significant main effect, but non-significant post-hoc effect, may imply that layer-specific changes are not large enough to meet the stricter p-value requirements of post-hoc multiple comparisons. In two-way ANOVA, a significant overall main effect can disappear in post-hoc tests, which I noticed when running Šídák's multiple comparisons test on the laminar distribution of NPY+ neurons in S1. This may occur because post-hoc tests are more conservative and are designed to control the increased risk of Type I error (false positive) when performing multiple comparisons. This means they use a stricter p-value threshold than the original ANOVA (Lee and Lee 2018; In and Lee 2017).

Interestingly, I noticed significant reductions in the soma area and perimeter of NPY+ interneurons in L5 of S1 at 12 weeks of age in the mutant mice relative to control mice (Figure 3.21. D). The soma area of NPY+ neurons was ~25% smaller in L5 in the *Snap25* cKO mice compared to ctrl mice, and there was a marked decrease in the perimeter of L5 NPY+ neurons in S1 (area, p=<0.0001; perimeter, p=0.0018; Kruskal-Wallis test with Dunn's multiple comparisons). Additionally, I observed that the NPY+ neurons in the L5-silenced mice had a markedly reduced circularity in L2/3 of S1 (Figure 3.21. D) (p=0.02, Kruskal-Wallis test with Dunn's multiple comparisons). It may be concluded that the morphological variations observed in L5 of S1 reflect long-term adaptations in NPY+ neurons, as the 'silenced' Rbp4-Cre+ neurons do not function properly and fail to interact with the inhibitory cells. The chronic silencing of L5 neurons, therefore, leads to long-term changes in the soma shape and size in S1, but not in M1.

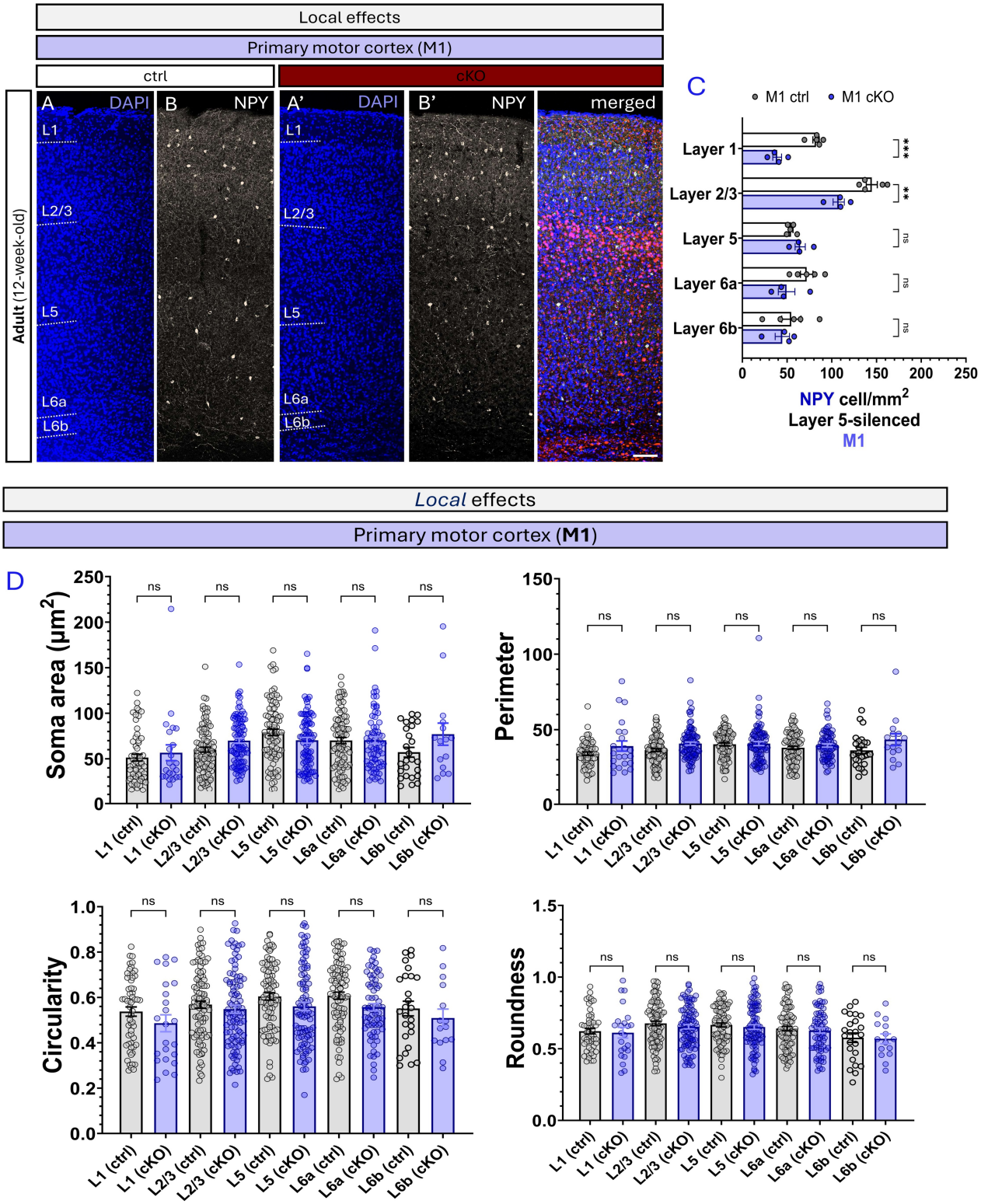
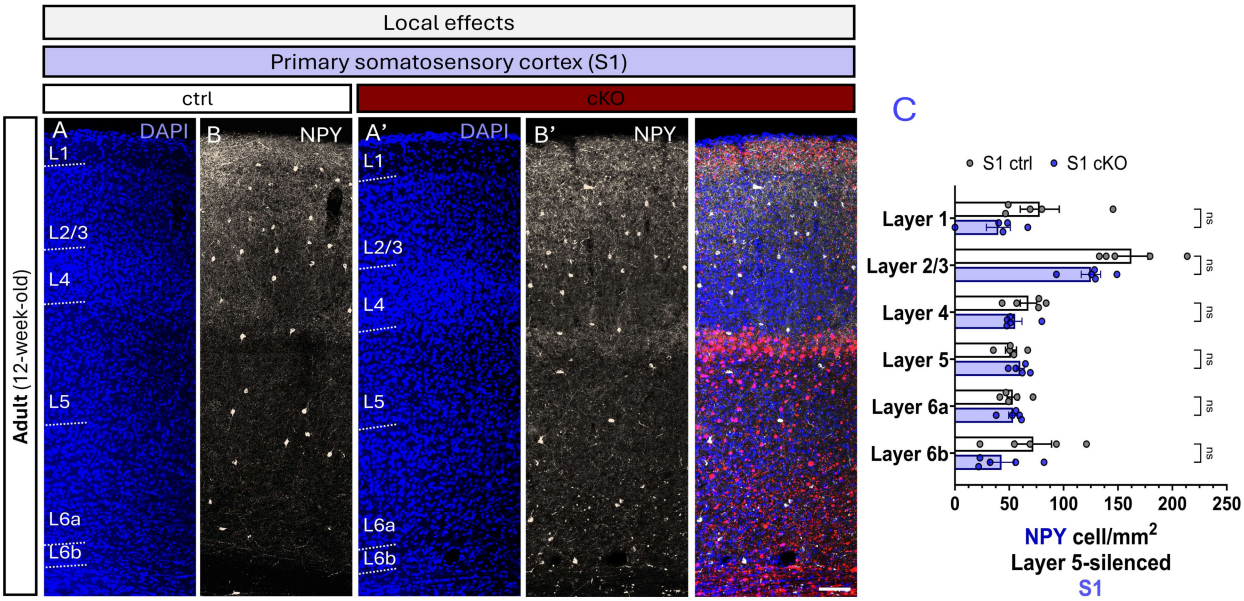


Figure 3.20. Chronic silencing of layer 5 projection neurons rearranges the laminar distribution of cortical NPY+ interneurons in the adult primary motor cortex. (A-B') Tiled maximum-intensity projected z-stack of the primary motor cortex displaying NPY-immunoreactive

neurons in the ctrl (A, B) and cKO mice (A, B') at 12 weeks of age. White dotted lines used to delineate cortical layer boundaries. (C) Quantification of the laminar density of NPY+ cells in M1. (D) Morphometric assessment of NPY+ neurons in M1. Scale bars =100 µm.



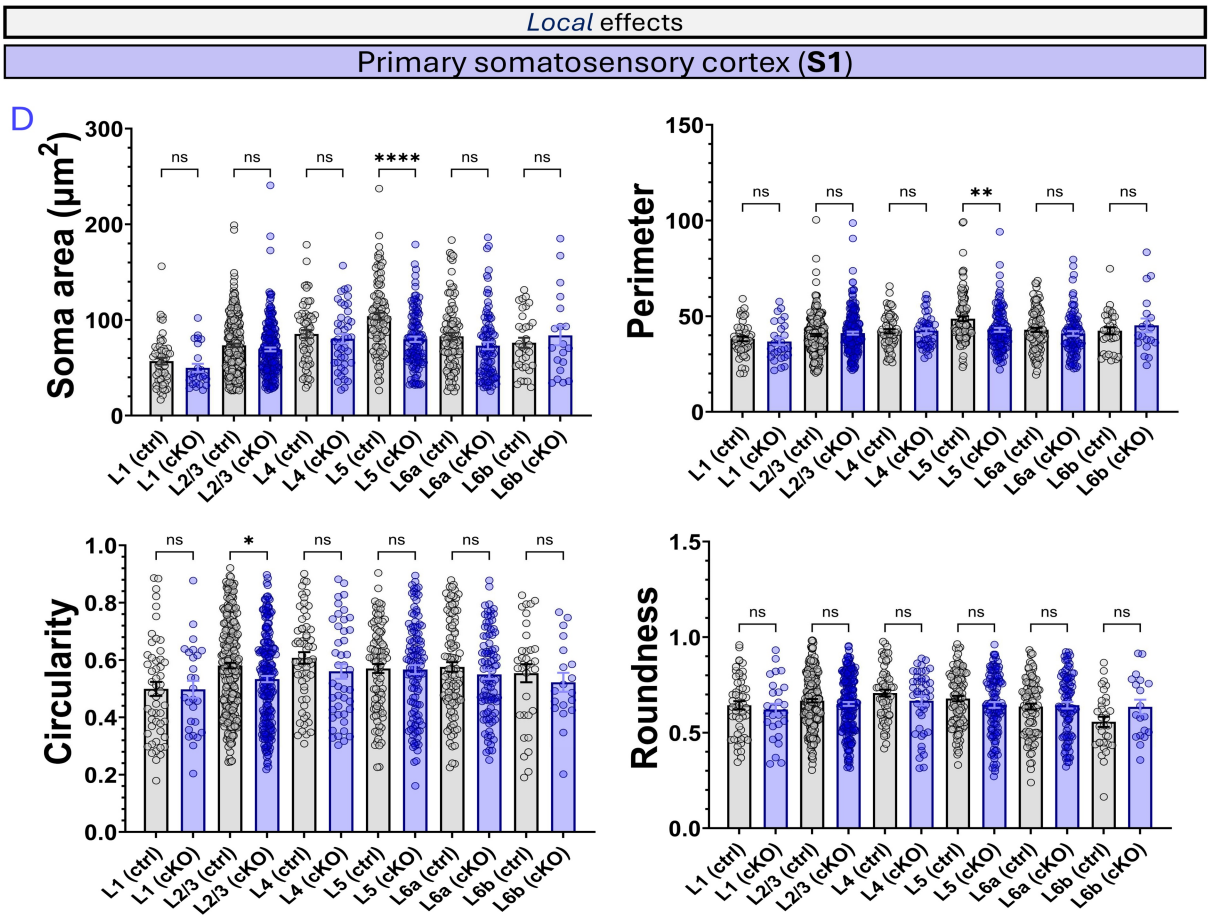


Figure 3.21. Chronic silencing of subsets of layer 5 neurons leaves the laminar positioning of cortical NPY+ interneurons in the adult primary somatosensory cortex intact. (A-B') Tiled maximum-intensity projected z-stack image of the primary somatosensory cortex illustrating NPY-immunoreactive neurons in the ctrl (A, B) and *Snap25* cKO mice (A, B') at 12 weeks of age. Cortical layer boundaries are indicated by white dotted lines. (C) Quantification of the laminar density of NPY+ cells across the somatosensory cortex. (D) Morphometric assessment of NPY+ neurons in S1 revealed significant modifications in the soma size and perimeter of NPY+ neurons in L5. Scale bars =100 µm.

3.4.5. The density of striatal NPY+ neurons remains unchanged following the deletion of Snap25 from Rbp4-Cre+ neurons

After examining the effects of genetically silencing Rbp4-Cre+ neurons on cortical NPY+ interneurons, I next assessed their effects on subcortical NPY+ neurons. I selected the caudoputamen as my subcortical ROI, given that it is densely innervated by the descending axonal projections of Rbp4-Cre+ neurons, which form *Vglut1*-positive glutamatergic synapses there. Consequently, cortical L5 projection neurons may exert a direct impact on NPY+ neurons within the caudoputamen. The absence of local glutamatergic neurons in the striatum was another significant selection factor, which begs the question of whether cortical excitatory inputs from L5 are involved in regulating the density of GABAergic neurons.

Contrary to expectations, the conditional silencing of Rbp4-Cre+ neurons did not result in significant changes in the density of NPY+ neurons (Figure 3.22. A1-A2', B). I found modest increases (~17%) in the circularity, roundness, and solidity values of striatal NPY+ neurons in the *Snap25* cKO mice at 12 weeks of age, suggesting subtle morphological changes in NPY+ neurons following the chronic silencing of L5 (Figure 3.22. C1-C2', D) (circularity, p=0.05; roundness, p=0.04; solidity, p=0.03; two-tailed Mann-Whitney test). The increase in circularity and roundness did not coincide with an increase in soma area or perimeter, indicating that the somata's shape - rather than the size of NPY+ neurons – was altered by the deletion of *Snap25* from Rbp4-Cre+ neurons. The loss of spatial information resulting from vibratome sectioning and 2D imaging of 3D structures is a potential confounding factor

in the results of morphological analysis. Certain tissue-processing steps, such as paraformaldehyde fixation, are known to cause tissue shrinkage (Tran et al. 2015), which can impact the accuracy of soma measurements. Similarly, vibratome sectioning of three-dimensional (3D) structures may lead to deformations in the tissue (Boyce et al. 2010), and two-dimensional (2D) sectioning further complicates the precise assessment of soma parameters. While techniques like tissue clearing or tissue expansion are ideal for preserving the intact 3D structure of cells and avoiding deformations during sectioning, I was unable to implement these methods due to the lack of appropriate equipment in our lab. Although I could not eliminate the possibility that fixation and sectioning result in some loss of spatial information, I employed 3D imaging to capture the complete profile of the soma. I acquired z-stack images using Nyquist sampling, which requires a sampling interval that is equal to twice the highest spatial frequency of the specimen being imaged to accurately preserve spatial resolution in the resulting digital image https://zeiss-campus.magnet.fsu.edu/articles/basics/digitalimaging.html. Therefore, I used the optimal interval calculated according to the Nyquist theorem for acquiring z-stack images for soma measurements, ensuring that the selected pixel size was sufficiently small to resolve the smallest details in my sample.

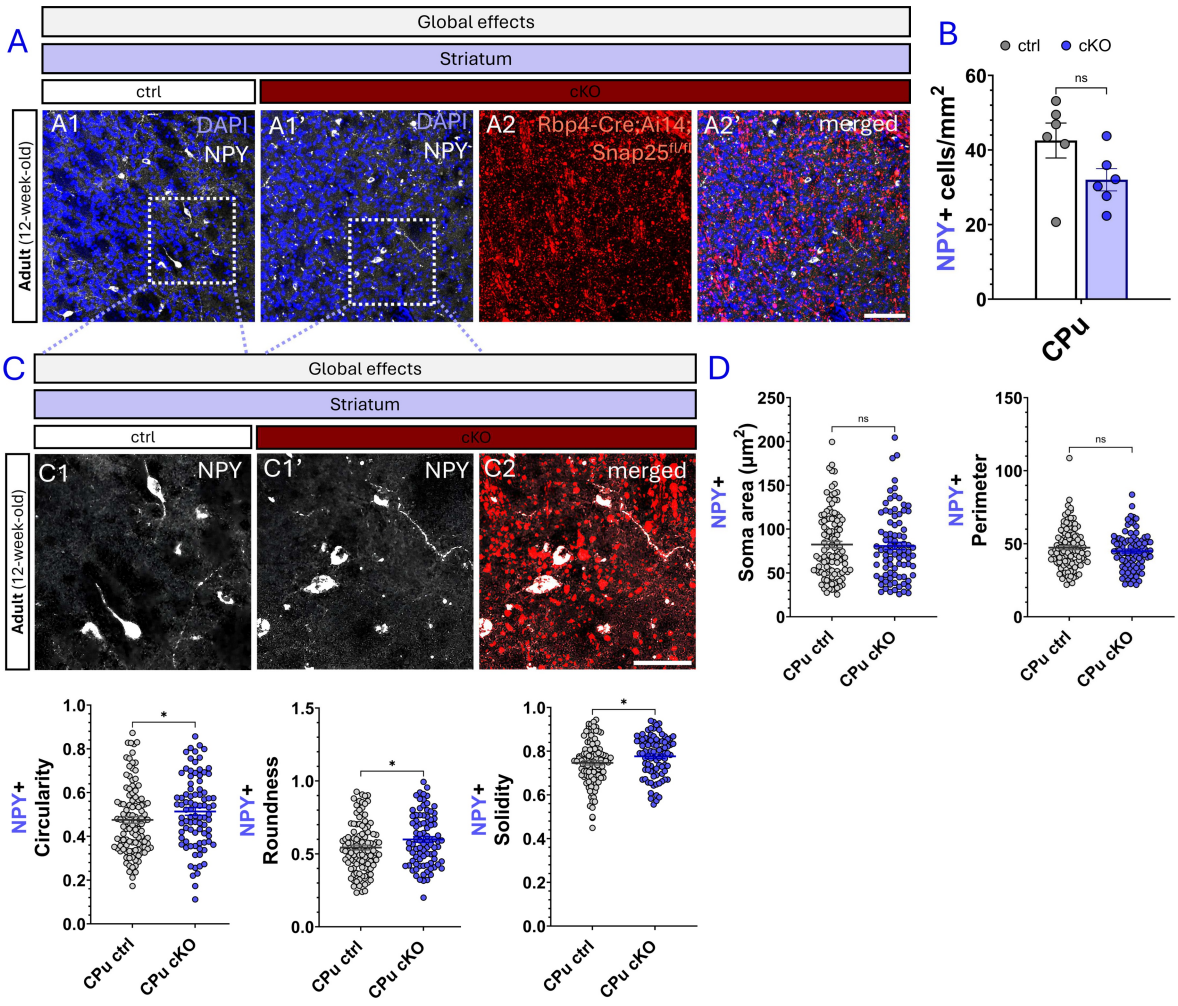


Figure 3.22. Chronic silencing of Rbp4-Cre+ layer 5 projection neurons has no long-term impact on the density of NPY+ neurons in the striatum at 12 weeks of age. Maximum-intensity projected z-stack images of NPY-immunoreactive cells in the dorsal striatum in the ctrl (A1, C1) and *Snap25* cKO mice (A1', C1'). Dotted squares denote the locations of NPY+ neurons shown in panel C. Maximum-intensity projected z-stack image of the tdTomato-positive projections of Rbp4-Cre+ pyramidal neurons in the striatum (A2, A2', C2). Quantification of the cell density of NPY-immunopositive neurons in the dorsal striatum at 12 weeks of age (B). Results of soma measurements of striatal NPY+ neurons (D). Scale bars = 100 µm.

3.6. The effects of genetically silencing the hippocampal mossy fibre pathway on GABAergic interneurons

In the previous sections, the research questions were centred around the role of layer 5 glutamatergic projection neurons in regulating the spatial and laminar organisation of GABAergic interneurons in developing and adult brains. I investigated the effects of genetically silencing layer 5 pyramidal neurons on the development, density, laminar distribution, and soma morphology of *parvalbumin* neurons. The chapter then explored the long-term effects on NPY-expressing neurons in the neocortex and the striatum. Since Cre is also expressed in the granule cells of the dentate gyrus in the Rbp4-Cre+ line, the loss of AP-dependent neurotransmitter release will affect not only the glutamatergic Rbp4-Cre+ layer 5 projection neurons but also the mossy fibre pathway. Therefore, I took advantage of the *Rbp4-Cre+,Ai14;Snap25*$^{fl/fl}$ cKO mice and employed them to investigate the effects of silencing the hippocampal granule cells.

In the next sections, I addressed the following research questions:

1) How does AP-dependent neurotransmitter release from hippocampal granule cells affect GABAergic neurons in the juvenile and adult hippocampus?

2) Are distinct subtypes of GABAergic neurons affected differently when the mossy fibre pathway is silenced? How do PV, NPY, and SST neurons respond to the genetic silencing of granule cells in the dentate gyrus?

Long-term effects on parvalbumin, somatostatin and neuropeptide-Y neurons

3.6.1. Genetic silencing of dentate gyrus granule cells does not affect the density of parvalbumin interneurons during development

First, I tested the hypothesis that chronic silencing of the mossy fibre pathway would impair the development of local PV+ neurons in the CA3 and the dentate gyrus during the early phases of development. Contrary to expectations, the density of PV+ neurons remained unaltered in the CA3 and dentate gyrus at P14 and P21 in the *Snap25* cKO mice relative to the control mice (Figure 3.23. D, H). At both ages, two-way ANOVA revealed a significant *region* but no *genotype* effect, without *interaction* between the two variables (*region*, P14, p=0.0002; P21, p<0.0001). Next, I assessed the developmental trajectory of PV+ interneurons. Control mice displayed a significant increase of ~44% in the density of PV+ neurons in the dentate gyrus between P14 and P21 (p=0.0352; two-way ANOVA with Šídák's multiple comparisons test) (Figure 3.23. M). A similar trend was observed in the *Snap25* cKO mice; however, it did not reach statistical significance (p=0.4947) (Figure 3.23. N). Between P14 and P21, the developmental trajectories of PV+ neurons in the CA3 did not differ significantly between control and cKO mice (Figure 3.23. M, N). These results suggest that the chronic silencing of hippocampal granule cells has no region-specific effect on the maturation of local PV+ neurons and allows for a normal developmental trajectory in both hippocampal regions.

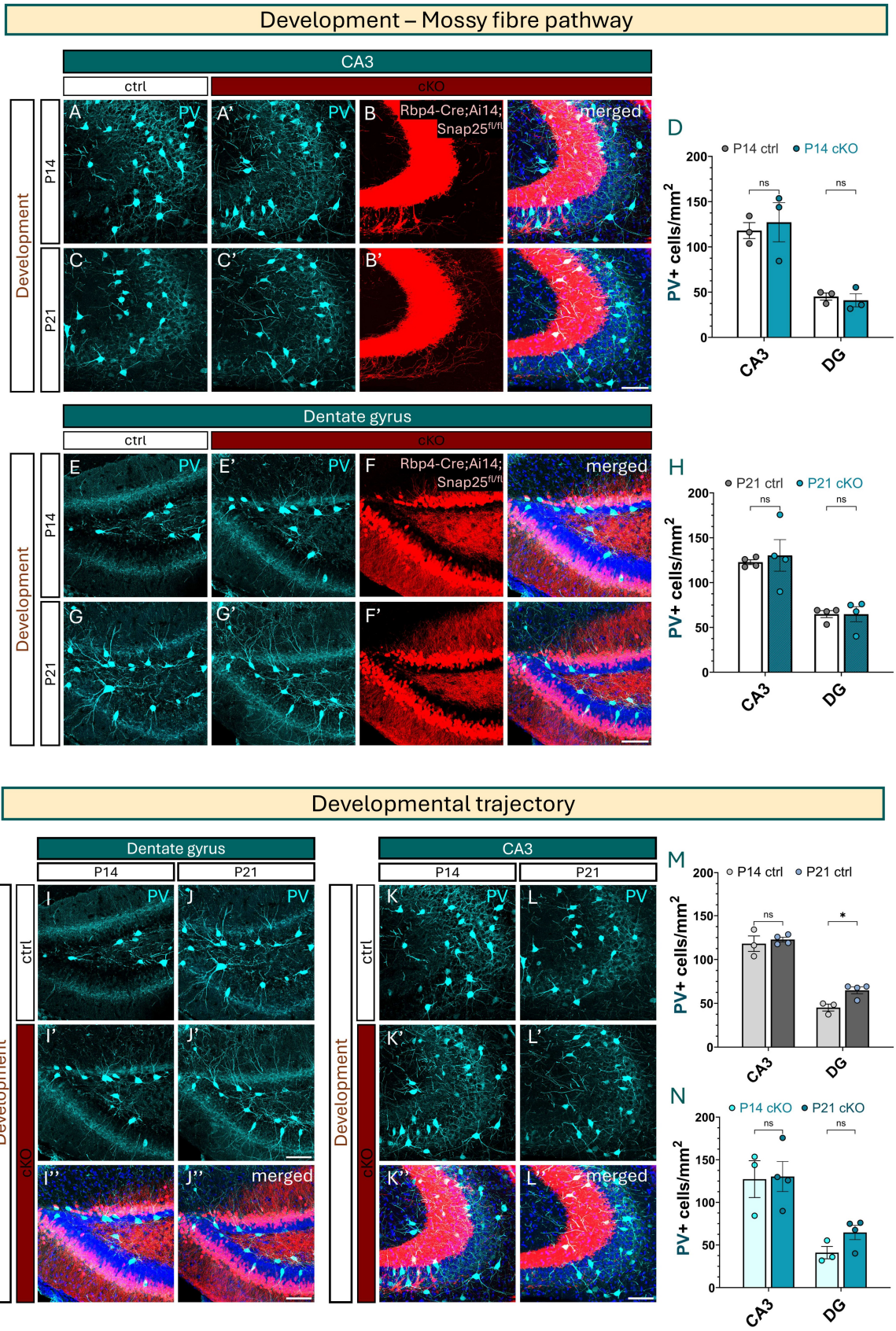

Development – Mossy fibre pathway
CA3
ctrl
cKO
Development
P14
P21
A
PV
A'
PV
B
Rbp4-Cre;Ai14;
Snap25fl/fl
merged
C
C'
B'
D
P14 ctrl
P14 cKO
PV+ cells/mm2
200
150
100
50
0
ns
ns
CA3
DG
Dentate gyrus
E
PV
E'
PV
F
Rbp4-Cre;Ai14;
Snap25fl/fl
merged
G
G'
F'
H
P21 ctrl
P21 cKO
PV+ cells/mm2
ns
ns
CA3
DG
Developmental trajectory
Dentate gyrus
CA3
P14
P21
ctrl
cKO
Development
I
PV
J
PV
K
PV
L
PV
I'
J'
K'
L'
I''
J''
merged
K''
L''
merged
M
P14 ctrl
P21 ctrl
PV+ cells/mm2
ns
*
CA3
DG
N
P14 cKO
P21 cKO
PV+ cells/mm2
ns
ns
CA3
DG

Figure 3.23. The density and developmental trajectories of parvalbumin interneurons are not affected by the chronic silencing of the mossy fibre pathway. Maximum-intensity projected z-stacks of PV-immunoreactive neurons at P14 and P21 in the CA3 and the dentate gyrus in control (A, C, E, G) and cKO mice (A', C', E', G'). Robust tdTomato+ expression in the *Snap25* cKO mice in the CA3 (B, B') and dentate gyrus (F, F'). Quantification of the cell density of PV+ neurons in the CA3 and dentate gyrus at P14 and P21 (D, H). Merged z-stack images of PV-immunopositive neurons between P14 and P21 in control and mutant mice in the dentate gyrus (I-J, I'-J") and CA3 area (K-L, K'-L"). Quantification of the developmental dynamics of PV+ neurons between P14 and P21 in the CA3 and dentate gyrus in the control and *Snap25* cKO mice (M, N). Scale bars = 50 μm.

3.6.2. The conditional silencing of hippocampal granule cells does not impact perineuronal nets in the adult hippocampus

Since the conditional silencing of the mossy fibre pathway did not influence the density and developmental dynamics of immature PV+ neurons, I wondered whether it might have a delayed effect on them that would only manifest in adulthood. In particular, whether mature PV+ neurons encapsulated by PNNs might be more affected by silencing the hippocampal granule cells. Two-way ANOVA tests only identified a significant *region* but no *genotype* effect on PV and VVA density in both the CA3 and dentate gyrus (PV, region, $p<0.0001$, genotype, $p=0.3879$; VVA, region, $p<0.0001$, genotype, $p=0.5497$; two-way ANOVA with Šídák's multiple comparisons test). *Post*-hoc tests detected no alterations in the density of PV+ and VVA+ cells in the CA3 and dentate gyrus at 12 weeks of age between the ctrl and *Snap25* cKO mice (Figure 3.24. A-D', G-J', E, F).

When differentiating between PV+ neurons that are enclosed by PNNs and those without PNNs, only a significant *region* effect was identified (CA3, $p=0.0039$; DG, $p=0.0041$; two-way ANOVA with Šídák's multiple comparisons test). *Post*-hoc comparisons did not find significant changes in the density of PV+ VVA+, PV+ VVA-, and PV- VVA+ cells (Figure 3.24. M-N', P- Q', O, R). These findings suggest that there is neither a short-term nor a long-term impact on the density of PV+ neurons or PNNs when *Snap25* is deleted from the hippocampal granule cells.

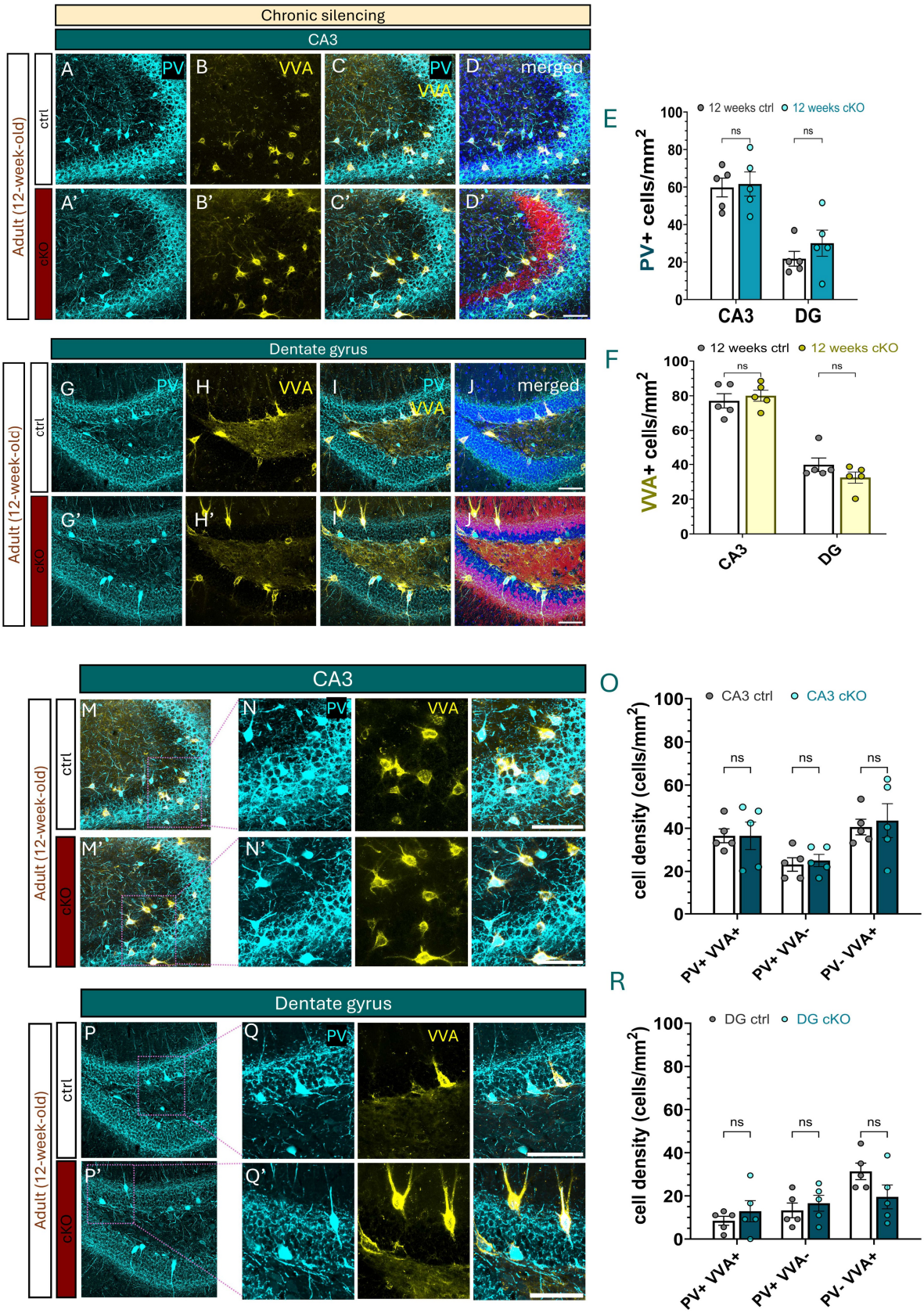

Chronic silencing
CA3
Adult (12-week-old)
ctrl
cKO
A
PV
B
VVA
C
PV
VVA
D
merged
A'
B'
C'
D'
E
12 weeks ctrl
12 weeks cKO
PV+ cells/mm2
ns
CA3
DG
Dentate gyrus
G
H
I
J
G'
H'
I'
F
VVA+ cells/mm2
CA3
DG
CA3
M
N
M'
N'
O
CA3 ctrl
CA3 cKO
cell density (cells/mm2)
PV+ VVA+
PV+ VVA-
PV- VVA+
Dentate gyrus
P
Q
P'
Q'
R
DG ctrl
DG cKO

Figure 3.24. Genetic silencing of granule cells does not have a long-term effect on parvalbumin neurons and the perineuronal nets within the hippocampus. (A-D) Collapsed z-stack images of parvalbumin-immunoreactive neurons in cyan (A, A') and *Vicia villosa* agglutinin (VVA)-labelled perineuronal nets in yellow (B, B') and their superimposed image (C, C') in the CA3 at 12 weeks of age in the ctrl and cKO mice. Maximum-intensity projected z-stacks of DAPI, PV, and VVA channels in the CA3 of ctrl mice (D, D'). Quantification of the mean cell density of PV-immunoreactive cells in the CA3 and dentate gyrus at 12 weeks of age (E). Quantification of the mean cell density of VVA-labelled PNN density in the CA3 and dentate gyrus at 12 weeks of age (F). Collapsed z-stack images illustrating parvalbumin-immunoreactive neurons and the perineuronal nets in the dentate gyrus at 12 weeks of age in the control (G, H, I) and cKO mice (G', H', I'). Maximum-intensity projected z-stacks of DAPI, PV, and VVA channels in the dentate gyrus of ctrl and cKO mice (J, J'). Zoom-in confocal z-stack images showing PV and VVA neurons (N, N') outlined in panel M (ctrl) and M' (mutant mice) in the CA3. (O) Quantification of the density of PV and VVA cells in the CA3 of ctrl and *Snap25* cKO mice. (P-P', Q-Q') Zoom-in images of PV and VVA neurons (Q, Q') outlined in panel P (ctrl) and P' (mutant mice) in the dentate gyrus. (R) Quantification of the mean cell density of PV+ neurons as well as PV+ cells with and without PNNs in the dentate gyrus. Scale bars = 50 μm.

3.6.3. The density of parvalbumin interneurons significantly declines in the CA3 of the hippocampus from development to adulthood, both under normal and chronic conditions

My next goal was to establish the trajectory of PV neurons from the third week of development to three months of age within the hippocampus. According to two-way ANOVA tests, *region* and *age* had a significant influence on PV+ cell density, and there was a significant *interaction* between the two components (region and age, $p<0.0001$; interaction, $p=0.0311$). Significant variations in the trajectory of PV+ neurons in the *control* mice between P21 and 12 weeks were detected by *post*-hoc Šidák's multiple comparisons test. In particular, the dentate gyrus's PV+ cell density decreased by almost 66%, whereas the CA3's was reduced by roughly 51% ($p<0.0001$) (Figure 3.25. E). The same pattern was identified in the CA3 of the mossy fibre-silenced mice, where the density of PV+ neurons was reduced by half ($p=0.0006$; two-way ANOVA with Šídák's multiple comparisons test) (Figure 3.25. F). The dentate gyrus of *Snap25* cKO mice showed a comparable reduction in PV+ cell density between P21 and 3 months, but it did not reach statistical significance (Figure 3.25. F) ($p=0.0581$). However, these results suggest that a marked reduction in PV+ cell density occurs both in control and *Snap25*

cKO mice.

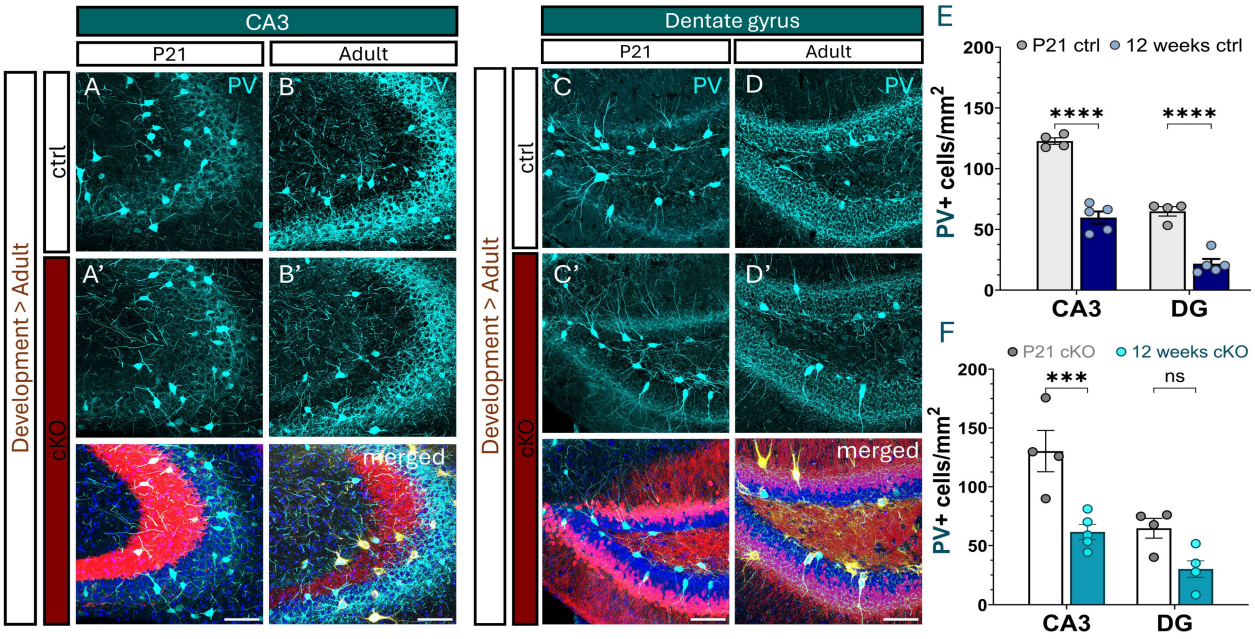


Figure 3.25. From development to adulthood, the density of parvalbumin interneurons in the CA3 area of the hippocampus decreases considerably both in the ctrl and *Snap25* cKO mice. (A-B) Comparison of the trajectory of PV-immunoreactive neurons in the CA3 from postnatal day 21 to 12 weeks of age in ctrl mice. Note the prominent decrease in the number of PV+ neurons in the adult brain, where the mossy fibre pathway remained intact. (A'-B') Comparison of the trajectory of PV-immunoreactive neurons in the CA3 from postnatal day 21 to 12 weeks of age in the *Snap25* cKO mice, where the mossy fibre pathway was chronically silenced. (C-D, C'-D') Comparison of the trajectory of PV-immunoreactive neurons in the dentate gyrus from postnatal day 21 to 12 weeks of age in the ctrl mice and mutant mice. (E-F) Quantification of the mean cell density of PV-immunostained neurons from development to adulthood in ctrl and mutant mice.

3.6.4. Chronic silencing of the hippocampal mossy fibre pathway does not uniformly affect the density of neuropeptide-Y interneurons within the hippocampus

To ascertain if the genetic silencing of granule cells had a distinct impact on the interneuron subtypes that do not express Ca^{2+}-binding proteins, I examined the long-term effects on NPY interneurons. I noted a significant decrease of ~28% in the density of NPY+ cells in the dentate gyrus of *Snap25* cKO mice relative to control mice (Figure 3.26. I) (p=0.0321; two-way ANOVA with Šídák's multiple comparisons test). Other regions did not show significant alterations in the density of NPY+ neurons between ctrl and cKO mice (CA3, p=0.9862; CA1, p>0.999). Since the genetic silencing of the mossy fibre pathway did not have any effect on the density of PV+ neurons in the hippocampal regions studied, the observed effect appears to be specific to the NPY-expressing subtype of GABAergic interneurons.

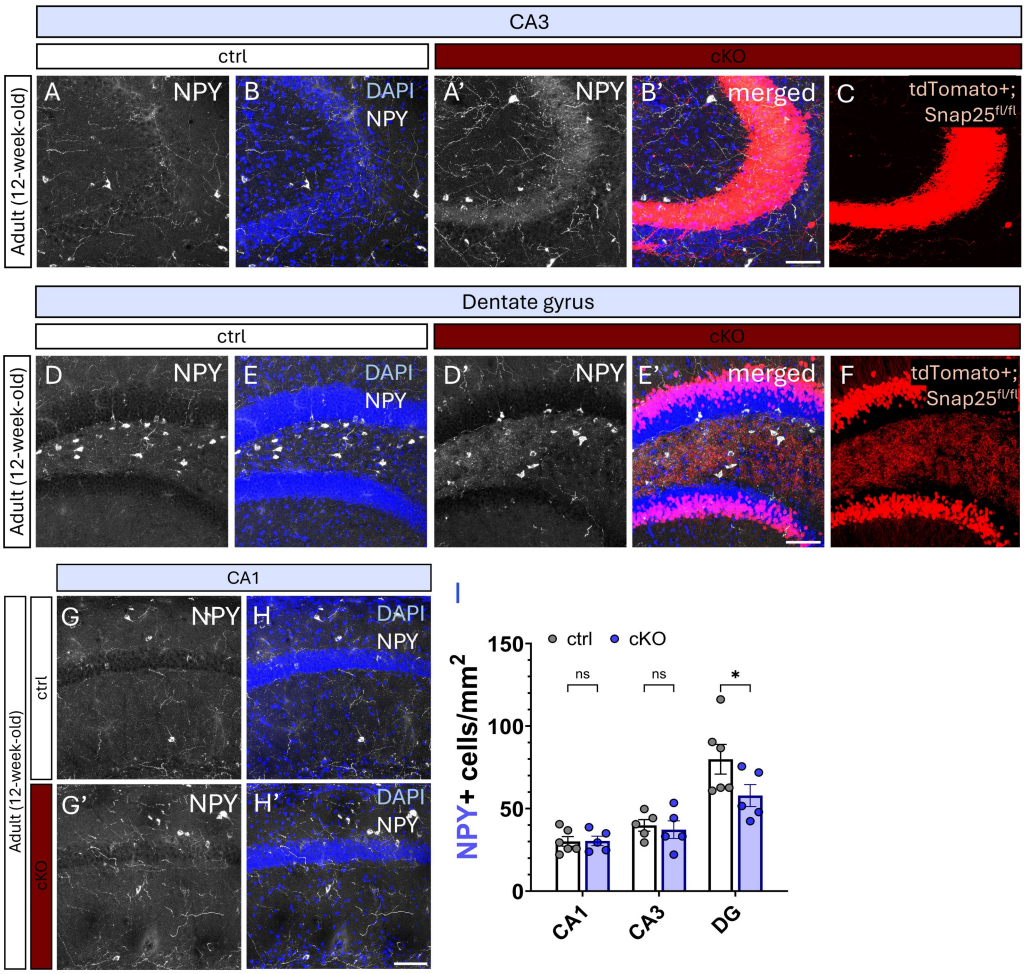


Figure 3.26. Neuropeptide-Y neurons in distinct regions of the hippocampus exhibit different responses to the deletion of *Snap25* from the granule cells of the dentate gyrus. Maximum-intensity projected z-stacks displaying NPY-immunoreactive cells in grey at 12 weeks of age in the CA3 and dentate gyrus in control (A, B, D, E) and mossy fibre-silenced mice (A', B', D', E'). Collapsed z-stack images showing tdTomato reporter expression in the CA3 and dentate gyrus in the *Rbp4-Cre;Ai14;Snap25*$^{fl/fl}$ mice (C, F). NPY-immunoreactive neurons in the CA1 of the hippocampus in the control (G, H) and *Snap25* cKO mice (G', H'). (I) PV+ cell density quantified at 12 weeks of age. Note that the reduction in PV+ density was only observed in the dentate gyrus, where AP-dependent neurotransmitter release was abolished.

3.6.5. The genetic silencing of hippocampal granule cells alters the density of somatostatin neurons in the dentate gyrus

Both SST+ and PV+ interneurons arise from the MGE during embryonic development; however, these two types of interneurons exhibit significant differences in their electrophysiological properties, input distribution, and circuit functions. SST+ interneurons are known for their pivotal roles in modulating incoming excitatory inputs and synaptic plasticity (Freund and Buzsáki 1996; Honoré et al. 2021), while PV interneurons are recognised for their fast inhibition, synchronising network oscillations, and controlling the spiking of pyramidal neurons (McBain and Fisahn 2001; Bartos et al. 2007). Given these differences, I postulated that the genetic silencing of granule cells—key excitatory neurons in the hippocampus—would have a more prominent impact on the survival of SST+ interneurons compared to their PV counterparts. This hypothesis stems from the notion that the loss of granule cell input to SST+ neurons may reduce the excitatory drive to SST+ neurons, potentially leading to disrupted feedback inhibition (Yuan et al. 2017; Drake et al. 2024). To ascertain whether SST+ neurons were indeed more vulnerable to the genetic silencing of dentate gyrus granule cells, I quantified their numbers within the hippocampus.

A two-way ANOVA test revealed a significant *region* and *genotype* influence on SST+ density within the hippocampus, with no interaction (region, p=0.0171; genotype, p=0.0023). *Post*-hoc multiple comparisons test found that the dentate gyrus of *Snap25* cKO mice contained ~39% fewer SST+ neurons compared to control mice (p=0.0256) (Figure 3.27. M). Considering that PV+

interneurons in the dentate gyrus did not exhibit such changes, it may be inferred that the chronically silenced mossy fibre pathway exclusively affects the neuropeptide-expressing subtypes of inhibitory cells (NPY and SST) and does not influence the Ca^{2+}-binding subgroups (PV).

3.6.6. Perineuronal nets surround SST neurons in the hippocampus and are not exclusively present around PV interneurons

To determine whether the presence of perineuronal nets is restricted to the parvalbumin subtype of interneurons, I performed double-histochemical staining for SST and VVA (Figure 3.27. A-D, A'-D'). I found evidence for SST-immunoreactive neurons that are enclosed by PNNs both in the control and mossy fibre-silenced mice at 12 weeks of age. Interestingly, CA3 exhibited the highest degree of co-localisation between SST and VVA (Figure 3.27. E-H, E'-H', N) and hence, had the highest number of SST cells surrounded by PNNs (Figure 3.27. O). The dentate gyrus barely contained any examples of SST-immunoreactive neurons that were positive for VVA (Figure 3.27. I-L, I'-L'). The relationship between SST and VVA in the CA3 is intriguing, as it raises the question of the role of PNNs around SST+ interneurons. First, it seems that the observed phenomenon is confined to the hippocampal CA3 region, suggesting that SST and VVA co-expression is exclusive to specific regions and cell types. Secondly, since SST interneurons do not have the same high metabolic demands as PV neurons, ECM/PNNs may not provide protection against oxidative stress for SST interneurons, or their co-localisation may serve a different function. It is conceivable that PNNs around SST+ neurons in the hippocampus play a role in the regulation of synaptic plasticity, stability, or memory retention.

3.6.7. Somatostatin neurons with perineuronal nets are unaffected by the genetic silencing of the mossy fibre pathway

Previous results have revealed that the genetic silencing of hippocampal granule cells leads to a significant reduction in the density of SST+ neurons exclusively in the dentate gyrus. To ascertain whether SST+ neurons that co-localise with PNNs respond differently to the chronic silencing, I assessed the density of SST+ VVA+ neurons. Two-way ANOVA testing found a significant *region* effect ($p<0.0001$), but neither the *genotype* ($p=0.2937$) nor the *interaction* ($p=0.7704$) between the two factors had a significant effect on the density of SST+ VVA+ neurons (Figure 3.27. N, O). *Post*-hoc Šídák's multiple comparisons test showed no significant alterations in the density of SST+ VVA+ cells at 12 weeks of age in any hippocampal region (Figure 27 N, O). It remains unclear if PNNs that physically enclose SST+ interneurons make them less responsive to shifts in network activity or plasticity. It would be interesting to know if SST+ neurons without PNNs in the adult cortex and hippocampus have different electrophysiological properties and are more adaptive than SST+ neurons with PNNs.

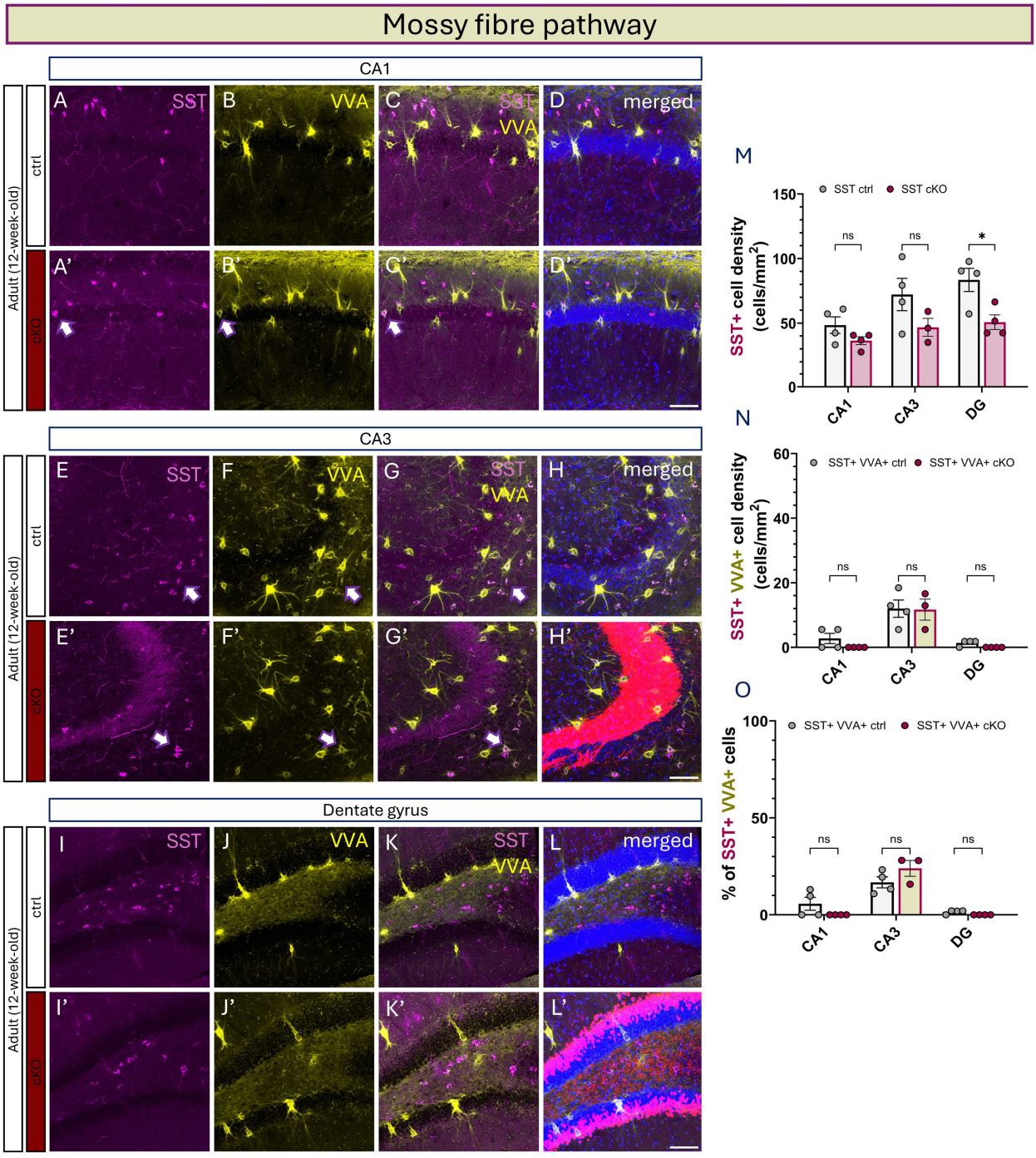


Figure 3.27. Genetic silencing of the mossy fibre pathway exclusively affects SST+ interneurons that are not encapsulated by perineuronal nets. Maximum-intensity projected z-stack images illustrating somatostatin-immunoreactive neurons in magenta in the control and mossy fibre-silenced mice in the CA1 (A, A'), CA3 (E, E'), and dentate gyrus (I, I'). Maximum-intensity projected z-stack images of *Vicia villosa* agglutinin-labelled perineuronal nets in yellow in the control and mossy fibre-silenced mice in the CA1 (B, B'), CA3 (F, F'), and dentate gyrus (J, J'). Collapsed z-stack images showing the perineuronal nets superimposed on the somatostatin signal in the ctrl and *Snap25* cKO mice at 12 weeks of age in the CA1 (C, C', D, D'), CA3 (G, G', H, H'), and dentate gyrus (K, K', L, L'). Note the

tdTomato+ reporter expression in the *Rbp4-Cre;Ai14;Snap25*$^{fl/fl}$ mice in the CA3 and dentate gyrus (H', L'). Quantification of the density of somatostatin-immunoreactive neurons in various regions of the hippocampus at 12 weeks of age (M). Quantification of the density of double-positive somatostatin-immunoreactive neurons surrounded by perineuronal nets (N). (O) Percentage of somatostatin-immunoreactive neurons surrounded by perineuronal nets in the CA1, CA3, and dentate gyrus. Scale bars = 50 μm.

3.7. Discussion

3.7.1. The effects of chronically silencing layer 5 projection neurons on parvalbumin interneurons in the *juvenile* brain

One central notion in interneuron research is that the maturation of interneurons and the formation of inhibitory circuits are not solely defined by genetically controlled mechanisms, and the 'fate' of developmental processes can be overridden by manipulating the interaction between pyramidal cells and interneurons in the embryonic and early postnatal brain. For instance, increased network activity has been shown to have a pro-survival effect on cortical GABAergic interneurons by reducing the number of interneurons undergoing apoptosis and increasing their survival rate in the forebrain (Denaxa et al. 2018; Wong and Marín 2019). Enhanced levels of network activity by the synchronised activation of pyramidal cells and interneurons in the nascent cortex have been documented to have a similar pro-survival effect on both glutamatergic and GABAergic cells (Duan et al. 2020). It has also been revealed that the removal of pyramidal cell inputs to developing cortical interneurons affects their survival and density (Duan et al. 2020; De Marco García et al. 2011).

To elucidate the role of infragranular cortical projection neurons in modulating the spatial and laminar distribution of GABAergic interneurons, I used a triple transgenic mouse model (*Rbp4-Cre+;Ai14,Snap25*$^{fl/fl}$) where AP-dependent neurotransmitter release was abolished in a restricted subset of corticostriatal pyramidal neurons in layer 5 as well as in the granule cells of the dentate gyrus. I found that the density and development of GABAergic PV+ interneurons were not altered in the selected cortical and subcortical output regions of layer 5 at P14 and P21. However, chronic silencing of subsets of layer 5 neurons had a long-term impact on the laminar distribution of PV+ cells in the adult brain. The primary motor and somatosensory cortices had different rearrangements in the distribution of PV+ neurons and PNNs; therefore, these effects may vary depending on the laminar and regional location of the interneurons in the cortex.

The following reasons might account for the lack of effects on the density of immature PV+ interneurons. First, PV+ interneurons may be able to compensate for the absence of glutamatergic inputs during the early periods of development, when the inhibitory circuits are highly plastic and are still under construction. In the context of diminished input from layer 5 pyramidal neurons, various compensatory mechanisms may be activated, including alternative excitatory signals originating from other cortical layers. Notably, PV+ neurons receive robust glutamatergic input not only from local layer 5 pyramidal neurons but also through translaminar connections facilitated by excitatory neurons located in layers 2 and 3 (Naka and Adesnik 2016). By partially compensating for the reduced L5 drive, increased activity from these alternate sources can maintain PV firing's ability to inhibit networks. Besides local and translaminar inputs, PV+ interneurons also receive long-range afferent inputs from a wide array of cortical regions, such as the visual cortex, somatosensory areas, premotor area, or the auditory cortex (Wall et al. 2016; Lu et al. 2014; Hafner et al. 2019). These long-range cortical as well as the thalamocortical inputs may be able to substitute for the diminished excitatory input from layer 5.

Other compensatory mechanisms may entail PV-PV autaptic or self-innervating connections, as PV+ interneurons are known to form synaptic connections onto themselves. With the PV-PV synapses, the glutamatergic drive can be distributed throughout the PV network, potentially preserving coordinated inhibitory output in the event that a fraction of PV inputs declines (Micheva et al. 2021; Bacci and Huguenard 2006). The decreased inputs from layer 5 may also promote the recruitment of different subtypes of GABAergic cells, such as SST+ and VIP+ interneurons, or increase the excitability and synaptic strength of PV+ neurons (Lu et al. 2014). Furthermore, the redistribution of excitatory signals to maintain the equilibrium between excitation and inhibition (E/I balance) may also occur through network-level homeostasis (Gainey and Feldman 2017). Collectively, these mechanisms may serve as compensatory strategies to mitigate the impact of diminished excitation from layer 5 pyramidal neurons.

Silencing layer 5 neurons may not influence cortical GABAergic interneurons since *Snap25* deletion occurs at or around birth and hence, does not happen during the CP of interneuron cell death (P5-P10). Previous research supports this by demonstrating that chemogenetic alteration of pyramidal neuron activity, when regulated after the closure of programmed cell death of GABAergic interneurons, has no impact on the distribution of PV+ interneurons (Wong et al. 2018; Sreenivasan et al. 2022).

However, it has to be noted that pyramidal cell activity is chronically silenced in our model and therefore, our results cannot be directly compared to the results of studies using transient modulation of pyramidal cell activity (Wong et al. 2018; Sreenivasan et al. 2022). Nevertheless, the varying influences of pyramidal neuron activity on the distribution of interneurons indicate the sensitivity of GABAergic cells to developmental periods and the importance of studying their organisation at distinct stages of development. Investigating the number of parvalbumin interneurons during the peak of GABAergic interneuron cell death would not have been feasible, as the accurate detection of PV interneurons at P8 is limited by several factors. One limit is the sensitivity of immunohistochemistry, which is unable to capture low-expressing PV neurons accurately during such early stages of development. Furthermore, the late commencement of PV protein expression (P14) makes it technically difficult to identify interneurons in the cortex that express PV at P8 (Vogt Weisenhorn et al. 1998; del Río et al. 1994). The delayed onset of Cre recombinase expression in the PV-Cre or PV-CreERT2 strains makes genetic labelling techniques and the use of PV-specific Cre-driver lines impractical because they do not produce adequate PV labelling at P8 either (Tanahira et al. 2009; Taniguchi et al. 2011). One promising transgenic mouse line is the G42 PV-expressing reporter strain. This strain shows high specificity for PV basket interneurons and can be used to identify PV cells and their presynaptic boutons prior to P14 (Chattopadhyaya et al. 2004; Miyamae et al. 2017). Notably, GFP-expressing cells are present in the neocortex at birth (Chattopadhyaya et al. 2004). Transcription factors that are expressed early in development play a crucial role in PV fate specification, migration,

and differentiation, which can serve as markers for PV neuron precursors, allowing for accurate inference of PV identity even before the detection of PV protein expression in the developing cortex becomes possible. Some key developmental lineage markers include *Lhx6, Sox6, Nkx2.1, Satb1, Mafb,* and *Tox2* (Azim et al. 2009; Paul et al. 2017; Sussel et al. 1999; Butt et al. 2008). However, these transcription factors should be used alongside other molecular markers, as they are also expressed in SST cells. Recent advances in single-cell RNA sequencing have identified additional transcription factors unique to the PV lineage, such as *Lmo2, Ppargc1a, Rora, Pthlh, Tac1, Syt2,* and *Adm* (Paul et al. 2017). These factors can also help distinguish PV cells before the onset of PV protein expression.

3.7.2. The effects of chronically silencing layer 5 projection neurons on distinct subtypes of GABAergic interneurons in the adult brain

My findings indicate that developmental perturbations can have a long-lasting effect on inhibitory neurons. Specifically, I found that the genetic silencing of subsets of Rbp4-Cre+ neurons in layer 5 had a delayed effect on PV neurons and the perineuronal nets that only emerged in adulthood. It has to be noted, however, that chronic silencing of layer 5 neurons only disrupts the laminar positioning of PV neurons without altering their number. This is an interesting finding because pathological changes in a variety of neuropsychiatric illnesses, including bipolar disorder and schizophrenia, have been linked to significant reductions in the number of GABAergic interneurons (Enwright et al. 2016; Benes and Berretta 2001; Lodge et al. 2009; Dienel and Lewis 2019; Sakai et al. 2008). While it was beyond the scope of this thesis to investigate the effects of silencing layer 5 pyramidal neurons on MGE vs. CGE-derived interneurons in the postnatal brain, I found that NPY+ cells in the adult *Snap25* cKO brains were affected in an opposing manner in S1. The laminar distribution of PV+ and PV+ VVA+ neurons was significantly increased in layer 4 of S1 at 12 weeks of age, whereas the laminar positioning of NPY+ remained unchanged. However, in M1, the laminar distribution of NPY+ neurons was significantly decreased in layer 1 and layer 2/3, whereas PV+

neurons were unaltered. It remains to be determined why different subtypes of GABAergic cells respond differently to the conditional silencing of layer 5 neurons. Additionally, it is important to understand the factors that contribute to the regional and laminar differences observed between the responses of PV+ and NPY+ neurons to layer 5 silencing. The area- and layer-specific microcircuits in the neocortex, along with the functional specialisation of PV+ and NPY+ cells, can play a role in their varying responses when the excitatory drive from layer 5 neurons is diminished. Besides mediating precise feedback and feedforward inhibition, fast-spiking PV+ interneurons are crucial for modulating the firing of pyramidal cells and the gain of cortical output (Hu et al. 2014; Freund 2003). Given that FS PV+ interneurons modulate pyramidal cell spiking and synchronise network oscillations (Tremblay et al. 2016), their function heavily relies on the activity of pyramidal neurons and excitatory drive from these cells (Selten et al. 2025). In contrast, NPY+ neurons provide slow, volume-transmitted inhibition and neuromodulation, which contribute to overall network stability (Aoki and Pickel 1989; Karagiannis et al. 2009). As a result, NPY+ neurons may be less sensitive to changes in the activity of excitatory neurons.

Additionally, differences in synaptic connectivity between PV+ and NPY+ interneurons influence their dependence on excitatory inputs. For example, PV+ neurons receive local, direct glutamatergic inputs from pyramidal neurons within the same layer, as well as inputs from different layers, integrating them deeply into inhibitory cortical circuits (Gupta et al. 2000). While PV+ interneurons demonstrate activity-dependent plasticity (Selten et al. 2025), NPY+ neurons are implicated in compensatory adjustments within the network and hence, rely on less direct, diffuse excitatory inputs (Bacci et al. 2002). Thus, the response of PV+ and NPY+ interneurons to the genetic silencing of Rbp4-Cre+ neurons may be influenced by differences in input dependency, functional specialisation, and synaptic connections.

3.7.3. The effects of manipulating the hippocampal mossy fibre pathway on different subtypes of GABAergic interneurons in the adult brain

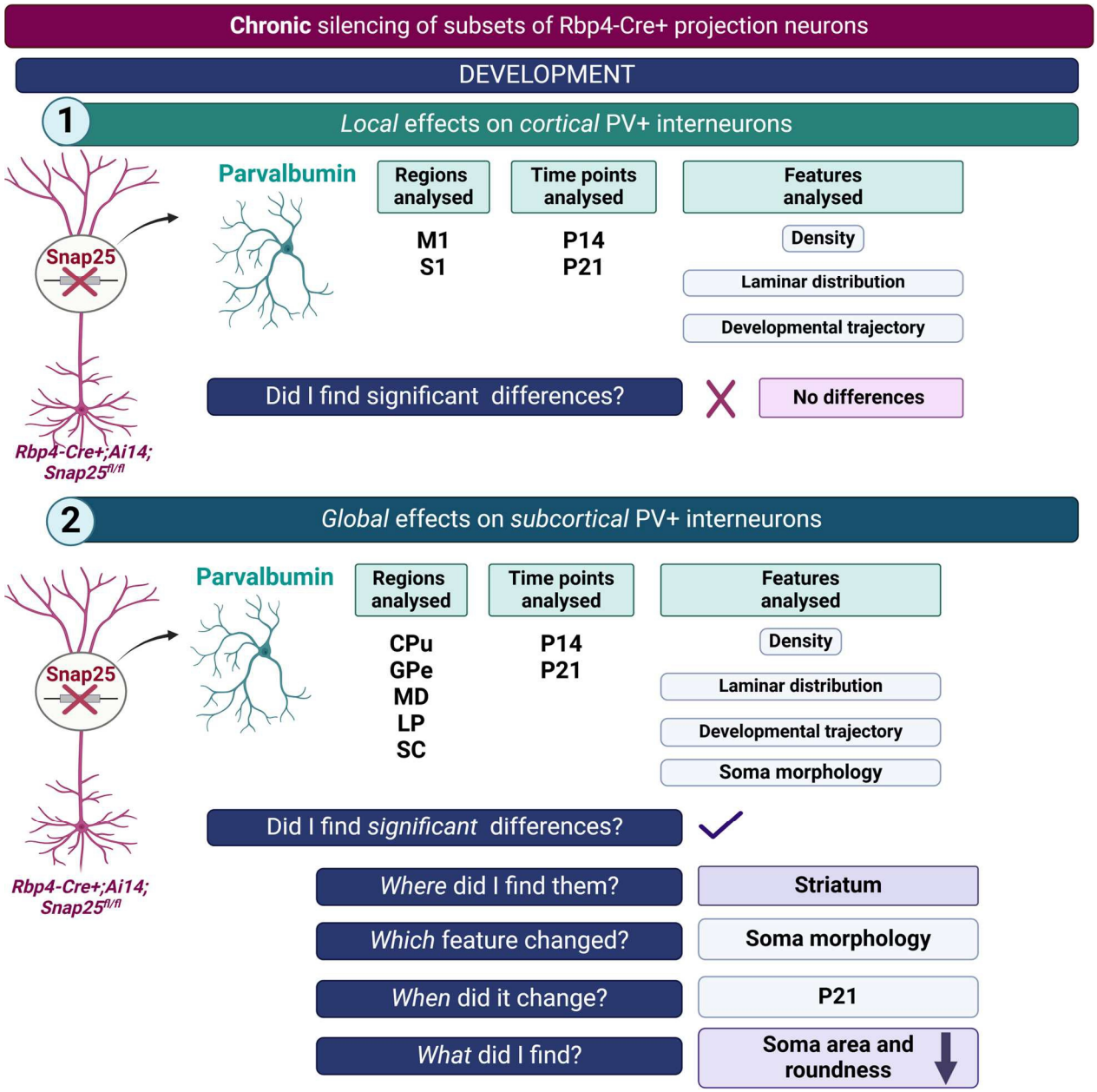
The results point to the importance of studying GABAergic neurons beyond the neocortex. I found that the density of NPY+ and SST+ neurons significantly decreased in the dentate gyrus in the *Snap25* cKO mice compared to the control mice. Considering that the dentate gyrus is not a projection region of Rbp4-Cre+ pyramidal neurons, I attribute the observed effect to chronically silencing the mossy fibre tract and eliminating the ability of granule cells in the dentate gyrus to release synaptic vesicles. Therefore, hippocampal-related alterations are unlikely to be derived from the genetic silencing of layer 5 projection neurons. Furthermore, hippocampal pyramidal neurons are not manipulated in the *Rbp4-Cre+;Ai14,Snap25*$^{fl/fl}$ mice, suggesting that modifications in the neuropeptide-expressing GABAergic interneurons resulted from silencing the granule cells.

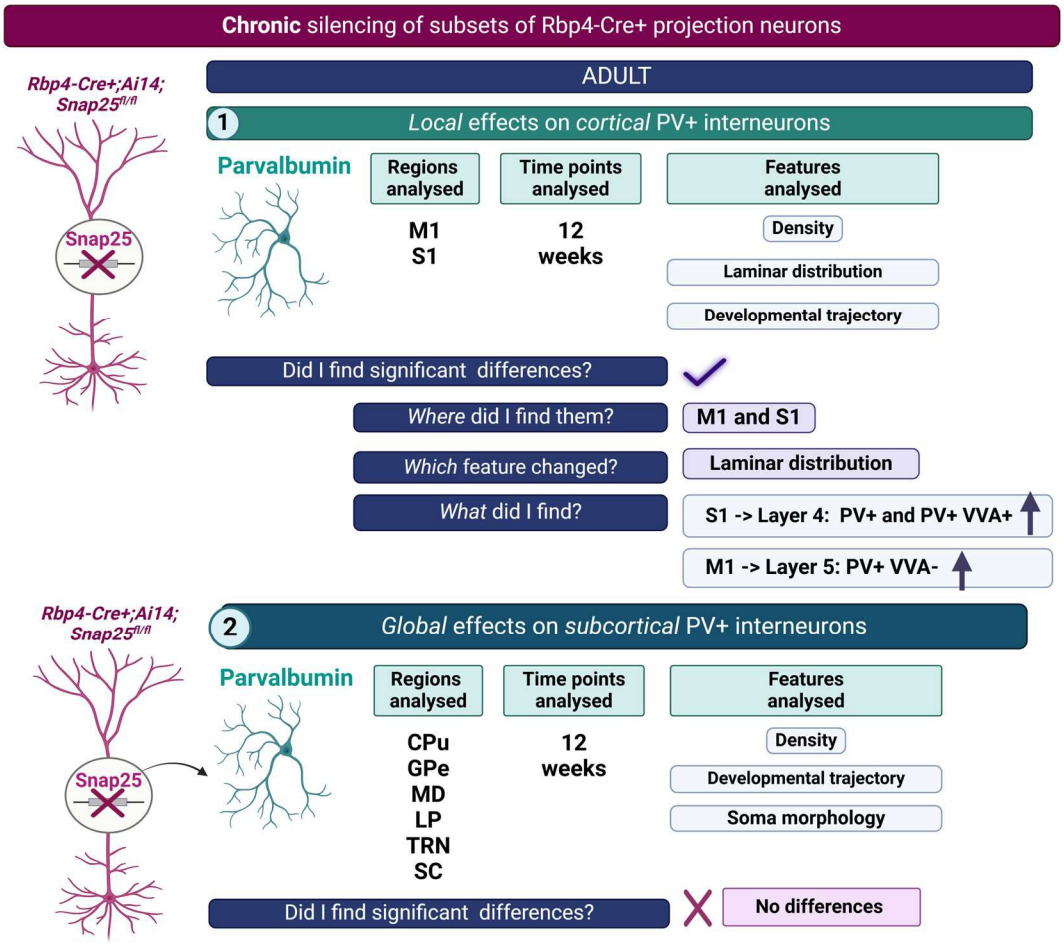
It would be interesting to know whether the significant decline in the density of NPY+ and SST+ neurons detected in the dentate gyrus is correlated with changes in inhibitory synapses. Since the excitatory drive to inhibitory neurons is diminished when the dentate gyrus granule cells are genetically silenced, NPY+ and SST+ neurons are deprived of the excitation necessary to sustain their inhibitory roles. The elimination of excitation leads to a statistically significant decrease in the density of NPY+ neurons in the dentate gyrus, suggesting either activity-dependent maintenance of NPY+ expression or potential cell loss due to the reliance on local excitatory input from the dentate granule cells. In addition to NPY+ neurons, there were notable reductions in the density of SST+ interneurons, similarly in the dentate gyrus. Given that SST+ interneurons provide dendritic inhibition to principal neurons, they play a pivotal role in filtering and modulating glutamatergic inputs, thereby modulating the integration of synaptic inputs and affecting network dynamics (Keijser and Sprekeler 2023). When the activity of granule cells is genetically silenced, it deprives SST+ interneurons of a key source of excitatory transmission, and the decrease in SST+ density seems to reflect a direct response to the removal of glutamatergic input. This suggests that SST+ interneurons are not only dependent on

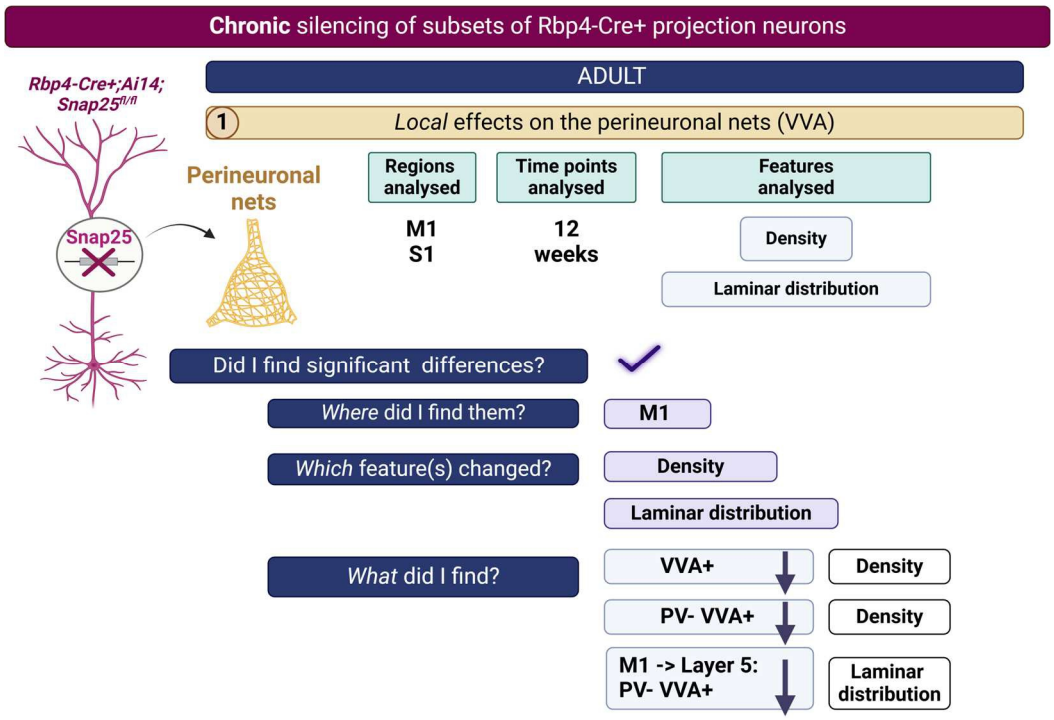
neuronal and network activity but also require excitatory input for their survival (Asgarihafshejani et al. 2022; Grigoryan et al. 2023; Urban-Ciecko and Barth 2016).

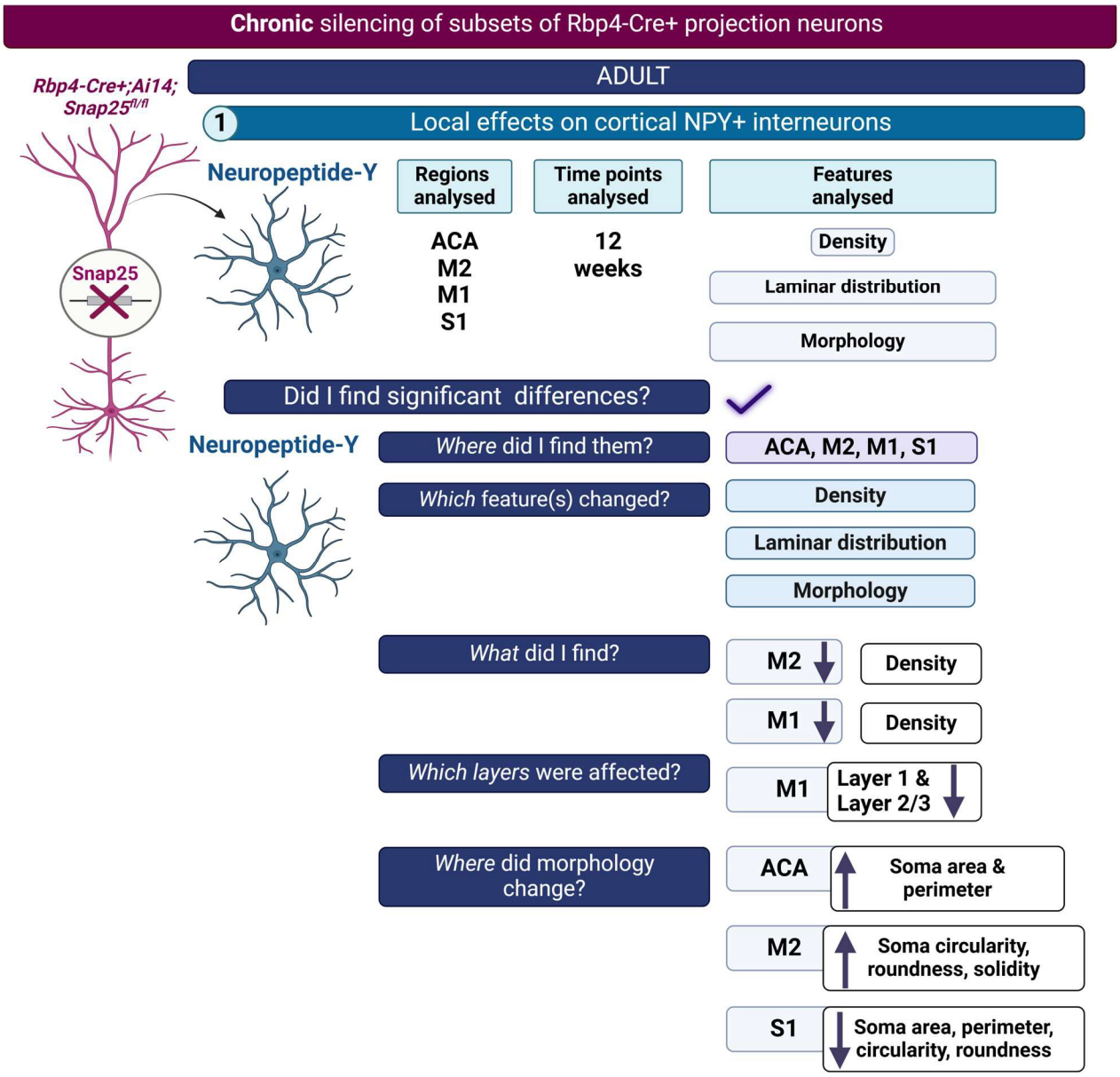
Long-term chemogenetic suppression of SST-expressing interneurons in the hilus of the dentate gyrus has led to deficiencies in learning and memory (Lyu et al. 2023). Interestingly, neither the chronic nor the acute manipulation of the hippocampal mossy fibre pathway affected PV+ interneurons in the hippocampus. However, further research needs to be conducted to reveal how acute, short-term manipulations of pyramidal neuron activity in the adult brain may cause circuit abnormalities, synaptic defects, or maladaptive behaviours.

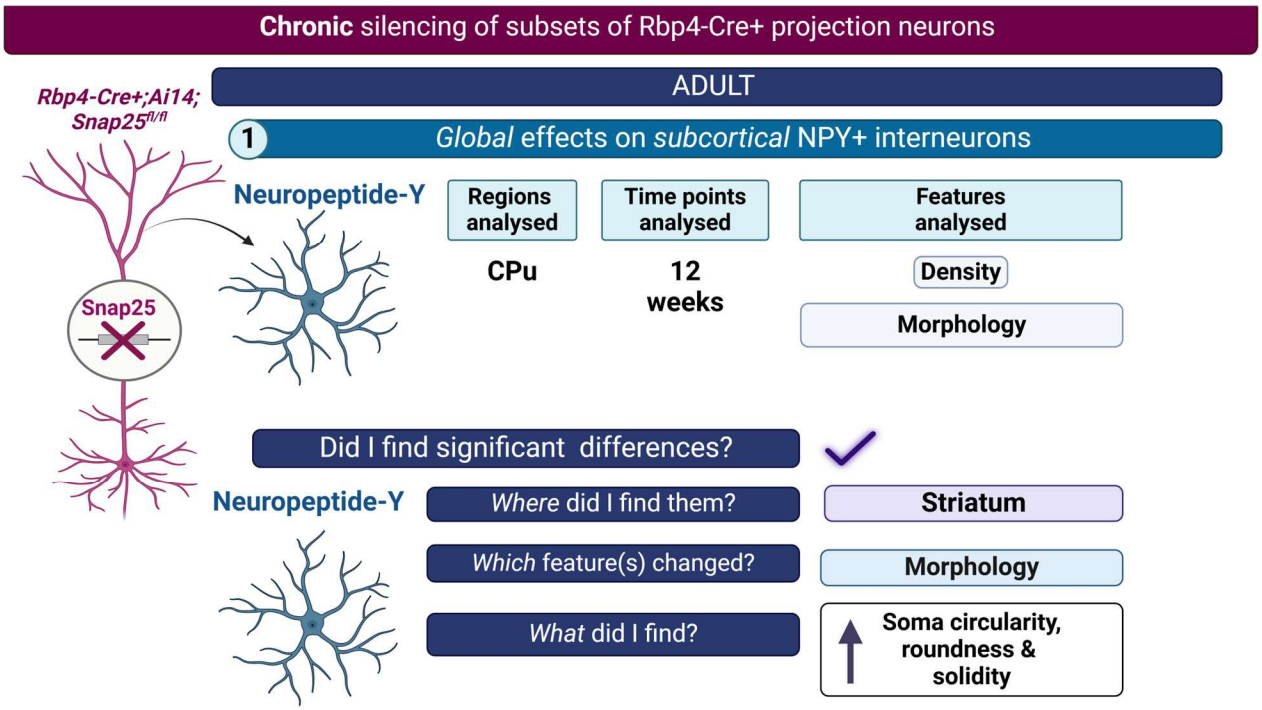
3.8. OVERVIEW OF RESULTS

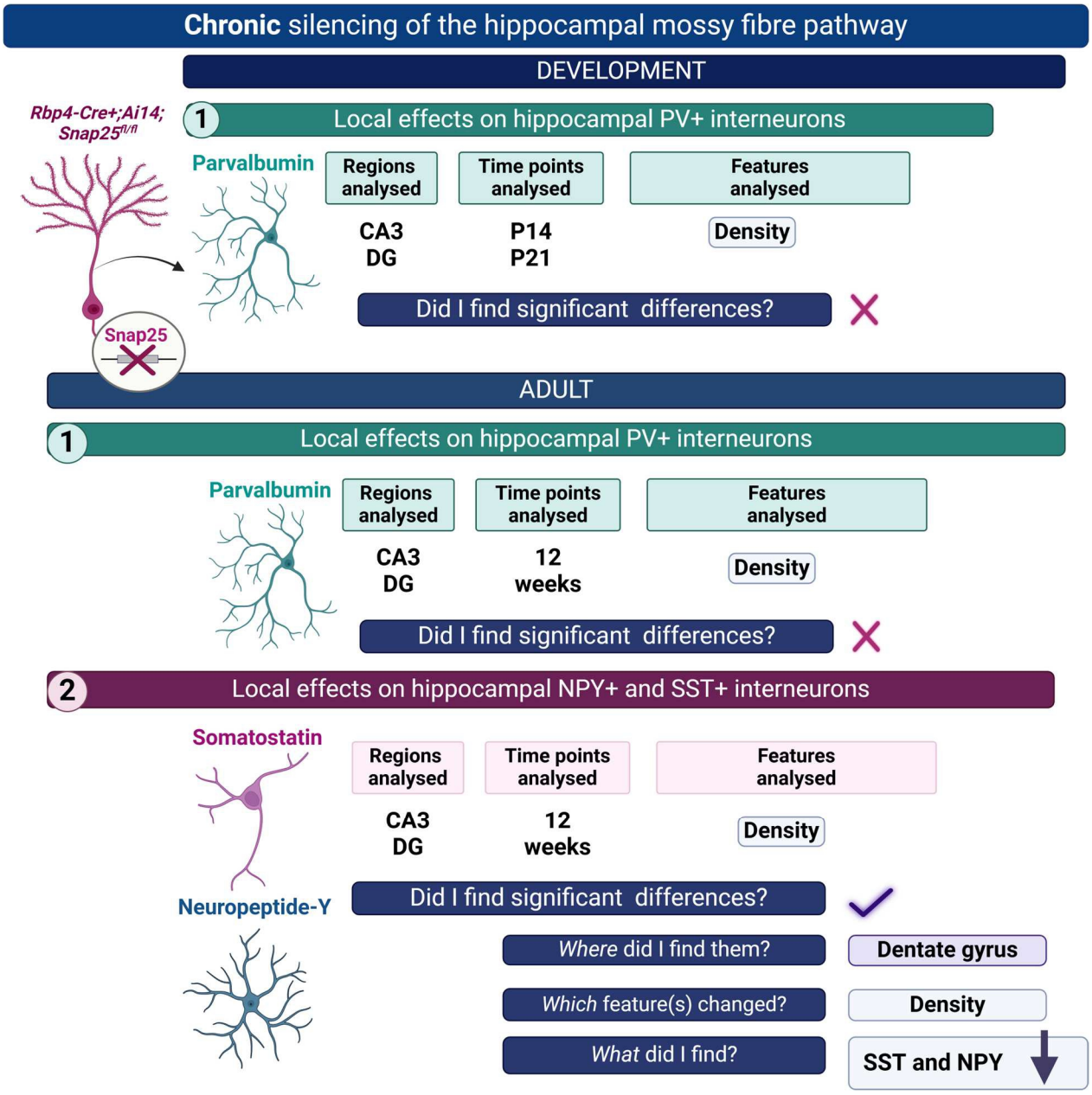



Chronic silencing of subsets of Rbp4-Cre+ projection neurons
Rbp4-Cre+;Ai14; Snap25fl/fl
ADULT
1
Local effects on cortical PV+ interneurons
Parvalbumin
Snap25
Regions analysed
Time points analysed
Features analysed
M1
S1
12 weeks
Density
Laminar distribution
Developmental trajectory
Did I find significant differences?
Where did I find them?
M1 and S1
Which feature changed?
Laminar distribution
What did I find?
S1 -> Layer 4: PV+ and PV+ VVA+
M1 -> Layer 5: PV+ VVA-
Rbp4-Cre+;Ai14; Snap25fl/fl
2
Global effects on subcortical PV+ interneurons
Parvalbumin
Snap25
Regions analysed
Time points analysed
Features analysed
CPu
GPe
MD
LP
TRN
SC
12 weeks
Density
Developmental trajectory
Soma morphology
Did I find significant differences?
No differences


Chronic silencing of subsets of Rbp4-Cre+ projection neurons
Rbp4-Cre+;Ai14; Snap25fl/fl
ADULT
1
Local effects on the perineuronal nets (VVA)
Perineuronal nets
Snap25
Regions analysed
Time points analysed
Features analysed
M1
S1
12 weeks
Density
Laminar distribution
Did I find significant differences?
Where did I find them?
M1
Which feature(s) changed?
Density
Laminar distribution
What did I find?
VVA+
Density
PV- VVA+
Density
M1 -> Layer 5: PV- VVA+
Laminar distribution


Chronic silencing of subsets of Rbp4-Cre+ projection neurons
Rbp4-Cre+;Ai14; Snap25fl/fl
ADULT
1
Local effects on cortical NPY+ interneurons
Neuropeptide-Y
Regions analysed
Time points analysed
Features analysed
ACA
M2
M1
S1
12 weeks
Density
Laminar distribution
Morphology
Snap25
Did I find significant differences?
Neuropeptide-Y
Where did I find them?
ACA, M2, M1, S1
Which feature(s) changed?
Density
Laminar distribution
Morphology
What did I find?
M2
Density
M1
Density
Which layers were affected?
M1
Layer 1 & Layer 2/3
Where did morphology change?
ACA
Soma area & perimeter
M2
Soma circularity, roundness, solidity
S1
Soma area, perimeter, circularity, roundness


Chronic silencing of subsets of Rbp4-Cre+ projection neurons
Rbp4-Cre+;Ai14; Snap25fl/fl
ADULT
1
Global effects on subcortical NPY+ interneurons
Neuropeptide-Y
Regions analysed
Time points analysed
Features analysed
CPu
12 weeks
Density
Morphology
Snap25
Did I find significant differences?
Neuropeptide-Y
Where did I find them?
Striatum
Which feature(s) changed?
Morphology
What did I find?
Soma circularity, roundness & solidity


Chronic silencing of the hippocampal mossy fibre pathway
DEVELOPMENT
Rbp4-Cre+;Ai14; Snap25fl/fl
1
Local effects on hippocampal PV+ interneurons
Parvalbumin
Regions analysed
Time points analysed
Features analysed
CA3
DG
P14
P21
Density
Did I find significant differences?
Snap25
ADULT
1
Local effects on hippocampal PV+ interneurons
Parvalbumin
Regions analysed
Time points analysed
Features analysed
CA3
DG
12 weeks
Density
Did I find significant differences?
2
Local effects on hippocampal NPY+ and SST+ interneurons
Somatostatin
Regions analysed
Time points analysed
Features analysed
CA3
DG
12 weeks
Density
Neuropeptide-Y
Did I find significant differences?
Where did I find them?
Dentate gyrus
Which feature(s) changed?
Density
What did I find?
SST and NPY

3.9. Summary

In this chapter, I have presented the findings regarding the chronic abolition of AP-dependent neurotransmitter release from glutamatergic layer 5 projection neurons on distinct subtypes of GABAergic interneurons. I have investigated the short-and long-term effects of silencing layer 5 on cortical and subcortical PV+ neurons at different ages. I have also discussed the chronic manipulation of the mossy fibre pathway and its effects on local PV+, NPY+, and SST+ interneurons.

In Chapter 4, I will explore the effects of chronically silencing a different subtype of deep-layer projection neurons in layer 6 of the cortex. These are the excitatory Drd1a-Cre+ corticothalamic pyramidal neurons that selectively innervate the higher-order thalamic nuclei (Hoerder-Suabedissen et al. 2018). Together with layer 5 projection neurons, layer 6 projection neurons are the main output neurons of the cerebral cortex and are ideally situated to influence GABAergic neurons, both inside and outside the neocortex.

Chapter 4 ..... Results

Chronic silencing of a subgroup of glutamatergic layer 6 cortical projection neurons

4.1. Introduction

In the previous chapter, I demonstrated that genetic silencing of Rbp4-Cre+ projection neurons affected the laminar organisation of GABAergic interneurons and the perineuronal nets after development. These results prompted enquiries into whether the observed modifications in the laminar positioning of PV+ and NPY+ interneurons were specific to layer 5, and whether long-term silencing of a different subtype of cortical projection neurons resulted in a comparable rearrangement of interneuron cell distribution.

4.2. Aims and Objectives

In this chapter, I will investigate the role of a restricted subset of glutamatergic cortical layer 6 projection neurons in instructing the development and distribution of GABAergic neurons. In particular, I will examine

1) whether the conditional deletion of *Snap25* from Drd1a-Cre+ neurons interferes with the development and maturation of the GABAergic neurons
2) whether the loss of AP-dependent neurotransmitter release from Drd1a-Cre+ layer 6 neurons alters the density, distribution, or morphology of GABAergic neurons
3) short- and long-term effects of genetically silencing a subset of layer 6 pyramidal neurons on distinct subtypes of GABAergic neurons

4) whether silencing excitatory projection neurons in cortical *layer 6* vs *layer 5* has differing effects on inhibitory neurons

5) The distribution of ionotropic GABA-$_A$ and metabotropic GABA-$_B$ receptors to explore changes in GABAergic transmission in the juvenile neocortex

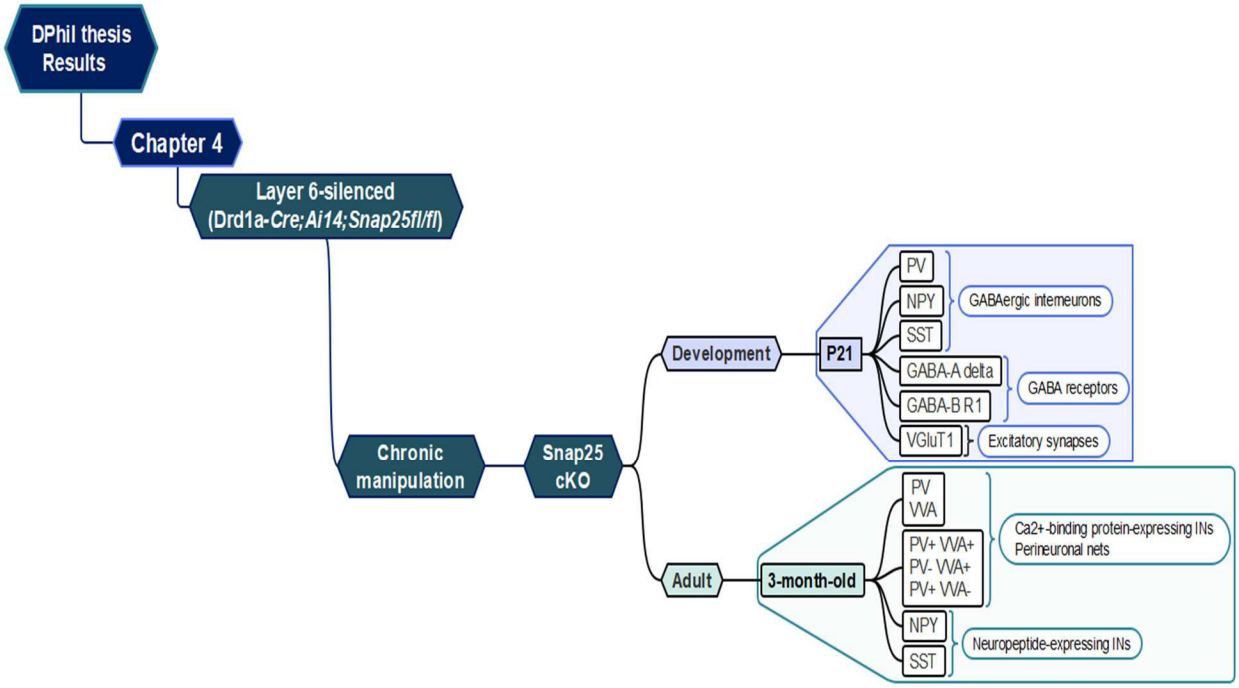


Figure 4.1. Schematic drawing showing the structure of Chapter 4. The diagram serves to illustrate how the chapter is organised and gives an overview of the various subtypes of GABAergic neurons examined during *development* (postnatal day 21) and *adulthood* (3 months of age). The main research theme of each section is indicated in parentheses (e.g., GABA receptors for the GABA-$_A$ δ and GABA-$_B$ R1 results examined at P21 in the *Drd1a-Cre;Ai14;Snap25$^{fl/fl}$* mice).

4.3. The effects of chronically silencing a subset of layer 6 projection neurons on GABAergic neurons in the juvenile brain

4.3.1. Targeting layer 6b neurons (Drd1a-Cre lines)

When considering the different BAC-Cre-driver lines that target the D1 receptor, specifically the Drd1_EY217, Drd1_EY262, Drd1_FK150, and Drd1_FK164 founder lines, there is significant variability in the recombination patterns of the inserted transgenes, as well as in the types of cells and the specific neuronal projection pathways that are labelled. For example, the *Tg(Drd1-cre)FK150Gsat/Mmucd* strain (Founder Line FK150) exhibits Cre expression that aligns with the endogenous Drd1a expression, particularly labelling cortical pyramidal neurons in layer 6 of the cerebral cortex. However, it also inadvertently labels a substantial number of layer 5 cell populations (Gerfen et al. 2013). Consequently, this strain is more commonly utilised to trace direct striatonigral projection pathways rather than layer-specific corticothalamic projection systems (Gong et al. 2007; Gerfen et al. 2013). Therefore, the *Tg(Drd1a-cre)FK164Gsat/Mmucd* (Founder Line FK164) was selected to selectively manipulate layer 6b projection neurons throughout the thesis since it has been well-characterised and labels a subpopulation of neurons targeting the higher-order thalamic nuclei (Hoerder-Suabedissen et al. 2018; Viswanathan et al. 2017; Killackey and Sherman 2003). Given that layer 6a neurons do not innervate the higher-order thalamic nuclei but target the first-order thalamic nuclei (Zhang and Deschênes 1997; Chevée et al. 2018; Ansorge et al. 2020), it can be posited that the Cre+ neurons identified outside of layer 6b in my samples are more accurately categorised as layer 6b neurons, both functionally and anatomically, rather than layer 6a.

Regarding the Cre recombinase pattern of expression in the Drd1a-Cre+ line, it is primarily restricted to layer 6b neurons within the cerebral cortex https://www.gensat.org/cre.jsp;jsessionid=7C1E87166E67E838C6F8CCB2F78DCE3C. Higher numbers of Drd1a-Cre+ neurons are seen in the frontal, motor, and anterior somatosensory regions, while lower numbers are found in the visual and posterior parietal association areas. For examining

Cre expression and the distribution of Drd1a-Cre+ neurons in the Tg *(Drd1a-cre)FK164Gsat/Mmucd* (Founder Line FK164) line, please refer to the GENSAT Gene Expression Nervous Atlas System https://www.gensat.org/cre.jsp;jsessionid=7C1E87166E67E838C6F8CCB2F78DCE3C.

4.3.2. Selecting my regions of interest

When deciding on the cortical regions of interest (ROIs), various cortical regions may have been considered, from the anterior prefrontal cortex to the posterior visual areas. However, I aimed to investigate two morphologically and functionally distinct cortical regions where there was a high percentage of silenced Drd1a-Cre+ neurons. Thus, I kept the primary motor (M1) and the primary somatosensory cortices (S1) as my cortical ROIs (Figure 4.2. A1-A4) to be able to compare the effects of chronically silencing a subpopulation of *layer 5* versus a subpopulation of *layer 6* projection neurons on GABAergic neurons. To determine whether silencing Drd1a-Cre+ neurons in *association* vs *sensory* cortical areas had a different impact on GABAergic neurons, I chose to investigate the anterior cingulate areas (ACA) of the prefrontal cortex (PFC) in addition to M1 and S1 (Figure 4.2. A5-A8). The high abundance of interneurons and perineuronal nets in these cortical areas also justified the selection of these regions (Figure 4.2. A2, A3, A6, A7).

To locate the regions where corticothalamic projection neurons of neocortical layer 6 may exert an influence on the number and distribution of GABAergic interneurons, I mapped the axonal projections of Drd1a-Cre+ neurons in the *Snap25*-cKO mice. Upon leaving the cortex, the Drd1a-Cre+ axons travel through the striatum and the internal capsule (ic) before reaching the thalamus, as previously described in normal controls (Hoerder-Suabedissen et al. 2018). Despite having less dense innervation than the thalamus, the external section of the globus pallidus (GPe) that borders the striatum also displayed the presence of tdTomato+ fibres (Figure 4.2. B1, B5, B9). The striatum and the GPe were retained as *subcortical* ROIs in the layer 6-silenced mice due to the abundance of inhibitory neurons in these regions, especially those expressing parvalbumin (Figure 4.2. B2, B6, B10). These PV-rich subcortical areas showed strong PNN labelling. (Figure 4.2. B3, B7, B11). The presence

of PV+ neurons adjacent to the red fibres of the silenced Drd1a-Cre+ neurons can be seen in the striatum, the GPe, and the thalamic reticular nucleus (TRN) (Figure 4.2. B4, B8, B12).

The reason for mapping the axonal projections of Drd1a-Cre+ neurons in the *Drd1a-Cre+;Ai14;Snap25*$^{fl/fl}$ mice was that the control mice (*Drd1a-Cre-;Ai14;Snap25*$^{fl/fl}$) used throughout my DPhil research were Cre-negative animals, hence there is no tdTomato fluorescence following Cre recombination. Thus, it was not feasible to map the axonal projections of Drd1a-Cre+ neurons using control animals, as they lacked the red fluorescence signal and the tdTomato-labelled Drd1a-Cre+ neurons. Considering that the *Drd1a-Cre;Ai14;Snap25*$^{fl/fl}$ transgenic mice were bred on a double homozygous background for the *Snap25* and *Ai14* alleles, no conditional heterozygous mice were generated that could have been used as control animals with tdTomato expression. The *Drd1a-Cre;Ai14* reporter line could have been used as a suitable control; however, breeding issues precluded the collection of brains for these experiments.

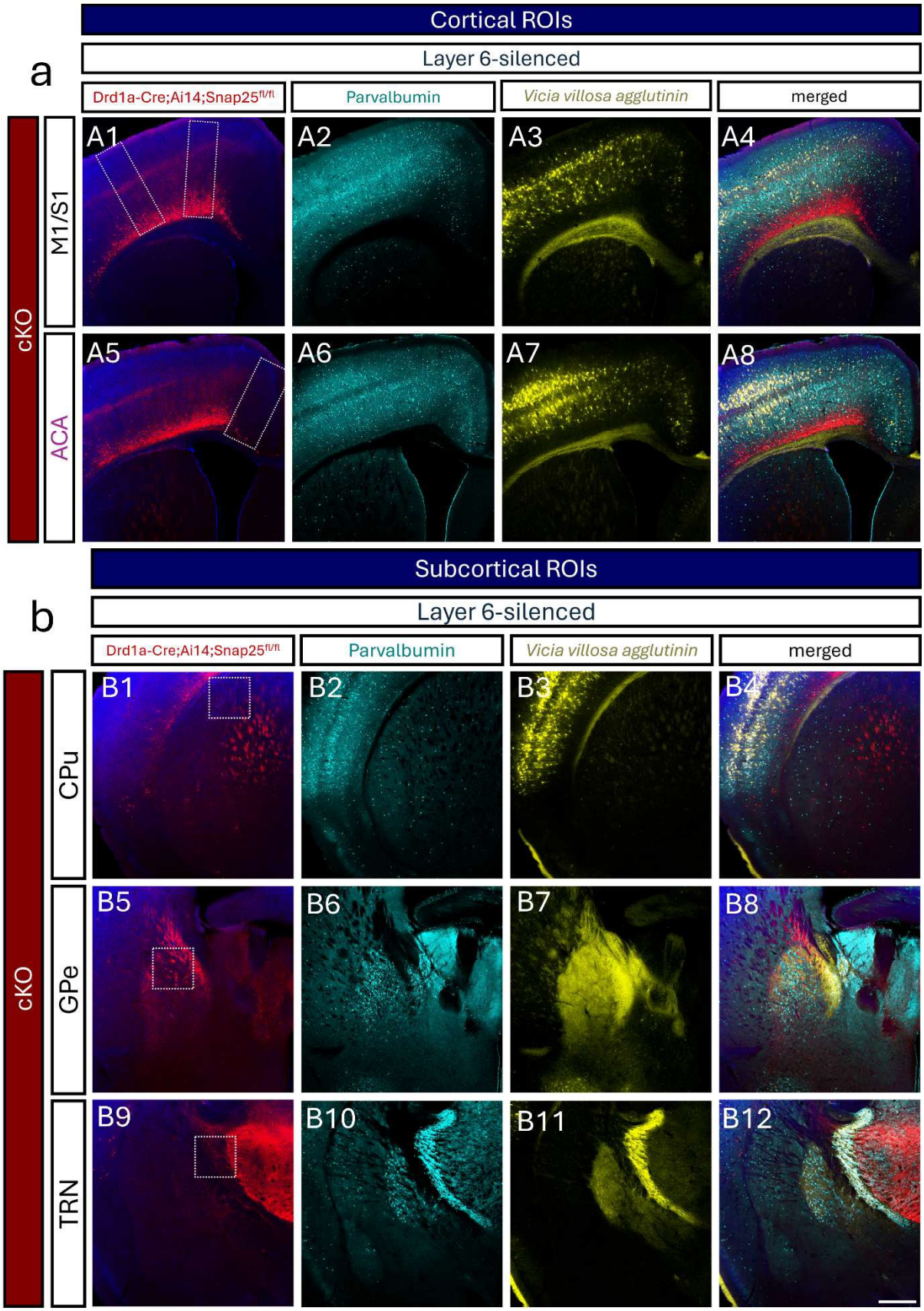

Cortical ROIs
a
Layer 6-silenced
Drd1a-Cre;Ai14;Snap25fl/fl
Parvalbumin
Vicia villosa agglutinin
merged
cKO
M1/S1
ACA
A1
A2
A3
A4
A5
A6
A7
A8
Subcortical ROIs
b
Layer 6-silenced
Drd1a-Cre;Ai14;Snap25fl/fl
Parvalbumin
Vicia villosa agglutinin
merged
cKO
CPu
GPe
TRN
B1
B2
B3
B4
B5
B6
B7
B8
B9
B10
B11
B12

Figure 4.2. a. Selected *cortical* regions of interest in *Drd1a-Cre;Ai14;Snap25*$^{fl/fl}$ mice. (A1) Confocal image representing the silenced subset of *Drd1a-Cre;Ai14;Snap25*$^{fl/fl}$ neurons (red) in the primary motor and somatosensory cortices in the cKO mice. (A2) Parvalbumin-immunoreactive neurons are seen in cyan and (A3) their perineuronal nets in yellow in the cKO mice. (A4) Merged image showing parvalbumin neurons and the perineuronal nets superimposed on the silenced layer 6 projection neurons in M1 and S1. (A5) Confocal image illustrating *Drd1a-Cre;Ai14;Snap25*$^{fl/fl}$ neurons in the ACA. (A6) Parvalbumin-immunoreactive neurons and (A7) their perineuronal nets in the ACA in the *Snap25* cKO mice. (A8) Merged image showing all four channels (DAPI, *Drd1-Cre;Snap25*$^{fl/fl}$, PV, PNNs).

Figure 4.2. b. Selected *subcortical* regions of interest in *Drd1a-Cre;Ai14;Snap25*$^{fl/fl}$ mice. Confocal image depicting the long-range projections of Drd1a-Cre+ neurons in the *Snap25* cKO mice traversing through the caudoputamen (B1), the GPe (B5), and the TRN (B9). Parvalbumin-immunopositive neurons and their perineuronal nets in the caudoputamen (B2, B3), the GPe (B6, B7), and the TRN (B10, B11). Overlay confocal images representing the presence of parvalbumin neurons and perineuronal nets near the axon terminals of the silenced layer 6 pyramidal neurons (B4, B8, B12). Scale bar = 200 µm.

Previous studies have revealed that Drd1a-Cre+ neurons densely and selectively innervate the higher-order thalamic nuclei and avoid the first-order nuclei (Hoerder-Suabedissen et al. 2018; Viswanathan et al. 2017). Despite the dense innervation of the lateral dorsal (LD), ventral anterior lateral (VAL), ventral medial (VM)(Figure 4.3. C1, C1', C4, C4') and posterior nucleus of the thalamus (PO), none of the previously described regions was selected as *subcortical* ROIs due to the scarcity of GABAergic interneurons and PNNs in the thalamus (Figure 4.3. C2, C2', C3, C3'). Considering that *Rbp4-Cre;Snap25*$^{fl/fl}$ neurons target the same higher-order nuclei as the *Drd1a-Cre;Snap25*$^{fl/fl}$ neurons via their long-range projections, the effect of chronically manipulating a subset of *layer 5* versus *layer 6* projection neurons on thalamic PV+ interneurons is not expected to differ considerably. The lack of effect of silencing layer 5 projection neurons on PV neurons in the LP and MD nuclei provided additional rationale for not retaining the higher-order thalamic nuclei as *subcortical* ROIs in the layer 6-silenced mice (please refer to Chapter 3). Figure 4.3. d compares the cortical and subcortical ROIs directly in *layer 5* and *layer 6-silenced* animals. Please refer to Figure 4.3. e for the ROIs selected for investigating PV and NPY interneurons in the *Rbp4-Cre;Snap25*$^{fl/fl}$ and *Drd1a-Cre;Snap25*$^{fl/fl}$ mice, respectively.

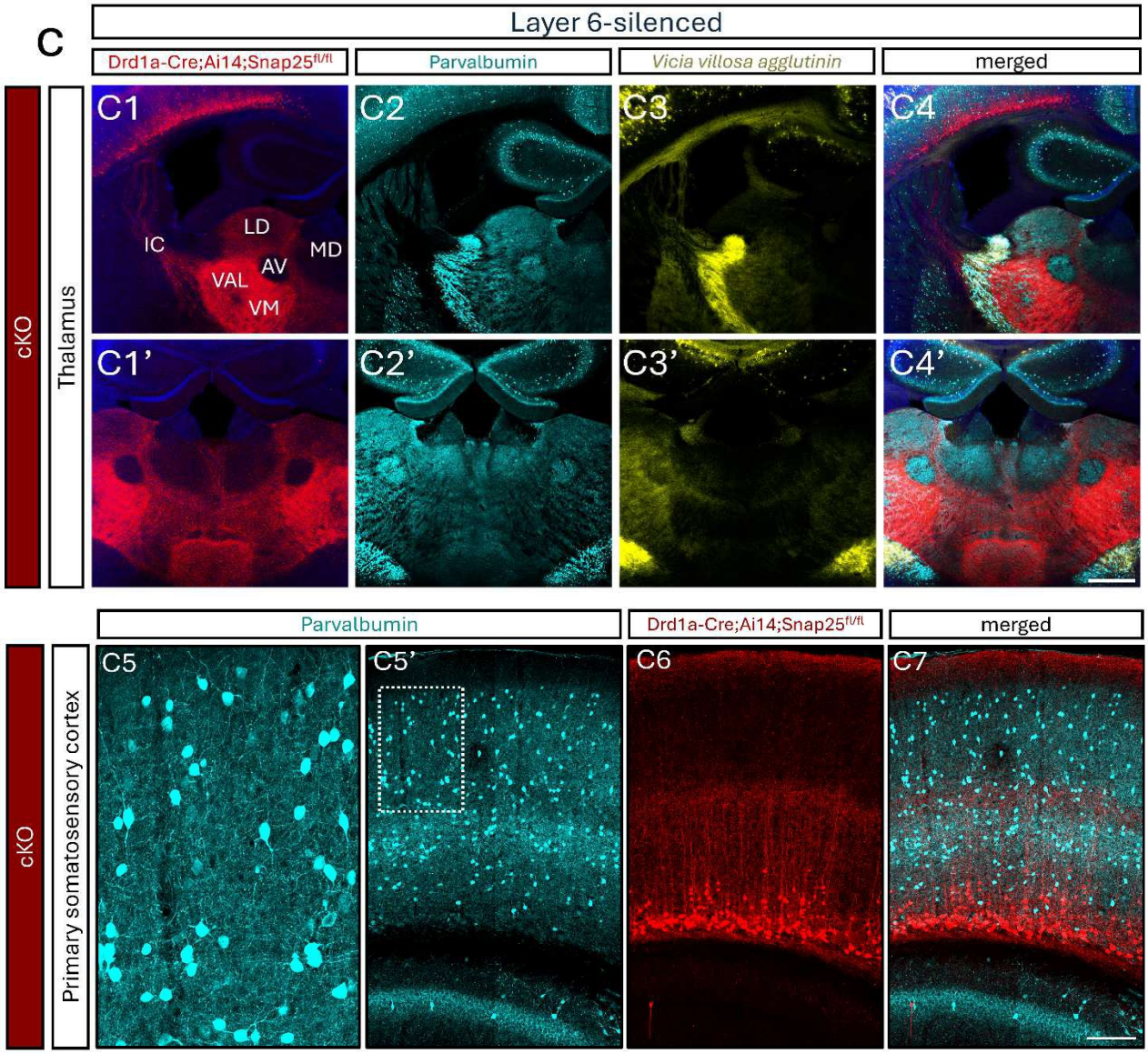


Figure 4.3. c. The selective innervation of the higher-order thalamic nuclei is retained in the Drd1a-Cre-silenced mice. *Snap25*-deficient subgroup of layer 6 corticothalamic neurons retained the selective targeting of the higher-order nuclei in the thalamus. Note the dense innervation of the ventral anterior lateral (VAL) and the ventral medial nucleus (VM) of the thalamus, as well as the absence of the red fibres in the first-order anterior ventral nucleus (AV) in the silenced layer 6-mice (C1, C1'). Parvalbumin-immunopositive neurons and perineuronal nets are highly abundant in the thalamic reticular nucleus but virtually absent from the higher-order nuclei (C2, C2', C3, C3'). Confocal images depicting the absence of overlap between the distribution of parvalbumin interneurons and the terminals of *Drd1a-Cre;Snap25*$^{fl/fl}$ neurons (C4, C4'). Zoom-in and high-magnification maximum-projected z-stack images of PV-immunoreactive neurons in cyan and Snap25-deleted Drd1a-Cre+ neurons in red. Scale bar = 200 µm. IC: internal capsule, LD: lateral dorsal nucleus, MD: mediodorsal nucleus, VAL: ventral anterior lateral nucleus, VM: ventral medial nucleus, AV: anterior ventral nucleus.

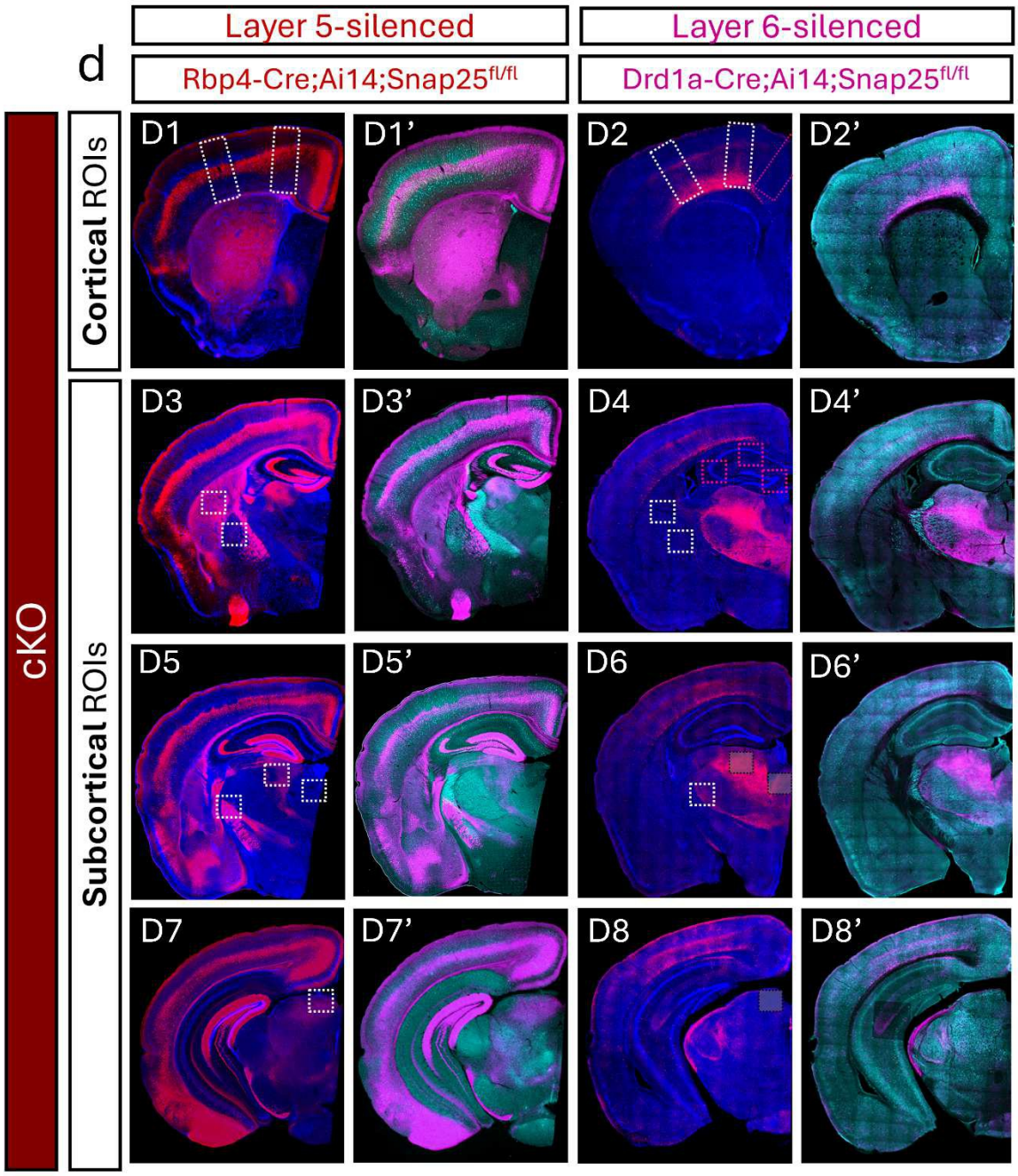


Figure 4.3. d. Comparisons of the chosen cortical and subcortical regions of interest between layer 5 and layer 6-silenced mice. Low-power epifluorescence micrographs showing hemisections of the *Snap25* cKO brains in rostro-caudal order, where subsets of *layer 5* or *layer 6* projection neurons were selectively silenced. Silenced populations of *Rbp4-Cre;Snap25*$^{fl/fl}$ (D1) and *Drd1a-Cre;Snap25*$^{fl/fl}$ (D2) projection neurons in the primary motor and somatosensory cortices. Cortical areas of interest (ROIs) that were the same in layer 5 and layer 6 silenced mice are shown by white dotted rectangles. Boxes in magenta represent new cortical ROIs in layer 6-silenced mice. Parvalbumin interneurons surround *Rbp4-Cre;Snap25*$^{fl/fl}$ (D1') and *Drd1a-Cre;Snap25*$^{fl/fl}$ (D2') projection neurons in anterior cortical areas, as seen in merged green and red channel images. *Rbp4-Cre;Snap25*$^{fl/fl}$ corticofugal neurons have long-range projections to various subcortical regions, of which the caudoputamen (D3), the GPe (D3), the TRN (D5), the higher-order thalamic nuclei (D5), and the superior colliculus (D7)

were selected as my *subcortical* ROIs. Axon terminals of *Drd1a-Cre;Snap25*$^{fl/fl}$ corticothalamic pyramidal neurons pass through the caudoputamen (D4), the GPe (D4), and the TRN (D6). The lateral posterior and mediodorsal nuclei that were examined in the layer 5-silenced mice were no longer analysed in the layer 6-silenced mice due to the sparse number of interneurons in the thalamus (D3, D3', D4, D6'). ROIs that have been discarded in *Drd1a-Cre;Ai14;Snap25*$^{fl/fl}$ mice are highlighted with grey boxes. Descending projections of *Rbp4-Cre;Snap25*$^{fl/fl}$ target the superior colliculus (D7), where they intersect parvalbumin interneurons (D7'). The superior colliculus receives innervation from *Drd1a-Cre;Snap25*$^{fl/fl}$ projection neurons as well (D8), but this region was not retained in the layer 6-silenced mice. Merged confocal image illustrating the distribution of parvalbumin interneurons and the long-range projections of *Drd1a-Cre;Ai14;Snap25*$^{fl/fl}$ neurons in the midbrain (D8').

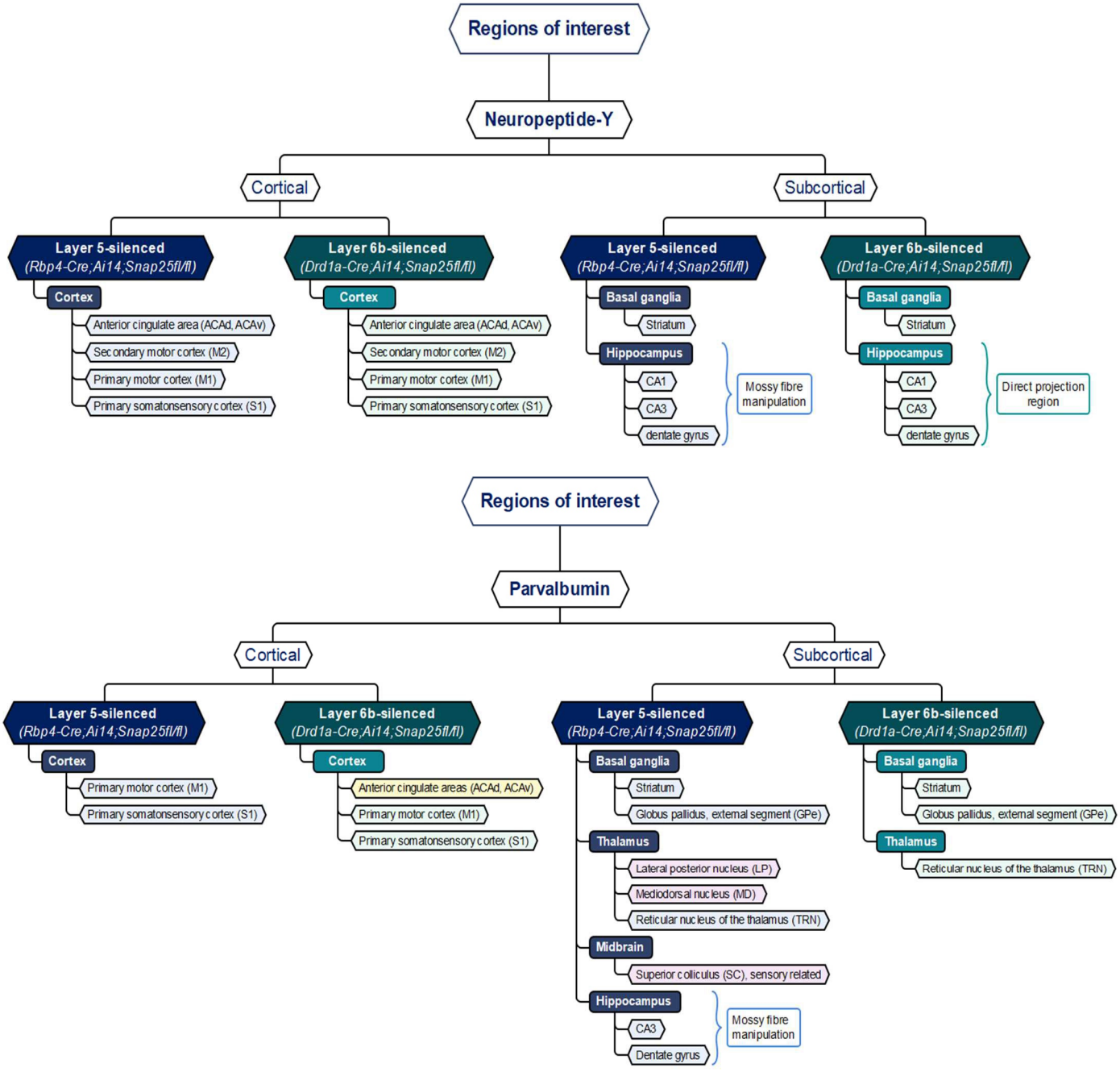


Figure 4.3. e. Overview of the cortical and subcortical regions of interest selected in layer 5 and layer 6-silenced mice. Upper schematic illustrating the cortical and subcortical ROIs chosen in layer 5 and layer 6-silenced mice for the investigation of parvalbumin interneurons. Lower schematic illustrating the cortical and subcortical ROIs selected in layer 5 and layer 6-silenced mice for the investigation of neuropeptide-Y interneurons. Regions were colour-coded to distinguish between original and new ROIs. Light blue represents layer 5 ROIs, while light green represents layer 6 ROIs. New ROIs are indicated in yellow, while aborted ROIs are highlighted in magenta in the Drd1a-Cre-silenced mice. Note that all hippocampal ROIs in the *Rbp4-Cre;Ai14;Snap25*$^{fl/fl}$ animals were chosen to investigate the effects of the chronic silencing of the mossy fibre pathway rather than being direct projection sites of layer 5 cortical neurons. In contrast to the *Rbp4-Cre;Ai14;Snap25*$^{fl/fl}$ mice, the hippocampal regions in the *Drd1a-Cre;Ai14;Snap25*$^{fl/fl}$ mice were selected as direct projection regions to examine the effects of the chronic silencing of layer 6 neurons on interneurons.

4.3.3. Drd1a-Cre+ tdTomato+ fibres are present in the stratum lacunosum-moleculare of CA1, CA2, and CA3

Contrary to *Rbp4-Cre;Ai14;Snap25*$^{fl/fl}$ mice, *Drd1a-Cre;Ai14;Snap25*$^{fl/fl}$ mice lack Cre expression in the hippocampus, making them suitable for interrogating the effects of genetically silencing layer 6 neurons on hippocampal interneurons. Previous research has revealed that layer 6b neurons in the adult murine entorhinal cortex monosynaptically connect the principal neurons in the hippocampus and innervate all subregions of the hippocampal formation (Ben-Simon et al. 2022). This has shed light on a previously unidentified layer 6b cortico-hippocampal pathway implicated in spatial coding and memory formation. Another notable finding was that the subpopulation of layer 6b neurons in the entorhinal cortex that projects to the hippocampal formation appears to be a remnant of the subplate, which survived into adulthood (Ben-Simon et al. 2022). While these hippocampal-projecting layer 6b cells were positive for the Connective Tissue Growth Factor (CTGF), Drd1a-Cre;tdTomato+ neurons in layer 6b co-localise with CTGF-expressing cells. In particular, 34% of Drd1a-Cre;tdTomato+ neurons express CTGF in the primary somatosensory cortex at P8 (Hoerder-Suabedissen et al. 2018). Considering that around one-third of Drd1a-Cre+ neurons in layer 6b overlap with CTGF+ neurons, chronic manipulation of Drd1a-Cre+ neurons and their axon terminals might lead to similar alterations in the hippocampal and parahippocampal networks.

To investigate whether tdTomato+ fibres were present in the hippocampal regions in the *Drd1a-Cre;Ai14;Snap25*$^{fl/fl}$ mice, I examined the distribution of their axonal projections. Although the higher-order thalamic nuclei receive the densest innervation of all subcortical regions, tdTomato+ fibres were visible in the CA3 in the layer 6-silenced mice (Figure 4.4. a) Since the image acquisition parameters were set to the tdTomato+ fibres in the thalamus, the presence of axon terminals in the CA3 is not readily apparent because of the extremely intense red fluorescence signal in the higher-order nuclei. However, careful investigation of the hippocampal regions revealed that the stratum lacunosum-moleculare (s.l.m.) of CA1, CA2, and CA3 contained red fibres of *Drd1a-Cre;Snap25*$^{fl/fl}$ neurons (Figure 4.4. b). Cre-expressing tdTomato+ pyramidal neurons were also detected in the stratum pyramidale (s.p.) of CA1, specifically in posterior sections which were selected at the level of the primary visual cortex (V1) and posterior parietal association regions (PTL) in the adult *Drd1a-Cre;Ai14;Snap25*$^{fl/fl}$ mice (Figure 4.4. c). A noncanonical circuit motif in the hippocampus has been shown by recent studies, wherein the subiculum and the ventral CA1 send back projections to the excitatory neurons in CA1 and CA3 (Xu et al. 2016). Additionally, it was shown that the subiculum and the ventral CA1 provide monosynaptic, noncanonical inputs to CA3 inhibitory neurons (Lin et al. 2023).

While the Drd1a-Cre transgenic strain predominantly labels cortical layer 6b neurons, it has to be acknowledged that a small number of Drd1a-Cre+ neurons can also be detected outside of the neocortex, mainly in the dorsal striatum, the CA1, the anterior pretectal nucleus, and the superior colliculus (Hoerder-Suabedissen et al. 2018). The presence of Drd1a-Cre+ neurons outside the cortex raises the possibility that subcortical Drd1a-Cre+ neurons may contribute to any observed effects after the deletion of *Snap25*. However, since these neurons are very sparse in number, it is unlikely that they would have a significant impact on the cells being studied.

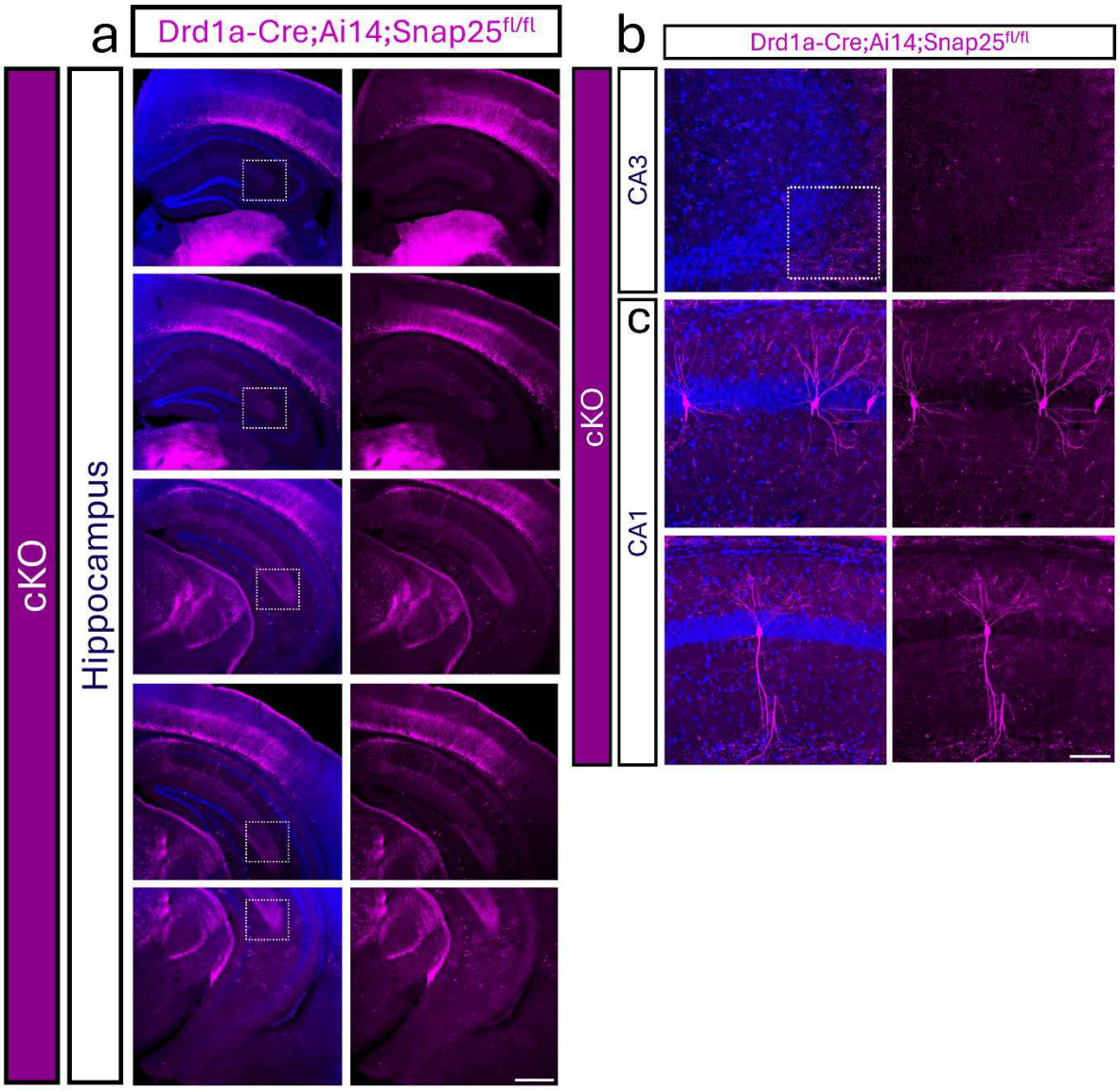


Figure 4.4. tdTomato+ fibres are present in the stratum lacunosum-moleculare of CA1, CA2, and CA3 in the *Drd1a-Cre;Ai14;Snap25$^{fl/fl}$* mice. (a) Confocal images illustrating the projections of silenced layer 6 neurons at 12 weeks of age in the hippocampus. Hemisections are presented in rostrocaudal order. (b) Maximum-intensity z-stacks showing the presence of tdTomato+ terminals of *Drd1a-Cre;Snap25$^{fl/fl}$* neurons in the stratum lacunosum-moleculare of CA1, CA2, and CA3. (c) tdTomato-positive Cre-expressing pyramidal neurons in the stratum pyramidale of CA1 in the adult *Drd1a-Cre;Ai14;Snap25$^{fl/fl}$* mice. Scale bars = 200 μm (a), 100 μm (c).

4.3.4. *Drd1a-Cre;Ai14;Snap25*$^{fl/fl}$ neurons form excitatory synapses in subregions of the basal ganglia and the thalamic reticular nucleus

The presence of tdTomato+ fibres in the striatum, GPe, and TRN prompted the question of whether *Drd1a-Cre;Ai14;Snap25*$^{fl/fl}$ neurons formed synapses in the selected subcortical regions. Given that the primary targets of the descending projections of layer 6b are the higher-order nuclei, it is conceivable that these terminals do not branch in these regions and only pass through subregions of the basal ganglia and the TRN *en route* to the thalamus. To ascertain whether *Drd1a-Cre;Ai14*;*Snap25*$^{fl/fl}$ neurons formed glutamatergic synapses in the selected subcortical ROIs, I performed immunohistochemical staining for the vesicular glutamate transporter, type 1 (VGluT1), which is the predominant isoform in the cerebral cortex as well as the hippocampus (Martineau et al. 2017).

I found that the axon terminals of *Drd1a-Cre;Ai14*;*Snap25*$^{fl/fl}$ neurons expressed VGluT1+ in all three subcortical regions; however, the degree of co-localisation between the terminals of *Drd1a-Cre;Ai14*;*Snap25*$^{fl/fl}$ neurons and the excitatory presynaptic marker varied greatly. The striatum showed the least degree of co-localisation at P21 (Figure 4.5.) as the presence of VGluT1+ synapses was only observed in a few fibre bundles of *Drd1a-Cre;Ai14*;*Snap25*$^{fl/fl}$ neurons (Figure 4.5. A1-A4, A1'-A4'). The TRN exhibited low to moderate co-localisation between the terminals of *Drd1a-Cre;Ai14*;*Snap25*$^{fl/fl}$ neurons and VGluT1+ (Figure 4.6. A1-A4, A1'-A4'). The presence of excitatory synapses in the TRN is an unanticipated finding due to the absence of axon collaterals of Drd1a-Cre+ neurons in this nucleus (Hoerder-Suabedissen et al. 2018). This implies the possibility of topographical variations within the TRN or the variable expression of VGluT1+ synapses by distinct subsets of layer 6 neurons. The existence of VGluT1+ synapses established by *Drd1a-*

Cre;Ai14;S*nap25*$^{fl/fl}$ neurons further justified TRN as a subcortical ROI to be explored, and it is the most densely populated subcortical nucleus with PV+ interneurons (Figure 4.6. A5, A5'). The highest degree of co-localisation was seen in the GPe, where a significant proportion of *Drd1a-Cre;Ai14*;S*nap25*$^{fl/fl}$ neurons had projections expressing VGluT1+ (Figure 4.7. A1-A4, A1'-A4', d). Many of these excitatory synapses were found to be near PV+ interneurons, raising the possibility of direct control of layer 6 over PV+ cells in the GPe (Figure 4.7. A5-A5'). Interestingly, the GPe contained more VGluT1+ synapses, albeit tdTomato+ fibres were more prevalent in the caudoputamen (Figure 4.8.). The scarcity of VGluT1+ synapses in the caudoputamen suggests that the genetic silencing of subsets of layer 6 neurons may not have a robust effect on GABAergic interneurons in the caudoputamen.

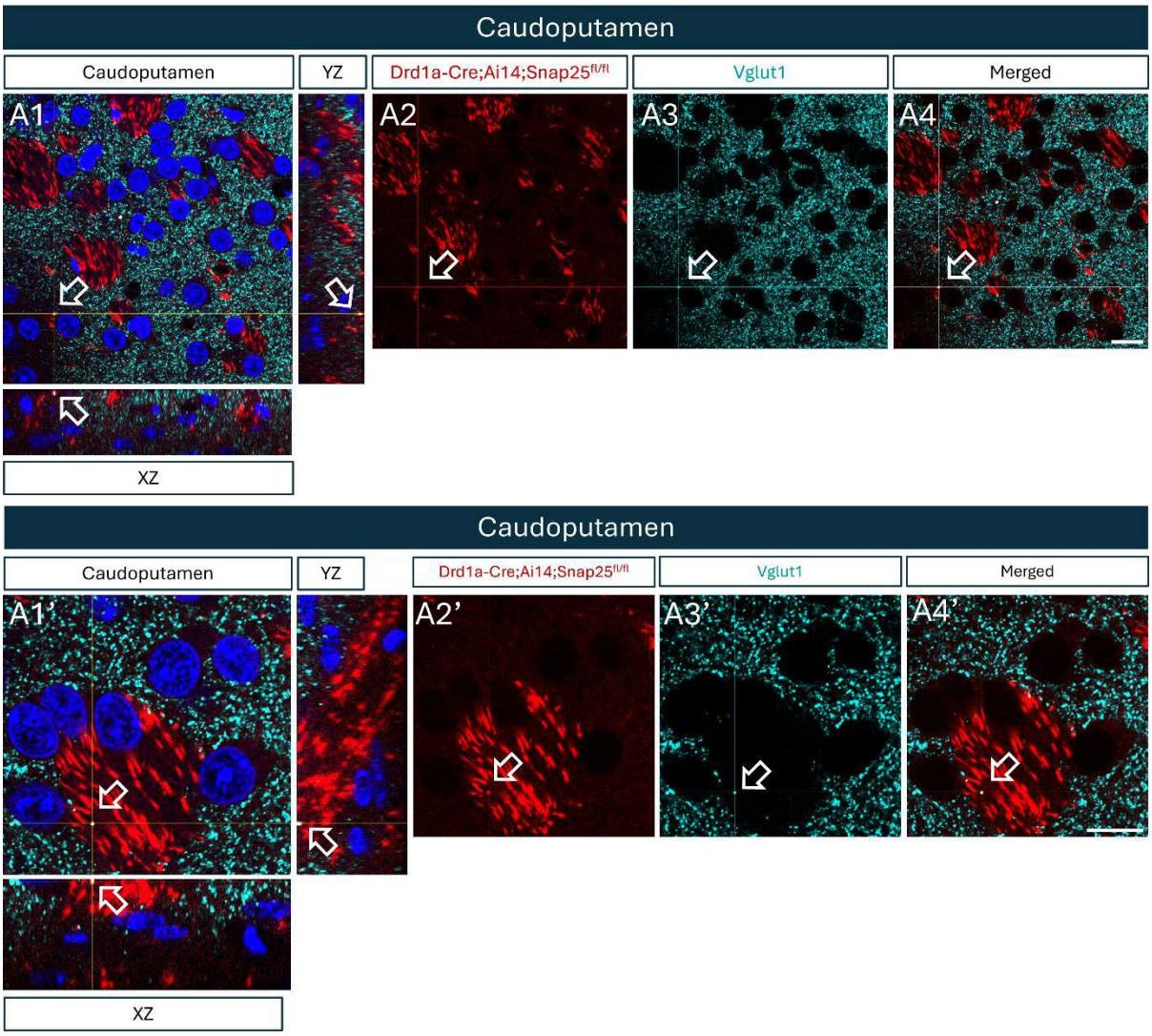


Figure 4.5. *Drd1a-Cre;Snap25$^{fl/fl}$* projection neurons form VGluT1-positive synapses in the caudoputamen. Single image of a confocal z-stack of the glutamatergic axon projections of *Drd1a-Cre;Snap25$^{fl/fl}$* neurons (red) and VGluT1+ punctae (cyan) along with DAPI counterstaining (blue) in the *Snap25* cKO brains (A1, A1'). Orthogonal projections of the confocal z-stack onto the YZ and XZ planes are placed around the image. Axon fibre bundles of *Drd1a-Cre;Ai14;Snap25$^{fl/fl}$* neurons in the caudoputamen at P21 (A2, A2'). VGluT1-expressing punctae labelling shows glutamatergic presynaptic transporter proteins in the caudoputamen (A3, A3'). Examples of VGluT+ tdTomato+ punctae at P21 in the *Drd1a-Cre;Ai14;Snap25$^{fl/fl}$* mice (A4, A4'). Scale bar = 20 µm (A4, A4').

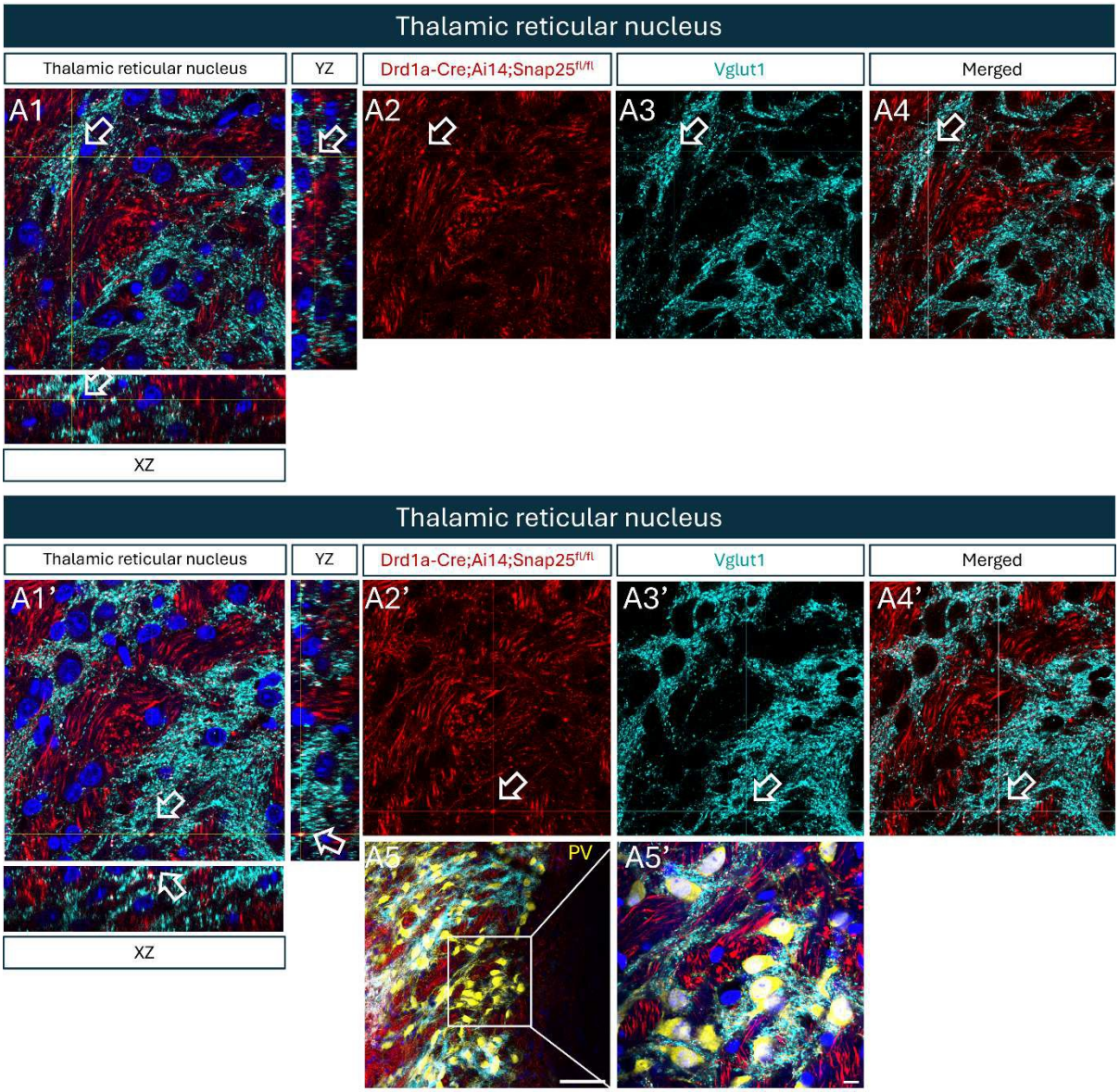


Figure 4.6. Thalamus-projecting *Drd1a-Cre;Ai14;Snap25$^{fl/fl}$* neurons make excitatory synapses in the thalamic reticular nucleus. Individual confocal z-stack image showing DAPI counterstaining, VGluT1+ labelling, and tdTomato+ fibres of *Drd1a-Cre;Snap25$^{fl/fl}$* cortical neurons in the *Snap25* cKO brains at P21 (A1, A1'). Encircling the picture are orthogonal views of the confocal z-stack image onto the YZ and XZ planes. Presence of glutamatergic projections of *Drd1a-Cre;Ai14;Snap25$^{fl/fl}$* neurons in the TRN in the *Snap25* cKO mice (A2, A2'). Intense VGluT1+ labelling in the TRN indicates the presence of excitatory presynaptic boutons (A3, A3'). Example of Drd1a-Cre+ tdTomato+ punctae co-localising with the presynaptic VGluT1+ marker (A4, A4'). Confocal merged image highlighting parvalbumin-immunoreactive neurons near the tdTomato+ fibres of *Drd1a-Cre;Ai14;Snap25$^{fl/fl}$* cortical neurons (A5, A5'). The white rectangle illustrates the imaging location. Scale bars = 50 µm (A5), 20 µm (A5').

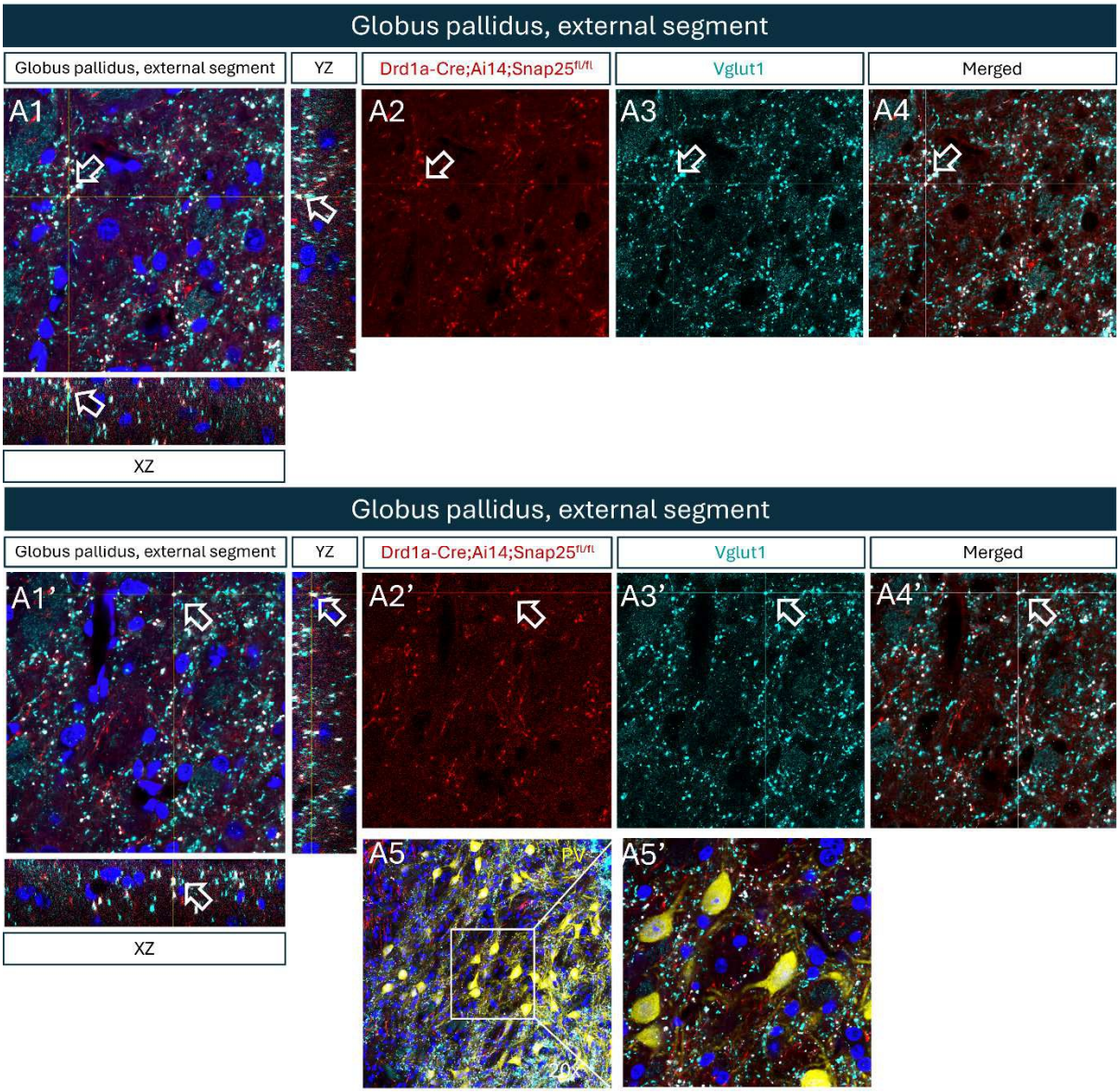


Figure 4.7. VGluT1-positive synapses are formed by *Drd1a-Cre;Ai14;Snap25$^{fl/fl}$* projection neurons in the external segment of the globus pallidus. Single image of a z-stack along with orthogonal projections of the z-stack illustrating tdTomato+ fibres and VGluT1+ labelling in the GPe at P21 (A1, A1'). tdTomato+ punctae and VGluT1+ glutamatergic synapses are visible in the layer 6-silenced mice at P21 in the GPe (A2, A2', A3, A3'). VGluT1-immunopositive synapses formed by *Drd1a-Cre;Ai14;Snap25$^{fl/fl}$* neurons (A4, A4'). Parvalbumin-immunoreactive neurons close to the tdTomato+ fibres of *Drd1a-Cre;Snap25$^{fl/fl}$* cortical neurons (A5, A5'). The imaging site is shown by the white rectangle.

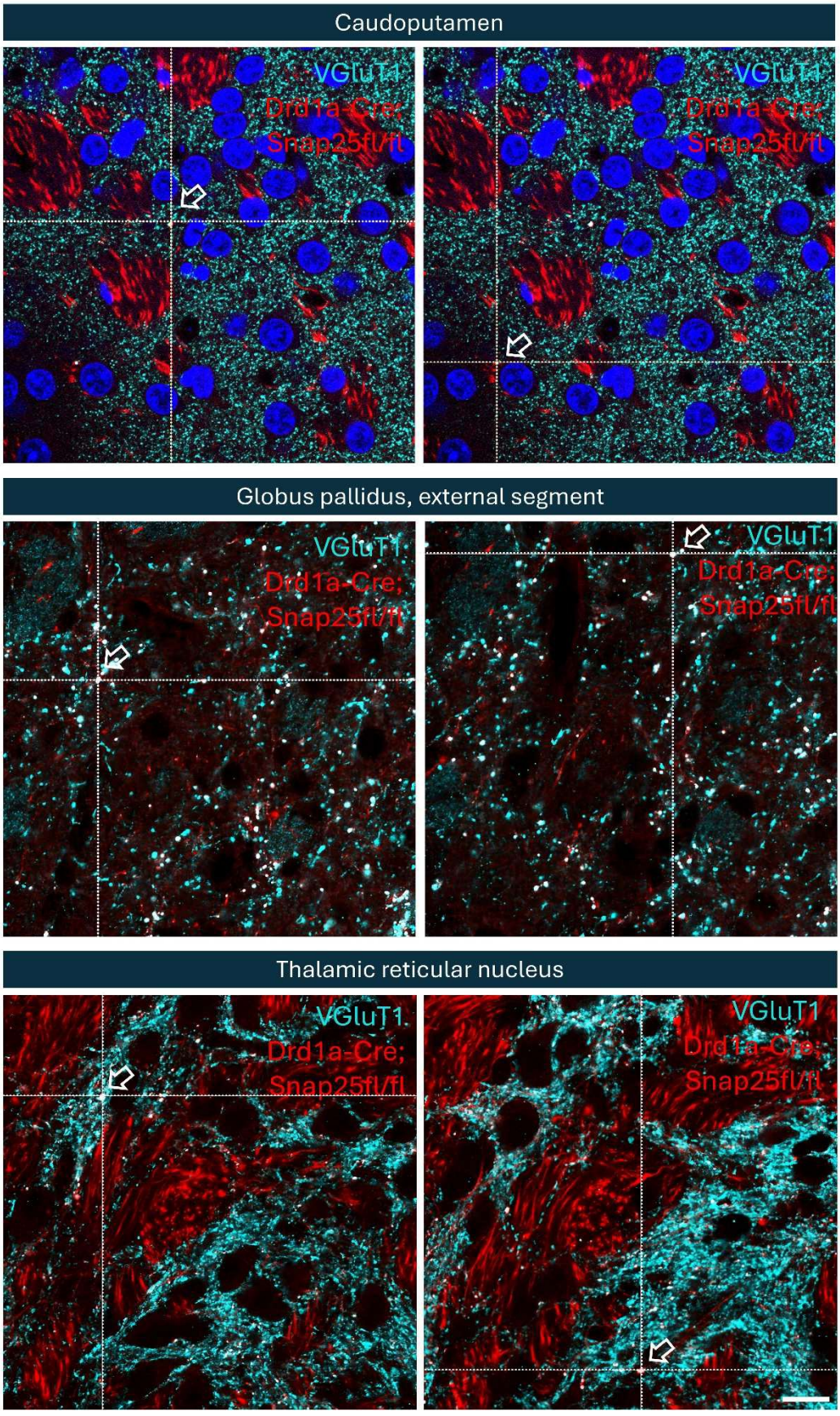

Caudoputamen
VGluT1
Drd1a-Cre;
Snap25fl/fl
VGluT1
Drd1a-Cre;
Snap25fl/fl
Globus pallidus, external segment
VGluT1
Drd1a-Cre;
Snap25fl/fl
VGluT1
Drd1a-Cre;
Snap25fl/fl
Thalamic reticular nucleus
VGluT1
Drd1a-Cre;
Snap25fl/fl
VGluT1
Drd1a-Cre;
Snap25fl/fl

Figure 4.8. Comparison of the excitatory synapses formed by *Drd1a-Cre;Ai14;Snap25$^{fl/fl}$* neurons in the selected subcortical regions of interest. For each subcortical area, two examples showing co-localisation between the tdTomato+ punctae (red) and the excitatory presynaptic marker VGluT1(cyan) are presented. Excitatory synapses of *Drd1a-Cre;Ai14;Snap25$^{fl/fl}$* neurons are shown in the caudoputamen, the GPe, and the TRN at P21 in the layer 6-silenced mice. Note the varying degrees of co-localisation throughout the subcortical ROIs in the *Snap25* cKO mice. Scale bar = 20 µm.

4.3.5. Regional variations in the density of *Drd1a-Cre+;Ai14;Snap25$^{fl/fl}$* neurons

There are different proportions of glutamatergic cortical neurons in different cortical areas and layers. To assess how the number of Drd1a-Cre+ neurons varied by cortical area, I quantified their density in M1 and S1 at P21. In line with expectations, the density and laminar distribution of *Drd1a-Cre;Ai14;Snap25$^{fl/fl}$* neurons significantly differed between M1 and S1. The density of *Drd1a-Cre;Ai14;Snap25$^{fl/fl}$* neurons was found to be ~38% higher in M1 compared to S1 at P21 in the *Snap25* cKO mice (Figure 4.9. A, B) ($p=0.0441$, two-tailed unpaired student's t-test with Welch correction). Corresponding to the increased density, layer 6b of M1 contained ~39% more *Drd1a-Cre;Ai14;Snap25$^{fl/fl}$* neurons than layer 6 of S1 at P21 in the *Snap25* cKO mice (Figure 4.9. C), $p<0.0001$, ordinary two-way ANOVA with Šídák's multiple comparisons test). When distinguishing layer 6a from layer 6b, I utilised both cytoarchitectural and morphological differences between the two sublaminae. Layer 6b forms a narrow band of densely packed cells located just above the white matter, and this thin line of cells is easily observable in most cortical regions. In terms of morphological characteristics, Drd1a-Cre+ neurons in layer 6b are comprised of both horizontally and vertically oriented neurons that are irregularly arranged and unevenly distributed. In contrast, layer 6a neurons are fewer in number and have a more homogeneous appearance. There is also a small gap between the end of layer 6b and the beginning of layer 6a, which marks the transition from one layer to the other. Additionally, the DAPI nuclear counterstain helps to differentiate the two sublaminae, with layer 6b displaying lower nuclear density and more sparsely spaced nuclei.

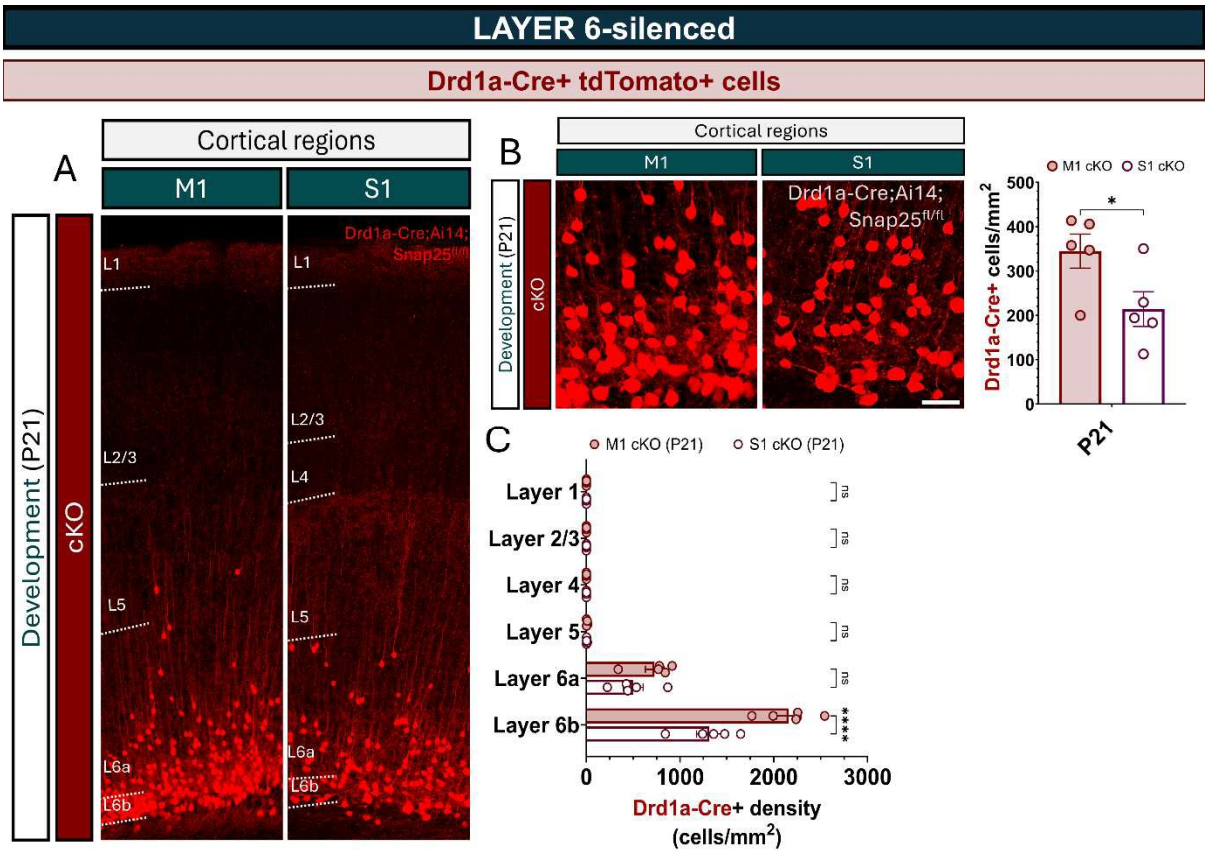


Figure 4.9. Regional variations in the density of Drd1a-Cre+ neurons. (A) Confocal images of the entire depth of the primary motor and primary somatosensory cortices at postnatal day 21, illustrating Drd1a-Cre+ tdTomato-expressing neurons in the *Drd1a-Cre;Ai14;Snap25*$^{fl/fl}$ mice. (B) Examples of *Drd1a-Cre;Ai14;Snap25*$^{fl/fl}$ neurons in M1 and S1 at P21. Bar graphs representing the density of *Drd1a-Cre;Ai14;Snap25*$^{fl/fl}$ neurons in the *Snap25* cKO in M1 and S1 at P21. (C) Quantification of the laminar distribution of *Drd1a-Cre;Ai14;Snap25*$^{fl/fl}$ neurons in M1 and S1 at P21**.** Note the significant difference in the density of Drd1a-Cre+ neurons in cortical layer 6b between M1 and S1 in the *Snap25* cKO mice. Scale bar = 50 µm.

4.3.6. The effects of silencing Drd1a-Cre+ neurons on cortical parvalbumin interneurons during development

4.3.6.1. Genetically silencing Drd1a-Cre+ neurons reorganises the laminar distribution of parvalbumin neurons in S1 at P21

To continue investigating the role of deep-layer projection neurons in instructing the spatial distribution of inhibitory neurons, I chronically manipulated a subset of Drd1a-Cre+ projection neurons in layers 6a and 6b of the neocortex. First, I examined the effects on cortical parvalbumin interneurons during development. I observed no significant changes in the density of PV+ neurons at P21 in M1 and S1 (Figure 4.10. D). The new cortical ROI, i.e., the ACA, did not show a significant alteration in PV+ cell density either (Figure 4.10. E). Since the number of PV+ neurons remained stable following the genetic silencing of Drd1a-Cre+ neurons, I set out to investigate their laminar positioning in M1 and S1. No laminar alterations were detected in M1 at P21 (Figure 4.10. F). Two-way ANOVA testing identified a significant *layer* effect ($p<0.0001$) and a significant *interaction* between *layer* and *genotype* in S1 ($p=0.0038$). Šídák's multiple *post*-hoc comparisons test showed that there was a significant decrease of ~34% in the density of PV+ interneurons in layer 5 of S1 in the *Snap25* cKO mice compared to control mice (Figure 4.10. G) ($p=0.0025$). Since the overall cell density of PV+ neurons in S1 did not change at P21, this suggests a possible redistribution of PV+ neurons across cortical layers. PV+ neurons may shift their laminar locations between layer 5 and layer 6 to compensate for the long-term loss of excitatory inputs from Drd1a-Cre+ neurons.

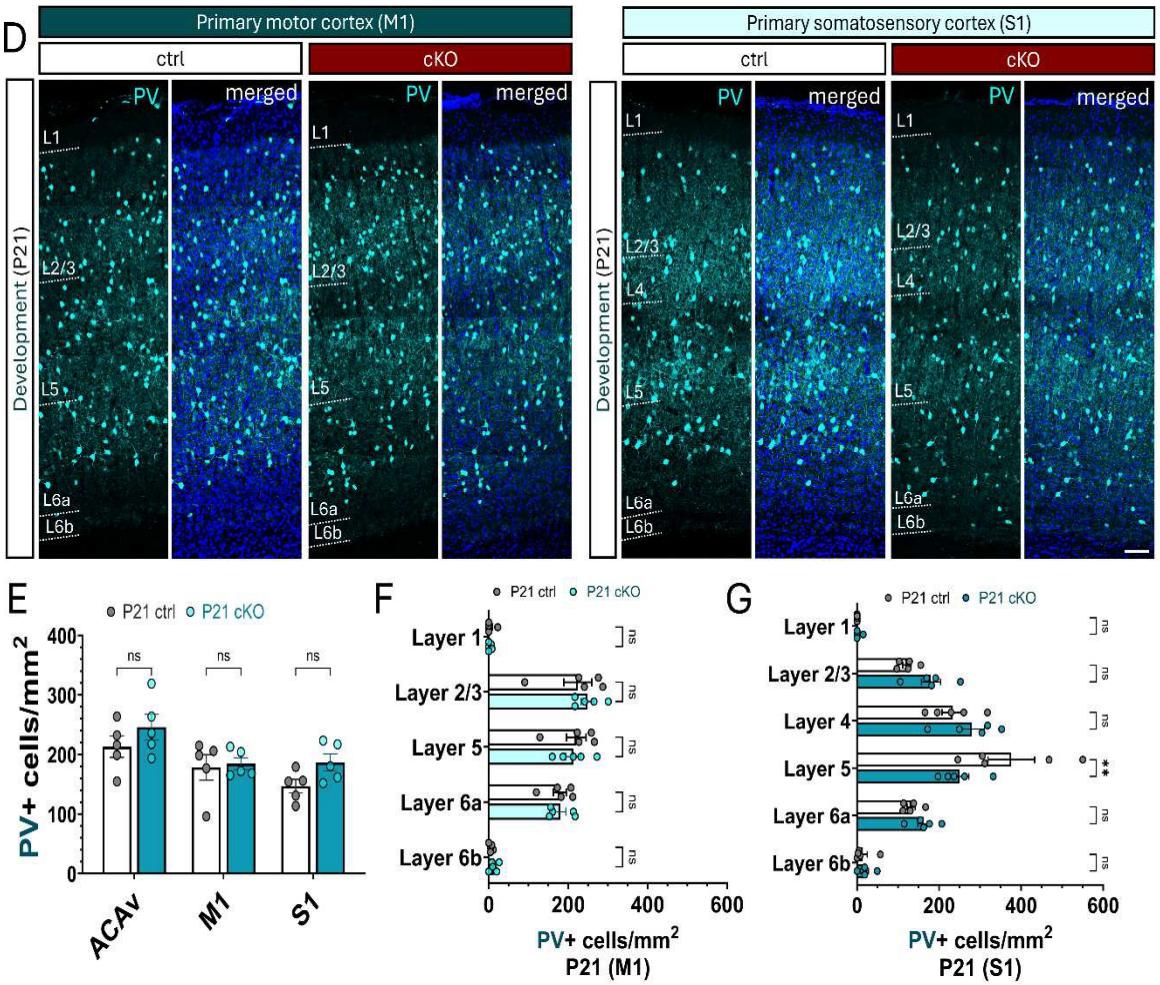


Figure 4.10. The laminar positioning of parvalbumin interneurons following the chronic silencing of a subset of layer 6 projection neurons is altered in layer 5 of S1 at P21. (D) Parvalbumin-immunopositive neurons in cyan in M1 and S1 at P21. White lines mark cortical layer boundaries. (E) Bar graphs representing the density of parvalbumin interneurons quantified in selected cortical ROIs. (F, G) Quantification of the laminar distribution of parvalbumin interneurons in M1 and S1 at P21. Scale bar = 100 µm.

4.3.7. The effects of silencing Drd1a-Cre+ neurons on subcortical parvalbumin neurons during development

4.3.7.1. The soma morphology of striatal parvalbumin interneurons is altered at P21, without corresponding changes in their density

Next, I investigated whether the genetic silencing of Drd1a-Cre+ neurons led to changes in the soma parameters of PV+ neurons in the caudoputamen during development. I sought to examine PV+ morphology at P21 since this is the age when the silencing of Rbp4-Cre+ projection neurons had a transient effect on the soma features of PV+ cells (please refer to Chapter 3). Moreover, the descending axon terminals of Rbp4-Cre+ and Drd1a-Cre+ neurons both form VGluT1+ excitatory synapses in the caudoputamen, pointing to the possibility of cortical control over subcortical GABAergic neurons in the CPu.

Morphometric analyses of PV+ neurons revealed significant alterations in the soma area, perimeter, and roundness values of PV+ cells in the *Snap25* cKO mice relative to control mice at P21 (Figure 4.11. A1, A1', B1, B1', C) (soma area, p=0.0206; soma perimeter, p=0.0398; roundness, p=0.0261; two-tailed Mann-Whitney test). The decreased soma area and perimeter of PV+ neurons in the mutant mice imply that the 'silenced' *Drd1a-Cre;Ai14;Snap25*$^{fl/fl}$ neurons adopted a smaller, less rounded, and more compact soma shape. I also aimed to determine whether the morphological alterations were accompanied by alterations in their number. I found no significant differences in the density of PV+ neurons in the caudoputamen at P21 in the *Drd1a-Cre;Ai14;Snap25*$^{fl/fl}$ mice compared to controls. Despite the existence of excitatory synapses formed by Drd1a-Cre+ terminals, neither the GPe nor the TRN demonstrated significant changes in the density of PV+ neurons (Figure 4.11. D1, D1', E1, E1', F). In concert, these results suggest that the genetic silencing of Drd1a-Cre+ projection neurons alters the soma size of striatal PV+ neurons, without affecting their number. However, it remains to be determined whether these morphological alterations in striatal PV+ neurons are rescued during development or persist into adulthood.

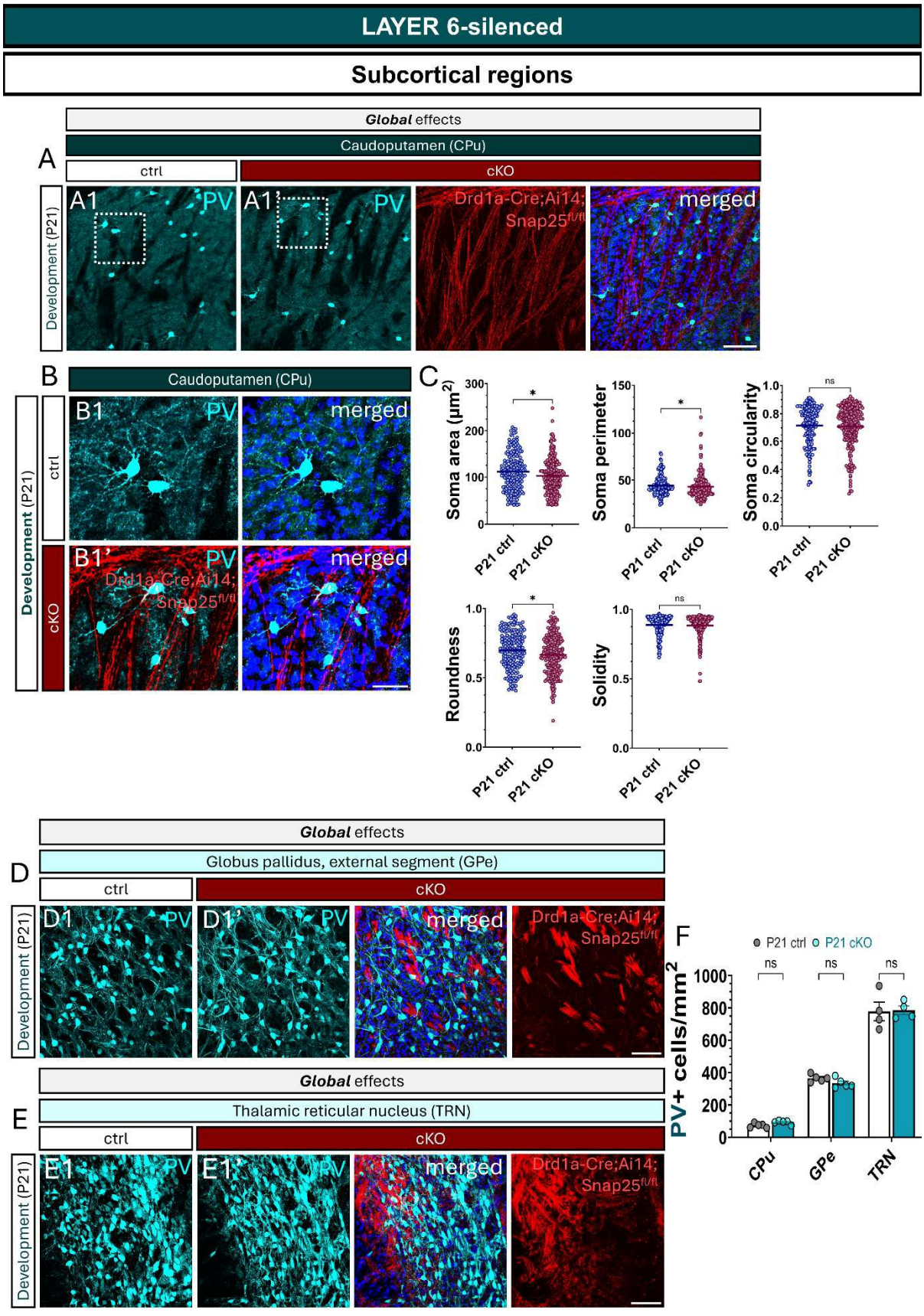

LAYER 6-silenced
Subcortical regions
Global effects
Caudoputamen (CPu)
A
ctrl
cKO
Development (P21)
A1
PV
Drd1a-Cre;Ai14;
Snap25fl/fl
merged
B
Caudoputamen (CPu)
B1
B1'
C
Soma area (µm2)
Soma perimeter
Soma circularity
Roundness
Solidity
P21 ctrl
P21 cKO
ns
Global effects
Globus pallidus, external segment (GPe)
D
D1
D1'
Global effects
Thalamic reticular nucleus (TRN)
E
E1
E1'
F
P21 ctrl
P21 cKO
PV+ cells/mm2
CPu
GPe
TRN

Figure 4.11. Loss of AP-dependent neurotransmitter release from a subset of layer 6 pyramidal neurons leads to decreased soma size in striatal parvalbumin interneurons. (A1) Merged z-stack images depicting parvalbumin immunostained neurons in the caudoputamen at P21 in control brains. (A1') Maximum-intensity projected z-stack displaying parvalbumin immunoreactive neurons in cyan and the long-range projections of *Drd1a-Cre;Ai14;Snap25*$^{fl/fl}$ neurons in red in the *Snap25* cKO mice. Parvalbumin-positive neurons shown at greater magnification in (B) are indicated by white dotted boxes. (B1) Representative examples of parvalbumin-immunoreactive neurons in the caudoputamen in control mice. (B1') Merged confocal images illustrating parvalbumin-expressing neurons being in proximity to the silenced red fibres of Drd1a-Cre+ neurons at P21. (C) Morphometric analyses of parvalbumin neurons in the caudoputamen during development. (D1) Maximum-intensity projected z-stack of parvalbumin neurons in the GPe in control mice. (D1') Parvalbumin-positive neurons are displayed in cyan, while long-range projections of *Drd1a-Cre;Ai14;Snap25*$^{fl/fl}$ neurons are in red in the GPe of the *Snap25* cKO mice. (E1) Confocal z-stack images of parvalbumin neurons in the TRN in control mice at P21. (E1') Maximum-intensity projected z-stack showing the red fibres of *Drd1a-Cre;Ai14;Snap25*$^{fl/fl}$ neurons in the *Snap25* cKO mice and parvalbumin-immunoreactive neurons in cyan in the TRN. (F) Bar graphs representing the mean cell density of parvalbumin neurons across different subcortical regions of interest. Scale bars = 100 µm.

4.3.8. The effects of silencing Drd1a-Cre+ neurons on GABA-$_B$ receptors in the juvenile cortex

4.3.8.1. The density of GABA-$_B$ receptors decreased in the primary motor and somatosensory regions in the layer 6-silenced mice during development

Previous research has demonstrated that pyramidal neuron fate transition leads to the abnormal lamination of MGE-derived interneurons and disruptions in GABAergic inhibition (Lodato et al. 2011). Therefore, I sought to examine whether the laminar rearrangement of PV+ cells detected in layer 5 correlated with alterations in the distribution of GABA-$_A$ and GABA-$_B$ receptors. GABA Type-B Receptor Subunit 1 (GABA-B R1) signalling in PV neurons plays a crucial role in not only regulating presynaptic GABA release, but also dynamically modulating the excitability of PV neurons and controlling output synchronisation (Booker et al. 2013; Bartos et al. 2007; Bassetti 2022). Thus, GABA-$_B$ R1 receptors can modulate PV interneuron function through presynaptic as well as postsynaptic mechanisms.

First, I investigated the receptor density of GABA-$_B$ R1 in layer 5 of M1. The measurements of GABA-B R1 in layer 5 of M1 refer to the number of receptors counted per unit area. Since the Drd1a-Cre+ line does not label pyramidal neurons in layer 5, I did not quantify the number of pyramidal cells or the density of GABA-B R1 on these cells. Two-way ANOVA testing revealed significant effects of *cell type* ($p<0.0001$) and *genotype* ($p=0.0037$), along with a significant *interaction* ($p=0.0428$) between these two factors. Šídák's multiple comparisons test found a significant decline in the density of GABA-$_B$ R1 receptors in layer 5 of M1 at P21 in the layer 6-silenced mice compared to control mice (Figure 4.12. A, C) ($p=0.0119$).

Next, I aimed to determine whether PV+ neurons had fewer GABA-$_B$ R1 receptors and therefore quantified PV+ neurons which co-localised with GABA-$_B$ R1. Šídák's multiple comparisons test revealed no differences in the density of PV+ GABA-$_B$ R1+ neurons in layer 5 of M1 between *Snap25* cKO and control mice (Figure 4.12. C). Similarly, no reductions were detected in the density of PV+ GABA-$_B$ R1- neurons in layer 5 of M1 in the layer 6-silenced mice compared to control mice. However, the density of PV- GABA-$_B$ R1+ receptors that were not co-localised with PV+ neurons decreased significantly by approximately 19% (Figure 4.12. C) ($p=0.0254$, two-way ANOVA with Šídák's multiple comparisons test). Two-way ANOVA testing showed that the density of GABA-$_B$ R1 was significantly influenced by both *genotype* and *cell type* ($p<0.0001$, $p=0.0037$), but only the *GABA-$_B$ R1+* that was *not* co-located with PV+ showed a significant reduction. These results indicate that silencing of Drd1a-Cre+ neurons does not appear to influence PV+ GABA-$_B$ R1+ neurons located in layer 5 in M1. It is yet to be determined what kind of PV-negative GABA-$_B$ R1+ cells decreased in layer 5.

After investigating GABA-$_B$ R1+ receptors in M1, I analysed their density in S1. Using two-way ANOVA testing, significant *genotype* and *cell type* effects were found, along with significant *interactions* (all values $p<0.0001$). Šídák's multiple comparisons test detected a robust ~36% decrease in the density of both GABA-$_B$ R1+ receptors and PV- GABA-$_B$ R1+ receptors in layer 5 of S1 at P21 (Figure

4.12. D) ($p<0.0001$). These are the same populations that were altered in M1 as well. *Post*-hoc tests did not identify significant alterations in the density of PV+ GABA-$_B$ R1+ ($p=0.9972$) and PV+ GABA-$_B$ R1- ($p=0.9997$) in layer 5 between *Snap25* cKO and control mice (Figure 4.12. D). When comparing the percentages of PV+ GABA-$_B$ R1+ populations between M1 and S1, two-way ANOVA found a significant *region* effect ($p=0.0034$). Uncorrected Fisher's LSD *post*-hoc tests found that both the control and mutant mice had more PV+ GABA-$_B$ R1+neurons in S1 at P21. (Figure 4.12. E, F, G) (ctrl, $p=0.0288$; cKO, $p=0.0264$). Taken together, these results imply that the chronic silencing of a specific subset of layer 6 neurons selectively affects the GABA-$_B$ R1+ receptors both in M1 and S1. It is worth noting that the effect of silencing Drd1a-Cre+ neurons appears to be more robust in layer 5 of S1, which is the region where the distribution of PV+ neurons was altered at P21.

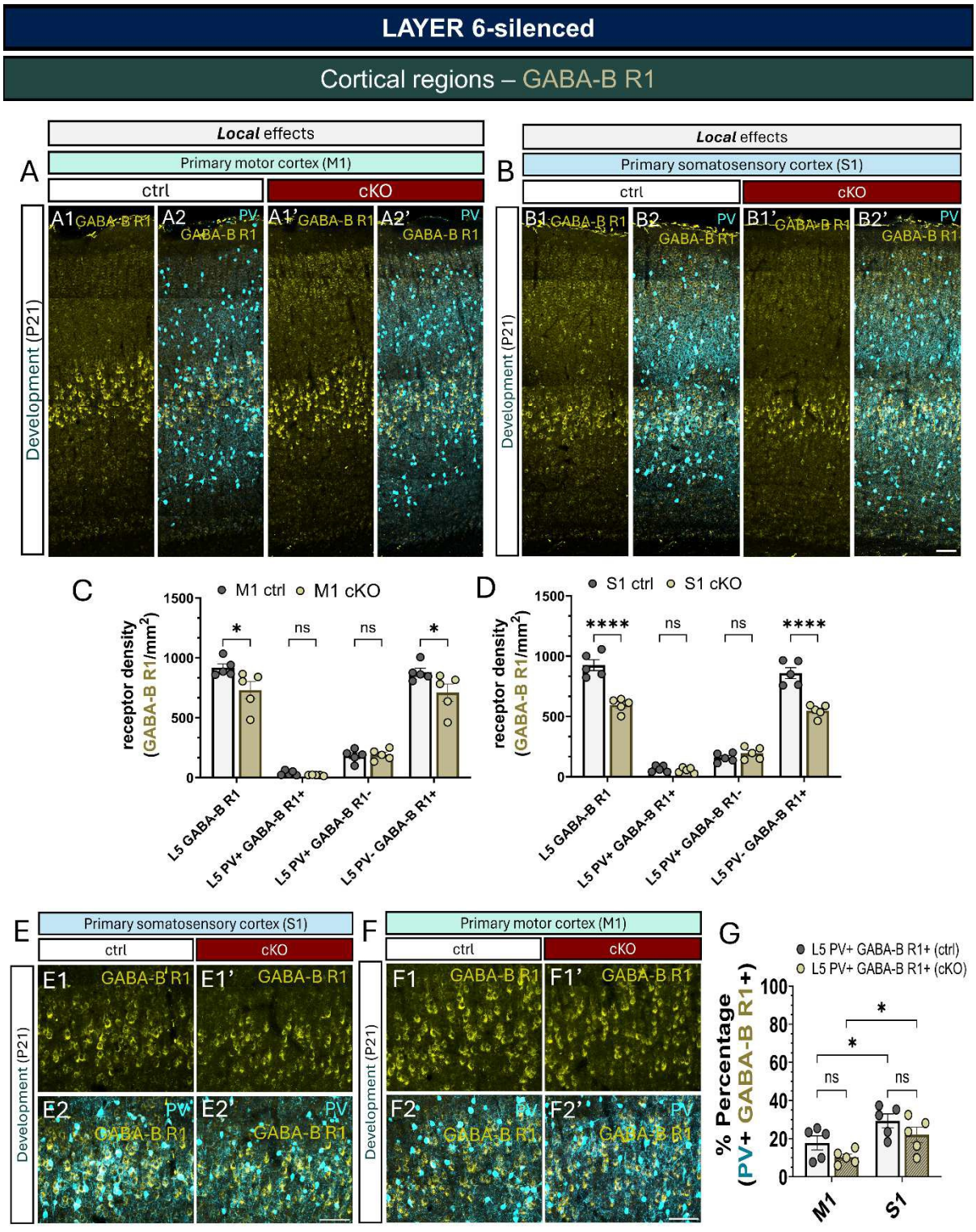


Figure 4.12. GABA-$_B$ R1 receptors are significantly reduced in layer 5 of the primary motor and somatosensory cortices following the genetic silencing of layer 6 projection neurons. Confocal images of the whole depth of the primary motor and somatosensory cortices illustrating GABA-$_B$ R1+ receptors in yellow and parvalbumin-immunoreactive neurons in cyan at P21 in layer 5 in the control (A1, A2, B1, B2) and the *Drd1a-Cre;Ai14;Snap25$^{fl/fl}$* mice (A1', A2', B1', B2'). Quantification of the mean

density of GABA-$_B$ R1+ receptors, GABA-$_B$ R1+ positive for PV+ neurons, PV+ neurons negative for GABA-$_B$ R1+, and GABA-$_B$ R1+ negative for PV+ neurons in layer 5 in M1 (C) and S1 at P21 (D). Representative examples of GABA-$_B$ R1+ receptors in cortical layer 5 in S1 and M1 in the control mice (E1, E2, F1, F2) and the layer 6-silenced mice (E1', E2', F1', F2'). Percentages of PV-immunoreactive neurons co-localising with GABA-B R1 in M1 and S1 in the control and layer 6-silenced mice. Scale bars = 200 μm.

4.3.9. The effects of silencing Drd1a-Cre+ neurons on GABA-$_A$ receptors in the juvenile cortex

4.3.9.1. Ionotropic GABA-$_A$ receptors in the juvenile neocortex remained unaffected by the genetic silencing of Drd1a-Ce+ neurons

To determine whether the genetic silencing of Drd1a-Cre+ neurons affected the ionotropic GABA-$_A$ receptors, I set out to examine the GABA-$_A$ δ subunit, which is enriched in GABAergic PV neurons and PT-type of glutamatergic layer 5 neurons (https://celltypes.brain-map.org/rnaseq/mouse_ctxhpf_10x?selectedVisualization=Heatmap&colorByFeature=Gene+Expression&colorByFeatureValue=Gabrd). Contrary to GABA-$_B$ R1 receptors, two-way ANOVA testing did not detect a significant *region* (p=0.0943) or *genotype* effect (p=0.2155). Šídák's *post*-hoc tests showed that GABA-$_A$ δ receptor density did not differ significantly between control and layer 6-silenced mice at P21 in layer 6 of M1 and S1 (p=0.1834 and p=0.9980) (Figure 4.13. A, B, C). Based on the absence of impact on the GABA-$_A$ receptors, it can be inferred that chronic silencing of layer 6 neurons selectively affects the GABA-$_B$ receptors in M1 and S1.

Then, in layer 6 of the Drd1a-Cre+-silenced mice, I counted the number of Drd1a-Cre+ neurons that co-localised with the GABA-$_A$ δ receptor and investigated whether there were regional differences in the density of Drd1a-Cre+;GABA-$_A$ δ+ neurons. The primary reason for investigating Drd1a-Cre+;GABA-$_A$ δ+ neurons in the *Snap25* cKO mice was the absence of tdTomato+ fluorescence in the Drd1a-Cre control mice. Compared to S1 cKO, M1 of *Snap25* cKO mice had a considerably higher density of the subsets of Drd1a-Cre+ neurons expressing the GABA-$_A$ δ receptors. Consequently, S1 of the *Snap25* cKO mice contained ~44% fewer Drd1a-Cre+;GABA-$_A$ δ+ neurons in layer 6 relative to layer

6 of M1 at P21 (Figure 4.13. G) (p=0.0174, two-tailed student's t-test with Welch's correction). The noticeably greater density of Drd1a-Cre+;GABA-$_A$ δ+ neurons in layer 6 M1 compared to layer 6 S1 in the *Snap25* cKO mice is not surprising. This is expected since the density of silenced Drd1a-Cre+ neurons varies significantly across cortical regions, and *Drd1a-Cre;Ai14;Snap25*$^{fl/fl}$ neurons are more prevalent in M1 (Figure 4.13. F) (p=0.0104, two-tailed student's t-test with Welch's correction).

Taken together, these results indicate that chronically silencing layer 6 corticothalamic neurons differentially impacts the metabotropic and ionotropic GABA receptors during development. Ablation of *Snap25* from subsets of layer 6 neurons led to significant reductions in the density of GABA-$_B$ R1 in layer 5 of M1 and S1 at P21; however, it left GABA-$_A$ δ receptors in layer 6 intact. It remains to be discovered whether other subunits of the GABA-$_A$ receptors may be impacted by the genetic silencing of Drd1-Cre+ neurons.

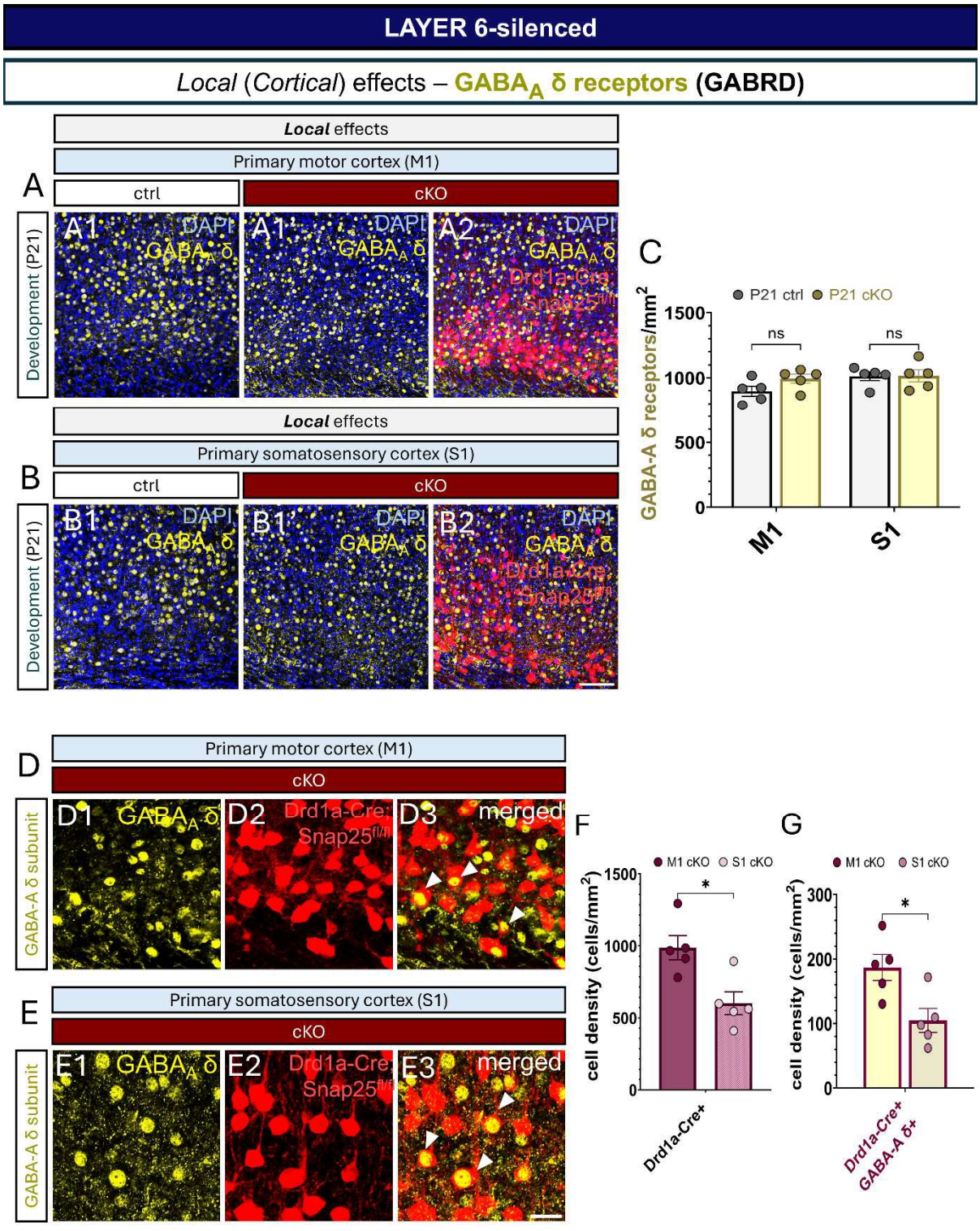


Figure 4.13. Loss of AP-dependent neurotransmitter release from cortical layer 6 neurons leaves the ionotropic GABA-$_A$ δ receptors in layer 6 intact during development. Maximum-intensity projected z-stacks showing DAPI nuclear counterstain and GABA-$_A$ δ receptors at P21 in M1 and S1 in control (A1, B1) and *Snap25* cKO mice (A1', B1'). Merged z-stack image illustrating *Drd1a-*

Cre;Ai14;Snap25$^{fl/fl}$ neurons (red) in layer 6, along with GABA-$_A$ δ receptors in M1 and S1 (A2, B2). Quantification of GABA-$_A$ δ receptor density in cortical layer 6 in M1 and S1 (C). Examples of GABA-$_A$ δ receptors and *Drd1a-Cre;Ai14;Snap25*$^{fl/fl}$ neurons in cortical layer 6 of M1 and S1 (D1, D2, E1, E2). Merged confocal image representing co-localisation between GABA-$_A$ δ receptors and *Drd1a-Cre;Ai14;Snap25*$^{fl/fl}$ neurons (D3, E3). (F) Quantification of the density of Drd1a-Cre+ neurons in M1 and S1 in the mutant mice. (G) Quantification of the density of Drd1a-Cre+ neurons co-localising with GABA-$_A$ δ receptors in the mutant M1 and S1.

4.3.10. The effects of silencing Drd1a-Cre+ neurons on cortical neuropeptide-Y interneurons during development

4.3.10.1. Neuropeptide-Y interneurons significantly increased in layer 6b of the primary somatosensory cortex in the Snap25 cKO mice at P21

To continue investigating whether the genetic silencing of a restricted subtype of layer 6 neurons affected other subtypes of GABAergic interneurons, I first examined the spatial and laminar organisation of NPY+ neurons at P21. Of the selected cortical ROIs, there was a significant *region* (p=0.0011) and *genotype* effect (p=0.0070), albeit with no *interaction* (p=0.4056), on the density of NPY+ interneurons in ACA and M2. Šídák's multiple comparisons test revealed a significant increase of ~42% in the density of NPY+ interneurons in the secondary motor cortex (M2) but not in ACA (p=0.2212) at P21 in the *Drd1a-Cre;Ai14;Snap25*$^{fl/fl}$ mice compared to control mice (Figure 4.14. A, B) (p=0.0262). In the rest of the cortical ROIs, i.e., M1 and S1, the results of the two-way ANOVA indicate a significant effect of *genotype* (p=0.0074), with no *region* effect (p=0.3586), on NPY+ cell density. Interestingly, Šídák's multiple comparisons test did not find significant alterations in NPY+ cell density in M1 and S1 in the *Drd1a-Cre;Ai14;Snap25*$^{fl/fl}$ mice relative to control mice (Figure 4.14. C, D, E, G); however, S1 approached, but did not reach statistical significance (p=0.0514).

Analysis of the laminar distribution of NPY+ interneurons revealed significant effects of *layer* (p<0.0001) and *genotype* (p=0.0032) without *interaction* (p=0.0870), as demonstrated by two-way ANOVA testing. Šídák's multiple comparisons tests found a prominent increase in the density of NPY+ interneurons in layer 6b of S1 in the *Snap25* cKO mice compared to control mice (Figure 4.14. D, H)

(p=0.0199). No such alteration was observed in M1, where the density of NPY+ neurons between the control and the *Snap25* cKO mice did not differ significantly across cortical layers (Figure 4.14. C, F) at P21. These findings indicate a significant redistribution of interneurons in S1 when excitatory inputs from layer 6 are eliminated. This suggests that interneurons respond to changes in cortical connectivity and changes in the excitation received from the same or adjacent layers. Notably, alterations in the density of cortical NPY+ neurons were only observed in layer 6b of S1. This is intriguing given that calcium-dependent neurotransmission in Drd1a-Cre-positive neurons was disrupted in both layer 6a and layer 6b. However, it remains to be seen whether the observed repositioning of NPY+ neurons in S1 persists into adulthood. Additionally, it is unclear if the increased presence of NPY+ neurons in layer 6b is offset by some compensatory mechanisms that may come into play during various developmental stages. Further studies are necessary to clarify these dynamics and their implications for cortical organisation and function.

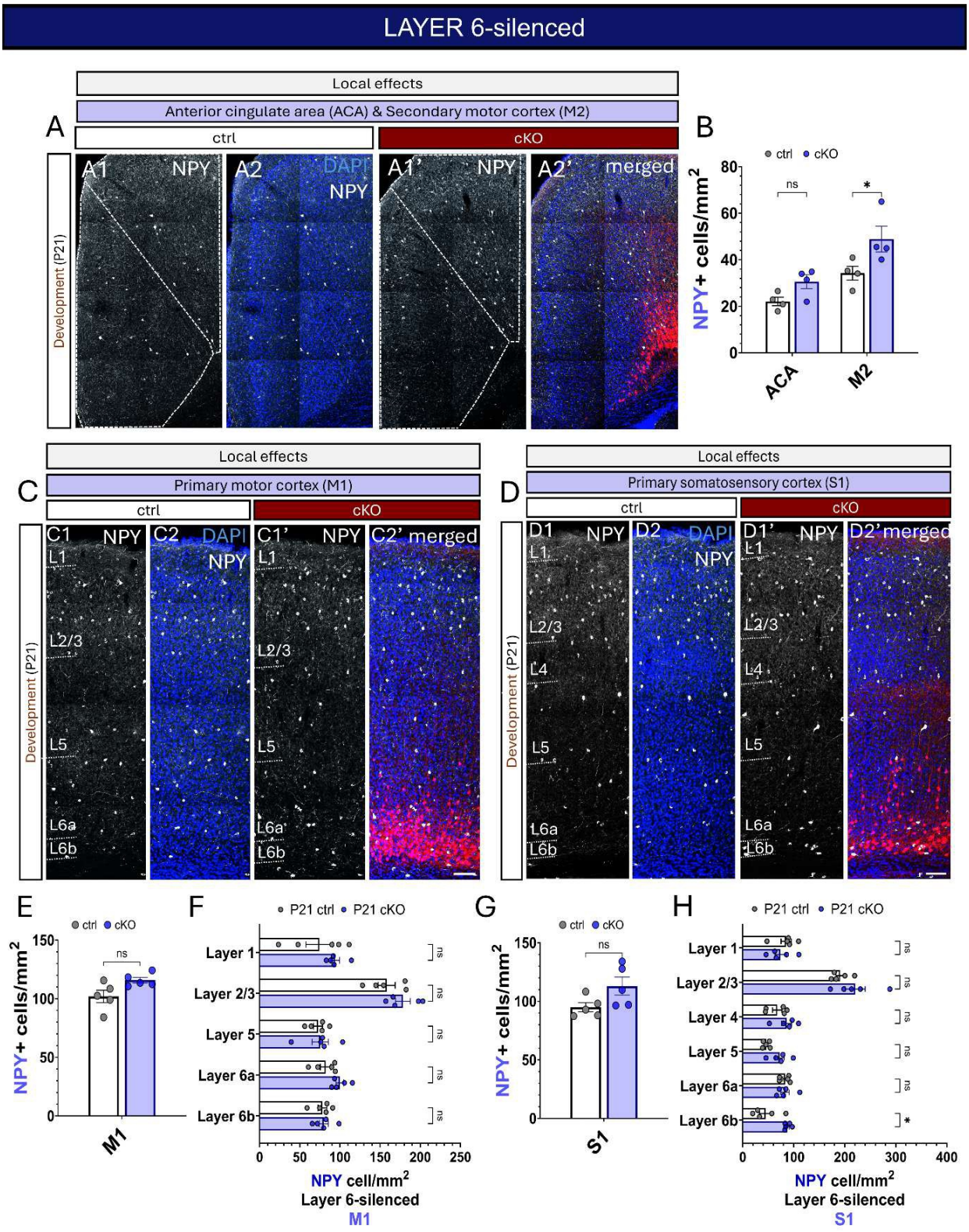


Figure 4.14. Neuropeptide-Y interneurons within distinct cortical regions demonstrate different susceptibility to the genetic silencing of Drd1a-Cre+ neurons. (A) Tile scan images

depicting the anterior cingulate area and the secondary motor cortex. Neuropeptide-Y-immunoreactive neurons are displayed in grey at P21 in the control (A1, A2) and the layer 6-silenced mice (A1', A2'). Quantification of the density of neuropeptide-Y-immunopositive neurons in the ACA and M2. Combined tile scan and z-stack images of M1 illustrating neuropeptide-Y-immunopositive neurons across different cortical layers in the control (C1, C2) and the *Snap25* cKO mice (C1', C2') at P21. White lines mark layer boundaries. Tiled z-stack images of neuropeptide-Y-immunopositive neurons across different cortical layers in M1 and S1 in the control (C1, C2, D1, D2) and the *Snap25* cKO mice (C1', C2', D1', D2') at P21. Merged images indicate silenced *Drd1a-Cre;Ai14;Snap25*$^{fl/fl}$ neurons in red (C2', D2'). Bar graphs illustrating the mean cell density of neuropeptide-Y-immunopositive neurons in M1 and S1 at P21 (E, G). Quantification of the laminar distribution of neuropeptide-Y-immunopositive neurons in M1 and S1 (F, H). Scale bar = 100 µm.

4.3.11. The effects of silencing Drd1a-Cre+ neurons on subcortical neuropeptide-Y neurons during development

4.3.11.1. Chronic silencing of Drd1a-Cre+ neurons influences the density and soma morphology of striatal neuropeptide-Y neurons at P21

In the preceding sections, I examined how NPY+ interneurons in the neocortex were affected by the conditional deletion of *Snap25* from Drd1a-Cre+ neurons. In this section, I looked at NPY+ neurons outside of the neocortex. I selected the hippocampus and caudoputamen as my ROIs in order to compare the effects of silencing layer 6 projection neurons on NPY+ neurons with those of SST+ and CR+ interneurons that I investigated in the same regions. Interestingly, I found a notable yet unexpected increase of ~22% in the density of NPY+ neurons in the caudoputamen at P21 in the *Drd1a-Cre;Ai14;Snap25*$^{fl/fl}$ mice relative to control mice (Figure 4.15. A, B, C) (p=0.0328, unpaired student's t-test with Welch correction). The increased density of NPY+ neurons was concomitant with alterations in the soma characteristics of NPY+ neurons. At P21, chronic silencing of Drd1a-Cre+ neurons led to a significant increase in the soma area and perimeter of NPY+ neurons in the striatum in the *Snap25* cKO mice (Figure 4.15. D) (soma area, p=0.0092; soma perimeter, p=0.0064; two-tailed unpaired Mann-Whitney test). The alterations observed in striatal NPY+ interneurons may suggest that their development is partially dependent on extrinsic signals from cortical glutamatergic projection neurons. However, additional research is required to ascertain the degree to which the

maintenance and maturation of NPY+ neurons in subcortical nuclei are modulated by cortical excitatory inputs.

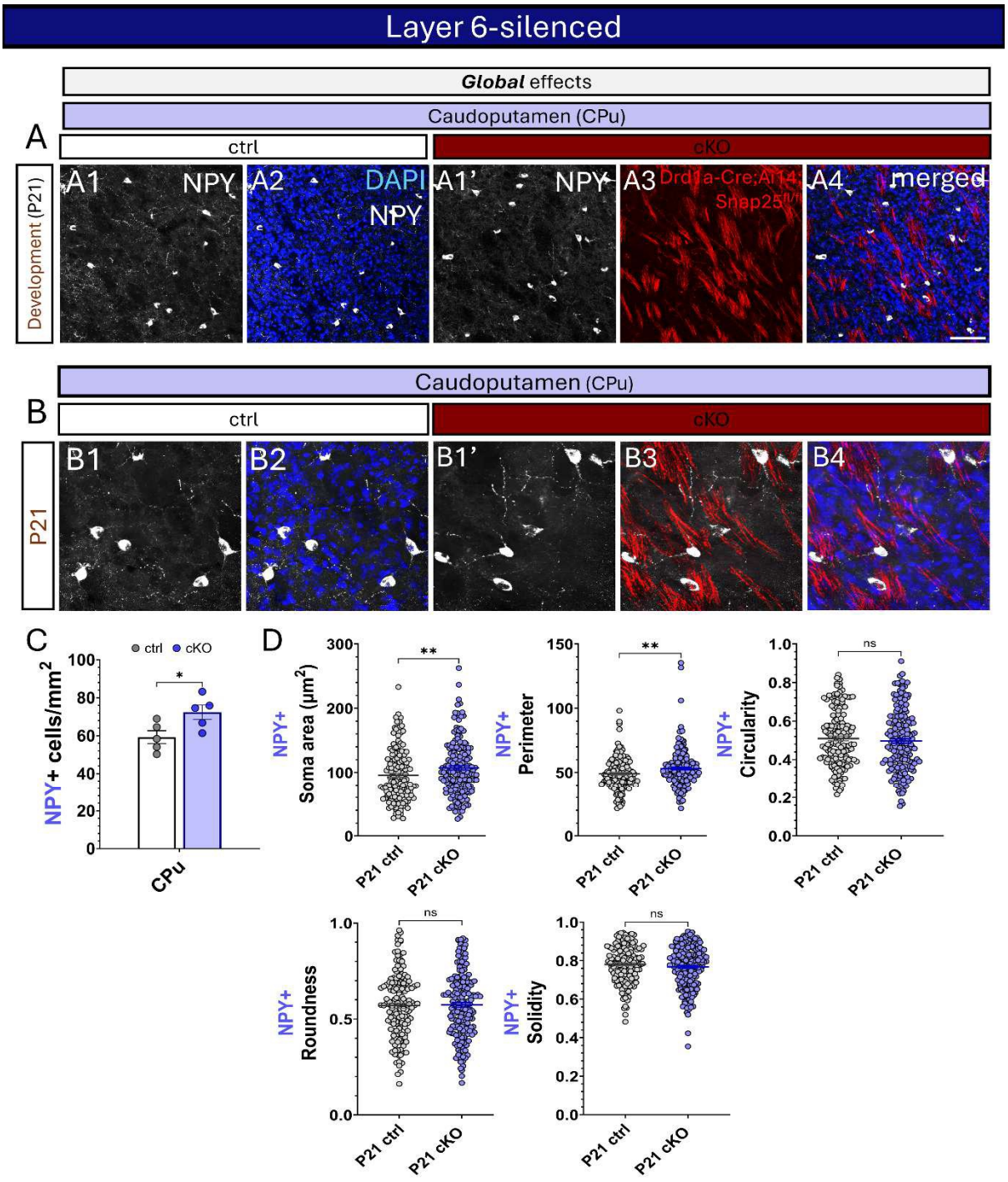


Figure 4.15. Striatal neuropeptide-Y interneurons react to the chronic silencing of layer 6 projection neurons during development. Maximum-intensity projected z-stacks of neuropeptide-Y-immunoreactive neurons in the caudoputamen in the control mice (A1, A2) and the *Drd1a*-

Cre;Ai14;Snap25$^{fl/fl}$ mice (A1'). Red fibre bundles of *Drd1a-Cre;Ai14;Snap25*$^{fl/fl}$ neurons, where evoked neurotransmitter release was abolished (A3). Superimposed z-stack image showing DAPI counterstain in blue, neuropeptide-Y-immunoreactive neurons in grey, and the silenced *Drd1a-Cre;Ai14;Snap25*$^{fl/fl}$ neurons in red (A4). Confocal z-stack images illustrating the soma morphology of neuropeptide-Y-immunoreactive neurons in the caudoputamen at postnatal day 21 in the control (B1, B2) and the layer 6-silenced mice (B1'). Merged maximum-intensity projected z-stacks of the silenced tdTomato+ fibres of *Drd1a-Cre;Ai14;Snap25*$^{fl/fl}$ intersecting NPY+ neurons (B3, B4). Bar graph representing the mean cell density of NPY+ neurons in the control and *Snap25* cKO mice at P21 (C). Soma measurements of striatal NPY+ neurons shown by scatter plots (D). Scale bar = 100 µm.

4.3.11.2. Upregulation of NPY+ interneuron expression in the dentate gyrus at P21 following the conditional deletion of Snap25 from Drd1a-Cre+ neurons

To investigate the impact of the genetic silencing of a subset of layer 6 cortical projection neurons on NPY+ interneurons in the hippocampus, I assessed their distribution in the CA1, CA3, and dentate gyrus at P21 (Figure 4.16. A, B, C). Two-way ANOVA results indicated that both *genotype* ($p=0.0010$) and *region* ($p<0.0001$) significantly influenced NPY+ cell density, with no *interaction* between the two factors ($p=0.4724$). Šídák's multiple comparisons test identified a significant rise in NPY+ interneurons in the dentate gyrus of the *Drd1a-Cre;Ai14;Snap25*$^{fl/fl}$ mice, following the genetic silencing of Drd1a-Cre+ neurons (Figure 4.16. C1, C2, C1', C2', D) ($p=0.0230$). Neither the CA1 ($p=0.0747$) nor the CA3 ($p=0.5704$) exhibited significant alterations in the density of NPY+ interneurons at P21 (Figure 4.16. A1, A2, A1'-A2', B1, B2, B1', B2'). The significant increase in the density of NPY+ cells observed specifically within the dentate gyrus may be linked to the presence of tdTomato+ fibres in the hippocampus, indicating axonal projections from Drd1a-Cre+ neurons. However, to confirm whether a direct synaptic connection exists between Drd1a-Cre+ layer 6b pyramidal neurons and the hippocampus, further investigation using virus-assisted anatomical tracing and/or optogenetic circuit mapping is necessary. Given the relatively low abundance of Cre-expressing tdTomato+ neurons in CA1, it is likely that the NPY+ interneurons are responding to the genetic silencing of Drd1a-Cre+ neurons in layer 6b, rather than to the possible silencing of the sparse Cre+ pyramidal neurons in CA1 (Figure 4.16. A3).

The upregulation in NPY+ neuron expression detected within the dentate gyrus is rather paradoxical, given that these neurons are devoid of glutamatergic inputs following the deletion of *Snap25* from Drd1a-Cre+ neurons. One would expect to observe the opposite effect, with the density of NPY+ neurons declining and probable cell death occurring due to reduced excitation. Given that interneuron function is highly reliant on network activity and extrinsic cues from principal neurons (De Marco García and Fishell 2025), corresponding changes in interneuron numbers and function are anticipated to maintain E/I balance and network homeostasis. Since NPY is known to modulate both excitatory and inhibitory synaptic transmission (Tu et al. 2005; Colmers et al. 1991; Sperk et al. 2007; El Bahh et al. 2002), NPY-mediated signalling can increase the inhibitory tone onto excitatory granule cells while concurrently modulating the dynamics of other inhibitory neurons (Bacci et al. 2002). Under reduced glutamatergic drive, NPY+ may suppress granule cell excitation and simultaneously decrease the amplitude of inhibitory postsynaptic currents (IPSCs) to fast-spiking and low-threshold-spiking (LTS) interneurons (Bacci et al. 2002). The decreased inhibition, i.e., disinhibition, of PV+ and LTS neurons can modulate inhibitory output and assist network-level stabilisation. To maintain circuit stability in the hippocampus when excitation is reduced, NPY+ may thus initiate circuit-level adaptations and modify network dynamics by directly regulating excitatory granule neurons and indirectly regulating other interneurons, such as LTS, FS PV+, and SST+ cells (Bacci et al. 2002).

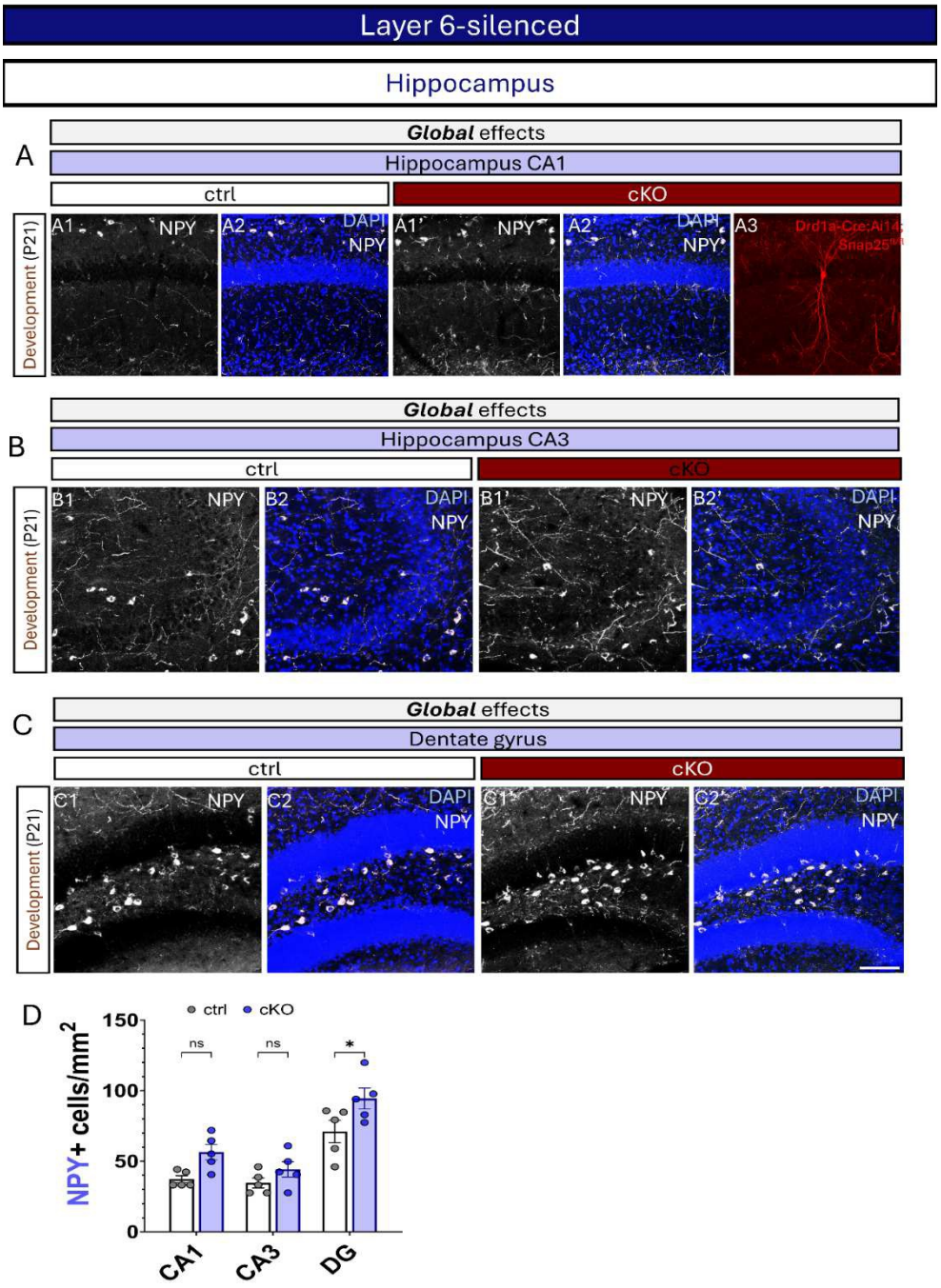


Figure 4.16. Silencing a subset of layer 6 projection neurons selectively affects neuropeptide-Y interneurons in the dentate gyrus, while leaving the CA1 and CA3 intact. Z-stack images illustrating neuropeptide-Y interneurons in the CA1 at P21 in control (A1, A2) and layer 6-silenced mice (A1', A2'). Example of a Cre-expressing tdTomato+ pyramidal neuron in the stratum pyramidale of CA1 in the *Drd1a-Cre;Ai14;Snap25*$^{fl/fl}$ mice (A3). Maximum-intensity projected z-stacks of neuropeptide-Y interneurons in the CA3 and dentate gyrus in control (B1, B2, C1, C2) and *Snap25* cKO (B1', B2', C1', C2'). Quantification of the cell density of neuropeptide-Y-immunopositive neurons in the hippocampal regions (D). Scale bar = 100 μm.

4.3.12. The effects of silencing Drd1a-Cre+ neurons on somatostatin and calretinin-positive neurons during development

4.3.12.1. Chronic silencing of glutamatergic layer 6 projection neurons selectively affects the soma size of calretinin-positive interneurons in the striatum

I previously showed that when excitatory driving from Drd1a-Cre+ neurons is significantly decreased, the developing hippocampus and striatum exhibit higher levels of NPY+ expression. I then looked into the SST+ and CR+ subtypes to examine whether this effect was exclusive to NPY+ neurons. I retained the striatum as my subcortical ROI since the distribution of SST and CR inhibitory neurons in the CPu intersects with the red fibre bundles of the silenced Drd1a-Cre+ neurons (Figure 4.17. A, B, C). SST+ and CR+ neuron density did not differ significantly between the control and *Snap25* cKO animals at P21 (p=0.9777, p=0.3716; t-test with Welch's correction) (Figure 4.17. D, E), despite the possibility that glutamatergic inputs may affect GABAergic interneurons in the striatum. This agrees with the finding on striatal parvalbumin neurons whose number remained unaffected when *Snap25* was ablated from either layer 5 or layer 6 projection neurons (please refer to Chapter 3).

Chronic silencing of layer 5 and layer 6b neurons resulted in morphological changes in PV+ neurons at P21, prompting the question of whether similar morphological alterations could be observed in CR+ neurons. Loss of *Snap25* from Drd1a-Cre+ neurons resulted in increased soma area and perimeter in CR+ neurons in the *Snap25* cKO mice compared to control mice at P21 (Figure 4.17. F) (soma area, p=0.0027; soma perimeter, p=0.0041; two-tailed unpaired Mann-Whitney test). Although the approximately 14% increase in the soma area of striatal CR+ neurons cannot be deemed robust, it may suggest that inhibitory cells adapt to the reduced excitation from layer 6 neurons through morphological changes rather than alterations in their density. It is interesting to note that these morphological changes during development were observed in the Ca^{2+}-binding protein-expressing subtype of GABAergic neurons, i.e., parvalbumin and calretinin. Inferring the interactions

between glutamatergic deep-layer projection neurons and Ca^{2+}-binding protein-expressing interneurons is an important topic that merits further investigation.

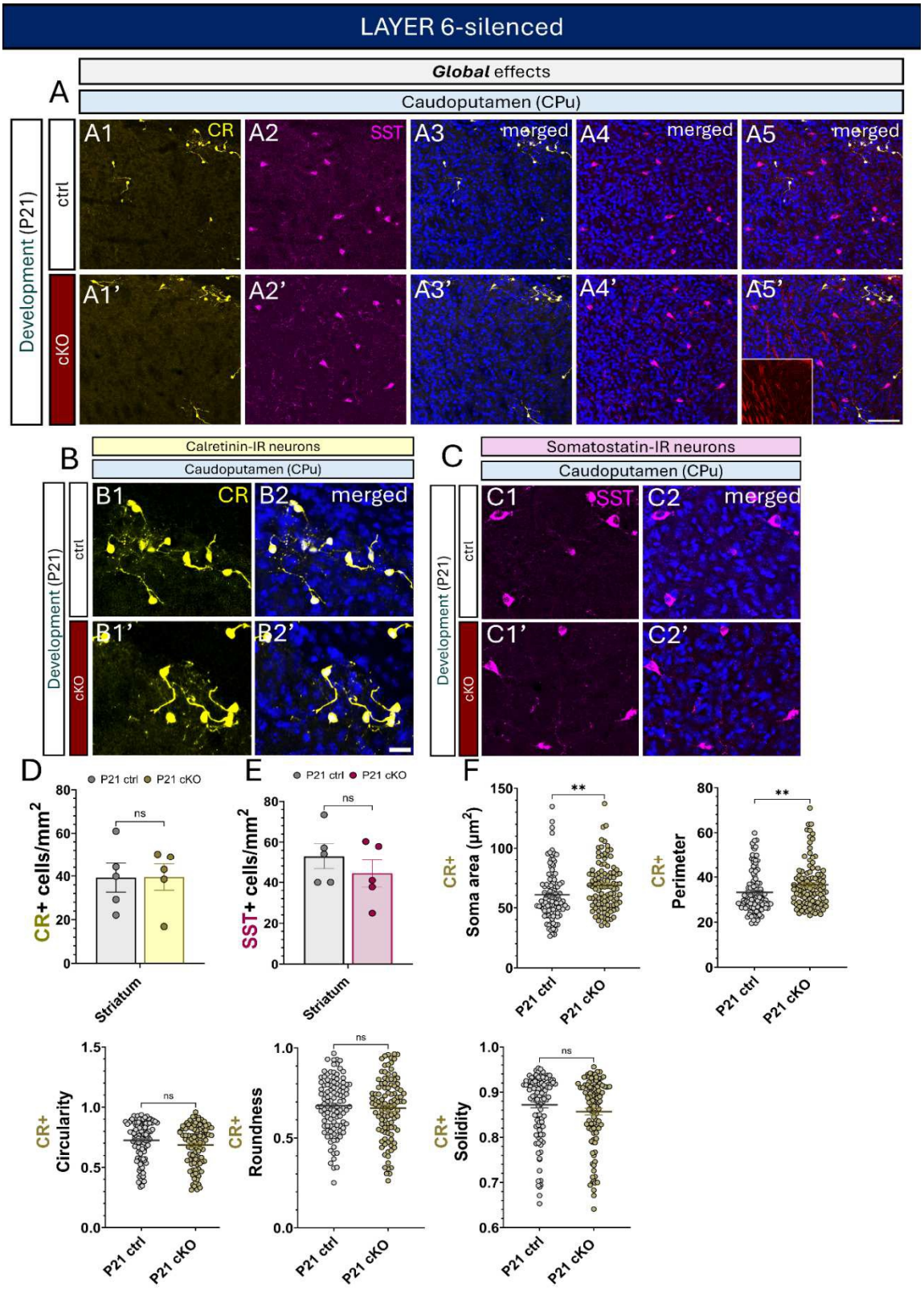


Figure 4.17. Differential impact of the chronic silencing of a subset of layer 6 projection neurons on somatostatin and calretinin-expressing interneurons in the caudoputamen during development. Collated z-stacks of calretinin-immunoreactive neurons in yellow and somatostatin-immunoreactive neurons in magenta in the caudoputamen with DAPI counterstain at P21 in the control (A1-A5) and *Snap25* cKO mice (A1'-A5'). Representative examples of striatal calretinin and somatostatin-immunostained neurons in the control (B1, B2, C1, C2) and layer 6-silenced mice (B1', B2', C1', C2'). Quantification of the cell density of calretinin and somatostatin neurons in the caudoputamen at P21 (D, E). Scatter plots representing different soma parameters of striatal calretinin neurons measured at postnatal day 21 (F). Scale bars = 100 µm (A5'), 50 µm (B2').

4.3.12.2. Hippocampal calretinin and somatostatin-positive neurons are differentially affected by the genetic silencing of cortical Drd1a-Cre+ neurons

The presence of tdTomato+ fibres in the s.l.m. of CA1 and CA3 in the *Drd1a-Cre;Ai14;Snap25*$^{fl/fl}$ mice may suggest that layer 6b neurons could exert a direct influence on the GABAergic cell populations in the hippocampus. To examine the effects of chronically silencing layer 6 projection neurons on hippocampal SST+ and CR+ interneurons, I investigated their distribution in the CA1 region during development. The CA1 region saw a marked increase in the density of CR-expressing neurons (p=0.0004) in the *Drd1a-Cre; Ai14;Snap25*$^{fl/fl}$ mice compared to control mice at P21 (unpaired t-test with Welch's correction) (Figure 4.18. A, B, D). SST neurons changed in the opposite direction; their density significantly decreased by ~15% in the *Drd1a-Cre;Ai14;Snap25*$^{fl/fl}$ mice relative to control mice in CA1 (p=0.0195, unpaired t-test with Welch's correction) (Figure 4.18. A, C, E). Due to their unique circuit roles, input specificity, and plasticity mechanisms, SST+ and CR+ interneurons in the CA1 appear to react differently to the reduced excitation coming from cortical excitatory neurons. Through homeostatic plasticity, SST+ interneurons typically maintain or modify their inhibitory control in the presence of decreased excitation (Honoré et al. 2021). In contrast, CR interneurons, which are more implicated in interneuron-interneuron inhibition, may exhibit diminished function, resulting in disrupted inhibitory signalling within the hippocampal circuit (Honoré et al. 2021; Chamberland et al. 2024; Tóth and Maglóczky 2014; Harris et al. 2018).

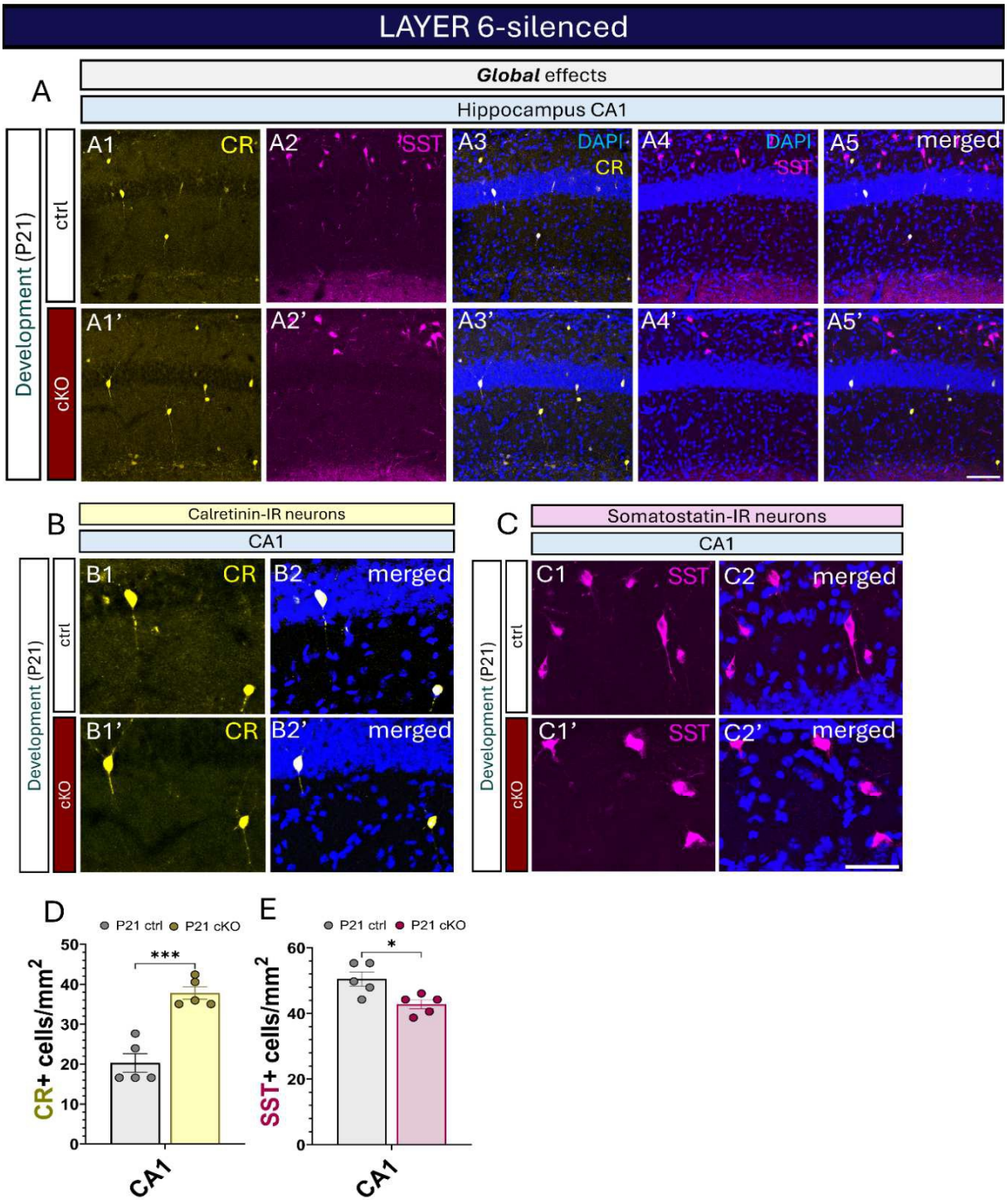


Figure 4.18. Hippocampal calretinin and somatostatin-positive neurons in CA1 demonstrate notable changes in their density after silencing Drd1a-Cre+ neurons. Collated confocal z-stacks illustrating calretinin and somatostatin-immunoreactive neurons along with DAPI nuclear counterstain in the CA1 at P21 in the control (A1-A5) and *Snap25* cKO mice (A1'-A5'). Representative examples of calretinin and somatostatin-immunoreactive cells in the control (B1, B2, C1, C2) and layer 6-silenced mice (B1', B2', C1', C2') at P21. Bar graphs showing the mean cell density of somatostatin-immunopositive neurons at P21 in the CA1 (E). Scale bars = 50 μm.

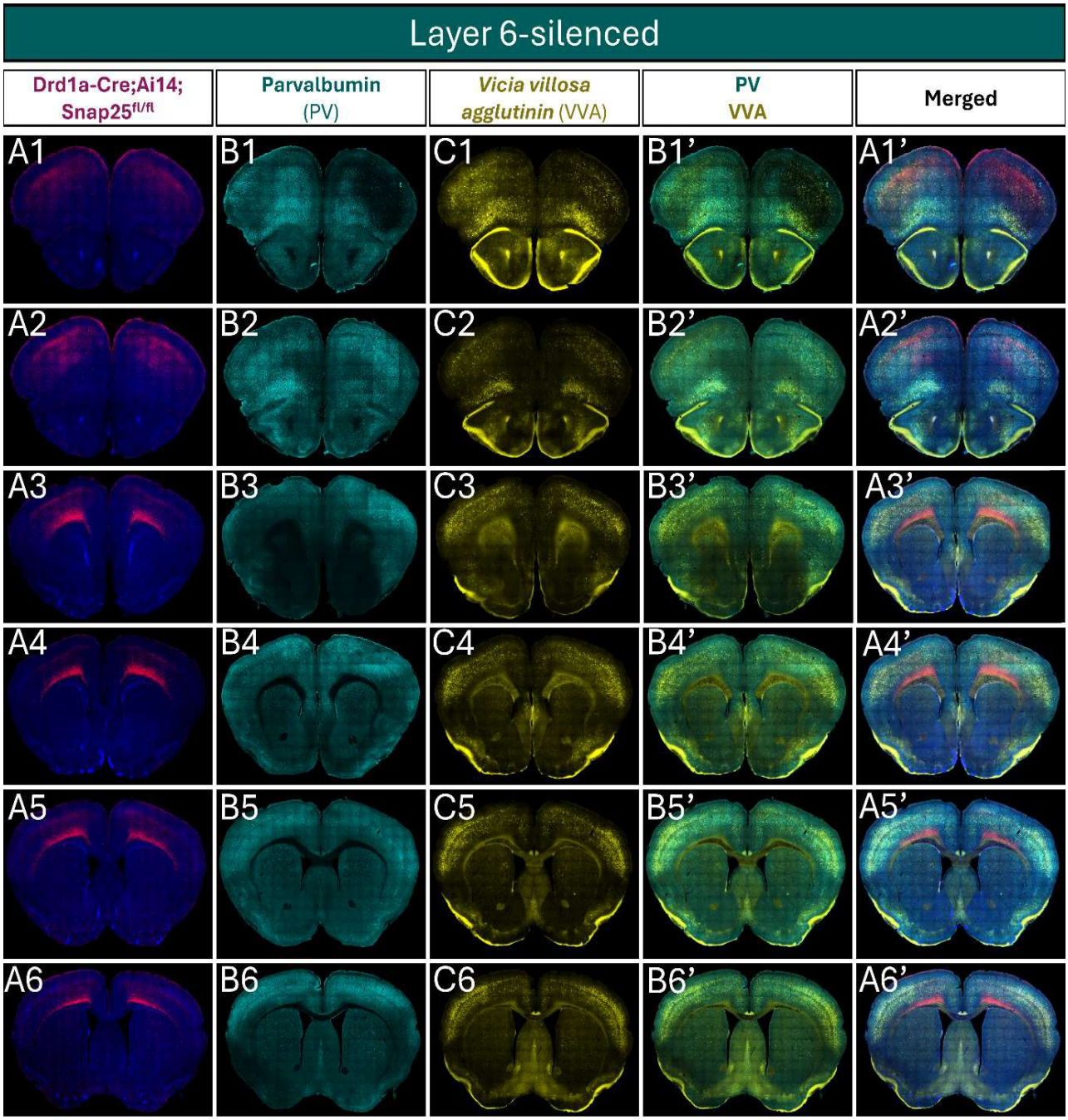
4.4. The effects of chronically silencing a subset of layer 6 projection neurons on GABAergic interneurons in the adult brain

4.4.1. Mapping the brain-wide distribution of Drd1a-Cre+ neurons, PV interneurons, and the perineuronal nets in the *Snap25* cKO mice

It has been demonstrated that conditional deletion of *Snap25* results in progressive neurodegeneration and axon terminal fragmentation of Rbp4-Cre+ neurons (Hoerder-Suabedissen et al. 2019). I aimed to determine whether the same genetic manipulation of Drd1a-Cre+ neurons resulted in similar neurodegenerative events in the adult layer 6-silenced brain. Qualitative analysis of the red fibres of *Drd1a-Cre;Ai14;Snap25*$^{fl/fl}$ corticothalamic neurons along the rostrocaudal axis revealed no signs of degeneration and/or fragmentation at 12 weeks of age in the *Snap25* cKO mice (Figure 4.19. A1-A12, A1'-A12'). Given that the conditional deletion of *Snap25* did not affect the long-range projections of Drd1a-Cre+ neurons, any effects on GABAergic interneurons are likely due to the chronic silencing of layer 6 neurons rather than neurodegenerative processes.

After establishing the distribution of the axonal projections of Drd1a-Cre+ neurons, I documented the brain-wide distribution of parvalbumin interneurons as well as the VVA-labelled perineuronal nets at 12 weeks of age in the *Drd1a-Cre;Ai14;Snap25*$^{fl/fl}$ mice. In the neocortex, parvalbumin interneurons and the PNNs were particularly enriched in the ventral and dorsal parts of the anterior cingulate area (ACAv, ACAd), the barrel field of the primary somatosensory, and the supplemental somatosensory area (SSt) (Figure 4.19. B1-B6, C1-C6, B1'-B6', A1'-A6'). In posterior brain regions, PV interneurons were also abundant in the ventral and dorsal parts of the retrosplenial area (RSPv, RSPd), the posterior parietal association area (PTLp), the anteromedial (VISam), anterolateral (VISal), and primary visual area (VISp) (Figure 4.19. B7-B12, C7-C12, B7'-B12', C7'-C12'). The abundance of PV neurons was moderate in the primary and secondary motor areas (M1, M2) as well as in the dorsal auditory area (AUDd), the ventral auditory area (AUDv), and the primary auditory

cortex (AUDp). The abundance of parvalbumin neurons and the PNNs was low to very low in the temporal association areas (TEa), the ectorhinal area (ECT), the perirhinal area (PERI), and the entorhinal area (ENTI) (Figure 4.19. B7-B12, C7-C12, B7'-B12', C7'-C12'). The distribution of the PNNs followed that of the PV interneurons. PNNs were highly abundant in areas with a high concentration of PV interneurons, including the ACAd, ACAv, SSp, SSt, or Visp (Figure 4.19. B7-B12, C7-C12, B7'-B12', C7'-C12'). Of the subcortical regions, PV interneurons and PNNs were significantly concentrated in the medial septal nucleus (MS) and the diagonal band nucleus (DNB) (Figure 4.19. B5-B6, C5-C6, B5'-B6', C5'-C6'). Despite the scarcity of PV neurons in the thalamus, the TRN had the highest concentration of PV and PNNs of all subcortical nuclei. The caudoputamen, the GPe, the CA3, CA1, and the dentate gyrus of the hippocampus contained a considerable number of PV interneurons (Figure 4.19. B7-B9, C7-C9, B7'-B9', C7'-C9'). PV neurons and PNNs were also prevalent in the zona incerta (ZI), the basolateral amygdala (BLA), and the anterior pretectal nucleus (APN) (Figure 4.19. B10-B12, C10-C12, B10'-B12', C10'-C12').


Layer 6-silenced
Drd1a-Cre;Ai14; Snap25fl/fl
Parvalbumin (PV)
Vicia villosa agglutinin (VVA)
PV VVA
Merged
A1
B1
C1
B1'
A1'
A2
B2
C2
B2'
A2'
A3
B3
C3
B3'
A3'
A4
B4
C4
B4'
A4'
A5
B5
C5
B5'
A5'
A6
B6
C6
B6'
A6'

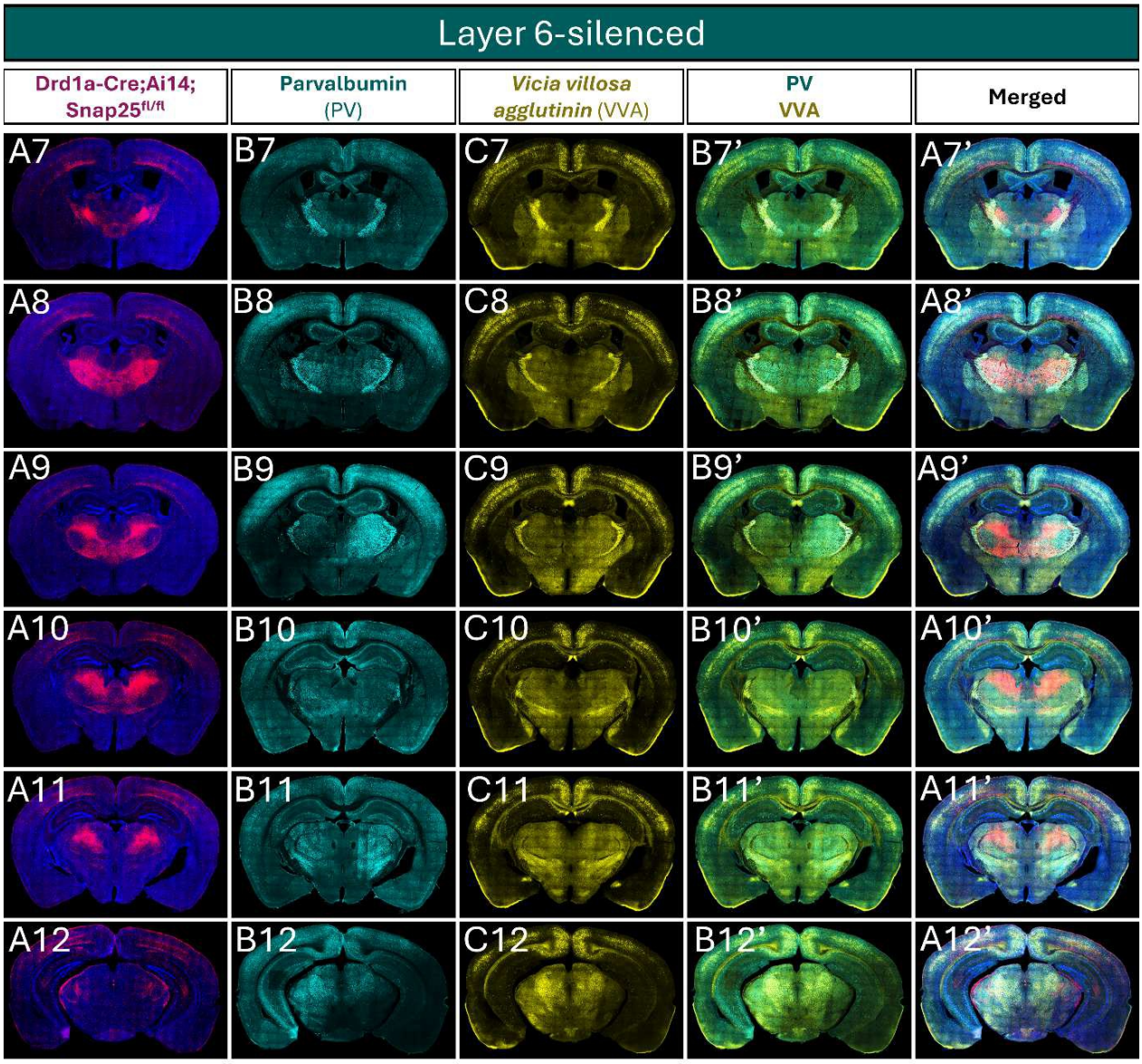


Figure 4.19. Brain-wide mapping of the long-range projections of Drd1a-Cre+ corticothalamic neurons as well as the distribution of parvalbumin interneurons and the perineuronal nets in the adult *Drd1a-Cre;Ai14;Snap25*$^{fl/fl}$ mice. (A1-A12) Red fibres of the silenced Drd1a-Cre+ neurons traced along the rostrocaudal axis in the *Drd1a-Cre;Ai14;Snap25*$^{fl/fl}$ mice at 12 weeks of age. Note the dense innervation in the higher-order thalamic nuclei, including the lateral posterior nucleus, the posterior complex of the thalamus, and the ventral anterior-lateral complex of the thalamus (A7-A11, A7'-A11'). Spatial distribution of parvalbumin-immunoreactive neurons in cyan along the rostrocaudal axis in the *Drd1a-Cre;Ai14;Snap25*$^{fl/fl}$ mice (B1-B6, B7-B12). Brain-wide distribution of the perineuronal nets visualised by *Vicia villosa* agglutinin in the *Drd1a-Cre;Ai14;Snap25*$^{fl/fl}$ mice (C1-C6, C7-C12). Note the high abundance of perineuronal nets in the barrel field of the primary somatosensory cortex and the supplemental somatosensory cortex (C7-C11). Merged spinning-disk confocal images showing the brain-wide distribution of the axonal projections of Drd1a-Cre+ neurons, parvalbumin-immunoreactive neurons, and *Vicia villosa* agglutinin-labelled perineuronal nets in the *Drd1a-Cre;Ai14;Snap25*$^{fl/fl}$ mice (A1'-A6', A7'-A12').

4.4.2. Regional and laminar differences in the number of Drd1a-Cre+ projection neurons in different subdivisions of the primary somatosensory cortex

The *Snap25* cKO mice exhibit a significant reduction in the number of Rbp4-Cre+ neurons by the time they are eight months old, whereas the Drd1a-Cre-silenced mice do not exhibit cell loss at such an age (Hoerder-Suabedissen et al. 2019). To determine whether the conditional ablation of *Snap25* affected Drd1a-Cre+ neurons well before eight months of age, I established the developmental trajectory of the silenced Drd1a-Cre+ neurons from P21 to 12 weeks of age. The laminar density of Drd1a-Cre+ neurons did not differ significantly in any cortical layers in S1 in the *Drd1a-Cre;Ai14;Snap25$^{fl/fl}$* mice from development to adulthood (L6a, p=0.9867; L6b, p=0.4175; two-way ANOVA with Šídák's multiple comparisons test) (Figure 4.20. A, B). Similarly, there was no discernible difference in S1 in the total density of Drd1a-Cre+ neurons between P21 and 12 weeks of age (p=0.8152, t-test with Welch's correction) (Figure 4.20. C, D1, D1'). These findings demonstrate that the Drd1a-Cre+-silenced neurons do not undergo apoptosis when AP-dependent neurotransmitter release from layer 6 is chronically abolished, as both the overall density and the laminar distribution of Drd1a-Cre+ neurons remain unchanged between P21 and 12 weeks of age (Figure 4.20. B, C). The results agree with (Hoerder-Suabedissen et al. 2019).

After establishing the lack of apoptosis in the *Drd1a-Cre;Ai14;Snap25$^{fl/fl}$* mice in S1, I aimed to quantify the number of Cre-expressing cells in different subregions of S1. The Drd1a-Cre+ transgenic strain exhibits apparent variations in the number of tdTomato-expressing cells across the lower limb (S1LL), upper limb (S1UL), barrel field (S1BF), and supplemental somatosensory area (SS). Considering that the shift in the density of Cre+ neurons appears to be the most prominent between S1LL and S1UL/S1BF, I selected these regions to quantify the change in the density of Drd1a-Cre+ neurons. Significant *layer* and *region* effects were detected by two-way ANOVA testing (p<0.0001), along with significant *interactions* between the two tested parameters (p<0.0001). Šídák's multiple comparisons test revealed that both layers 6a and 6b had significantly lower densities of Drd1a-Cre+

neurons at 12 weeks of age in S1UL/S1BF compared to S1LL in the *Snap25* cKO mice. S1UL/S1BF contained ~64% fewer Drd1a-Cre+ neurons in layer 6a, and ~42% fewer in layer 6b relative to S1LL in the *Drd1a-Cre;Ai14;Snap25*$^{fl/fl}$ mice (Figure 4.20. E, F) (layer 6a, $p<0.0001$; layer 6b, $p<0.0001$; two-way ANOVA with Šídák's multiple comparisons test). The laminar difference observed in the density of Drd1a-Cre+ neurons in layers 6a and 6b in S1UL/S1BF of the *Snap25* cKO mice was correlated with changes in the total density of Drd1a-Cre+ neurons in S1UL/S1BF. I found that the density of Drd1a-Cre+ neurons was ~56% lower in S1UL/S1BF compared to S1LL at 12 weeks of age in the *Drd1a-Cre;Ai14;Snap25*$^{fl/fl}$ mice ($p=0.0011$, unpaired t-test with Welch's correction) (Figure 4.20. G, H1, H1').

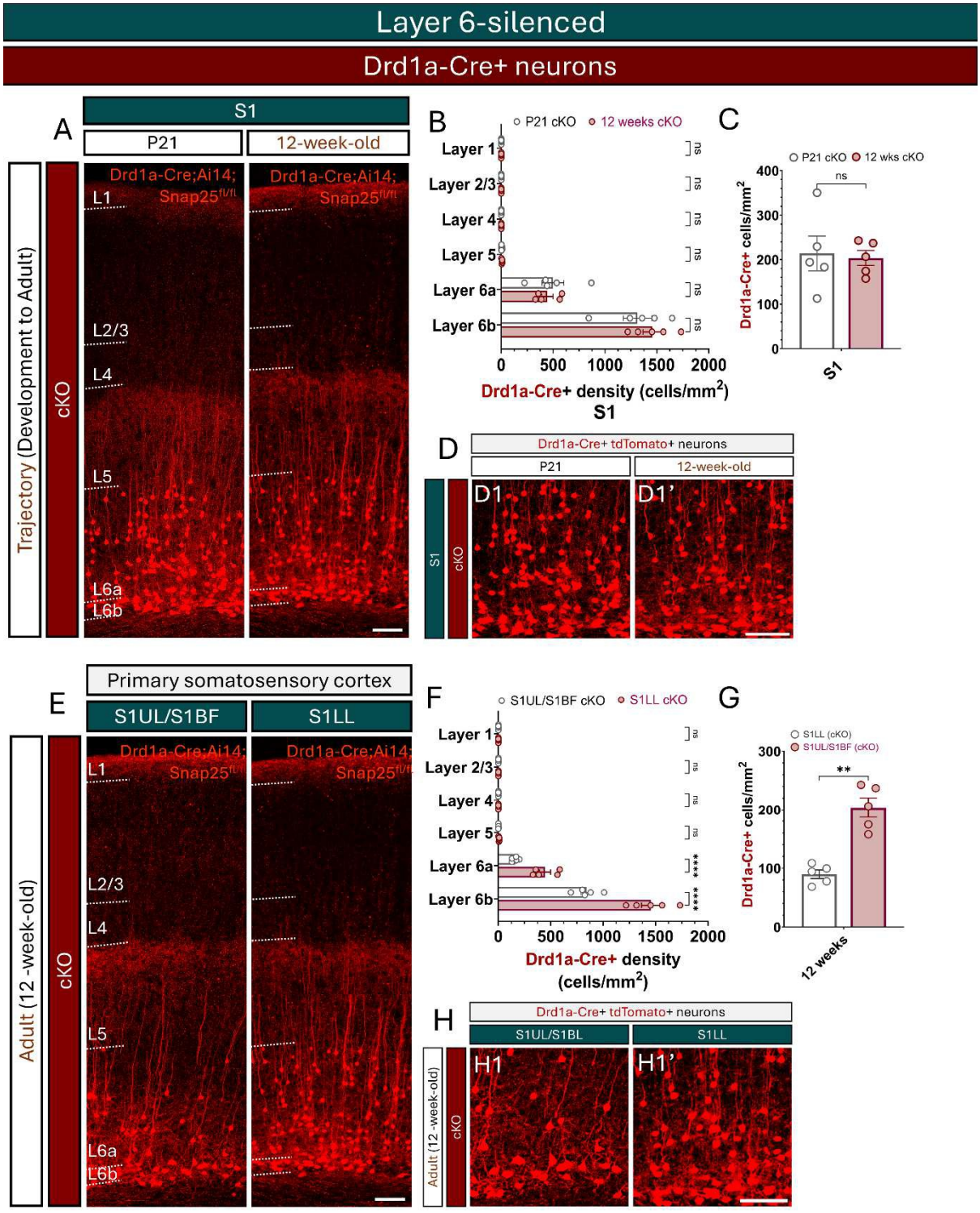


Figure 4.20. Chronic silencing of subsets of layer 6 neurons does not cause cell death in Drd1a-Cre+ neurons, which exhibit regional variations across distinct fields of the primary somatosensory cortex. (A) Tiled z-stack images of S1 showing *Drd1a-Cre;Ai14;Snap25*$^{fl/fl}$ neurons in the juvenile and the adult S1 region. (B) Developmental profile of the laminar distribution of the silenced Drd1a-Cre+ neurons at P21 and 12 weeks in S1 of the *Snap25* cKO mice. (C) Total density of

Drd1a-Cre+ neurons in S1 from development to adulthood. (D) Representative examples of *Drd1a-Cre;Ai14;Snap25*$^{fl/fl}$ neurons in S1 at P21 (D1) and 12 weeks of age (D1'). Tile-scan images of the lower and the upper limb/barrel field of S1 illustrating *Drd1a-Cre;Ai14;Snap25*$^{fl/fl}$ neurons at 12 weeks of age in the *Snap25* cKO mice (E). (F) Laminar density of Drd1a-Cre+ neurons in S1UL/S1BF relative to S1LL in the *Snap25* cKO mice. (G) Bar graphs illustrating the total density of *Drd1a-Cre;Ai14;Snap25*$^{fl/fl}$ neurons in S1UL/S1BF and S1LL of the *Snap25* cKO mice. (H) Representative examples of the silenced Drd1a-Cre+ neurons in layers 6a and 6b in S1LL (H1) and S1UL/S1BF (H1') at 12 weeks in the mutant mice. Scale bars = 100 µm.

4.4.3. The effects of silencing Drd1a-Cre+ neurons on parvalbumin interneurons and the perineuronal nets in the adult neocortex

4.4.3.1. The genetic silencing of Drd1a-Cre+ neurons alters the density of those parvalbumin interneurons which are surrounded by perineuronal nets in layer 5 of M1

In the following sections, I have investigated the *long*-term effects of the conditional deletion of *Snap25* from Drd1a-Cre+ neurons on PV interneurons in the adult neocortex. When examining the anterior cingulate area, I found no significant differences in the density of PV+ neurons (p=0.2646) and PNNs (p=0.1871, unpaired t-test with Welch's correction) between the control and *Drd1a-Cre,Ai14;Snap25*$^{fl/fl}$ mice at 12 weeks of age (Figure 4.21. A, B, C). After distinguishing between PV+ neurons with and without PNNs, I found a significant *cell type* but no *genotype* effect (p<0.0001, p=0.4011, two-way ANOVA with Šídák's multiple comparisons test). No significant alterations were discovered in the density of PV+ VVA+, PV+ VVA-, PV- VVA+ cells in the ACA of the *Snap25* cKO mice compared to control mice after *post*-hoc testing (Figure 4.21. D).

I then set out to investigate whether *motor* areas were affected differently by the genetic silencing of layer 6 neurons than *association* areas. In M1, the total density of PV+ interneurons and VVA+ cells did not differ significantly between the control and *Snap25* cKO mice at 12 weeks of age (Figure 4.21. E, F, G). However, when differentiating PV+ neurons from those lacking PNNs, I found a marked reduction in the density of PV+ VVA+ neurons in M1 of the Drd1a-Cre+-silenced mice relative to control mice (Figure 4.21. H) (p=0.0187, two-way ANOVA with Šídák's multiple comparisons test).

These findings imply a region-specific effect on PV interneurons and PNNs, showing variations between motor and prefrontal regions.

Following the density analysis, I aimed to determine whether the laminar positioning of PV+ and VVA+ cells was altered in M1. While no significant alterations were identified in the density of VVA+ and PV- VVA+ neurons (Figure 4.21. L, K), the decreased total cell density of PV+ VVA+ in M1 correlated with changes in their laminar distribution. Two-way ANOVA testing highlighted a significant *layer* and *genotype* effect ($p<0.0001$, $p=0.0058$), but there was no *interaction* between layer and genotype ($p=0857$). Šídák's multiple comparisons tests showed a ~37% reduction in the density of PV+ VVA+ neurons in layer 5 of M1 in the *Drd1a-Cre,Ai14;Snap25*$^{fl/fl}$ mice relative to the control mice (Figure 4.21. J) ($p=0.0036$). Other PV+ neurons remained unaltered (Figure 4.21. I, K). These results demonstrate that the chronic silencing of layer 6 neurons selectively alters the distribution of PV+ neurons in the adjacent cortical layer (L5), which are synaptically connected to Drd1a-Cre+ neurons in layer 6b (Zolnik et al. 2020; Zolnik et al. 2024).

Finally, I established the developmental trajectory of PV+ interneurons between P21 and 12 weeks of age. Neither the control nor the *Drd1a-Cre,Ai14;Snap25*$^{fl/fl}$ mice displayed significant changes in the laminar arrangement of PV+ interneurons (Figure 4.21. N, O). These results imply that the laminar organisation of PV+ interneurons remains stable after developmental cell death, and the developmental profile of PV+ interneurons in the mutant mice matches that of the control mice.

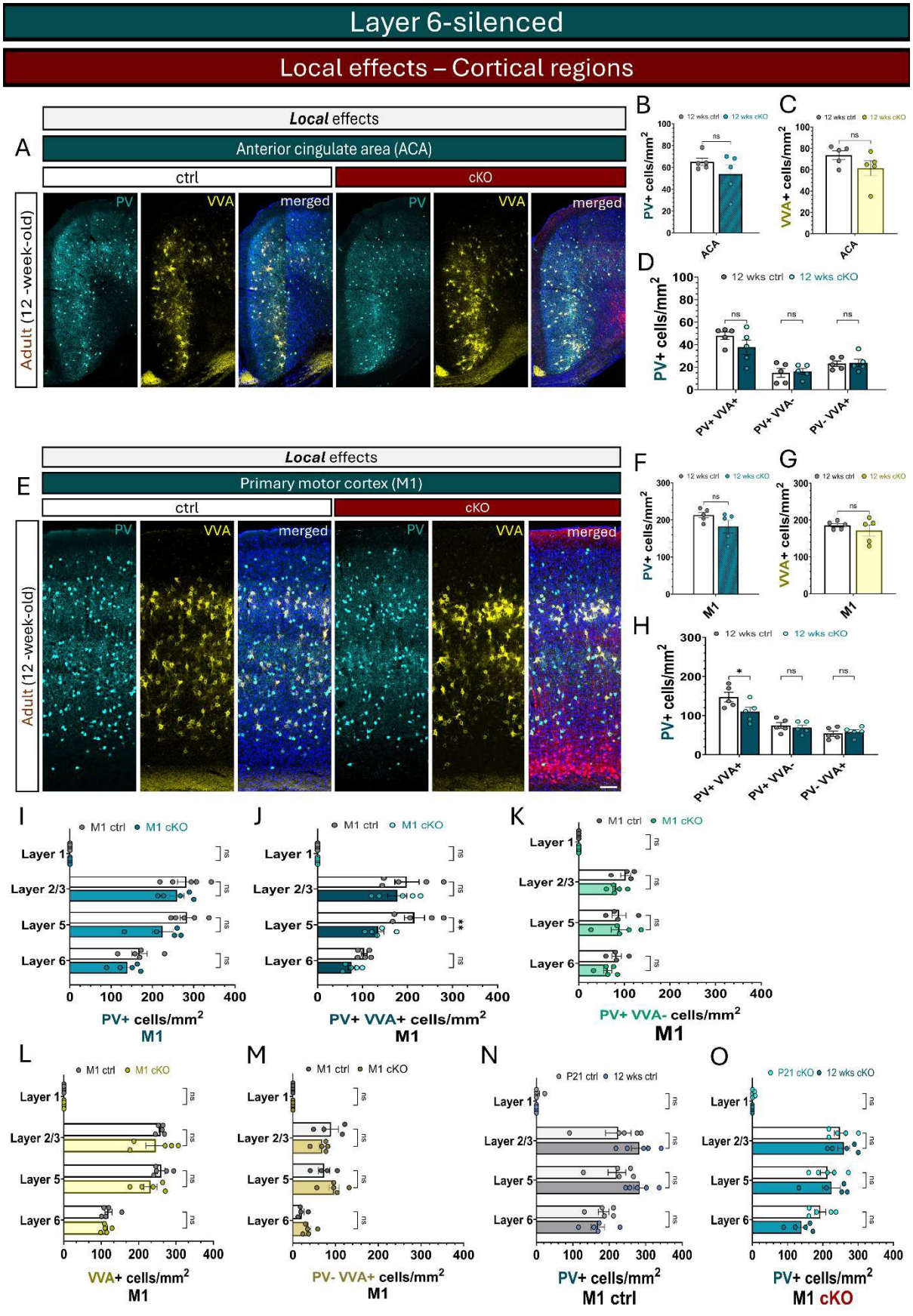

Layer 6-silenced
Local effects – Cortical regions
A
Local effects
Anterior cingulate area (ACA)
ctrl
cKO
Adult (12 -week-old)
PV
VVA
merged
B
C
D
12 wks ctrl
12 wks cKO
PV+ cells/mm2
VVA+ cells/mm2
ACA
PV+ VVA+
PV+ VVA-
PV- VVA+
E
Primary motor cortex (M1)
F
G
H
M1
I
J
K
M1 ctrl
M1 cKO
Layer 1
Layer 2/3
Layer 5
Layer 6
PV+ cells/mm2
M1
PV+ VVA+ cells/mm2
PV+ VVA- cells/mm2
L
M
N
O
P21 ctrl
12 wks ctrl
P21 cKO
12 wks cKO
VVA+ cells/mm2
PV- VVA+ cells/mm2
M1 ctrl
M1 cKO

Figure 4.21. The genetic silencing of Drd1a-Cre+ neurons selectively affects the distribution of layer 5 PV+ interneurons in the primary motor cortex. (A) Tile-scan of the anterior cingulate area illustrating parvalbumin interneurons in cyan and *Vicia villosa* agglutinin-labelled perineuronal nets in yellow in the control and *Snap25* cKO mice. (B, C) Quantification of the cell density of parvalbumin-immunopositive neurons (B) and *Vicia villosa agglutinin*-positive cells in the ACA at 12 weeks of age. (D) Quantification of the cell density of parvalbumin-immunoreactive neurons in the ACA. (E) Tile-scan images of M1 illustrating parvalbumin interneurons in cyan and *Vicia villosa* agglutinin+ cells in yellow in the control and *Snap25* cKO mice at 12 weeks of age. (F, G) Bar graphs showing the mean cell density of PV+ and VVA+ in M1. (H) Quantification of the cell density of parvalbumin-immunoreactive neurons with and without perineuronal nets in M1 at 12 weeks of age (H). Quantification of the laminar density of parvalbumin interneurons in M1 in control and *Drd1a-Cre,Ai14;Snap25*$^{fl/fl}$ mice (I). Quantification of the laminar density of parvalbumin interneurons with perineuronal nets in M1 in control and *Drd1a-Cre,Ai14;Snap25*$^{fl/fl}$ mice. (J) Quantification of the laminar density of parvalbumin interneurons devoid of perineuronal nets in M1 in control and *Drd1a-Cre,Ai14;Snap25*$^{fl/fl}$ mice (K). Quantification of the laminar density of perineuronal nets in M1. (L) Quantification of the laminar density of *Vicia villosa agglutinin*-positive cells, which do not co-localise with parvalbumin interneurons in M1 (M). Developmental trajectory of the laminar distribution of parvalbumin-immunopositive neurons between P21 and 12 weeks of age in control and *Drd1a-Cre,Ai14;Snap25*$^{fl/fl}$ mice (N, O). Scale bar = 100 µm.

4.4.3.2. Distinct subdivisions of S1 exhibit changes in perineuronal net density in layer 4 upon the chronic silencing of layer 6 neurons

Previously, I have demonstrated that the S1UL/S1BF contained fewer Drd1a-Cre+ neurons than S1LL in layer 6a and layer 6b. Since the density of Drd1a-Cre+ neurons varies greatly by region and layer, the number of silenced Drd1a-Cre+ neurons would also vary depending on which region or layer is being silenced. For instance, regional differences in the number of Drd1a-Cre+ neurons would lead to more silenced Drd1a-Cre+ neurons in S1LL, where the abundance of Drd1a-Cre+ neurons is *high*. To determine whether A) the number of 'silenced' Drd1a-Cre+ neurons matters and B) whether areas with *high* versus *low* numbers of silenced Drd1a-Cre+ neurons influence PV interneurons differently, I assessed PV+ density and laminar allocation in S1UL/S1BF and S1LL.

First, I examined the total cell density of PV+ interneurons and the PNNs. No significant alterations were observed in the density of PV+ and VVA+ cells between the control and the *Drd1a-Cre,Ai14;Snap25*$^{fl/fl}$ mice in S1LL and S1UL/S1BF either at 12 weeks of age (Figure 4.22. A, B, C, D). When comparing the density of PV+ interneurons between S1LL and S1UL/S1BF, there was a

significant *region* (p=0.0100) but no *genotype* effect (p=0.2393). I found that S1UL/S1BF had a lower density of PV+ neurons in the mutant mice (Figure 4.22. C) (p=0.0387, two-way ANOVA with uncorrected Fisher's LSD test). Similarly, there was a significant *region* effect on the density of PNNs in S1UL/S1BF compared to S1LL (Figure 4.22. D) (p=0.0031, two-way ANOVA with uncorrected Fisher's LSD test). There was an increased density of PNNs in S1UL/S1BF relative to S1LL in the *Snap25* cKO mice (p=0.0062). Interestingly, no such differences were detected between S1LL and S1UL/S1BF in the control mice. These results suggest that the *Snap25* cKO mice might have altered levels of PNNs in different subdivisions of S1. Next, I investigated whether PV+ interneurons that are either ensheathed by or lacking PNNs were affected differently by the genetic silencing of Drd1a-Cre+ neurons. Although no significant differences were observed in S1LL (Figure 4.22. E), S1UL/S1BF revealed a significant increase in the density of PV- VVA+ cells at 12 weeks of age between the control and the *Drd1a-Cre,Ai14;Snap25*$^{fl/fl}$ mice (Figure 4.22. F) (p=0.0321, two-way ANOVA with Šídák's multiple comparisons test). Based on these data, it appears that the perineuronal nets that do not surround PV+ neurons are selectively altered following the genetic silencing of Drd1a-Cre+ neurons.

Next, I investigated the laminar arrangement of PV+ interneurons. PV+, PV+ VVA+, and PV+ VVA- cell density did not differ significantly in any cortical layer between the control and *Drd1a-Cre;Ai14;Snap25*$^{fl/fl}$ mice at 12 weeks of age in S1LL and S1UL/S1BF either (Figure 4.22. G, G', I, I', K, K'). The lack of influence on their laminar positioning suggests that the quantity of Drd1a-Cre+ neurons that are silenced is irrelevant for the PV+ cells. This is supported by the observation that cortical regions, such as S1LL and M1, that have a high density of Drd1a-Cre+ neurons do not seem to have a greater effect on PV+ interneurons. It follows that there is no correlation between the effect size and the quantity of Drd1a-Cre+ neurons that have been silenced. My next question was whether the laminar arrangement of PNNs appears to be more affected by cortical regions with a high density of Drd1a-Cre+ neurons, such as S1LL. Two-way ANOVA testing identified a significant *layer* effect (p<0.0001) with a *significant* interaction (p=0.0102) between *layer* and *genotype* on the density of

PNNs but not on PV+ density. Šídák's multiple comparisons test revealed a ~18% increase in the density of VVA+ cells in layer 4 of S1LL in the *Snap25* cKO mice relative to control mice at 12 weeks of age (Figure 4.22. H) (p=0.0163, two-way ANOVA with Šídák's multiple comparisons test). No such alteration was detected in S1UL/S1BF (Figure 4.22. H').

However, significant *layer* (p<0.0001) and *genotype* (p=0.0015) effects were detected by two-way ANOVA testing in S1UL/S1BF on the density of PV- VVA+ cells. Šídák's *post*-hoc tests found a prominent increase of ~27% in the density of PV- VVA+ neurons in layer 4 exclusively in S1UL/S1BF in the *Drd1a-Cre;Ai14;Snap25*$^{fl/fl}$ mice compared to control mice (Figure 4.22. J') (p=0.0090). Interestingly, chronic silencing of Drd1a-Cre+ neurons impacted PNNs in layer 4 solely, both in S1LL and S1UL/S1BF. The increase in the laminar density of PV- VVA+ neurons in layer 4 in S1UL/S1BF was correlated with an increase in the total density of PV- VVA+ neurons in S1UL/S1BF. This may indicate the presence of two distinct mechanisms in S1LL versus S1UL/S1BF: 1) *redistribution* of PNNs in S1LL, 2) *upregulation* of the ECM proteins in S1UL/S1BF to compensate for the reduced excitatory drive from layer 6 neurons.

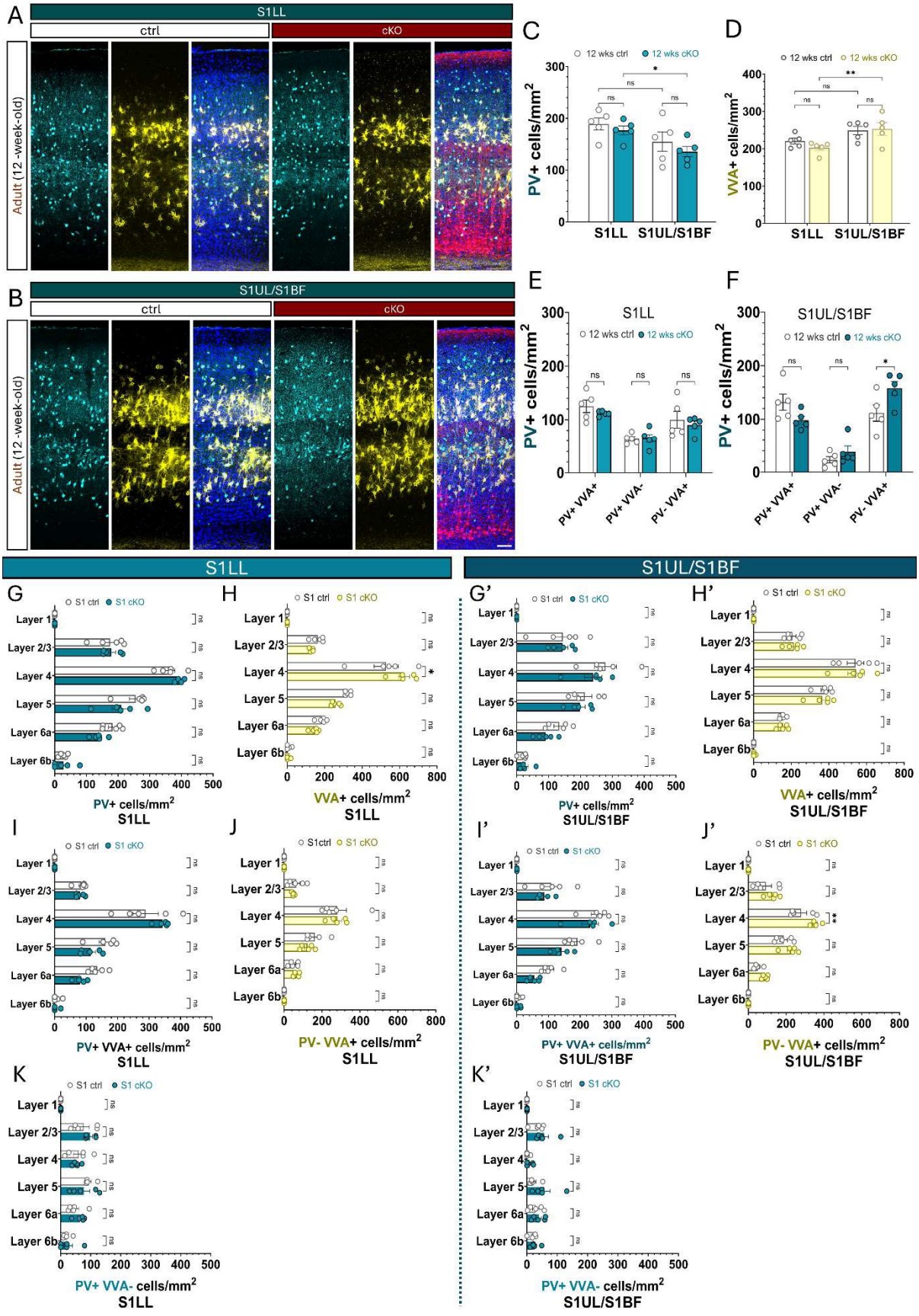

A
S1LL
ctrl
cKO
Adult (12 -week-old)
B
S1UL/S1BF
ctrl
cKO
Adult (12 -week-old)
C
12 wks ctrl
12 wks cKO
PV+ cells/mm2
S1LL
S1UL/S1BF
D
12 wks ctrl
12 wks cKO
VVA+ cells/mm2
S1LL
S1UL/S1BF
E
S1LL
12 wks ctrl
12 wks cKO
PV+ cells/mm2
PV+ VVA+
PV+ VVA-
PV- VVA+
F
S1UL/S1BF
12 wks ctrl
12 wks cKO
PV+ cells/mm2
PV+ VVA+
PV+ VVA-
PV- VVA+
S1LL
S1UL/S1BF
G
S1 ctrl
S1 cKO
Layer 1
Layer 2/3
Layer 4
Layer 5
Layer 6a
Layer 6b
PV+ cells/mm2
S1LL
H
VVA+ cells/mm2
S1LL
G'
PV+ cells/mm2
S1UL/S1BF
H'
VVA+ cells/mm2
S1UL/S1BF
I
PV+ VVA+ cells/mm2
S1LL
J
PV- VVA+ cells/mm2
S1LL
I'
PV+ VVA+ cells/mm2
S1UL/S1BF
J'
PV- VVA+ cells/mm2
S1UL/S1BF
K
PV+ VVA- cells/mm2
S1LL
K'
PV+ VVA- cells/mm2
S1UL/S1BF

Figure 4.22. Different subfields of S1 display changes in perineuronal net density in layer 4 following *Snap25* deletion from a subset of layer 6 neurons. (A) Tiled z-stack images of the lower limb of the primary somatosensory cortex (S1LL), where the density of silenced Drd1a-Cre+ neurons is high. The cyan channel indicates parvalbumin-immunoreactive neurons, while the yellow channel shows *Vicia villosa* agglutinin-labelled perineuronal nets in control and *Drd1a-Cre,Ai14;Snap25*$^{fl/fl}$ mice. (B) Tiled z-stack images of the upper limb and the barrel field of S1 (S1UL/S1BF), where the density of silenced Drd1a-Cre+ neurons is low. (C, D) Bar graphs showing the density of parvalbumin-immunoreactive neurons and VVA+ cells in S1LL and S1UL/S1BF between control and *Drd1a-Cre,Ai14;Snap25*$^{fl/fl}$ mice. (E, F) Bar graphs representing parvalbumin-immunoreactive neurons with and without PNNs in S1 *dense* and S1 *sparse* at 12 weeks of age. Quantification of the laminar distribution of parvalbumin-immunopositive neurons (G, G') and the perineuronal nets (H, H') in S1LL and S1UL/S1BF at 12 weeks of age. Quantification of the laminar distribution of parvalbumin-immunopositive neurons ensheathed by PNNs in S1LL and S1UL/S1BF between control and *Drd1a-Cre,Ai14;Snap25*$^{fl/fl}$ mice (I, I'). Quantification of the laminar distribution of *Vicia villosa* agglutinin cells in S1LL and S1UL/S1BF, which do not ensheathe parvalbumin-immunopositive neurons (J, J'). Quantification of the laminar distribution of parvalbumin-immunopositive neurons that are devoid of perineuronal nets in S1LL and S1UL/S1BF between control and *Drd1a-Cre,Ai14;Snap25*$^{fl/fl}$ mice (K, K'). Scale bar = 100 μm.

4.4.4. The effects of silencing Drd1a-Cre+ neurons on neuropeptide-Y interneurons in the adult neocortex

4.4.4.1. The genetic silencing of Drd1a-Cre+ neurons does not have a long-term effect on neuropeptide-Y neurons in the adult prefrontal and secondary motor cortex

This section of the chapter centres around cortical NPY+ interneurons. My objectives were to: 1) compare the long-term effects of silencing a subset of layer 6 neurons on NPY+ with those of PV+ interneurons; and 2) investigate whether effects specific to specific cell types and layers may be identified in the neocortex. I postulated that the genetic silencing of Drd1a-Cre+ neurons would influence NPY+ and PV+ interneurons in a layer-and cell-type-specific manner, as they occupy distinct cortical layers and have differential innervation patterns. While the processes of NPY+ neurons are primarily restricted to layer 1 and the top band of layer 2 (Torigoe et al. 2016; Llorca and Deogracias 2022), the terminals of PV+ interneurons are not only localised within their own layer but also show cross-laminar innervation patterns (Scheuer et al. 2024). The morphoelectric and transcriptomic classification of cortical GABAergic neurons conducted by the Allen Brain Institute has revealed that one key characteristic that sets apart various GABAergic met-types is their layer-specific axon innervation pattern (Gouwens et al. 2020). It has also been shown that the majority of transcriptome types (t-types) have distinct laminar locations in the visual cortex and display identical transcriptomic, morphological, and electrophysiological characteristics (Gouwens et al. 2020). The differential laminar innervation pattern of interneurons may therefore determine how a particular cell type reacts to changes in excitatory inputs.

First, I examined NPY+ neuron density in the association (ACA) as well as the motor regions (M2, M1) to see if their responses to the reduced excitatory drive from layer 6 neurons differed regionally. There was only a significant *region* ($p=0.0015$) but no *genotype* effect ($p=0.9445$) on NPY+ density. Thus, the mean cell density of NPY+ neurons did not differ significantly between the control

and *Drd1a-Cre,Ai14;Snap25*$^{fl/fl}$ mice in the ACA and M2 at 12 weeks of age, as shown by two-way ANOVA Šídák's *post*-hoc tests (Figure 4.23. A, B).

Next, I investigated the developmental trajectory of NPY+ neurons to determine whether their total cell number changes from development to adulthood. In the control mice, neither the ACA nor the M2 exhibited significant alterations in NPY+ cell density from P21 to 12 weeks of age (Figure 4.23. C). However, two-way ANOVA revealed a significant *region* (p=0.0018) and *age* effect (p=0.0003), without interaction (p=0.0891), on the density of NPY+ neurons in the *Snap25* cKO mice. Šídák's *post*-hoc tests detected a significant decline in the cell density of NPY+ neurons from P21 to 12 weeks in M2 relative to control mice (Figure 4.23. D) (p=0.0007). The distinct developmental course from development to adulthood in the mutant mice was anticipated, given the greater density of NPY+ interneurons in the *Snap25* cKO animals in M2 at P21. No such alterations in the developmental trajectory of NPY+ neurons were detected in ACA of the *Snap25* cKO mice (Figure 4.23. D).

Following the density and trajectory analysis, I looked for potential morphological alterations in NPY+ neurons. Morphometric investigation of NPY+ neurons confirmed the density results, as there were no significant variations in the soma area, perimeter, circularity, and roundness of NPY+ neurons between the control and *Snap25* cKO mice in the adult ACA (Figure 4.23. E, F). Modifications were only detected in the soma solidity of NPY+ neurons in the mutant mice at 12 weeks of age (p=0.0383, unpaired Mann-Whitney test); however, it remains to be seen whether this change has functional significance. The absence of variations in NYP+ neuron density and soma size in M2 further supports the observation that the Drd1a-Cre+ neurons do not control NPY+ neuron numbers in ACA and M2 (Figure 4.23. G, H).

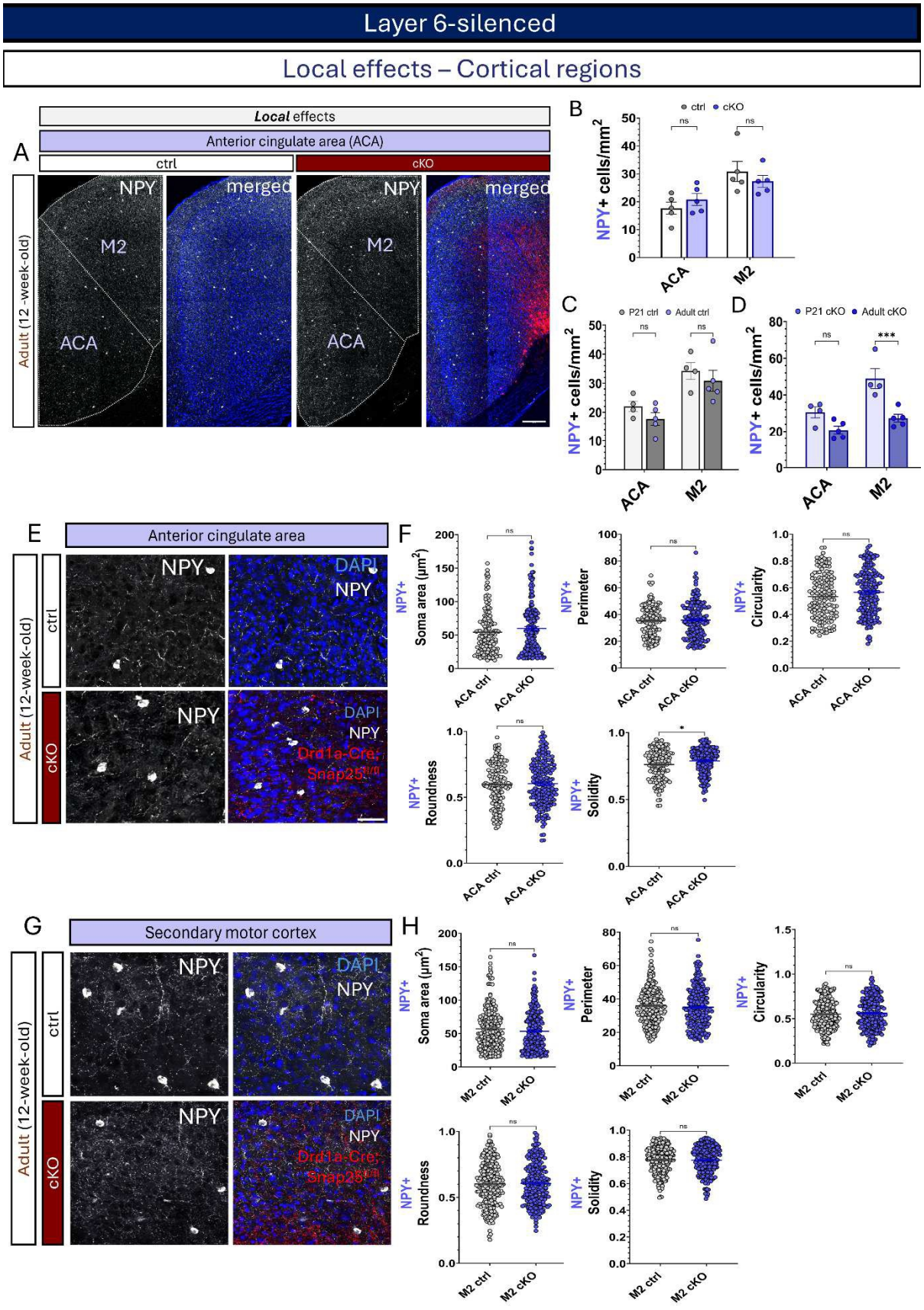

Layer 6-silenced
Local effects – Cortical regions
A
Local effects
Anterior cingulate area (ACA)
ctrl
cKO
Adult (12 -week-old)
NPY
merged
M2
ACA
B
ctrl
cKO
NPY+ cells/mm2
ns
ACA
M2
C
P21 ctrl
Adult ctrl
D
P21 cKO
Adult cKO
***
E
Anterior cingulate area
DAPI
Drd1a-Cre;
Snap25fl/fl
F
NPY+
Soma area (µm2)
Perimeter
Circularity
Roundness
Solidity
ACA ctrl
ACA cKO
G
Secondary motor cortex
H
M2 ctrl
M2 cKO

Figure 4.23. Neuropeptide-Y interneurons in the anterior cingulate and secondary motor cortex are not dependent on AP-dependent neurotransmitter release from Drd1a-Cre+ neurons in the adult brain. (A) Tile-scans of the anterior cingulate area and the secondary motor cortex illustrating neuropeptide-Y-immunoreactive neurons in grey at 12 weeks of age in control and *Drd1a-Cre+*-silenced mice. (B) Quantification of neuropeptide-Y immunopositive neurons in control and *Drd1a-Cre+*-silenced mice in ACA and M2. (C) Bar graphs of the developmental trajectory of neuropeptide-Y immunopositive neurons in control mice. (D) Bar graphs of the developmental trajectory of neuropeptide-Y immunopositive neurons from P21 to 12 weeks in the *Snap25* cKO mice. (E, G) Examples of neuropeptide-Y neurons in ACA and M2 at 12 weeks of age in control and *Drd1a-Cre+*-silenced mice. Merged images showing tdTomato+ fibres of the silenced Drd1a-Cre+ neurons in the *Snap25* cKO mice. (F, H) Scatter plots representing soma measurements of neuropeptide-Y interneurons in the ACA and M2.

4.4.4.2. Neuropeptide-Y interneurons display density and laminar changes in layer 2/3 of the primary motor and somatosensory cortices from development to adulthood

To further explore the long-term effects on cortical NPY+ interneurons, I assessed their spatial and laminar distribution in M1 and S1 after development. I found no significant modifications in the density of NPY+ neurons in the layer 6-silenced mice compared to control mice in M1 and S1 at 12 weeks of age (Figure 4.24. A, B, C). When analysing how the total cell density of NPY+ neurons changed from development to adulthood, two-way ANOVA testing identified a significant *age* effect but no *region* effect, with no *interaction* between the two parameters in both control (p=0.5045) and mutant mice (p=0.3919). However, *age* accounted for 60.97% of the total variance (p<0.0001) in the cKO mice, whereas it was only 30.35% in the control mice (p=0.0138). Šídák's *post*-hoc testing only revealed notable reductions in NPY+ mean cell density between P21 and 3 months in M1 and S1 in the *Drd1a-Cre,Ai14;Snap25$^{fl/fl}$* mice. Specifically, there was a ~30% decrease in NPY+ cell density in M1, and a ~22% decrease in S1 from development to adulthood in the *Drd1a-Cre,Ai14;Snap25$^{fl/fl}$* mice (Figure 4.24. D, E) (M1, p=0.0012; S1, p=0.0164). In S1, the non-significant elevation in the cell counts of NPY+ interneurons in mutant S1 at P21 may contribute to the altered developmental trajectory. Conversely, in M1, the lack of a significant difference in NPY+ density between control and mutant mice at P21 may suggest that the observed variations in the mutant trajectory may be attributable to accelerated maturation rather than an inherent baseline discrepancy in cell nunber at this age.

After establishing their trajectory, I investigated whether their laminar positioning was altered over time. Only a significant *layer* ($p<0.0001$), but no *genotype* effect was shown by two-way ANOVA tests in M1 and S1. *Post*-hoc comparisons, therefore, did not find significant modifications in the laminar distribution of NPY+ interneurons between the control and *Drd1a-Cre+*-silenced mice in the adult M1 and S1 (Figure 4.24. F, G). It can be concluded that silencing layer 6 projection neurons has no long-term impact on the density of NPY+ neurons in layer 6b and does not result in a long-term rearrangement of the laminar positioning of NPY+ neurons in S1.

I continued investigating the long-term effects on the laminar profile of NPY+ interneurons from development to adulthood. Two-way ANOVA testing yielded a significant *layer* effect ($p<0.0001$) but no *age* effect in *control* mice (Figure 4.24. J, L) in both M1 ($p=0.1496$) and S1 ($p=0.7689$). However, it found a significant *layer* ($p<0.0001$) and *age* effect (M1, $p<0.0001$; S1, $p=0.0010$), which significantly interacted ($p=0.0055$), in the *Snap25* cKO mice in M1 as well as S1. Šídák's multiple comparisons test showed that the density of NPY+ neurons in layer 2/3 of M1 declined by ~34%, while the density of layer 6a NPY+ neurons decreased by ~40% from P21 to 12 weeks in the layer 6-silenced mice (Figure 4.24. H, K) (cKO, layer 2/3, $p<0.0001$; cKO, layer 6a, $p=0.0022$). No such alterations in layer 2/3 and layer 6a of M1 in control mice were seen from P21 to 12 weeks (Figure 4.24. H, J). Comparable to M1, S1 of the *Snap25* cKO mice also exhibited a notable decrease in the density of layer 2/3 neurons between P21 and 12 weeks (Figure 4.24. L, M) ($p<0.0001$, two-way ANOVA with Šídák's multiple comparisons test). Since *layer* accounts for over 60% of the total variance, the observed differences in layer 2/3 NPY+ neurons in mutant M1 and S1 are predominantly driven by *layer* and not *age*.

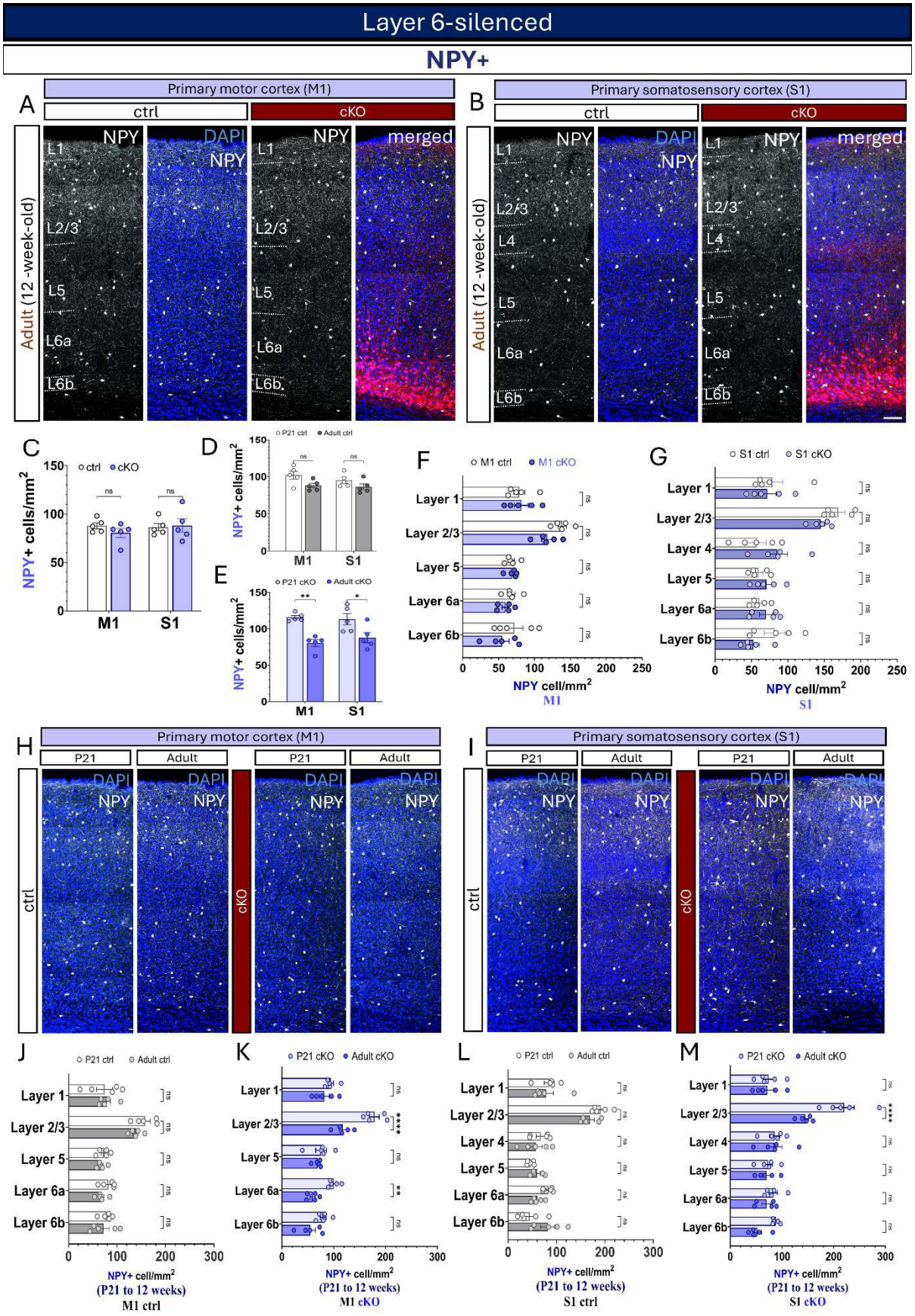

Layer 6-silenced
NPY+
A
Primary motor cortex (M1)
ctrl
cKO
Adult (12 -week-old)
NPY
DAPI
merged
L1
L2/3
L5
L6a
L6b
B
Primary somatosensory cortex (S1)
L4
C
NPY+ cells/mm2
M1
S1
D
E
P21 ctrl
Adult ctrl
P21 cKO
Adult cKO
F
M1 ctrl
M1 cKO
Layer 1
Layer 2/3
Layer 4
Layer 5
Layer 6a
Layer 6b
NPY cell/mm2
M1
G
S1 ctrl
S1 cKO
S1
H
Primary motor cortex (M1)
P21
Adult
I
Primary somatosensory cortex (S1)
J
K
L
M
NPY+ cell/mm2
(P21 to 12 weeks)
M1 ctrl
M1 cKO
S1 ctrl
S1 cKO

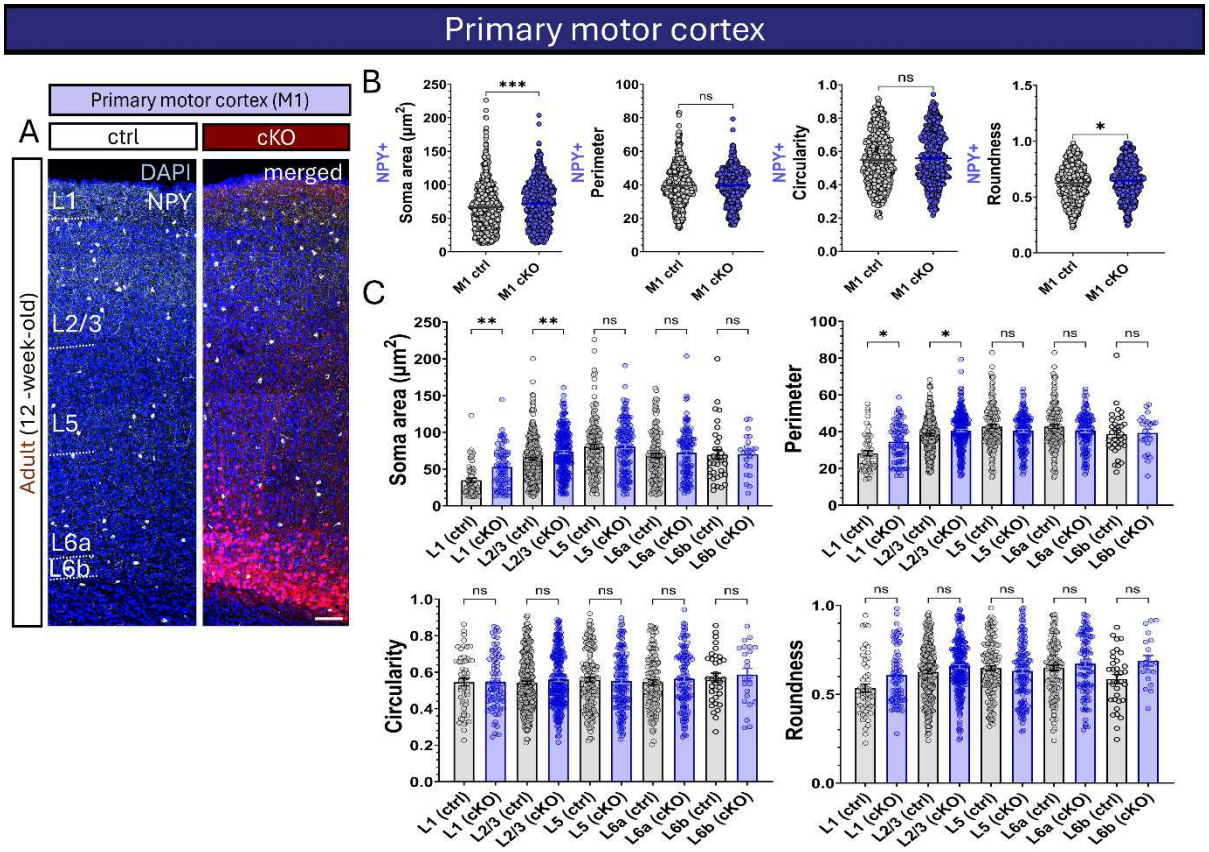
Figure 4.24. Laminar maturation of neuropeptide-Y interneurons in layer 2/3 of the primary motor and somatosensory cortices is different in the cKO mice. (A, B) Tiled z-stacks of the entire depths of the primary motor and somatosensory cortices representing neuropeptide-Y-immunopositive neurons in grey and DAPI nuclear counterstain in blue in control and *Snap25* cKO mice. (C) Bar graphs representing the mean cell density of neuropeptide-Y interneurons. (D, E) Trajectory of NPY+ cell density between P21 and 12 weeks in control and cKO mice. (F, G) Laminar distribution of NPY+ neurons quantified in M1 and S1 at 12 weeks of age. (H, I) Tiled z-stacks showing neuropeptide-Y interneurons and DAPI counterstaining in M1 and S1 at P21 and 12 weeks in control and *Snap25* cKO mice. (J-M) Bar graphs showing the trajectory of the laminar distribution of neuropeptide-Y interneurons in control and *Drd1a-Cre,Ai14;Snap25*$^{fl/fl}$ mice between P21 and 12 weeks in M1 (J, K) and S1 (L, M). Scale bar = 100 μm.

4.4.4.3. Conditional deletion of Snap25 from Drd1a-Cre+ neurons leads to morphological alterations in the soma area of NPY+ neurons in layer 2/3 of the adult primary motor cortex

In the preceding sections, I examined the laminar distribution and developmental dynamics of cortical NPY+ interneurons. Next, I sought to determine whether silencing Drd1a-Cre+ neurons altered the soma size or shape of NPY+ neurons in the neocortex. First, I found a substantial increase in the soma area of NPY+ interneurons in M1 in the layer 6-silenced mice relative to control mice at 12 weeks of age (Figure 4.25. A, B) (p=0.0002; unpaired Mann-Whitney test). There was a corresponding increase in the soma roundness of NPY+ neurons in M1 in the *Drd1a-Cre,Ai14;Snap25*$^{fl/fl}$ mice (Figure 4.25. B) (p=0.0259; unpaired Mann-Whitney test).

My next objective was to identify the cortical layers in which NPY+ interneurons showed a significant change in soma area. Given the high concentration of NPY+ neurons in layers 2/3 and 6a, I postulated that NPY+ neurons in these layers would be significantly affected by the long-term silencing of layer 6 neurons. I observed significant morphological alterations in the soma area and perimeter in the superficial layers 1 and 2/3 of M1 in the *Drd1a-Cre,Ai14;Snap25*$^{fl/fl}$ mice compared to control mice at 12 weeks of age (Figure 4.25. C) (L1, p=0.0042; L2/3, p=0.0028; one-way ANOVA Kruskal-Wallis test with Dunn's multiple comparisons test). According to these findings, NYP+ interneurons in layers 1 and 2/3 are likely driving the overall increase seen in the soma area in M1.

To ascertain whether these changes were unique to M1, I performed the same morphometric analysis on NPY+ neurons in S1. The soma perimeter and area were significantly lower in the *Drd1a-Cre+*-silenced mice at 12 weeks of age (Figure 4.25. D, E) (area, p=0.0052; perimeter, p=0.0344; unpaired Mann-Whitney test). I then aimed to identify the cortical layers where NPY+ interneurons displayed a marked decrease in soma area and perimeter. I discovered that NPY+ neurons in layer 6a of the *Drd1a-Cre+*-silenced mice had a smaller soma area in comparison to control mice (Figure 4.25. F) (p=0.0084, Kruskal-Wallis test with Dunn's multiple comparisons test). These findings imply that NPY+ interneurons in M1 and S1 are affected in a region-dependent manner by the genetic silencing of Drd1a-Cre+ neurons. When layer 6 neurons are silenced, the soma area of NYP+ neurons in M1 increases, but NPY+ neurons in S1 experience the opposite impact, with their soma size shrinking significantly by three months of age. Their morphology seems to be shaped by the removed excitation from layer 6 neurons in those cortical layers where NPY+ neurons are abundant. The opposing effects on M1 and S1 draw attention to regional differences between cortical layers and regions. However, further experiments are needed to investigate how and if the long-term morphological modifications in NPY+ neurons affect their intrinsic electrophysiological characteristics.


Primary motor cortex
A
Primary motor cortex (M1)
ctrl
cKO
Adult (12 -week-old)
DAPI
NPY
merged
L1
L2/3
L5
L6a
L6b
B
NPY+
Soma area (µm²)
Perimeter
Circularity
Roundness
M1 ctrl
M1 cKO
C
L1 (ctrl)
L1 (cKO)
L2/3 (ctrl)
L2/3 (cKO)
L5 (ctrl)
L5 (cKO)
L6a (ctrl)
L6a (cKO)
L6b (ctrl)
L6b (cKO)

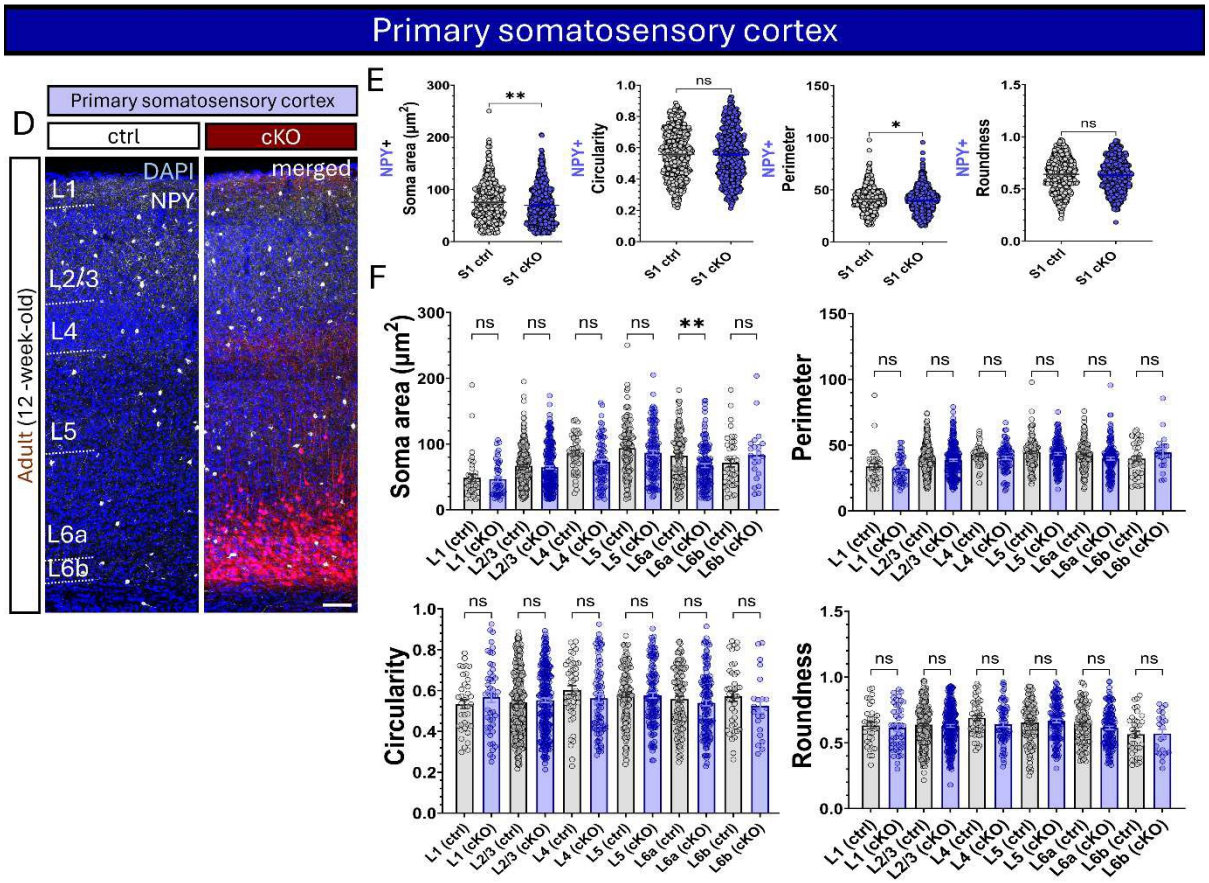

Primary somatosensory cortex
D
Primary somatosensory cortex
ctrl
cKO
Adult (12 -week-old)
DAPI
NPY
merged
L1
L2/3
L4
L5
L6a
L6b
E
NPY+
Soma area (µm²)
Circularity
Perimeter
Roundness
S1 ctrl
S1 cKO
F
L1 (ctrl)
L1 (cKO)
L2/3 (ctrl)
L2/3 (cKO)
L4 (ctrl)
L4 (cKO)
L5 (ctrl)
L5 (cKO)
L6a (ctrl)
L6a (cKO)
L6b (ctrl)
L6b (cKO)

Figure 4.25. Loss of AP-dependent neurotransmitter release from layer 6 neurons differentially affects the soma size of NPY+ interneurons in layer 2/3 and layer 6a in the primary motor and somatosensory cortex. (A) Tile-scan of the whole depth of the primary motor cortex showing neuropeptide-Y interneurons at 12 weeks of age in control and *Snap25* cKO mice. *Snap25*-deleted Drd1a-Cre+ neurons in cortical layer 6a and layer 6b are depicted in red. (B) Scatter plots showing soma measurements of neuropeptide-Y-immunopositive neurons in M1. (C) Morphometric analysis of neuropeptide-Y-immunopositive neurons in the upper and lower layers of M1 at 12 weeks of age. (D) Tile-scan of the whole depth of the primary somatosensory cortex illustrating neuropeptide-Y interneurons in control and *Snap25* cKO mice. White lines delineate cortical layer boundaries. (E) Scatter plots displaying soma measurements of neuropeptide-Y-immunopositive neurons in S1. (F) Morphometric analysis of neuropeptide-Y-immunopositive neurons in the upper and lower layers of S1 between control and *Drd1a-Cre,Ai14;Snap25*$^{fl/fl}$ mice. Scale bars = 100 µm.

4.4.5. The effects of silencing Drd1a-Cre+ neurons on subcortical parvalbumin neurons in the adult brain

In the preceding sections, I have demonstrated the long-term effects of ablating *Snap25* from Drd1a-Cre+ neurons on **cortical** inhibitory neurons in the adult neocortex. I will now discuss the findings on the **subcortical** GABAergic neurons. I will specifically focus on the density and soma characteristics of PV+, NPY+, and SST+ interneurons following the chronic silencing of a subset of layer 6 neurons.

4.4.5.1. Conditional deletion of Snap25 from a subset of Drd1a-Cre+ neurons has no long-term influence on the density and morphology of striatal PV+ interneurons

I started my investigation with the distribution of PV+ interneurons in the output regions of Drd1a-Cre+ neurons and quantified their density in the caudoputamen. Since striatal PV+ cell density was not altered at P21, I anticipated that silencing Drd1a-Cre+ neurons would not alter PV+ density at 12 weeks of age either. In line with the developmental results, PV+ cell density did not significantly differ between the control and the *Drd1a-Cre,Ai14;Snap25*$^{fl/fl}$ mice in the adult caudoputamen (Figure 4.26. A, B, C). Similarly, there were no significant variations in the soma morphology of PV+ neurons either (Figure 4.26. D). Considering that the reductions in striatal PV+ soma area and perimeter were

only detected at P21, it seems that silencing of Drd1a-Cre+ neurons has no long-term impact on the soma area of PV+ interneurons. It does not appear to control their number either, implying that striatal PV+ neurons are unaffected by the removal of excitatory inputs from layer 6 neurons.

Next, I established the developmental trajectory of the density of PV+ interneurons. In the control mice, the density of striatal PV+ interneurons remained unchanged between P21 and 12 weeks of age (Figure 4.26. E, F), suggesting that PV+ neuron numbers stabilise in the striatum after development. In *Drd1a-Cre,Ai14;Snap25*$^{fl/fl}$ mice, however, I observed a marked decrease in PV+ cell density in the striatum by 12 weeks of age (Figure 4.26. E, G) (p=0.0188, unpaired student's t-test with Welch correction). There appears to be a trend toward reduced cell density in adult cKO mice, but the specific factors contributing to the observed decrease in cell density by 12 weeks in the *Snap25* cKO mice are not clear. It is to be determined whether these differences imply an altered developmental trajectory of PV+ neurons within the striatum. When comparing the developmental dynamics of the morphology of striatal PV+ interneurons between P21 and 12 weeks of age, no significant alterations were detected between the control and *Drd1a-Cre,Ai14;Snap25*$^{fl/fl}$ mice (Figure 4.26. H, I).

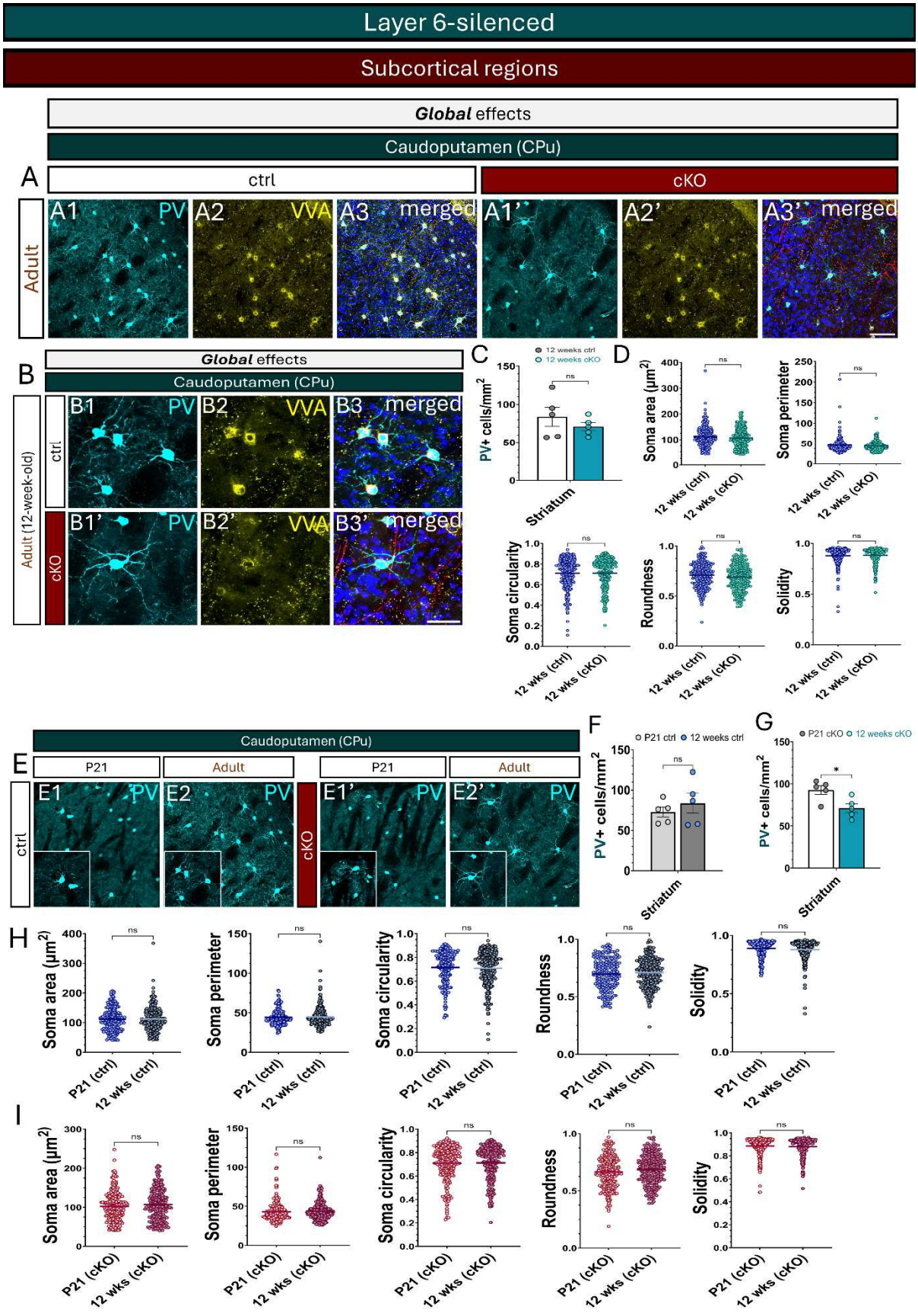

Layer 6-silenced
Subcortical regions
Global effects
Caudoputamen (CPu)
A
ctrl
cKO
Adult
A1
PV
A2
VVA
A3
merged
A1'
A2'
A3'
B
Adult (12-week-old)
ctrl
cKO
B1
B2
B3
B1'
B2'
B3'
C
12 weeks ctrl
12 weeks cKO
PV+ cells/mm2
Striatum
D
Soma area (µm2)
Soma perimeter
Soma circularity
Roundness
Solidity
12 wks (ctrl)
12 wks (cKO)
E
P21
Adult
E1
E2
E1'
E2'
F
P21 ctrl
12 weeks ctrl
G
P21 cKO
12 weeks cKO
H
P21 (ctrl)
12 wks (ctrl)
I
P21 (cKO)
12 wks (cKO)
ns

Figure 4.26. Silencing Drd1a-Cre+ neurons does not lead to long-term changes in the soma area of striatal parvalbumin interneurons. Maximum-intensity projected images of parvalbumin-immunoreactive neurons and *Vicia villosa* agglutinin-labelled perineuronal nets in the adult striatum in control (A1-A3, B1-B3) and *Drd1a-Cre,Ai14;Snap25*$^{fl/fl}$ mice (A1'-A3', B1'-B3'). Merged confocal images illustrating the silenced tdTomato+ fibre bundles of *Drd1a-Cre,Ai14;Snap25*$^{fl/fl}$ neurons (A3', B3'). Quantification of parvalbumin interneuron cell density in the caudoputamen at 12 weeks of age (C). Morphometric analysis of the soma parameters of parvalbumin neurons in control and *Drd1a-Cre,Ai14;Snap25*$^{fl/fl}$ mice (D). Z-stack images showing parvalbumin-immunopositive neurons in the caudoputamen in control mice at P21 and 12 weeks (E1, E2). Bar graph showing the trajectory of parvalbumin-immunopositive neurons in control and *Snap25* cKO mice between P21 and 12 weeks (G). Morphometric measurements of parvalbumin neurons between P21 and 12 weeks in control and cKO mice (H, I). Scale bar = 100 µm.

4.4.5.2. The density of parvalbumin neurons substantially decreases in the thalamic reticular nucleus both in control and Snap25 cKO mice from development to adulthood

After demonstrating that the reduced excitatory drive from Drd1a-Cre+ neurons does not influence the spatial distribution and soma area of striatal PV+ neurons, I investigated whether it affected PV+ neurons in other subcortical regions. There was a significant *region* ($p<0.0001$) but no *genotype* effect ($p=0.3525$) on PV+ cell density in the GPe and TRN at 12 weeks of age. Šídák's multiple comparison tests, accordingly, did not detect significant differences between control and *Drd1a-Cre+*-silenced mice in the GPe and TRN (Figure 4.27. A, B, C). Given that the TRN has the highest concentration of PV+ neurons among the subcortical areas, the *region* effect is to be expected. These findings further demonstrate that the spatial arrangement of subcortical PV+ interneurons is not affected either during or after development by the chronic silencing of a subgroup of layer 6 neurons. Next, I examined the developmental trajectory of PV+ interneurons in the GPe and the TRN (Figure 4.27. D, E). Interestingly, both the TRN and the GPe exhibited a significant reduction in the density of PV+ interneurons from P21 to 12 weeks in the control mice, which were primarily driven by significant *region* ($p<0.0001$) and *age* effects ($p=0.0001$) (Figure 4.27. F) (GPe, $p=0.0188$; TRN, $p=0.0011$, two-way ANOVA with Šídák's multiple comparisons test). The *Snap25* cKO displayed the same alteration in the density of PV+ neurons in the TRN, where I detected a ~27% decrease in PV+ cell density from P21 to 12 weeks (Figure 4.27. G) (p=GPe, $p=0.1160$; TRN, $p=0.0011$; two-way ANOVA

with Šídák's multiple comparisons test). However, no substantial reduction in the total density of PV+ neurons was observed in the GPe of *Drd1a-Cre,Ai14;Snap25*$^{fl/fl}$ mice (Figure 4.27. G). The results indicate that the density of PV+ interneurons in the TRN exhibits significant alterations during the transition from development to adulthood in both control and cKO mice. However, this reduction does not appear to be associated with the genetic silencing of Drd1a-Cre+ neurons. Instead, it may be attributed to substantial *regional* and *age*-related effects. Therefore, how the developmental trajectory of GABAergic interneurons varies across different subcortical regions needs more investigation.

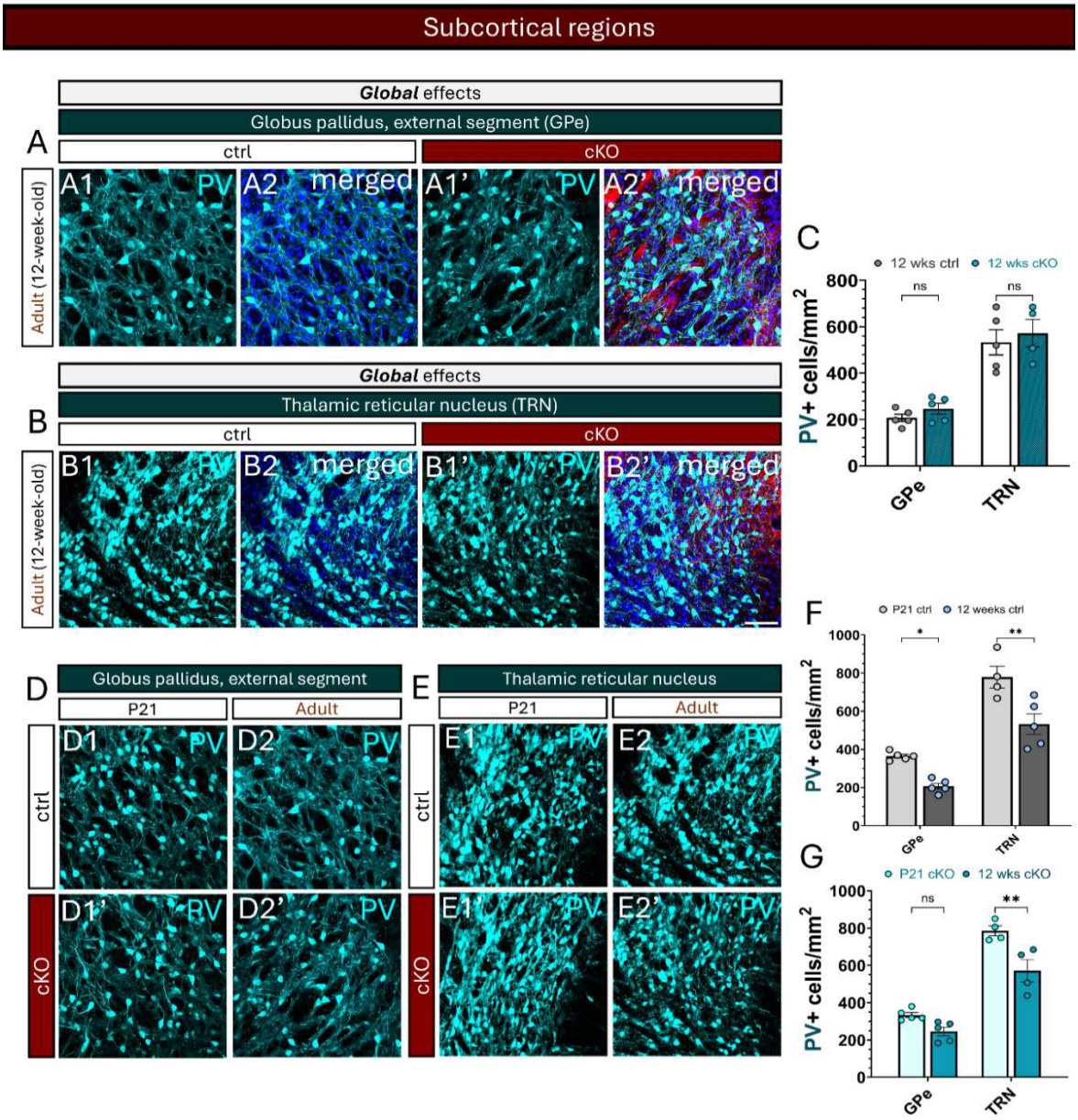


Figure 4.27. The developmental trajectory of parvalbumin interneurons indicates notable changes in the TRN, both in control and layer 6-silenced mice, from development to adulthood. Confocal images depicting parvalbumin-immunoreactive neurons in the external segment of the globus pallidus and the thalamic reticular nucleus in control (A1, A2, B1, B2) and *Drd1a-Cre,Ai14;Snap25*$^{fl/fl}$ mice (A1', A2', B1', B2'). Bar graphs of the mean cell density of parvalbumin-immunoreactive neurons in select subcortical ROIs (C). Parvalbumin-immunoreactive neurons in the GPe and TRN at P21 and 12 weeks of age in control (D1, D2, E1, E2) and *Drd1a-Cre,Ai14;Snap25*$^{fl/fl}$ mice (D1', D2', E1', E2'). Bar graphs representing the trajectory of parvalbumin neurons from development to adulthood in control (F) and cKO mice (G). Scale bar = 100 µm.

4.4.6. The effects of silencing Drd1a-Cre+ neurons on NPY+ neurons in the adult striatum and hippocampus

4.4.6.1. Silencing Drd1a-Cre+ neurons does not cause long-term alterations in the density and soma parameters of neuropeptide-Y interneurons in the adult striatum

To ascertain whether the alterations observed in the density and soma parameters of NPY+ interneurons at P21 persisted into adulthood, I assessed their density and soma morphology again at 12 weeks. I detected no significant changes between the control and layer 6-silenced striatum (p=0.0654, unpaired t-test with Welch's correction), indicating that the previously observed developmental increase in striatal NPY+ density in the Snap25 cKO mice was no longer present in the adult brain (Figure 4.28. A, C). Similarly, no long-term alterations were observed on the soma morphology of NPY+ neurons at 12 weeks in *Drd1a-Cre+*-silenced mice relative to control mice (Figure 4.28. D, E). Finally, I established the cell trajectory of NPY+ interneurons from development to adulthood. Interestingly, both control and *Drd1a-Cre,Ai14;Snap25*$^{fl/fl}$ mice exhibited prominent reductions in the mean cell density of striatal NPY+ neurons between P21 and 3 months. The *Drd1a-Cre+*-silenced animals showed a higher decline in the density of NPY+ interneurons in comparison to the control mice (Figure 4.28. B, C) (ctrl, p=0.0023; cKO, p=0.0002; two-tailed student's t-test with Welch correction). The cell trajectory of NPY+ neurons showed that the number of these neurons does fluctuate significantly in the striatum from development to maturity, suggesting that the decrease in cell density is primarily an age effect.

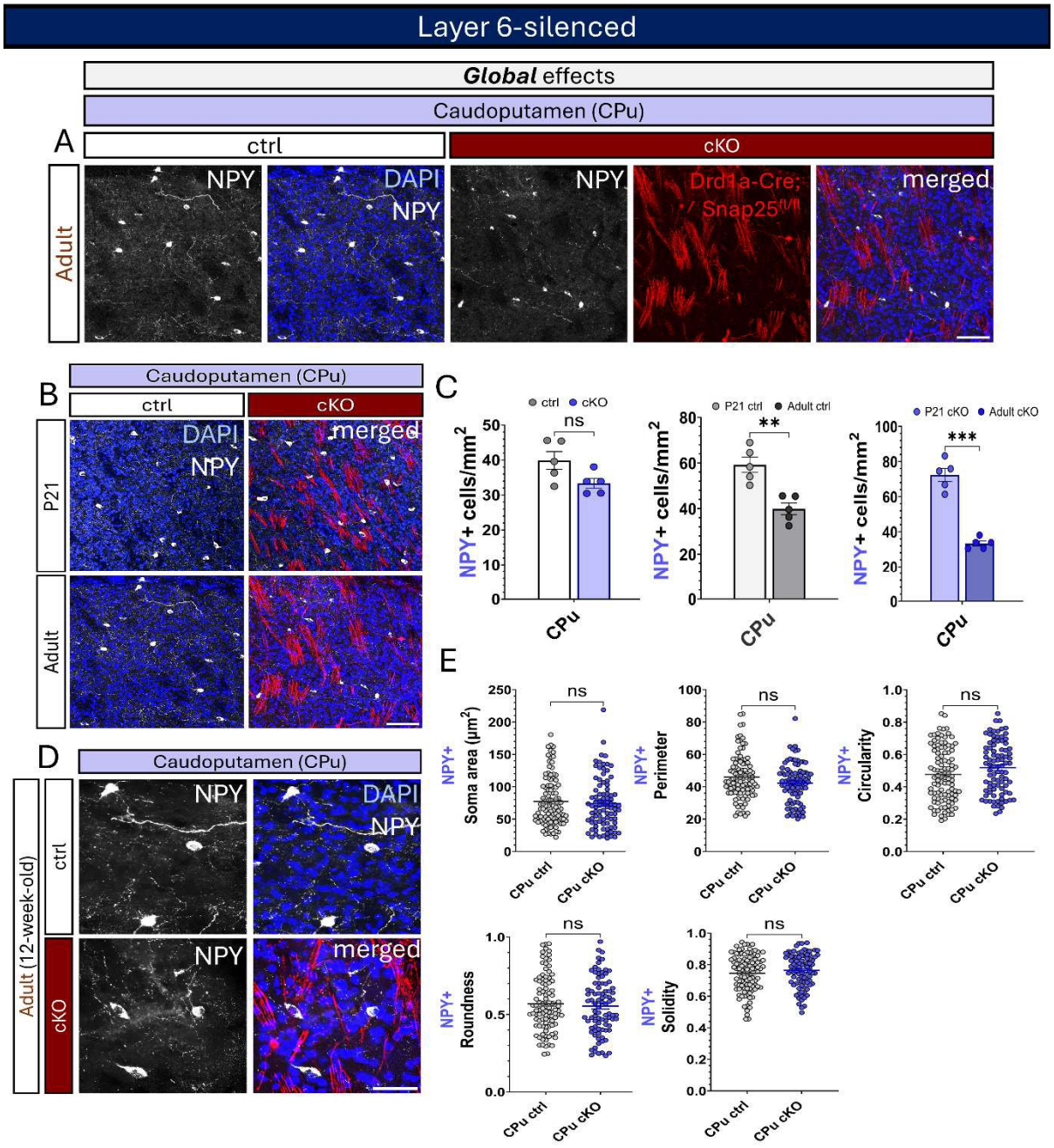


Figure 4.28. The density and soma characteristics of neuropeptide-Y interneurons in the adult striatum do not exhibit long-term changes in the cKO mice. (A) Maximum-intensity projected z-stacks of neuropeptide-Y-immunostained neurons in control and *Snap25* cKO mice in the adult caudoputamen. tdTomato+ fibre bundles of the silenced Drd1a-Cre+ neurons in the *Snap25* cKO mice. (B) Z-stacks depicting neuropeptide-Y-immunoreactive neurons and the silenced terminals of Drd1a-Cre+ neurons in the caudoputamen in control and *Snap25* cKO mice at P21 and 3 months. (C) Bar graphs showing the mean cell density and the developmental trajectory of neuropeptide-Y neurons in control and *Drd1a-Cre,Ai14;Snap25$^{fl/fl}$* mice. (D) Representative examples of neuropeptide-Y-immunopositive neurons at 12 weeks of age in control and *Drd1a-Cre,Ai14;Snap25$^{fl/fl}$* mice. Note the descending fibres of Drd1a-Cre+ neurons intersect neuropeptide-Y interneurons. (E) Scatter plots of individual soma measurements of striatal NPY+ neurons. Scale bars = 100 µm.

4.4.6.2. The density of neuropeptide-Y interneurons in adult hippocampal regions is not altered by silencing Drd1a-Cre+ neurons

In this section, I set out to examine the long-term effects on hippocampal NPY+ neurons. Previously, I demonstrated that the density of NPY+ neurons in the CA1 region significantly increased at P21 in the *Snap25* cKO mice. Interestingly, I found no significant changes in the density of NPY+ interneurons between the control and *Drd1a-Cre,Ai14;Snap25*$^{fl/fl}$ mice at 12 weeks of age in the CA1, CA3, and dentate gyrus (Figure 4.29. A, B). Thus, silencing layer 6 appears to have only a short-term impact on hippocampal NPY+ neurons that can no longer be detected after development.

Finally, I traced the development of NPY+ neurons in the hippocampus to determine if there were any notable fluctuations in their number from development to adulthood. I observed no significant alterations in the cell density of NPY+ neurons in any hippocampal regions between P21 and 3 months in control brains (Figure 4.29. C, D). However, two-way ANOVA testing identified a significant *region* ($p<0.0001$) and *age* effect ($p=0.0008$), with no interaction ($p=0.3762$), in the *Snap25* cKO mice. Šídák's multiple comparisons tests detected a prominent decrease in the density of NPY+ neurons from development to adulthood in mutant CA1 ($p=0.0147$) (Figure 4.29. C, D), which exhibited elevated NPY+ density at P21. Whilst a similar trend was observed in the CA3 and dentate gyrus of the *Snap25* cKO mice, the decline in their number did not reach statistical significance.

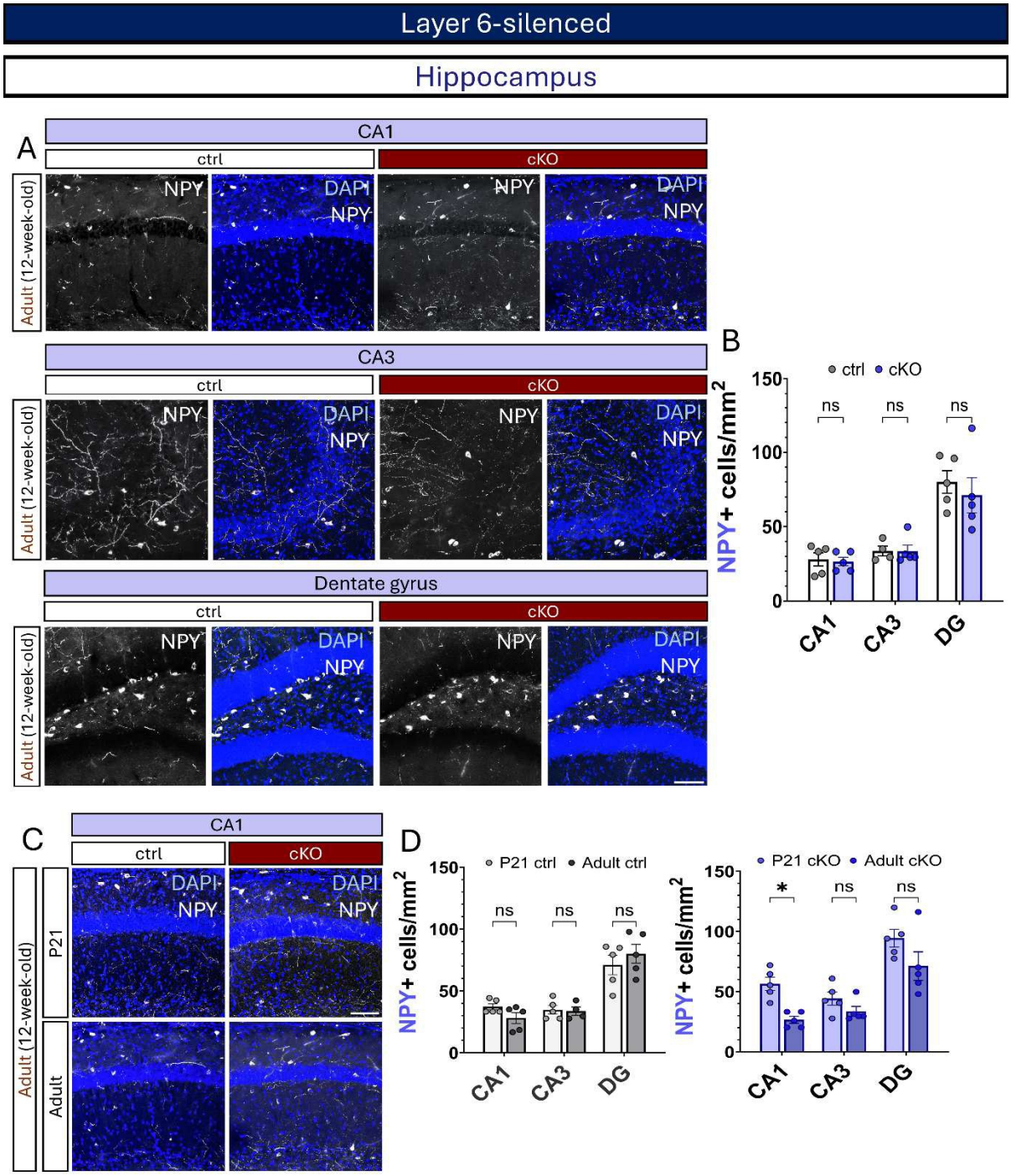


Figure 4.29. Silencing Drd1a-Cre+ neurons had no long-term effect on the density of neuropeptide-Y interneurons in the hippocampal regions. (A) Maximum-intensity projected images of neuropeptide-Y-immunoreactive neurons in grey and DAPI nuclear counterstaining in blue in the CA1, CA3, and dentate gyrus in control and *Drd1a-Cre+*-silenced mice. (B) Quantification of the mean cell density of neuropeptide-Y-immunoreactive neurons within the hippocampus at 12 weeks. (C) Z-stack images of neuropeptide-Y-immunoreactive neurons in the CA1 region in control and *Drd1a-Cre,Ai14;Snap25*$^{fl/fl}$ mice at P21 and 12 weeks. (D) Trajectory of neuropeptide-Y-immunopositive neurons in control and *Drd1a-Cre,Ai14;Snap25*$^{fl/fl}$ mice. Scale bars = 100 µm.

4.4.7. The effects of silencing Drd1a-Cre+ neurons on somatostatin interneurons in adult striatum and hippocampus

4.4.7.1. Somatostatin interneurons in the dentate gyrus are selectively affected by the long-term absence of Ca2+-dependent neurotransmission from Drd1a-Cre+ neurons in the adult hippocampus

In the last section, I continued investigating the long-term effects of silencing Drd1a-Cre+ neurons on hippocampal GABAergic interneurons. A significant *region* (p=0.0093) and *genotype* effect (p=0.0240), with significant *interaction* (p=0.0127), was found on SST+ density in the adult hippocampus using two-way ANOVA testing. Šídák's *post*-hoc tests yielded significant reductions in the density of SST+ neurons solely in the dentate gyrus in the *Drd1a-Cre,Ai14;Snap25$^{fl/fl}$* mice (Figure 4.30. B, C), which contained ~39% fewer SST+ interneurons compared to control mice (p=0.0020). The same prominent reduction in the number of SST+ neurons in the dentate gyrus was detected in the adult *Rbp4-Cre,Ai14;Snap25$^{fl/fl}$* mice (Figure 4.30. F, G). These results may indicate that external cues from deep-layer projection neurons are likely required for the maintenance of SST+ interneurons located in the dentate gyrus. This was observed specifically in the *Drd1a-Cre,Ai14;Snap25$^{fl/fl}$* mice, suggesting that layer 6 may play a crucial role in regulating the population of SST+ interneurons within the adult hippocampus. This highlights the importance of inter-neuronal communication and extrinsic factors in sustaining neural populations in mature brain regions.

To determine whether PNNs may enwrap inhibitory neurons that are not PV-positive, I examined the distribution of PNNs around SST+ interneurons in the hippocampus at 12 weeks of age. In the CA3, I observed multiple instances of co-localisation between SST+ interneurons and VVA+ cells, indicating that PNNs surround non-fast-spiking GABAergic interneurons in the hippocampus (Figure 4.30. D, E). Next, I quantified the number of SST+ neurons co-localising with VVA+ cells in the CA3 and noted a significant increase of ~47% in the SST+ VVA+ cells in the *Drd1a-Cre,Ai14;Snap25$^{fl/fl}$* mice compared to control mice (Figure 4.30. H) (p=0.0429, unpaired student's t-test with Welch correction). The

Snap25 cKO mice exhibited a significantly higher proportion of PNN-bearing SST+ interneurons in the CA3 region (Figure 4.30. I) (p = 0.0431, unpaired t-test with Welch correction). It appears that the removed excitatory input from layer 6 neurons leads to the upregulation of SST+ interneurons, accompanied by an overexpression of PNNs.

Finally, I established the developmental trajectory of SST+ interneurons in the CA1 and the striatum. With no significant *region* (p=0.8186) and *age* effects (p=0.2110), two-way ANOVA Šídák's multiple comparisons test detected no significant alterations in the density of SST+ interneurons in the striatum and CA1 of control mice, implying that SST+ cell density remained constant from development to adulthood (Figure 4.30. J). The *Drd1a-Cre,Ai14;Snap25*$^{fl/fl}$ mice followed the developmental trajectory of that of the control brains (Figure 4.30. K).

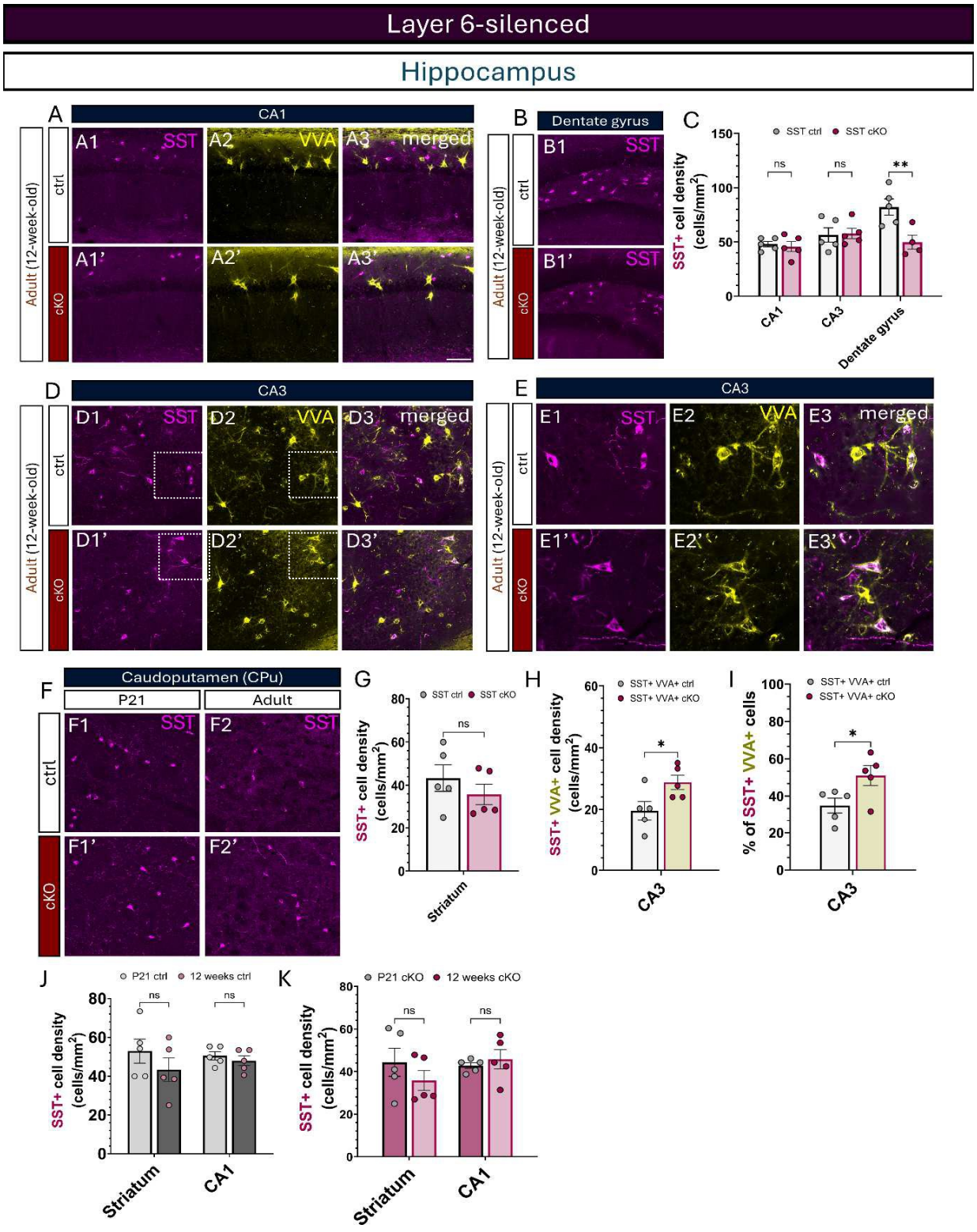


Figure 4.30. Somatostatin interneurons in the CA3 are enwrapped by perineuronal nets, and the number of perineuronal net-bearing somatostatin neurons increases when layer 6 projection neurons are persistently silenced. Confocal images illustrating somatostatin-immunoreactive neurons in magenta and perineuronal nets in yellow in the CA1 and dentate gyrus in

control (A1-A3, B1) and *Drd1a-Cre,Ai14;Snap25*$^{fl/fl}$ mice (A1'-A3', B1'). Quantification of the density of somatostatin-immunopositive neurons in the CA1, CA3, and dentate gyrus (C). Confocal z-stacks and zoom-in images of somatostatin-immunoreactive neurons and perineuronal nets in the CA3 in control (D1-D3, E1-E3) and *Drd1a-Cre,Ai14;Snap25*$^{fl/fl}$ mice (D1'-D3', E1'-E3'). Co-localising somatostatin interneurons with *Vicia villosa* agglutinin-positive cells in control (E3) and *Drd1a-Cre,Ai14;Snap25*$^{fl/fl}$ mice (E3'). Somatostatin-immunoreactive neurons at P21 and 12 weeks in control (F1, F2) and *Drd1a-Cre,Ai14;Snap25*$^{fl/fl}$ mice (F1', F2'). Quantification of the cell density of somatostatin-immunopositive neurons in the caudoputamen at 12 weeks of age (G). Bar graphs representing the mean cell density of somatostatin-immunoreactive neurons enwrapped by perineuronal nets in the CA3 (H). Bar graphs representing the percentage of somatostatin interneurons co-localising with *Vicia villosa* agglutinin-positive cells in the CA3 (I). Developmental trajectory of somatostatin interneurons in the striatum and the CA1 in control and cKO mice (J, K). Scale bar = 100 μm.

4.4.8. Discussion

Overview

The purpose of this chapter was to clarify how a subset of layer 6 corticothalamic neurons shapes the development of inhibitory networks and directs the laminar and spatial organisation of GABAergic neurons inside and outside the neocortex. Thus, I manipulated layer 6 pyramidal neurons in a cell-type-specific manner. By conditionally deleting *Snap25* from Drd1a-Cre+ projection neurons, I genetically 'silenced' both layers 6a and 6b neurons throughout the cortical mantle. The chronic manipulation of Drd1a-Cre+ neurons enabled me to assess the short-term and long-term effects on cortical and subcortical GABAergic neurons. A major question in this chapter was to determine whether the genetic silencing of Drd1a-Cre+ neurons led to layer-and cell-type-specific alterations in GABAergic neuron number and laminar distribution. To this end, I examined three distinct subtypes of GABAergic neurons, namely parvalbumin, somatostatin, and neuropeptide-Y interneurons, during and after development.

Excitatory synaptic contacts formed by Drd1a-Cre+;Ai14;Snap25$^{fl/fl}$ neurons in subcortical regions

The first question in this chapter was to find the cortical and subcortical regions of interest where GABAergic interneurons may be influenced by layer 6 projection neurons. Prior to selecting the subcortical ROIs, I mapped the long-range projections of the silenced Drd1a-Cre+ neurons in the *Snap25* cKO mice. One unanticipated finding was that the descending terminals of Drd1a-Cre+ neurons, which target the higher-order thalamic nuclei, form VGluT1-positive synapses in the striatum, the GPe, and the TRN. These results are unexpected since the terminals of Drd1a-Cre+ neurons do not branch in the TRN (Hoerder-Suabedissen et al. 2018), and the absence of side collaterals would indicate the absence of synaptic contact in the TRN. This unexpected finding may be due to potential topographic variations in the TRN. For instance, cortical projections derived from prefrontal areas target particular rostrocaudal and mediolateral sectors within the TRN, which are

distinct from the projections arising from the sensory and motor areas that terminate in the central and caudal sectors of the TRN (Zikopoulos and Barbas 2006). These projections are modality-specific and demonstrate a clear spatial arrangement, providing evidence for the presence of functionally and spatially distinct sectors within the TRN (Crabtree 2018). Thus, the TRN exhibits topographical variations in the spatial organisation of its afferent and efferent connections (Phillips et al. 2019; Zikopoulos and Barbas 2006). Additionally, certain spatial regions within the TRN are selectively innervated by subtypes of layer 6 CT neurons, which reflect their projection patterns to particular thalamic nuclei (Whilden et al. 2021; Martinetti et al. 2024). The descending axon terminals of Drd1a-Cre+neurons may exhibit similar topographical variations, and the presence of Vglut1+ synapses may be dependent on which sector of the TRN is being investigated. I investigated the anteromedial sections of the TRN at the level of the ventral anterior-lateral complex of the thalamus, which may have been different from the sector and level studied by Hoerder-Suabedissen et al. 2018).

Another plausible explanation for the excitatory synapses found in the TRN in the Drd1a-Cre+-silenced mice may originate from layer 6a rather than layer 6b neurons. Previous studies on tracing corticothalamic connections have shown that layer 6 corticothalamic neurons directly innervate the TRN and the thalamic relay cells (Bourassa et al. 1995; Deschênes et al. 1998; Veinante et al. 2000; Zhang and Deschênes 1997; Groh et al. 2014; Antunes and Malmierca 2021). Layer 6 corticothalamic neurons give side collaterals to the TRN and form glutamatergic synapses (Ojima 1994; Rouiller and Welker 2000; Hazama et al. 2004). Since the distribution of Drd1a-Cre+ neurons is not restricted to layer 6b and there are a few Cre+ neurons in layer 5 as well, further studies need to identify the exact populations of corticothalamic neurons that form these glutamatergic synapses in the TRN. It is also known that layer 5 has a direct excitatory projection to the TRN (Hádinger et al. 2023; Groh et al. 2014; Rovó et al. 2012), which complicates the anatomical and functional dissection of these cortico-thalamo-cortical networks and the synapses that arise from corticothalamic neurons. However, Cre+ driver lines specific to layer 6a will help differentiate between layer 6a and layer 6b-specific pathways.

Drd1a-Cre+ fibres are present in the stratum lacunosum moleculare of the hippocampus

The hippocampus was not an obvious choice among the regions of interest, given that the primary targets of the long-range projections of Drd1a-Cre+ neurons are the higher-order thalamic nuclei rather than the hippocampus. However, examining the brain-wide projections of Drd1a-Cre+ neurons has revealed tdTomato+ fibres in the stratum lacunosum moleculare of CA1, CA2, and CA3 (section 4.3.3.). Direct excitatory projections from entorhinal cortex layer 6b neurons have been demonstrated to target the s.l.m. of CA3 (Ben-Simon et al. 2022); however, this study utilised a *Ctgf-2A-dgCre* driver line to demonstrate the existence of the layer 6b-hippocampal pathway. While Ctgf+ neurons do co-localise with Drd1a-Cre+ neurons (at least in S1), it is not known whether Drd1a-Cre+ neurons project to the hippocampus. Layer 6b neurons in the entorhinal cortex are not labelled by the FK164 line, making it an imperfect tool for studying the connections between the entorhinal cortex layer 6b and the hippocampus. Therefore, to ascertain if Drd1a-Cre+ layer 6b neurons provide direct or indirect inputs to the hippocampus, more research utilising anatomical tracing, genetic tagging, and electrophysiological techniques is required, along with alternative Cre-driver lines. The source of the Drd1a-Cre+ axon projections in my samples is yet to be identified.

The effects of silencing Drd1a-Cre+ neurons on cortical parvalbumin interneurons during and after development

ACA, M1, and S1 were the three cortical ROIs that I chose to evaluate the impact of silencing a subset of layer 6 neurons on cortical PV+ interneurons. The very first Cre-expressing cells in the *Drd1a-Cre;Ai14* line are seen in the anterior and medial cortex at P1, but the density of Drd1a-Cre+ tdTomato+ cells is low at P1 and P3 and only resembles adult-like density in the majority of cortical areas at P8 (Hoerder-Suabedissen et al. 2018). The ablation of *Snap25* and the subsequent genetic silencing of a subset of layer 6 pyramidal neurons in the Drd1a-*Cre;Ai14;Snap25*$^{fl/fl}$ line may therefore

occur between P8 and P11, which is just around or slightly outside the window of interneuron cell death. GABAergic interneurons are particularly susceptible to changes in pyramidal cell number, function, or network activity during the critical window of programmed cell death, which spans from P5 to P10, with a notable surge in apoptosis at approximately P7 (Wong et al. 2018). Prior research has indicated that the timing of the chemogenetic modulation of pyramidal neurons was critical in determining whether cortical PV+ and SST+ interneurons were affected (Wong et al. 2018; Wong et al. 2022; Sreenivasan et al. 2022). If the loss of *Snap25* mRNA and proteins and the subsequent silence of Drd1a-Cre+ neurons happen to coincide with interneuron cell death, it is unclear why the development of inhibitory neurons has not been impacted. One possible interpretation is that AP-dependent neurotransmitter release is dispensable for the development of GABAergic neurons. The developmental data confirm this, demonstrating that the maturation and total density of PV+ interneurons in the neocortex were unaffected by the loss of AP-dependent synaptic vesicle release from Drd1a-Cre+ or Rbp4-Cre+ projection neurons during early postnatal development. Other conditional knockout models that targeted SNARE complex synaptic proteins other than *Snap25* provide additional support for the idea that interneuron numbers are not altered in the absence of synaptic vesicle exocytosis. The density of PV+ and SST+ interneurons in the adult *Munc18-1* (also known as STXBP1) haploinsufficient mice remained unaltered, suggesting that cortical interneuron survival is not perturbed by *Munc18-1* haploinsufficiency (Chen et al. 2020). It is interesting to note that Munc18-1 haploinsufficient mice exhibit severe abnormalities in PV and SST-mediated inhibition, as seen by reduced PV+ synaptic strength and decreased SST+ interneuron connection to pyramidal neurons (Chen et al. 2020). These findings suggest that whereas disruptions in synaptic transmission permit the regular survival and maintenance of inhibitory neurons, they result in GABAergic synaptic dysfunction. It would be interesting to know whether similar alterations in PV-and SST-mediated inhibition occur in the *Snap25* cKO mice. Examining the effects of the conditional deletion of other SNARE-associated synaptic proteins, such as *Vamp2* and *Syntaxin1*, on interneuron survival and

GABAergic inhibition would therefore aid our understanding of the role of evoked and spontaneous neurotransmission in the formation of GABAergic circuits.

While the genetic silencing of Drd1a-Cre+ neurons left the overall numbers of cortical PV+ neurons intact, it did significantly alter their laminar positioning in layer 5 of S1 at P21. PV+ interneurons in S1 may have rearranged or redistributed, orienting themselves to their layer 6 synaptic partners, which could account for the observed result. However, no significant changes in PV+ laminar distribution were seen at 12 weeks of age, suggesting that the reorganisation of PV+ interneurons in S1 was transient in the *Snap25* cKO mice. Given that the chronic abolition of AP-dependent neurotransmission has no long-term impact on the laminar positioning of PV+ neurons, compensatory effects deriving from local or translaminar connections may account for the lack of effect in the adult S1. Furthermore, it is likely that the loss of AP-dependent neurotransmitter release results in functional rather than structural changes in GABAergic neurons, such as changes in synaptic strength or laminar connectivity, which are yet to be examined.

The effects of silencing Drd1a-Cre+ neurons on the perineuronal nets after development

Examining the perineuronal nets and the laminar architecture of PV+ neurons in the adult neocortex has shown notable regional differences between cortical layers and regions. The density and laminar distribution of PV+ interneurons in the developing primary motor cortex did not differ significantly between control and *Snap25* cKO mice; however, by 12 weeks of age, the density of PV+ interneurons enwrapped by PNNs had dramatically decreased in M1. Remarkably, PV+ interneurons that co-localised with VVA-positive cells were the only cells impacted. The existence of PNNs surrounding PV+ interneurons may theoretically limit their capacity to adapt to changes in the external environment following the closure of crucial periods, given that PNNs function as a brake on synaptic plasticity (Carulli and Verhaagen 2021; Oohashi et al. 2015). However, the expression of

PNNs and PV+ neurons is both activity-dependent, suggesting a dynamic ECM structure in the adult brain (Devienne et al. 2021). This may partially account for the significant change detected in the density of PV+ VVA+ neurons in M1 in the adult *Snap25* cKO mice. These results support the notion that manipulation of pyramidal neuron activity can elicit changes in PNN density even in the adult brain and that ECM alterations can remodel local microcircuits through activity-dependent mechanisms (Devienne et al. 2019; Devienne et al. 2021).

The transient changes in the laminar distribution of PV+ interneurons in S1 at P21 raised the question of whether the density of PNNs might have been remodelled in the adult somatosensory cortex. PNNs are particularly dense in the upper limb and barrel field of S1, and layer 4 contains extremely condensed PNNs. Therefore, the significant alterations observed in layer 4 of S1LL and S1UL/S1BF at 12 weeks of age were not unanticipated findings. What was unexpected, though, was the opposing ways that layer 6 controlled PNN density. In S1LL, the genetic silencing of a subset of layer 6 neurons only affected the density of PNNs in layer 4, without changing the total number of VVA+ cells. However, in S1UL/S1BF, it altered the density of PV- VVA+ cells in layer 4, which resulted in a corresponding increase in the total density of PV- VVA+ cells in S1UL/S1BF. In S1LL, there appears to be a remodelling of PNN density in the long-term absence of AP-dependent neurotransmitter release from Drd1a-Cre+ neurons. The shift in the overall PV-VVA+ cell count in S1UL/S1BF suggests PNN overexpression and a possible compensatory mechanism. These results indicate that PNNs may respond to perturbations in network and pyramidal neuron activity in two distinct manners: 1) redistribution or remodelling of PNN expression, and 2) overexpression or upregulation of PNN density. These results underscore the intricate mechanisms controlling PNN expression in the adult cortex as well as the *intra*- and *inter*regional differences among distinct cortical regions.

The differential effects on PNN expression in S1LL and S1UL/S1BF may imply that functionally distinct subdomains of S1 exhibit different forms and degrees of plasticity. Variations in plasticity may stem from differences in sensory modalities and the subfield circuitry (Erzurumlu and Gaspar 2012).

Plasticity is influenced by both vertical and horizontal connections in various layers (Bernardo et al. 1990; Kolb et al. 2010). For instance, selective whisker-trimming paradigms suggest that intracortical pathways are the main mediators of experience-dependent cortical plasticity, but it is not known if these connections originate from layer IV, the supragranular layers, or both (Erzurumlu and Gaspar 2012). The columnar organisation and intrinsic differences in intracortical connections may differ between the barrel field and the hindlimb area, potentially leading to varying forms of plasticity within different subdomains of S1. This may be one of the underlying reasons why the response of different S1 subfields to trauma or altered sensory experiences varies. For example, after peripheral sensory loss, the barrel field reorganises differently than the cortex of the forelimb or hindlimb (Kolb et al. 2010; Mohammed and Hollis 2018).

The effects of silencing Drd1a-Cre+ neurons on subcortical parvalbumin neurons during and after development

Assessing the effects of the genetic silencing of Drd1a-Cre+ neurons on subcortical PV+ neurons did not reveal significant alterations in PV+ density in the CPu, GPe, and TRN. The findings at 12 weeks of age were consistent with the developmental results. The lack of significant differences in the output regions of Drd1a-Cre+ neurons implies that subcortical PV+ neurons are not under the control of long-range cortical projections from layer 6. Additionally, it is conceivable that the maintenance of PV+ neurons in the chosen subcortical locations is not regulated by AP-dependent neurotransmission. Although I demonstrated that the terminals of Drd1a-Cre+ neurons form VGluT1+ glutamatergic synapses in the striatum, the GPe, and the TRN, the number of VGluT1+ synapses seemed to be relatively sparse in the striatum and the TRN as well.

One interesting finding was that the genetic silencing of layer 5 or layer 6 projection neurons had a similar impact on the soma morphology of striatal PV+ neurons. Both had a short-term effect on the soma area and roundness of striatal PV+ interneurons at P21; however, these changes did not persist

into adulthood. In alignment with the density results, chronic silencing of layer 5 or layer 6 projection neurons does not cause long-term morphological alterations in striatal PV+ neurons. Although the soma characteristics of PV+ neurons were the exclusive focus of the morphometric studies in this thesis, it is yet to be seen how silencing layer 5 or layer 6 projection neurons may affect the dendritic processes and arborisation of PV+ neurons.

Ionotropic and metabotropic GABA receptors in the Drd1a-Cre+ silenced mice

Since defects in GABAergic transmission and GABA receptor abnormalities have been shown to underlie the aetiology of neuropsychiatric disorders, the structure and function of GABA receptors have consistently garnered a lot of attention. Schizophrenia, dyslexia, and juvenile myoclonic epilepsy are among the neurodevelopmental disorders that are associated with the human GABABR1 gene on chromosome 6p21.3 (Martin et al. 2001). GABA-$_B$ receptors are especially abundant in the thalamus, the cerebellum, the hippocampal regions, and monoaminergic brainstem nuclei (Wang et al. 2022; Bettler et al. 2004; Margeta-Mitrovic et al. 1999). In the present chapter, I focused on the primary motor and somatosensory cortices to examine the local effects of silencing a subset of layer 6 neurons on the GABA-$_A$ and GABA-$_B$ receptors. I have observed significant reductions in GABA-$_B$ R1+ receptor density in layer 5 of M1 and S1 in the *Snap25* cKO mice relative to control mice at P21. In layer 5 of S1, the decline in receptor density was more pronounced. However, GABA-$_B$ R1 receptors were not decreased on PV+ interneurons, given that the density of GABA-$_B$ R1-expressing PV+ neurons remained unaffected in layer 5 at P21. Since GABA-$_B$ receptors are expressed by both glutamatergic and GABAergic neurons, it is equally likely that long-term silencing of Drd1a-Cre+ neurons resulted in a decrease in GABA-B R1+ on glutamatergic neurons or non-fast-spiking interneurons.

GABA-$_B$ receptor agonists and antagonists have been shown in earlier studies to have cell-type-specific effects on GABAergic interneurons. GABA-$_B$ receptor agonist and antagonist application

selectively altered certain intrinsic electrophysiological properties of PV+ neurons but did not affect SST+ interneurons (Kanigowski et al. 2023). This is an intriguing finding given that the low number of PV+ interneurons co-localised with GABA-B R1 in my samples would have predicted the contrary. However, the exact cell type that expresses GABA-$_B$ receptors and was markedly diminished in the Drd1a-Cre+-silenced mice is yet to be identified. Future research will also be needed to examine whether the decreased GABA-B receptor density leads to dysfunctions in the R1 subunit and/or perturbations in GABAergic transmission.

The effects of silencing Drd1a-Cre+ neurons on somatostatin interneurons during and after development

Another main objective of the present thesis was to distinguish the effects of the genetic silencing of Drd1a-Cre+ neurons on distinct subtypes of interneurons during and after development. I chose to investigate SST+ interneurons in the hippocampus and the caudoputamen at P21 and 12 weeks. The significant decrease in the density of CA1 SST+ interneurons in the *Snap25* cKO mice seems to be a transient change during development. No such alterations were detected in the adult Snap25 cKO mice in the CA1. Contrary to CA1, SST+ interneurons in the dentate gyrus remained intact throughout development and only showed a significant decrease in density in the adult brain. These results demonstrate that silencing a subset of layer 6 projection neurons has a long-term effect on SST+ interneurons in the dentate gyrus, but only a short-term effect on SST+ interneurons in the CA1. Since SST+ interneurons receive reduced excitation due to the removal of glutamatergic inputs from Drd1a-Cre+ neurons, the decrease in their density/downregulation of the somatostatin peptide is likely to reflect a homeostatic adaptation. SST+ interneurons may thus exhibit homeostatic plasticity when their synaptic input is reduced to preserve their firing rate and overall network stability (Leighton et al. 2021; Scheyltjens and Arckens 2016). While electrophysiological recordings were beyond the scope of the present thesis, it would be interesting to see whether the decreased SST+

interneurons in the dentate gyrus led to disruptions in hippocampal network dynamics and plasticity in the *Snap25* cKO mice. Similarly, reduced dendritic inhibition of the dentate gyrus circuitry may lead to the hyperactivity of pyramidal neurons and induce pathological changes both at a cellular and behavioural level. For instance, chemogenetic silencing of adult SST+ interneurons in the dentate gyrus hilus revealed prominent reductions in the density of SST+ interneurons and resulted in cognitive impairments and memory deficits (Lyu et al. 2023). Although my results cannot be directly compared to research that uses chemogenetic silencing, they do indicate that SST+ interneurons in the dentate gyrus undergo selective modifications when either pyramidal neurons or interneurons are altered. It is also worth noting that at least two opposing forms of SST+ interneurons exist within the dentate gyrus, each with unique morphological and functional characteristics (Yuan et al. 2017). In addition to the conventional feedback-inhibitory SST+ neurons, which are implicated in the dendritic inhibition of granule cells, there is a distinct group of SST+ neurons (termed hilus-associated) that inhibit local GABAergic neurons through perisomatic inhibition (Yuan et al. 2017).

An interesting observation was the presence of perineuronal nets around SST+ interneurons in the CA3. Since the co-localisation between SST+ and VVA+ cells was only apparent in the CA3, different subregions of the hippocampus probably show variations in PNN-enwrapped SST+ neurons. Previous studies have reported that PNNs enwrap hippocampal excitatory pyramidal neurons as well as inhibitory neurons in the dorsal region of the CA2 (Carstens et al. 2016); however, very little was found in the literature on SST+ interneurons in the CA3. Interestingly, sex-and age-specific differences have been reported in the CA1 region, proving the heterogeneity in PNN expression between developmental and adult, female and male mice (Li et al. 2024) (Carstens et al. 2016). Although the challenges of obtaining sufficient brain samples from male and female mice have prevented me from examining sex-specific differences in my data, the adult hippocampus was found to have well-developed PNNs around SST+ neurons. The CA3 region of adult *Snap25* cKO mice exhibited an increased density of SST+ VVA+ neurons, which may indicate that PNN overexpression surrounding

SST+ neurons is elicited by the genetic silencing of Drd1a-Cre+ neurons. The upregulation of PNNs around the SST+ cell may serve as a mechanism to 'secure' or preserve active afferent synapses.

The effects of silencing Drd1a-Cre+ neurons on neuropeptide-Y interneurons during and after development

The last sections of this chapter sought to unravel changes in the spatial and laminar distribution of NPY+ interneurons. I postulated that subtypes of interneurons that produce neuropeptides may be differentially affected by the silencing of layer 6 neurons, compared to subtypes that express proteins that bind Ca^{2+} ions. Parvalbumin functions as a high-capacity, slow calcium buffer (Lee et al. 2000). It binds incoming Ca^{2+}, which facilitates the removal of calcium from the cytoplasm following each spike, thereby aiding in promptly restoring intracellular calcium levels (Chard et al. 1993). Parvalbumin and other calcium-binding proteins play a crucial role in maintaining intracellular calcium homeostasis and preventing toxic calcium excess during high-frequency firing (Juarez and Martínez Cerdeño 2022). Since the rapid firing of PV+ interneurons causes frequent Ca^{2+} influxes and significant calcium fluctuations, effective calcium buffering is of paramount importance for fast-spiking PV+ interneurons (Chard et al. 1993). Besides firing at high frequencies, parvalbumin also endows PV+ neurons with the capacity of having rapid, precise control over the timing of pyramidal neuron spiking and synchronising network oscillations (Druga et al. 2023).

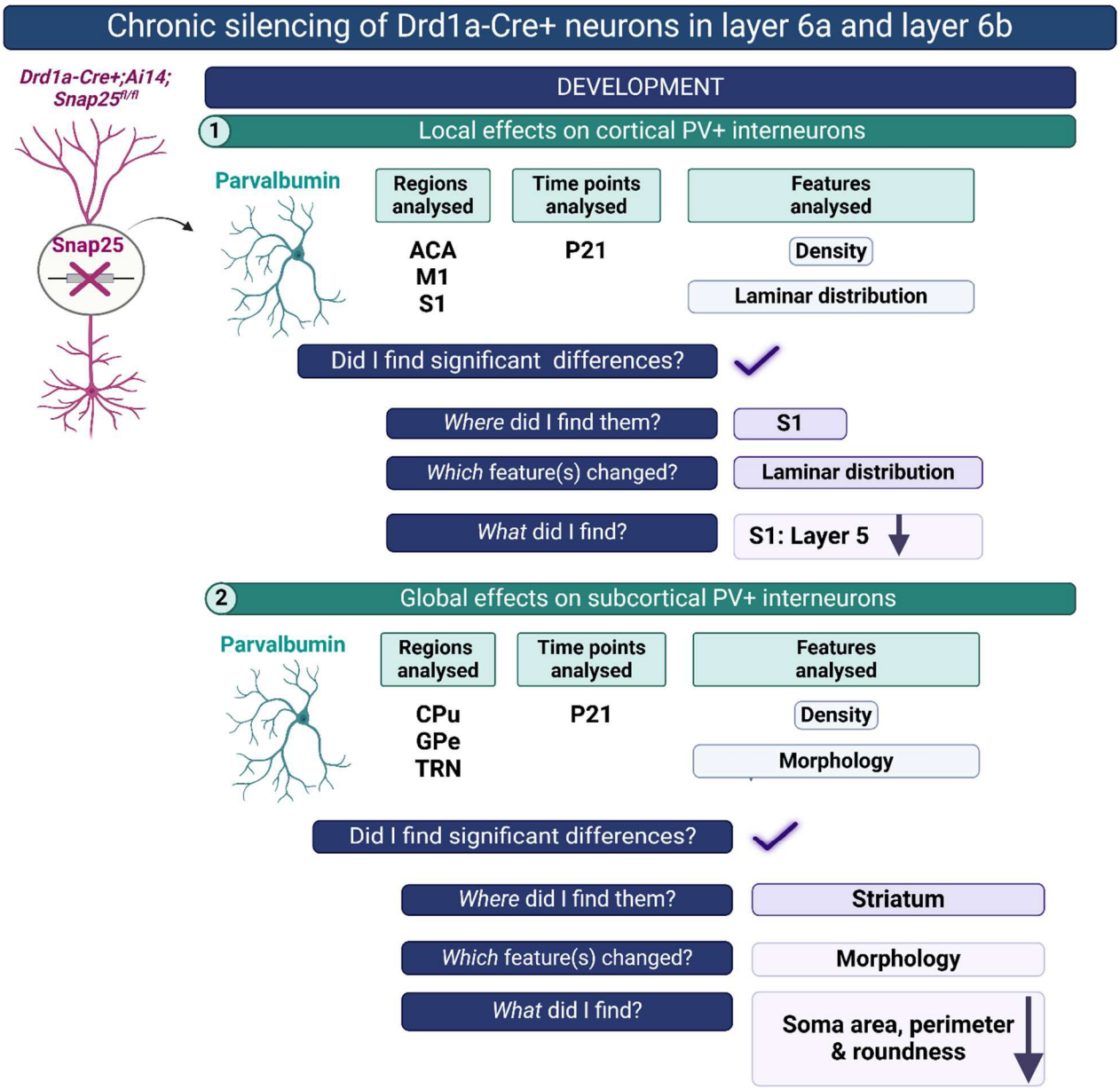
Contrary to calcium-binding proteins, which act as calcium buffers and facilitate rapid synaptic transmission, neuropeptides act as crucial neuromodulators that allow GABAergic interneurons to act more slowly and regulate brain activity across broad spatial and temporal scales (Kepecs and Fishell 2014). The neuromodulatory function enables the peptide-expressing interneurons to strengthen or weaken synaptic activity and dynamically modulate the overall excitability of neuronal networks. The neuropeptides secreted by GABAergic interneurons are also involved in preventing overexcitation of the network, stabilising network activity, and ensuring E/I

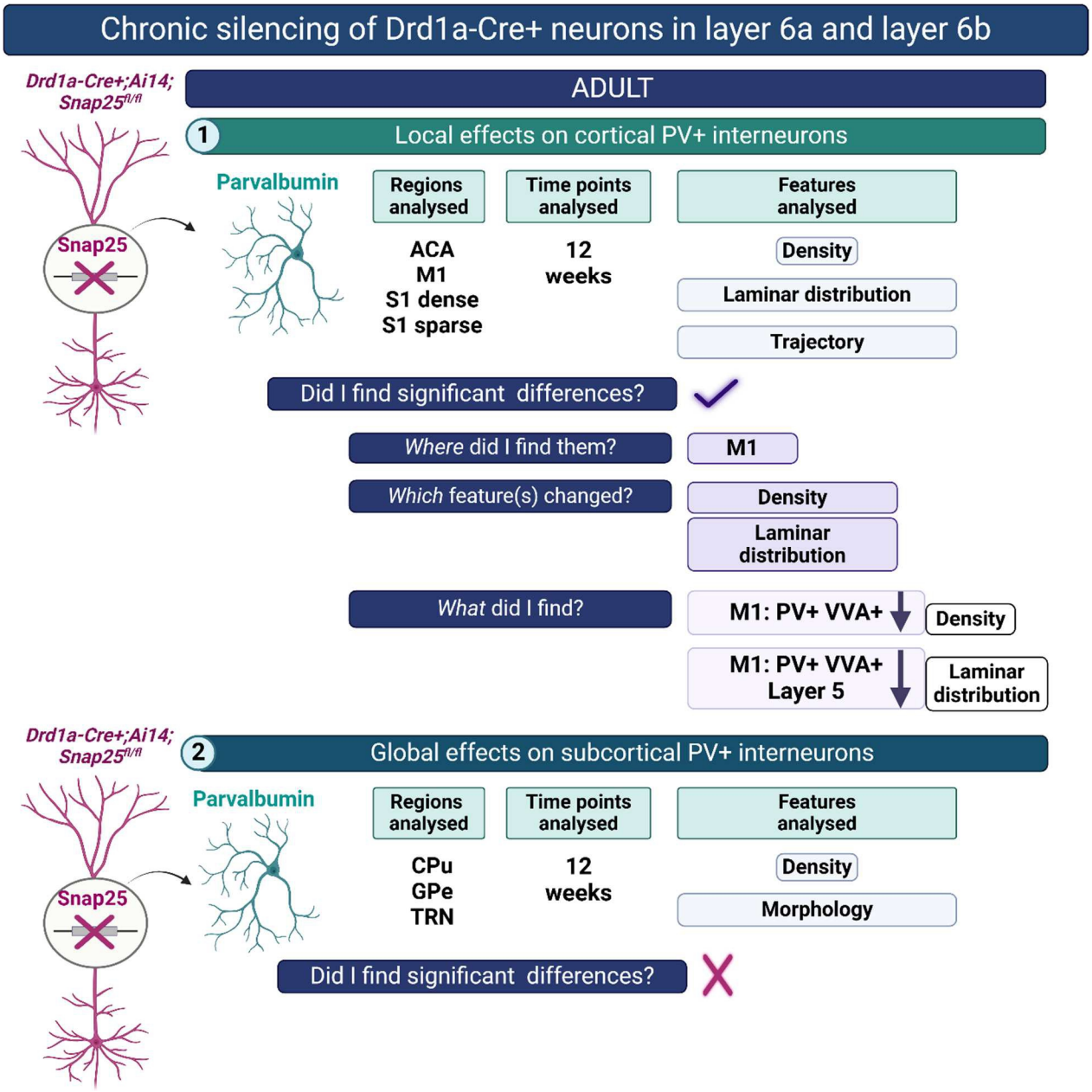
balance (Baraban and Tallent 2004). For instance, the distal dendrite-targeting SST+ interneurons play a crucial role in controlling the integration of sensory inputs, gating information flow in the cortex, and disinhibiting other interneurons (Urban-Ciecko and Barth 2016; Jiang et al. 2021; Song et al. 2021). NPY-expressing interneurons are implicated in shaping network excitability and reducing excessive excitation, thereby maintaining network homeostasis (Bacci et al. 2002; Karagiannis et al. 2009). NPY-expressing cells have anti-epileptic properties and are also involved in pain and itch modulation (Baraban et al. 1997), showing their diverse roles in a wide array of physiological processes. In addition to neuromodulation and circuit stability, neuropeptides are capable of volume transmission, i.e., altering the activity of numerous neurons at once, which affects neuronal ensembles rather than simply nearby cells (Baraban and Tallent 2004).

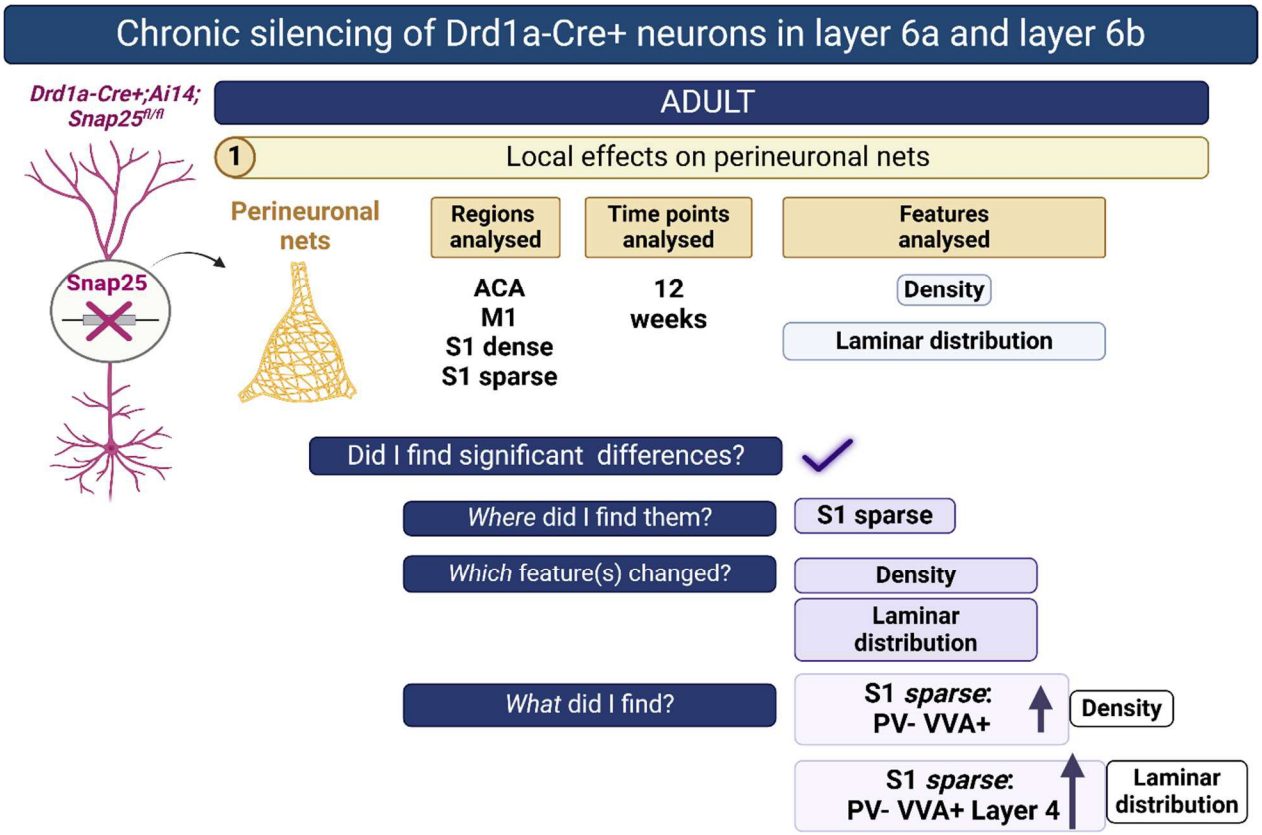
Another factor that supported the selection of this interneuron subtype is that layer 6b contains a great number of NPY+ interneurons, where I conducted the genetic manipulation of Drd1a-Cre+ projection neurons. If the interaction between GABAergic interneurons and pyramidal neurons is defined by their laminar allocation, then alterations in pyramidal neurons will probably impact GABAergic neurons in those layers where they normally reside. The results obtained from developmental brains support this hypothesis. The density of NPY+ interneurons in S1 significantly increased in layer 6b in *Snap25* cKO mice compared to control mice at P21. These results may imply that the loss of synaptic transmission from pyramidal cells affects intralaminar NPY+ interneurons instead of translaminar ones. Since specific synaptic connections between interneurons and pyramidal neurons are formed according to their areal and laminar location, special microcircuits may exist in the cortex where NPY+ interneurons are regulated by deep-layer projection neurons (Wu et al. 2024). However, it has to be noted that the genetic silencing of Drd1a-Cre+ neurons only transiently reorganises the laminar distribution of NPY+ neurons in S1. This transient effect can be explained as follows: 1) the absence of evoked vesicle release from layer 6 causes short-term alterations in the laminar arrangement of NPY+ neurons, and 2) the absence of AP-dependent neurotransmitter release

is not detrimental to NPY+ neuron number and function over time. It is unclear why, at 12 weeks of age, there was no genotype influence on the total density of NPY+ neurons in M1 and S1, suggesting that the total number of GABAergic neurons cannot easily be altered. Rather than experiencing cell death or downregulating their expression, GABAergic interneurons seem to be reacting to changes in their external environment by altering their distribution, trajectory, or morphology. Dissecting the interaction between GABAergic interneurons and deep-layer projection neurons will require more research.

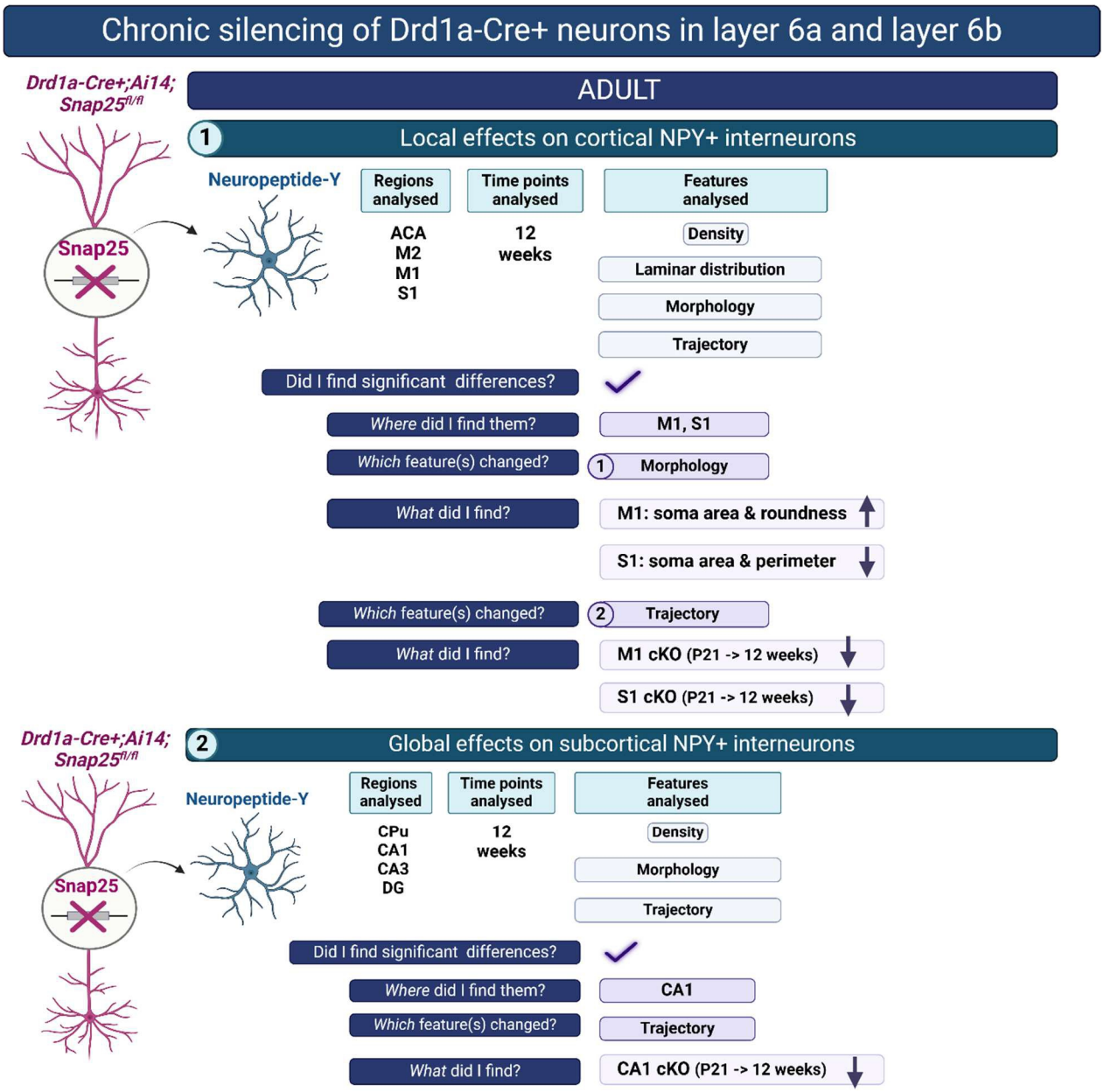
Summary of results – PARVALBUMIN INTERNEURONS



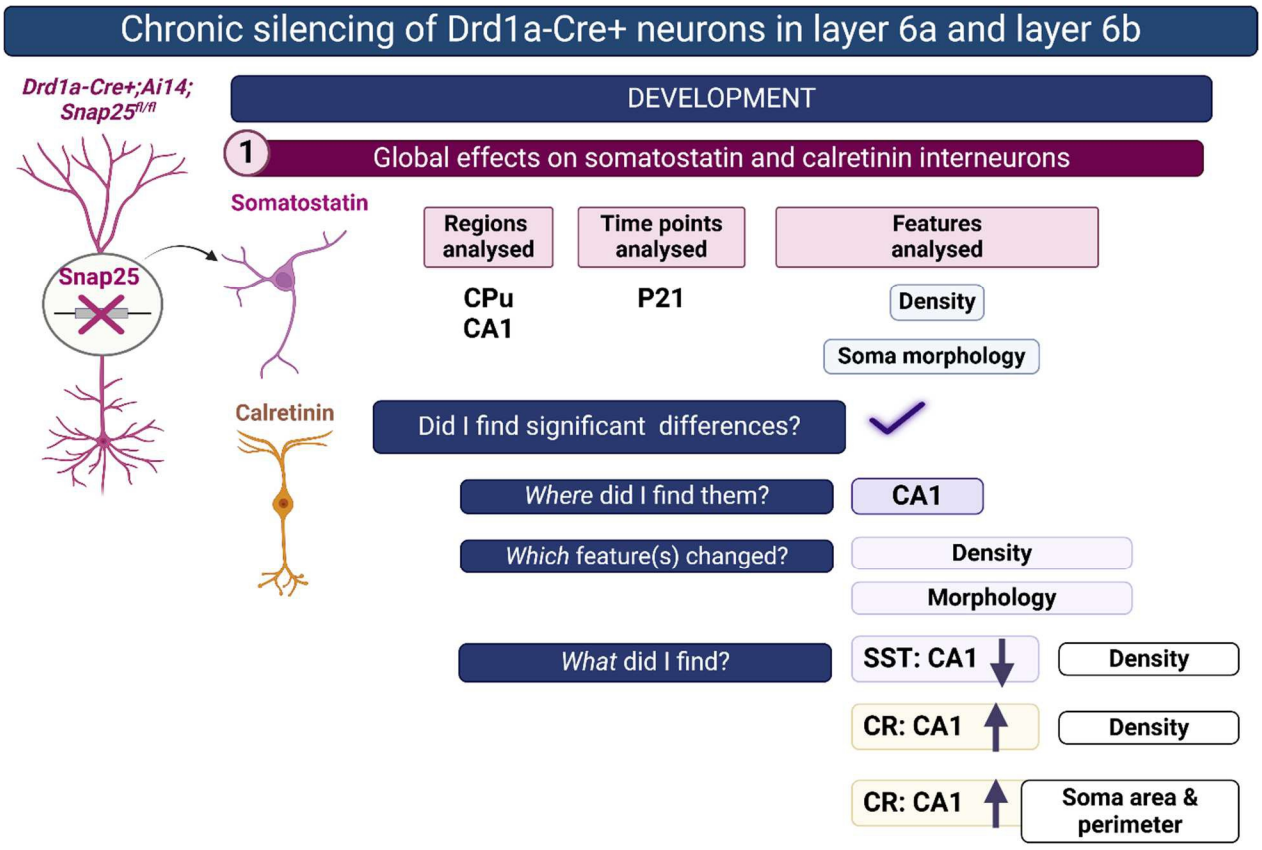

Chronic silencing of Drd1a-Cre+ neurons in layer 6a and layer 6b
Drd1a-Cre+;Ai14; Snap25fl/fl
ADULT
1
Local effects on cortical PV+ interneurons
Parvalbumin
Snap25
Regions analysed
Time points analysed
Features analysed
ACA
M1
S1 dense
S1 sparse
12 weeks
Density
Laminar distribution
Trajectory
Did I find significant differences?
Where did I find them?
M1
Which feature(s) changed?
Density
Laminar distribution
What did I find?
M1: PV+ VVA+
Density
M1: PV+ VVA+ Layer 5
Laminar distribution
Drd1a-Cre+;Ai14; Snap25fl/fl
2
Global effects on subcortical PV+ interneurons
Parvalbumin
Snap25
Regions analysed
Time points analysed
Features analysed
CPu
GPe
TRN
12 weeks
Density
Morphology
Did I find significant differences?

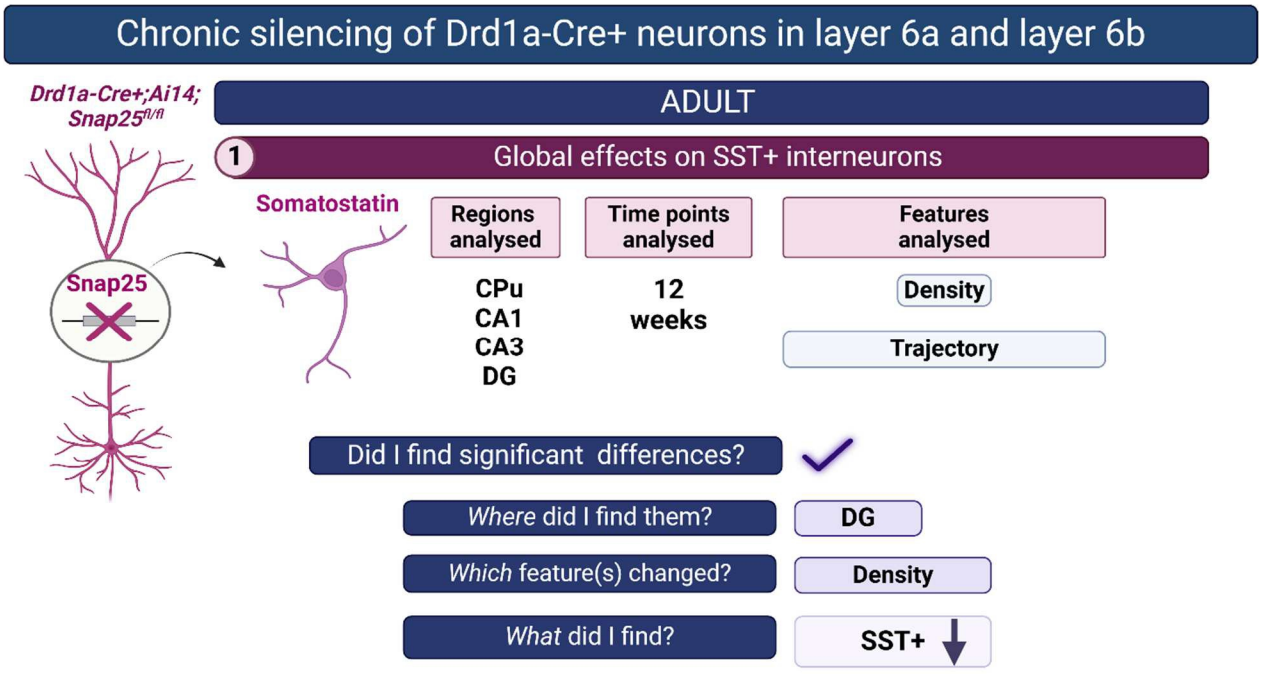

Chronic silencing of Drd1a-Cre+ neurons in layer 6a and layer 6b
Drd1a-Cre+;Ai14; Snap25fl/fl
ADULT
1
Local effects on perineuronal nets
Perineuronal nets
Snap25
Regions analysed
Time points analysed
Features analysed
ACA
M1
S1 dense
S1 sparse
12 weeks
Density
Laminar distribution
Did I find significant differences?
Where did I find them?
S1 sparse
Which feature(s) changed?
Density
Laminar distribution
What did I find?
S1 sparse: PV- VVA+
Density
S1 sparse: PV- VVA+ Layer 4
Laminar distribution

Summary of results – NEUROPEPTIDE-Y INTERNEURONS

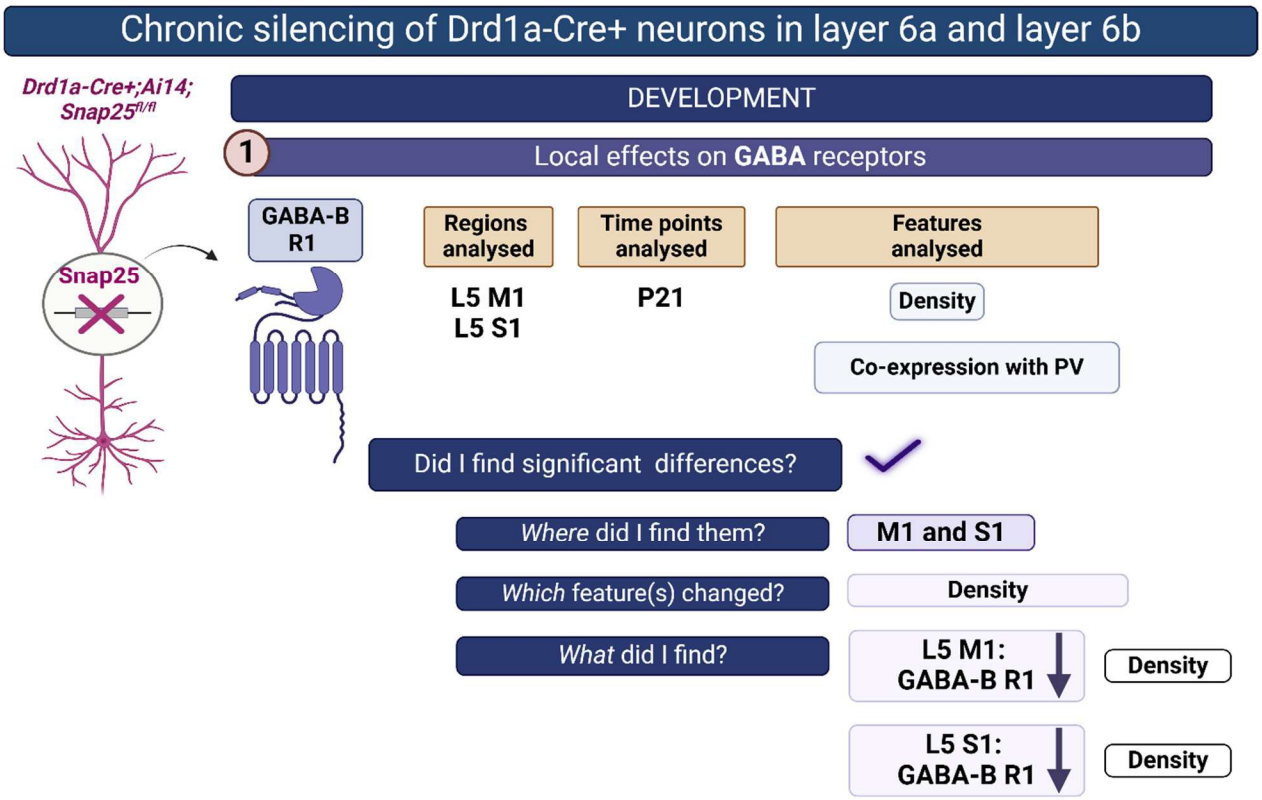


Summary of results – SOMATOSTATIN INTERNEURONS





Summary of results – GABA RECEPTORS



Chapter 5 ..... Results

Chronic augmentation of a subset of glutamatergic Drd1a-Cre+ layer 6 projection neurons

5.1. Introduction

Programmed cell death is responsible for eliminating approximately one-third of cortical GABAergic interneurons between P5 and P10 in the mouse neocortex (Wong et al. 2018; Wong and Marín 2019; Southwell et al. 2012); however, Bax/Bak-dependent apoptosis is not the sole mechanism governing interneuron survival. Non-cell-autonomous mechanisms also act in concert with programmed cell death to adjust the total number of inhibitory neurons in the developing cortex. Cell-surface molecules, neuronal activity, and pro-survival pathways have been demonstrated to shape the number of interneurons during a critical window of interneuron cell death (Southwell et al. 2012; Denaxa et al. 2018; Wong et al. 2018; Wong et al. 2022; Carriere et al. 2020; Priya et al. 2018; Wagner-Golbs and Luhmann 2012).

5.1.1. The PI3K/AKT/mTOR pathway

One such pro-survival pathway is the phosphatidylinositol-3-OH kinase (PI3K)/AKT (protein kinase B) signalling pathway. This highly conserved pathway controls a plethora of intracellular processes, including cell cycle progression, growth, proliferation, vesicle trafficking, metabolism, and cancer progression (Martini et al. 2014; Vanhaesebroeck et al. 2010; Hemmings and Restuccia 2012; Engelman et al. 2006). The PI3K/AKT pathway can be activated by a vast array of external stimuli, including hormones, cytokines, insulin-like growth factor, or epidermal growth factor (EGF) (Guo et al. 2015). G protein-coupled receptors (GPCRs) and monomeric GTPases are other well-known

upstream activators (Luo et al. 2003; Vanhaesebroeck et al. 2010; Yang et al. 2019; Guo et al. 2015; Fritsch et al. 2013).

A key signalling element, downstream of growth factor-activated receptor tyrosine kinases (RTKs), is phosphoinositide 3-kinase (PI3K) (Luo et al. 2003). Following the activation of particular RTKs or GPCRs, class I PI3Ks, consisting of a catalytic p110 subunit and a regulatory p85 subunit, are recruited to the plasma membrane. Upon activation, PI3K uses its p110 domain to convert phosphatidylinositol (3,4)-bisphosphate (PIP2) lipids into phosphatidylinositol (3,4,5)-trisphosphate (PIP3). Acting as a second messenger, PIP3 then binds to the pleckstrin-homology (PH) domains of various downstream proteins, especially the serine-threonine kinases AKT and the 3-phosphoinositide-dependent protein kinase-1 (PDK1) (Luo et al. 2003; Yang et al. 2019; Martini et al. 2014). By phosphorylating Akt at threonine 308 (Thr308), PDK1 achieves the partial activation of Akt (Alessi et al. 1997). Full activation of AKT requires additional phosphorylation at serine 473 (Ser473) by the mammalian target of rapamycin (mTOR) complex 2 (mTORC2) (Guo et al. 2015; Martini et al. 2014). Tuberous sclerosis (TSC) complex ½ is then phosphorylated upon activation of AKT. After TSC1/2 is phosphorylated by AKT, Ras-enriched in brain (Rheb) small GTPase is released from the inhibition of TSC1/2 (Franke 2008). The subsequent activation of the Rheb protein triggers the activation of mTOR complex 1 (mTORC1). AKT can also stimulate mTORC1 by phosphorylating the 40 kDa proline-rich AKT substrate (PRAS40). (Vander Haar et al. 2007; Guo et al. 2015). Two key substrates of mTORC1 are eukaryotic translation initiation factor 4E-binding protein 1 (4E-BP1) and ribosomal protein S6 kinase, 70 kDa, polypeptide 1 (S6K1). The mTORC1 complex upregulates protein synthesis and promotes cell growth by the direct phosphorylation of S6K and inhibition of 4E-BP1 (Luo et al. 2003). The phosphorylation of ribosomal protein S6 (S6) by S6K elevates protein translation and leads to cell proliferation (Hemmings and Restuccia 2012). While stimulation of mTORC1 increases protein synthesis and promotes cellular growth, mTORC2 signalling regulates cell

survival, cytoskeleton organisation, and glucose metabolism (Laplante and Sabatini 2012). For a schematic diagram of the PI3K/Akt/mTOR pathway, please refer to Figure 5.1.

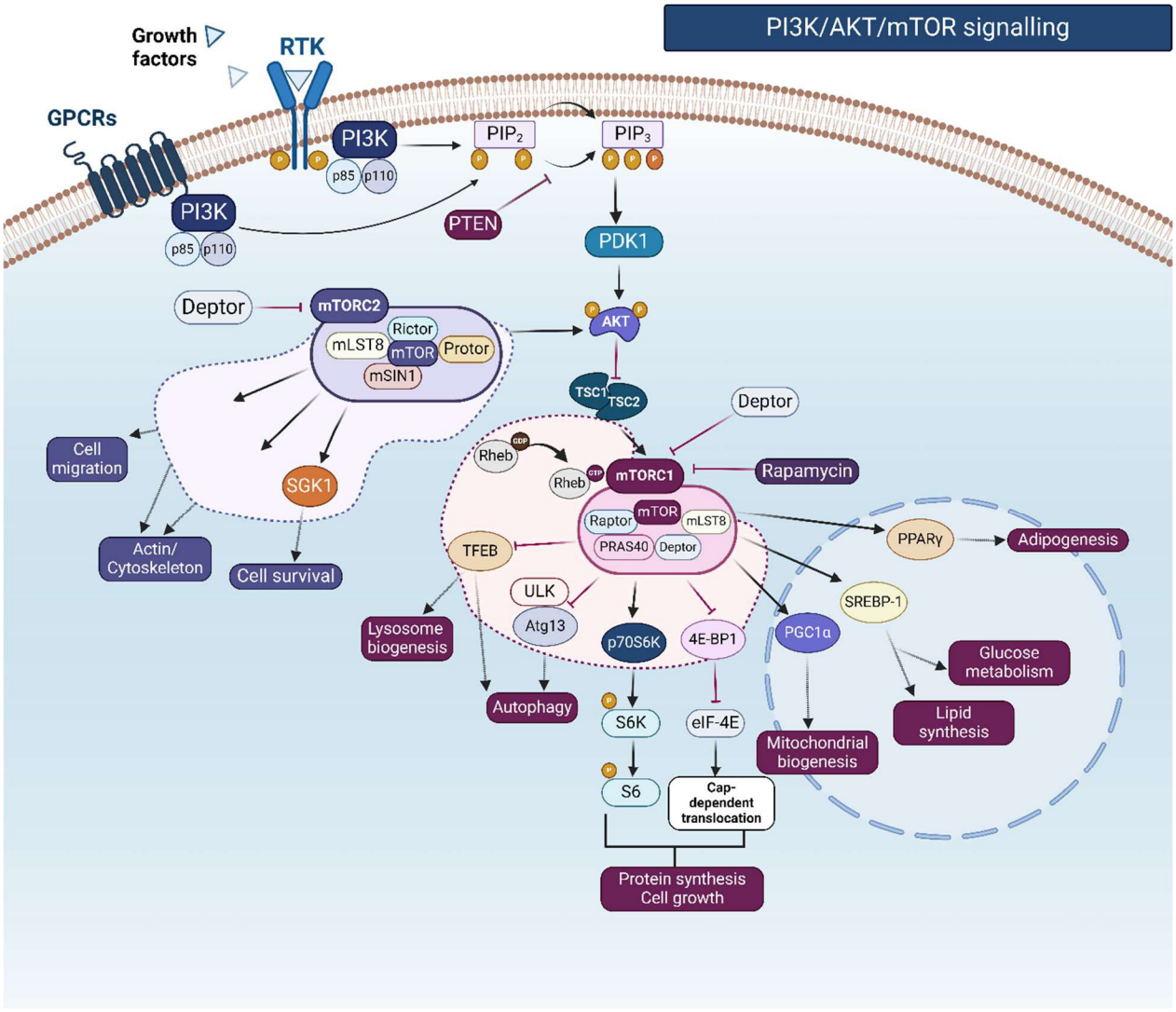


Figure 5.1. Schematic of the PI3K/AKT/mTOR pathway along with the intracellular events it regulates. Upon autophosphorylation of receptor tyrosine kinases, PI3K is recruited to the plasma membrane, where it phosphorylates PIP_2. The conversion of PIP_2 to PIP_3 attracts the serine-threonine protein kinases AKT and PDK1. The lipid phosphatase Pten can antagonise the PI3K/AKT/mTOR pathway by converting PIP_3 back to PIP_2. PTEN is an essential negative regulator of mTOR signalling and plays a critical role in controlling cell proliferation, growth, and tumour signal transduction. Numerous substrates can be phosphorylated by activated AKT. One such substrate is the mTORC1 complex. Upon phosphorylation and inhibition of the TSC1/2 complex, the small GTPase Rheb protein is released, leading to the activation of mTORC1. The subsequent phosphorylation of p70 ribosomal S6 kinase (p70S6K) and eIF4E-binding proteins promotes mRNA translation, cell proliferation, and cellular growth (Franke 2008; Martini et al. 2014). Created with BioRender.

5.1.2. Germline mutations of *PTEN* and its associated diseases

The phosphatase and tensin homologue deleted on chromosome 10 (PTEN) is a crucial negative regulator of the PI3K/AKT/mTOR pathway. Compromised *PTEN* function and insufficient AKT inhibition result in the constitutive activation of the downstream effectors of the PI3K pathway. Such dysregulation fosters an oncogenic environment that promotes tumour formation and facilitates cancer progression (He et al. 2021; Fruman and Rommel 2014). *PTEN* has a high mutation or deletion rate, making it the second most commonly mutated tumour suppressor in cancers, following p53 (Fruman and Rommel 2014; Guo et al. 2015). In addition to the germline mutations of *PTEN* being associated with hamartomas and malignancies, *PTEN* gene mutations occur in 5-10% of individuals with autism spectrum disorder (ASD) (Kreis et al. 2014; Butler et al. 2005). The genetic aetiology of ASD exhibits considerable heterogeneity, with approximately 80% of cases categorised as idiopathic (Frazier 2019). Nonetheless, a significant association has been established between germline heterozygous mutations in the *PTEN* gene and the manifestation of macrocephaly/autism syndrome (Busch et al. 2013; Buxbaum et al. 2007; Hobert et al. 2014). Missense mutations exhibit variable severity, leading to a range of phenotypic outcomes. Point mutations in the *PTEN* gene associated with ASDs do not completely abolish the lipid phosphatase activity of PTEN, resulting in only a partial loss of protein function (Zhou and Parada 2012). Conversely, more severe *PTEN* mutations can lead to the accumulation of stable, inactive PTEN proteins, thereby increasing the likelihood of significant developmental abnormalities and malignancies (Leslie and Longy 2016).

5.1.3. Conditional deletion of *Pten* from select cell populations

Numerous transgenic mouse models have been developed to explore the consequences of dysregulated PI3K/AKT signalling. These mouse models have been instrumental in discovering the phenotypes of *heterozygous* versus *homozygous* deletions. Homozygous *Pten* deletions are lethal, causing embryonic lethality at 7.5 or 9.5 days of gestation due to defects in *Pten*$^{-/-}$ embryonic stem (ES) cells (Di Cristofano et al. 1998; Podsypanina et al. 1999; Suzuki et al. 1998). While heterozygous

germline deletion of *Pten* does not cause embryo-lethality, *Pten*$^{+/-}$ mice developed spontaneous gonadostromal, thyroid, and colon tumours (Di Cristofano et al. 1998).

The generation of conditional knockout mice has revealed further insights into the role of *Pten* in regulating growth-associated signal transduction pathways. The ***Gfap-Cre;Pten$^{fl/fl}$*** mice resulted in the homozygous deletion of *Pten* from granule cells in the dentate gyrus and cerebellum, with additional deletions in populations of cortical neurons. Various histological and neurological abnormalities have been detected in the *Gfap-Cre;Pten$^{fl/fl}$* mutant mice, including seizures, ataxia, macrocephaly, and soma hypertrophy (Backman et al. 2001).

The ***Emx1-Cre;Pten$^{fl/+}$*** mice demonstrated an increase in cerebral cortical mass and total brain mass, accompanied by cortical overgrowth and elevated β-catenin signalling (Chen et al. 2015). Conditional homozygous deletion of *Pten* from forebrain excitatory neurons using the *Nex-Cre,Pten$^{loxP/loxP}$* mice recapitulated certain hallmark features of ASD. However, homozygous knockout mice (KO) experience premature death, indicating that conditional homozygous deletions of *Pten* in excitatory neurons are lethal (Kazdoba et al. 2012).

Another conditional knockout mouse model targeting forebrain excitatory neurons includes the ***CamKII-Cre$^{+/-}$;Pten$^{loxP/loxP}$;Thy1-GFP*** mice. The knockout mice revealed lamina-specific alterations in the morphology of cortical pyramidal neurons in layer 2/3 following the postnatal loss of *Pten* (Chow et al. 2009).

The ***Nse-Cre;Pten$^{loxP/loxP}$*** mouse model effectively replicates key behavioural features of autism, including hypersensitivity to sensory stimuli and hippocampus-related cognitive impairments (Takeuchi et al. 2013; Kwon et al. 2006). Cre is expressed under the neuron-specific enolase (Nse) promoter driving conditional *Pten* deletion in subpopulations of postmitotic cortical neurons, hippocampal granule cells, and CA3 pyramidal cells (Kwon et al. 2006). Excessive mTOR

signalling, neuronal hypertrophy, increased spine density, and ectopic expression of axon projections have all been noted in the *Nse-Cre;Pten$^{loxP/loxP}$* mouse (Takeuchi et al. 2013; Kwon et al. 2006).

There is a limited number of models that are specifically directed at progenitors of inhibitory neurons or subtypes of GABAergic interneurons. One such animal model is the ***Nkx2.1-Cre;Pten$^{flox/flox}$*** mice, where Cre expression is driven by the Nkx2.1 promoter to interneuron progenitors in the ventricular zone. *Pten* loss in cortical interneuron progenitors did not result in macrocephaly, spontaneous seizures, or anxiety-like behaviour (Kwon et al. 2006). Deletion of *Pten* from postmitotic interneurons did not result in changes to interneuron numbers (Vogt et al. 2015), but it altered the ratio of PV+ and SST+ interneurons.

Other significant mouse models contributing to the understanding of ASD include the ***PV-Cre;Pten$^{flox/flox}$*** and ***SST-Cre;Pten$^{flox/flox}$*** mice. Both cKO mice displayed key autism-associated phenotypes, including repetitive behaviours and decreased social novelty preference (Shin et al. 2021). The deletion of *Pten* from PV+ interneurons is associated with deficits in motor learning and a reduction in anxiolytic behaviours. Loss of *Pten* from SST+ interneurons is linked to the manifestation of anxiety-like behavioural traits (Shin et al. 2021).

For a concise summary of the mouse models, please refer to Table 5.1. The table is available in its entirety in the Supplements. For an overview of the cellular effects of the loss of *Pten* on brain development and morphology, please see (van Diepen and Eickholt 2008).

SUMMARY OF CONDITIONAL DELETION OF *PTEN*
IN DIFFERENT BRAIN REGIONS AND CELL TYPES

LOSS OF *PTEN* FUNCTION EXPERIMENTS

MOUSE MODEL	Experimental strategy	Type & time of deletion	Targeted cells	Region of deletion	Behavioural phenotype	Anatomical & physiological alterations	Reference
***Pten*$^{-/-}$**	gene targeting techniques in the mouse germ line and mouse ES cells (inactivation *via* homologue recombination)	homozygous deletion; embryonic	somatic	whole-body knockout	embryonic lethality at days 3.5 and 9.5	impaired ability of ES cells to differentiate into endodermal, ectodermal and mesodermal derivatives; hyperplastic-dysplastic changes in the intestinal mucosa, testis atrophy, skin hyperkeratosis spontaneous development of germ cell, gonadostromal, thyroid, and colon tumours	Di Cristofano et al. 1998
***Pten*$^{+/-}$**	gene targeting deletion of PTEN in exon 5	heterozygous deletion; embryonic	germline	whole-body knockout	N/A embryonic lethality in Pten-/- mice occurs by day 6.5	A variety of tumours lymphomas, dysplastic intestinal polyps, endometrial complex atypical hyperplasia, prostatic intraepithelial neoplasia, and thyroid neoplasms	Podsypanina et al. 1999
Gfap-Cre; Pten$^{fl/fl}$	Cre-*loxP* system homozygous *Pten flox* mice *Pten$^{loxP/loxP}$*) crossed	tissue-specific deletion; conditional knockout	deletion targeted to glial cells, but Pten loss is limited to	granule cells of the dentate gyrus and the cerebellum	neurological defects, including seizures and ataxia,	macrocephaly, cell-autonomous increase in soma size,	(Backman et al. 2001)

	with *Gfap-Cre* transgenic mice	(homozygous), by P0-P14	neuronal cells instead of astrocytes	The extent of *Pten* loss is greater in the dentate gyrus, plus some cortical neurons	developed by 9 weeks of age, status epilepticus	increased phosphorylation of Akt, thickened cerebellar folia, dysplasia of granule cells, dysplastic Purkinje cells, hypertrophied glial cells and oligodendrocytes with aberrant myelination	
Gfap-Cre; Pten$^{fl/fl}$	Cre-*loxP* system (homozygous *Pten flox* mice (*Pten$^{loxP/loxP}$*) crossed with *Gfap-Cre* transgenic mice)	tissue-specific deletion, conditional knockout (homozygous), by P14	astrocytes 80–90% of neurons in the hippocampus and cerebellar granule neurons, 50–80% of pyramidal neurons	astrocytes throughout the brain, dentate gyrus, cerebellum and the cerebral cortex	seizures, ataxia, premature death	altered morphology and neuronal hypertrophy, increased ribosome density, increased spine density, myelination defects, enlarged presynaptic terminals, marked decreased synaptic transmission, increased astrocyte proliferation	(Fraser et al. 2008; Fraser et al. 2004)
Emx1-Cre; Pten$^{fl/+}$	Cre-*loxP* system (*Pten$^{loxP/loxP}$*) crossed with *Emx1$^{tm1(cre)Krj}$* (*Emx1-Cre)* transgenic mice)	tissue-specific deletion, conditional knockout (heterozygous) *Emx1-Cre^{+}; Pten$^{loxP/loxP}$* Mice are not viable after P10.	cortical neural progenitor cells and their descendants, including pyramidal neurons, astrocytes, and oligodendrocytes, plus a subset of cells in the olfactory bulb	cerebral cortex (no region-specificity)	social behavioural deficits	overgrowth of the cerebral cortex, increased total brain mass and cerebral cortex mass, excess neurons at birth and excess glia in adulthood	(Chen et al. 2015)
Nex-Cre, Pten$^{loxP/+}$;	crossing homozygous NEX-*Cre* knock-in mice with Cre-negative	tissue-specific deletion, conditional knockout	excitatory neurons immediately after they	all forebrain (no region-specificity)	premature lethality of homozygous	macrocephaly and neuronal hypertrophy NEX-Cre+; Pten$^{loxP/loxP}$	(Kazdoba et al. 2012)

Nex-Cre, Pten$^{loxP/loxP}$	conditional neuron subset-specific *Pten* (NS-*Pten*) knockout mice (Pten$^{loxP/loxP}$)	(homozygous (NEX-Cre+; Pten$^{loxP/loxP}$) kn ockout mice die within 1 week after birth	become postmitotic		Pten knockout mice	mice, intact migration but overmigration into the marginal zone and distortion of cortical cellular layers, MAP2 upregulation, higher levels of the NMDA receptor subunits 2A and 2B	
Nse-Cre; Pten$^{loxP/loxP}$	Both alleles of the *Pten* gene contain loxP sites, and *Cre* is expressed under the neuron-specific enolase promoter	conditional knockout mouse, tissue-specific deletion; late-onset model	granule cell, pyramidal neurons in the CA3, select populations of postmitotic neurons in the cortex	hippocampal dentate gyrus, CA3, and the entorhinal cortex	autism-relevant behaviours, spontaneous seizures and deficits in hippocampus-based social and cognitive behaviours, hypersensitivit y to sensory stimuli, and anxiety	macrocephaly of the dentate gyrus and the overlying neocortex, reduced dendritic arborization of DG neurons, overactivation of mTOR in DGCs and CA3 pyramidal neurons, neuronal hypertrophy, enhanced LTP, impaired LTD	(Takeuchi et al. 2013)
Nse-Cre; Pten$^{loxP/loxP}$	*Neuron-specific enolase* (*Nse*) promoter-driven *Cre* transgenic mouse line	conditional knockout mouse, tissue-specific deletion; by 4 weeks of age	subsets of differentiated neurons in the cortex and hippocampus (30-60% of forebrain neurons by 4 weeks of age)	layers III to V of the cerebral cortex and in the CA3, dentate gyrus granular layer (GL), and polymorphic layer (PML) of the hippocampal formation	ASD phenotype, including exaggerated reaction to sensory stimuli, anxiety-like behaviours, seizures, decreased learning; deficits in nest formation, less interaction with the novel target mouse,	macrocephaly, neuronal hypertrophy, axonal and dendritic growth, ectopic positioning of dentate axons, increased spine density, altered polarity of neuronal processes	(Kwon et al. 2006)

					and defects in maternal care		
Gli1-Cre-ERT2::* *Pten$^{flox/flox}$	Gli1-CreER^{T2} hemizygous: PTEN$^{wt/flox}$ mice crossed to PTEN$^{wt/flox}$ mice to generate Gli1CreER^{T2} Hemizygous:: PTEN$^{flox/flox}$ mice	conditional, Cre-inducible knockout; tissue-specific deletion, Injection of tamoxifen at P14	a subset of granule cells (deletion of Pten from ~27% of hippocampal granule cells)	hippocampus	epilepsy	increased intrinsic excitability of Pten-deficient cells, lower input resistance, tendency towards burst firing, overlapping dendritic branches, impaired excitation/inhibiti on balance, increased sEPSC frequency, sexual dimorphism, females (both control and KOs) receiving more sEPSCs and sIPSCs	(Santos et al. 2017)
CamKII-Cre+/-; Pten$^{loxP/loxP}$; Thy1-GFP	Mice with a Pten$^{loxp/loxp}$ allele flanking exon 5 crossed with mice carrying both an αCamKII-driven Cre transgene and a Thy1-driven green fluorescent protein	conditional knockout; tissue-specific deletion (*Camk2a*) promoter driving Cre recombinase expression in the forebrain, including CA1 pyramidal neurons in the hippocampus	excitatory forebrain neurons	cerebral cortex and hippocampus, no region-specificity	not tested	laminar-specific, large-scale growth of apical dendrites in *Pten$^{-/-}$* mice; longer apical dendrites detected only in layer 2/3 pyramidal neurons, No effect on basal dendritic length, mature cortical neurons exhibit constitutively active growth-promoting pathways	(Chow et al. 2009); (Sperow et al. 2012)
Nkx2.1-Cre* × *Pten$^{flox/flox}$	crossing *Pten^{Flox}* mice to *Nkx2.1-Cre* mice; *Ai14* Cre-dependent reporter line to	conditional knockout; tissue-specific deletion (*Nkx2.1-Cre* BAC transgenic line	interneuron progenitors in the ventricular zone; MGE-and POA-derived	ventricular zone	deficits in social interaction, reduced social behaviour,	increased AKT signalling; differential impact on SST^{+} and PV^{+} interneurons;	(Vogt et al. 2015)

	label Cre-expressing cells	drives Cre expression in the ventricular zone (VZ) of the MGE and POA (beginning on embryonic day ~9.5)	GABAergic interneurons		but normal levels of exploratory activity, locomotion, and anxiety	increased PV^+/SST^+ ratio, ectopic PV^+ processes in layer 1; increased inhibition of neocortical pyramidal neurons	
PV-Cre × Pten$^{flox/flox}$; ***SST-Cre × Pten$^{flox/flox}$***	$Pten^{fl/fl}$ mice crossed to Sst-$Cre^{+/+}$ mice to generate Sst-$Cre^{+/+}/Pten^{fl/+}$ mice; three types of experimental mice generated 1) Sst-$Cre^{+/+}/Pten^{+/+;}$ 2) Sst-$Cre^{+/+}/Pten^{fl/+;}$ 3) Sst-$Cre^{+/+}/Pten^{fl/fl}$; same breeding strategy applied to breed PV-$Cre^{+/+}/Pten^{fl/+}$ breeders and their offspring	Cre/loxP recombination system; conditional knockout; cell type-specific deletion	parvalbumin and somatostatin interneurons	no region specificity	autism-like symptoms; PV-Pten-KO mice exhibiting hyperactivity, impairment in motor coordination/ learning, anxiolytic-like behaviors; Sst-Pten-KO displaying anxiety-like behavior	not tested	(Shin et al. 2021)

5.2. Selective deletion of *Pten* from subsets of cortical Drd1a-Cre+ projection neurons in layer 6

The discovery that pyramidal neurons are critical regulators of interneuron survival by inhibiting *Pten* during developmental programmed cell death (Wong et al. 2018) is a significant advancement in our understanding of the mechanisms governing the total number of inhibitory neurons in the developing neocortex. This raises important questions about which population of pyramidal neurons is responsible for controlling interneuron survival. Despite various animal models with conditional *Pten* deletion, the majority of these models failed to achieve selective targeting of specific cell populations. This poses a significant challenge, as *Pten* deletion occurs in various neuronal and/or glial populations, making it difficult to isolate the contributions of specific cell types to the observed phenotype. Moreover, the mouse models with conditional deletion of *Pten* from subsets of pyramidal neurons are scarce.

Therefore, in collaboration with Professor Britta Eickholt at the Charité - Universitätsmedizin Berlin, we set out to engineer a novel conditional knockout strain to investigate the effects of deleting *Pten* from a subset of excitatory projection neurons in cortical layer 6. This is the first conditional knockout strain to date that achieved *Pten* deletion from a specific subset of pyramidal neurons. The generation of the *Drd1a-Cre;Ai9;Pten$^{fl/fl}$* mice opened up new avenues to study *Pten* deletions in a layer-specific manner.

5.2.1. Generating a novel conditional knockout strain to study the effects of *Pten* deletion from subsets of Drd1a-Cre+ projection neurons

To generate a novel *Pten* cKO mouse model where *Pten* has been conditionally deleted from subsets of layer 6 projection neurons, first, a *Tg(Drd1a-cre)FK164Gsat/Mmucd* (Drd1a-Cre) driver line that drives Cre expression under the dopamine receptor D1 (Drd1) promoter was crossed to B6.Cg-*Gt(ROSA)26Sor$^{tm9(CAG-tdTomato)Hze}$*/J (Ai9) Cre reporter line (https://www.jax.org/strain/007909) expressing tandem dimer tomato (tdTomato) fluorescence following Cre recombination. The resulting

strain (*Drd1a-Cre;Ai9*) labels a mixed subset of Drd1a-Cre+ neurons in layers 6b and 6a in red. By utilising the Drd1a-Cre line, it has been shown that layer 6b contains separate subcircuits that comprise diverse subpopulations, such as L1a-projecting L6b-Drd1 neurons, POm/L5a-projecting L6b-Drd1 neurons, and a smaller subset of SC-projecting L6b cells (Zolnik et al. 2024). Although it should be emphasised that not all Drd1a-Cre+ layer 6b neurons are depolarised by orexin, the Drd1a-Cre line also identified an orexin-sensitive subpopulation of layer 6b cells (79% of Drd1a-Cre+ cells in S1) (Zolnik et al. 2024). To obtain conditional homozygous and heterozygous mice, a B6.129S4-*Pten^{tm1Hwu}*/J (Pten^{flox}) mouse harbouring loxP-flanked exon 5 of the *Pten* gene was crossed to *Drd1a-Cre;Ai9* mice. The resulting tissue-specific *Drd1a-Cre;Ai9,Pten$^{fl/fl}$* knockout mice therefore delete *Pten* exclusively from subsets of Drd1a-Cre+ neurons. The schematic diagram illustrating the breeding strategy of *Pten* cKO mice is shown below (Figure 5.2.).

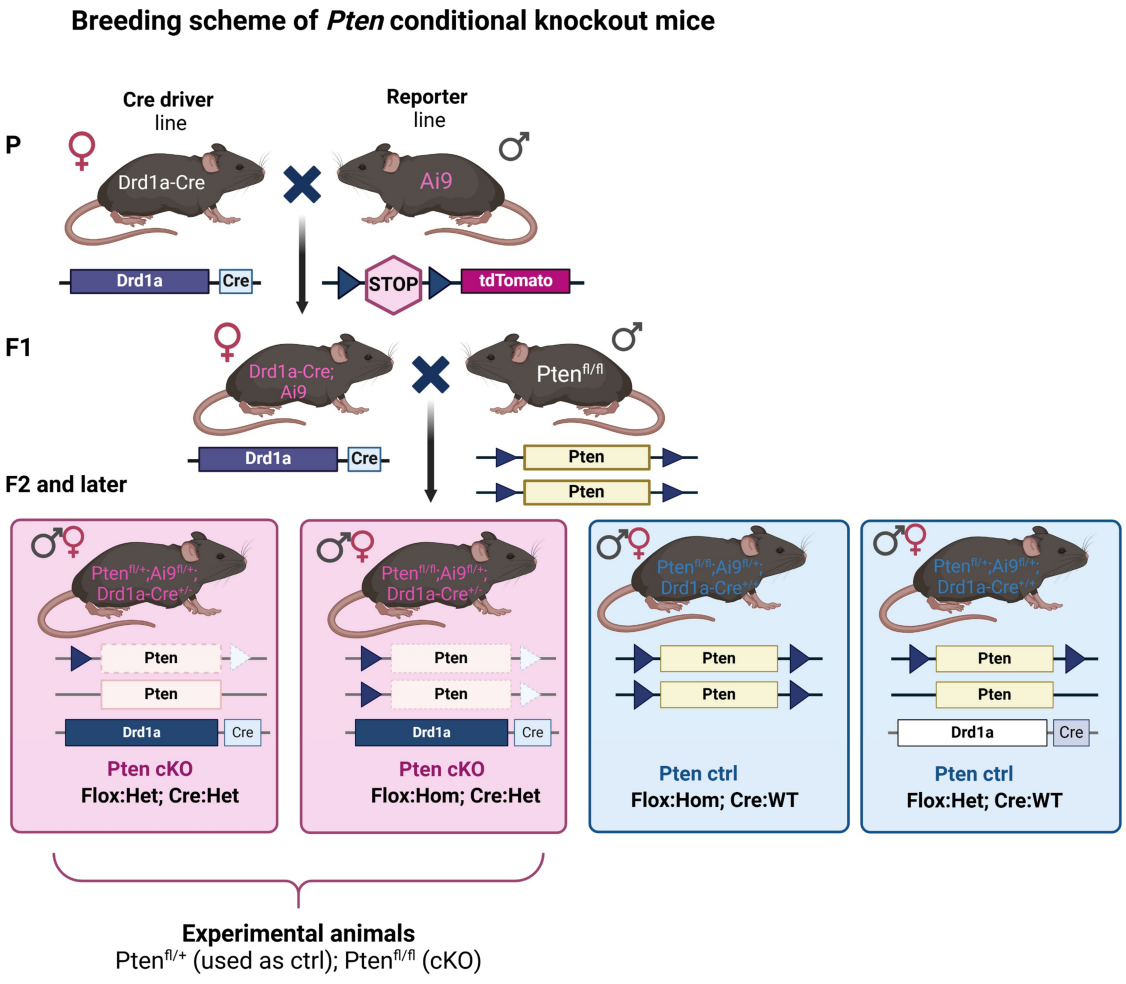


Figure 5.2. Schematic illustration of the breeding of the *Drd1a-Cre;Ai9,Pten$^{fl/fl}$* conditional knockout mice. Selective deletion of the *Pten* gene from a subtype of corticothalamic projection neurons in layers 6a and 6b was achieved by crossing *Pten$^{fl/fl}$* mice with *Drd1a-Cre;Ai9* mice. Note that conditional heterozygous mice (*Drd1a-Cre$^{+/-}$;Ai9,Pten$^{fl/+}$)* were used as controls throughout the thesis instead of *Drd1a-Cre$^{+/+}$;Ai9,Pten$^{fl/+}$* or *Drd1a-Cre$^{+/+}$;Ai9,Pten$^{fl/fl}$* due to the absence of tdTomato expression in these animals.

5.2.2. Estimating the time of *Pten* removal from Drd1a-Cre+ neurons in the *Pten* cKO mice

It is important to ascertain when *Pten* gets deleted from our targeted cell population in the newly engineered *Drd1a-Cre;Ai9,Pten$^{fl/fl}$* mice. The *Drd1a-Cre;Ai14* mice display a considerable increase in the density of tdTomato+ cells between postnatal days 3 and 8, albeit Cre-expressing cells only become numerous in the subplate/L6b at P8 and beyond (Hoerder-Suabedissen et al. 2018). To get a better estimate of when *Pten* gets removed from Drd1a-Cre+ neurons, it is essential to know the half-life of Pten mRNA and protein levels. However, a variety of reasons make it difficult to obtain a precise estimate of Pten half-life, which results in inconsistent findings and numbers in the literature. One such complication arises from the absence of information on whether the half-life of the Pten protein refers to *cytoplasmic* or *nuclear* Pten. Besides the subcellular localisation, another factor affecting the consistency of results on the half-life of Pten is the variety of cell lines and conditions used to conduct such measurements. Pten half-life, as determined by cell line experiments, ranges from 2-3 hours to 24-72 hours (please refer to Table 5.2.). Wu et al. calculated the half-life of Pten protein to be between 48 and 72 hours, but Ho et al. reported an average half-life of 7-8 hours regardless of normal or mutant/transfected cells. Since tdTomato+ Drd1a-Cre+ cells are only abundant in the *Drd1a-Cre;Ai14* mice in M1 and the anterior somatosensory cortex at P8 (Hoerder-Suabedissen et al. 2018), the complete removal of Pten mRNA and Pten protein levels is expected to occur between P8 and P11 in the *Drd1a-Cre;Ai9,Pten$^{fl/fl}$* mice (within 48-72 hours following Cre-mediated recombination of the floxed alleles in Drd1a-Cre+ neurons). Therefore, the genetic deletion of *Pten* from Drd1a-Cre+ neurons in the *Pten* cKO mice is likely to coincide with the developmental

programmed cell death of GABAergic interneurons (P7-P10). Note that the peak of cell death in the subplate occurs within the same time window (~P8) (Hoerder-Suabedissen and Molnár 2013).

Pten	Localisation	Half-life		References
		Wild-type	Mutant	
Protein	not indicated	>8 hours	~2 hours	(Xu et al. 2010)
Protein	cytoplasmic	~7.5 hours	N.A.	(Trotman et al. 2007)
Protein	nuclear	~7.5 hours	N.A.	
Protein	forced cytoplasmic	N.A.	4.5 hours (cycloheximide (CHX) treatment)	
Protein	forced nuclear	N.A.	15 hours (cycloheximide (CHX) treatment)	
Protein	not indicated	N.A.	~8 hours (Pten missense mutations L108P and L112P)	(Spinelli et al. 2015)
Protein	nuclear	N.A.	~3 hours (cycloheximide (CHX) treatment)	(Ge et al. 2020)
Protein	not indicated	>2 hours	N.A.	(Georgescu et al. 1999)
Protein	not indicated	~6 hours (293T cells)	3-4 hours (Pten missense mutants H118P, I135R, D252G, and N276S)	(Wong et al. 2020)
mRNA	N.A.	3 hours (BT474 cell)	5.6 hours (after overexpression of RBM38)	(Zhou et al. 2017)
mRNA	N.A.	1.9 hours (MDA-MB-453 cell)	3.3. hours (after overexpression of RBM38)	
mRNA	N.A.	5.1 hours (BT474 cell)	1.9 hours (after RBM38 knockdown)	
mRNA	N.A.	2.6 hours (MDA-MB-453 cell)	1.7 hours (after RBM38 knockdown)	
Protein	not indicated	N.A.	48-72 hours (full-length PTEN C124S protein,	(Wu et al. 2000)

			catalytically inactive mutant)	
Protein	not indicated	N.A.	12-24 hours (PTEN C124S 1–377 mutant, truncation)	(Birle et al. 2002)
Protein	not indicated	~2 hours (inactive PTEN-C124G)	~1.5 hours (S385A mutants, 50 µg/ml cycloheximide treatment)	
Protein	not indicated	N.A.	~1 hour (S380A mutants, 50 µg/ml cycloheximide treatment)	
Protein	not indicated	N.A.	~45 minutes (double S380A/S385A (SA/SA) mutants)	
Protein	not indicated	2-4 hours (cell type-dependent)	N.A.	(Yu et al. 2009)
Protein	not indicated	~10 hours (TGF-β1 untreated cells; hepatocarcinoma cell line SMMC-7721)	~4 hours (TGF-β1 treated cells; hepatocarcinoma cell line SMMC-7721)	(Yang et al. 2009)
Protein	not indicated	>24 hours	<4 hours (Y336F mutant treated with CHX)	(Yim et al. 2009)
Protein	not indicated	>24 hours	<4 hours (Rak knockdown)	
mRNA	N.A.	4.4 hours (A549 cells, 5 µg/ml actinomycin D treatment)	1.7 hours (ATXN3 depletion, A549 cells, 5 µg/ml actinomycin D treatment)	(Sacco et al. 2014)
Protein	not indicated	>20 hours (A549 cells)	similar to WT (ATXN3 depletion)	
Protein	not indicated	~20 hours	similar to WT after PI3K inhibitors	(Mukherjee et al. 2021)
Protein	not indicated	~5.5 hours (293T cells)	~2 hours (I101T mutants)	(Wong et al. 2018)

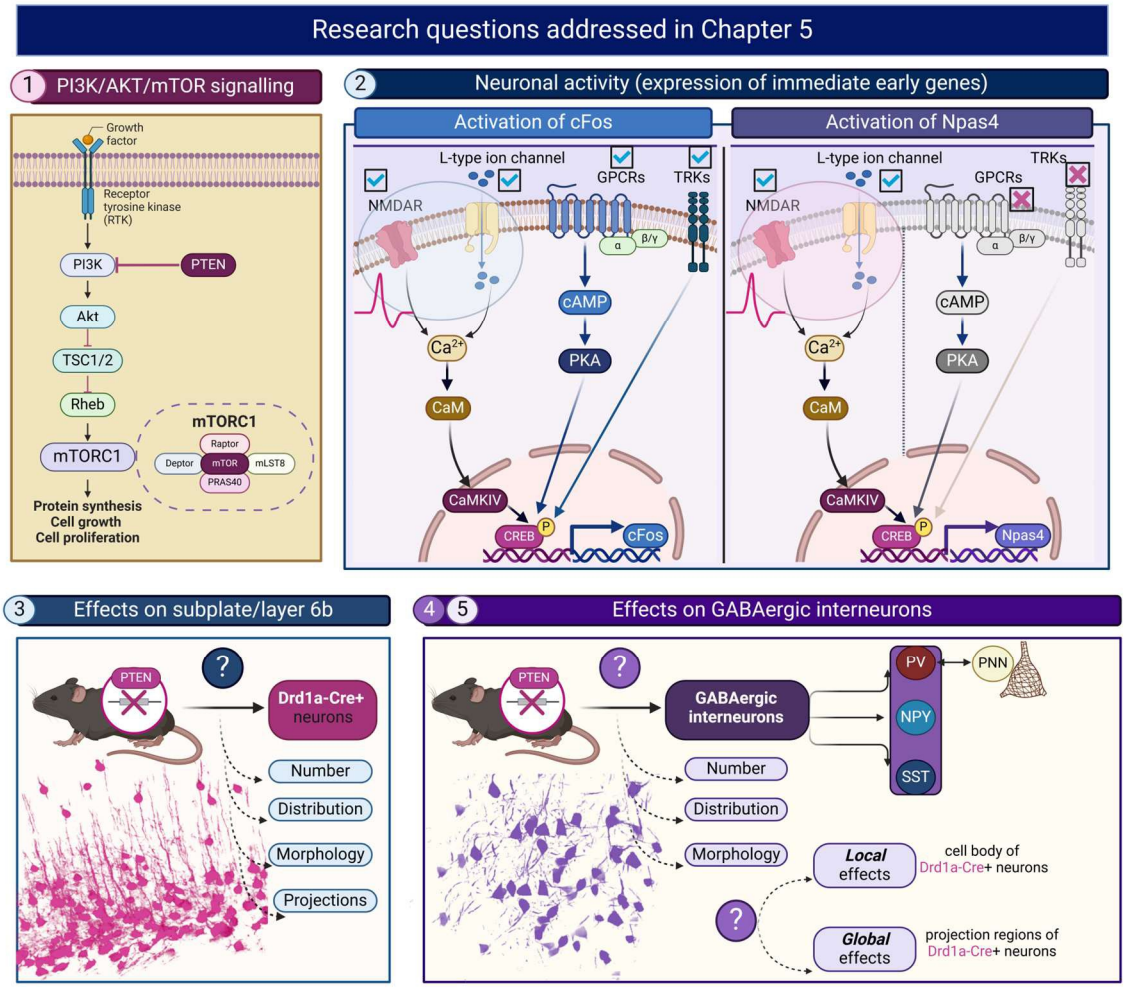
Table 5.2. Half-lives of Pten mRNA and protein. The table gives an overview of the $t_{1/2}$ values of Pten mRNA and protein determined in WT and mutant cells. Note that Pten half-life varies significantly across different cell lines, experimental conditions, and studies.

5.3. Aims and Objectives

I deleted *Snap25* from Drd1a-Cre+ neurons in Chapter 4 to genetically 'silence' subsets of layer 6 projection neurons. In this chapter, I removed *Pten* from Drd1a-Cre+ neurons in order to genetically 'enhance' the same subgroups of layer 6 projection neurons. Our preliminary findings have shown that the conditional deletion of *Pten* from Drd1a-Cre+ neurons altered the morphology and intrinsic electrophysiological properties of Drd1a-Cre+ neurons in layers 6a and 6b. Specifically, *Pten*-ablated Drd1a-Cre+ neurons exhibited an increase in the number of dendritic spines and had thicker dendrites. Furthermore, *Pten*-ablated Drd1a-Cre+ neurons had more local inputs than long-range ones (unpublished data, Zolnik TA) and *Pten* deletion significantly elevated the maximal firing rate of Drd1a-Cre+ neurons in cKO animals compared to control mice (unpublished data, Zolnik TA).

In Chapter 5, I set out to examine the following questions:

1) How does the conditional deletion of *Pten* from subsets of Drd1a-Cre+ neurons during postnatal development affect mTOR signalling?
2) Does the conditional ablation of *Pten* from subsets of Drd1a-Cre+ neurons lead to increased neuronal activity in layer 6b?
3) Does the conditional deletion of *Pten* from subsets of Drd1a-Cre+ neurons alter the number, laminar distribution, and axonal projections of Drd1a-Cre+ neurons in layer 6b?
4) How do distinct subtypes of GABAergic interneurons respond to the deletion of *Pten* from subsets of Drd1a-Cre+ neurons?
5) What are the long-term consequences of the loss of *Pten* from subsets of Drd1a-Cre+ neurons on PV+, SST+, and NPY+ interneurons?



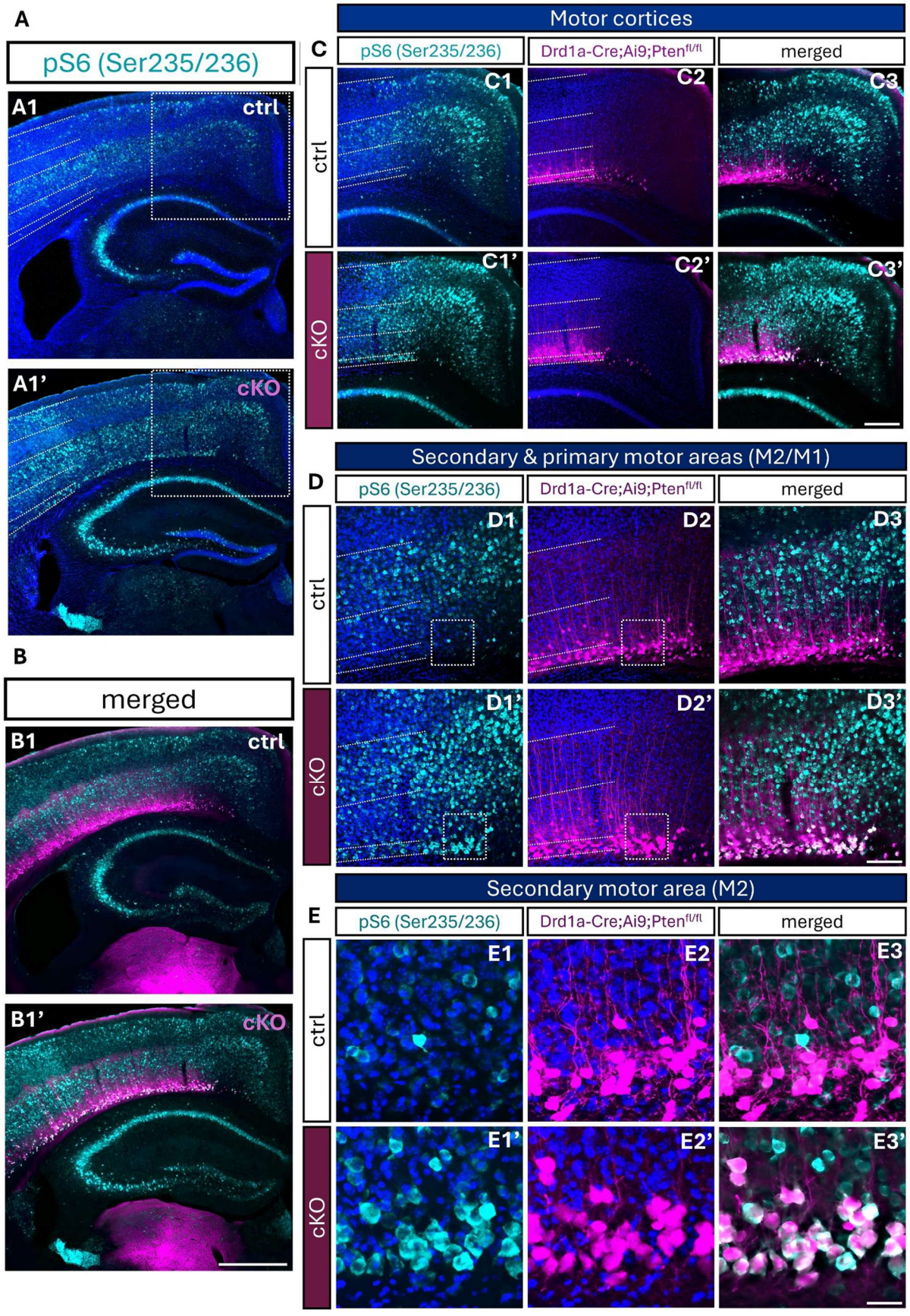
For a summary of research objectives, please refer to Figure 5.3.

Figure 5.3. Schematic illustration of the research questions addressed in Chapter 5. The first two questions of this chapter are concerned with the characterisation of the novel conditional knockout strain (*Drd1a-Cre;Ai9;Pten$^{fl/fl}$*) engineered to study the effects of the loss of *Pten* from layer 6b neurons on subplate survival and inhibitory networks. The first question pertains to the PI3K/AKT pathway and whether *Pten*-deleted layer 6b neurons exhibit increased mTOR signalling. The second question addresses whether the deletion of *Pten* from subsets of Drd1a-Cre+ neurons induces the expression of immediate early genes. The third major question focuses on the effects of the loss of *Pten* on layer 6b neurons, especially on their number, distribution, and soma morphology. The fourth and fifth questions seek to answer how the deletion of *Pten* from Drd1a-Cre+ neurons affects different subtypes of GABAergic interneurons in the adult brain. *Created with BioRender*.

5.4. Characterisation of the novel *Pten* conditional knockout mice

5.4.1. Elevated levels of phospho-S6 in subsets of cortical layer 6b neurons after *Pten* deletion

To determine whether the genetic ablation of *Pten* from a subset of cortical neurons in layer 6 resulted in the persistent activation of the PI3K/AKT/mTOR pathway, I performed immunohistochemical staining for the active form of the ribosomal protein S6 (S6) phosphorylated at serine residues 235 and 236 (pS6$^{235/236}$). pS6 has conventionally been used as a readout of hyperactive mTOR signalling (Gutilla and Steward 2016). Qualitative assessment of pS6$^{235/236}$ immunostaining revealed enhanced pS6 signal intensity in Drd1a-Cre+ neurons in the adult primary motor (Figure 5.4. A-B, C-E) and somatosensory cortices of homozygous *Pten* cKO mice (*Drd1a-Cre$^{+/-}$;Ai9;Pten$^{fl/fl}$)* relative to control mice (*Drd1a-Cre$^{+/-}$;Ai9;Pten$^{fl/+}$)* (Figure 5.4. F-H). The upregulation of pS6$^{235/236}$ levels was primarily observed in tdTomato-expressing neurons in layer 6b across M1 and anterior S1 in *Pten* cKO mice (Figure 5.4. E1-E3, E1'-E3', H1-H3, H1'-H3'); however, a few Drd1a-Cre+ pS6+ co-localising neurons were also detected in layer 6a and layer 5 at ~4 months of age (Figure 5.4. D1-D3, D1'-D3', G1-G3, G1'-G3'). Interestingly, both the knockout and control cortex exhibited intense pS6$^{235/236}$ staining in cortical layer 5a and layer 2 (Figure 5.4. C1-C3, C1'-C3', F1-F3, F1'-F3'). This suggests that neurons in layer 5 may have increased phosphorylation of S6, which is not induced by the selective deletion of *Pten* from subsets of Drd1a-Cre+ neurons. However, the intense levels of pS6 in layer 6b demonstrate that loss of *Pten* leads to a defective PI3K/AKT pathway, which results in hyperactive mTOR signalling. Since pS6 staining intensity was assessed in the adult brain, the postnatal deletion of *Pten* appears to lead to the constitutive, persistent activation of the mTORC1 complex well beyond postnatal development.


A
pS6 (Ser235/236)
A1
ctrl
A1'
cKO
B
merged
B1
ctrl
B1'
cKO
Motor cortices
C
pS6 (Ser235/236)
Drd1a-Cre;Ai9;Ptenfl/fl
merged
ctrl
C1
C2
C3
cKO
C1'
C2'
C3'
Secondary & primary motor areas (M2/M1)
D
pS6 (Ser235/236)
Drd1a-Cre;Ai9;Ptenfl/fl
merged
ctrl
D1
D2
D3
cKO
D1'
D2'
D3'
Secondary motor area (M2)
E
pS6 (Ser235/236)
Drd1a-Cre;Ai9;Ptenfl/fl
merged
ctrl
E1
E2
E3
cKO
E1'
E2'
E3'

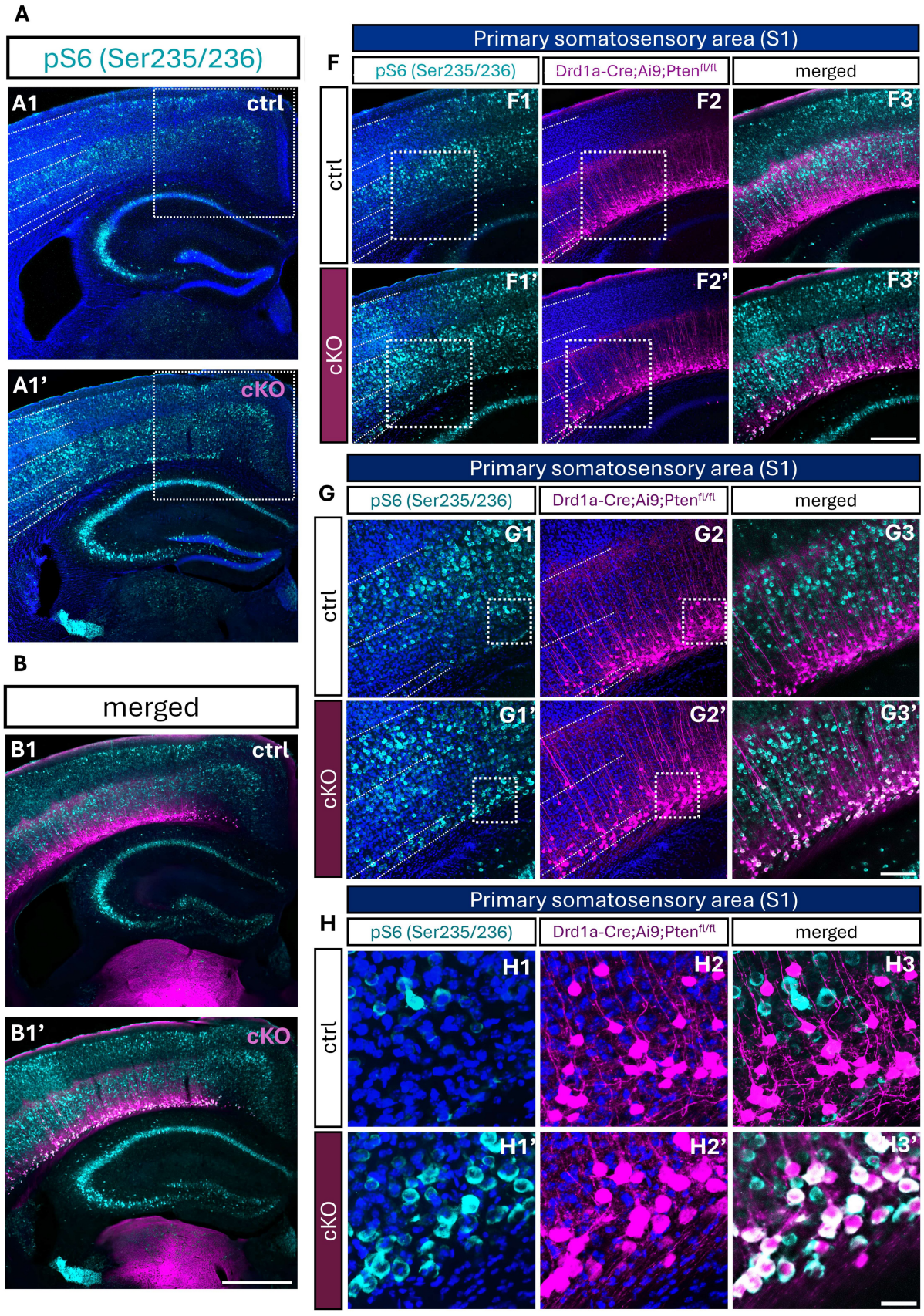
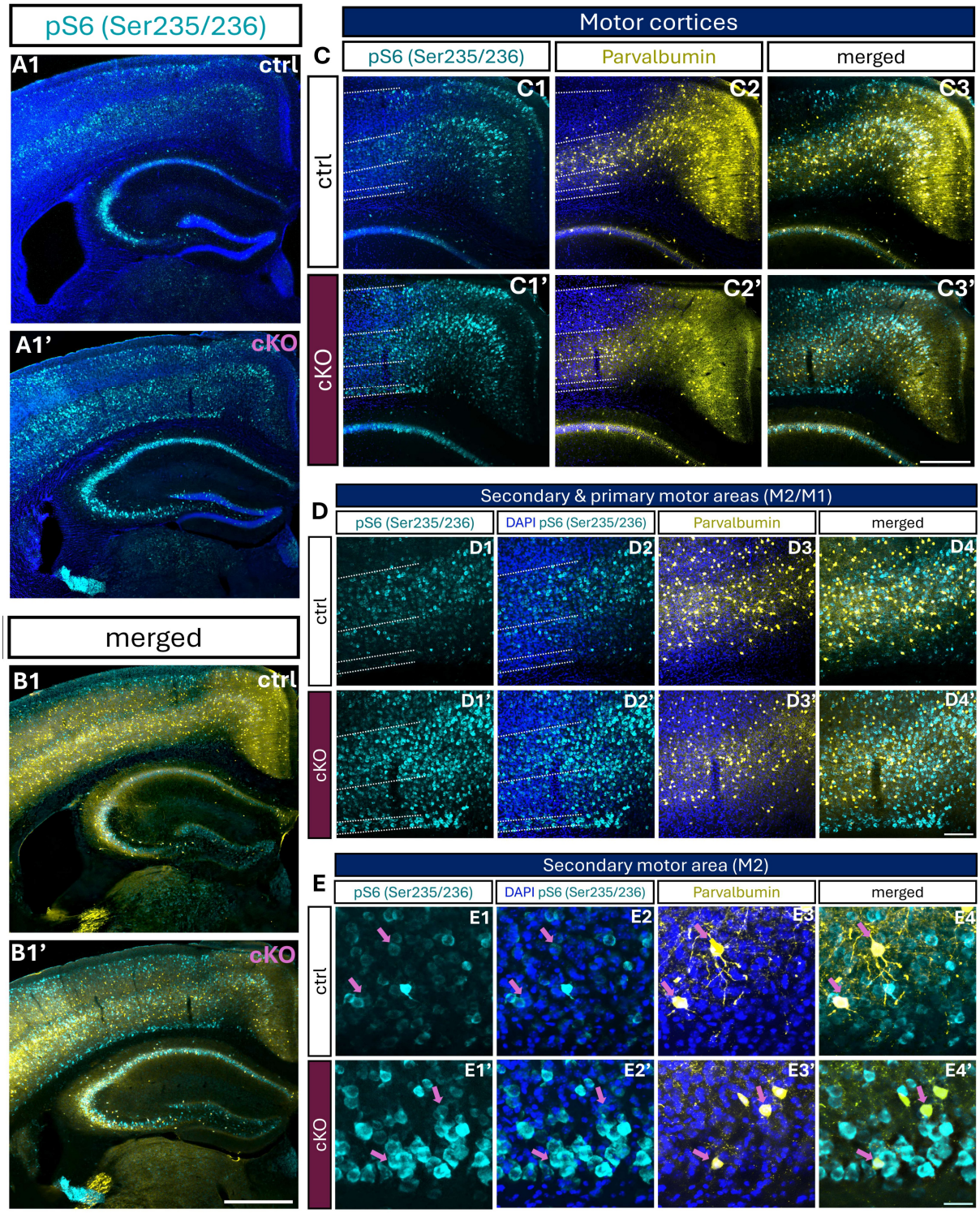

A
pS6 (Ser235/236)
A1
ctrl
A1'
cKO
B
merged
B1
ctrl
B1'
cKO
F
Primary somatosensory area (S1)
pS6 (Ser235/236)
Drd1a-Cre;Ai9;Ptenfl/fl
merged
ctrl
cKO
F1
F2
F3
F1'
F2'
F3'
G
Primary somatosensory area (S1)
pS6 (Ser235/236)
Drd1a-Cre;Ai9;Ptenfl/fl
merged
ctrl
cKO
G1
G2
G3
G1'
G2'
G3'
H
Primary somatosensory area (S1)
pS6 (Ser235/236)
Drd1a-Cre;Ai9;Ptenfl/fl
merged
ctrl
cKO
H1
H2
H3
H1'
H2'
H3'

Figure 5.4. Elevated levels of phosphorylated ribosomal protein S6 in layer 6b of the *Pten* cKO mice indicate hyperactive mTOR signalling. Confocal single-scans representing phospho-S6 immunostaining (cyan) and Drd1a-Cre+ neurons (magenta) in the primary and secondary motor cortices and the primary somatosensory cortex in the control (C1-C3, D1-D3, E1-E3, F1-F3, G1-G3, H1-H3) and *Pten* cKO mice (C1'-C3', D1'-D3', F1'-F3', G1'-G3', H1'-H3'). Merged confocal images displaying pS6 signal overlain on tdTomato channel (C3, C3', D3, D3', E3, E3', F3, F3', G3, G3', H3, H3'). White dotted squares indicate the location of imaging sites of zoom-in images in Panels B and G. Scale bars = 50 μm.

5.4.2. A subset of phospho-S6-expressing Drd1a-Cre-negative neurons are parvalbumin-positive GABAergic interneurons

In the previous section, I detected pS6+ cells in the infragranular layers of M1 and S1, which were not Cre+ neurons. To determine whether the pS6-expressing Cre- neurons were GABAergic interneurons, I performed immunofluorescence staining for pS6 and parvalbumin (Figure 5.5. B1, B1', C, F). Previous research has demonstrated that PV+ neurons display elevated levels of pS6 in comparison to SST+ interneurons (Malik et al. 2019). Although the high pS6-expressing cells were PV-negative, I found examples of PV+ neurons co-localising with pS6 in layer 6a and occasionally in layer 6b of M1 and S1 in the control and *Pten* cKO mice (Figure 5.5. E1-E4, E1'-E4', H1-H4, H1'-H4'). pS6 expression varied among PV+ interneurons, ranging from moderate to low levels. Interestingly, I only observed a few instances of co-localisation between PV+ and pS6 signal in layer 5, which exhibited enhanced pS6 labelling (Figure 5.5. D1-D4, D1'-D4', G1-G4, G1'-G4'). These results suggest that some of the pS6-expressing Drd1a-Cre-negative neurons in M1 and S1 are PV+ interneurons; however, they appear to be less common in cortical layer 5.


pS6 (Ser235/236)
A1
ctrl
A1'
cKO
merged
B1
ctrl
B1'
cKO
Motor cortices
C
pS6 (Ser235/236)
Parvalbumin
merged
ctrl
C1
C2
C3
cKO
C1'
C2'
C3'
Secondary & primary motor areas (M2/M1)
D
pS6 (Ser235/236)
DAPI pS6 (Ser235/236)
Parvalbumin
merged
ctrl
D1
D2
D3
D4
cKO
D1'
D2'
D3'
D4'
Secondary motor area (M2)
E
pS6 (Ser235/236)
DAPI pS6 (Ser235/236)
Parvalbumin
merged
ctrl
E1
E2
E3
E4
cKO
E1'
E2'
E3'
E4'

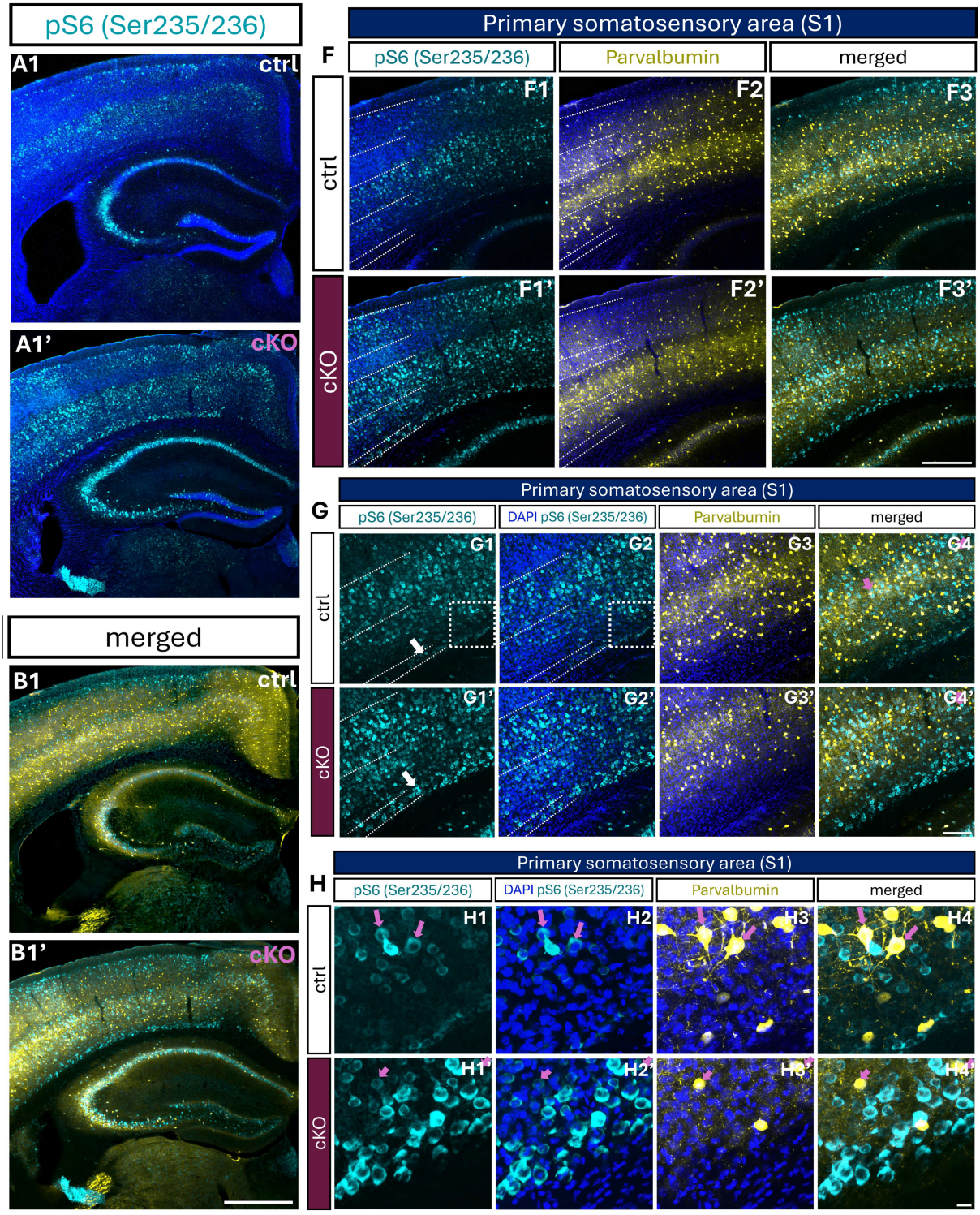


Figure 5.5. Parvalbumin-positive interneurons comprise a subgroup of Drd1a-Cre-negative phospho-S6-expressing neurons in cortical layer 6. Confocal single-scans and merged images showing the distribution of pS6-positive cells in cyan and parvalbumin-immunoreactive neurons in yellow control and *Pten* cKO mice in the motor (C1-C3, C1'-C3', D1-D4, D1'-D4', E1-E4, E1'-E4') and somatosensory cortices (F1-F3, F1'-F3', G1-G4, G1'-G4', H1-H4, H1'-H4'). White arrows point to cortical layer 6b (G1, G1'). High-magnification confocal images depicting pS6-immunostained cells

and parvalbumin interneurons in the motor and somatosensory cortices in control (E1-E4, H1-H4) and mutant mice (E1'-E4', H1'-H4'). Blue signal indicates DAPI nuclear counterstaining (A1-A1'). Double-positive neurons (pS6+ PV+) are highlighted by arrows in magenta (E1-E4, E1'-E4', H1-H4, H1'-H4'). White squares indicate imaging sites of zoom-in images (G1, G2). Scale bars = 50 µm.

5.4.3. *Pten* cKO mice display immediate early gene activation in cortical regions

To examine whether hyperactive mTOR signalling leads to enhanced neuronal activity, I performed immunostaining for the c-Fos protein. I noticed enhanced c-Fos expression in layer 2/3, layer 4, and layer 6 in M1 and anterior S1 in the *Pten* cKO mice at ~4 months of age (Figure 5.6.). Since c-Fos can be activated by a wide array of stimuli unrelated to neuronal activation, I decided to use a different marker of neural activity, which is 1) neuron-specific, 2) induced solely by neural activity, and 3) rapidly activated.

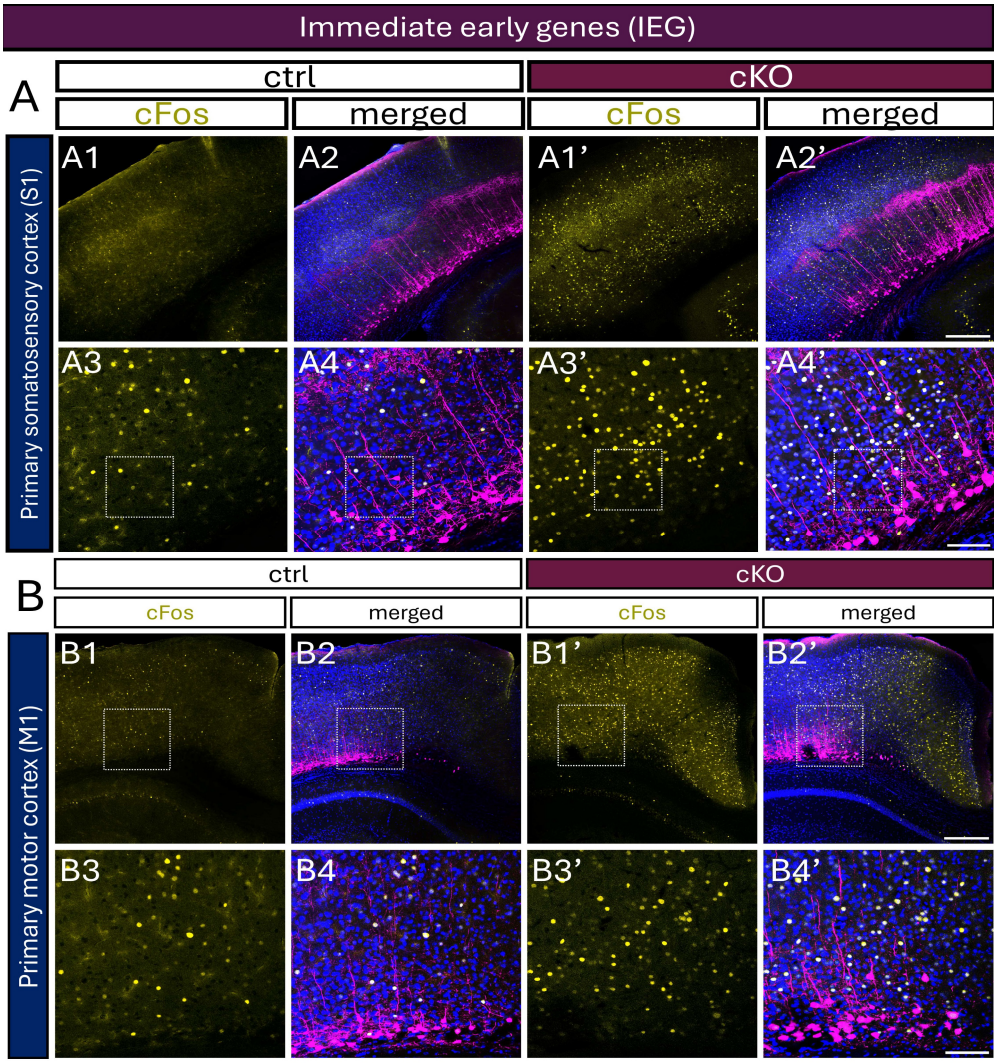


Figure 5.6. Conditional deletion of *Pten* from Drd1a-Cre+ neurons results in increased levels of c-Fos expression both in the supra- and infragranular layers. Low and high-magnification confocal images of the primary somatosensory and motor cortex displaying c-Fos-immunoreactive neurons in yellow in control (A1-A4, B1-B4) and *Pten*-ablated mice (A1'-A4', B1'-B4'). Superimposed images showing DAPI counterstain and Drd1a-Cre+ neurons in magenta in the primary somatosensory and motor cortex in control (A2, A4, B2, B4) and mutant mice (A2', A4', B2', B4'). Imaging sites of high-magnification panels are indicated by white squares. Scale bars = 200 μm (A2', B2'), 100 μm (A4, B4').

5.4.4. Activation of Npas4 expression in the *Pten* cKO mice supports increased neuronal activation following *Pten* deletion

To confirm that conditional deletion of *Pten* from subsets of Drd1a-Cre+ neurons did, in fact, cause IEG transcription and result in increased neural activation, I sought to employ an alternative marker that is only triggered by neuronal activity. Neuronal PAS domain protein 4 (Npas4) has proven to be a reliable marker for measuring neuronal activity, given its expression is not induced by neurotrophins or growth factors (Lin et al. 2008; Sun and Lin 2016). Npas4 is not expressed in non-neuronal cells and Ca^{2+}-influx selectively induces its expression in excitatory neurons through the activation of L-type voltage-sensitive calcium channels (L-VSCCs) as well as Ca^{2+}-permeable N-methyl-d-aspartic acid (NMDA) type glutamate receptors (Leslie and Nedivi 2011; Maya-Vetencourt 2013; Lin et al. 2008; Spiegel et al. 2014). The most significant distinctions between the induction of Npas4 and c-Fos expression are summarised below in Figure 5.7. To examine whether the expression of Npas4 was induced in response to the loss of *Pten* from Drd1a-Cre+ neurons, I performed immunohistochemical staining for Npas4. Consistent with the results of c-Fos immunohistochemistry, the *Pten*-deleted mice displayed increased Npas4 expression in M1 and S1 compared to control mice (Figure 5.8. A, B). Interestingly, Npas4-immunoreactive neurons were primarily expressed in deep cortical layers such as layers 6a and 6b, where *Pten* deletion occurred in Drd1a-Cre+ neurons (Figure 5.8. A3', A6', B3', B6'). A small number of Npas+ cells were also noted in layer 5 in M1 and S1 in the

Pten cKO mice (Figure 5.8. A1'-A3'). These results suggest that the loss of *Pten* leads to enhanced neuronal activity and induces the expression of IEGs, including Npas4 and c-Fos.

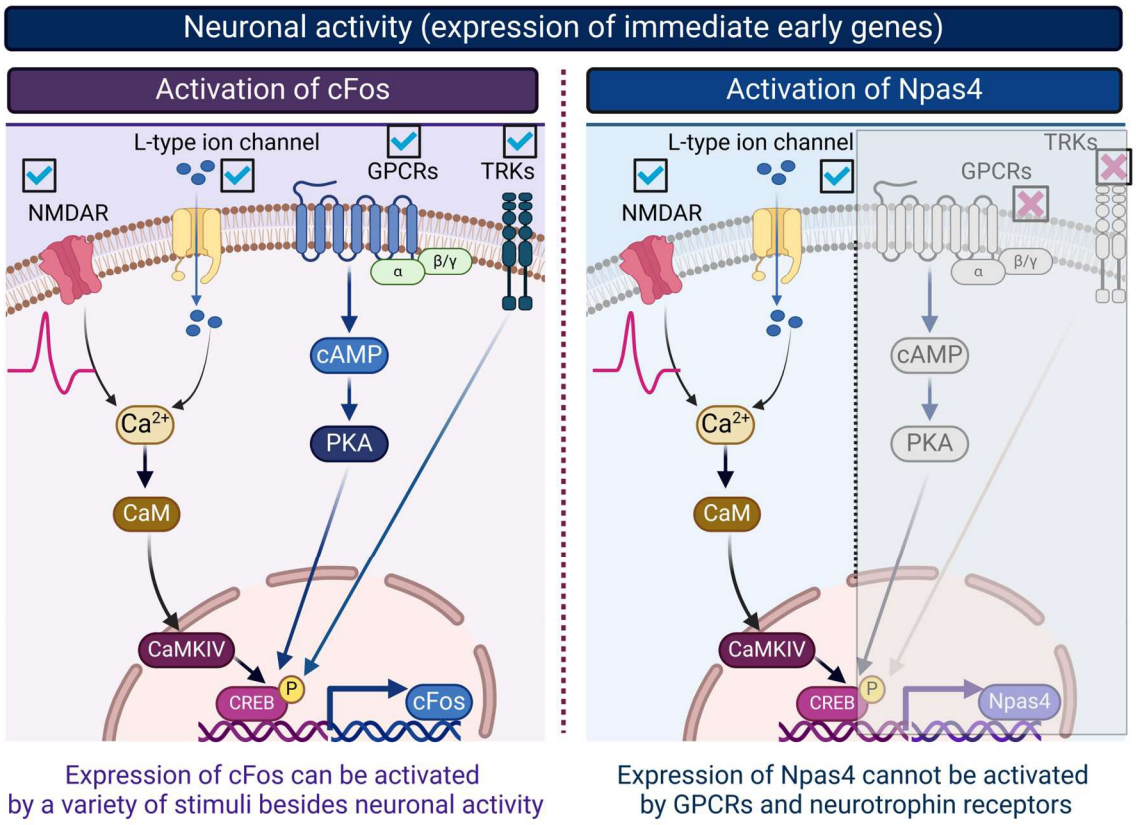
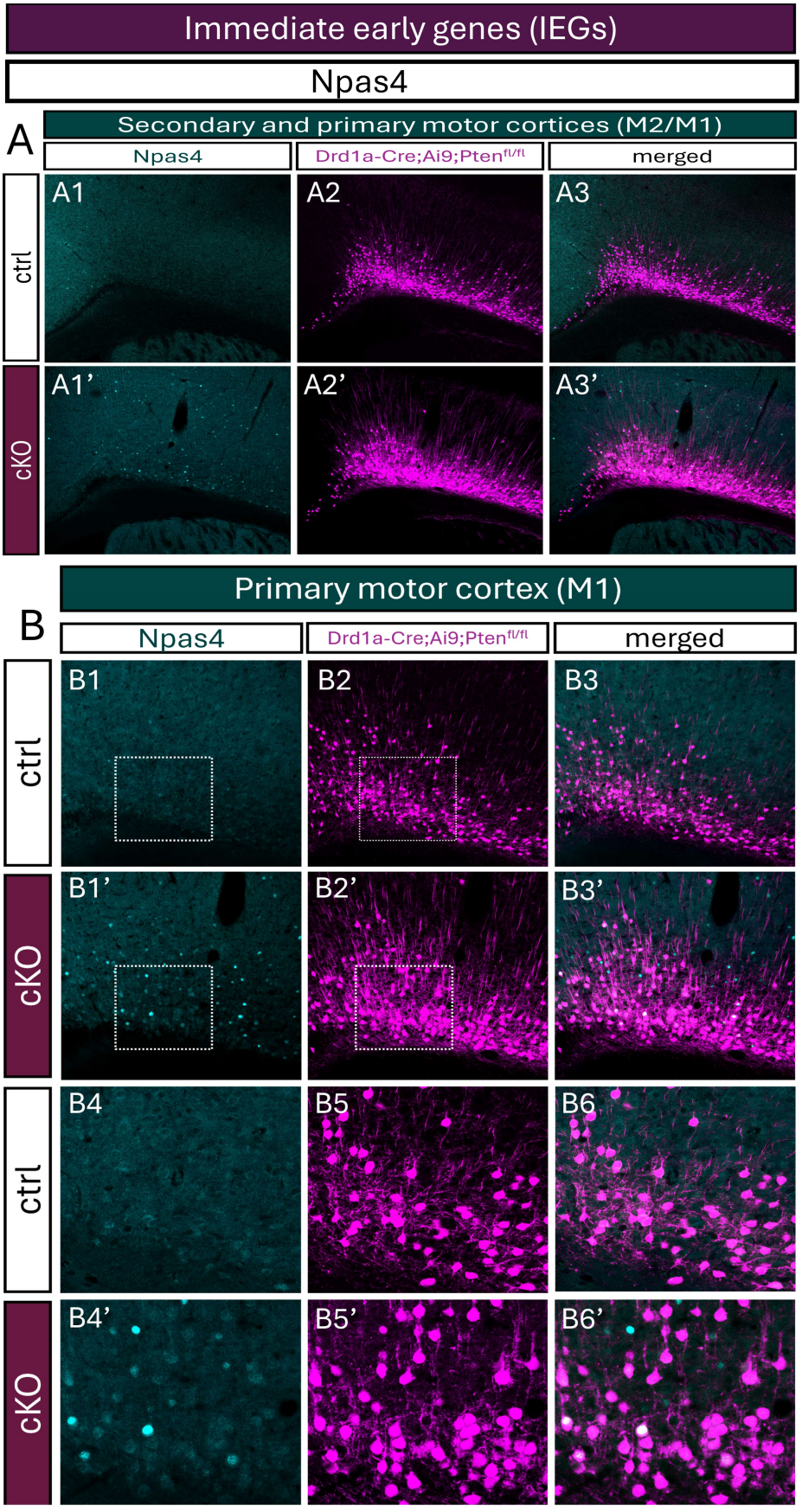


Figure 5.7. Differential activation of two activity-dependent immediate early genes, i.e., c-Fos and Npas4. Besides Ca^{2+}-permeable NMDA receptors and voltage-sensitive Ca^{2+} channels, c-Fos transcription can be induced by a broad array of extracellular stimuli through ligand-gated G protein-coupled receptors (GPCRs) or by neurotrophins through transmembrane receptors tyrosine kinases (RTKs). Depending on the external stimuli, different signal transduction pathways induce different intracellular signalling cascades, such as the activation of protein kinase A (PKA) or the calcium/calmodulin-dependent protein kinase IV (CaMKIV). These Ca^{2+}-dependent pathways then all converge on the nucleus to phosphorylate the cAMP-responsive element binding protein (CREB), leading to the transcription of IEGs, including c-Fos. However, the transcriptional activation of Npas4 can only occur via influx of extracellular Ca^{2+} through L-VSCCs or NMDA receptors. Compared to c-Fos, Npas4 is therefore a more accurate indicator of neuronal activity.


Immediate early genes (IEGs)
Npas4
A
Secondary and primary motor cortices (M2/M1)
Npas4
Drd1a-Cre;Ai9;Pten fl/fl
merged
ctrl
cKO
A1
A2
A3
A1'
A2'
A3'
B
Primary motor cortex (M1)
Npas4
Drd1a-Cre;Ai9;Pten fl/fl
merged
ctrl
cKO
ctrl
cKO
B1
B2
B3
B1'
B2'
B3'
B4
B5
B6
B4'
B5'
B6'

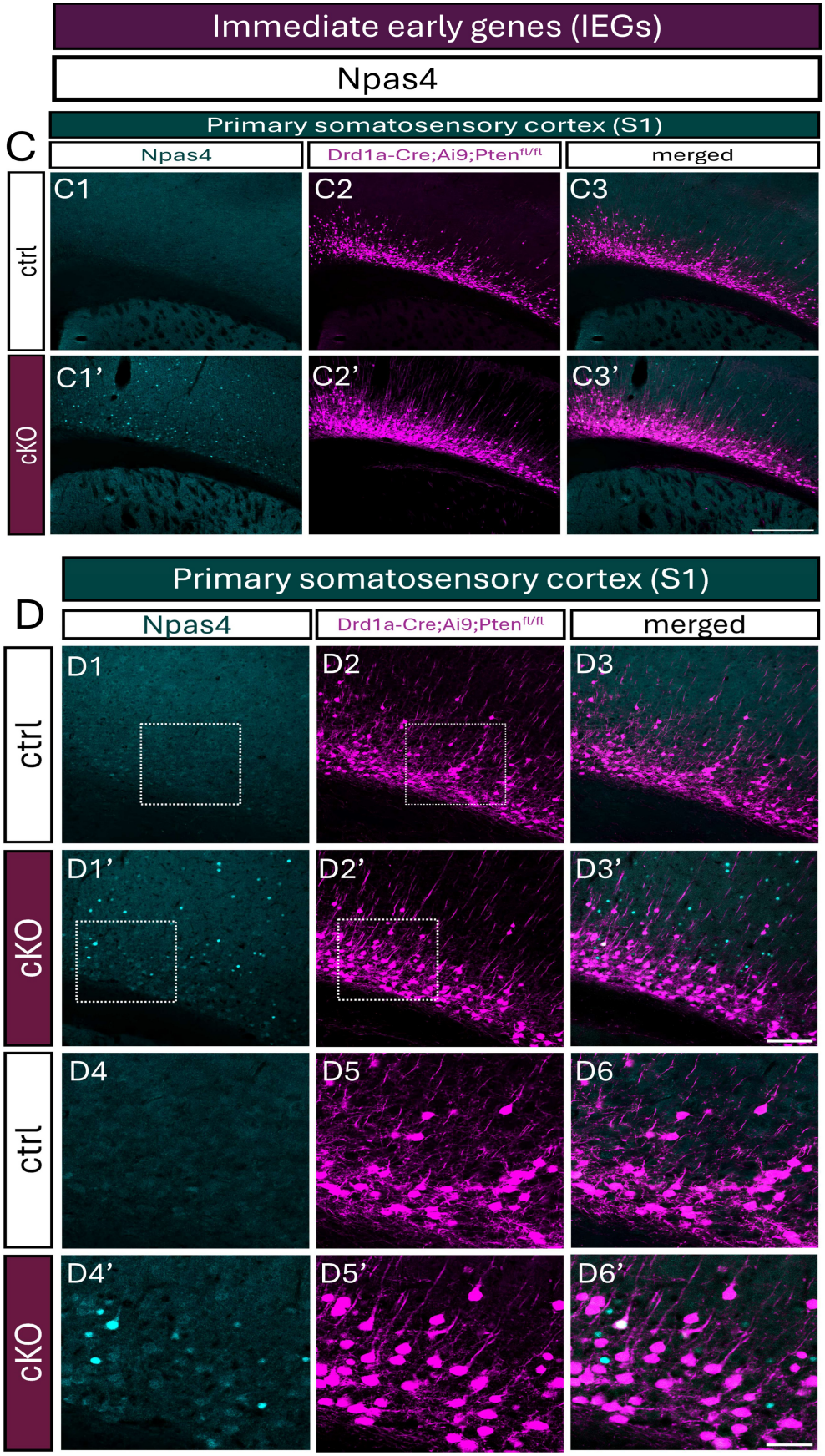
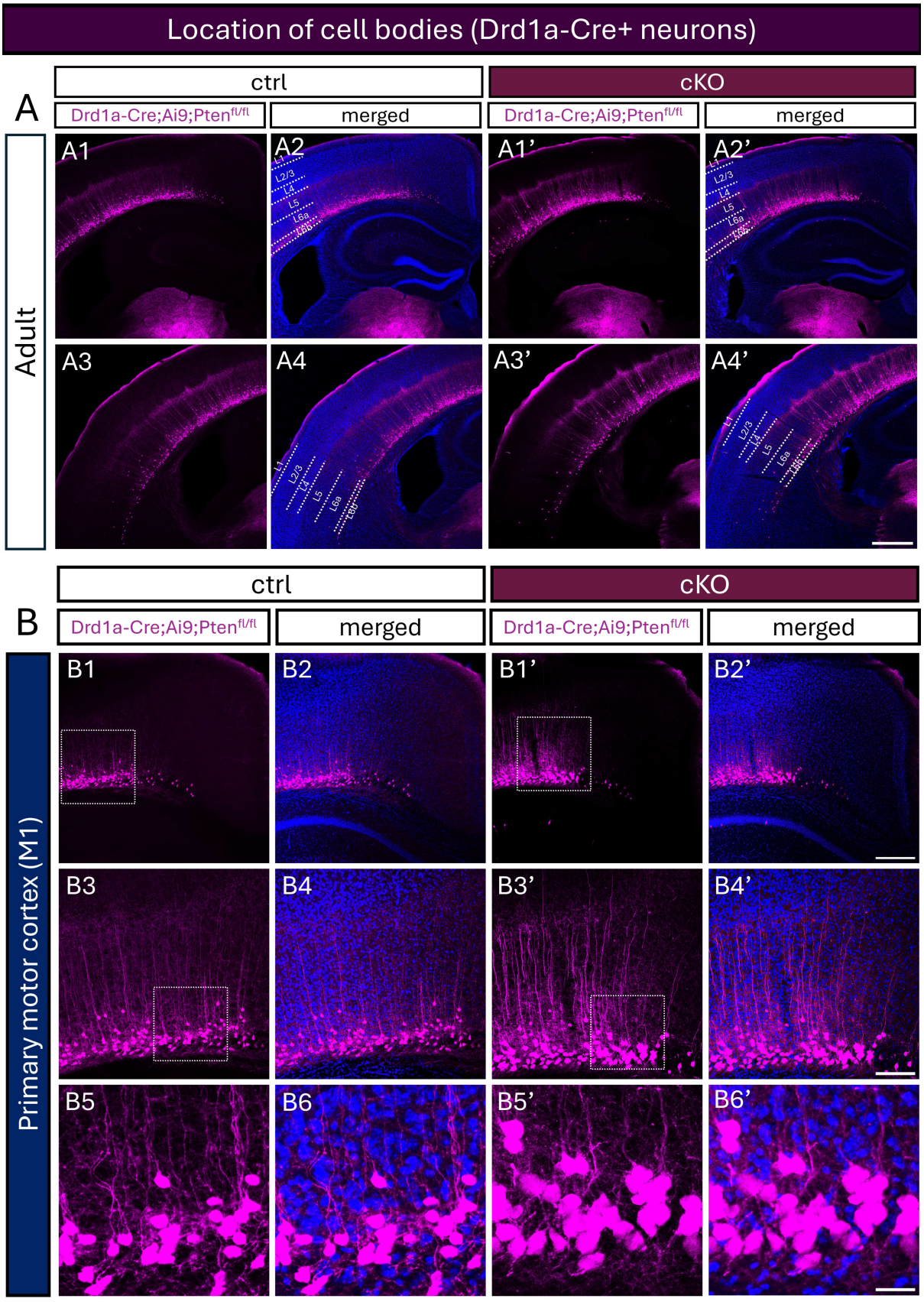

Immediate early genes (IEGs)
Npas4
C
Primary somatosensory cortex (S1)
Npas4
Drd1a-Cre;Ai9;Ptenfl/fl
merged
ctrl
cKO
C1
C2
C3
C1'
C2'
C3'
D
Primary somatosensory cortex (S1)
Npas4
Drd1a-Cre;Ai9;Ptenfl/fl
merged
ctrl
cKO
ctrl
cKO
D1
D2
D3
D1'
D2'
D3'
D4
D5
D6
D4'
D5'
D6'

Figure 5.8. Upregulation of Npas4 in the *Pten* cKO mice supports the transcriptional activation of immediate early genes and increased neuronal activation following the deletion of *Pten* from Dr1a-Cre+ neurons. Confocal images of the primary motor cortex at different magnifications at ~4 months of age, representing Npas4-immunoreactive neurons in cyan and Drd1a-Cre+ neurons in magenta in control (A1-A3, B1-B3, B4-B6) and cKO mice (A1'-A3', B1'-B3', B4'-B6'). Confocal images of the primary somatosensory cortex illustrating Npas4-immunoreactive neurons and Drd1a-Cre+ neurons in control (C1-C3, D1-E3, D4-D6) and cKO mice (C1'-C3', D1'-D3', D4'-D6'). Merged confocal images showing Npas4-expressing Drd1a-Cre+ neurons in *Pten* cKO mice (B3', B6', D3', D6'). Scale bars = 500 µm (C3'), 50 µm (D3', D6').

5.4.5. Constitutive activation of mTOR signalling causes neuronal hypertrophy in *Pten*-deleted Drd1a-Cre+ neurons

After demonstrating that the conditional deletion of *Pten* from Drd1a-Cre+ neurons results in the transcriptional activation of immediate early genes and elevated pS6 levels, my next aim was to investigate whether the augmented mTOR signalling influenced the soma size of Drd1a-Cre+ neurons. Consistent with the majority of *Pten* cKO models, hyperactive mTOR signalling led to the enlargement of cell bodies in the *Drd1a-Cre;Ai9;Pten$^{fl/fl}$* mice (qualitative assessment) (Figure 5.9. B1'-B4'). The somatic overgrowth, however, did not lead to macrocephaly as the size of *Pten* cKO brains appeared to be normal and indistinguishable from the control brains to the naked eye. The exact weights of the brains were not measured since formaldehyde perfusion and tissue shrinkage following dissection are compounding factors that can skew results. No signs of defects for cortical lamination were seen in M1 and S1 as the *Pten* cKO mice exhibited normal cortical layering (Figure 5.9. A1-A4, A1'-A4'). The enlarged somata of *Pten*-deleted Drd1a-Cre+ neurons in M1 and S1 imply that mTOR signalling continues to remain hyperelevated months after the deletion of *Pten* (Figure 5.9. B1-B6, B1'-B6'). The apical dendrites of *Pten*-ablated Drd1a-Cre+ neurons in the cKO mice terminated in the same layers as those of the control mice, namely layer 1 and the uppermost part of layer 5 (Figure 5.9. C1-C1'). Since the Drd1a-Cre+ neurons are genetically labelled, the bright layer 1 signal cannot be an artefact of immunofluorescence staining. The destination layers of the apical dendrites of Drd1a-Cre+ neurons reflect the two distinct subpopulations of layer 6b neurons that are captured by the Drd1a-Cre line, i.e., the POm/L5a-projecting Drd1 neurons and L1a-projecting Drd1 neurons (Zolnik et al. 2024).


Location of cell bodies (Drd1a-Cre+ neurons)
A
ctrl
cKO
Drd1a-Cre;Ai9;Pten$^{fl/fl}$
merged
Drd1a-Cre;Ai9;Pten$^{fl/fl}$
merged
Adult
A1
A2
A1'
A2'
A3
A4
A3'
A4'
L1
L2/3
L4
L5
L6a
L6b
B
ctrl
cKO
Drd1a-Cre;Ai9;Pten$^{fl/fl}$
merged
Drd1a-Cre;Ai9;Pten$^{fl/fl}$
merged
Primary motor cortex (M1)
B1
B2
B1'
B2'
B3
B4
B3'
B4'
B5
B6
B5'
B6'

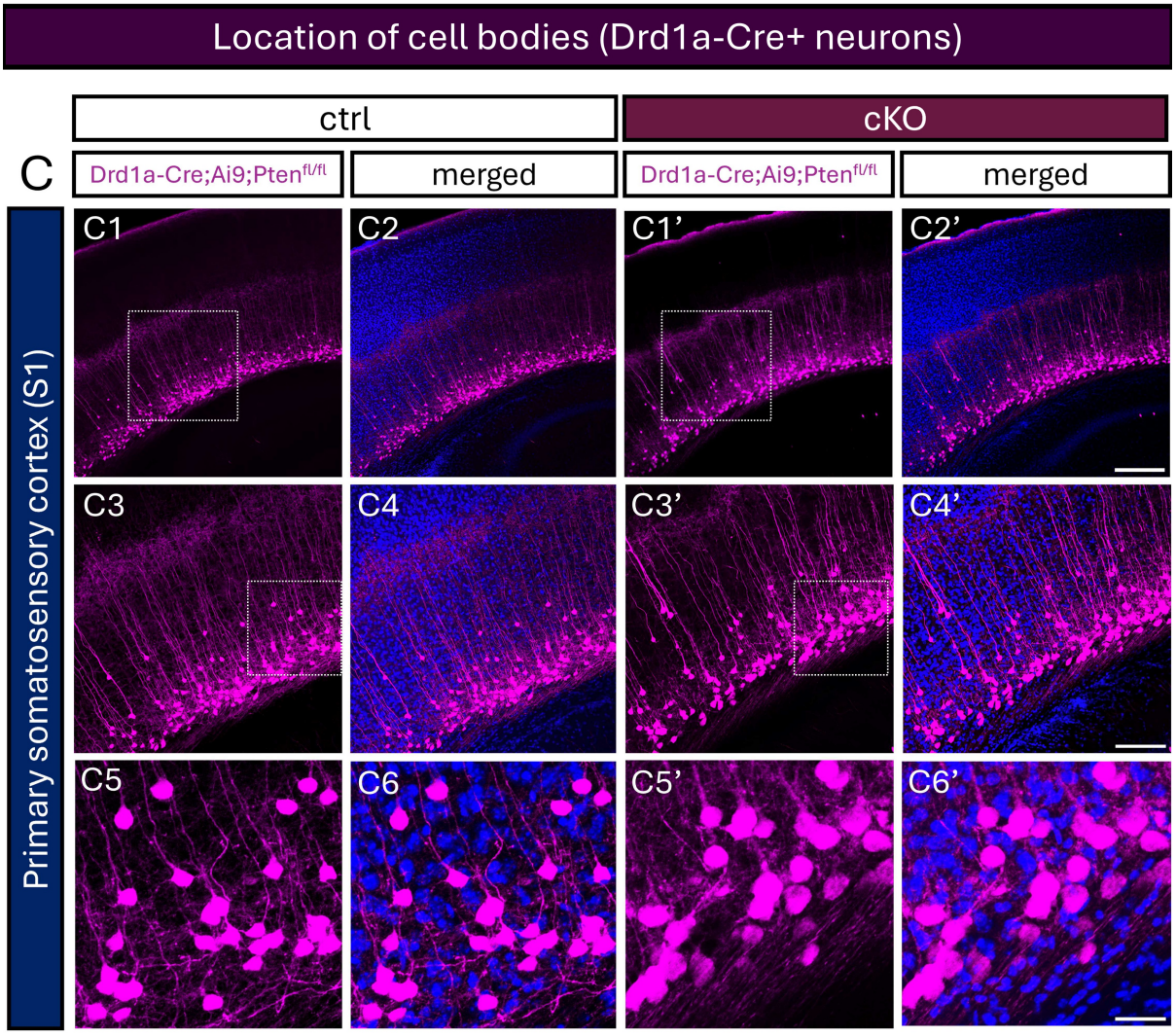
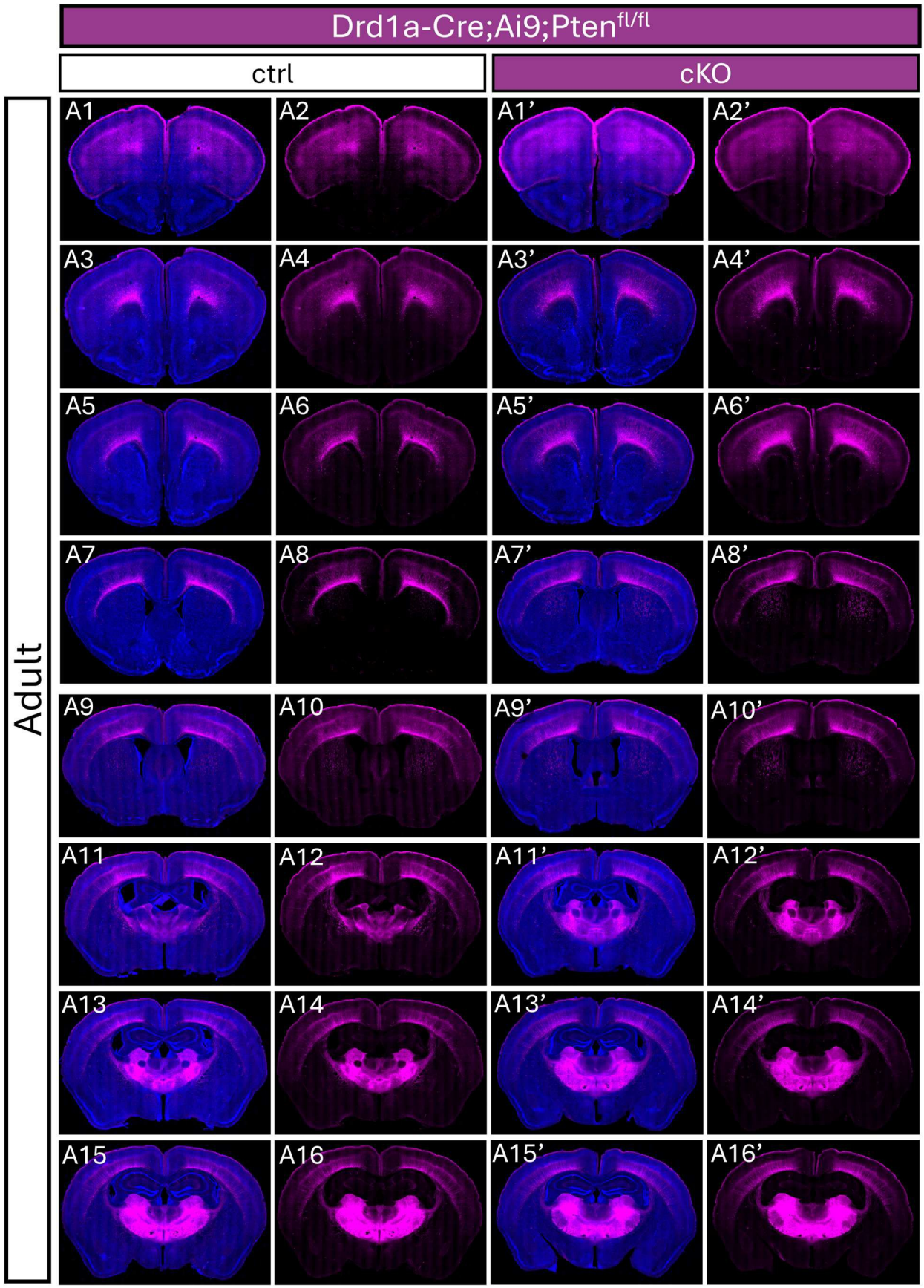


Figure 5.9 Postnatal deletion of *Pten* from Drd1a-Cre+ projection neurons leads to neuronal hypertrophy and enlarged cell bodies in the adult cKO mice. Low-magnification confocal scans displaying the distribution of Drd1a-Cre+ neurons in the anterior and the lateral neocortex in control (A1-A4) and cKO mice (A1'-A4'). White dotted lines indicate cortical layer boundaries. Confocal high-magnification and zoom-in images illustrating Drd1a-Cre+ projection neurons in the primary motor cortex and somatosensory cortices in control (B1-B6, C1-C6) and mutant mice (B1'-B6', C1'-C6'). Locations of imaging sites are delineated by white squares. Scale bars = 200 µm (A4'), 100 µm (B2', C2', C4'), 50 µm (B4', B6', C6').

5.4.6. Loss of *Pten* from subsets of Drd1a-Cre+ projection neurons does not cause ectopic projections or misrouted axonal tracts

Next, I mapped the brain-wide projections of *Pten*-deficient neurons in the adult brain. Similarly to control mice, *Drd1a-Cre;Ai9;Pten$^{fl/fl}$* mice had dendrites terminating in the upper margin of layer 5a (Figure 5.10. A1-A22, A1'-A22'). Another distinguishing trait of a subgroup of Drd1a-Cre+ neurons is that their dendrites end in layer 1 (Zolnik et al. 2020; Zolnik et al. 2024; Hoerder-Suabedissen et al. 2018). *Pten* cKO mice displayed a similar pattern, with dendrites ending in layer 1 (Figure 5.10. A1-A22, A1'-A22'). Descending fibres of *Drd1a-Cre;Ai9;Pten$^{fl/fl}$* neurons exit the cortex through the internal capsule and find their way to the thalamus via the caudoputamen (Figure 5.10. A7-A10, A7'-A10'). *Drd1a-Cre;Ai9;Pten$^{fl/fl}$* neurons are similar to control neurons in that they avoid first-order thalamic nuclei and exclusively innervate higher-order thalamic nuclei (Figure 5.10. A11-A14, A11'-A14'). This matches the innervation pattern of wild-type Drd1a-Cre+ neurons. The selective innervation of the higher-order thalamus by Drd1a-Cre+ neurons has previously been discovered and described in detail by our lab (please refer to (Hoerder-Suabedissen et al. 2018). The loss of *Pten* does not result in axon misrouting in the adult *Pten* cKO mice, as evidenced by the projection pattern of *Drd1a-Cre;Ai9;Pten$^{fl/fl}$* neurons, which mirrored that of the wild-type *Drd1a-Cre;Ai14* neurons and the control neurons (*Drd1a-Cre;Ai9;Pten$^{fl/+}$*).


Drd1a-Cre;Ai9;Pten$^{fl/fl}$
ctrl
cKO
Adult
A1
A2
A1'
A2'
A3
A4
A3'
A4'
A5
A6
A5'
A6'
A7
A8
A7'
A8'
A9
A10
A9'
A10'
A11
A12
A11'
A12'
A13
A14
A13'
A14'
A15
A16
A15'
A16'

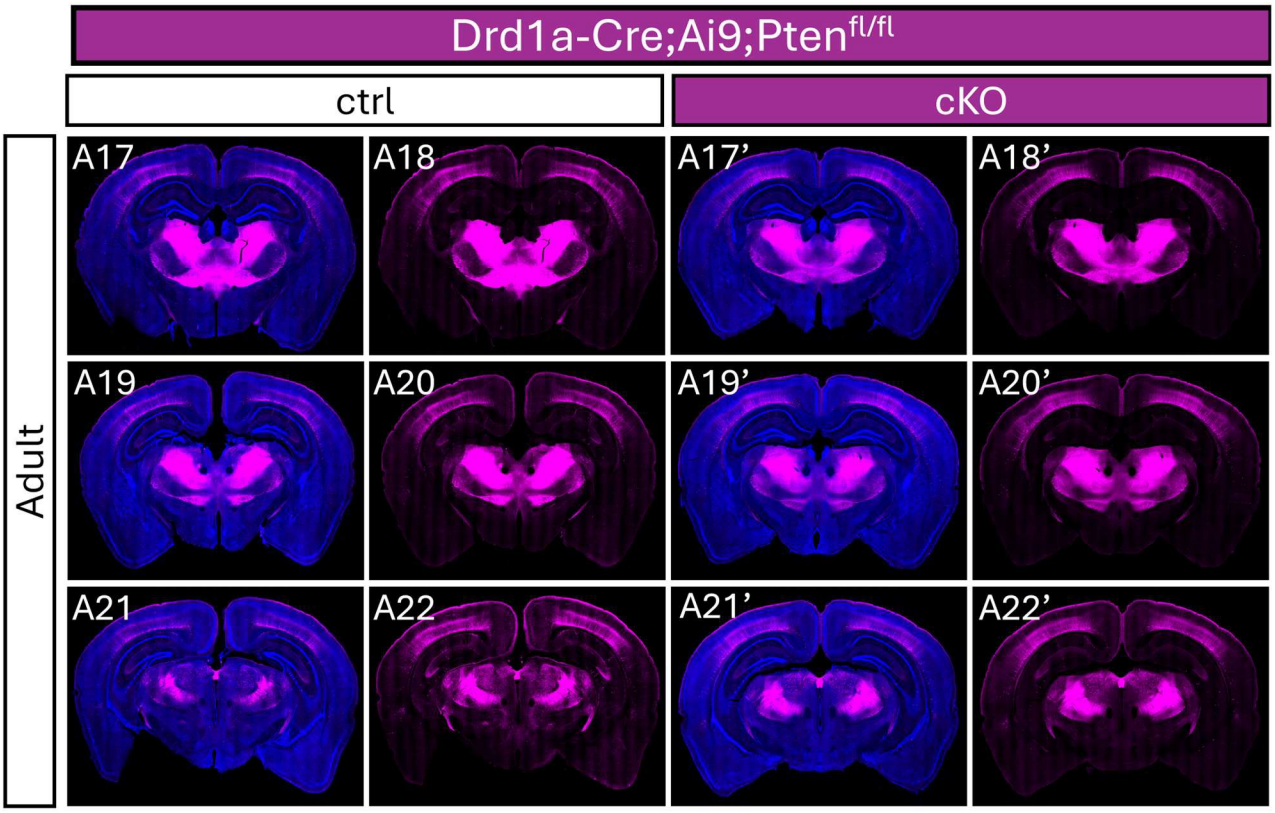


Figure 5.10. The long-range axonal projections of Drd1a-Cre+ neurons are not misrouted in the *Pten* cKO mice. Spinning disk images of full coronal slices of the brain-wide distribution of Drd1a-Cre+ neurons (magenta) and their long-range projections in control and *Pten* cKO mice. Merged images show DAPI signal superimposed on Drd1a-Cre+ neurons. Coronal slices are displayed along the rostrocaudal axis. The dendrites of Drd1a-Cre+ neurons terminate below layer 4 both in control (A1-A6) and mutant mice (A1'-A6'). Descending fibres of Drd1a-Cre+ neurons are apparent in the caudoputamen before reaching the thalamus in both control (A7-A9) and *Pten* cKO mice (A7'-A9'). Selective innervation of the higher-order nuclei and avoidance of the first-order nuclei are visible in control (A11-A18) and *Pten* cKO mice (A11'-A18'). Additionally, *Drd1a-Cre;Ai9;Pten$^{fl/fl}$* fibres can be seen in the rhomboid, nucleus reuniens (RE), mediadorsal nucleus of the thalamus (MD), and the central medial (CM). In caudal brain regions, the posterior complex (PO) and the parts of the parafascicular nucleus (PF) are innervated by Drd1a-Cre+ neurons both in control (A19, A20) and cKO mice (A19', A20'). The anterior pretectal nucleus of both control (A21, A22) and mutant mice has Cre+ neurons (A21', A22').

5.4.7. Selective loss of *Pten* from Drd1a-Cre+ neurons modifies their laminar distribution but does not increase their overall number

Following the documentation of the brain-wide distribution of the axonal projections of Drd1a-Cre+ neurons in the *Pten* cKO and control mice, I then performed an in-depth analysis of their number and laminar distribution. I sought to determine whether the enhanced soma size in *Pten*-deleted Drd1a-Cre+ neurons was followed by a corresponding change in their overall number. I postulated that the loss of *Pten* and the constitutive activation of the mTOR pathway would preclude subplate cells from undergoing cell death, leading to their enhanced survival. A significant proportion of subplate neurons undergoes programmed cell death in the murine neocortex (Price et al. 1997), and subplate neurons exhibit high rates of apoptosis between P5 and P8 (Spreafico et al. 1995). The earliest-born subplate neurons (E.11) are eliminated during the first postnatal week (Price et al. 1997); however, not all subplate cells disappear by cell death (Valverde et al. 1995). With the identification of subplate-specific molecular markers (Hoerder-Suabedissen et al. 2009), it has been revealed that a considerable fraction of subplate neurons labelled by Cplx3, Nurr1, and Lpar1-GFP selectively survive beyond the first week of postnatal development (Hoerder-Suabedissen and Molnár 2013). These markers have also been reported to label cells in the subplate layer in the adult cortex (Hoerder-Suabedissen et al. 2009). The surviving subplate neurons persist in cortical layer 6b (Friedlander and Torres-Reveron 2009; Luhmann et al. 2018), which is considered to be the remnant of the subplate (Marx et al. 2017). Therefore, it has to be noted that while the majority of subplate cells is eliminated by programmed cell death, developmental apoptosis does not affect all subplate neurons.

Since PTEN is a crucial regulator of cell growth and survival, it is vital for controlling pro-survival signalling, cell cycle progression, and antagonising the PI3K/AKT pathway. In the event of *Pten* loss, this brake on cell cycle control (G1/S and G2/M checkpoints) causes a persistent activation of AKT and its downstream effectors, resulting in overexpression of anti-apoptotic proteins and cell

survival (Stambolic et al. 1998). I hypothesised that the loss of *Pten* from Drd1a-Cre+ neurons and the consequent dysregulation of PI3K/AKT signalling would lead to an enhanced survival of layer 6 neurons. Contrary to previous expectations, neither the density nor the total number of Drd1a-Cre+ neurons differed significantly between control and *Pten* cKO mice in M1 (density, p=0.59; number, p=0.53; unpaired t-test with Welch's correction) (Figure 5.11. A, B, C).

Next, I aimed to determine the degree of regional variation in the number of Drd1a-Cre+ neurons across cortical regions. I found that the M1 in control and *Pten* cKO mice had a significantly higher number of Drd1a-Cre+ neurons than anterior S1 (lower limb region where Drd1a-Cre+ neurons are abundant, S1LL) (Figure 5.11. D). Significant differences were observed between *regions* but not *genotypes* (region, p<0.0001; genotype, p=0.5518), without *interaction* between them (p=0.7541). *Post-hoc* multiple comparisons test revealed a lower density of Drd1a-Cre+ neurons in S1 compared to M1 (ctrl, p=0.007; cKO, p=0.0015; two-way ANOVA with Šídák's multiple comparisons test). After assessing the regional effect, I then examined whether the loss of *Pten* modified the laminar distribution of Drd1a-Cre+ neurons in M1. There were significant differences between *genotypes* and *layers* (genotype, p=0.0045; layer, p<0.0001), with significant *interaction* between the two (p=0.0001) (Figure 5.11. E, F). *Post-hoc* multiple comparisons test found a significant decrease in the density of Drd1a-Cre+ neurons in layer 6b in *Pten* cKO mice compared to control mice (p<0.0001, two-way ANOVA with Šídák's multiple comparisons test). These results indicate that the conditional deletion of *Pten* from Drd1a-Cre+ neurons alters their laminar distribution in layer 6b of M1, without changing the total number of Drd1a-Cre+ neurons.

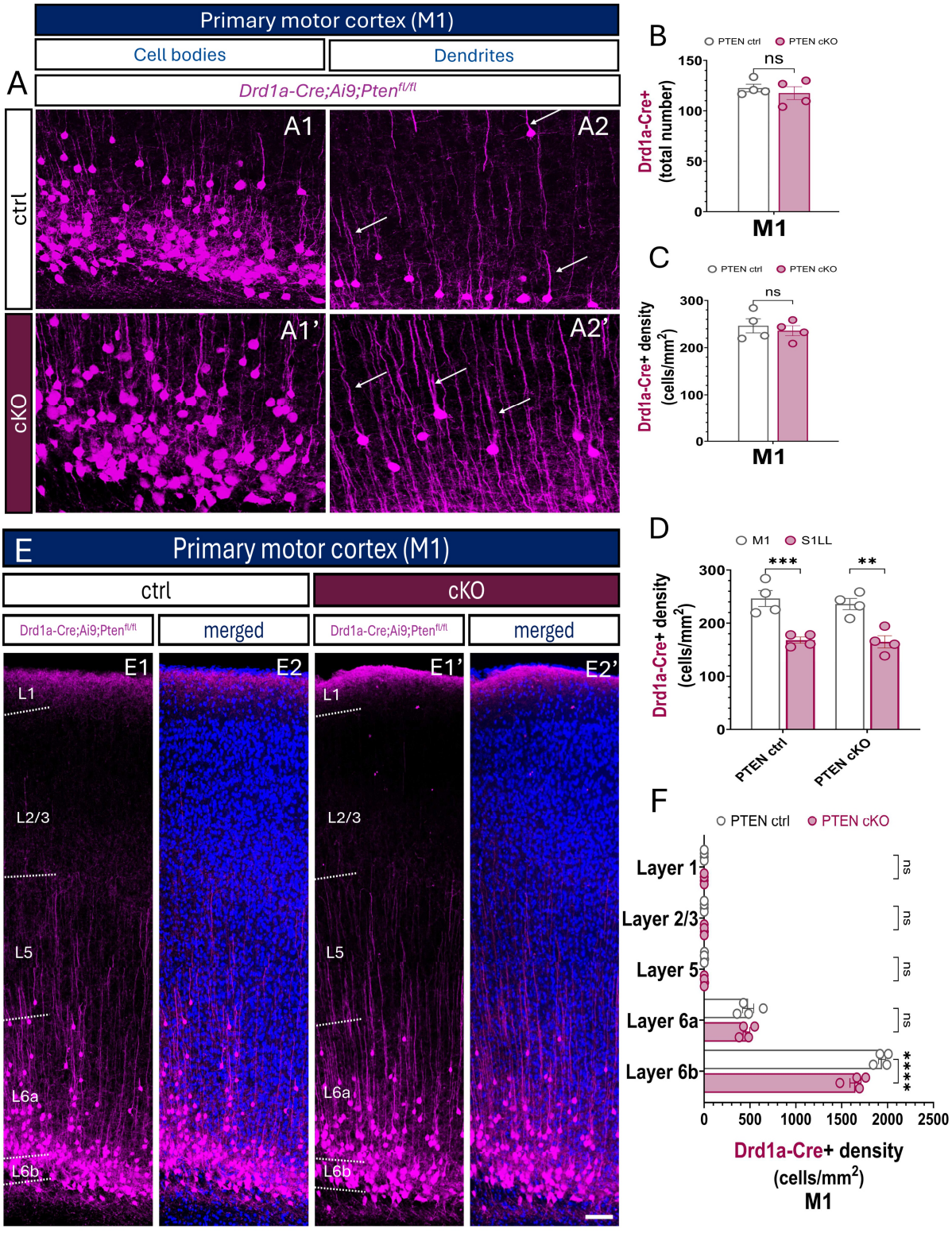


Figure 5.11. Without changing the overall amount of Drd1a-Cre+ neurons, the Pten cKO animals exhibit a change in the laminar distribution of these neurons in layer 6b of M1. Representative examples of the cell bodies and the apical dendrites of Drd1a-Cre+ projection neurons in the primary motor cortex of control (A1-A2) and *Pten* cKO mice (A1'-A2'). White arrows highlight the dendrites of Drd1-Cre+ neurons. Note the thickened dendrites in the *Pten*-deleted Drd1-Cre+

neurons (A2'). Bar graph showing the density of Drd1-Cre+ neurons in M1 (B). Bar graph showing the total number of Drd1-Cre+ neurons in M1 (C). Tiled z-stack confocal images of the entire depth of M1 illustrating Drd1-Cre+ neurons (magenta) and DAPI counterstaining (blue). White dotted lines denote layer boundaries. Bar graphs showing the laminar distribution of Drd1-Cre+ neurons in M1 (F). Scale bars = 50 μm (A2', E2').

5.4.8. The total number of Drd1a-Cre+ neurons does not change in different subfields of the primary somatosensory cortex following *Pten* ablation

To further investigate how the conditional deletion of *Pten* and the constitutive activation of the mTOR pathway affected Drd1a-Cre+ neurons, I examined their density and number in distinct subregions of S1. Similar to Chapter 4, I distinguished different subdomains of S1 based on the abundance of Drd1a-Cre+ neurons. S1LL refers to the lower limb region where the density of Drd1a-Cre+ neurons is high, whereas S1UL/S1BF refers to the barrel cortex where the density of Drd1a-Cre+ neurons tends to be low. The density and the total number of Drd1a-Cre+ neurons remained unchanged in S1 *total* (i.e., S1LL + S1UL/S1BF) in the adult *Pten*-ablated mice (Figure 5.12. A, C, D) (density, p=0.935; cell counts, p=0.9734). When distinguishing between S1LL and S1UL/S1BF, I found a significant effect of *region* but no effect of *genotype* on the density and the number of Drd1a-Cre+ neurons (density, region, p<0.0001; genotype, p=0.9099; total number, region, p<0.0001; genotype, p=0.6924). However, there was no significant *interaction* between *genotype* and *region* (density, interaction, p=0.6174; total number, interaction, p=0.6865) (Figure 5.12. F, G). The region effect can be explained by the greater density of Drd1a-Cre+ neurons in S1LL compared to S1UL/S1BF (Figure 5.12. E). In both control and cKO animals, *post-hoc* multiple comparisons test revealed a significant difference in the density of Drd1a-Cre+ neurons between S1LL and S1UL/S1BF (ctrl, p<0.0001; cKO, p<0.0001).

Interestingly, the loss of *Pten* appeared to have a differential impact on the laminar distribution of Drd1a-Cre+ neurons in S1LL and S1UL/S1BF. There was a significant effect of *layer* (p<0.0001) but no *genotype* (p=0.0516) on the density of Drd1a-Cre+ neurons in S1LL, with a

significant *interaction* between the two factors (p=0.0006) (Figure 5.12. J). *Post-hoc* tests indicated that layer 6b of *Pten* cKO mice had significantly fewer neurons relative to control mice in S1LL (p<0.0006, two-way ANOVA Šídák's multiple comparisons test). I noticed the same pattern in S1UL/S1BF. The density of Drd1a-Cre+ neurons in S1UL/S1BF was significantly influenced by *layer* (p<0.0001), but not by *genotype* (p=0.1050), and the two factors significantly *interacted* (p=0.016). In S1UL/S1BF, the density of Drd1a-Cre+ neurons was higher in layer 6b of *Pten* cKO mice than in control animals, as revealed by *post-hoc* analysis (Figure 5.12. K) (p=0.0006). I used both the cytoarchitecture and the morphology of the two sublaminae to differentiate layer 6a from layer 6b. In the majority of cortical regions, layer 6b is visible as a narrow band of closely spaced cells situated directly above the white matter. Morphologically speaking, Drd1a-Cre+ neurons in layer 6b appear to be dispersed and irregularly spaced, which contain both horizontally and vertically orientated cells. On the other hand, layer 6a neurons are more uniform in appearance and are fewer in number. The transition from one layer to the next is also indicated by a tiny space that separates the end of layer 6b from the start of layer 6a. Furthermore, layer 6b exhibits a lower nuclear density and more widely spaced nuclei, which aids in the differentiation of the two sublaminae using the DAPI nuclear counterstain.

It seems that the density of layer 6b neurons in S1UL/S1BF, where the density of Drd1a-Cre+ neurons was low, the deletion of *Pten* increased the density of Drd1a-Cre+ neurons in layer 6b. However, the reverse pattern emerged in S1LL. The deletion of *Pten* decreased the density of Drd1a-Cre+ neurons in layer 6b, where the density of Drd1a-Cre+ neurons was high. It has to be noted, however, that the loss of *Pten* did not increase or decrease the total number of Drd1a-Cre+ neurons in S1LL and S1UL/S1BF either.

Lastly, my goal was to examine whether the densities of Drd1a-Cre+ neurons in layer 6b and layer 6a varied depending on the subdivisions of S1 (lower limb vs. barrel cortex). In the *Pten* cKO mice, I noticed a significant effect of both *layer* and *region* on the laminar distribution of Drd1a-Cre+ neurons, with a significant *interaction* between them (layer, p<0.0001; region, p<0.0001; interaction,

p<0.0001) (Figure 5.12. L). *Post-hoc* multiple comparisons test showed that layers 6a and 6b of *Pten* cKO mice displayed lower densities of Drd1a-Cre+ neurons in S1UL/S1BF compared to S1LL (layer 6a, p=0.0002; layer 6b, p<0.0001). In control mice, I detected the same layer and genotype effect, with *post-hoc* tests indicating a lower density of Drd1a-Cre+ neurons in layer 6b in S1UL/S1BF relative to S1LL (p<0.0001) (Figure 5.12. M). These results indicate that *genotype, layer,* and *region* have a significant impact on the density of Drd1a-Cre+ neurons.

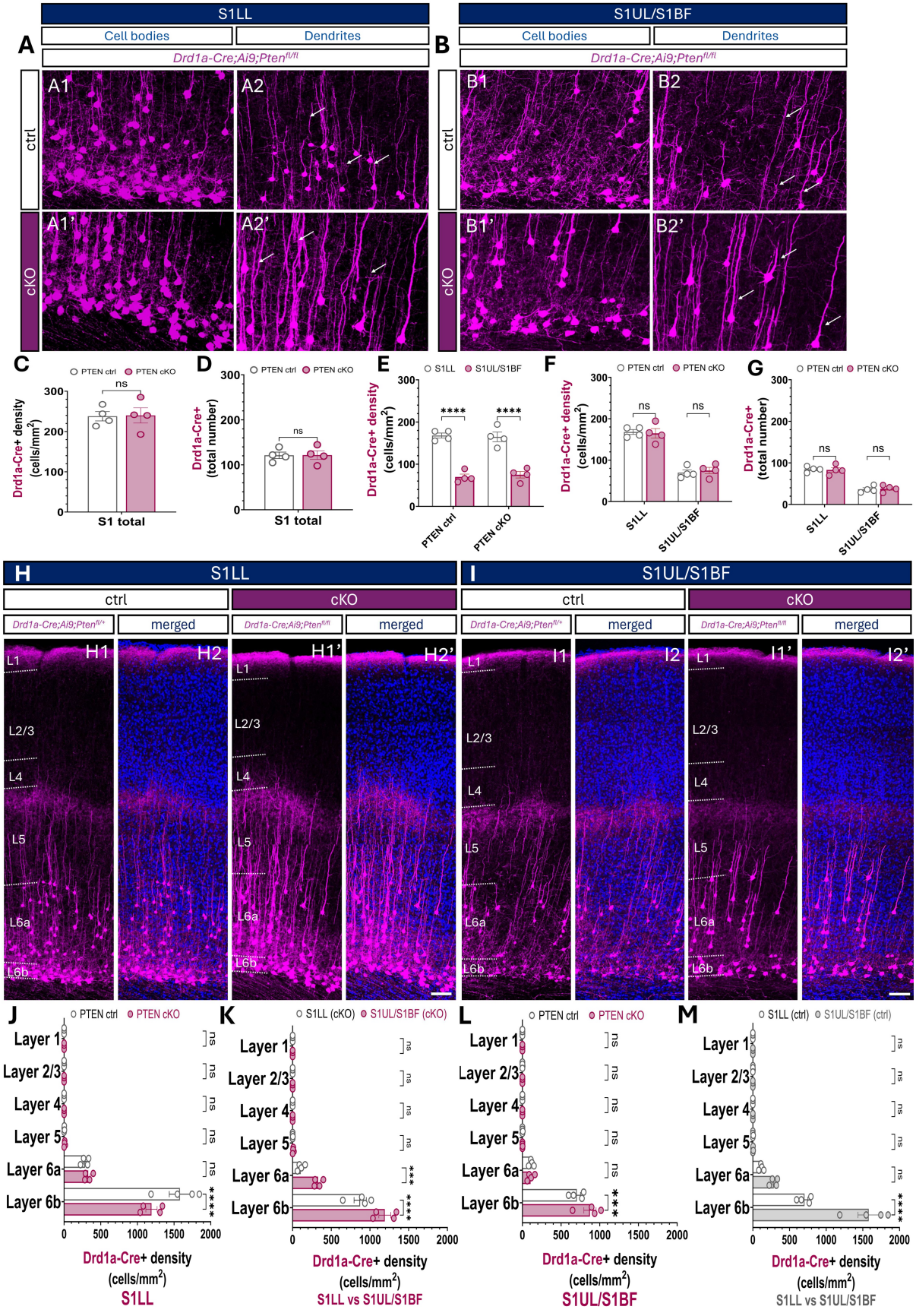

A
S1LL
Cell bodies
Dendrites
Drd1a-Cre;Ai9;Ptenfl/fl
ctrl
cKO
A1
A2
A1'
A2'
B
S1UL/S1BF
B1
B2
B1'
B2'
C
PTEN ctrl
PTEN cKO
ns
Drd1a-Cre+ density (cells/mm2)
S1 total
D
Drd1a-Cre+ (total number)
E
S1LL
S1UL/S1BF
****
F
G
H
I
merged
L1
L2/3
L4
L5
L6a
L6b
J
K
L
M
Layer 1
Layer 2/3
Layer 4
Layer 5
Layer 6a
Layer 6b
S1LL (cKO)
S1UL/S1BF (cKO)
S1LL (ctrl)
S1UL/S1BF (ctrl)
Drd1a-Cre+ density (cells/mm2)
S1LL
S1LL vs S1UL/S1BF
S1UL/S1BF

Figure 5.12. Chronic deletion of *Pten* modifies the laminar distribution of Drd1a-Cre+ neurons in layer 6b in distinct subregions of S1, without affecting their total cell number. Representative examples of the cell bodies and dendritic processes of Drd1a-Cre+ neurons (magenta) in S1LL versus S1UL/S1BF in control (A1-A2, B1-B2) and *Pten* cKO mice (A1'-A2', B1'-B2'). Note the thickened apical dendrites of Drd1a-Cre+ neurons, which are highlighted by white arrows (A2, A2', B2, B2'). Bar graphs displaying the density and the total cell number of Drd1a-Cre+ neurons in S1 *total* between control and mutant mice (C, D). Bar graphs comparing the number of Drd1a-Cre+ neurons between S1LL and S1UL/S1BF in control and cKO mice (region effect) (E). Bar graphs comparing the density and number of Drd1a-Cre+ neurons between *control* and *cKO* mice (genotype effect). Tiled z-stack images of S1LL and S1UL/S1BF showing the distribution of Drd1a-Cre+ neurons across the six cortical layers in control (H1, H2, I1, I2) and mutant mice (H1', H2', I1', I2'). Quantification of the laminar distribution of Drd1a-Cre+ neurons between control and *Pten* cKO mice in S1LL and S1UL/S1BF (J, K). Quantification of the laminar distribution of Drd1a-Cre+ neurons between S1LL and S1UL/S1BF in the *Pten* cKO (L) and control mice (M). Scale bars = 50 μm.

5.5. Elucidating the long-term consequences of conditionally deleting *Pten* from Drd1a-Cre+ projection neurons on GABAergic interneurons

In the previous sections, I have presented the results on the characterisation of a novel conditional knockout line (*Drd1a-Cre;Ai9;Pten$^{fl/fl}$*), which selectively deletes *Pten* from subsets of Drd1a-Cre+ projection neurons at around or slightly after the end of the first postnatal week. I have established that the loss of *Pten* from Drd1a-Cre+ neurons leads to the upregulation of pS6 phosphorylation in layer 6b and the activation of immediate early genes, including *c-Fos* and *Npas4*. Hyperactive mTOR signalling causes neuronal hypertrophy in Drd1a-Cre+ neurons following the loss of *Pten*; however, it did not alter the distribution of their long-range axonal projections or cause ectopic projections. Following the characterisation of the *Pten* cKO mice, I then turned my attention to quantifying the effects of the loss of *Pten* on GABAergic interneurons. The last section of this chapter, therefore, uncovers the effects of the conditional ablation of *Pten* from Drd1a-Cre+ neurons on PV, SST, and NPY-expressing interneurons. Table 5.3. highlights the ROIs selected for PV+ interneurons.

	CHAPTER 5		
	Regions of interest (ROIs)		
Strain	**Layer 6-enhanced** *(Drd1a-Cre;Ai9;Pten$^{fl/fl}$)*		
Interneurons	**Parvalbumin**	**Neuropeptide-Y**	**Somatostatin**
Cortical ROIs	ACA M1 S1 dense S1 sparse	ACA M2 M1 S1	ACA M1 S1
Subcortical and hippocampal ROIs	CPu GPe TRN	CA1 CA3 DG	CA1 CA3 DG

Table 5.3. Overview of the cortical, subcortical, and hippocampal ROIs selected for distinct subtypes of interneurons investigated in Chapter 5.

5.5. CORTICAL PARVALBUMIN INTERNEURONS

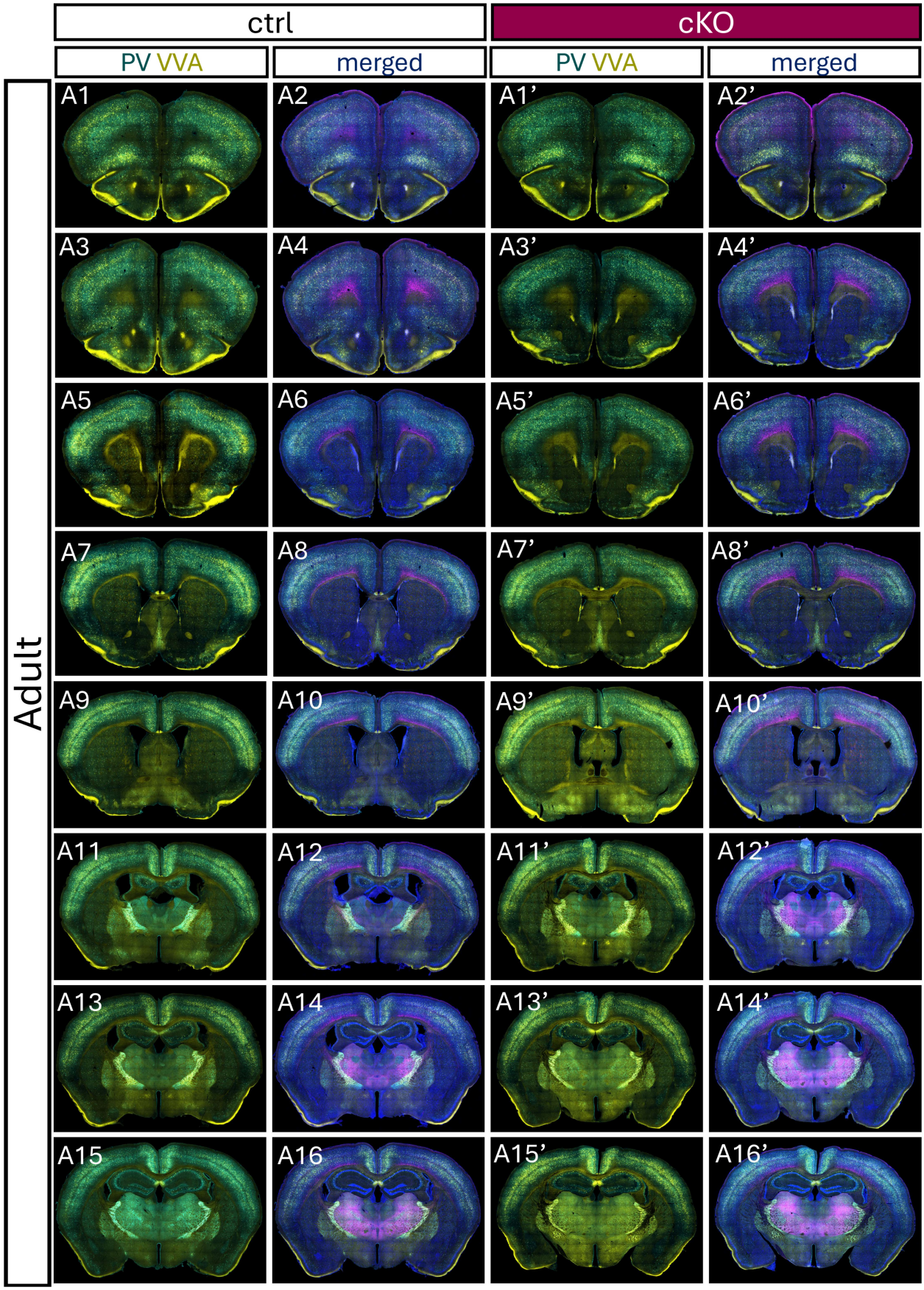
5.5.1. The brain-wide distribution of parvalbumin interneurons and the perineuronal nets in the *Pten* cKO mice does not differ from that of control mice

The majority of the monosynaptic input from L6b is received by L5 and L6 neurons. Of the layer 5 cells, the vast majority of neurons (64%) have been shown to be immunopositive for Satb2, while 22% express Ctip2 (Zolnik et al. 2024). This indicates that Drd1a-Cre+ layer 6b neurons primarily target L5-IT and L5-ET pyramidal neurons. On the contrary, the intracortical targets of layer 6b neurons in layer 6 are GABAergic interneurons, where PV+ account for 35% and SST+ for 17% of the targeted cells (Zolnik et al. 2024). As a result, the primary synaptic partners of layer 6b neurons in cortical layer 6b are PV+ and SST+ interneurons, with just a tiny proportion of the L6b-targeted cells in L5 being excitatory L5 pyramidal neurons. Corticothalamic pyramidal neurons in layer 6 preferentially form synapses with PV neurons in layers 5b and 6 (Kuramoto et al. 2022).

Deleting *Pten* from Drd1a-Cre+ neurons, therefore, may impact PV interneurons in deep cortical layers and their perineuronal nets (PNNs), prompting a mapping of their distribution to understand these effects. In the neocortex, the infralimbic (ILA), prelimbic (PL), and anterior cingulate areas (ACAd, ACAv) were rich in PV+ neurons and PNNs in both control and *Pten* cKO mice (Figure 5.13. A1-A10, A1'-A10'). PV neurons in the primary (S1) and supplemental somatosensory areas (SSt) were similarly prevalent in both groups. Moderate concentrations were found within the primary and secondary motor areas (M1, M2) and the auditory areas. In contrast, the temporal association areas had fewer PV neurons and PNNs (Figure 5.13. A11-A16, A11'-A16'). PV interneurons were prevalent in caudal cortical regions, including the retrosplenial area and primary visual regions, showing no significant differences between *Pten* cKO and control mice (Figure 5.13. A17-A22, A17'-A22'). The distribution of PNNs mirrored that of PV interneurons, especially in areas like ACAd, ACAv, and SSp.

Within subcortical regions, PV interneurons and PNNs were most concentrated in the thalamic reticular nucleus. Notably, PV neurons were also present in the caudoputamen, globus

pallidus externus, and several hippocampal areas without differences between the two mouse types (Figure 5.13. A11-A17, A11'-A17'). Hence, the loss of *Pten* from Drd1a-Cre+ neurons does not impact the overall distribution of PV neurons and PNNs.


ctrl
cKO
PV VVA
merged
PV VVA
merged
Adult
A1
A2
A1'
A2'
A3
A4
A3'
A4'
A5
A6
A5'
A6'
A7
A8
A7'
A8'
A9
A10
A9'
A10'
A11
A12
A11'
A12'
A13
A14
A13'
A14'
A15
A16
A15'
A16'

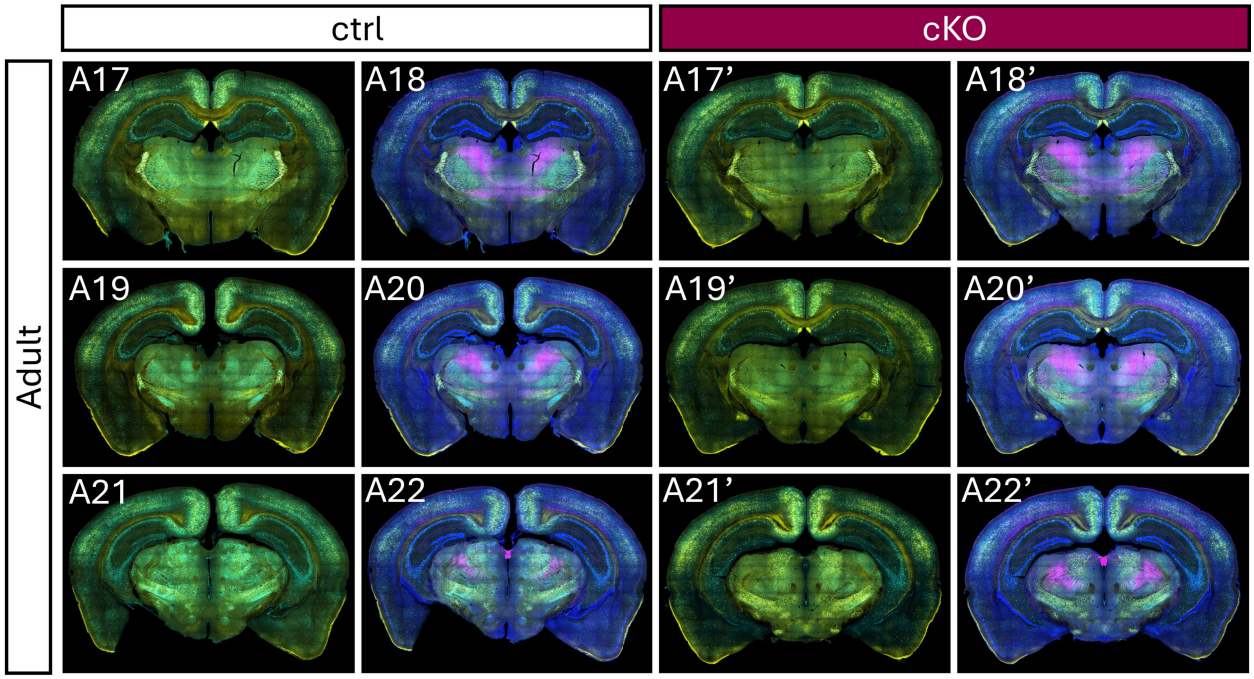


Figure 5.13. Mapping the brain-wide distribution of parvalbumin neurons and the perineuronal nets following the loss of *Pten* from Drd1a-Cre+ neurons. Spinning disk merged images showing the distribution of parvalbumin-immunopositive neurons (cyan), the perineuronal nets labelled by *Vicia villosa* agglutinin (yellow), Drd1a-Cre+ projection neurons (magenta), and DAPI nuclear counterstain (blue) in control (A2, A4, A6, A8, A10, A12, A14, A16, A18, A20, A22) and *Pten* cKO mice (A2', A4', A6', A8', A10', A12', A14', A16', A18', A20', A22'). The distribution of PV+ neurons and PNNs throughout the brain of the *Pten* cKO mice is identical to that of the control animals.

5.5.2. *Pten* deletion from Drd1a-Cre+ neurons slightly increases the soma area of PV+ interneurons in M1 without affecting their density

To understand the effects of ablating *Pten* from Drd1a-Cre+ neurons on cortical PV+ interneurons, I first assessed their spatial distribution in my selected cortical ROIs, i.e., ACA, M1, and S1. I detected a significant *region* effect but no *genotype* on the density of PV+ and VVA+ cells in ACA and M1 (Figure 5.14. C, D), without *interaction* (PV, region, $p<0.0001$; genotype, $p=0.6082$; interaction, $p=0.4242$; VVA, region, $p<0.0001$; genotype, $p=0.5721$; interaction, $p=0.2412$). Next, I sought to find out how long-term *Pten* ablation in Drd1a-Cre+ neurons affected those PV+ neurons covered by perineuronal nets and those without PNNs. The two-way ANOVA test revealed a significant *cell type* (PV+ VVA+, PV+ VVA-, PV- VVA+) effect but no *genotype* in ACA, with no significant *interaction*

between them (cell type, p=0.0141; genotype, p=0.5164; interaction, p=0.6909). Consequently, *post-hoc* did not find significant differences between control and *Pten* cKO mice (Figure 5.14. E).

In M1, *cell types* and *genotypes* in M1 did not differ significantly, and the two variables did not interact significantly (Figure 5.14. F) (cell type, p=0.0694; genotype, p=0.7105; interaction, p=0.3163; two-way ANOVA Šídák's multiple comparisons test). Although the density of PV+ neurons was not affected by *genotype*, the soma area of PV+ neurons in M1 in *Pten* cKO mice was considerably larger than in control mice (p=0.0302) (Figure 5.14. G, H).

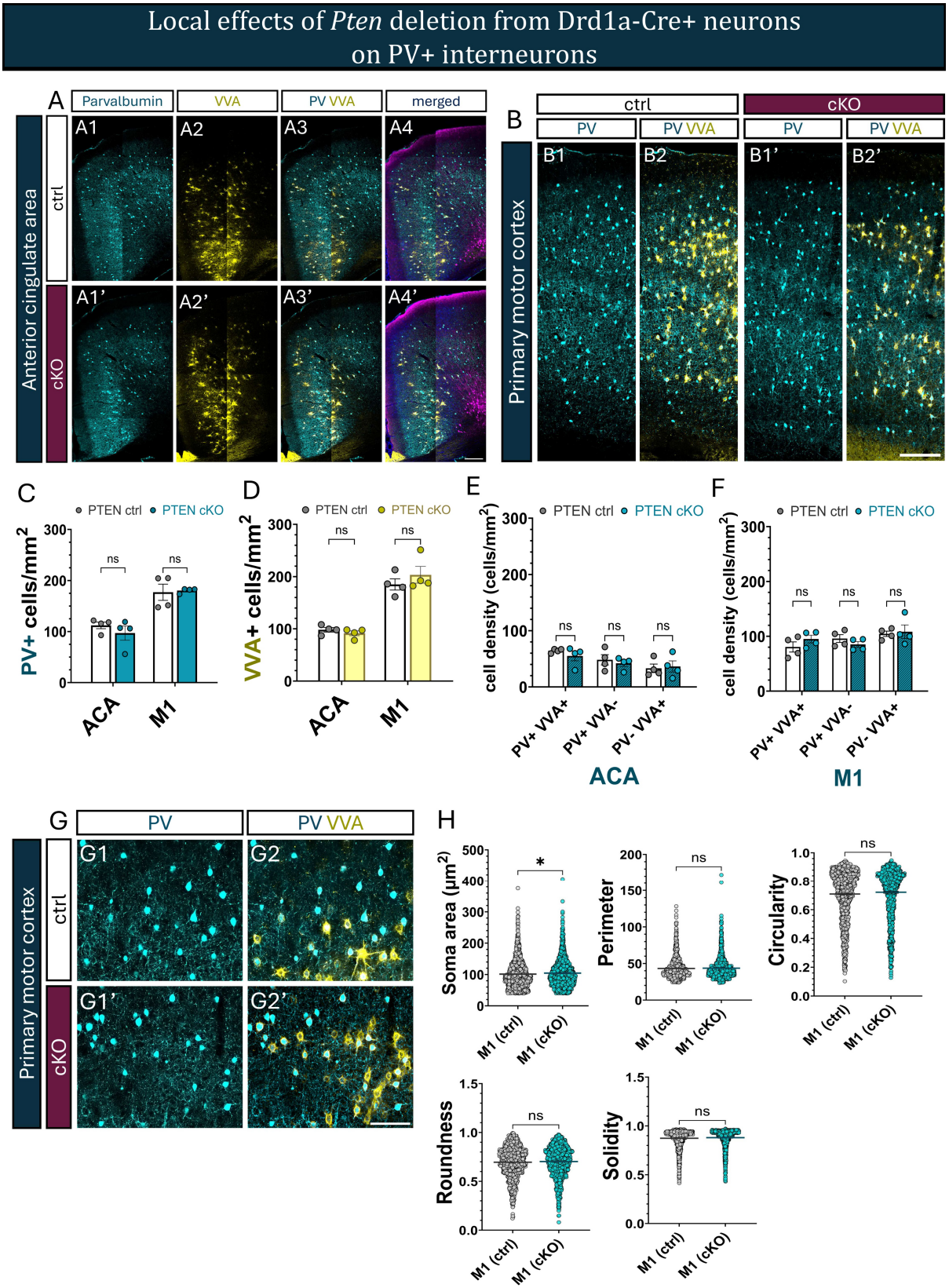

Local effects of Pten deletion from Drd1a-Cre+ neurons on PV+ interneurons
A
Parvalbumin
VVA
PV VVA
merged
Anterior cingulate area
ctrl
cKO
A1
A2
A3
A4
A1'
A2'
A3'
A4'
B
ctrl
cKO
PV
PV VVA
Primary motor cortex
B1
B2
B1'
B2'
C
PTEN ctrl
PTEN cKO
PV+ cells/mm2
ns
ACA
M1
D
VVA+ cells/mm2
E
cell density (cells/mm2)
PV+ VVA+
PV+ VVA-
PV- VVA+
ACA
F
M1
G
Primary motor cortex
G1
G2
G1'
G2'
H
Soma area (µm2)
*
Perimeter
Circularity
Roundness
Solidity
M1 (ctrl)
M1 (cKO)

Figure 5.14. Deleting *Pten* from Drd1a-Cre+ neurons leads to enlarged soma size in parvalbumin interneurons in M1 in *Pten* cKO mice. Tile-scans of the anterior cingulate area and the primary motor cortex illustrating parvalbumin interneurons in *cyan* and *Vicia villosa* agglutinin-labelled perineuronal nets in *yellow* in control (A1, A2, B1) and *Pten* cKO mice (A1', A2', B1'). Merged images showing parvalbumin neurons superimposed on the yellow channel (A3, A3', B2, B2') as well as DAPI counterstaining in blue, and Drd1a-Cre+ projection neurons in magenta in control (A4) and mutant mice (A4'). Quantification of the density of parvalbumin neurons and perineuronal nets in ACA and M1 between control and *Pten* cKO mice (C, D). Bar graphs displaying the density of double-positive (PV+ VVA+) and single positive (PV+ VVA-, VVA- PV+) cells in ACA and M1 between control and *Pten* cKO mice (E, F). Confocal images showing parvalbumin-immunopositive neurons and VVA-labelled PNNs in layer 2/3 of M1 in control (G1, G2) and mutant mice (G1', G2'). Scatter plots representing soma measurements of parvalbumin neurons in M1. Scale bar = 100 µm (A4', G2'), 50 µm (B2').

5.5.3. The laminar density of PV+ neurons bearing perineuronal nets is significantly increased in layer 2/3 of M1 following the loss of *Pten* from Drd1a-Cre+ neurons

My next goal was to investigate the long-term impact of *Pten* deletion on the laminar distribution of PV+ after establishing that the selective loss of Pten causes an increase in their soma size in M1. I discovered a significant *layer* ($p<0.0001$), but no *genotype* ($p=0.7852$) effect on the laminar density of PV+ interneurons in M1, with no *interaction* between the two factors ($p=0.4870$) (Figure 5.15. A, B). As indicated by Šídák's *post-hoc* multiple comparisons, the laminar density of PV+ neurons across the six cortical layers did not differ between control and cKO mice (please see Supplementary Materials for numerical values). The laminar distribution of PV+ neurons devoid of PNNs (PV+ VVA-) showed the same trend; *layer* factor having the only significant effect on the laminar density of PV+ VVA- neurons (layer, $p<0.0001$; genotype, $p=0.3291$; interaction, $p=0.0576$) (Figure 5.15. C). I did find a significant *layer* effect, albeit not a *genotype* effect, on the density of PV+ VVA+ cells in M1, and the two factors interacted (layer, $p<0.0001$; genotype, $p=0.0695$; interaction, $p=0.0393$). In comparison to control mice, *Pten* cKO animals had a greater PV+ VVA+ cell density in layer 2/3 of M1, according to *post-hoc* comparisons test ($p=0.0027$) (Figure 5.15. D).

Interestingly, VVA+ density in layer 2/3 of *Pten* cKO mice in M1 followed the same trend, showing a significant *layer* but no *genotype* effect and no *interaction* (layer, $p<0.0001$; genotype,

p=0.0885; interaction, p=0.2338). *Post-hoc* tests indicated significantly increased PNNs in layer 2/3 in M1 in the mutant mice (p=0.0361) (Figure 5.15. E). However, the density of those VVA+ cells not enwrapping PV+ interneurons (PV- VVA+) did not differ significantly between control and *Pten* cKO mice in any cortical layers (Figure 5.15. F).

In conclusion, the conditional ablation of *Pten* from Drd1a-Cre+ neurons results in an increased density of PV+ VVA+ neurons in layer 2/3, as well as a corresponding increase in the density of PNNs within the same layer in M1. The upregulation of PNNs in layer 2/3 may be due to the altered number of PV+ VVA+ neurons in layer 2/3. However, one has to consider that cortical layers have a significant impact on the distribution of these neurons. Layer-specific inhibitory circuit motifs exist within the cortex, which underlie how inhibitory circuits operate across cortical layers (Markram et al. 2004). While a reciprocal feedback loop is the dominant circuit motif between deep-layer pyramidal neurons and layer 5 PV+ cells, superficial PV+ neurons exert feedforward inhibition to pyramidal neurons after incoming excitation (Sempere-Ferràndez et al. 2019; Li et al. 2014). The laminar connectivity and input distribution of PV+ interneurons within a cortical column may also determine how they react to the loss of *Pten* from Drd1a-Cre+ neurons. Since the laminar distribution of PV+ interneurons was not affected in layers 5 and 6 in the *Pten* cKO mice, it appears that *Pten* deletion selectively altered superficial PV+ cells that receive substantial excitatory input from translaminar connections originating from layer 5 as well as from local pyramidal neurons within the same layers. The altered PV+ VVA+ density in layer 2/3 may have an indirect effect via translaminar interactions. It would be interesting to know whether *Pten* deletion alters the activity or the synaptic connectivity of the entire cortical column in M1.

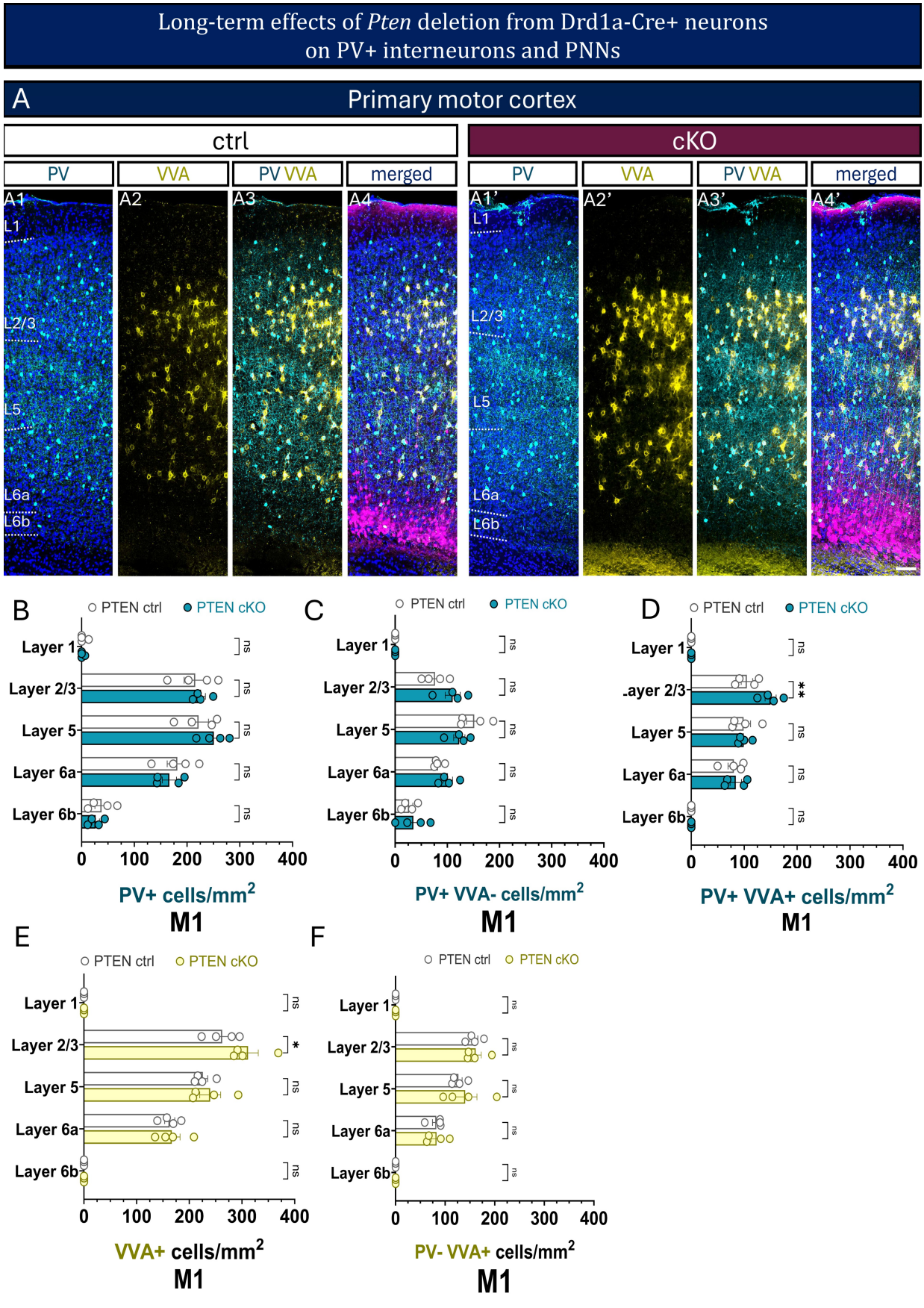

Long-term effects of *Pten* deletion from Drd1a-Cre+ neurons on PV+ interneurons and PNNs
A
Primary motor cortex
ctrl
cKO
PV
VVA
PV VVA
merged
A1
A2
A3
A4
A1'
A2'
A3'
A4'
L1
L2/3
L5
L6a
L6b
B
C
D
E
F
PTEN ctrl
PTEN cKO
Layer 1
Layer 2/3
Layer 5
Layer 6a
Layer 6b
ns
**
*
0
100
200
300
400
PV+ cells/mm2
PV+ VVA- cells/mm2
PV+ VVA+ cells/mm2
VVA+ cells/mm2
PV- VVA+ cells/mm2
M1

Figure 5.15. Permanent loss of *Pten* from Drd1a-Cre+ neurons selectively affects the laminar distribution of PV+ VVA+ neurons and PNNs in layer 2/3 of the adult primary motor cortex. Tiled z-stack confocal images of the entire depth of the primary motor cortex illustrating parvalbumin-immunoreactive neurons (cyan), DAPI counterstaining (blue), *Vicia villosa* agglutinin-labelled PNNs (yellow), and Drd1a-Cre+ projection neurons (magenta) in control (A1-A4) and *Pten*-deficient mice (A1'-A4'). Cortical layer boundaries are delineated by white lines. Quantification of the laminar distribution of PV-immunoreactive neurons in M1 between control and mutant mice (B). Bar graphs showing the laminar density of PV+ VVA- and PV+ VVA+ neurons in M1 between control and *Pten*-deleted mice (C, D). Quantification of the laminar distribution of *Vicia villosa* agglutinin-positive cells (VVA+) and PV- VVA+ cells in M1 between control and mutant mice (E, F). Scale bar = 50 μm.

5.5.4. Dysregulated mTORC1 signalling in layer 6b neurons does not have a lasting influence on the density and laminar distribution of PV neurons in the lower limb of S1

Since Drd1a-Cre+ neurons are highly abundant in the lower limb of S1 (S1LL), I first quantified the cell density of PV+ interneurons and PNNs in that region to investigate region-specific effects on PV+ cells following the loss of *Pten*. There were no significant differences in the density of PV+ interneurons and VVA+ cells between control and *Pten* cKO animals (Figure 5.16. A, B, C). The analysis of the density of PV+ neuron *with* and *without* perineuronal nets revealed no significant differences between control and *Pten* cKO mice within S1LL (Figure 5.16. D). Notably, a significant effect related to *cell type* was observed (p=0.0143); however, no interaction with *genotype* was detected (p=0.4099). Consequently, there appears to be no *genotype* effect, nor a long-term impact resulting from the loss of *Pten* in Drd1a-Cre+ neurons within S1LL.

As anticipated, two-way ANOVA tests identified a significant *layer* effect (p<0.0001) but no *genotype* effect on the following cell densities: PV+, VVA+, PV+ VVA+, PV+ VVA-, and PV- VVA+ (Figure 5.16. E, F, G, H, I). No interaction between *layer* and *genotype* was found in any of the five cell groups (For p-values, please see Appendices). However, Šídák's multiple comparisons test revealed a significant decrease in the density of PNNs not surrounding PV+ neurons (PV- VVA+) in cortical layer 5 of *Pten* cKO mice within S1LL (p=0.0374) (Figure 5.16. I).

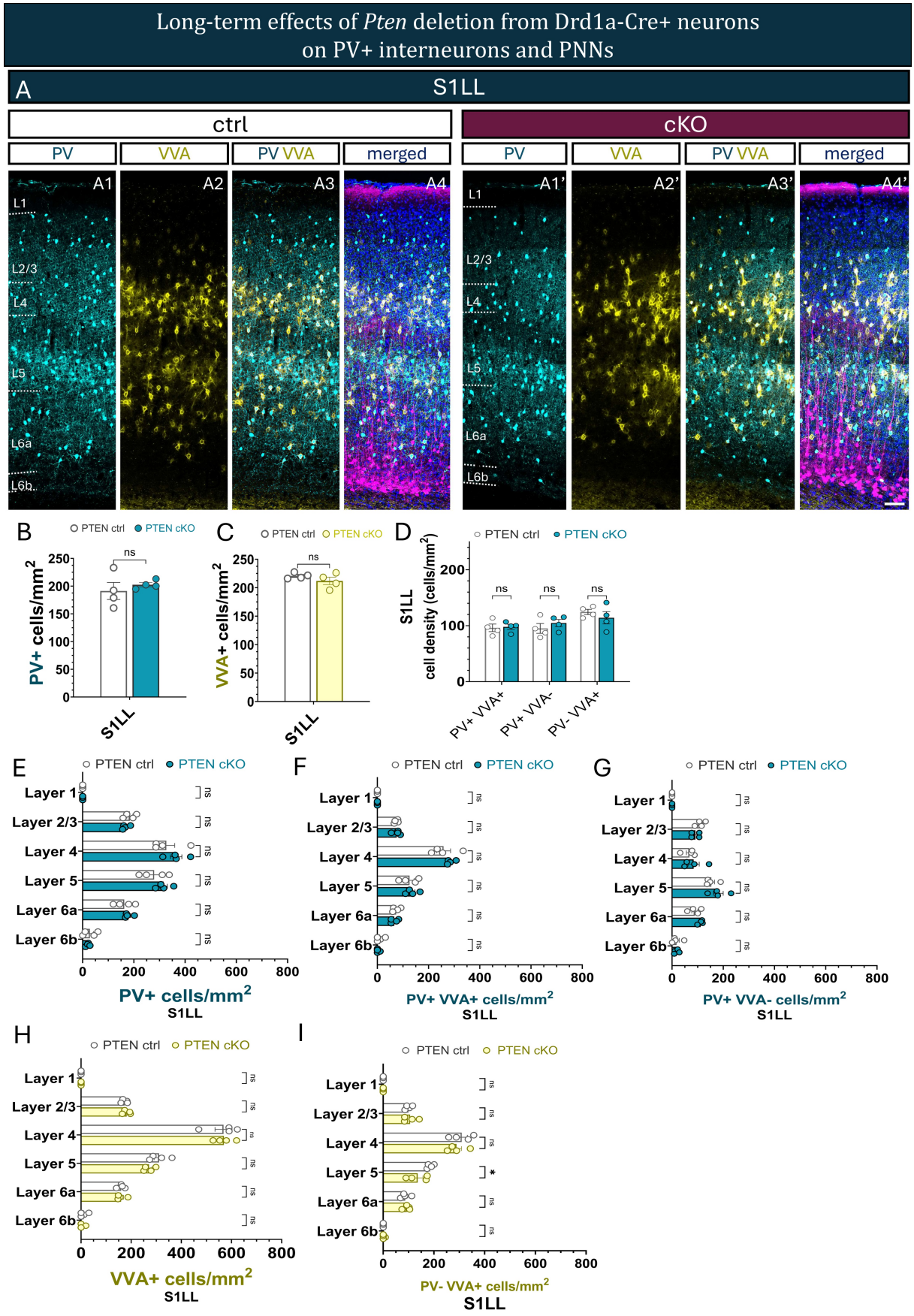

Long-term effects of Pten deletion from Drd1a-Cre+ neurons on PV+ interneurons and PNNs
A
S1LL
ctrl
cKO
PV
VVA
PV VVA
merged
A1
A2
A3
A4
A1'
A2'
A3'
A4'
L1
L2/3
L4
L5
L6a
L6b
B
C
D
PTEN ctrl
PTEN cKO
PV+ cells/mm2
VVA+ cells/mm2
cell density (cells/mm2)
ns
S1LL
PV+ VVA+
PV+ VVA-
PV- VVA+
E
F
G
Layer 1
Layer 2/3
Layer 4
Layer 5
Layer 6a
Layer 6b
PV+ cells/mm2
PV+ VVA+ cells/mm2
PV+ VVA- cells/mm2
H
I
VVA+ cells/mm2
PV- VVA+ cells/mm2
*

Figure 5.16. Parvalbumin interneurons in the lower limb of the primary somatosensory cortex remain unaffected by the loss of *Pten* from Drd1a-Cre+ projection neurons. Tile-scan & z-stack images displaying parvalbumin-immunoreactive interneurons in cyan and perineuronal nets visualised by *Vicia villosa* agglutinin in yellow in control (A1, A2, A3) and *Pten* cKO mice (A1', A2', A3') in the area of S1 where Drd1a-Cre+ neurons are abundant. Additionally, merged pictures show DAPI counterstaining in blue and Drd1a-Cre+ projection neurons (A4, A4'). White dotted lines indicate the boundaries of cortical layers. Quantification of the cell density of parvalbumin and *Vicia villosa* agglutinin-positive cells in control and *Pten*-deleted mice in S1LL (B, C). Quantification of the cell density of parvalbumin cells with and without PNNs in control and *Pten*-deleted mice in S1LL (D). Bar graphs showing the laminar distribution of PV+, VVA+, PV+ VVA+, PV+ VVA-, and PV- VVA+ cells across the six layers of S1LL in control and *Pten* cKO mice (E, F, G, H, I). Scale bar = 50 µm.

5.5.5. No soma hypertrophy was detected in PV+ interneurons in S1LL following the deletion of *Pten* from Drd1a-Cre+ neurons

Lastly, I investigated the soma morphology of PV+ neurons in S1LL. Contrary to M1, the soma area, perimeter, circularity, roundness, and solidity of PV+ neurons did not differ significantly between control and *Pten*-deficient mice at ~4 months of age (Figure 5.17. A, B).

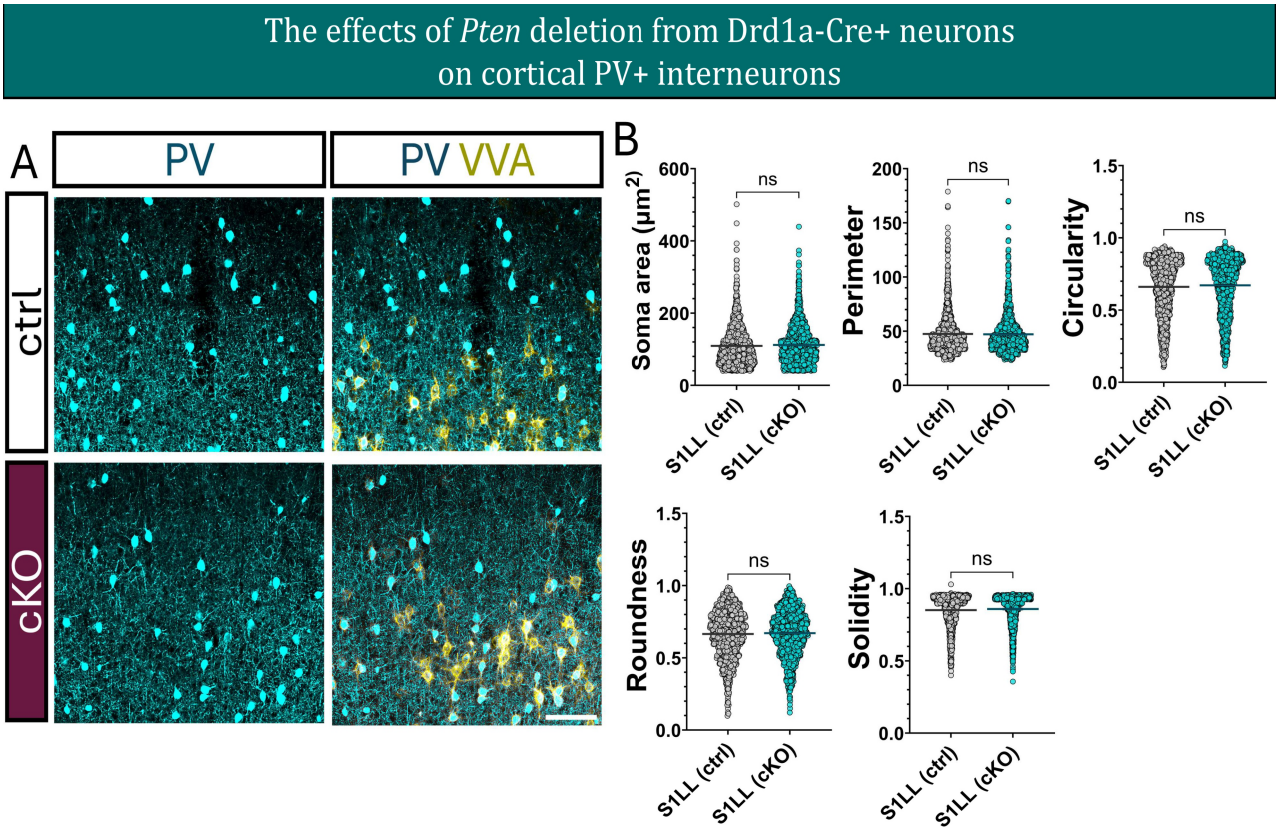


Figure 5.17. *Pten* deletion from Drd1a-Cre+ neurons does not alter the soma shape of parvalbumin interneurons in S1LL. Examples of parvalbumin interneurons and perineuronal nets in the lower limb of the primary somatosensory cortex in control and mutant mice in cortical layer 2/3 mice (A). Scatter plots showing individual cell measurements of selected soma features of parvalbumin-immunopositive neurons (B). Scale bar = 50 μm.

5.5.6. PV+ interneurons without perineuronal nets are elevated in layer 5 of the upper limb/barrel cortex of S1 when *Pten* from Drd1a-Cre+ neurons is deleted

To investigate how PV+ neurons in different subdivisions of S1 were affected by the loss of *Pten*, I continued analysing their density in S1. The next area that I investigated was S1UL/S1BF, which has significantly fewer Drd1a-Cre+ neurons than the lower limb field. The *Pten* cKO mice showed no significant alterations in the density of PV+ neurons or VVA-labelled PNNs compared to controls in S1UL/S1BF (Figure 5.18. A, B, C). When examining PV+ neurons with or without PNNs, no significant differences were found between the control and *Pten* cKO mice (Figure 5.18. D). Two-way ANOVA testing indicated a significant *layer* effect on the density of all PV+ cells in S1UL/S1BF (PV+, PV+ VVA+, PV+ VVA-, PV- VVA+) (Figure 5.18. E, F, G, I)($p<0.0001$), with only PV+ VVA- showing a significant *genotype* effect and *interaction* (genotype, $p=0.0495$; interaction, $p=0.0019$). Notably, *Pten* cKO mice exhibited a significant increase in PV+ VVA- neurons in layer 5 in S1UL/S1BF ($p<0.0001$) (Šídák's *post-hoc* multiple comparison tests) (Figure 5.18. G), suggesting that PV+ neurons in adjacent cortical layers that are devoid of PNNs were selectively altered by *Pten* loss. Additionally, *layer* effects on the laminar distribution of PNNs (VVA+ and PV- VVA+) were observed ($p<0.0001$), but no significant *genotype* effects or *interactions* were found (Figure 5.18. H, I).

Overall, PNNs in S1UL/S1BF appear unaffected by *Pten* deletion. The loss of *Pten* from Drd1a-Cre+ neurons seems to influence exclusively that subpopulation of PV+ neurons that are not enwrapped by PNNs. PNNs may operate as a brake on plasticity, allowing PV+ neurones without PNNs to respond to extracellular stimuli from excitatory pyramidal neurones and environmental changes with remarkable flexibility and adaptability (Carulli and Verhaagen 2021; Devienne et al. 2021). The

reason why layer 5 PV+ inhibitory neurons are upregulated while layer 6b projection neurons are chronically *Pten*-deficient may be explained by the anatomical and functional connectivity between layer 5 and layer 6b (Zolnik et al. 2020; Zolnik et al. 2024). Given that Drd1a-Cre+ layer 6b neurons preferentially target PV+ interneurons in layer 6, it is probable that the loss of *Pten* predominantly affects local and nearby PV+ neurons in layers adjacent to layer 6.

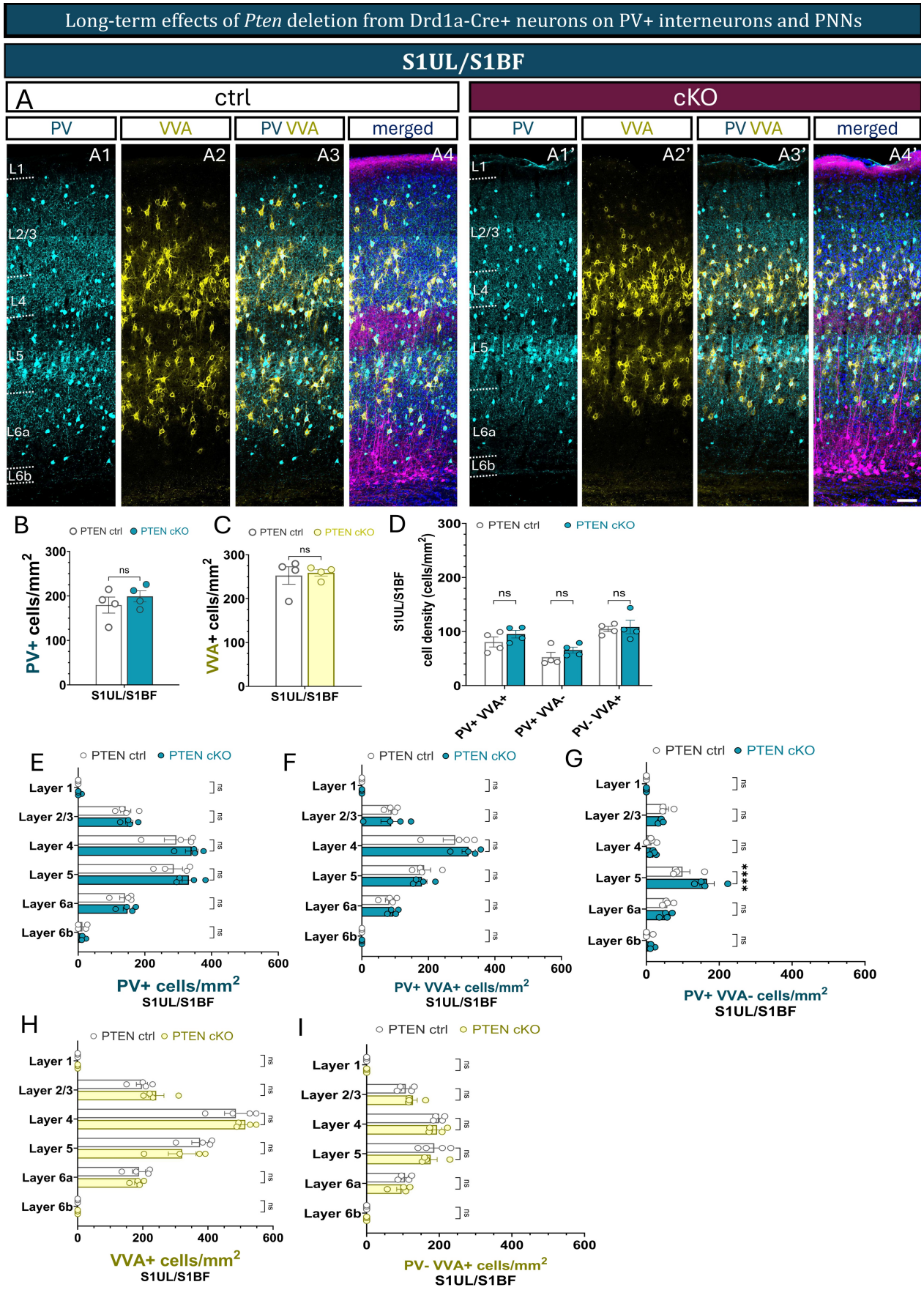

Long-term effects of Pten deletion from Drd1a-Cre+ neurons on PV+ interneurons and PNNs
S1UL/S1BF
A
ctrl
cKO
PV
VVA
PV VVA
merged
A1
A2
A3
A4
A1'
A2'
A3'
A4'
L1
L2/3
L4
L5
L6a
L6b
B
C
D
PTEN ctrl
PTEN cKO
PV+ cells/mm2
VVA+ cells/mm2
S1UL/S1BF cell density (cells/mm2)
ns
PV+ VVA+
PV+ VVA-
PV- VVA+
E
F
G
Layer 1
Layer 2/3
Layer 4
Layer 5
Layer 6a
Layer 6b
PV+ cells/mm2
S1UL/S1BF
PV+ VVA+ cells/mm2
PV+ VVA- cells/mm2
****
H
I
VVA+ cells/mm2
PV- VVA+ cells/mm2

Figure 5.18. Layer 5 in S1UL/S1BF indicates a significant increase in PV+ VVA- density following the ablation of *Pten* from Drd1a-Cre+ projection neurons. Tiled z-stack images of the entire depth of S1UL/S1BF illustrating parvalbumin-immunoreactive neurons, *Vicia villosa* agglutinin-positive cells, as well as merged images showing DAPI counterstaining and Drd1a-Cre+ projection neurons in control (A1-A4) and *Pten* cKO mice (A1'-A4'). Layer boundaries are denoted by white lines. Bar graphs showing the density of parvalbumin neurons and *Vicia villosa* agglutinin-positive cells in adult S1UL/S1BF between control and *Pten* cKO mice (B, C). Quantification of the density of parvalbumin neurons based on PNN expression in S1UL/S1BF between control and *Pten* cKO mice (D). Bar graphs illustrating the laminar distribution of PV+, PV+ VVA-, and PV+ VVA+ cells across S1UL/S1BF in control and *Pten*-deleted mice (E, F, G). Note the upregulation of PV+ VVA- cells in layer 5 of *Pten* cKO mice. Bar graphs showing the laminar distribution of VVA+ and PV- VVA+ cells in S1UL/S1BF at ~4 months of age between control and *Pten* cKO mice (H, I). Scale bar = 50 µm.

5.6. SUBCORTICAL PARVALBUMIN NEURONS

5.6.1. *Pten* deletion from Drd1a-Cre+ neurons results in altered soma shape in striatal PV+ interneurons

The impact on subcortical PV+ neurons brings this section to a close. I selected the striatum, the external segment of the globus pallidus (GPe), and the thalamic reticular nucleus (TRN) as my regions of interest (ROIs). As demonstrated in the previous chapter, the existence of VGlut1+ glutamatergic synapses generated by Drd1a-Cre+ axon terminals indicates that these are output regions of Drd1a-Cre+ layer 6 neurons. No significant differences were observed in the striatum and TRN between control and *Pten* cKO mice at ~4 months of age (CPu, p=0.4205; GPe, p=0. 8306) (Figure 5.19. A, B, C, F, H). However, I detected a significant increase in the density of PV+ neurons exclusively in the GPe in *Pten* cKO mice compared to control mice (p=0.0474) (Figure 5.19. E, G). I hypothesised that there might be morphological variations in striatal PV+ neurons in the mutant mice, despite no difference in overall density. My findings supported this, showing that the soma *perimeter* of striatal PV+ interneurons significantly decreased (p=0.0427), while *circularity* (p=0.0171) and *roundness* increased (p=0.0224) in the *Pten* cKO mice (unpaired Mann-Whitney test) (Figure 5.19. B, D). This suggests that PV+ neurons in the mutant striatum become more compact and rounded compared to

the control neurons. Thus, the conditional ablation of *Pten* from Drd1a-Cre+ neurons alters the soma shape of PV+ neurons in the adult striatum without affecting their cell density.

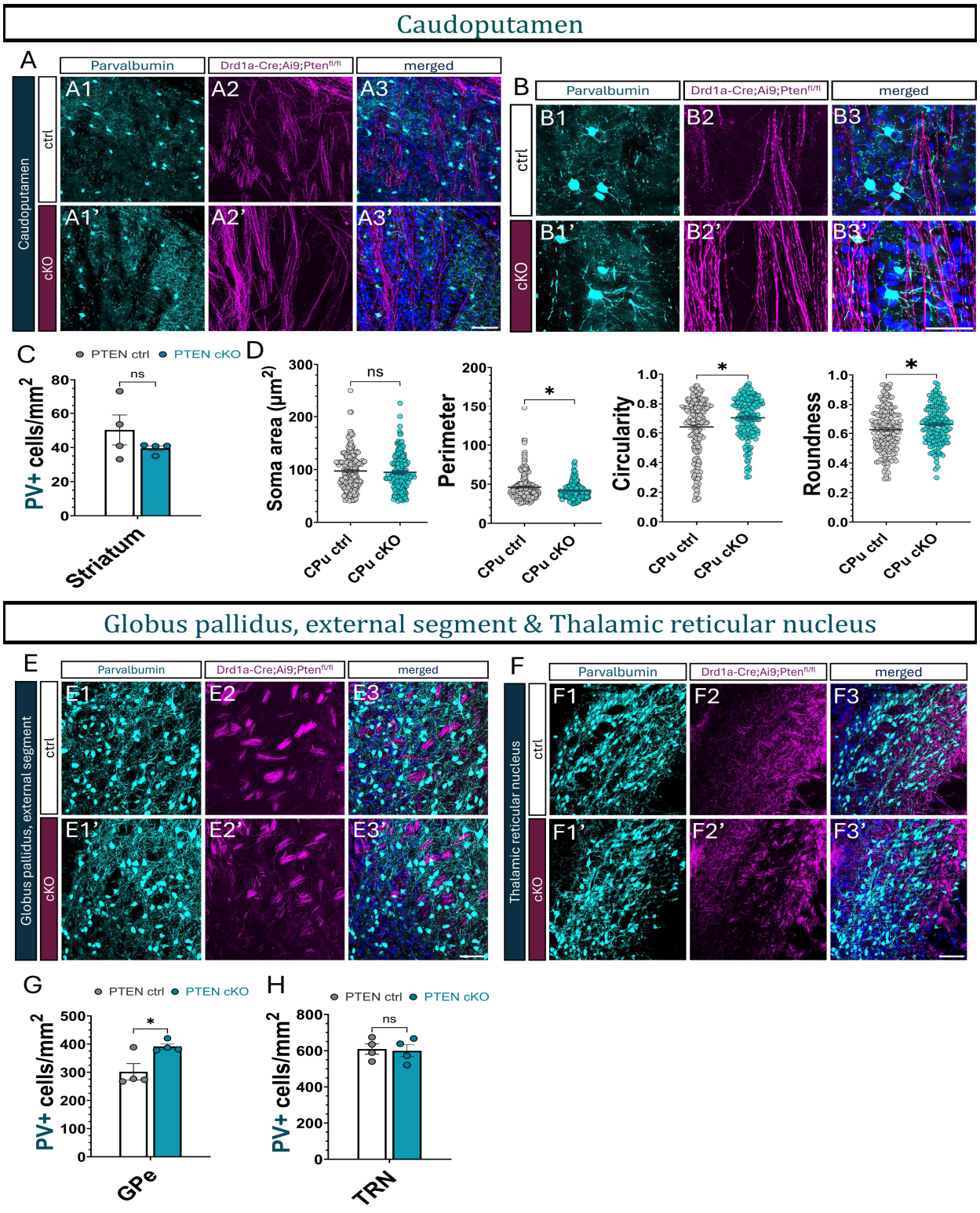


Figure 5.19. The soma shape of striatal parvalbumin interneurons is significantly altered following the deletion of *Pten* from Drd1a-Cre+ neurons. Confocal z-stacks and zoom-in images illustrating parvalbumin-immunoreactive neurons in cyan and the terminals of Drd1a-Cre+ neurons in magenta in the caudoputamen in control (A1-A3, B1-B3) and *Pten* cKO mice (A1'-A3', B1'-B3'). Quantification of the density of parvalbumin-immunoreactive neurons in the caudoputamen in control and *Pten* cKO mice (C). Scatter plots showing morphological characteristics of parvalbumin neurons measured in the caudoputamen of *Pten* cKO and control mice (D). Confocal z-stacks and zoom-in images displaying parvalbumin-immunoreactive neurons and the terminals of Drd1a-Cre+ neurons in the GPe and TRN in control (E1-E3, F1-F3) and *Pten* cKO mice (E1'-E3', F1'-F3'). Bar graphs of the total density of parvalbumin-immunoreactive neurons in the GPe and TRN between control and *Pten*-deleted mice (G, H). Scale bar = 100 μm (A3'), 50 μm (B3', E3', F3').

5.7. NEUROPEPTIDE-Y INTERNEURONS - Neocortex

In the following sections, I will present the results on the effects of *Pten* deletion on GABAergic interneurons which do *not* belong to the Ca^{2+}-binding protein-expressing subgroup. First, I will describe the effects of the loss of *Pten* on neuropeptide-Y interneurons, then move on to discuss its impact on somatostatin interneurons. This will increase our understanding of whether *Pten* ablation from Drd1a-Cre+ neurons results in cell-type-specific effects, which might be predicted given their layer-specific distribution, input selectivity, and specialised roles within the cortical microcircuits. Table 5.4. highlights the ROIs selected for NPY+ interneurons.

	CHAPTER 5		
	Regions of interest (ROIs)		
Strain	**Layer 6-enhanced** *(Drd1a-Cre;Ai9;Pten$^{fl/fl}$)*		
Interneurons	**Parvalbumin**	**Neuropeptide-Y**	**Somatostatin**
Cortical ROIs	ACA M1 S1 dense S1 sparse	ACA M2 M1 S1	ACA M1 S1
Subcortical and hippocampal ROIs	CPu GPe TRN	CA1 CA3 DG	CA1 CA3 DG

Table 5.4. Overview of cortical, subcortical, and hippocampal ROIs selected for NPY+ interneurons.

5.7.1. Loss of *Pten* from Drd1a-Cre+ neurons alters the soma area of NPY+ interneurons in the adult M2 without affecting their density

Regarding NPY+ cell density in ACA and M2, two-way ANOVA testing revealed a substantial *region* but no *genotype* effect, without *interaction* between the two factors (region, p=0.0003; genotype, p=0.3992; interaction, p=0.1607). Consequently, Šídák's multiple comparison tests did not

identify significant differences between control and mutant mice (Figure 5.20. A, B, C). Morphometric analysis of NPY+ neurons in ACA and M2 showed that the soma area of *Pten*-deficient NPY+ neurons in M2 was significantly larger than that of control neurons (unpaired Mann-Whitney test, p=0.0353) (Figure 5.20. D, E). These results indicate that hyperactive mTORC1 signalling in subsets of layer 6b neurons leads to somatic hypertrophy of NPY+ neurons selectively in M2.

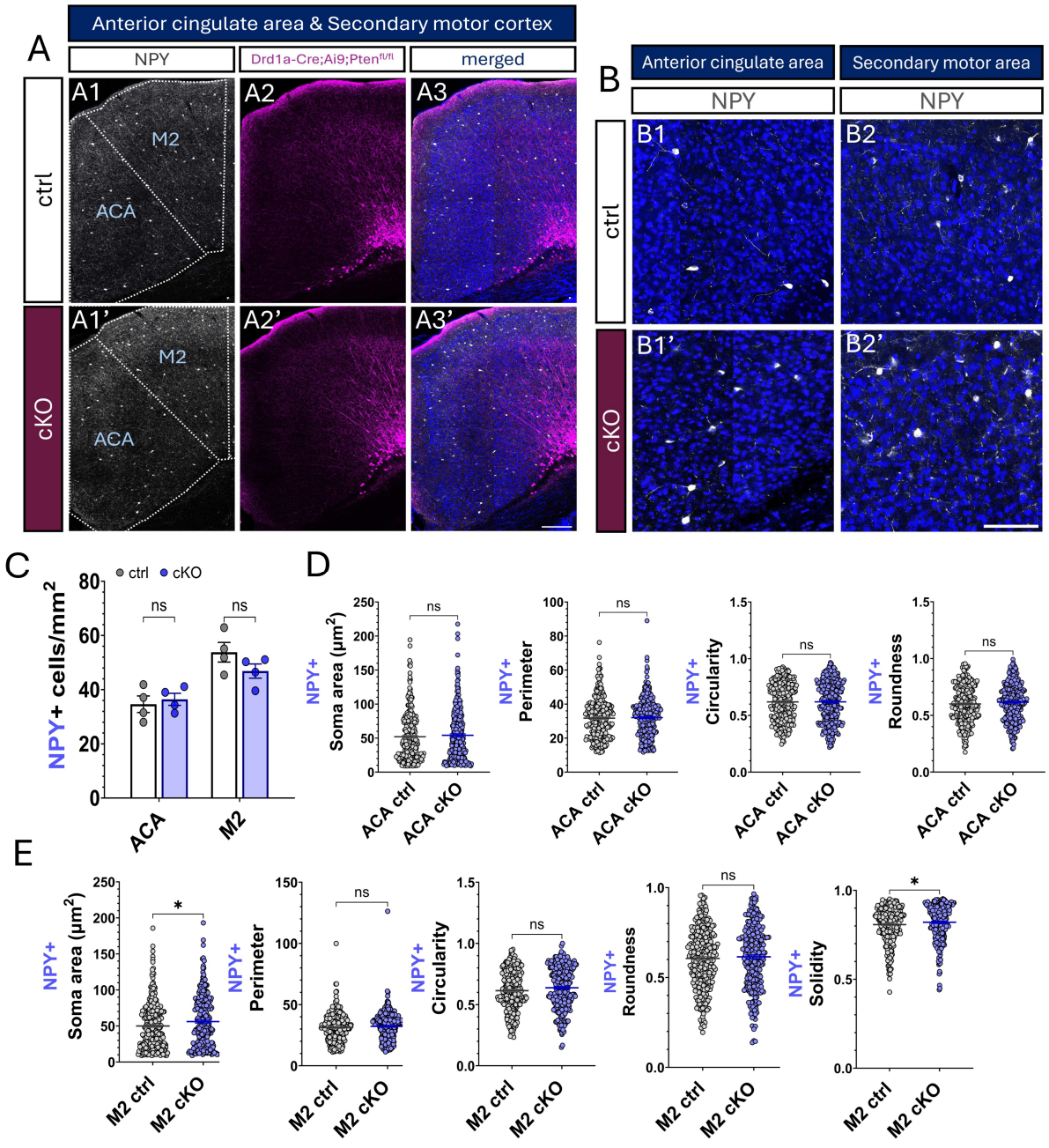


Figure 5.20. Slight increase in the soma area of neuropeptide-Y interneuron in the secondary motor cortex following *Pten* deletion from Drd1a-Cre+ neurons. Confocal images of the anterior cingulate area and the secondary motor cortex showing neuropeptide-Y-immunopositive neurons and Drd1a-Cre+ projection neurons in control (A1-A3, B1-B2) and *Pten* cKO mice (A1'-A3', B1'-B2'). Bar graphs showing the density of NPY+ neurons in ACA and M2 at ~4 months of age between control and *Pten* cKO mice (C). Morphometric analysis of NPY+ neurons in ACA and M2 (D, E). Scale bars = 100 µm.

5.7.2. NPY+ interneurons in M1 and S1 of *Pten*-deleted mice exhibit morphological changes but no laminar changes

Following ACA and M2, I next assessed NPY+ mean cell density in M1 and S1. Unlike PV+ interneurons, two-way ANOVA testing did not show a significant *region* effect on the density of NPY+ interneurons in M1 and S1. No differences existed between genotypes (Figure 5.21. A, B, C). Next, a significant effect of *layer* was observed on the cortical distribution of NPY+ neurons in M1 as well as S1 ($p<0.0001$), with no *genotype* or *interaction* effects (M1, genotype, $p=0.3281$; interaction, $p=0.5352$; S1, genotype, $p=0.2633$; interaction, $p=0.7439$) (Figure 5.21. D, E). Thus, the observed influence on NPY+ neurons seems to be determined significantly by the laminar arrangement of NPY+ neurons across layers, rather than by genetic differences.

Morphometric analysis of NPY+ neurons discovered significant alterations in the soma area of NPY+ cells in M1 and S1. Both regions of the *Pten* cKO mice showed a significant rise in soma area, with S1 exhibiting a prominent impact on NPY+ neurons (M1, $p=0.0105$; S1, $p<0.0001$, unpaired Mann-Whitney test) (Figure 5.21. F, G). *Pten*-deleted NPY+ neurons in S1 had significantly higher perimeter and roundness values, besides the increase in soma area (perimeter, $p=0.0001$; roundness, $p=0.0239$, unpaired Mann-Whitney test) (Figure 5.21. G). Somatic expansion in NPY+ interneurons in different parts of the neocortex may be caused by hyperactive mTOR signalling in *Pten* cKO mice.

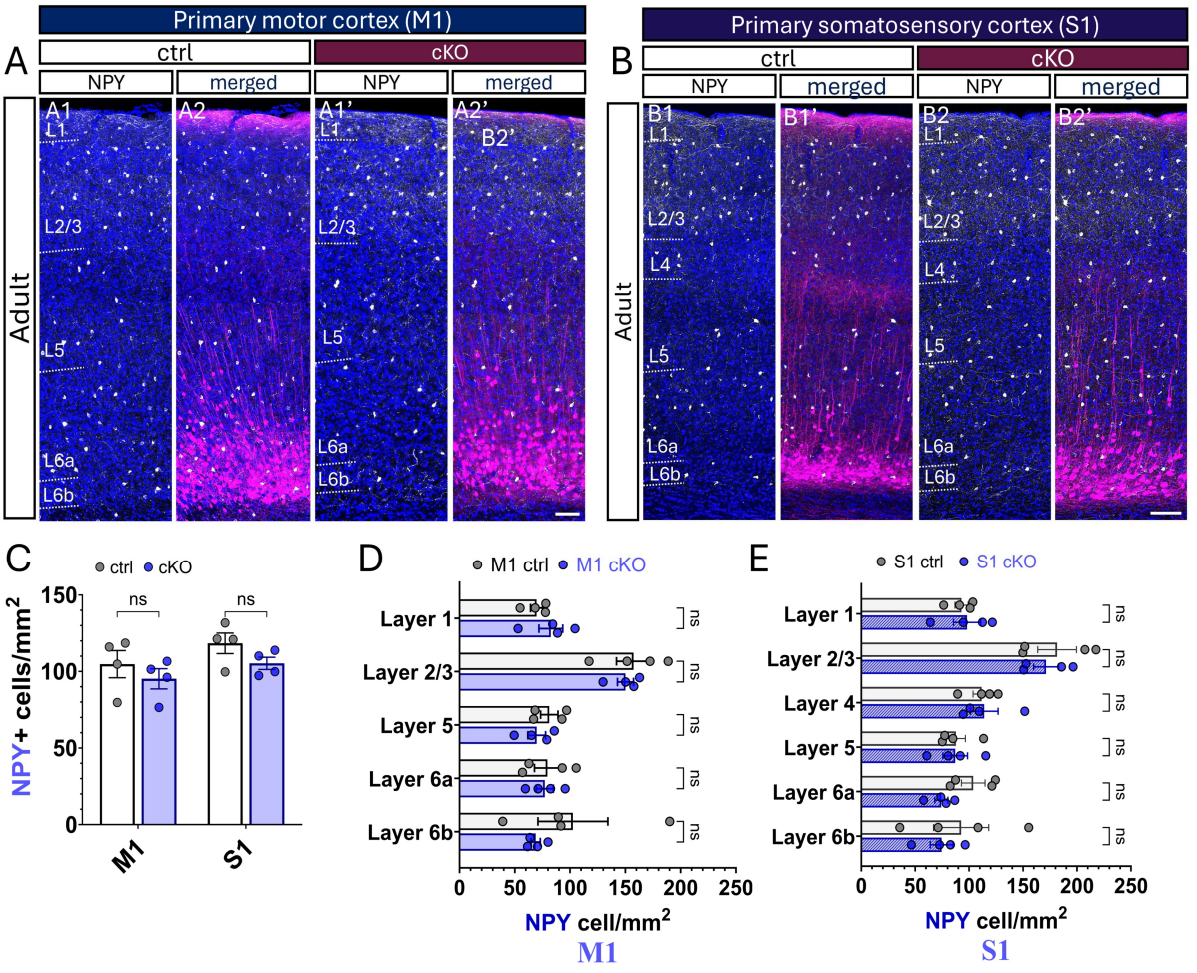

A
Primary motor cortex (M1)
ctrl
cKO
NPY
merged
NPY
merged
Adult
L1
L2/3
L5
L6a
L6b
B
Primary somatosensory cortex (S1)
ctrl
cKO
NPY
merged
NPY
merged
Adult
L1
L2/3
L4
L5
L6a
L6b
C
ctrl
cKO
NPY+ cells/mm2
150
100
50
0
ns
ns
M1
S1
D
M1 ctrl
M1 cKO
Layer 1
Layer 2/3
Layer 5
Layer 6a
Layer 6b
ns
0
50
100
150
200
250
NPY cell/mm2
M1
E
S1 ctrl
S1 cKO
Layer 1
Layer 2/3
Layer 4
Layer 5
Layer 6a
Layer 6b
ns
0
50
100
150
200
250
NPY cell/mm2
S1
Primary motor cortex
F
NPY+ Soma area (µm2)
*
NPY+ Perimeter
ns
NPY+ Circularity
ns
NPY+ Roundness
ns
NPY+ Solidity
ns
M1 ctrl
M1 cKO
Primary somatosensory cortex
G
NPY+ Soma area (µm2)
****
NPY+ Perimeter
***
NPY+ Circularity
ns
NPY+ Roundness
*
NPY+ Solidity
ns
S1 ctrl
S1 cKO

Figure 5.21. Deleting *Pten* from a subset of layer 6 projection neurons appears to result in somatic overgrowth in NPY+ interneurons in different areas of the cortex. Merged images of neuropeptide-Y-positive neurons in grey, Drd1a-Cre+ projection neurons in magenta, and DAPI counterstaining in adult primary motor and somatosensory cortices of control (A1-A2, B1-B2) and *Pten* cKO mice (A1'-A2', B1'-B2'). Bar graphs of the density of neuropeptide-Y-positive neurons in M1 and S1 between control and *Pten* cKO mice (C). Bar graphs of the laminar distribution of neuropeptide-Y-positive neurons across M1 and S1 between control and *Pten* cKO mice (D, E). Scatter plots of soma measurements of neuropeptide-Y-positive neurons in M1 and S1 (F, G). Scale bars = 50 µm.

5.7.3. NPY+ interneurons in layer 2/3 and layer 6 of S1 exhibit increased soma area and perimeter

Having established that the removal of *Pten* from Drd1a-Cre+ neurons leads to a significant increase in the soma area of NPY+ neurons in S1, I proceeded to identify the specific cortical layers where these affected neurons reside. In *Pten* cKO mice, NPY+ neurons within layers 2/3 exhibited a marked increase in soma area ($p=0.0005$, Kruskal-Wallis test with Dunn's multiple comparisons). Additionally, there was a corresponding increase in the perimeter of NPY+ neurons in both layer 2/3 ($p=0.0253$) and layer 6a ($p=0.0431$) in *Pten*-deficient mice (Kruskal-Wallis test with Dunn's multiple comparisons) (Figure 5.22. A, B). These findings suggest that the deletion of *Pten* primarily influences NPY+ neurons within these layers; however, the nature of the relationship between NPY+ neurons in layers 2/3 and 6a, along with any potential microcircuit connections with Drd1a-Cre+ neurons in layers 6a and 6b, will be interesting to elucidate.

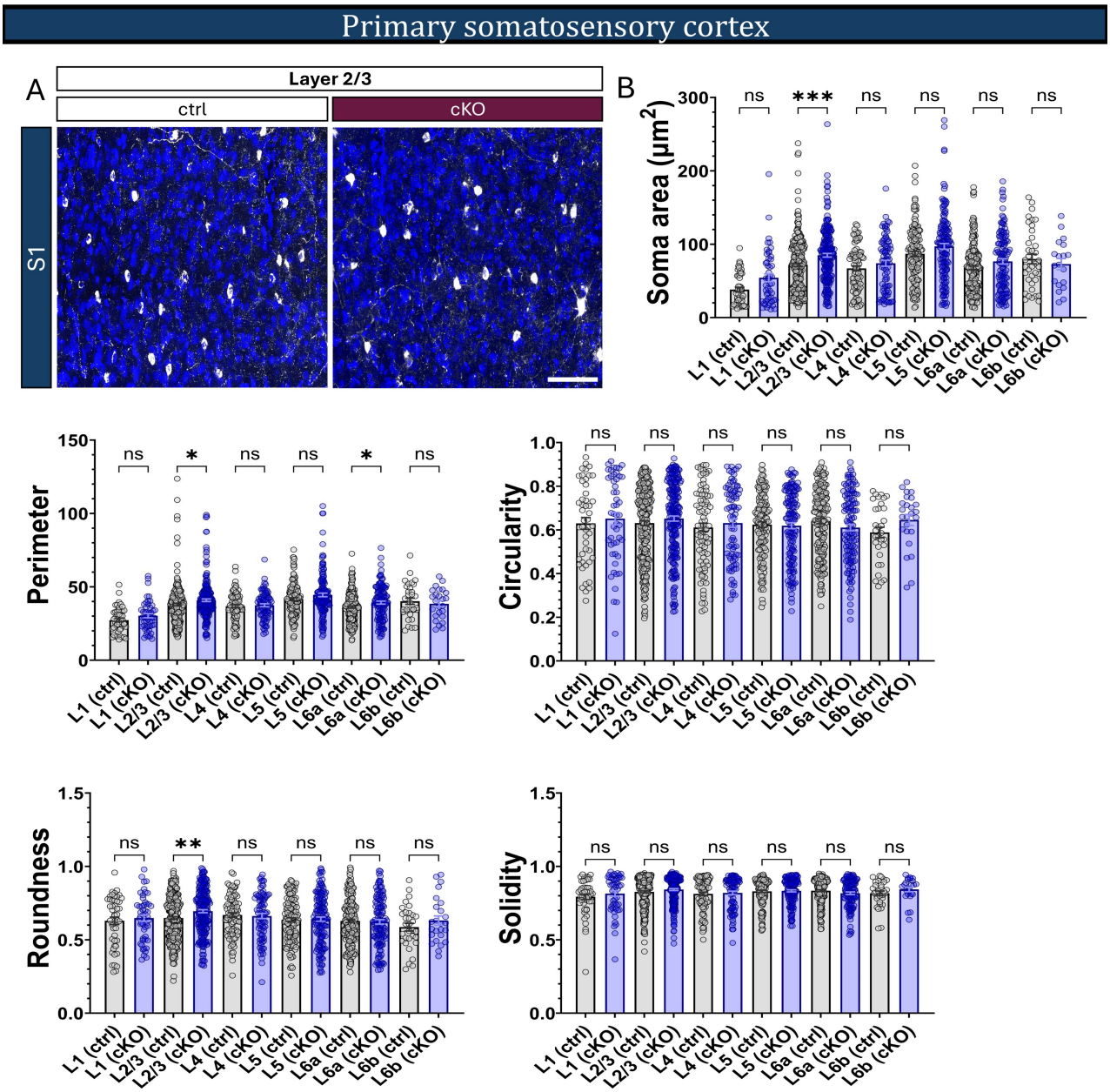
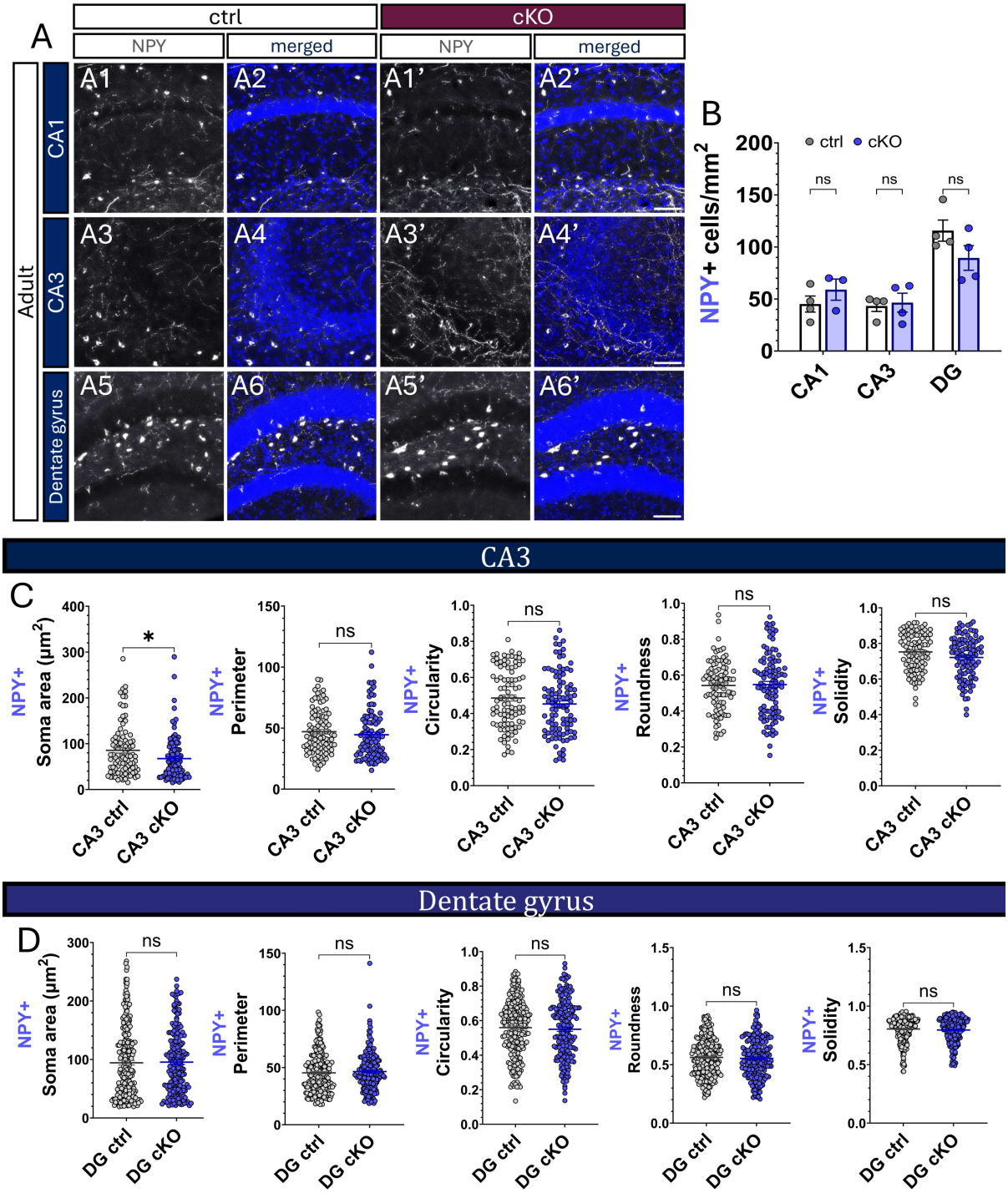


Figure 5.22. Layer 2/3 and layer 6a neuropeptide-Y interneurons have enlarged somata and perimeter in the primary somatosensory cortex of *Pten* cKO mice. (A) Representative examples of neuropeptide-Y-immunoreactive neurons in layer 2/3 of the primary somatosensory cortex in control and *Pten*-deleted mice. (B) Bar graphs showing the morphometric assessment of neuropeptide-Y-immunostained neurons across cortical layers of the primary somatosensory cortex in control and *Pten* cKO mice. Scale bar = 100 µm.

5.8. NEUROPEPTIDE-Y INTERNEURONS – CPu and hippocampus

5.8.1. Subtle changes in soma morphology with no alteration in cell number observed in NPY+ interneurons in the striatum and CA3 region after *Pten* deletion

The next aim was to assess whether *Pten* removal from Drd1a-Cre+ neurons had a long-term effect on NPY+ neurons outside of the cortex, specifically in the hippocampal regions and the dorsal striatum. Regarding the hippocampus, the density of NPY+ neurons varied significantly by *area* ($p<0.0001$) but not by *genotype* ($p=0.6905$), with no region-genotype *interaction* detected between the two factors ($p=0.1111$, two-way ANOVA with Šídák's multiple comparison). Thus, *Pten* loss did not affect NPY+ neuron density in the adult hippocampus (Figure 5.23. A, B). However, morphometric analysis revealed a notable reduction in the soma area of NPY+ neurons in the CA3 region of *Pten* cKO mice ($p=0.0123$, unpaired Mann-Whitney test), which contradicts expectations of a constitutive activation of the mTOR pathway leading to somatic and dendritic hypertrophy. In the dentate gyrus, soma parameters showed no significant differences between groups (Figure 5.23. C, D). The striatum showed a modest decrease in soma circularity of NPY+ neurons in *Pten* cKO mice ($p=0.0449$, unpaired Mann-Whitney test), but other morphological features and density remained unchanged (Figure 5.23. E, F, G). In conclusion, selective *Pten* ablation from Drd1a-Cre+ neurons did not alter the density of NPY+ neurons in their projection regions, suggesting that interneuron numbers and their protein expression do not appear to be regulated by cortical excitatory neurons in layers 6a and 6b.


A
ctrl
cKO
NPY
merged
NPY
merged
Adult
CA1
CA3
Dentate gyrus
A1
A2
A1'
A2'
A3
A4
A3'
A4'
A5
A6
A5'
A6'
B
ctrl
cKO
NPY+ cells/mm2
ns
CA1
CA3
DG
CA3
C
NPY+ Soma area (µm2)
NPY+ Perimeter
NPY+ Circularity
NPY+ Roundness
NPY+ Solidity
CA3 ctrl
CA3 cKO
Dentate gyrus
D
DG ctrl
DG cKO

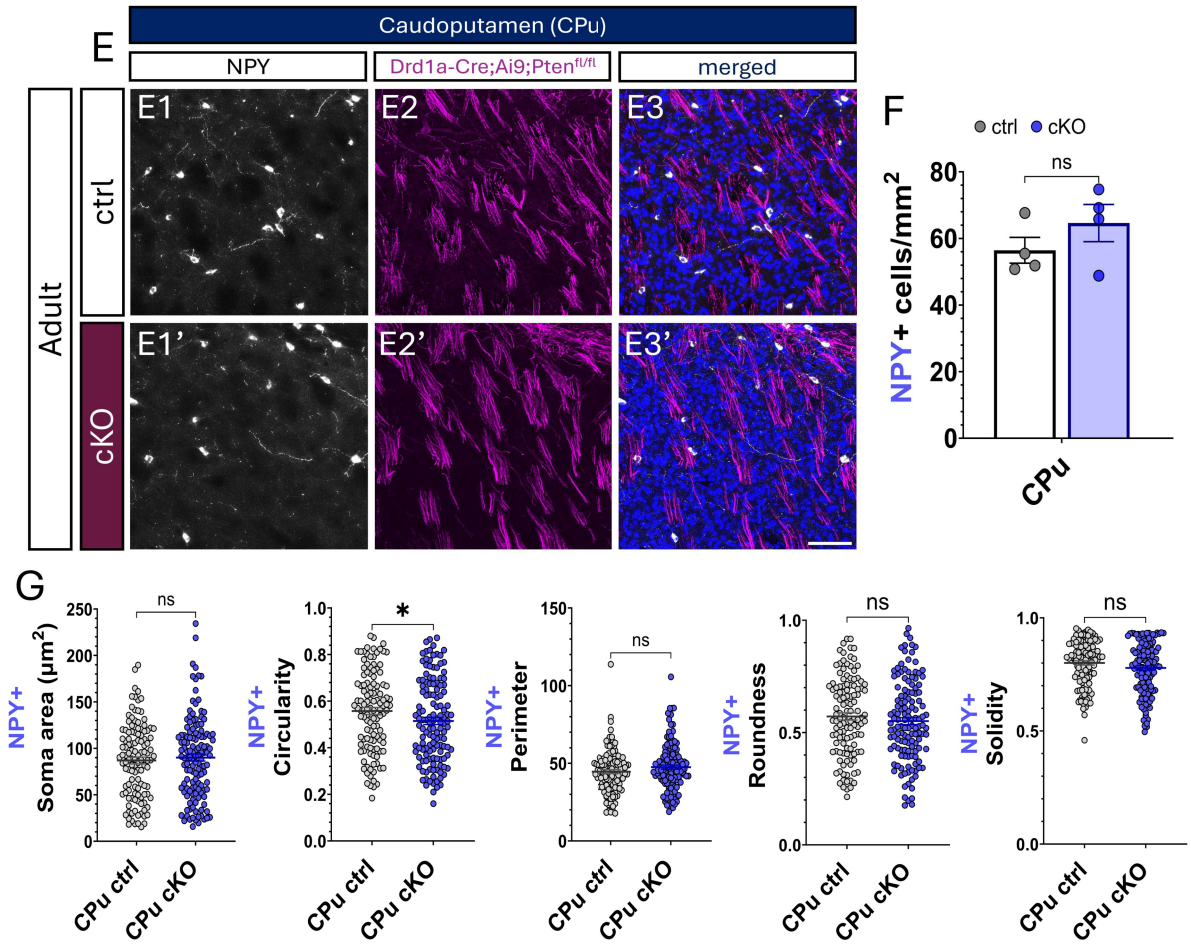


Figure 5.23. Conditional deletion of *Pten* from Drd1a-Cre+ projection neurons did not impact the overall density of NPY+ interneurons in the striatum and hippocampal areas. Maximum-intensity projected z-stack images illustrating neuropeptide-Y-immunoreactive neurons in grey and DAPI counterstaining in blue in the CA1, CA3, and dentate gyrus in control (A1-A6) and *Pten*-deleted mice (A1'-A6'). Quantification of the cell density of neuropeptide-Y-immunoreactive neurons in distinct regions of the hippocampus (B). Scatter plots displaying soma measurements of individual NPY+ neurons in the CA3 and dentate gyrus between control and *Pten* cKO mice (C, D). Z-stack images of neuropeptide-Y-immunoreactive neurons and terminals of Drd1a-Cre+ neurons in the striatum in control (E1-E3) and *Pten* cKO mice (E1'-E3'). Bar graphs of the density of striatal NPY+ neurons in control and *Pten* cKO mice (F). Scatter plots displaying soma measurements of individual NPY+ neurons within the striatum between control and mutant mice (G). Scale bars = 50 µm.

5.9. SOMATOSTATIN INTERNEURONS – Neocortex

This chapter concludes with a discussion of the somatostatin (SST) subtype of GABAergic neurons and the effects on their spatial and laminar distribution following the permanent loss of *Pten* from Drd1a-Cre+ neurons. By comparing PV+ to SST+ and NPY+ interneurons, I hope to clarify whether neuropeptide-expressing subtypes are more vulnerable than subtypes that produce Ca^{2+}-binding proteins to 1) dysfunctions in the PI3K/AKT/mTOR pathway and its downstream effectors, and 2) perturbations in glutamatergic deep-layer projection neurons.

5.9.1. Permanent loss of *Pten* from subsets of layer 6 neurons rearranges the laminar distribution of SST+ interneurons in layer 5 and layer 6b of M1

First, I assessed the long-term effects of *Pten* deletion on cortical SST+ interneurons in the anterior cingulate area at ~4 months of age. The density of ACA SST+ cells in the *Pten*-deleted mice did not differ significantly from that of the control mice (Figure 5.24. A, B). Next, I detected a substantial *genotype* effect (p=0.0183), but no region-genotype interaction or *region* effect when comparing the density of SST+ neurons in M1 and S1 (Figure 5.24. C, D, E). Interestingly, two-way ANOVA with Šídák's multiple comparisons revealed no significant differences between the *Pten* cKO and control mice. However, the *Pten* cKO animals did show a trend toward a decrease in SST+ density in M1, although it did not reach statistical significance (p=0.0581) (Figure 5.24. E). Next, I sought to determine whether the laminar distribution of SST+ neurons was altered in the *Pten* cKO brains. The density of SST+ neurons in M1 was significantly influenced by both *layer* and *genotype*, albeit there was no *interaction* between the two variables (layer, p<0.0001; genotype, p<0.0001). *Post-hoc* tests found that *Pten* cKO mice had reduced density of SST+ interneurons in layer 5 and layer 6b of M1 (layer 5, p=0.0053; layer 6b, p=0.0177; two-way ANOVA with Šídák's multiple comparisons) (Figure 5.24. C, F). Since the overall density of SST+ interneurons in M1 remained the same, these findings suggest that SST+ neurons are redistributing throughout the deep cortical layers in M1 rather than

decreasing in number. Interestingly, no significant differences between *genotypes* and *layers* were observed in adult S1 (Figure 5.24. D, G), indicating that the effect on SST+ neurons is specific to M1.

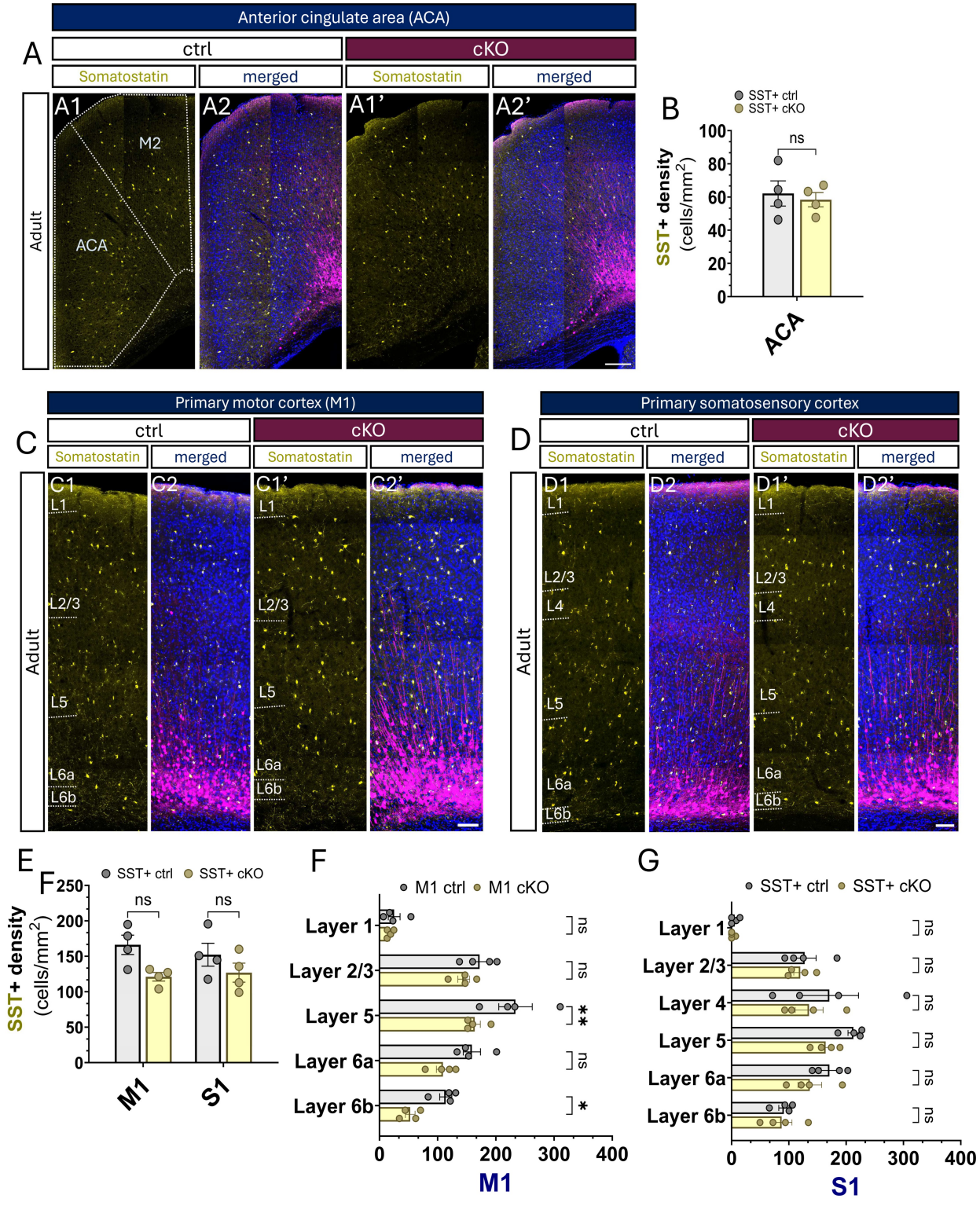


Figure 5.24. Loss of *Pten* from subsets of layer 6 neurons alters the distribution of somatostatin interneurons in layers 5 and 6b of the primary motor cortex. Tile-scans of the anterior cingulate area illustrating somatostatin-immunoreactive neurons in yellow in control and mutant mice (A1, A1'). Merged images displaying Drd1a-Cre+ projection neurons and DAPI counterstaining superimposed on the yellow signal (A2, A2'). Quantification of the cell density of somatostatin-immunoreactive neurons in the anterior cingulate area between control and *Pten* cKO mice (B). Tiled z-stack images of the entire depth of M1 and S1 depicting somatostatin-immunoreactive neurons in control (C1, D1) and *Pten* cKO mice (C1', D1'). Merged images showing Drd1a-Cre+ projection neurons and DAPI counterstaining overlaid on the somatostatin signal in M1 and S1 of control (C2, D2) and mutant mice (C2', D2'). Cortical layer boundaries are delineated by white lines. Bar graphs of the cell density of somatostatin-immunoreactive neurons in M1 and S1 between control and *Pten* cKO mice (E). Quantification of the laminar density of somatostatin-immunoreactive neurons in M1 and S1 between control and *Pten* cKO mice (F, G). Scale bars = 100 µm (A2'), 50 µm (C2', D2').

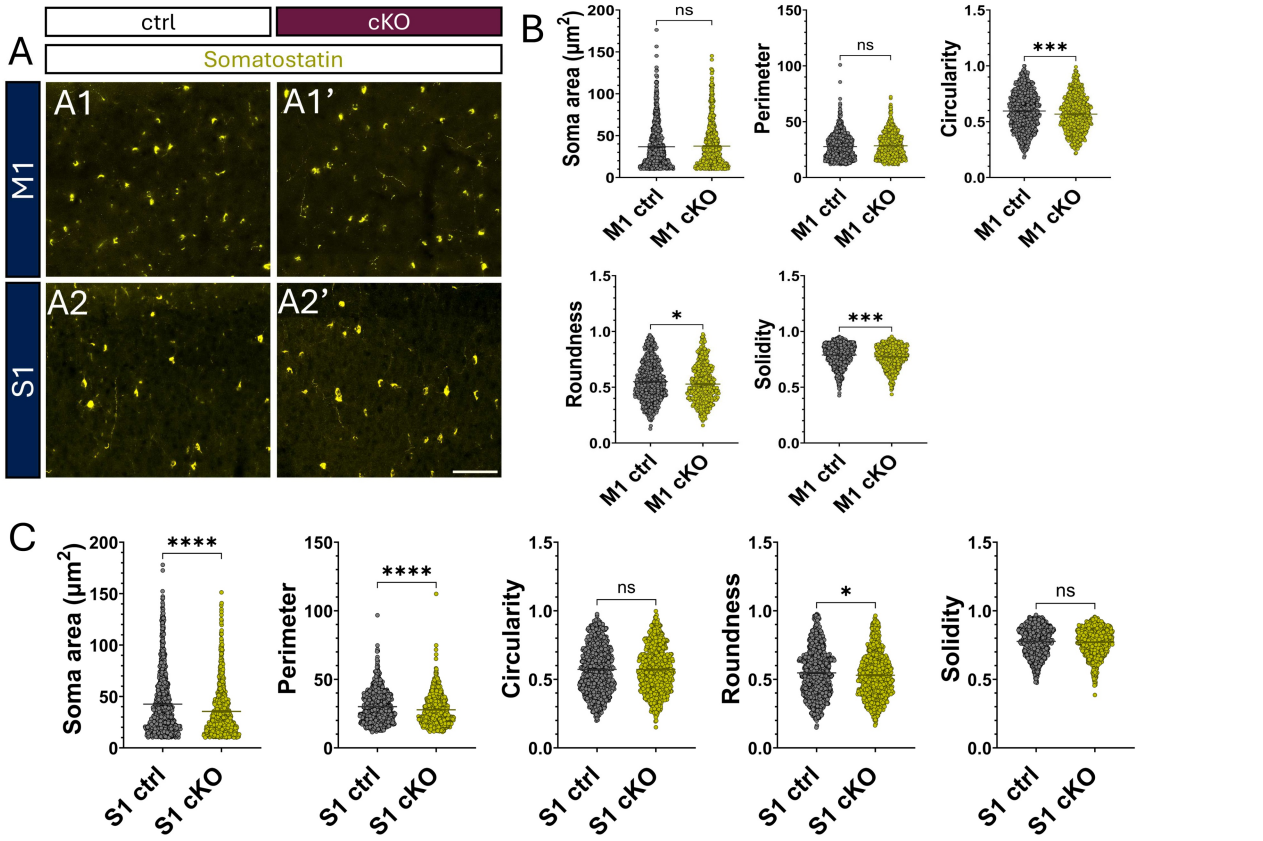
5.9.2. Morphological alterations in SST+ interneurons in the adult primary motor and somatosensory cortices after *Pten* deletion

Having established the long-term consequences of removing *Pten* from Drd1a-Cre+ neurons on the density and laminar distribution of SST+ interneurons, I next sought to assess the impact on their soma morphology. *Pten* cKO mice displayed significant reductions in the soma circularity, roundness, and solidity values of SST+ interneurons in M1 (circularity, p=0.0004; roundness, p=0.0139; solidity, p=0.0003; unpaired Mann-Whitney test) (Figure 5.25. A, B). These findings may suggest that after *Pten* deletion, SST+ interneurons typically exhibit asymmetrical soma morphologies. In contrast to M1, SST+ interneurons in S1 exhibited alterations in their soma perimeter and area, but not in their soma solidity or circularity (Figure 5.25. A, C). SST+ neurons in S1 in the *Pten*-deleted mice had smaller cell bodies and a reduced soma perimeter relative to control mice (area, p<0.0001; perimeter, p<0.0001; roundness, p=0.0376).

Next, I examined the laminar morphology of SST+ interneurons to see whether SST+ neurons with altered morphology in M1 and S1 were concentrated in the superficial or infragranular layers. Since the infragranular layers of M1 were the regions where the laminar density of SST+ neurons was impacted in the *Pten* cKO mice, I postulated that these layers included SST+ interneurons with changed circularity and solidity. In line with this, I noticed that SST+ interneurons in layer 6a

displayed reduced circularity and solidity in M1 of *Pten* cKO mice (L6a, circularity, p=0.0163; solidity, p=0.0373; perimeter, p=0.0200; Kruskal-Wallis test with Dunn's multiple corrections) (Figure 5.25. D). Interestingly, SST+ interneurons with decreased soma area and perimeter in the *Pten* cKO mice were located in the superficial, granular, and infragranular layers. In particular, SST+ interneurons in layer 4 and layer 6a of mutant S1 were found to have reduced soma size and perimeter (area, L2/3, p=0.0152; L4, p<0.0001; L6a, p=0.0089; perimeter, L4, p<0.0001; L6a, p=0.0043; Kruskal-Wallis test) (Figure 5.25. E).

It can be inferred that ablating *Pten* from Drd1a-Cre+ neurons has different effects on the laminar distribution and soma morphology of SST+ interneurons in M1 and S1. This suggests that the long-term effects of *Pten* deletion on SST+ interneurons vary by cortical regions. It remains to be seen whether the conditional removal of *Pten* from different types of deep-layer projection neurons in layer 5 or layer 6a leads to the same region- and layer-specific effects.


A
ctrl
cKO
Somatostatin
M1
S1
A1
A1'
A2
A2'
B
Soma area (µm²)
Perimeter
Circularity
Roundness
Solidity
ns
*
***
M1 ctrl
M1 cKO
C
****
S1 ctrl
S1 cKO
Primary motor cortex
D
L1 (ctrl)
L1 (cKO)
L2/3 (ctrl)
L2/3 (cKO)
L5 (ctrl)
L5 (cKO)
L6a (ctrl)
L6a (cKO)
L6b (ctrl)
L6b (cKO)

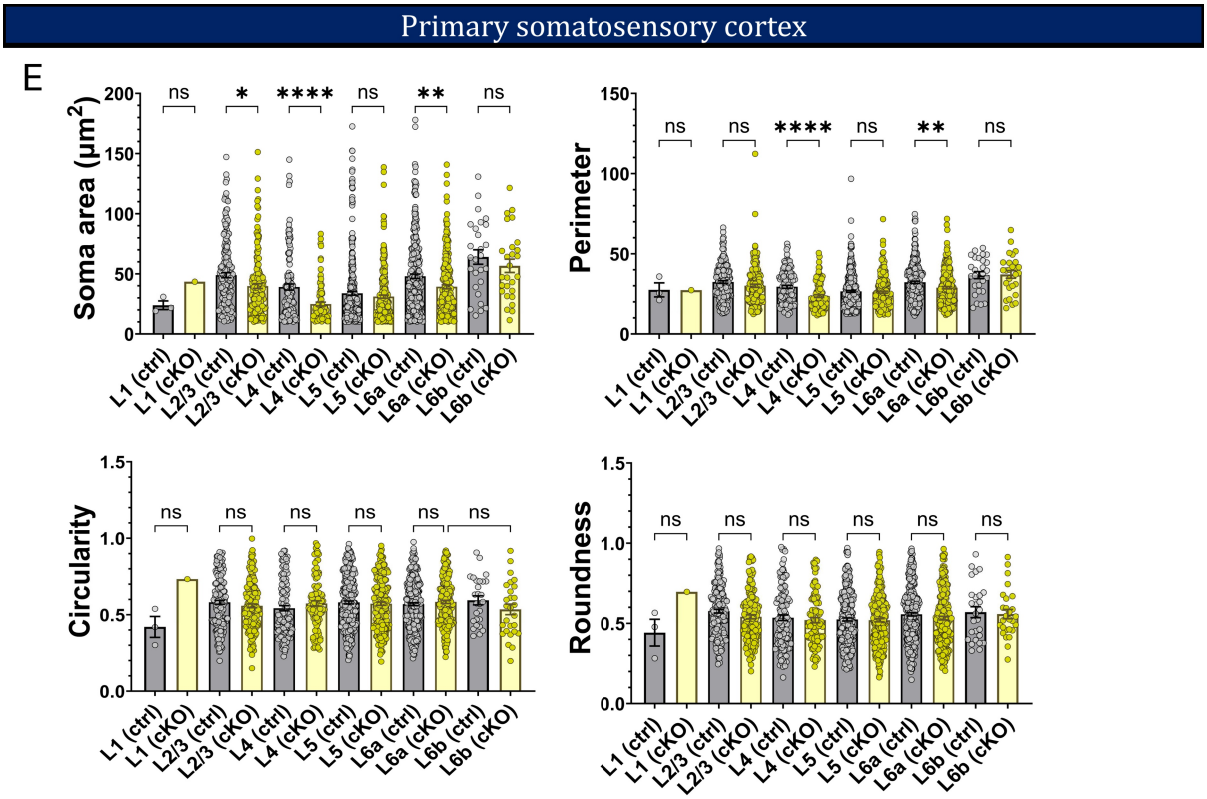


Figure 5.25. The soma area and shape of somatostatin interneurons are differentially affected by the long-term loss of *Pten* in the primary motor and somatosensory cortices. Representative images of somatostatin-immunostained neurons in layer 2/3 of the primary motor and somatosensory cortices in adult control (A1, A2) and *Pten*-deficient mice (A1', A2'). Morphometric analysis of somatostatin-immunostained neurons in M1 and S1 between control and *Pten* cKO mice. Scatter plots represent individual cell measurements (B, C). Morphometric analysis of somatostatin-immunostained neurons across the different cortical layers of M1 and S1 between control and *Pten* cKO mice. Scale bar = 50 µm.

5.10. SOMATOSTATIN INTERNEURONS – CPu and hippocampus

5.10.1. SST+ interneurons in the striatum are unaffected by the permanent loss of *Pten* from Drd1a-Cre+ neurons

Finally, I investigated how deleting *Pten* from Drd1a-Cre+ neurons impacts the density and morphology of SST+ interneurons in the projection regions of Drd1a-Cre+ neurons. The striatum did not reveal significant alterations in the density and soma morphology of SST+ interneurons between control and *Pten*-deleted mice at ~4 months of age (Figure 5.26. A, B, C, D). This indicates that the number of SST+ interneurons in the adult striatum is not regulated by glutamatergic Drd1a-Cre+ projection neurons in layer 6 via *Pten*.

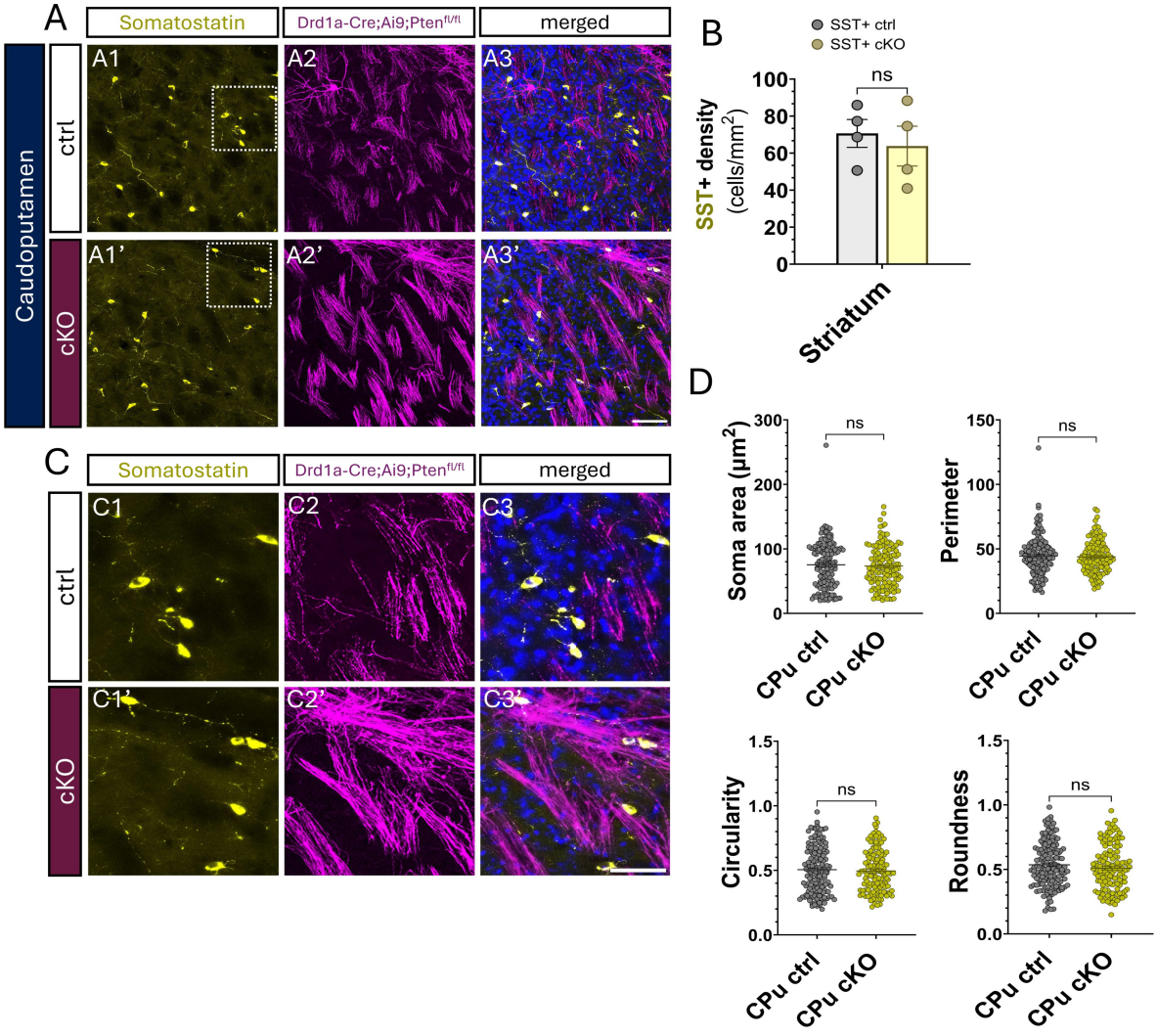


Figure 5.26. Drd1a-Cre+ neurons do not regulate the density and soma morphology of somatostatin interneurons in the adult caudoputamen. Maximum-intensity projected z-stacks of the caudoputamen showing somatostatin-immunoreactive neurons in yellow along with axon terminals of Drd1a-Cre+ neurons in magenta in control (A1-A3) and *Pten*-deficient mice (A1'-A3'). Cell density of SST+ neurons in the caudoputamen between control and *Pten*-deleted mice (B). Zoom-in images of somatostatin-immunoreactive neurons and fibre terminals of Drd1a-Cre+ neurons (C1-C3, C1'-C3'). Note the presence of SST+ neurons in the vicinity of Drd1a-Cre+ neuron terminals (C3, C3'). Morphometric assessment of striatal SST+ neurons (D). Scale bars = 50 µm (A3'), 30 µm (C3').

5.10.2. Subsets of SST+ interneurons are enwrapped by perineuronal nets in the hippocampus and remain unaffected by *Pten* deletion from Drd1a-Cre+ neurons

Previous research has indicated that PNNs encase a subtype of SST+ interneurons, as evidenced by *Wisteria floribunda* agglutinin (WFA) labelling (Berretta et al. 2015). This specific SST+ WFA+ group is especially intriguing as it contains the Kv3 voltage-gated potassium channel subunit, which might give them the ability to fire at high frequencies (Berretta et al. 2015), similar to the fast-spiking PV interneurons. Remarkably, I found several instances of SST+ interneurons in the CA3, CA1, and dentate gyrus, which were positive for VVA labelling in both control and *Pten* cKO mice (Figure 5.27. A). These double-positive SST+ neurons were mainly located in the CA1 region (Figure 5.27. A1-A3, A1'-A3'). Next, I quantified the density of SST+ neurons in the hippocampal regions and differentiated between SST+ neurons bearing PNNs (SST+ VVA+) versus those without PNNs (SST+ VVA-). The density of SST+ VVA+ neurons in the CA1 and CA3 regions was found to be significantly influenced by *region*, but not by *genotype* (Figure 5.27. B, C). Albeit there was a significant *region* effect, no *interaction* was observed between genotype and region (region, p=0.0073; genotype, p=0.9465; interaction, p=0.3906). The lack of *genotype* effect on the density of SST+ VVA+ neurons suggests that *Pten* removal does not perturb the number of SST+ VVA+ neurons in CA1 and CA3. Next, I analysed the subset of SST+ interneurons that lacked PNNs. However, there were no significant *regional* or *genotype* differences in the density and percentage of SST+ VVA- neurons between control and *Pten* cKO mice in the CA1 and CA3 (Figure 5.27. D, E). Similarly, *Pten* cKO mice did not exhibit significant differences in the total density of SST+ neurons across the hippocampal regions (genotype,

p=0.6977; region, p<0.0001; interaction, p=0.1324; two-way ANOVA with Šídák's multiple comparisons) (Figure 5.27. F). Therefore, it can be concluded that *regional* effects, rather than the irreversible loss of *Pten* from Drd1a-Cre+ neurons, were responsible for the notable variations in the density of SST+ and SST+ VVA+ neurons.

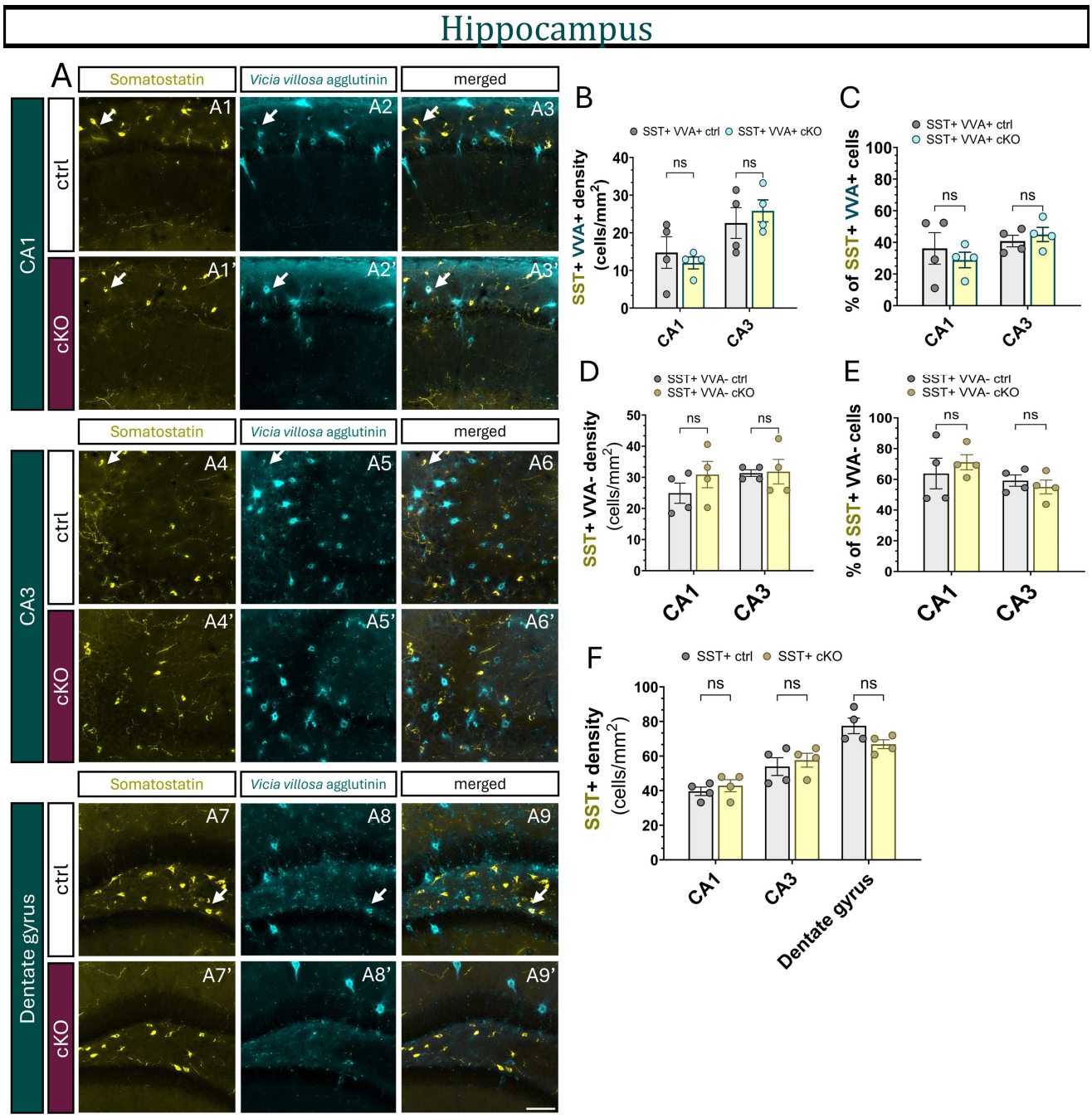


Figure 5.27. Perineuronal nets surround subsets of somatostatin interneurons in the hippocampus, but the loss of *Pten* from Drd1a-Cre+ neurons does not alter their density. Maximum-intensity projected z-stacks of somatostatin-immunostained neurons in yellow and *Vicia villosa* agglutinin-labelled perineuronal nets in cyan in the CA1, CA3, and dentate gyrus in control (A1-A3, A4-A6, A7-A9) and *Pten* cKO mice (A1'-A3', A4'-A6', A7'-A9'). PNN-bearing SST+ neurons co-localising with VVA+ cells are indicated by white arrows. Bar graphs showing the density and percentage of SST+ VVA+ neurons in the CA1 and CA3 between control and *Pten* cKO mice (B, C). Bar graphs showing the density and percentage of SST+ VVA- neurons in the CA1 and CA3 between control and *Pten* cKO mice (D, E). Quantification of the density of SST+ neurons in multiple hippocampal regions at ~4 months of age between control and *Pten* cKO mice (F). Scale bar = 50 µm.

5.10.3. Permanent deletion of *Pten* from Drd1a-Cre+ neurons selectively alters the soma area and shape of CA1 SST+ interneurons

Lastly, I performed a morphometric analysis of SST+ neurons within the hippocampus. I detected a substantial reduction in the soma area and perimeter of CA1 SST+ interneurons (area, p=0.0284; perimeter, p=0.0079; unpaired Mann-Whitney test), along with an increase in their circularity and roundness in the *Pten* cKO mice (circularity, p=0.0217; roundness, p=0.016) (Figure 5.28. A, B). Deleting *Pten* from Drd1a-Cre+ neurons did not affect the soma morphology of SST+ interneurons in the CA3 and dentate gyrus (Figure 5.28. C, D, E, F), suggesting that *Pten* deletion had a region-specific effect solely on CA1 SST+ interneurons.

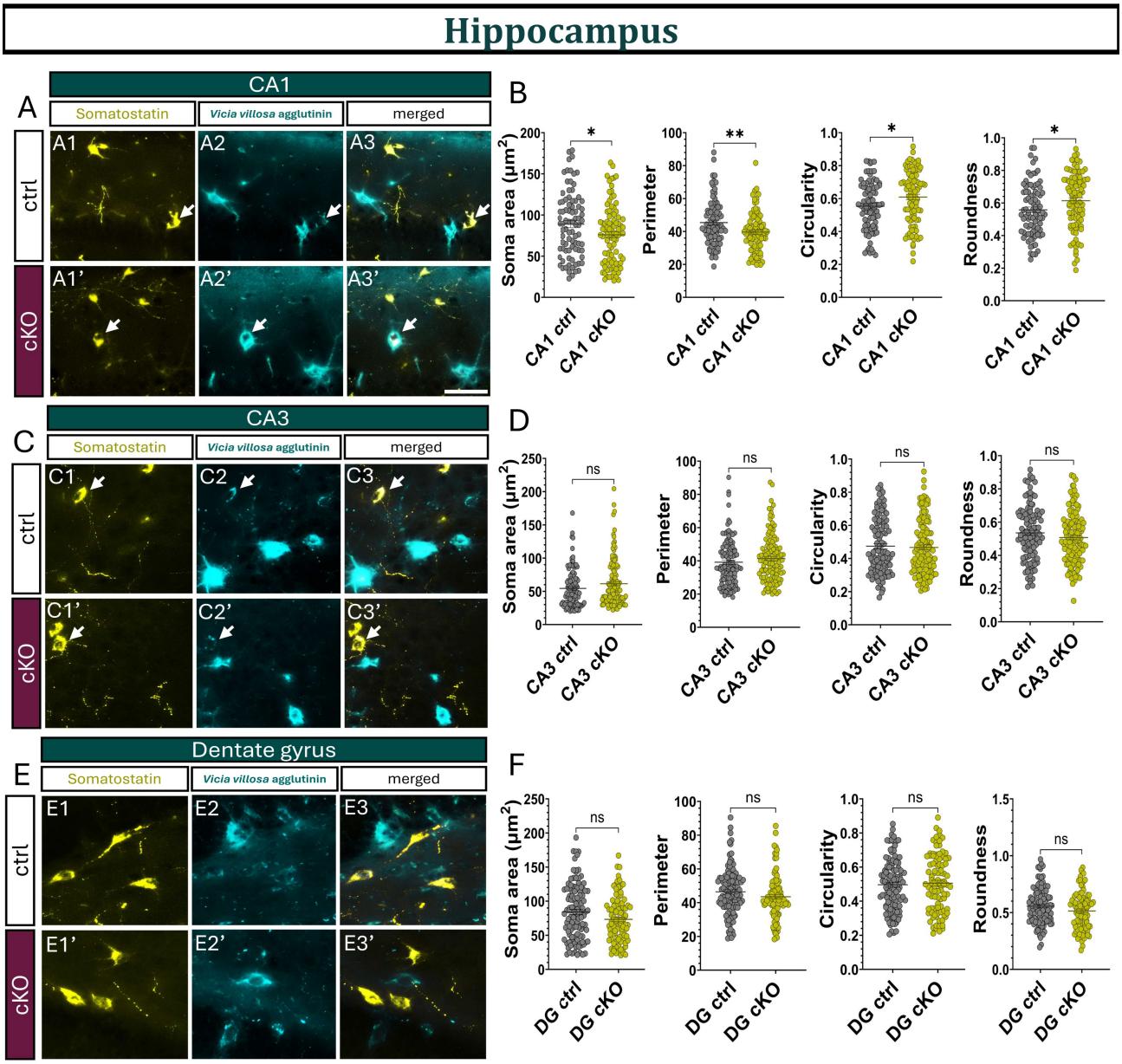


Figure 5.28. Loss of *Pten* from Drd1a-Cre+ neurons has a region-specific influence on the soma morphology of somatostatin interneurons in CA1. Representative images of somatostatin-immunostained neurons and perineuronal nets detected by *Vicia villosa* agglutinin in distinct regions of the adult hippocampus in control (A1-A3, C1-C3, E1-E3) and mutant mice (A1'-A3', C1'-C3', E1'-E3'). Scatter plots indicating individual cell measurements of somatostatin interneurons in the CA1, CA3, and dentate gyrus between control and *Pten* cKO mice (B, D, F). Scale bar = 30 µm.

5.11. Discussion

5.11.1. Generating a novel conditional knockout mouse strain where *Pten* is selectively deleted from Drd1a-Cre+ projection neurons

In this chapter, I have employed a novel cKO strain where *Pten* was selectively ablated from Drd1a-Cre+ cortical projection neurons shortly after the end of the first week of postnatal development. This is the first animal model to date to selectively delete *Pten* from subsets of deep-layer projection neurons in cortical layers 6a and 6b. *Pten* knockout mice targeting forebrain excitatory neurons have already been generated (e.g., NEX-*Pten* (Kazdoba et al. 2012) and *CamKIIα*-Cre;*Pten*$^{loxP/loxP}$ (Sperow et al. 2012; Chow et al. 2009)); however, *Pten* deletion in these animal models occurred in multiple subtypes of glutamatergic neurons, making it unfeasible to investigate cell type-specific effects. In our *Pten* cKO model, permanent deletion of *Pten* leads to disrupted PI3K/AKT signalling and constitutive activation of the mTORC1 complex. This was evidenced by the upregulation of pS6 in layer 6b at 4 months of age. Consistent with other models, I detected somatic overgrowth and thickened neuronal processes in the *Pten*-deleted Drd1a-Cre+ neurons. Interestingly, persistent mTOR activation did not lead to increased cell survival, thus leaving the total number of Drd1a-Cre+ neurons in the *Pten* cKO mice unaltered. However, it did result in the redistribution of Drd1a-Cre+ neurons in layer 6b, presumably as a result of the hypertrophic alterations in *Pten*-deficient neurons. *Pten* knockout models with increased cell proliferation exhibited severe brain overgrowth and migration defects that I did not observe in our cKO model (Wen et al. 2013; Huang et al. 2016; Skelton et al. 2020; Kwon et al. 2006). Our *Pten* cKO mouse model did not recapitulate the hallmark features of ASD, including macrocephaly, sociobehavioural impairments, or anxiety. However, Barnes maze tests showed that *Pten* cKO mice exhibited superior spatial learning and memory skills (results from Professor Britta Eickholt's research group and Dr Timothy Zolnik). These suggest that *Pten* deletion from distinct populations of cells causes a range of phenotypes, occasionally with no overt or severe pathologies. The phenotypes also seem to be significantly influenced by the time and severity of *Pten*

deletion. For a summary of the molecular, physiological, and behavioural phenotypes observed in our *Pten* cKO model, please refer to Figure 5.29.

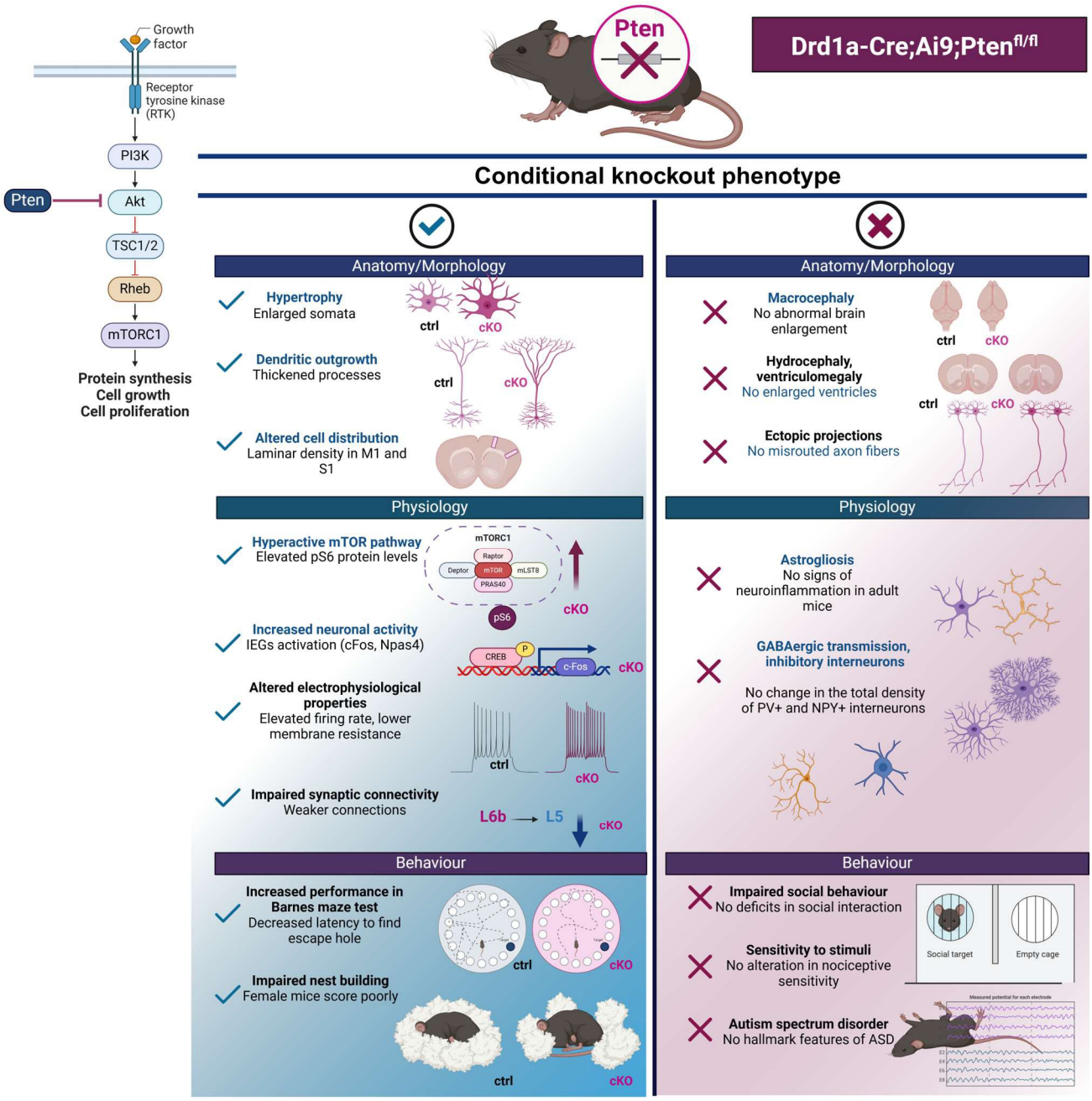


Figure 5.29. Summary of the anatomical, physiological, and behavioural phenotypes detected in our *Pten* cKO model. Conditional deletion of *Pten* from subsets of Drd1a-Cre+ neurons was achieved using the Drd1a promoter. Left blue column lists the phenotypes observed in the *Pten* cKO mice. Right magenta column lists the phenotypes absent in the *Pten* cKO mice. Phenotypes highlighted in blue colour (anatomy/morphology) are my qualitative and quantitative observations. Phenotypes

in black colour (physiology/behavioural studies) are results obtained by Professor Britta Eickholt's lab and Dr. Timothy Zolnik at Charité University, Berlin.

5.11.2. The long-term effects of *Pten* deletion from Drd1a-Cre+ neurons on parvalbumin interneurons

Considering that pyramidal neurons have been shown to modulate the number of PV+ and SST+ interneurons via *Pten* during postnatal development (Wong et al. 2018), I expected to detect a lasting effect on PV+ numbers in the *Pten* cKO mice. Remarkably, postnatal ablation of *Pten* from Drd1a-Cre+ neurons had no impact on the total density of cortical PV+ neurons and PNNs in any of the cortical regions investigated (i.e., ACA, M1, distinct subdivisions of S1).

One possible explanation is that the Drd1a-Cre+ projection neurons do not modulate cortical PV+ interneuron numbers. While corticocortical pyramidal neurons in layer 6a have been shown to establish local microcircuits with PV+ interneurons (Frandolig et al. 2019; Yang et al. 2022), these pyramidal neurons are concentrated in the upper layer 6a. Although the distribution of Drd1a-Cre+ neurons is not genuinely specific to layer 6b (a significant portion of tdTomato+ neurons resides in layer 6a in our model), previous research has shown that Drd1a-Cre+ neurons in layer 6a resemble Drd1a-Cre+ neurons in layer 6b. For instance, these neurons have the same projection pattern and sensitivity to wake-promoting neuropeptides, including orexin, like layer 6b neurons (Zolnik et al. 2020; Zolnik et al. 2024). Therefore, it could be argued that our model functionally targets layer 6b neurons and not layer 6a, which may explain why *Pten* deletion did not impact PV+ neurons, which are preferentially innervated by layer 6a pyramidal neurons. Since the two sublaminae of layer 6 harbour anatomically and functionally distinct populations of projection neurons, further research needs to be conducted to disentangle the connection between layer 6b neurons and PV+ interneurons.

The lack of change in the density of PV+ interneurons in the adult cortex may imply that transient changes in PV+ interneuron numbers during or after postnatal development may have been

offset by compensatory mechanisms and circuit-level adaptations to preserve network stability and E/I balance. One of the major limitations of the present chapter is that the distribution of GABAergic interneurons during early developmental stages was not examined, as the brains received from Berlin were from adult mice. Prior research on *Emx1-Cre+; Pten$^{loxP/+}$* mice supports the idea that the transient increase in neuron numbers is balanced out in adulthood. Specifically, although heterozygous *Pten* knockout mice had more Cux1+ neurons in upper cortical layers at birth, the total number of Cux1+ neurons in adult cortices was similar between control and Pten$^{+/-}$ mice (Chen et al. 2015).

It is conceivable that the excess number of GABAergic and/or glutamatergic neurons is eliminated during programmed cell death, or the extra number of cells is redistributed across the cortical layers to maintain E/I balance. In line with this theory, I found that adult *Pten* cKO mice had a significantly higher density of PV+ VVA+ neurons in layer 2/3 of M1, without a corresponding shift in the overall density of PV+ VVA+ neurons. I also found a significant increase in the density of PNNs in layer 2/3 of M1 in the *Pten*-deleted mice, indicating that PNNs may follow the reorganisation of PV+ neurons. Chen et al. (2015) reported a marked decrease in the density of upper and deep cortical layers in adult Pten$^{+/-}$ mice without a change in the total neuronal density. This further supports the laminar reorganisation of PV+ neurons in the adult cortex; however, the preservation of PV+ numbers and PV+ viability may be facilitated by intact excitatory drive from pyramidal cells that were not affected by *Pten* deletion. Considering that the Drd1a-Cre+ line utilised throughout Chapters 4 and 5 only labels a proportion of cortical projection neurons in layers 6a and 6b (tdTomato+ cells account for 24% of NeuN+ cells in the adult somatosensory cortex) (Hoerder-Suabedissen et al. 2018), the genetic deletion of *Pten* only affects a restricted subset of glutamatergic neurons, suggesting that compensatory effects from other glutamatergic pyramidal neurons could arise to maintain PV+ cell numbers and preserve circuit stability. Intact pyramidal cells may probably strengthen their existing connections to PV+ interneurons to compensate for the altered glutamatergic inputs deriving from *Pten* deletion (Barrows et al. 2017). Alterations in synaptic strength and connectivity can therefore

occur to fine-tune the balance between excitation and inhibition, which is crucial for maintaining PV interneurons. Synaptic plasticity and activity-dependent network adaptations are highly likely to contribute to preserving circuit homeostasis. This supports that the dynamic interplay between glutamatergic and GABAergic neurons is plastic and persists well beyond early postnatal development.

Pten-dependent pathways continue functioning after the first week of birth to regulate cell numbers and prevent over-inhibition by GABA in the network. For instance, PTEN has been demonstrated to play a pivotal role in the elimination of surplus PV interneurons, with its absence leading to a persistent excess of PV+ interneurons in the cortex (Magno et al. 2021). While PV numbers following *Cux2*-deletion return to normal by P30, they stay elevated in PTEN-only and compound (simultaneous deletion of CUX2 and PTEN) mutants, demonstrating that PV+ interneuron numbers do not normalise following the loss of *Pten* (Magno et al. 2021).

The absence of effect on PV+ cell density suggests that irreversible changes in PV+ neuron numbers and functions would only be detected if *Pten* were ablated during embryonic development. However, an earlier modification of deep-layer projection neurons would not be possible due to the comparatively late commencement of Cre recombinase expression in our strain. Further research using different Cre driver lines and reversible manipulation techniques will therefore be needed to determine both the short and long-term effects of *Pten* ablation on GABAergic interneurons. Nevertheless, it can be concluded that the conditional ablation of *Pten* from postmitotic neurons rather than progenitors does not seem to change the number of PV+ interneurons, indicating that the control over cell number and the role of PTEN in determining cell survival function at progenitor stages, while preserving postmitotic neurons. My findings on PV+ interneurons as well as PNNs after the permanent loss of *Pten* from Drd1a-Cre+ neurons are summarised in Figure 5.30.

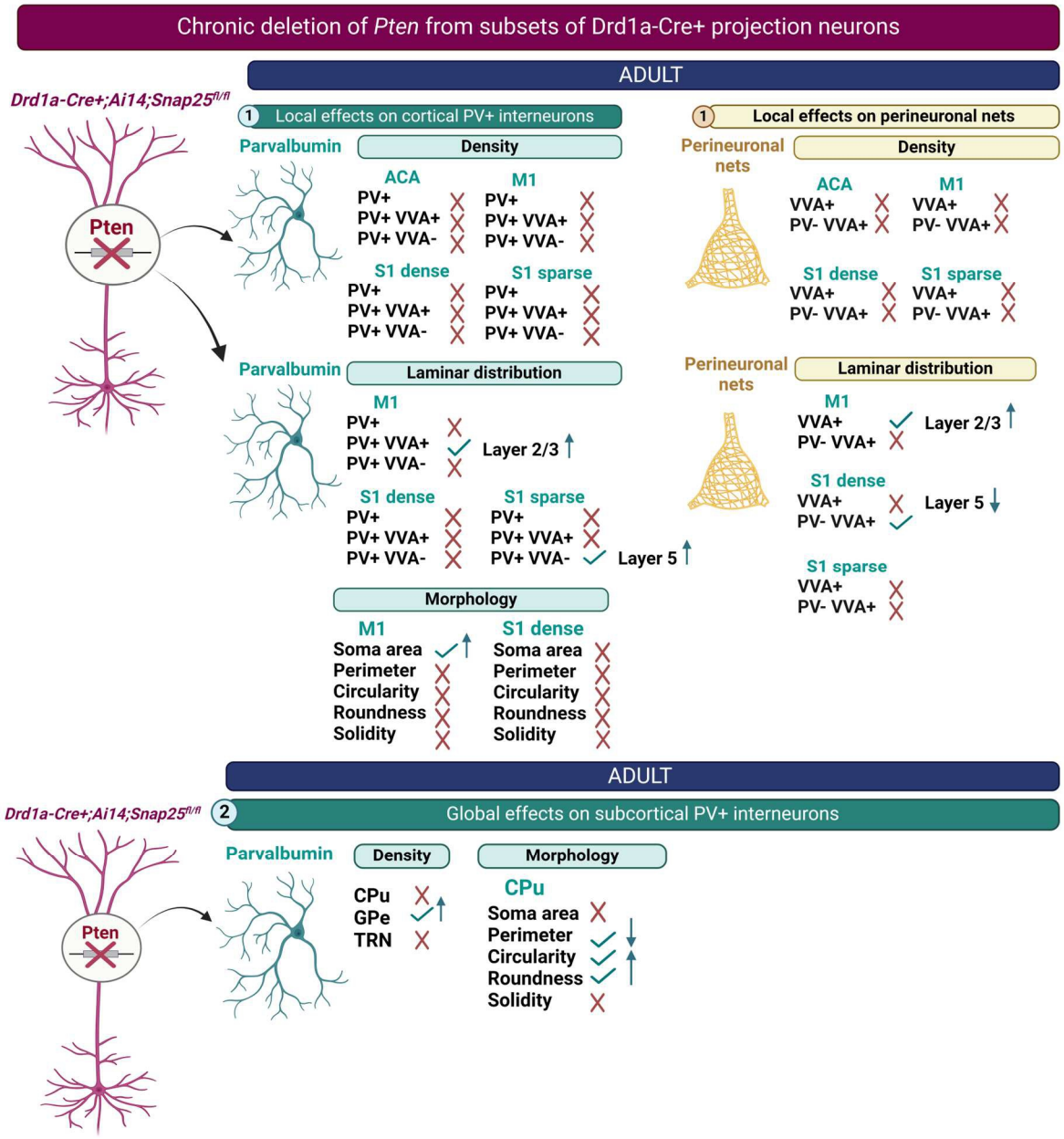


Figure 5.30. Schematic summarising the results of *Pten* deletion from Drd1a-Cre+ neurons on cortical and subcortical parvalbumin neurons in the adult brain. S1 dense refers to S1LL, while S1 sparse refers to S1UL/S1BB.

5.11.3. The long-term effects of *Pten* deletion from Drd1a-Cre+ neurons on somatostatin and neuropeptide-Y interneurons

The conditional deletion of *Pten* from Drd1a-Cre+ neurons raised another important question for the thesis: did this have a different effect on the neuropeptide-expressing subgroup of interneurons (SST+, NPY+) than on the subgroups that expressed Ca^{2+}-binding proteins (PV+)? The total cell density of SST+ interneurons in ACA, M1, and S1 was unaffected by *Pten* deletion, which is consistent with the findings on cortical PV+ neurons. It may be inferred that MGE-derived interneurons respond similarly to the removal of *Pten* from Drd1a-Cre+ neurons. However, cell type-specific differences emerged when I investigated the laminar distribution and the morphology of SST+ neurons. While the loss of *Pten* increased the density of PV+ neurons bearing PNNs in layer 2/3 of M1, it decreased the density of SST+ interneurons in layer 5 and layer 6b of M1. The results, therefore, suggest that *Pten* differentially regulates PV+ and SST+ neurons, and the effects observed on their laminar positioning may be related to their different vulnerability to *Pten* deletion stemming from their distinct maturational profiles and developmental lineage. Since *Pten* deletion in MGE-derived progenitors causes apoptosis in SST neurons but spares PV+ cells during late gestation and early neonatal stages (Vogt et al. 2015), PV+ cells may be inherently less susceptible to *Pten* dysfunction, suggesting that a selective vulnerability in GABAergic interneuron progenitors may exist, making them more or less resistant to *Pten* loss. SST+ interneuron numbers seem to decline rather than rise following *Pten* ablation, indicating that their early maturation makes them more dependent on PTEN for survival. Therefore, loss of *Pten* and perturbations in PI3K-Akt-mTOR signalling appear to have cell-autonomous effects on cortical GABAergic interneurons.

The tendency for SST+ neurons to decline following the loss of *Pten* was also demonstrated by previous research deleting *Cux2* and/or *Pten* from MGE-derived interneuron progenitors (Magno et al. 2021). Mice deficient in *Pten* exhibited a decrease in the density of SST+ neurons, while the density of PV+ interneurons increased at P17.5 and P30 (Magno et al. 2021). Our *Pten* cKO model similarly

demonstrated this bidirectional modulation of PV+ and SST+ interneurons, as the laminar density of PV+ and SST+ neurons shifted in the opposite manner.

Further evidence for the differential regulation of GABAergic interneurons by *Pten* is supported by the NPY+ data. Contrary to PV+ and SST+ interneurons, the permanent loss of *Pten* from Drd1a-Cre+ neurons had no long-term impact on NPY+ interneurons. Since distinct subgroups of NPY+ interneurons are derived from the CGE and the POA, it is tempting to conclude that *Pten* preferentially affects the MGE-derived subtypes of interneurons. An alternative explanation is that Drd1a-Cre+ neurons in layer 6b are dispensable for the development and maturation of NPY+ neurons. If that scenario is true, then *Pten* deletion is expected to have no temporary and permanent effects on the number, density, and laminar distribution of NPY+ interneurons. The morphological changes in the soma area of NPY+ neurons in the motor and somatosensory cortices are more likely due to the constitutive activation of the PI3K pathway and mTOR signalling rather than a direct impact of layer 6b neurons on NPY+ interneurons. Figure 5.31. shows the overview of results on SST+ and NPY+ neurons in the *Pten* cKO mice.

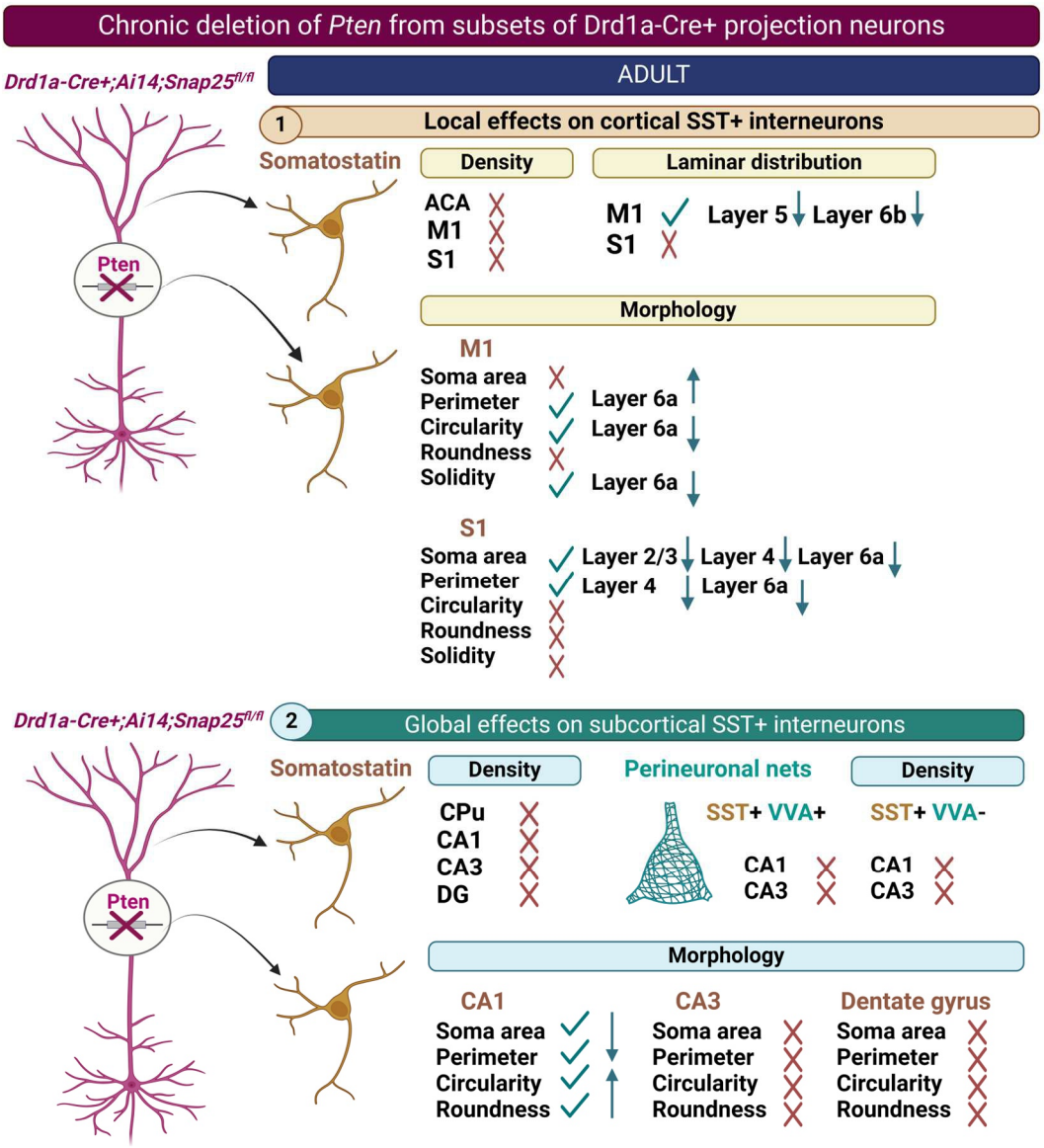


Figure 5.31 Overview of the results on somatostatin interneurons.

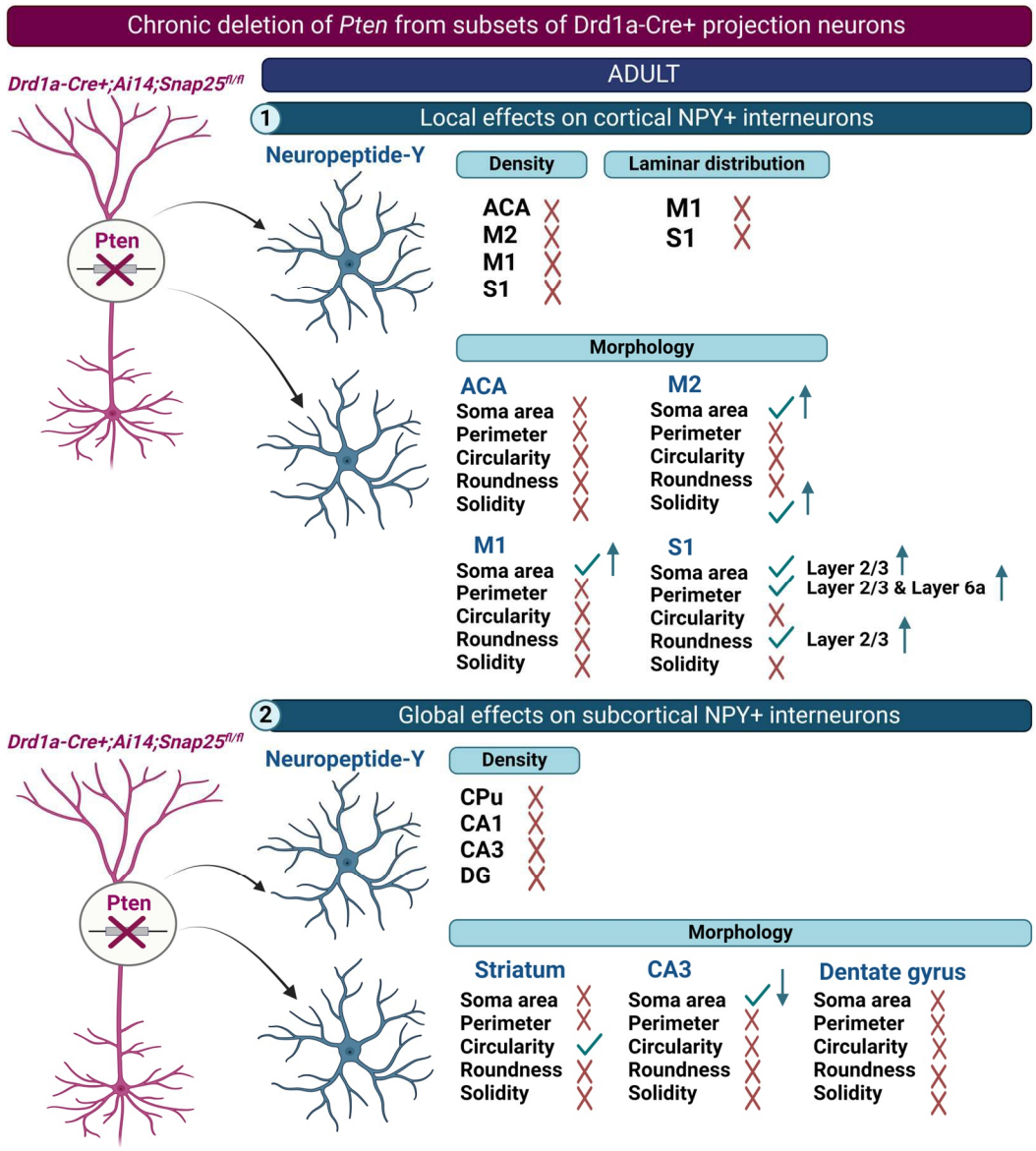


Figure 5.32. Overview of the results on neuropeptide-Y interneurons.

5.12. Conclusion

In closing, the conditional deletion of *Pten* from Drd1a-Cre+ neurons appears to have a region and cell-type-specific impact on GABAergic interneurons in the adult cortex. *Pten* appears to differently regulate MGE-derived interneurons, such as PV+ and SST+ interneurons, while having no effect on the laminar density of CGE-derived interneurons. Permanent loss of *Pten* from Drd1a-Cre+ neurons does not affect the total cell density of GABAergic interneurons but redistributes PV+ and SST+ neurons in distinct cortical layers. Additional research involving the removal of *Pten* from distinct subtypes of layer 6a and layer 6b neurons will aid our understanding of how deep-layer glutamatergic pyramidal neurons regulate the survival and number of interneurons.

Chapter 6 ..... General Discussion

6.1. Chronic manipulation of different subsets of glutamatergic deep-layer cortical projection neurons

6.1.1. Overview

Fundamental to my DPhil dissertation is understanding the mechanisms controlling the interplay between excitatory pyramidal neurons and inhibitory interneurons. I irreversibly manipulated deep-layer projection neurons to explore how they regulate the number and distribution of interneurons *during* and *after* development. Using different Cre driver lines specific to subsets of layer 5 or layer 6 pyramidal neurons, I achieved the selective ablation of *Snap25* from Rbp4-Cre+ and Drd1a-Cre+ projection neurons, respectively. By generating a novel cKO strain in collaboration with Professor Britta Eickholt and Dr Timothy Zolnik at Charité University, Berlin, we selectively deleted *Pten* from Drd1a-Cre+ pyramidal neurons. These animal models enabled me to investigate the short- and long-term effects of 1) the genetic silencing of Rbp4-Cre+ or Drd1a-Cre+ neurons on GABAergic interneurons (Chapters 3 & 4), and 2) the permanent loss of *Pten* from a restricted subset of layer 6 pyramidal neurons on GABAergic interneurons (Chapter 5). My PhD thesis aims to contribute to the growing area of research exploring the role of excitatory inputs and glutamatergic pyramidal neurons in the survival and development of GABAergic interneurons.

6.1.2. What is the significance of this DPhil research? Why study how projection neurons affect GABAergic neuron development?

The balance between inhibitory GABAergic neurons and excitatory glutamatergic pyramidal neurons is crucial for the proper function of cortical networks. Changes in pyramidal neuron activity can alter the number of GABAergic cells, potentially leading to abnormal cortical networks and long-term impairments (Lodato et al., 2011; Sreenivasan et al., 2022; Wong et al., 2018, 2022; Wu et al.,

2024). However, the mechanisms behind these changes, including how various subtypes of pyramidal neurons influence interneuron numbers in different cortical areas, remain unclear. Understanding these processes is vital, as insufficient inhibitory control can lead to disorders like epilepsy, autism, or schizophrenia. A new approach using cKO lines, such as selectively ablating *Pten* from Drd1a-Cre+ neurons, enabled me to investigate whether dysregulation of the PI3K/AKT pathway in subsets of layer 6 neurons leads to histological and morphological alterations.

6.1.3. The importance of the cell-type-specific targeting of pyramidal neurons

Little research has been done to examine how alterations in interneurons are accompanied by additional changes in their respective synaptic inputs, i.e., pyramidal neurons. Therefore, my DPhil thesis addressed how distinct cortical pyramidal neuron subtypes, which are just as varied as GABAergic interneurons, contribute to the formation of inhibitory circuits. For instance, there are notable distinctions between the way PV+ interneurons innervate supragranular and infragranular pyramidal neurons. In contrast to superficial pyramidal neurons in layer 2/3 that have both local and translaminar PV+ innervation, deep-layer pyramidal cells in the somatosensory cortex exclusively receive local PV+ innervation (Yetman et al., 2019). I sought to identify layer-specific trends in the structure of cortical networks by focusing on the interplay between deep-layer projection neurons and interneurons. Thus, my experimental methods of selectively manipulating infragranular projection neurons and identifying sublamina-specific patterns are essential elements of my DPhil research.

6.1.4. What were the *expected* outcomes?

Based on chemogenetic and post-mortem studies, I predicted significant reductions in the density of GABAergic interneurons, especially in the Ca^{2+}-binding protein-expressing subtypes. Chronic loss of AP-dependent neurotransmitter release could lead to two outcomes: 1) alterations in the ratio of excitatory to inhibitory neurons in the cerebral cortex, which would disrupt interneuron

numbers and distribution, or 2) a *transient, short-term* change in GABAergic interneurons with potential compensatory mechanisms arising from intact pyramidal neurons in the same or adjacent cortical layers or altered synaptic connectivity. I anticipated differential effects on soma-targeting PV+ interneurons and dendrite-contacting SST+ interneurons, as the location of inhibitory synapses on excitatory neurons influences the type and degree of inhibition they provide and hence endows them with highly specialised roles within the cortical microcircuits (McBain & Fisahn, 2001).

Upon conditional deletion of *Pten* from Drd1a-Cre+ projection neurons, I expected hyperactivation of the PI3K/AKT/mTOR pathway in layer 6b neurons, resulting in neuronal hypertrophy. I believed these effects would persist into adulthood without rapamycin treatment. The severity of the phenotype has been shown to be related to the timing and type of *Pten* deletion, leading me to postulate that loss from a subset of layer 6 projection neurons would result in a less severe phenotype than deletions in cortical and hippocampal neurons (see Table 5.1.).

6.1.5. What were the *actual* outcomes?

6.1.5.1. Chronic deletion of *Snap25* from subsets of Rbp4-Cre+ pyramidal neurons

First, I performed the genetic manipulation of subsets of layer 5 pyramidal neurons that comprise both intratelencephalic and pyramidal tract-type projection neurons. I assessed the *short-* and *long-term* effects of the loss of AP-dependent neurotransmitter release on GABAergic interneurons in the vicinity of the cell bodies and the long-range projections of layer 5 neurons. I have shown that the genetic silencing of Rbp4-Cre+ neurons allows for the normal development of cortical and subcortical PV+ neurons. However, silencing subsets of layer 5 pyramidal neurons has a lasting impact on the laminar arrangement of PV+ neurons and the perineuronal nets that are manifested at 3 months. These alterations are cell-type specific, given that the loss of AP-dependent neurotransmitter release from layer 5 affected distinct layers. The distribution of PV+ neurons was altered in layer 4 of S1 and layer 5 of M1, while NPY+ neurons showed specific alterations in layer 1

and layer 2/3 in the *Snap25* cKO mice. Contrary to PV+ neurons, the change in the laminar distribution of NPY+ neurons in M1 was followed by a decrease in their total cell density as well.

6.1.5.2. What can we learn from 'silencing' Rbp4-Cre+ pyramidal neurons?

1) Rbp4-Cre+ neurons in cortical layer 5 do not appear to regulate the development of parvalbumin interneurons

2) AP-dependent neurotransmitter release may not play a role in setting the final number of interneurons during development

3) Abolishing synaptic transmission from layer 5 may be compensated for by cortical plasticity, which could mask the true effects of silencing layer 5 neurons

4) The total number of parvalbumin neurons does not seem to be dependent on the activity of layer 5 projection neurons

5) Changes in the distribution of PV+ neurons and PNNs in the adult cortex imply long-term effects on the laminar positioning of interneurons

6) Loss of *Snap25* from subsets of layer 5 projection neurons differentially impacts PV+ and NPY+ neurons, indicating effects specific to individual inhibitory cell types

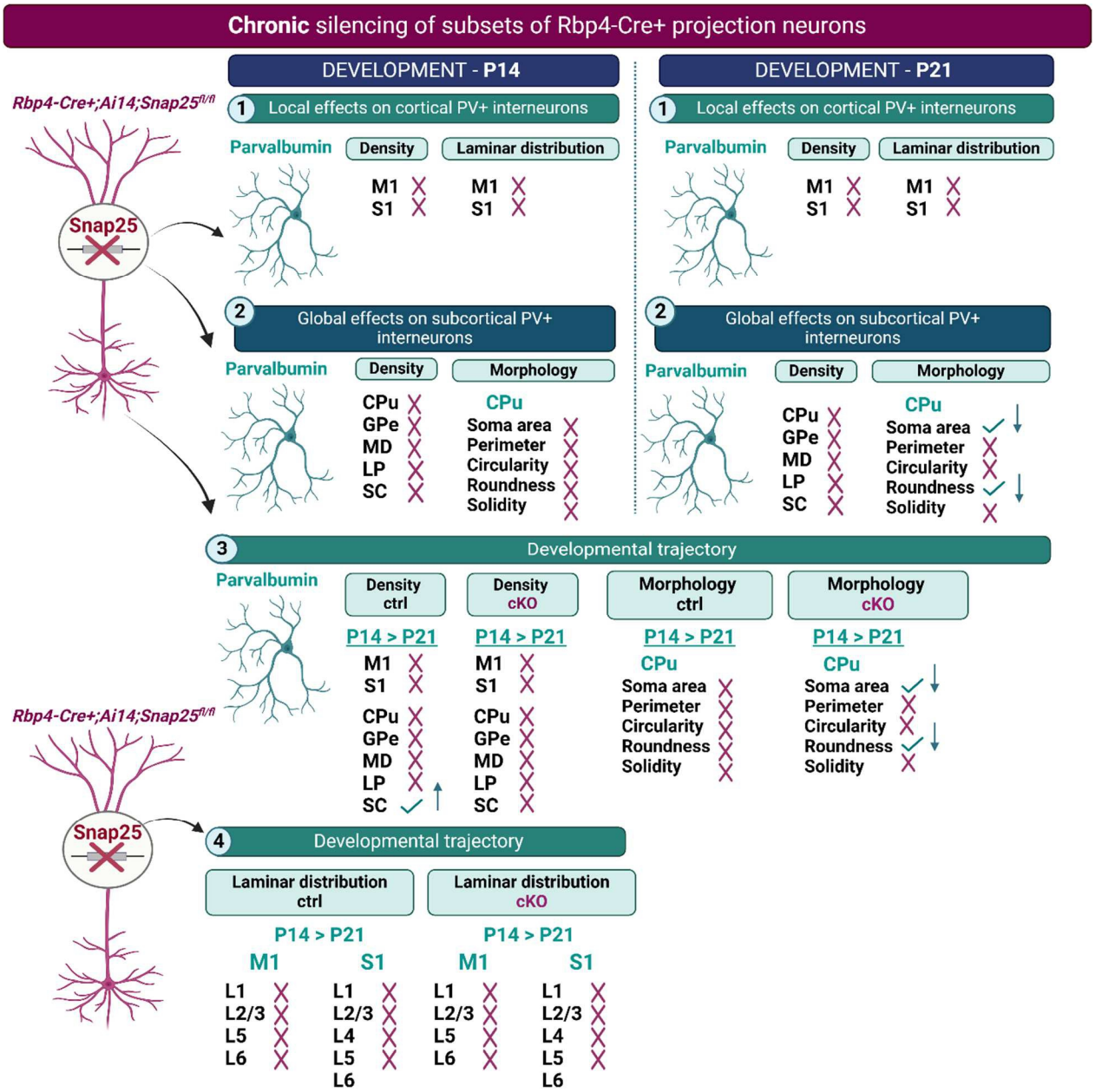


Figure 6.1. Overview of the developmental findings on the chronic silencing of Rbp4-Cre+ neurons on parvalbumin interneurons

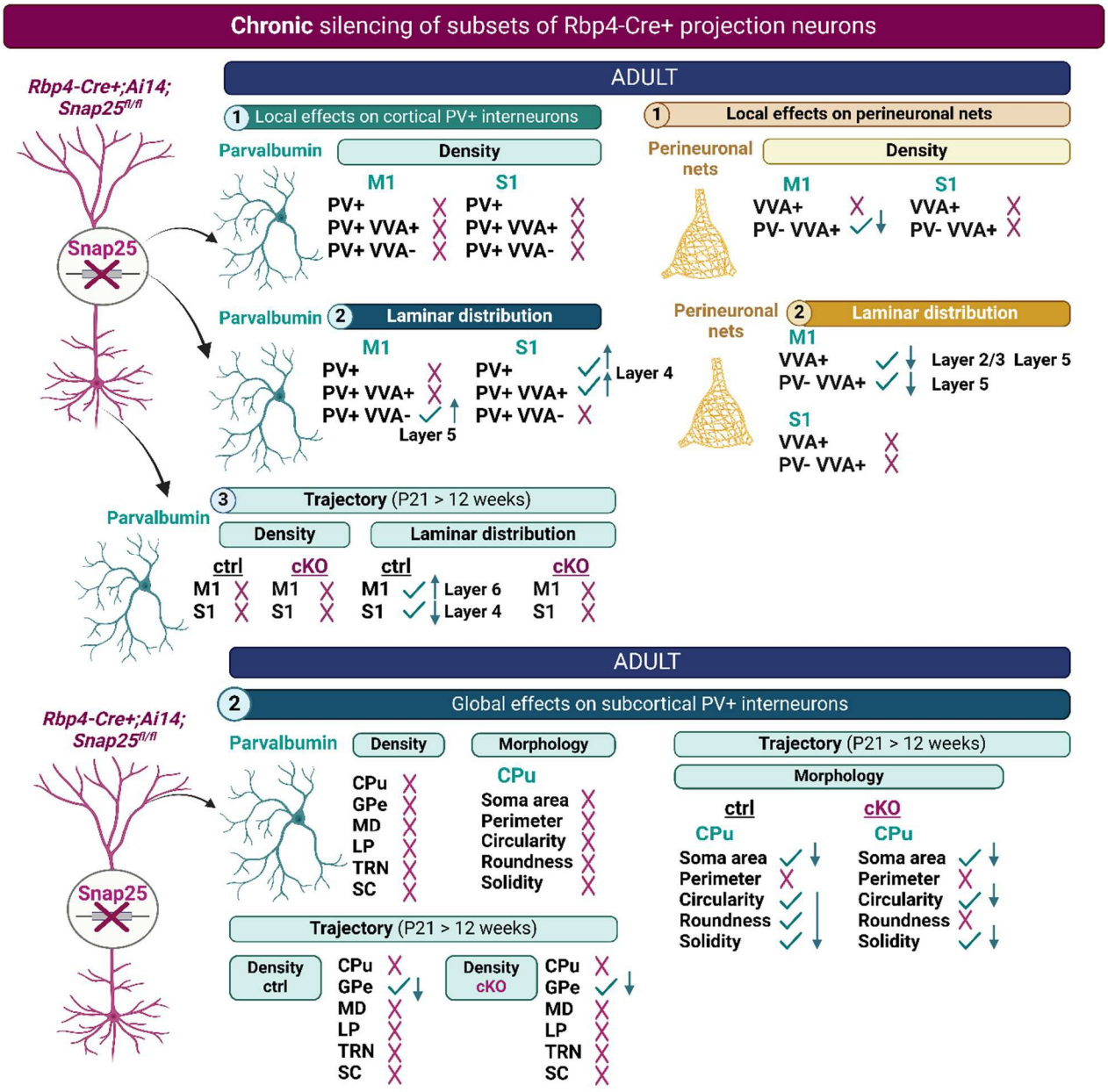


Figure 6.2. Overview of the adult findings on the chronic silencing of Rbp4-Cre+ neurons on parvalbumin interneurons

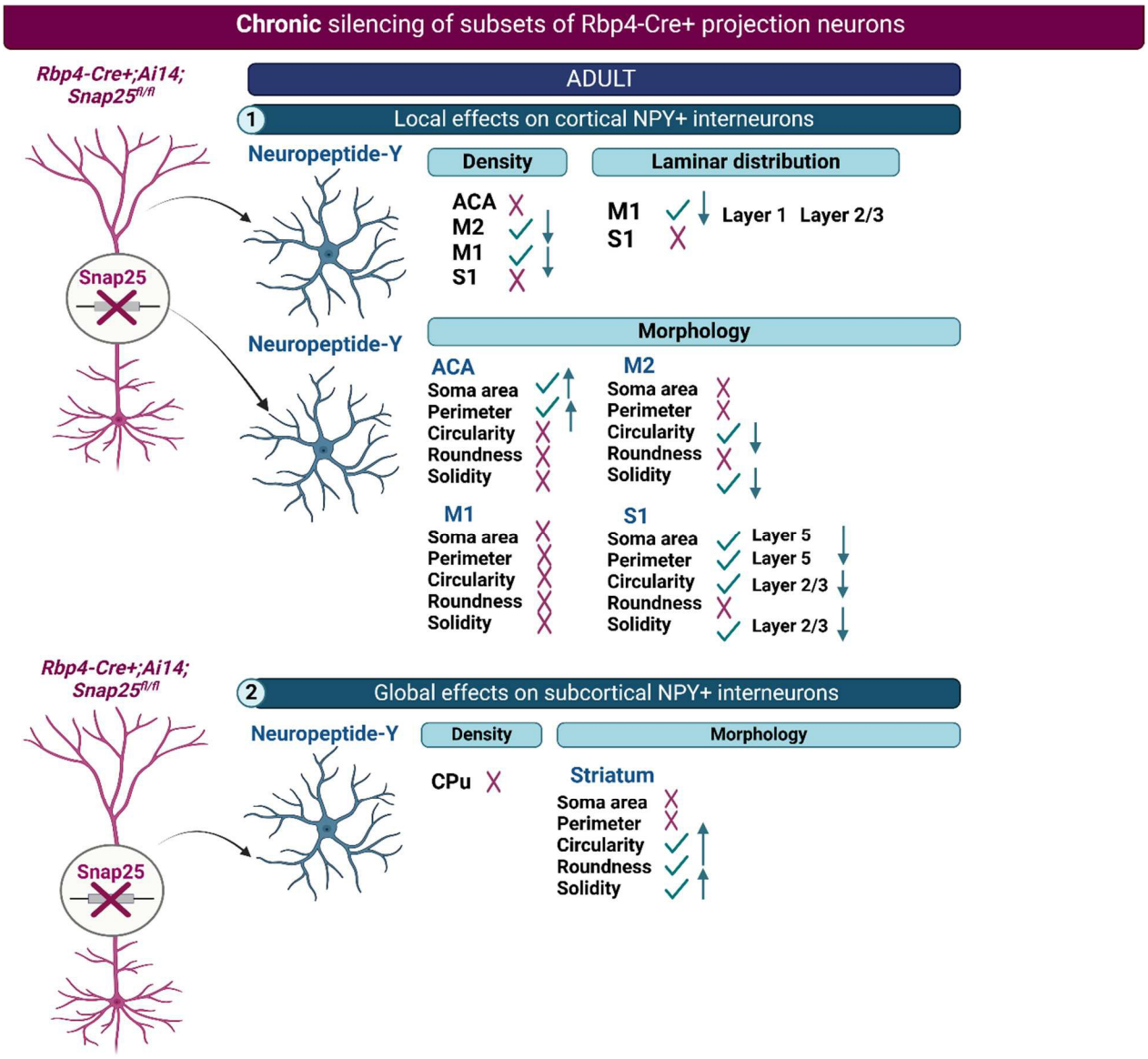


Figure 6.3. Overview of the adult findings on the chronic silencing of Rbp4-Cre+ neurons on neuropeptide-Y interneurons

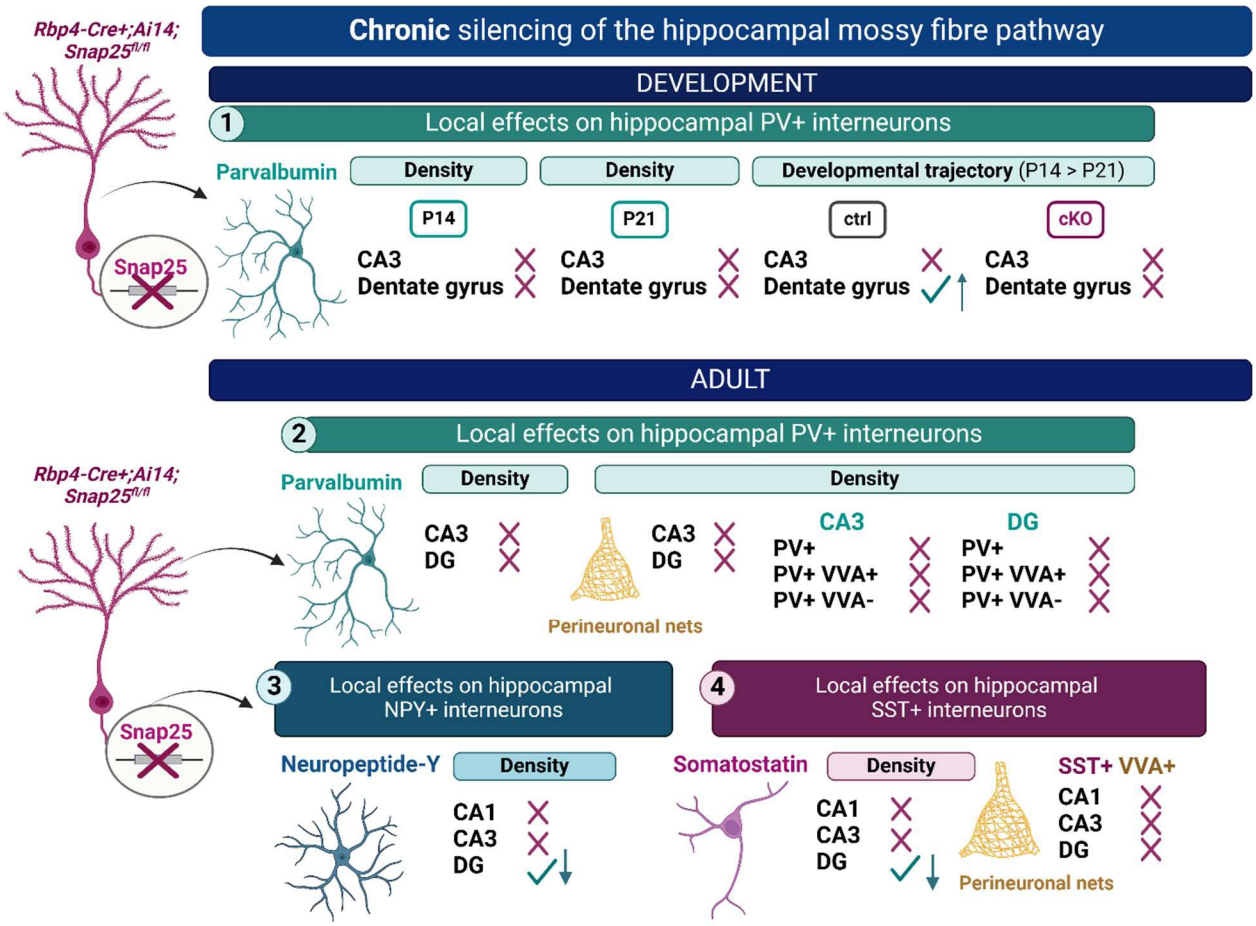


Figure 6.4. Overview of the developmental and adult findings on the chronic manipulation of the hippocampal mossy fibre pathway

6.1.5.3. Chronic deletion of *Snap25* from subsets of Drd1a-Cre+ pyramidal neurons

The above findings raised questions about whether the changes in the laminar distribution of PV+ and NPY+ neurons were genuinely specific to layer 5. Therefore, I manipulated a distinct subset of deep-layer projection neurons, i.e., *Drd1a*-Cre+ neurons in layers 6a and 6b. This allowed me to examine how changes in morphologically and functionally different subtypes of infragranular pyramidal neurons modified GABAergic neurons and so influenced the cytoarchitecture of the cerebral cortex. Abolishing AP-dependent neurotransmitter release from Drd1a-Cre+ neurons does not influence the total density of cortical and subcortical PV+ interneurons during development. Similar to layer 5, silencing layer 6 only affects the laminar distribution of PV+ interneurons long-term in layer 5 of M1. Contrary to layer 5, silencing subsets of layer 6 neurons changes the total density of PV+ VVA+ neurons in layer 5 of M1 as well as the density of PV- VVA+ cells in layer 4 of S1. I have found that the loss of synaptic transmission from Drd1a-Cre+ neurons affects the density of hippocampal NPY+, SST+, and CR+ interneurons in the CA1 region during development. However, I only detected changes in the density and the laminar distribution in cortical NPY+ interneurons at P21. Another important developmental finding is the significant reduction in the density of GABA-B R1 receptors in layer 5 of M1 and S1.

6.1.5.4. What can we learn from 'silencing' Drd1a-Cre+ pyramidal neurons?

1) Drd1a-Cre+ neurons in cortical layers 6a and 6b do not control the survival of parvalbumin interneurons during development
2) Silencing Drd1a-Cre+ neurons has region and layer-specific effects on the density and laminar distribution of PV+ neurons and the perineuronal nets
3) Loss of AP-dependent neurotransmitter release from subsets of layer 6a and layer 6b projection neurons seems to affect GABA-B receptor-mediated transmission in layer 5
4) Deletion of *Snap25* from Drd1a-Cre+ neurons has a short-term impact on the distribution of cortical NPY+ interneurons

5) Silencing Drd1a-Cre+ neurons appears to alter the trajectory of NPY+ interneurons from development to adulthood without changing their overall density
6) Loss of AP-dependent neurotransmitter release from Drd1a-Cre+ neurons affects SST+ interneurons in the adult dentate gyrus

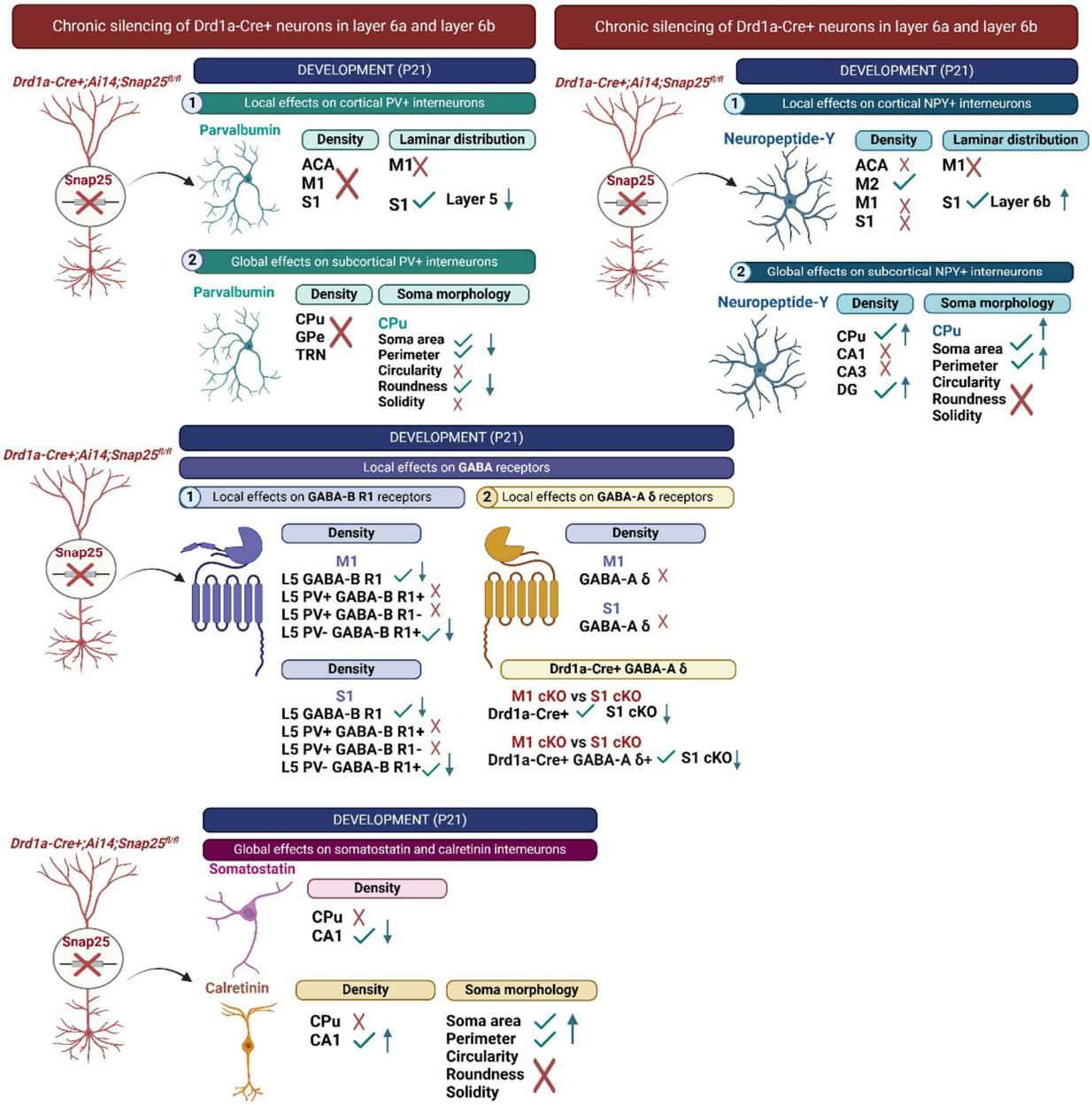


Figure 6.5. Summary of the developmental results on the chronic ablation of *Snap25* from Drd1a-Cre+ neurons at P21

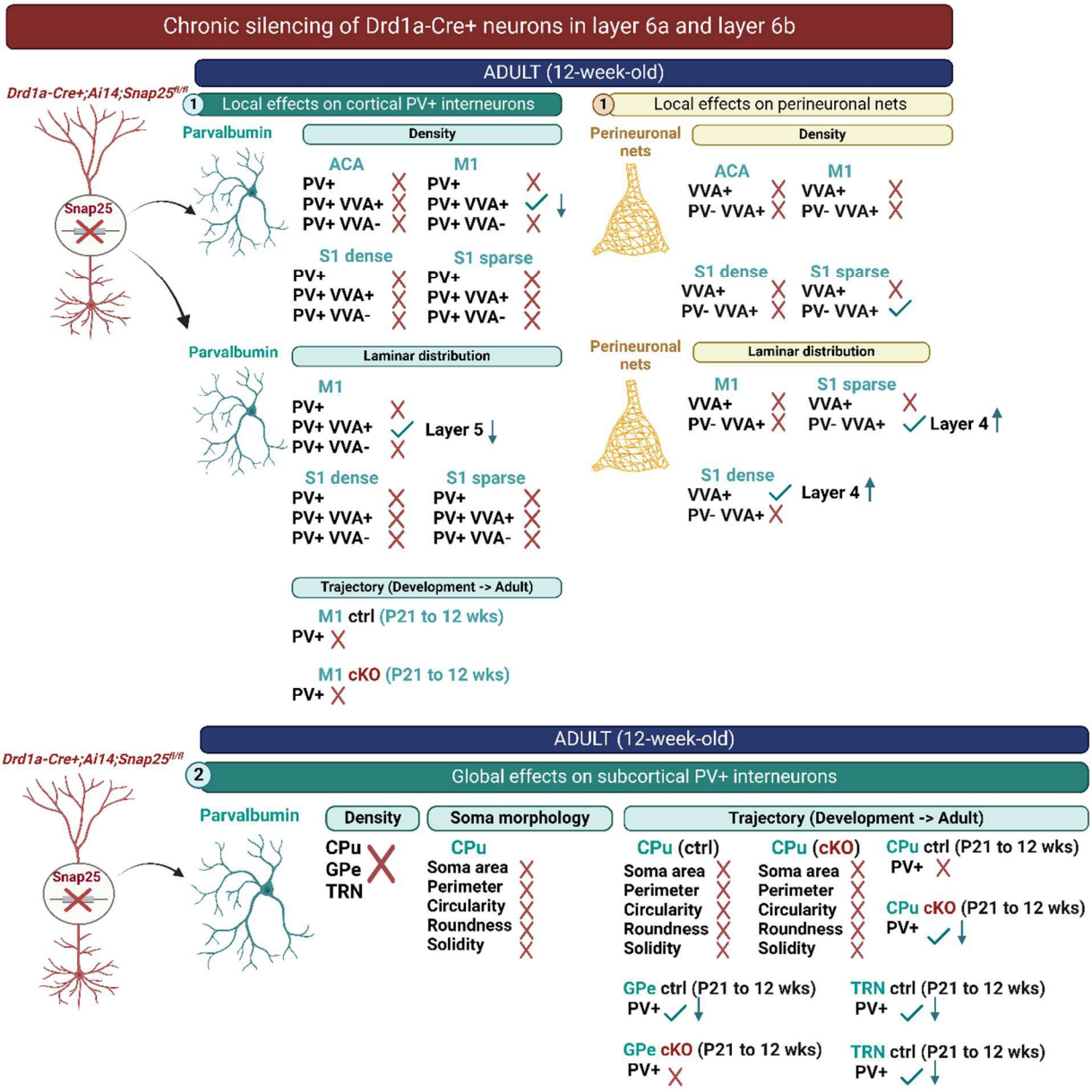


Figure 6.6. An overview of the adult findings on the effects of the chronic deletion of *Snap25* from Drd1a-Cre+ neurons on parvalbumin interneurons and the perineuronal nets

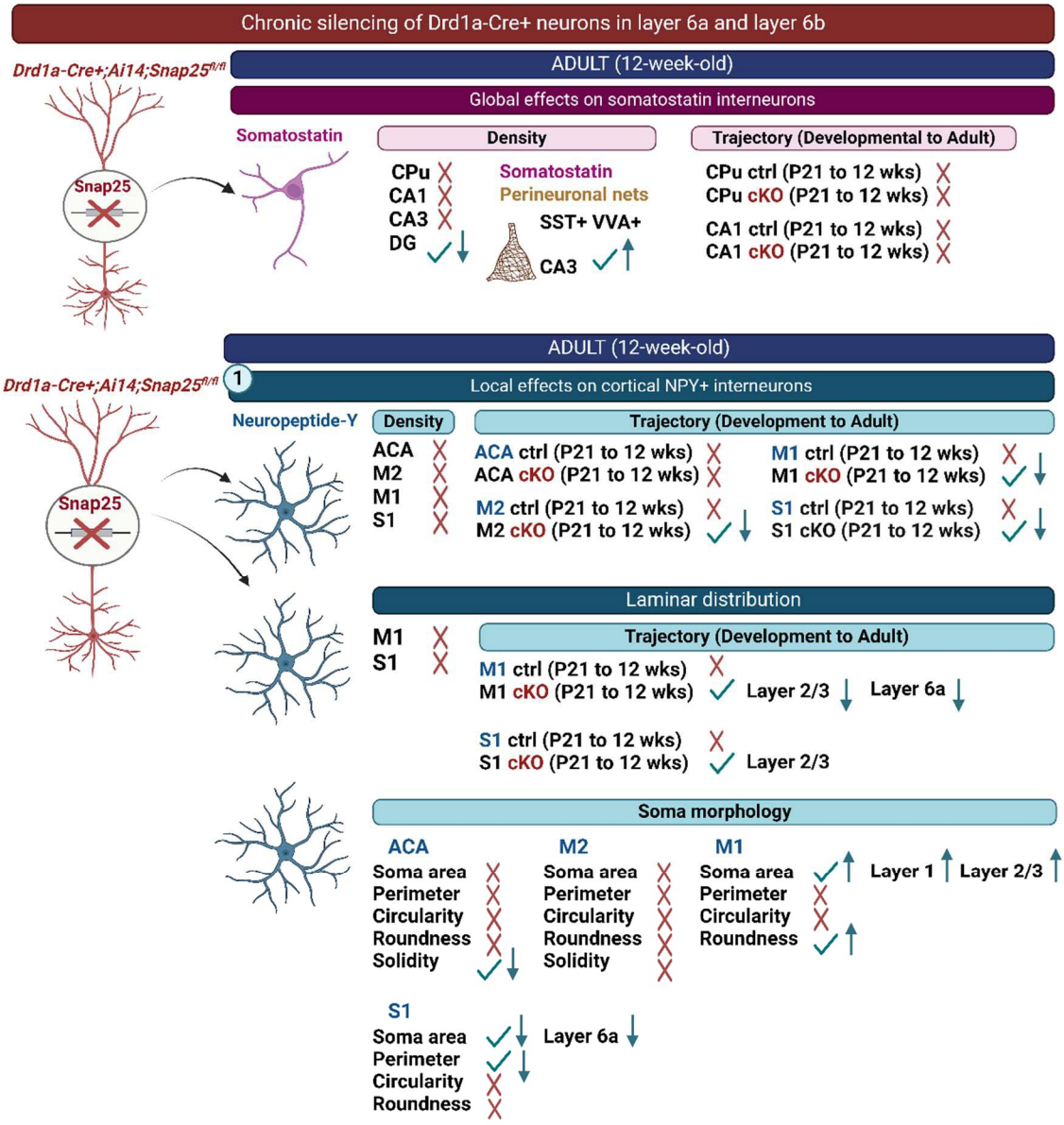


Figure 6.7. An overview of the adult findings on the effects of the chronic deletion of *Snap25* from Drd1a-Cre+ neurons on somatostatin and neuropeptide-Y interneurons

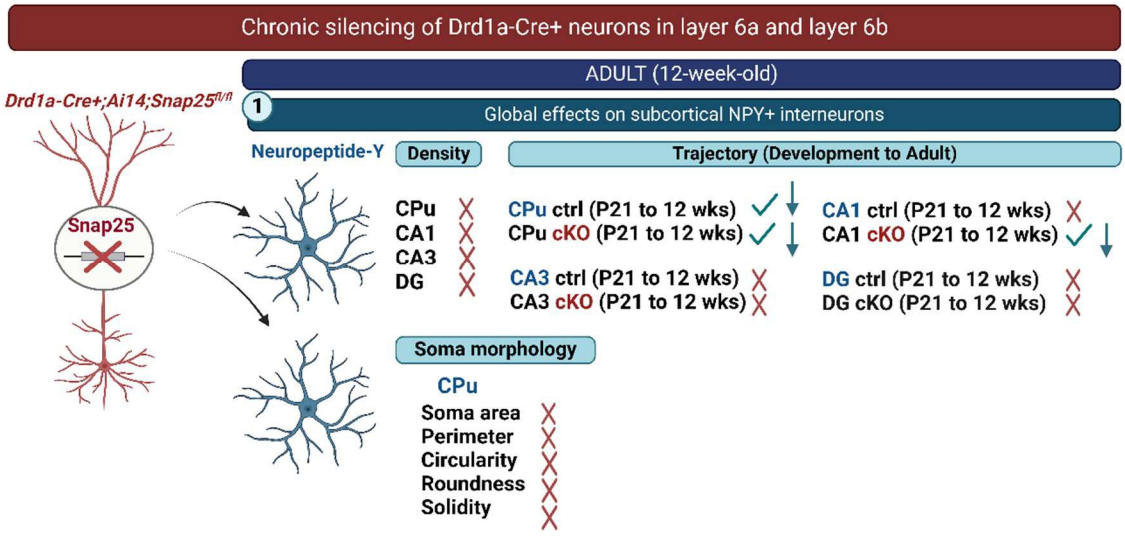


Figure 6.8. An overview of the adult findings on the effects of the chronic deletion of *Snap25* from Drd1a-Cre+ neurons on neuropeptide-Y interneurons in the striatum and the hippocampus

6.1.5.5. Chronic deletion of *Pten* from subsets of Drd1a-Cre+ pyramidal neurons

My DPhil research also examined how *Pten*-deficient layer 6 pyramidal neurons affected GABAergic interneurons. The *Pten;Ai9;Drd1a-Cre*$^{fl/fl}$ strain is a novel knockout model where the conditional deletion of *Pten* from layers 6a and 6b neurons leads to an overactive mTOR pathway. I have supported this by demonstrating the enhanced phosphorylation of S6 protein in layer 6b neurons. The persistent activation of the PI3K6/AKT/mTOR pathway results in neuronal hypertrophy and somatic overgrowth of Drd1a-Cre+ neurons; however, it does not cause the abnormal survival of Drd1a-Cre+ neurons. I have not observed signs of macrocephaly or defects in cortical lamination. Consistent with the findings of previous chapters, chronic loss of *Pten* has a long-term influence on the laminar allocation of GABAergic neurons. *Pten* deletion from Drd1a-Cre+ neuron alters PV+ VVA+ interneurons in layer 2/3 of M1 but affects SST+ interneurons in layer 5 and layer 6b of M1. It seems to affect PV+ interneurons differently in distinct subdomains of S1, where the density of Drd1a-Cre+ neurons differs. Loss of *Pten* does not seem to change the number of GABAergic interneurons in the

adult cortex; however, I have detected morphological changes in the soma area and shape of PV+, SST+, and NPY+ neurons months after *Pten* deletion.

6.1.5.6. What can we learn from 'overexciting' Drd1a-Cre+ pyramidal neurons?

1) Postnatal deletion of *Pten* from Drd1a-Cre+ neurons does not lead to enhanced survival of glutamatergic layer 6b neurons
2) Drd1a-Cre+ neurons do not seem to control interneuron numbers in cortical and subcortical regions
3) Laminar rearrangement of cortical interneurons is observed when *Pten* or *Snap25* are ablated from Drd1a-Cre+ neurons
4) Loss of *Pten* from Drd1a-Cre+ neurons affects MGE-derived interneurons
5) Morphological alterations are frequently observed in *Pten*-deficient mice
6) Subtle changes in interneurons are present in adulthood
7) The resulting phenotype depends on when *Pten* is deleted and from which cell type(s) *Pten* is ablated

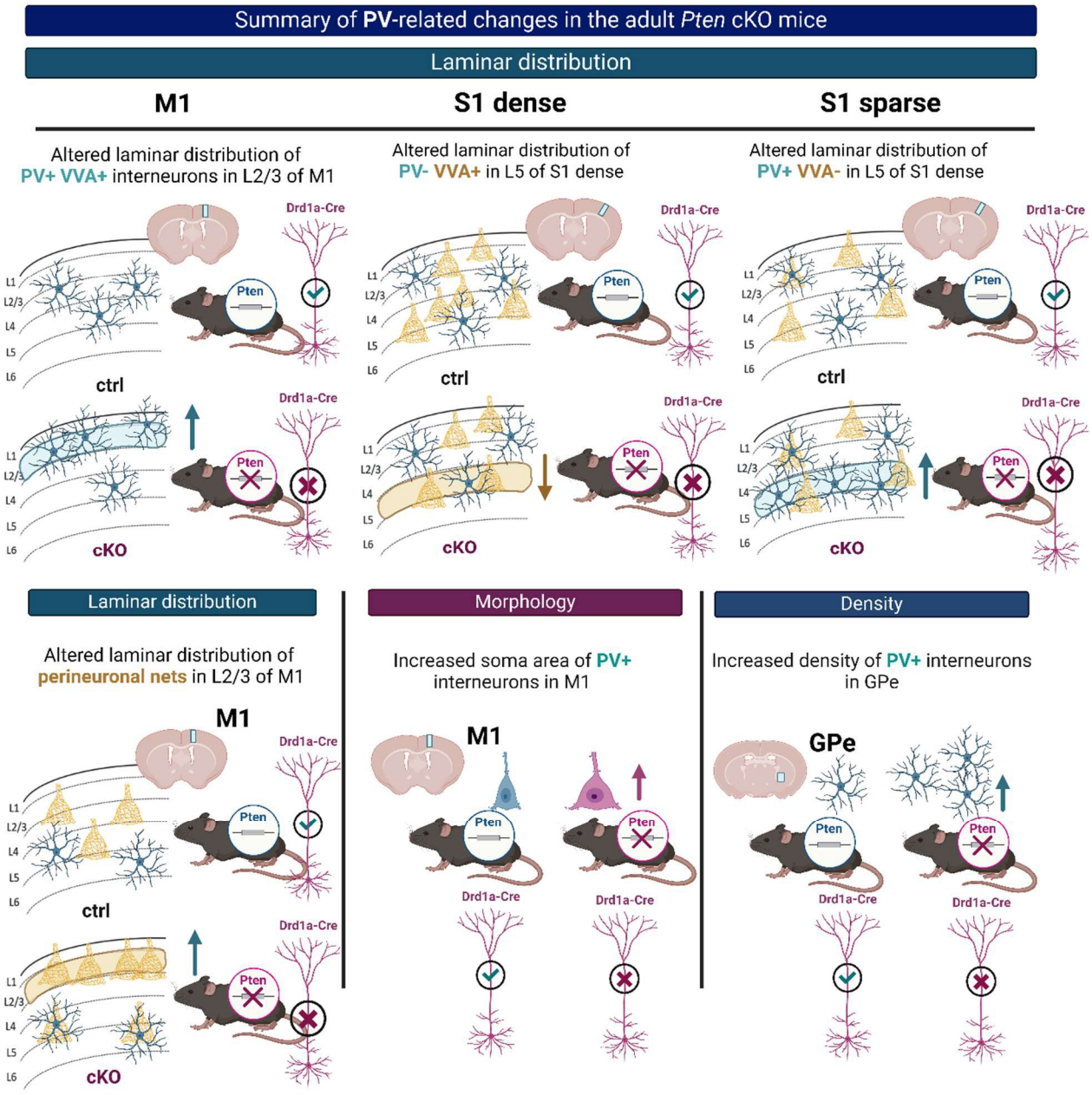


Figure 6.9. An overview of the results of the removal of *Pten* from Drd1a-Cre+ neurons on parvalbumin interneurons and perineuronal nets

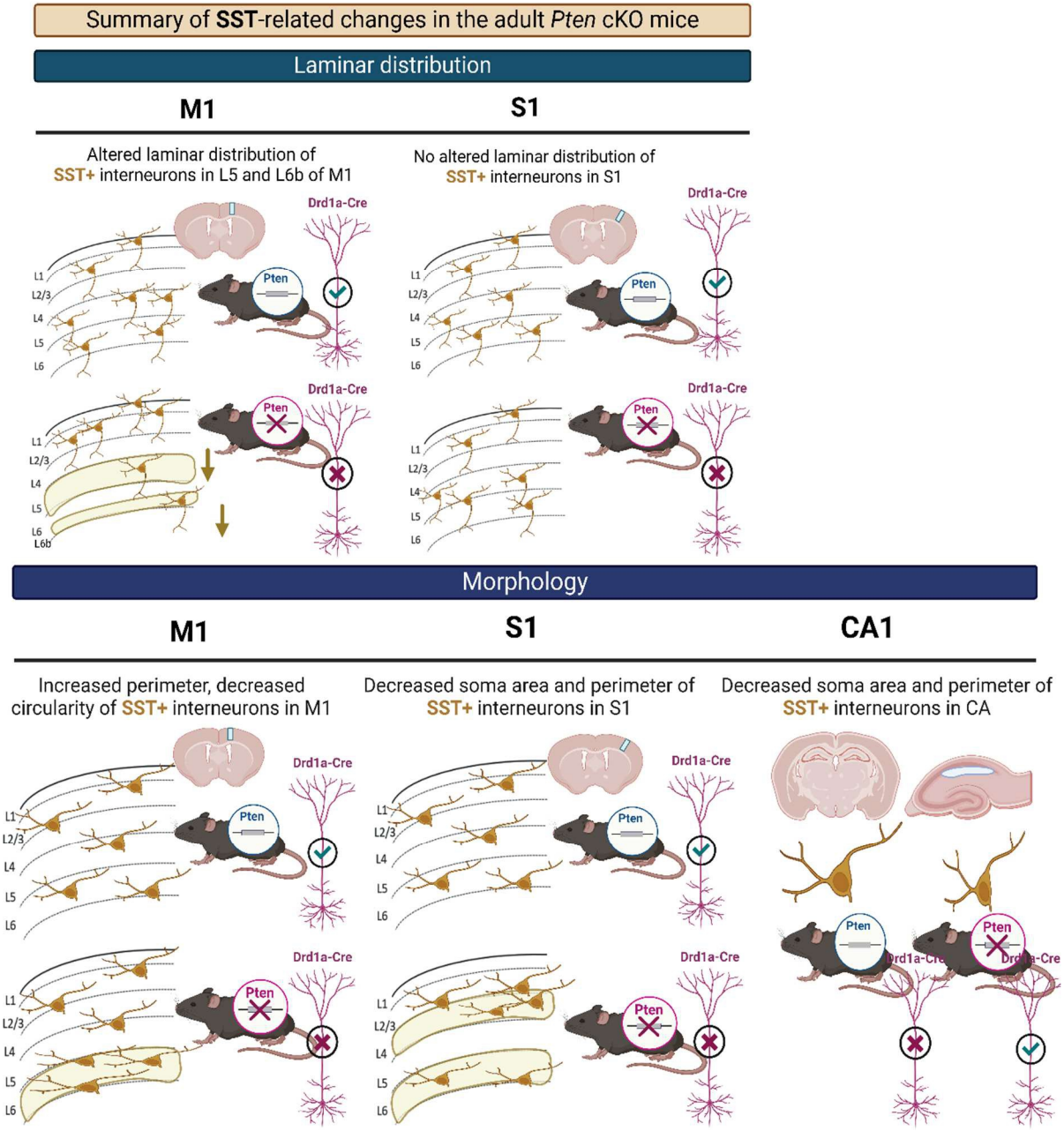


Figure 6.10. An overview of the results of the removal of *Pten* from Drd1a-Cre+ neurons on somatostatin interneurons

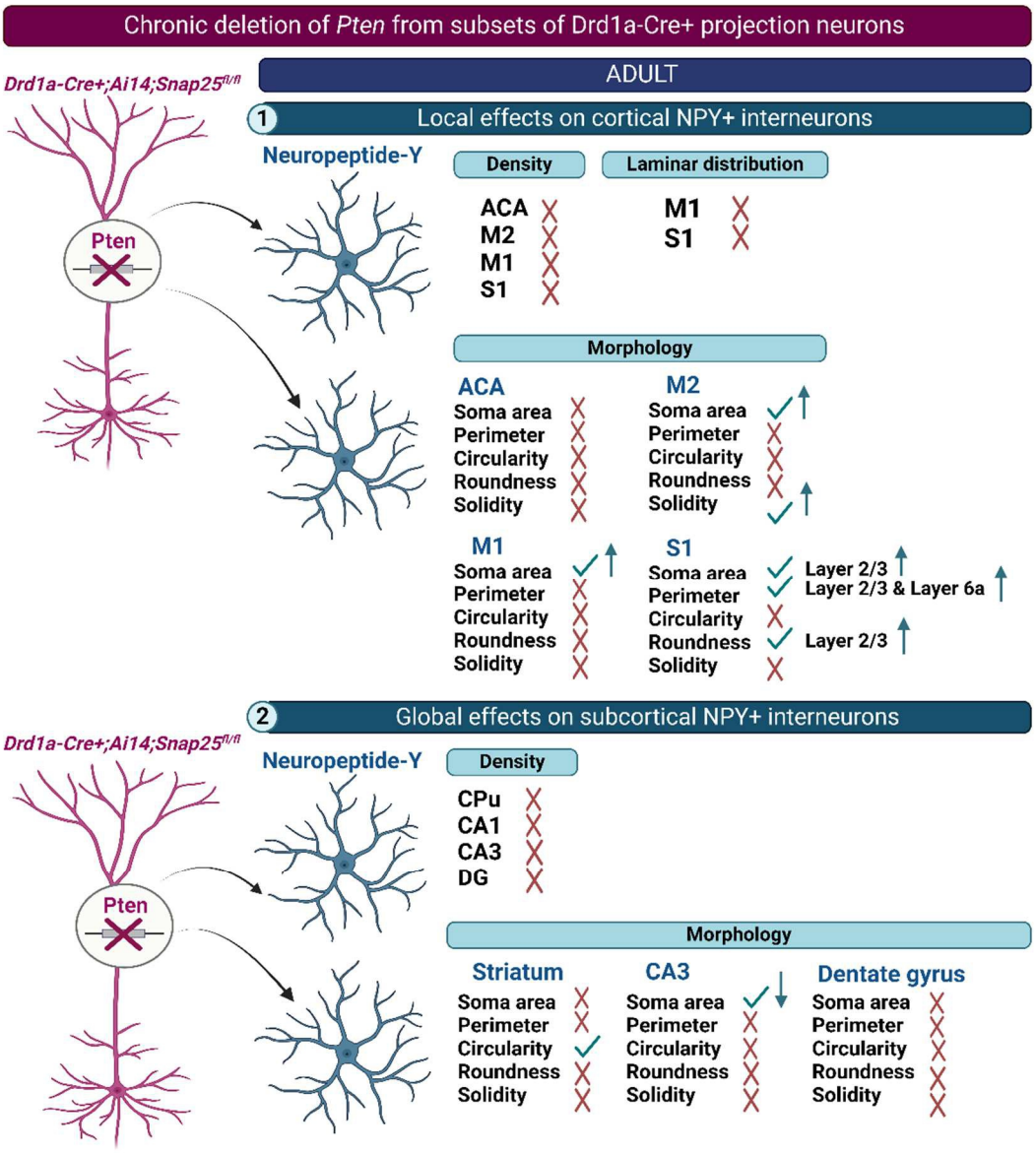


Figure 6.11. An overview of the results of the removal of *Pten* from Drd1a-Cre+ neurons on neuropeptide-Y interneurons

6.1.6. Investigating other SNARE proteins beyond Snap25

Loss of AP-dependent neurotransmitter release from subsets of layer 5 and layer 6b projection neurons did not alter interneuron cell density. My findings, therefore, imply that Snap25 and AP-dependent synaptic transmission are dispensable for interneuron survival. However, it remains unclear whether the number of GABAergic neurons is affected differently by the loss of other presynaptic SNARE proteins. For instance, Syntaxin 1A has been revealed to interact with neurotransmitter transporters, including the GABA transporter GAT1 (Deken et al., 2000; Geerlings et al., 2000). Syntaxin 1A negatively regulated the surface expression and subcellular localisation of GABA and glycine transporters (Deken et al., 2000; Geerlings et al., 2000). While it was beyond the scope of this thesis to investigate compensatory changes in the *Rbp4-Cre;Snap25* cKO mice, it is useful to note that other synaptic proteins might be altered when *Snap25* is ablated from infragranular projection neurons.

Loss-of-function studies on SNARE proteins have been hindered by the lack of appropriate knockout animal models and embryonic lethality. While it is known that both Syntaxin1 and Munc18-1 loss result in neuronal lethality *in vitro*, the rate and onset of cell loss were more advanced upon Syntaxin1 deletion, which caused Stx1A/1B double KO neurons to die earlier than Munc18-deficient neurons (Mishima et al., 2014; Verhage et al., 2000). The synaptobrevin-2/VAMP2 isoform is particularly abundant in the hippocampal formation, the dentate gyrus, the lateral geniculate and the posterior complex of the thalamus, and cortical layer 1 and layer 6 of the somatosensory areas (Raptis et al., 2005). Surprisingly, VAMP2 mutants showed a decreased sleep phenotype in addition to notable deficiencies in switching states of vigilance (Banks et al., 2020). Given that VAMP2 appears to be abundant in layer 6 and that the mutant mice exhibit a noticeable sleep phenotype, it would be intriguing to observe the effects of *VAMP2;Drd1a-Cre* cKO mice on hippocampal somatostatin interneurons. It is conceivable that different components of the SNARE system have distinct effects on GABAergic transmission and interneuron survival. A desirable future goal to better understand the

consequences of interrupting synaptic fusion proteins on interneuron development may be to generate novel conditional knockout models of other crucial components of the presynaptic machinery.

6.1.7. Does synaptic transmission play a role in interneuron development?

Ablating *Snap25* only affects regulated synaptic exocytosis. Thus, it is tempting to speculate that more severe perturbations in synaptic transmission would lead to a more severe phenotype. A plausible explanation for the absence of significant alterations in interneurons could be that *Snap25* deletion only impacts a subset of L5 and L6b pyramidal neurons. Considering that the rest of the non-Rbp4-Cre+ pyramidal neurons remain capable of regulated vesicle release, I speculate that these L5 pyramidal neurons may compensate for the cessation of activity of Rbp4-Cre+ L5 projection neurons. This might explain why interneurons survive the chronic abolition of synaptic transmission and remain unaffected in cortical and subcortical regions. Interestingly, the conditional ablation of *Munc18-1* from Rbp4-Cre+ L5 neurons subtly affected striatal PV+ neuron density (Sreenivasan et al., 2022). This is interesting considering that the genetic removal of *Munc18-1* results in the total cessation of neurotransmitter secretion (Verhage et al., 2000). It seems that the abolition of both *evoked* and *spontaneous* vesicle release from Rbp4-Cre+, counterintuitively, does not have a more severe impact on GABAergic interneurons. It will be interesting to examine whether the subtype of projection neurons or the timing of genetic modulation has a bigger impact on the development of inhibitory circuits.

6.1.8. Clinical implications of research

6.1.8.1. The link between SNAP25 and neuropsychiatric diseases

SNAP25 has been indicated to have a direct involvement in attention deficit and other common mental disorders by several linkage and genome-wide association studies (Faraone & Mick, 2010; Feng et al., 2005; Spencer et al., 2007). Different single-nucleotide polymorphisms (SNPs) affecting transcription factor binding sites in the SNAP25 gene locus (i.e., rs3746544, rs362549) have also been associated with ADHD traits (Thapar et al., 2005; Zhang et al., 2011). Other intronic SNAP25 polymorphisms, including rs363039, rs363050, have been shown to be further related to cognitive impairments in autistic children (Antonucci et al., 2016; Braida et al., 2015; Gosso et al., 2006). Besides genetic variations, decreased protein levels of SNAP25 and the subsequent disruption in monoamine transmissions may alter synaptic signalling and perturb network dynamics (Raber et al., 1997; Steffensen et al., 1999). Patients with Alzheimer's disease, Down syndrome, and frontotemporal dementia have also been shown to exhibit a significant reduction in SNAP25 expression (Greber et al., 1999; Sinclair et al., 2015). Postmortem brain analysis revealed altered SNAP25 expression in various brain regions of schizophrenic patients (Thompson et al., 2003; Young et al., 1998). The involvement of SNAP25 in the pathology of bipolar disorder has also been proposed due to the elevated protein levels of SNAP25 observed in the human prefrontal cortex (Scarr et al., 2006).

6.1.8.2. Deep-layer pyramidal neurons in mental disorders

Remarkably, dopamine 1 (D1) and dopamine 2 (D2) receptors are particularly enriched in cortical layer 5 and layer 6 glutamatergic pyramidal neurons (Ciliax et al., 1995; Gaspar et al., 1995; Le Moine & Gaspar, 1998). Selective ablation of Drd1a-expressing cortical neurons has been shown to induce several motor-related and behavioural impairments irrespective of the striatal pathways (Jiang et al., 2015). Cortical layer 6b cell populations merit further investigations as schizophrenia susceptibility genes, including *neuregulin-1*, *Drd1a*, *Notch2*, and *Slc1a2,* are enriched in subplate neurons that give

rise to layer 6 (Hoerder-Suabedissen et al., 2013). Similarly, autism-associated genes, including *Tbr1*, *Foxp1*, and *Bcl11*, have been identified with dominant expression levels in layer 5 and layer 6 projection neurons within the prefrontal cortex (Willsey et al., 2013).

6.1.9. Unresolved questions

6.1.9.1. Pyramidal neuron identity and/or activity driving interneuron distribution?

Previous studies have demonstrated that fate-converting subcerebral projection neurons to callosal projection neurons altered the laminar distribution of GABAergic interneurons (Lodato et al., 2011; Wester et al., 2019). These point to the role of glutamatergic pyramidal neuron identity in instructing the laminar arrangement of inhibitory neurons. Since long-term silencing of subsets of layer 5 neurons altered the laminar location of PV+ and NPY+ cells throughout development, it seems that inhibitory neurons are reallocated upon *Snap25*-ablation. This rearrangement might be required to compensate for the 'silent' glutamatergic neurons in the deep layers of the cortex. Both pyramidal neuron identity and activity may orchestrate interneuron distribution.

6.1.9.2. Loss of cell number or downregulation of protein expression?

The lack of effect of the chronic manipulation of layer 5 and layer 6b on PV total cell density in the adult brain indicates that alterations in PV cell number are highly unlikely once the final number of GABAergic interneurons is determined during early development. Since parvalbumin interneurons and PNNs are activity-dependent, I would argue that density changes are not driven by cell loss, but by a dynamic up-or downregulation of the parvalbumin protein and the PNNs that are responding to changes in the cortical network and changes in pyramidal neuron activity. This is supported by recent research showing that parvalbumin interneurons are not eliminated in a mouse model of autism spectrum disorder, and the downregulation of the parvalbumin protein expression is the cause of the apparent cell loss (Filice et al., 2016).

6.1.9.3. PV regulating PNNs or PNNs regulating PV neurons?

Since transcriptomic studies showed that PV neurons express several of the essential PNN lecticans and linkers, as well as membrane and secretory proteases, it has been suggested that PV interneurons may control the structure and expression of PNNs surrounding them (Devienne et al., 2021; Dityatev et al., 2010; Ferrer-Ferrer & Dityatev, 2018; Kwok et al., 2012). The subtypes of PV neurons (PV+ VVA+, PV+ VVA-, PV- VVA+) might reflect the individual response of PV neurons to pyramidal neuron activity as they up- or downregulate their PNNs depending on the network state. It is probable that the PV+ VVA- subtype is more plastic and so retains its ability to change to network disturbances, while the PV+ VVA+ subtype has limited plasticity as it is consolidated by PNNs. Therefore, the PNNs may endow PV neurons with distinct properties depending on whether they are surrounded by proteoglycans or not. Previous studies have discovered that through its control on potassium channel localisation and synaptic AMPA receptor levels, brevican alters the intrinsic characteristics of PV+ interneurons and modulates PV function and excitability (Favuzzi et al., 2017).

6.1.9.4. Why do deep-layer projection neurons have different susceptibility to Snap25 ablation?

The *Snap25*-ablated Drd1a-Cre cKO brains show the least severe signs of cell death and axonal degradation at 8 months. These symptoms are more noticeable in the *Ntsr1Cre;Snap25*$^{fl/fl}$ strain (layer 6a), and most prominent in the *Rbp4-Cre;Snap25*$^{fl/fl}$ mice (Hoerder-Suabedissen et al., 2019). It remains unclear why the chronic abolition of evoked vesicle release leads to the degeneration and cell death of Rbp4-Cre+ neurons. In particular, what makes the IT-and PT-type projection neurons in layer 5 more vulnerable to the conditional ablation of *Snap25*. These results imply that the chronic abolition of AP-dependent neurotransmission from distinct subtypes of deep-layer projection neurons has very different consequences on the projection neurons themselves.

6.1.10. Limitations of the DPhil thesis

One of the major limitations of the present study is that the Rbp4-Cre is a pan L5 line and, therefore, it is not truly restrictive to a specific subset of L5 pyramidal neurons. Since the Rbp4-Cre line is unable to differentiate between IT vs ET-type L5 projection neurons, other transgenic models with more precise genetic targeting of L5 pyramidal neurons will be needed. Tlx3_PL56, Ebf2_NP183, and Grp_KH288 Cre lines allow for the selective targeting of the IT-type of L5 neurons, while the Sim1_KJ18, Chrna2_OE25, Efr3a_NO108, and Rcan2_ON50 strains give genetic access to the PT-type of cortical L5 neurons (Gerfen et al., 2013). Another limiting factor is the chronic manipulation of pyramidal neuron activity. The *Rbp4-Cre;Snap25 cKO* mice only permit the permanent and irreversible manipulation of pyramidal neuron activity. Engineering of new CreERT mouse lines will allow us to manipulate pyramidal neurons in an acute fashion and perturb pyramidal neuron function with temporal precision. While the axonal projections of Rbp4-Cre+ neurons remained intact in the *Snap25* cKO mice until P21, severe neurodegeneration was detected in the adult brain. This makes it more difficult to distinguish between the effects of persistently silencing L5 projection neurons on PV interneurons and the impacts of cell death and inflammation, which may have an indirect impact on PV density, rather than the absence of layer 5 activity.

6.1.11. Conclusion

The *Snap25* cKO strains employed throughout the thesis remain vital models for researching the interplay between interneurons and pyramidal neurons, as they allow the layer-specific manipulation of pyramidal neurons. They can further reveal the individual distribution of deep-layer projection neurons in the establishment of cortical circuits. Since they perturb only evoked vesicle release, these models can also differentiate between different forms of neuroexocytosis. Further studies examining PV and PNN interactions will uniquely inform us about the plasticity of cortical circuits and the differential survival capacity of interneurons. These cKO models will also shed light on the pathophysiological changes underpinning neuropsychiatric disorders with synaptopathies.

References

Alcamo, E. A., Chirivella, L., Dautzenberg, M., Dobreva, G., Fariñas, I., Grosschedl, R., & McConnell, S. K. (2008). Satb2 regulates callosal projection neuron identity in the developing cerebral cortex. *Neuron*, *57*(3), 364–377. https://doi.org/10.1016/j.neuron.2007.12.012

Alessi, D. R., James, S. R., Downes, C. P., Holmes, A. B., Gaffney, P. R., Reese, C. B., & Cohen, P. (1997). Characterization of a 3-phosphoinositide-dependent protein kinase which phosphorylates and activates protein kinase Balpha. *Current Biology*, *7*(4), 261–269. https://doi.org/10.1016/s0960-9822(06)00122-9

Anastasiades, P. G., Marques-Smith, A., Lyngholm, D., Lickiss, T., Raffiq, S., Kätzel, D., Miesenböck, G., & Butt, S. J. B. (2016). GABAergic interneurons form transient layer-specific circuits in early postnatal neocortex. *Nature Communications*, *7*, 10584. https://doi.org/10.1038/ncomms10584

Anderson, S. A., Marín, O., Horn, C., Jennings, K., & Rubenstein, J. L. (2001). Distinct cortical migrations from the medial and lateral ganglionic eminences. *Development*, *128*(3), 353–363. https://doi.org/10.1242/dev.128.3.353

Angevine, J. B., & Sidman, R. L. (1961). Autoradiographic study of cell migration during histogenesis of cerebral cortex in the mouse. *Nature*, *192*, 766–768. https://doi.org/10.1038/192766b0

Antonucci, F., Corradini, I., Fossati, G., Tomasoni, R., Menna, E., & Matteoli, M. (2016). SNAP-25, a Known Presynaptic Protein with Emerging Postsynaptic Functions. *Frontiers in Synaptic Neuroscience*, *8*, 7. https://doi.org/10.3389/fnsyn.2016.00007

Aoki, C., & Pickel, V. M. (1989). Neuropeptide Y in the cerebral cortex and the caudate-putamen nuclei: ultrastructural basis for interactions with GABAergic and non-GABAergic neurons. *The Journal of Neuroscience*, *9*(12), 4333–4354. https://doi.org/10.1523/JNEUROSCI.09-12-04333.1989

Arlotta, P., Molyneaux, B. J., Chen, J., Inoue, J., Kominami, R., & Macklis, J. D. (2005). Neuronal subtype-specific genes that control corticospinal motor neuron development in vivo. *Neuron*, *45*(2), 207–221. https://doi.org/10.1016/j.neuron.2004.12.036

Asgarihafshejani, A., Honoré, È., Michon, F.-X., Laplante, I., & Lacaille, J.-C. (2022). Long-term potentiation at pyramidal cell to somatostatin interneuron synapses controls hippocampal network plasticity and memory. *IScience*, *25*(5), 104259. https://doi.org/10.1016/j.isci.2022.104259

Ayala, R., Shu, T., & Tsai, L.-H. (2007). Trekking across the brain: the journey of neuronal migration. *Cell*, *128*(1), 29–43. https://doi.org/10.1016/j.cell.2006.12.021

Azim, E., Jabaudon, D., Fame, R. M., & Macklis, J. D. (2009). SOX6 controls dorsal progenitor identity and interneuron diversity during neocortical development. *Nature Neuroscience*, *12*(10), 1238–1247. https://doi.org/10.1038/nn.2387

Bacci, A., & Huguenard, J. R. (2006). Enhancement of spike-timing precision by autaptic transmission in neocortical inhibitory interneurons. *Neuron*, *49*(1), 119–130. https://doi.org/10.1016/j.neuron.2005.12.014

Bacci, A., Huguenard, J. R., & Prince, D. A. (2002). Differential modulation of synaptic transmission by neuropeptide Y in rat neocortical neurons. *Proceedings of the National Academy of Sciences of the United States of America*, *99*(26), 17125–17130. https://doi.org/10.1073/pnas.012481899

Baccini, G., Foggetti, A., Wernet, N., Engelhardt, K.-A., Steinecke, C.-S., Edelmann, E., Balueva, K., Kronenbitter, K., Michels, J., Kulik, A., Wozny, C., & Wulff, P. (2025). Parvalbumin expression identifies subicular principal cells with high projection specificity. *Cell Reports*, *44*(8), 116004. https://doi.org/10.1016/j.celrep.2025.116004

Backman, S. A., Stambolic, V., Suzuki, A., Haight, J., Elia, A., Pretorius, J., Tsao, M. S., Shannon, P., Bolon, B., Ivy, G. O., & Mak, T. W. (2001). Deletion of Pten in mouse brain causes seizures, ataxia and defects in soma size resembling Lhermitte-Duclos disease. *Nature Genetics*, *29*(4), 396–403. https://doi.org/10.1038/ng782

Banks, S. M. L., Medeiros, A. T., McQuillan, M., Busch, D. J., Ibarraran-Viniegra, A. S., Sousa, R., Lafer, E. M., & Morgan, J. R. (2020). Hsc70 Ameliorates the Vesicle Recycling Defects Caused by Excess α-Synuclein at Synapses. *ENeuro*, *7*(1). https://doi.org/10.1523/ENEURO.0448-19.2020

Banks, S. M. L., Medeiros, A. T., McQuillan, M., Busch, D. J., Ibarraran-Viniegra, A. S., Sousa, R., Lafer, E. M., & Morgan, J. R. (2020). Hsc70 Ameliorates the Vesicle Recycling Defects Caused by Excess α-Synuclein at Synapses. *ENeuro*, *7*(1). https://doi.org/10.1523/ENEURO.0448-19.2020

Baraban, S C, Hollopeter, G., Erickson, J. C., Schwartzkroin, P. A., & Palmiter, R. D. (1997). Knock-out mice reveal a critical antiepileptic role for neuropeptide Y. *The Journal of Neuroscience*, *17*(23), 8927–8936. https://doi.org/10.1523/JNEUROSCI.17-23-08927.1997

Baraban, Scott C, & Tallent, M. K. (2004). Interneuron Diversity series: Interneuronal neuropeptides--endogenous regulators of neuronal excitability. *Trends in Neurosciences*, *27*(3), 135–142. https://doi.org/10.1016/j.tins.2004.01.008

Barrows, C. M., McCabe, M. P., Chen, H., Swann, J. W., & Weston, M. C. (2017). PTEN loss increases the connectivity of fast synaptic motifs and functional connectivity in a developing hippocampal

network. *The Journal of Neuroscience*, *37*(36), 8595–8611. https://doi.org/10.1523/JNEUROSCI.0878-17.2017

Bartos, M., Vida, I., & Jonas, P. (2007). Synaptic mechanisms of synchronized gamma oscillations in inhibitory interneuron networks. *Nature Reviews. Neuroscience*, *8*(1), 45–56. https://doi.org/10.1038/nrn2044

Baruchin, L. J., Ghezzi, F., Kohl, M. M., & Butt, S. J. B. (2022). Contribution of Interneuron Subtype-Specific GABAergic Signaling to Emergent Sensory Processing in Mouse Somatosensory Whisker Barrel Cortex. *Cerebral Cortex*, *32*(12), 2538–2554. https://doi.org/10.1093/cercor/bhab363

Bassetti, D. (2022). Keeping the balance: GABAB receptors in the developing brain and beyond. *Brain Sciences*, *12*(4). https://doi.org/10.3390/brainsci12040419

Bédard, A., & Parent, A. (2004). Evidence of newly generated neurons in the human olfactory bulb. *Brain Research. Developmental Brain Research*, *151*(1–2), 159–168. https://doi.org/10.1016/j.devbrainres.2004.03.021

Benes, F. M., & Berretta, S. (2001). GABAergic interneurons: implications for understanding schizophrenia and bipolar disorder. *Neuropsychopharmacology*, *25*(1), 1–27. https://doi.org/10.1016/S0893-133X(01)00225-1

Ben-Simon, Y., Kaefer, K., Velicky, P., Csicsvari, J., Danzl, J. G., & Jonas, P. (2022). A direct excitatory projection from entorhinal layer 6b neurons to the hippocampus contributes to spatial coding and memory. *Nature Communications*, *13*(1), 4826. https://doi.org/10.1038/s41467-022-32559-8

Bernardo, K. L., McCasland, J. S., Woolsey, T. A., & Strominger, R. N. (1990). Local intra- and interlaminar connections in mouse barrel cortex. *The Journal of Comparative Neurology*, *291*(2), 231–255. https://doi.org/10.1002/cne.902910207

Berretta, S., Pantazopoulos, H., Markota, M., Brown, C., & Batzianouli, E. T. (2015). Losing the sugar coating: potential impact of perineuronal net abnormalities on interneurons in schizophrenia. *Schizophrenia Research*, *167*(1–3), 18–27. https://doi.org/10.1016/j.schres.2014.12.040

Bettler, B., Kaupmann, K., Mosbacher, J., & Gassmann, M. (2004). Molecular structure and physiological functions of GABA(B) receptors. *Physiological Reviews*, *84*(3), 835–867. https://doi.org/10.1152/physrev.00036.2003

Bloodgood, B. L., Sharma, N., Browne, H. A., Trepman, A. Z., & Greenberg, M. E. (2013). The activity-dependent transcription factor NPAS4 regulates domain-specific inhibition. *Nature*, *503*(7474), 121–125. https://doi.org/10.1038/nature12743

Booker, S. A., Gross, A., Althof, D., Shigemoto, R., Bettler, B., Frotscher, M., Hearing, M., Wickman, K., Watanabe, M., Kulik, Á., & Vida, I. (2013). Differential GABAB-receptor-mediated effects in perisomatic- and dendrite-targeting parvalbumin interneurons. *The Journal of Neuroscience*, *33*(18), 7961–7974. https://doi.org/10.1523/JNEUROSCI.1186-12.2013

Bourassa, J., Pinault, D., & Deschênes, M. (1995). Corticothalamic projections from the cortical barrel field to the somatosensory thalamus in rats: a single-fibre study using biocytin as an anterograde tracer. *The European Journal of Neuroscience*, *7*(1), 19–30. https://doi.org/10.1111/j.1460-9568.1995.tb01016.x

Boyce, R. W., Dorph-Petersen, K.-A., Lyck, L., & Gundersen, H. J. G. (2010). Design-based stereology: introduction to basic concepts and practical approaches for estimation of cell number. *Toxicologic Pathology*, *38*(7), 1011–1025. https://doi.org/10.1177/0192623310385140

Braida, D., Guerini, F. R., Ponzoni, L., Corradini, I., De Astis, S., Pattini, L., Bolognesi, E., Benfante, R., Fornasari, D., Chiappedi, M., Ghezzo, A., Clerici, M., Matteoli, M., & Sala, M. (2015). Association between SNAP-25 gene polymorphisms and cognition in autism: functional consequences and potential therapeutic strategies. *Translational Psychiatry*, *5*(1), e500. https://doi.org/10.1038/tp.2014.136

Britanova, O., de Juan Romero, C., Cheung, A., Kwan, K. Y., Schwark, M., Gyorgy, A., Vogel, T., Akopov, S., Mitkovski, M., Agoston, D., Sestan, N., Molnár, Z., & Tarabykin, V. (2008). Satb2 is a postmitotic determinant for upper-layer neuron specification in the neocortex. *Neuron*, *57*(3), 378–392. https://doi.org/10.1016/j.neuron.2007.12.028

Bronner, M., & Hatten, M. E. (2013). Neurogenesis and Migration. In *Fundamental Neuroscience* (pp. 339–361). Elsevier. https://doi.org/10.1016/B978-0-12-385870-2.00015-9

Buonomano, D. V., & Merzenich, M. M. (1998). Cortical plasticity: from synapses to maps. *Annual Review of Neuroscience*, *21*, 149–186. https://doi.org/10.1146/annurev.neuro.21.1.149

Busch, R. M., Chapin, J. S., Mester, J., Ferguson, L., Haut, J. S., Frazier, T. W., & Eng, C. (2013). Cognitive characteristics of PTEN hamartoma tumor syndromes. *Genetics in Medicine*, *15*(7), 548–553. https://doi.org/10.1038/gim.2013.1

Butler, M. G., Dasouki, M. J., Zhou, X. P., Talebizadeh, Z., Brown, M., Takahashi, T. N., Miles, J. H., Wang, C. H., Stratton, R., Pilarski, R., & Eng, C. (2005). Subset of individuals with autism spectrum disorders

and extreme macrocephaly associated with germline PTEN tumour suppressor gene mutations. *Journal of Medical Genetics*, *42*(4), 318–321. https://doi.org/10.1136/jmg.2004.024646

Butt, S. J. B., Cobos, I., Golden, J., Kessaris, N., Pachnis, V., & Anderson, S. (2007). Transcriptional regulation of cortical interneuron development. *The Journal of Neuroscience*, *27*(44), 11847–11850. https://doi.org/10.1523/JNEUROSCI.3525-07.2007

Butt, S. J. B., Fuccillo, M., Nery, S., Noctor, S., Kriegstein, A., Corbin, J. G., & Fishell, G. (2005). The temporal and spatial origins of cortical interneurons predict their physiological subtype. *Neuron*, *48*(4), 591–604. https://doi.org/10.1016/j.neuron.2005.09.034

Butt, S. J. B., Sousa, V. H., Fuccillo, M. V., Hjerling-Leffler, J., Miyoshi, G., Kimura, S., & Fishell, G. (2008). The requirement of Nkx2-1 in the temporal specification of cortical interneuron subtypes. *Neuron*, *59*(5), 722–732. https://doi.org/10.1016/j.neuron.2008.07.031

Butt, S. J., Stacey, J. A., Teramoto, Y., & Vagnoni, C. (2017). A role for GABAergic interneuron diversity in circuit development and plasticity of the neonatal cerebral cortex. *Current Opinion in Neurobiology*, *43*, 149–155. https://doi.org/10.1016/j.conb.2017.03.011

Buxbaum, J. D., Cai, G., Chaste, P., Nygren, G., Goldsmith, J., Reichert, J., Anckarsäter, H., Rastam, M., Smith, C. J., Silverman, J. M., Hollander, E., Leboyer, M., Gillberg, C., Verloes, A., & Betancur, C. (2007). Mutation screening of the PTEN gene in patients with autism spectrum disorders and macrocephaly. *American Journal of Medical Genetics. Part B, Neuropsychiatric Genetics*, *144B*(4), 484–491. https://doi.org/10.1002/ajmg.b.30493

Bystron, I., Blakemore, C., & Rakic, P. (2008). Development of the human cerebral cortex: Boulder Committee revisited. *Nature Reviews. Neuroscience*, *9*(2), 110–122. https://doi.org/10.1038/nrn2252

Carriere, C. H., Wang, W. X., Sing, A. D., Fekete, A., Jones, B. E., Yee, Y., Ellegood, J., Maganti, H., Awofala, L., Marocha, J., Aziz, A., Wang, L.-Y., Lerch, J. P., & Lefebvre, J. L. (2020). The γ-Protocadherins Regulate the Survival of GABAergic Interneurons during Developmental Cell Death. *The Journal of Neuroscience*, *40*(45), 8652–8668. https://doi.org/10.1523/JNEUROSCI.1636-20.2020

Carstens, K. E., Phillips, M. L., Pozzo-Miller, L., Weinberg, R. J., & Dudek, S. M. (2016). Perineuronal nets suppress plasticity of excitatory synapses on CA2 pyramidal neurons. *The Journal of Neuroscience*, *36*(23), 6312–6320. https://doi.org/10.1523/JNEUROSCI.0245-16.2016

Carulli, D., & Verhaagen, J. (2021). An extracellular perspective on CNS maturation: perineuronal nets and the control of plasticity. *International Journal of Molecular Sciences*, *22*(5). https://doi.org/10.3390/ijms22052434

Castro-Alamancos, M. A., Donoghue, J. P., & Connors, B. W. (1995). Different forms of synaptic plasticity in somatosensory and motor areas of the neocortex. *The Journal of Neuroscience*, *15*(7 Pt 2), 5324–5333. https://doi.org/10.1523/JNEUROSCI.15-07-05324.1995

Chamberland, S., Grant, G., Machold, R., Nebet, E. R., Tian, G., Stich, J., Hanani, M., Kullander, K., & Tsien, R. W. (2024). Functional specialization of hippocampal somatostatin-expressing interneurons. *Proceedings of the National Academy of Sciences of the United States of America*, *121*(17), e2306382121. https://doi.org/10.1073/pnas.2306382121

Chard, P. S., Bleakman, D., Christakos, S., Fullmer, C. S., & Miller, R. J. (1993). Calcium buffering properties of calbindin D28k and parvalbumin in rat sensory neurones. *The Journal of Physiology*, *472*, 341–357. https://doi.org/10.1113/jphysiol.1993.sp019950

Chattopadhyaya, B., Di Cristo, G., Higashiyama, H., Knott, G. W., Kuhlman, S. J., Welker, E., & Huang, Z. J. (2004). Experience and activity-dependent maturation of perisomatic GABAergic innervation in

primary visual cortex during a postnatal critical period. *The Journal of Neuroscience*, *24*(43), 9598–9611. https://doi.org/10.1523/JNEUROSCI.1851-04.2004

Chen, W., Cai, Z.-L., Chao, E. S., Chen, H., Longley, C. M., Hao, S., Chao, H.-T., Kim, J. H., Messier, J. E., Zoghbi, H. Y., Tang, J., Swann, J. W., & Xue, M. (2020). Stxbp1/Munc18-1 haploinsufficiency impairs inhibition and mediates key neurological features of STXBP1 encephalopathy. *ELife*, *9*. https://doi.org/10.7554/eLife.48705

Chen, Y., Huang, W.-C., Séjourné, J., Clipperton-Allen, A. E., & Page, D. T. (2015). Pten Mutations Alter Brain Growth Trajectory and Allocation of Cell Types through Elevated β-Catenin Signaling. *The Journal of Neuroscience*, *35*(28), 10252–10267. https://doi.org/10.1523/JNEUROSCI.5272-14.2015

Chow, D. K., Groszer, M., Pribadi, M., Machniki, M., Carmichael, S. T., Liu, X., & Trachtenberg, J. T. (2009). Laminar and compartmental regulation of dendritic growth in mature cortex. *Nature Neuroscience*, *12*(2), 116–118. https://doi.org/10.1038/nn.2255

Ciliax, B. J., Heilman, C., Demchyshyn, L. L., Pristupa, Z. B., Ince, E., Hersch, S. M., Niznik, H. B., & Levey, A. I. (1995). The dopamine transporter: immunochemical characterization and localization in brain. *The Journal of Neuroscience*, *15*(3 Pt 1), 1714–1723. https://doi.org/10.1523/JNEUROSCI.15-03-01714.1995

Contamina, P., & Boada, E. (1992). Time of origin of cortico-collicular projection neurons in the rat visual cortex. *The Journal of Comparative Neurology*, *323*(4), 570–576. https://doi.org/10.1002/cne.903230409

Corbin, J. G., Gaiano, N., Machold, R. P., Langston, A., & Fishell, G. (2000). The Gsh2 homeodomain gene controls multiple aspects of telencephalic development. *Development*, *127*(23), 5007–5020. https://doi.org/10.1242/dev.127.23.5007

Crabtree, J. W. (2018). Functional diversity of thalamic reticular subnetworks. *Frontiers in Systems Neuroscience*, *12*, 41. https://doi.org/10.3389/fnsys.2018.00041

Dantzker, J. L., & Callaway, E. M. (2000). Laminar sources of synaptic input to cortical inhibitory interneurons and pyramidal neurons. *Nature Neuroscience*, *3*(7), 701–707. https://doi.org/10.1038/76656

De Marco García, N. V., Karayannis, T., & Fishell, G. (2011). Neuronal activity is required for the development of specific cortical interneuron subtypes. *Nature*, *472*(7343), 351–355. https://doi.org/10.1038/nature09865

Deken, S. L., Beckman, M. L., Boos, L., & Quick, M. W. (2000). Transport rates of GABA transporters: regulation by the N-terminal domain and syntaxin 1A. *Nature Neuroscience*, *3*(10), 998–1003. https://doi.org/10.1038/79939

del Río, J. A., de Lecea, L., Ferrer, I., & Soriano, E. (1994). The development of parvalbumin-immunoreactivity in the neocortex of the mouse. *Brain Research. Developmental Brain Research*, *81*(2), 247–259. https://doi.org/10.1016/0165-3806(94)90311-5

Denaxa, M., Neves, G., Rabinowitz, A., Kemlo, S., Liodis, P., Burrone, J., & Pachnis, V. (2018). Modulation of apoptosis controls inhibitory interneuron number in the cortex. *Cell Reports*, *22*(7), 1710–1721. https://doi.org/10.1016/j.celrep.2018.01.064

Devienne, G., Picaud, S., Cohen, I., Piquet, J., Tricoire, L., Testa, D., Di Nardo, A. A., Rossier, J., Cauli, B., & Lambolez, B. (2021). Regulation of perineuronal nets in the adult cortex by the activity of the cortical network. *The Journal of Neuroscience*, *41*(27), 5779–5790. https://doi.org/10.1523/JNEUROSCI.0434-21.2021

Di Cristofano, A., Pesce, B., Cordon-Cardo, C., & Pandolfi, P. P. (1998). Pten is essential for embryonic development and tumour suppression. *Nature Genetics*, *19*(4), 348–355. https://doi.org/10.1038/1235

Dienel, S. J., & Lewis, D. A. (2019). Alterations in cortical interneurons and cognitive function in schizophrenia. *Neurobiology of Disease*, *131*, 104208. https://doi.org/10.1016/j.nbd.2018.06.020

Ding, C., Emmenegger, V., Schaffrath, K., & Feldmeyer, D. (2021). Layer-Specific Inhibitory Microcircuits of Layer 6 Interneurons in Rat Prefrontal Cortex. *Cerebral Cortex*, *31*(1), 32–47. https://doi.org/10.1093/cercor/bhaa201

Ding, S.-L., Yao, Z., Hirokawa, K. E., Nguyen, T. N., Graybuck, L. T., Fong, O., Bohn, P., Ngo, K., Smith, K. A., Koch, C., Phillips, J. W., Lein, E. S., Harris, J. A., Tasic, B., & Zeng, H. (2020). Distinct Transcriptomic Cell Types and Neural Circuits of the Subiculum and Prosubiculum along the Dorsal-Ventral Axis. *Cell Reports*, *31*(7), 107648. https://doi.org/10.1016/j.celrep.2020.107648

Dityatev, A., Seidenbecher, C. I., & Schachner, M. (2010). Compartmentalization from the outside: the extracellular matrix and functional microdomains in the brain. *Trends in Neurosciences*, *33*(11), 503–512. https://doi.org/10.1016/j.tins.2010.08.003

Drake, A. W., Jerow, L. G., Ruksenas, J. V., McCoy, C., & Danzer, S. C. (2024). Somatostatin interneuron fate-mapping and structure in a Pten knockout model of epilepsy. *Frontiers in Cellular Neuroscience*, *18*, 1474613. https://doi.org/10.3389/fncel.2024.1474613

Druga, R., Salaj, M., & Al-Redouan, A. (2023). Parvalbumin - Positive Neurons in the Neocortex: A Review. *Physiological Research / Academia Scientiarum Bohemoslovaca*, *72*(Suppl 2), S173–S191. https://doi.org/10.33549/physiolres.935005

Duan, Z. R. S., Che, A., Chu, P., Modol, L., Bollmann, Y., Babij, R., Fetcho, R. N., Otsuka, T., Fuccillo, M. V., Liston, C., Pisapia, D. J., Cossart, R., & De Marco García, N. V. (2020). Gabaergic restriction of network dynamics regulates interneuron survival in the developing cortex. *Neuron*, *105*(1), 75-92.e5. https://doi.org/10.1016/j.neuron.2019.10.008

Dwivedi, D., Dumontier, D., Sherer, M., Lin, S., Mirow, A. M. C., Qiu, Y., Xu, Q., Liebman, S. A., Joseph, D., Datta, S. R., Fishell, G., & Pouchelon, G. (2024). Metabotropic signaling within somatostatin interneurons controls transient thalamocortical inputs during development. *Nature Communications*, *15*(1), 5421. https://doi.org/10.1038/s41467-024-49732-w

Engelman, J. A., Luo, J., & Cantley, L. C. (2006). The evolution of phosphatidylinositol 3-kinases as regulators of growth and metabolism. *Nature Reviews. Genetics*, *7*(8), 606–619. https://doi.org/10.1038/nrg1879

Enwright, J. F., Sanapala, S., Foglio, A., Berry, R., Fish, K. N., & Lewis, D. A. (2016). Reduced Labeling of Parvalbumin Neurons and Perineuronal Nets in the Dorsolateral Prefrontal Cortex of Subjects with Schizophrenia. *Neuropsychopharmacology*, *41*(9), 2206–2214. https://doi.org/10.1038/npp.2016.24

Erzurumlu, R. S., & Gaspar, P. (2012). Development and critical period plasticity of the barrel cortex. *The European Journal of Neuroscience*, *35*(10), 1540–1553. https://doi.org/10.1111/j.1460-9568.2012.08075.x

Fairén, A., Cobas, A., & Fonseca, M. (1986). Times of generation of glutamic acid decarboxylase immunoreactive neurons in mouse somatosensory cortex. *The Journal of Comparative Neurology*, *251*(1), 67–83. https://doi.org/10.1002/cne.902510105

Faraone, S. V., & Mick, E. (2010). Molecular genetics of attention deficit hyperactivity disorder. *The Psychiatric Clinics of North America*, *33*(1), 159–180. https://doi.org/10.1016/j.psc.2009.12.004

Favuzzi, E., Marques-Smith, A., Deogracias, R., Winterflood, C. M., Sánchez-Aguilera, A., Mantoan, L., Maeso, P., Fernandes, C., Ewers, H., & Rico, B. (2017). Activity-Dependent Gating of Parvalbumin Interneuron Function by the Perineuronal Net Protein Brevican. *Neuron*, *95*(3), 639-655.e10. https://doi.org/10.1016/j.neuron.2017.06.028

Fazel Darbandi, S., Robinson Schwartz, S. E., Qi, Q., Catta-Preta, R., Pai, E. L.-L., Mandell, J. D., Everitt, A., Rubin, A., Krasnoff, R. A., Katzman, S., Tastad, D., Nord, A. S., Willsey, A. J., Chen, B., State, M. W., Sohal, V. S., & Rubenstein, J. L. R. (2018). Neonatal tbr1 dosage controls cortical layer 6 connectivity. *Neuron*, *100*(4), 831-845.e7. https://doi.org/10.1016/j.neuron.2018.09.027

Feldman, D. E. (2009). Synaptic mechanisms for plasticity in neocortex. *Annual Review of Neuroscience*, *32*, 33–55. https://doi.org/10.1146/annurev.neuro.051508.135516

Feng, Y., Crosbie, J., Wigg, K., Pathare, T., Ickowicz, A., Schachar, R., Tannock, R., Roberts, W., Malone, M., Swanson, J., Kennedy, J. L., & Barr, C. L. (2005). The SNAP25 gene as a susceptibility gene contributing to attention-deficit hyperactivity disorder. *Molecular Psychiatry*, *10*(11), 998–1005, 973. https://doi.org/10.1038/sj.mp.4001722

Ferrer-Ferrer, M., & Dityatev, A. (2018). Shaping synapses by the neural extracellular matrix. *Frontiers in Neuroanatomy*, *12*, 40. https://doi.org/10.3389/fnana.2018.00040

Filice, F., Vörckel, K. J., Sungur, A. Ö., Wöhr, M., & Schwaller, B. (2016). Reduction in parvalbumin expression not loss of the parvalbumin-expressing GABA interneuron subpopulation in genetic parvalbumin and shank mouse models of autism. *Molecular Brain*, *9*, 10. https://doi.org/10.1186/s13041-016-0192-8

Fishell, G., & Rudy, B. (2011). Mechanisms of inhibition within the telencephalon: "where the wild things are". *Annual Review of Neuroscience*, *34*, 535–567. https://doi.org/10.1146/annurev-neuro-061010-113717

Flames, N., Pla, R., Gelman, D. M., Rubenstein, J. L. R., Puelles, L., & Marín, O. (2007). Delineation of multiple subpallial progenitor domains by the combinatorial expression of transcriptional codes. *The Journal of Neuroscience*, *27*(36), 9682–9695. https://doi.org/10.1523/JNEUROSCI.2750-07.2007

Fogarty, M., Grist, M., Gelman, D., Marín, O., Pachnis, V., & Kessaris, N. (2007). Spatial genetic patterning of the embryonic neuroepithelium generates GABAergic interneuron diversity in the adult cortex. *The Journal of Neuroscience*, *27*(41), 10935–10946. https://doi.org/10.1523/JNEUROSCI.1629-07.2007

Frandolig, J. E., Matney, C. J., Lee, K., Kim, J., Chevée, M., Kim, S.-J., Bickert, A. A., & Brown, S. P. (2019). The synaptic organization of layer 6 circuits reveals inhibition as a major output of a neocortical sublamina. *Cell Reports*, *28*(12), 3131-3143.e5. https://doi.org/10.1016/j.celrep.2019.08.048

Franke, T. F. (2008). PI3K/Akt: getting it right matters. *Oncogene*, *27*(50), 6473–6488. https://doi.org/10.1038/onc.2008.313

Frazier, T. W. (2019). Autism Spectrum Disorder Associated with Germline Heterozygous PTEN Mutations. *Cold Spring Harbor Perspectives in Medicine*, *9*(10). https://doi.org/10.1101/cshperspect.a037002

Freund, T F, & Buzsáki, G. (1996). Interneurons of the hippocampus. *Hippocampus*.

Freund, Tamás F. (2003). Interneuron Diversity series: Rhythm and mood in perisomatic inhibition. *Trends in Neurosciences*, *26*(9), 489–495. https://doi.org/10.1016/S0166-2236(03)00227-3

Friedlander, M. J., & Torres-Reveron, J. (2009). The changing roles of neurons in the cortical subplate. *Frontiers in Neuroanatomy*, *3*, 15. https://doi.org/10.3389/neuro.05.015.2009

Fritsch, R., de Krijger, I., Fritsch, K., George, R., Reason, B., Kumar, M. S., Diefenbacher, M., Stamp, G., & Downward, J. (2013). RAS and RHO families of GTPases directly regulate distinct phosphoinositide 3-kinase isoforms. *Cell*, *153*(5), 1050–1063. https://doi.org/10.1016/j.cell.2013.04.031

Fruman, D. A., & Rommel, C. (2014). PI3K and cancer: lessons, challenges and opportunities. *Nature Reviews. Drug Discovery*, *13*(2), 140–156. https://doi.org/10.1038/nrd4204

Fujiwara, T., Mishima, T., Kofuji, T., Chiba, T., Tanaka, K., Yamamoto, A., & Akagawa, K. (2006). Analysis of knock-out mice to determine the role of HPC-1/syntaxin 1A in expressing synaptic plasticity. *The Journal of Neuroscience*, *26*(21), 5767–5776. https://doi.org/10.1523/JNEUROSCI.0289-06.2006

Fujiwara, T., Snada, M., Kofuji, T., Yoshikawa, T., & Akagawa, K. (2010). HPC-1/syntaxin 1A gene knockout mice show abnormal behavior possibly related to a disruption in 5-HTergic systems. *The European Journal of Neuroscience*, *32*(1), 99–107. https://doi.org/10.1111/j.1460-9568.2010.07269.x

Gainey, M. A., & Feldman, D. E. (2017). Multiple shared mechanisms for homeostatic plasticity in rodent somatosensory and visual cortex. *Philosophical Transactions of the Royal Society of London. Series B, Biological Sciences*, *372*(1715). https://doi.org/10.1098/rstb.2016.0157

Gall, C., Lauterborn, J., Isackson, P., & White, J. (1990). Seizures, neuropeptide regulation, and mRNA expression in the hippocampus. *Progress in Brain Research*, *83*, 371–390. https://doi.org/10.1016/s0079-6123(08)61263-7

Gaspar, P., Bloch, B., & Le Moine, C. (1995). D1 and D2 receptor gene expression in the rat frontal cortex: cellular localization in different classes of efferent neurons. *The European Journal of Neuroscience*, *7*(5), 1050–1063. https://doi.org/10.1111/j.1460-9568.1995.tb01092.x

Geerlings, A., López-Corcuera, B., & Aragón, C. (2000). Characterization of the interactions between the glycine transporters GLYT1 and GLYT2 and the SNARE protein syntaxin 1A. *FEBS Letters*, *470*(1), 51–54. https://doi.org/10.1016/s0014-5793(00)01297-7

Gerber, S. H., Rah, J.-C., Min, S.-W., Liu, X., de Wit, H., Dulubova, I., Meyer, A. C., Rizo, J., Arancillo, M., Hammer, R. E., Verhage, M., Rosenmund, C., & Südhof, T. C. (2008). Conformational switch of syntaxin-1 controls synaptic vesicle fusion. *Science*, *321*(5895), 1507–1510. https://doi.org/10.1126/science.1163174

Gerfen, C. R., Paletzki, R., & Heintz, N. (2013). GENSAT BAC cre-recombinase driver lines to study the functional organization of cerebral cortical and basal ganglia circuits. *Neuron*, *80*(6), 1368–1383. https://doi.org/10.1016/j.neuron.2013.10.016

Gosso, M. F., de Geus, E. J. C., van Belzen, M. J., Polderman, T. J. C., Heutink, P., Boomsma, D. I., & Posthuma, D. (2006). The SNAP-25 gene is associated with cognitive ability: evidence from a family-

based study in two independent Dutch cohorts. *Molecular Psychiatry*, *11*(9), 878–886. https://doi.org/10.1038/sj.mp.4001868

Gouwens, N. W., Sorensen, S. A., Baftizadeh, F., Budzillo, A., Lee, B. R., Jarsky, T., Alfiler, L., Baker, K., Barkan, E., Berry, K., Bertagnolli, D., Bickley, K., Bomben, J., Braun, T., Brouner, K., Casper, T., Crichton, K., Daigle, T. L., Dalley, R., … Zeng, H. (2020). Integrated morphoelectric and transcriptomic classification of cortical gabaergic cells. *Cell*, *183*(4), 935-953.e19. https://doi.org/10.1016/j.cell.2020.09.057

Greber, S., Lubec, G., Cairns, N., & Fountoulakis, M. (1999). Decreased levels of synaptosomal associated protein 25 in the brain of patients with Down Syndrome and Alzheimer's disease. *ELECTROPHORESIS*.

Grigoryan, G., Harada, H., Knobloch-Bollmann, H. S., Kilias, A., Kaufhold, D., Kulik, A., Eyre, M. D., & Bartos, M. (2023). Synaptic plasticity at the dentate gyrus granule cell to somatostatin-expressing interneuron synapses supports object location memory. *Proceedings of the National Academy of Sciences of the United States of America*, *120*(51), e2312752120. https://doi.org/10.1073/pnas.2312752120

Groh, A., Bokor, H., Mease, R. A., Plattner, V. M., Hangya, B., Stroh, A., Deschenes, M., & Acsády, L. (2014). Convergence of cortical and sensory driver inputs on single thalamocortical cells. *Cerebral Cortex*, *24*(12), 3167–3179. https://doi.org/10.1093/cercor/bht173

Guo, H., German, P., Bai, S., Barnes, S., Guo, W., Qi, X., Lou, H., Liang, J., Jonasch, E., Mills, G. B., & Ding, Z. (2015). The PI3K/AKT pathway and renal cell carcinoma. *Journal of Genetics and Genomics = Yi Chuan Xue Bao*, *42*(7), 343–353. https://doi.org/10.1016/j.jgg.2015.03.003

Guo, J., & Anton, E. S. (2014). Decision making during interneuron migration in the developing cerebral cortex. *Trends in Cell Biology*, *24*(6), 342–351. https://doi.org/10.1016/j.tcb.2013.12.001

Gupta, A., Wang, Y., & Markram, H. (2000). Organizing principles for a diversity of GABAergic interneurons and synapses in the neocortex. *Science*, *287*(5451), 273–278. https://doi.org/10.1126/science.287.5451.273

Gutilla, E. A., & Steward, O. (2016). Selective neuronal PTEN deletion: can we take the brakes off of growth without losing control? *Neural Regeneration Research*, *11*(8), 1201–1203. https://doi.org/10.4103/1673-5374.189160

Hádinger, N., Bősz, E., Tóth, B., Vantomme, G., Lüthi, A., & Acsády, L. (2023). Region-selective control of the thalamic reticular nucleus via cortical layer 5 pyramidal cells. *Nature Neuroscience*, *26*(1), 116–130. https://doi.org/10.1038/s41593-022-01217-z

Hafner, G., Witte, M., Guy, J., Subhashini, N., Fenno, L. E., Ramakrishnan, C., Kim, Y. S., Deisseroth, K., Callaway, E. M., Oberhuber, M., Conzelmann, K.-K., & Staiger, J. F. (2019). Mapping Brain-Wide Afferent Inputs of Parvalbumin-Expressing GABAergic Neurons in Barrel Cortex Reveals Local and Long-Range Circuit Motifs. *Cell Reports*, *28*(13), 3450-3461.e8. https://doi.org/10.1016/j.celrep.2019.08.064

Hanganu-Opatz, I. L., Butt, S. J. B., Hippenmeyer, S., De Marco García, N. V., Cardin, J. A., Voytek, B., & Muotri, A. R. (2021). The logic of developing neocortical circuits in health and disease. *The Journal of Neuroscience*, *41*(5), 813–822. https://doi.org/10.1523/JNEUROSCI.1655-20.2020

Harris, K. D., Hochgerner, H., Skene, N. G., Magno, L., Katona, L., Bengtsson Gonzales, C., Somogyi, P., Kessaris, N., Linnarsson, S., & Hjerling-Leffler, J. (2018). Classes and continua of hippocampal CA1

inhibitory neurons revealed by single-cell transcriptomics. *PLoS Biology*, *16*(6), e2006387. https://doi.org/10.1371/journal.pbio.2006387

Hartmann, M., Heumann, R., & Lessmann, V. (2001). Synaptic secretion of BDNF after high-frequency stimulation of glutamatergic synapses. *The EMBO Journal*, *20*(21), 5887–5897. https://doi.org/10.1093/emboj/20.21.5887

Hatanaka, Y., & Murakami, F. (2002). In vitro analysis of the origin, migratory behavior, and maturation of cortical pyramidal cells. *The Journal of Comparative Neurology*, *454*(1), 1–14. https://doi.org/10.1002/cne.10421

Haubensak, W., Attardo, A., Denk, W., & Huttner, W. B. (2004). Neurons arise in the basal neuroepithelium of the early mammalian telencephalon: a major site of neurogenesis. *Proceedings of the National Academy of Sciences of the United States of America*, *101*(9), 3196–3201. https://doi.org/10.1073/pnas.0308600100

Hazama, M., Kimura, A., Donishi, T., Sakoda, T., & Tamai, Y. (2004). Topography of corticothalamic projections from the auditory cortex of the rat. *Neuroscience*, *124*(3), 655–667. https://doi.org/10.1016/j.neuroscience.2003.12.027

He, Y., Sun, M. M., Zhang, G. G., Yang, J., Chen, K. S., Xu, W. W., & Li, B. (2021). Targeting PI3K/Akt signal transduction for cancer therapy. *Signal Transduction and Targeted Therapy*, *6*(1), 425. https://doi.org/10.1038/s41392-021-00828-5

Hemmings, B. A., & Restuccia, D. F. (2012). PI3K-PKB/Akt pathway. *Cold Spring Harbor Perspectives in Biology*, *4*(9), a011189. https://doi.org/10.1101/cshperspect.a011189

Hendry, S. H., Jones, E. G., & Emson, P. C. (1984). Morphology, distribution, and synaptic relations of somatostatin- and neuropeptide Y-immunoreactive neurons in rat and monkey neocortex. *The Journal of Neuroscience*, *4*(10), 2497–2517. https://doi.org/10.1523/JNEUROSCI.04-10-02497.1984

Hess, E. J., Jinnah, H. A., Kozak, C. A., & Wilson, M. C. (1992). Spontaneous locomotor hyperactivity in a mouse mutant with a deletion including the Snap gene on chromosome 2. *The Journal of Neuroscience*, *12*(7), 2865–2874. https://doi.org/10.1523/JNEUROSCI.12-07-02865.1992

Hobert, J. A., Embacher, R., Mester, J. L., Frazier, T. W., & Eng, C. (2014). Biochemical screening and PTEN mutation analysis in individuals with autism spectrum disorders and macrocephaly. *European Journal of Human Genetics*, *22*(2), 273–276. https://doi.org/10.1038/ejhg.2013.114

Hoerder-Suabedissen, A., & Molnár, Z. (2013). Molecular diversity of early-born subplate neurons. *Cerebral Cortex*, *23*(6), 1473–1483. https://doi.org/10.1093/cercor/bhs137

Hoerder-Suabedissen, A., Hayashi, S., Upton, L., Nolan, Z., Casas-Torremocha, D., Grant, E., Viswanathan, S., Kanold, P. O., Clasca, F., Kim, Y., & Molnár, Z. (2018). Subset of cortical layer 6b neurons selectively innervates higher order thalamic nuclei in mice. *Cerebral Cortex*, *28*(5), 1882–1897. https://doi.org/10.1093/cercor/bhy036

Hoerder-Suabedissen, A., Korrell, K. V., Hayashi, S., Jeans, A., Ramirez, D. M. O., Grant, E., Christian, H. C., Kavalali, E. T., Wilson, M. C., & Molnár, Z. (2019). Cell-Specific Loss of SNAP25 from Cortical Projection Neurons Allows Normal Development but Causes Subsequent Neurodegeneration. *Cerebral Cortex*, *29*(5), 2148–2159. https://doi.org/10.1093/cercor/bhy127

Hoerder-Suabedissen, A., Oeschger, F. M., Krishnan, M. L., Belgard, T. G., Wang, W. Z., Lee, S., Webber, C., Petretto, E., Edwards, A. D., & Molnár, Z. (2013). Expression profiling of mouse subplate reveals

a dynamic gene network and disease association with autism and schizophrenia. *Proceedings of the National Academy of Sciences of the United States of America*, *110*(9), 3555–3560. https://doi.org/10.1073/pnas.1218510110

Hoerder-Suabedissen, A., Wang, W. Z., Lee, S., Davies, K. E., Goffinet, A. M., Rakić, S., Parnavelas, J., Reim, K., Nicolić, M., Paulsen, O., & Molnár, Z. (2009). Novel markers reveal subpopulations of subplate neurons in the murine cerebral cortex. *Cerebral Cortex*, *19*(8), 1738–1750. https://doi.org/10.1093/cercor/bhn195

Honoré, E., Khlaifia, A., Bosson, A., & Lacaille, J.-C. (2021). Hippocampal Somatostatin Interneurons, Long-Term Synaptic Plasticity and Memory. *Frontiers in Neural Circuits*, *15*, 687558. https://doi.org/10.3389/fncir.2021.687558

Hsu, R., Schofield, C. M., Dela Cruz, C. G., Jones-Davis, D. M., Blelloch, R., & Ullian, E. M. (2012). Loss of microRNAs in pyramidal neurons leads to specific changes in inhibitory synaptic transmission in the prefrontal cortex. *Molecular and Cellular Neurosciences*, *50*(3–4), 283–292. https://doi.org/10.1016/j.mcn.2012.06.002

Hu, H., Gan, J., & Jonas, P. (2014). Fast-spiking, parvalbumin^{+} GABAergic interneurons: from cellular design to microcircuit function. *Science*, *345*(6196), 1255263. https://doi.org/10.1126/science.1255263

Huang, W.-C., Chen, Y., & Page, D. T. (2016). Hyperconnectivity of prefrontal cortex to amygdala projections in a mouse model of macrocephaly/autism syndrome. *Nature Communications*, *7*, 13421. https://doi.org/10.1038/ncomms13421

Ikonomidou, C., Bosch, F., Miksa, M., Bittigau, P., Vöckler, J., Dikranian, K., Tenkova, T. I., Stefovska, V., Turski, L., & Olney, J. W. (1999). Blockade of NMDA receptors and apoptotic neurodegeneration in the developing brain. *Science*, *283*(5398), 70–74. https://doi.org/10.1126/science.283.5398.70

In, J., & Lee, S. (2017). Statistical data presentation. *Korean Journal of Anesthesiology*, *70*(3), 267–276. https://doi.org/10.4097/kjae.2017.70.3.267

Jeans, A. F., Oliver, P. L., Johnson, R., Capogna, M., Vikman, J., Molnár, Z., Babbs, A., Partridge, C. J., Salehi, A., Bengtsson, M., Eliasson, L., Rorsman, P., & Davies, K. E. (2007). A dominant mutation in Snap25 causes impaired vesicle trafficking, sensorimotor gating, and ataxia in the blind-drunk mouse. *Proceedings of the National Academy of Sciences of the United States of America*, *104*(7), 2431–2436. https://doi.org/10.1073/pnas.0610222104

Jiang, C., Wang, X., Le, Q., Liu, P., Liu, C., Wang, Z., He, G., Zheng, P., Wang, F., & Ma, L. (2021). Morphine coordinates SST and PV interneurons in the prelimbic cortex to disinhibit pyramidal neurons and enhance reward. *Molecular Psychiatry*, *26*(4), 1178–1193. https://doi.org/10.1038/s41380-019-0480-7

Jiang, L., O'Leary, C., Kim, H. A., Parish, C. L., Massalas, J., Waddington, J. L., Ehrlich, M. E., Schütz, G., Gantois, I., Lawrence, A. J., & Drago, J. (2015). Motor and behavioral phenotype in conditional mutants with targeted ablation of cortical D1 dopamine receptor-expressing cells. *Neurobiology of Disease*, *76*, 137–158. https://doi.org/10.1016/j.nbd.2015.02.006

Juarez, P., & Martínez Cerdeño, V. (2022). Parvalbumin and parvalbumin chandelier interneurons in autism and other psychiatric disorders. *Frontiers in Psychiatry*, *13*, 913550. https://doi.org/10.3389/fpsyt.2022.913550

Kanatani, S., Yozu, M., Tabata, H., & Nakajima, K. (2008). COUP-TFII is preferentially expressed in the caudal ganglionic eminence and is involved in the caudal migratory stream. *The Journal of Neuroscience*, *28*(50), 13582–13591. https://doi.org/10.1523/JNEUROSCI.2132-08.2008

Kanold, P. O., & Luhmann, H. J. (2010). The subplate and early cortical circuits. *Annual Review of Neuroscience*, *33*, 23–48. https://doi.org/10.1146/annurev-neuro-060909-153244

Kanold, P. O., & Shatz, C. J. (2006). Subplate neurons regulate maturation of cortical inhibition and outcome of ocular dominance plasticity. *Neuron*, *51*(5), 627–638. https://doi.org/10.1016/j.neuron.2006.07.008

Karagiannis, A., Gallopin, T., Dávid, C., Battaglia, D., Geoffroy, H., Rossier, J., Hillman, E. M. C., Staiger, J. F., & Cauli, B. (2009). Classification of NPY-expressing neocortical interneurons. *The Journal of Neuroscience*, *29*(11), 3642–3659. https://doi.org/10.1523/JNEUROSCI.0058-09.2009

Katz, L. C., & Shatz, C. J. (1996). Synaptic activity and the construction of cortical circuits. *Science*, *274*(5290), 1133–1138. https://doi.org/10.1126/science.274.5290.1133

Kawaguchi, Y. (2017). Pyramidal cell subtypes and their synaptic connections in layer 5 of rat frontal cortex. *Cerebral Cortex*, *27*(12), 5755–5771. https://doi.org/10.1093/cercor/bhx252

Kazdoba, T. M., Sunnen, C. N., Crowell, B., Lee, G. H., Anderson, A. E., & D'Arcangelo, G. (2012). Development and characterization of NEX- Pten, a novel forebrain excitatory neuron-specific knockout mouse. *Developmental Neuroscience*, *34*(2–3), 198–209. https://doi.org/10.1159/000337229

Keijser, J., & Sprekeler, H. (2023). Cortical interneurons: fit for function and fit to function? Evidence from development and evolution. *Frontiers in Neural Circuits*, *17*, 1172464. https://doi.org/10.3389/fncir.2023.1172464

Kepecs, A., & Fishell, G. (2014). Interneuron cell types are fit to function. *Nature*, *505*(7483), 318–326. https://doi.org/10.1038/nature12983

Kessaris, N. (2022). Human cortical interneuron development unraveled. *Science*, *375*(6579), 383–384. https://doi.org/10.1126/science.abn6333

Kessaris, N., & Denaxa, M. (2023). Cortical interneuron specification and diversification in the era of big data. *Current Opinion in Neurobiology*, *80*, 102703. https://doi.org/10.1016/j.conb.2023.102703

Kessaris, N., Fogarty, M., Iannarelli, P., Grist, M., Wegner, M., & Richardson, W. D. (2006). Competing waves of oligodendrocytes in the forebrain and postnatal elimination of an embryonic lineage. *Nature Neuroscience*, *9*(2), 173–179. https://doi.org/10.1038/nn1620

Kessaris, N., Magno, L., Rubin, A. N., & Oliveira, M. G. (2014). Genetic programs controlling cortical interneuron fate. *Current Opinion in Neurobiology*, *26*(100), 79–87. https://doi.org/10.1016/j.conb.2013.12.012

Killackey, H. P., & Sherman, S. M. (2003). Corticothalamic projections from the rat primary somatosensory cortex. *The Journal of Neuroscience*, *23*(19), 7381–7384. https://doi.org/10.1523/JNEUROSCI.23-19-07381.2003

Kim, E. J., Juavinett, A. L., Kyubwa, E. M., Jacobs, M. W., & Callaway, E. M. (2015). Three Types of Cortical Layer 5 Neurons That Differ in Brain-wide Connectivity and Function. *Neuron*, *88*(6), 1253–1267. https://doi.org/10.1016/j.neuron.2015.11.002

Kofuji, T., Fujiwara, T., Sanada, M., Mishima, T., & Akagawa, K. (2014). HPC-1/syntaxin 1A and syntaxin 1B play distinct roles in neuronal survival. *Journal of Neurochemistry*, *130*(4), 514–525. https://doi.org/10.1111/jnc.12722

Kolb, B., Teskey, G. C., & Gibb, R. (2010). Factors influencing cerebral plasticity in the normal and injured brain. *Frontiers in Human Neuroscience*, *4*, 204. https://doi.org/10.3389/fnhum.2010.00204

Kon, K., Ode, K. L., Mano, T., Fujishima, H., Takahashi, R. R., Tone, D., Shimizu, C., Shiono, S., Yada, S., Matsuzawa, K., Yoshida, S. Y., Yoshida Garçon, J., Kaneko, M., Shinohara, Y., Yamada, R. G., Shi, S., Miyamichi, K., Sumiyama, K., Kiyonari, H., … Ueda, H. R. (2024). Cortical parvalbumin neurons are responsible for homeostatic sleep rebound through CaMKII activation. *Nature Communications*, *15*(1), 6054. https://doi.org/10.1038/s41467-024-50168-5

Kreis, P., Leondaritis, G., Lieberam, I., & Eickholt, B. J. (2014). Subcellular targeting and dynamic regulation of PTEN: implications for neuronal cells and neurological disorders. *Frontiers in Molecular Neuroscience*, *7*, 23. https://doi.org/10.3389/fnmol.2014.00023

Kriegstein, A. R., & Noctor, S. C. (2004). Patterns of neuronal migration in the embryonic cortex. *Trends in Neurosciences*, *27*(7), 392–399. https://doi.org/10.1016/j.tins.2004.05.001

Krone, L. B., Yamagata, T., Blanco-Duque, C., Guillaumin, M. C. C., Kahn, M. C., van der Vinne, V., McKillop, L. E., Tam, S. K. E., Peirson, S. N., Akerman, C. J., Hoerder-Suabedissen, A., Molnár, Z., &

Vyazovskiy, V. V. (2021). A role for the cortex in sleep-wake regulation. *Nature Neuroscience*, *24*(9), 1210–1215. https://doi.org/10.1038/s41593-021-00894-6

Kroon, T., Sanalidou, S., Maeso, P., Garces, T., Yang, H., & Rico, B. (2024). Activity-dependent expression of *Fezf2* regulates inhibitory synapse formation in pyramidal cells. *BioRxiv*. https://doi.org/10.1101/2024.01.11.575171

Kuramoto, E., Tanaka, Y. R., Hioki, H., Goto, T., & Kaneko, T. (2022). Local Connections of Pyramidal Neurons to Parvalbumin-Producing Interneurons in Motor-Associated Cortical Areas of Mice. *ENeuro*, *9*(1). https://doi.org/10.1523/ENEURO.0567-20.2021

Kwok, J. C. F., Warren, P., & Fawcett, J. W. (2012). Chondroitin sulfate: a key molecule in the brain matrix. *The International Journal of Biochemistry & Cell Biology*, *44*(4), 582–586. https://doi.org/10.1016/j.biocel.2012.01.004

Kwon, C.-H., Luikart, B. W., Powell, C. M., Zhou, J., Matheny, S. A., Zhang, W., Li, Y., Baker, S. J., & Parada, L. F. (2006). Pten regulates neuronal arborization and social interaction in mice. *Neuron*, *50*(3), 377–388. https://doi.org/10.1016/j.neuron.2006.03.023

Laplante, M., & Sabatini, D. M. (2012). mTOR signaling in growth control and disease. *Cell*, *149*(2), 274–293. https://doi.org/10.1016/j.cell.2012.03.017

Larsen, B., Sydnor, V. J., Keller, A. S., Yeo, B. T. T., & Satterthwaite, T. D. (2023). A critical period plasticity framework for the sensorimotor-association axis of cortical neurodevelopment. *Trends in Neurosciences*, *46*(10), 847–862. https://doi.org/10.1016/j.tins.2023.07.007

Lavdas, A. A., Grigoriou, M., Pachnis, V., & Parnavelas, J. G. (1999). The medial ganglionic eminence gives rise to a population of early neurons in the developing cerebral cortex. *The Journal of Neuroscience*, *19*(18), 7881–7888. https://doi.org/10.1523/JNEUROSCI.19-18-07881.1999

Le Moine, C., & Gaspar, P. (1998). Subpopulations of cortical GABAergic interneurons differ by their expression of D1 and D2 dopamine receptor subtypes. *Molecular Brain Research*, *58*(1–2), 231–236. https://doi.org/10.1016/S0169-328X(98)00118-1

Lee, S. H., Rosenmund, C., Schwaller, B., & Neher, E. (2000). Differences in Ca2+ buffering properties between excitatory and inhibitory hippocampal neurons from the rat. *The Journal of Physiology*, *525 Pt 2*(Pt 2), 405–418. https://doi.org/10.1111/j.1469-7793.2000.t01-3-00405.x

Lee, S., & Lee, D. K. (2018). What is the proper way to apply the multiple comparison test? *Korean Journal of Anesthesiology*, *71*(5), 353–360. https://doi.org/10.4097/kja.d.18.00242

Leighton, A. H., Cheyne, J. E., Houwen, G. J., Maldonado, P. P., De Winter, F., Levelt, C. N., & Lohmann, C. (2021). Somatostatin interneurons restrict cell recruitment to retinally driven spontaneous activity in the developing cortex. *Cell Reports*, *36*(1), 109316. https://doi.org/10.1016/j.celrep.2021.109316

Leslie, J. H., & Nedivi, E. (2011). Activity-regulated genes as mediators of neural circuit plasticity. *Progress in Neurobiology*, *94*(3), 223–237. https://doi.org/10.1016/j.pneurobio.2011.05.002

Leslie, N. R., & Longy, M. (2016). Inherited PTEN mutations and the prediction of phenotype. *Seminars in Cell & Developmental Biology*, *52*, 30–38. https://doi.org/10.1016/j.semcdb.2016.01.030

Letinic, K., Zoncu, R., & Rakic, P. (2002). Origin of GABAergic neurons in the human neocortex. *Nature*, *417*(6889), 645–649. https://doi.org/10.1038/nature00779

Li, L., Ji, X., Liang, F., Li, Y., Xiao, Z., Tao, H. W., & Zhang, L. I. (2014). A feedforward inhibitory circuit mediates lateral refinement of sensory representation in upper layer 2/3 of mouse primary auditory cortex. *The Journal of Neuroscience*, *34*(41), 13670–13683. https://doi.org/10.1523/JNEUROSCI.1516-14.2014

Li, X., Wu, X., Lu, T., Kuang, C., Si, Y., Zheng, W., Li, Z., & Xue, Y. (2024). Perineuronal nets in the CNS: architects of memory and potential therapeutic target in neuropsychiatric disorders. *International Journal of Molecular Sciences*, *25*(6). https://doi.org/10.3390/ijms25063412

Lim, L., Mi, D., Llorca, A., & Marín, O. (2018). Development and functional diversification of cortical interneurons. *Neuron*, *100*(2), 294–313. https://doi.org/10.1016/j.neuron.2018.10.009

Lin, X., Cyrus, N., Avila, B., Holmes, T. C., & Xu, X. (2023). Hippocampal CA3 inhibitory neurons receive extensive noncanonical synaptic inputs from CA1 and subicular complex. *The Journal of Comparative Neurology*, *531*(13), 1333–1347. https://doi.org/10.1002/cne.25510

Lin, Y., Bloodgood, B. L., Hauser, J. L., Lapan, A. D., Koon, A. C., Kim, T.-K., Hu, L. S., Malik, A. N., & Greenberg, M. E. (2008). Activity-dependent regulation of inhibitory synapse development by Npas4. *Nature*, *455*(7217), 1198–1204. https://doi.org/10.1038/nature07319

Llorca, A., & Deogracias, R. (2022). Origin, development, and synaptogenesis of cortical interneurons. *Frontiers in Neuroscience*, *16*, 929469. https://doi.org/10.3389/fnins.2022.929469

Lodato, S., Rouaux, C., Quast, K. B., Jantrachotechatchawan, C., Studer, M., Hensch, T. K., & Arlotta, P. (2011). Excitatory projection neuron subtypes control the distribution of local inhibitory interneurons in the cerebral cortex. *Neuron*, *69*(4), 763–779. https://doi.org/10.1016/j.neuron.2011.01.015

Lodge, D. J., Behrens, M. M., & Grace, A. A. (2009). A loss of parvalbumin-containing interneurons is associated with diminished oscillatory activity in an animal model of schizophrenia. *The Journal of Neuroscience*, *29*(8), 2344–2354. https://doi.org/10.1523/JNEUROSCI.5419-08.2009

Lois, C., & Alvarez-Buylla, A. (1994). Long-distance neuronal migration in the adult mammalian brain. *Science*, *264*(5162), 1145–1148. https://doi.org/10.1126/science.8178174

Lois, C., García-Verdugo, J. M., & Alvarez-Buylla, A. (1996). Chain migration of neuronal precursors. *Science*, *271*(5251), 978–981. https://doi.org/10.1126/science.271.5251.978

López-Bendito, G., Sturgess, K., Erdélyi, F., Szabó, G., Molnár, Z., & Paulsen, O. (2004). Preferential origin and layer destination of GAD65-GFP cortical interneurons. *Cerebral Cortex*, *14*(10), 1122–1133. https://doi.org/10.1093/cercor/bhh072

Lu, J., Tucciarone, J., Lin, Y., & Huang, Z. J. (2014). Input-specific maturation of synaptic dynamics of parvalbumin interneurons in primary visual cortex. *Proceedings of the National Academy of Sciences of the United States of America*, *111*(47), 16895–16900. https://doi.org/10.1073/pnas.1400694111

Luhmann, H. J., & Khazipov, R. (2018). Neuronal activity patterns in the developing barrel cortex. *Neuroscience*, *368*, 256–267. https://doi.org/10.1016/j.neuroscience.2017.05.025

Luhmann, H. J., Kirischuk, S., & Kilb, W. (2018). The superior function of the subplate in early neocortical development. *Frontiers in Neuroanatomy*, *12*, 97. https://doi.org/10.3389/fnana.2018.00097

Luhmann, H. J., Kirischuk, S., Sinning, A., & Kilb, W. (2014). Early GABAergic circuitry in the cerebral cortex. *Current Opinion in Neurobiology*, *26*, 72–78. https://doi.org/10.1016/j.conb.2013.12.014

Luhmann, H. J., Sinning, A., Yang, J.-W., Reyes-Puerta, V., Stüttgen, M. C., Kirischuk, S., & Kilb, W. (2016). Spontaneous Neuronal Activity in Developing Neocortical Networks: From Single Cells to Large-Scale Interactions. *Frontiers in Neural Circuits*, *10*, 40. https://doi.org/10.3389/fncir.2016.00040

Luo, J., Manning, B. D., & Cantley, L. C. (2003). Targeting the PI3K-Akt pathway in human cancer: rationale and promise. *Cancer Cell*, *4*(4), 257–262. https://doi.org/10.1016/s1535-6108(03)00248-4

Lyu, J., Nagarajan, R., Kambali, M., Wang, M., & Rudolph, U. (2023). Selective inhibition of somatostatin-positive dentate hilar interneurons induces age-related cellular changes and cognitive dysfunction. *PNAS Nexus*, *2*(5), pgad134. https://doi.org/10.1093/pnasnexus/pgad134

Magno, L., Asgarian, Z., Pendolino, V., Velona, T., Mackintosh, A., Lee, F., Stryjewska, A., Zimmer, C., Guillemot, F., Farrant, M., Clark, B., & Kessaris, N. (2021). Transient developmental imbalance of cortical interneuron subtypes presages long-term changes in behavior. *Cell Reports*, *35*(11), 109249. https://doi.org/10.1016/j.celrep.2021.109249

Malik, R., Pai, E. L.-L., Rubin, A. N., Stafford, A. M., Angara, K., Minasi, P., Rubenstein, J. L., Sohal, V. S., & Vogt, D. (2019). Tsc1 represses parvalbumin expression and fast-spiking properties in somatostatin lineage cortical interneurons. *Nature Communications*, *10*(1), 4994. https://doi.org/10.1038/s41467-019-12962-4

Margeta-Mitrovic, M., Mitrovic, I., Riley, R. C., Jan, L. Y., & Basbaum, A. I. (1999). Immunohistochemical localization of GABAB receptors in the rat central nervous system. *Journal of Comparative Neurology*.

Marín, O, & Rubenstein, J. L. (2001). A long, remarkable journey: tangential migration in the telencephalon. *Nature Reviews. Neuroscience*, *2*(11), 780–790. https://doi.org/10.1038/35097509

Marín, O, Yaron, A., Bagri, A., Tessier-Lavigne, M., & Rubenstein, J. L. (2001). Sorting of striatal and cortical interneurons regulated by semaphorin-neuropilin interactions. *Science*, *293*(5531), 872–875. https://doi.org/10.1126/science.1061891

Marin, O., Anderson, S. A., & Rubenstein, J. L. (2000). Origin and molecular specification of striatal interneurons. *The Journal of Neuroscience*, *20*(16), 6063–6076. https://doi.org/10.1523/JNEUROSCI.20-16-06063.2000

Marín, Oscar, & Rubenstein, J. L. R. (2003). Cell migration in the forebrain. *Annual Review of Neuroscience*, *26*, 441–483. https://doi.org/10.1146/annurev.neuro.26.041002.131058

Marin-Padilla, M. (1971). Early prenatal ontogenesis of the cerebral cortex (neocortex) of the cat (Felis domestica). A Golgi study. I. The primordial neocortical organization. *Zeitschrift Fur Anatomie Und Entwicklungsgeschichte*, *134*(2), 117–145. https://doi.org/10.1007/BF00519296

Marin-Padilla, M., & Marin-Padilla, T. M. (1982). Origin, prenatal development and structural organization of layer I of the human cerebral (motor) cortex. A Golgi study. *Anatomy and Embryology*, *164*(2), 161–206. https://doi.org/10.1007/BF00318504

Markram, H., Toledo-Rodriguez, M., Wang, Y., Gupta, A., Silberberg, G., & Wu, C. (2004). Interneurons of the neocortical inhibitory system. *Nature Reviews. Neuroscience*, *5*(10), 793–807. https://doi.org/10.1038/nrn1519

Marques-Smith, A., Lyngholm, D., Kaufmann, A.-K., Stacey, J. A., Hoerder-Suabedissen, A., Becker, E. B. E., Wilson, M. C., Molnár, Z., & Butt, S. J. B. (2016). A transient translaminar gabaergic interneuron circuit connects thalamocortical recipient layers in neonatal somatosensory cortex. *Neuron*, *89*(3), 536–549. https://doi.org/10.1016/j.neuron.2016.01.015

Martin, S. C., Russek, S. J., & Farb, D. H. (2001). Human GABABR genomic structure: evidence for splice variants in GABABR1 but not GABABR2. *Gene*, *278*(1–2), 63–79. https://doi.org/10.1016/S0378-1119(01)00678-3

Martineau, M., Guzman, R. E., Fahlke, C., & Klingauf, J. (2017). VGLUT1 functions as a glutamate/proton exchanger with chloride channel activity in hippocampal glutamatergic synapses. *Nature Communications*, *8*(1), 2279. https://doi.org/10.1038/s41467-017-02367-6

Martinetti, L. E., Autio, D. M., & Crandall, S. R. (2024). Motor control of distinct layer 6 corticothalamic feedback circuits. *ENeuro*, *11*(7). https://doi.org/10.1523/ENEURO.0255-24.2024

Martínez-Cerdeño, V., & Noctor, S. C. (2018). Neural progenitor cell terminology. *Frontiers in Neuroanatomy*, *12*, 104. https://doi.org/10.3389/fnana.2018.00104

Martini, M., De Santis, M. C., Braccini, L., Gulluni, F., & Hirsch, E. (2014). PI3K/AKT signaling pathway and cancer: an updated review. *Annals of Medicine*, *46*(6), 372–383. https://doi.org/10.3109/07853890.2014.912836

Marx, M., Qi, G., Hanganu-Opatz, I. L., Kilb, W., Luhmann, H. J., & Feldmeyer, D. (2017). Neocortical Layer 6B as a Remnant of the Subplate - A Morphological Comparison. *Cerebral Cortex*, *27*(2), 1011–1026. https://doi.org/10.1093/cercor/bhv279

Maya-Vetencourt, J. F. (2013). Activity-dependent NPAS4 expression and the regulation of gene programs underlying plasticity in the central nervous system. *Neural Plasticity*, *2013*, 683909. https://doi.org/10.1155/2013/683909

McBain, C. J., & Fisahn, A. (2001). Interneurons unbound. *Nature Reviews. Neuroscience*, *2*(1), 11–23. https://doi.org/10.1038/35049047

Meng, X., Solarana, K., Bowen, Z., Liu, J., Nagode, D. A., Sheikh, A., Winkowski, D. E., Kao, J. P. Y., & Kanold, P. O. (2020). Transient subgranular hyperconnectivity to L2/3 and enhanced pairwise correlations during the critical period in the mouse auditory cortex. *Cerebral Cortex*, *30*(3), 1914–1930. https://doi.org/10.1093/cercor/bhz213

Meyer, G., Soria, J. M., Martínez-Galán, J. R., Martín-Clemente, B., & Fairén, A. (1998). Different origins and developmental histories of transient neurons in the marginal zone of the fetal and neonatal rat cortex. *Journal of Comparative Neurology*.

Mi, D., Li, Z., Lim, L., Li, M., Moissidis, M., Yang, Y., Gao, T., Hu, T. X., Pratt, T., Price, D. J., Sestan, N., & Marín, O. (2018). Early emergence of cortical interneuron diversity in the mouse embryo. *Science*, *360*(6384), 81–85. https://doi.org/10.1126/science.aar6821

Micheva, K. D., Kiraly, M., Perez, M. M., & Madison, D. V. (2021). Extensive Structural Remodeling of the Axonal Arbors of Parvalbumin Basket Cells during Development in Mouse Neocortex. *The Journal of Neuroscience*, *41*(45), 9326–9339. https://doi.org/10.1523/JNEUROSCI.0871-21.2021

Miller, M. W. (1985). Cogeneration of retrogradely labeled corticocortical projection and GABA-immunoreactive local circuit neurons in cerebral cortex. *Brain Research*, *355*(2), 187–192. https://doi.org/10.1016/0165-3806(85)90040-9

Mishima, T., Fujiwara, T., Kofuji, T., & Akagawa, K. (2012). Impairment of catecholamine systems during induction of long-term potentiation at hippocampal CA1 synapses in HPC-1/syntaxin 1A knock-out mice. *The Journal of Neuroscience*, *32*(1), 381–389. https://doi.org/10.1523/JNEUROSCI.2911-11.2012

Mishima, T., Fujiwara, T., Sanada, M., Kofuji, T., Kanai-Azuma, M., & Akagawa, K. (2014). Syntaxin 1B, but not syntaxin 1A, is necessary for the regulation of synaptic vesicle exocytosis and of the readily

releasable pool at central synapses. *Plos One*, *9*(2), e90004. https://doi.org/10.1371/journal.pone.0090004

Miyamae, T., Chen, K., Lewis, D. A., & Gonzalez-Burgos, G. (2017). Distinct Physiological Maturation of Parvalbumin-Positive Neuron Subtypes in Mouse Prefrontal Cortex. *The Journal of Neuroscience*, *37*(19), 4883–4902. https://doi.org/10.1523/JNEUROSCI.3325-16.2017

Miyoshi, G., & Fishell, G. (2011). GABAergic interneuron lineages selectively sort into specific cortical layers during early postnatal development. *Cerebral Cortex*, *21*(4), 845–852. https://doi.org/10.1093/cercor/bhq155

Miyoshi, G., Butt, S. J. B., Takebayashi, H., & Fishell, G. (2007). Physiologically distinct temporal cohorts of cortical interneurons arise from telencephalic Olig2-expressing precursors. *The Journal of Neuroscience*, *27*(29), 7786–7798. https://doi.org/10.1523/JNEUROSCI.1807-07.2007

Miyoshi, G., Hjerling-Leffler, J., Karayannis, T., Sousa, V. H., Butt, S. J. B., Battiste, J., Johnson, J. E., Machold, R. P., & Fishell, G. (2010). Genetic fate mapping reveals that the caudal ganglionic eminence produces a large and diverse population of superficial cortical interneurons. *The Journal of Neuroscience*, *30*(5), 1582–1594. https://doi.org/10.1523/JNEUROSCI.4515-09.2010

Moberg, S., & Takahashi, N. (2022). Neocortical layer 5 subclasses: From cellular properties to roles in behavior. *Frontiers in Synaptic Neuroscience*, *14*, 1006773. https://doi.org/10.3389/fnsyn.2022.1006773

Mohammed, H., & Hollis, E. R. (2018). Cortical reorganization of sensorimotor systems and the role of intracortical circuits after spinal cord injury. *Neurotherapeutics*, *15*(3), 588–603. https://doi.org/10.1007/s13311-018-0638-z

Molnár, Z, Adams, R., & Blakemore, C. (1998). Mechanisms underlying the early establishment of thalamocortical connections in the rat. *The Journal of Neuroscience*, *18*(15), 5723–5745. https://doi.org/10.1523/JNEUROSCI.18-15-05723.1998

Molnár, Z., & Cheung, A. F. P. (2006). Towards the classification of subpopulations of layer V pyramidal projection neurons. *Neuroscience Research*, *55*(2), 105–115. https://doi.org/10.1016/j.neures.2006.02.008

Molnár, Zoltán, López-Bendito, G., Small, J., Partridge, L. D., Blakemore, C., & Wilson, M. C. (2002). Normal development of embryonic thalamocortical connectivity in the absence of evoked synaptic activity. *The Journal of Neuroscience*, *22*(23), 10313–10323. https://doi.org/10.1523/JNEUROSCI.22-23-10313.2002

Molnár, Zoltán, Luhmann, H. J., & Kanold, P. O. (2020). Transient cortical circuits match spontaneous and sensory-driven activity during development. *Science*, *370*(6514). https://doi.org/10.1126/science.abb2153

Molyneaux, B. J., Arlotta, P., Hirata, T., Hibi, M., & Macklis, J. D. (2005). Fezl is required for the birth and specification of corticospinal motor neurons. *Neuron*, *47*(6), 817–831. https://doi.org/10.1016/j.neuron.2005.08.030

Molyneaux, B. J., Arlotta, P., Menezes, J. R. L., & Macklis, J. D. (2007). Neuronal subtype specification in the cerebral cortex. *Nature Reviews. Neuroscience*, *8*(6), 427–437. https://doi.org/10.1038/nrn2151

Nadarajah, B., Brunstrom, J. E., Grutzendler, J., Wong, R. O., & Pearlman, A. L. (2001). Two modes of radial migration in early development of the cerebral cortex. *Nature Neuroscience*, *4*(2), 143–150. https://doi.org/10.1038/83967

Naka, A., & Adesnik, H. (2016). Inhibitory circuits in cortical layer 5. *Frontiers in Neural Circuits*, *10*, 35. https://doi.org/10.3389/fncir.2016.00035

Noctor, S C, Flint, A. C., Weissman, T. A., Dammerman, R. S., & Kriegstein, A. R. (2001). Neurons derived from radial glial cells establish radial units in neocortex. *Nature*, *409*(6821), 714–720. https://doi.org/10.1038/35055553

Noctor, Stephen C, Martínez-Cerdeño, V., Ivic, L., & Kriegstein, A. R. (2004). Cortical neurons arise in symmetric and asymmetric division zones and migrate through specific phases. *Nature Neuroscience*, *7*(2), 136–144. https://doi.org/10.1038/nn1172

Ohtaka-Maruyama, C., Okamoto, M., Endo, K., Oshima, M., Kaneko, N., Yura, K., Okado, H., Miyata, T., & Maeda, N. (2018). Synaptic transmission from subplate neurons controls radial migration of neocortical neurons. *Science*, *360*(6386), 313–317. https://doi.org/10.1126/science.aar2866

Ojima, H. (1994). Terminal morphology and distribution of corticothalamic fibers originating from layers 5 and 6 of cat primary auditory cortex. *Cerebral Cortex*, *4*(6), 646–663. https://doi.org/10.1093/cercor/4.6.646

Oohashi, T., Edamatsu, M., Bekku, Y., & Carulli, D. (2015). The hyaluronan and proteoglycan link proteins: Organizers of the brain extracellular matrix and key molecules for neuronal function and plasticity. *Experimental Neurology*, *274*(Pt B), 134–144. https://doi.org/10.1016/j.expneurol.2015.09.010

Parnavelas, J. G. (2002). The origin of cortical neurons. *Brazilian Journal of Medical and Biological Research*, *35*(12), 1423–1429. https://doi.org/10.1590/s0100-879x2002001200003

Patton, M. H., Blundon, J. A., & Zakharenko, S. S. (2019). Rejuvenation of plasticity in the brain: opening the critical period. *Current Opinion in Neurobiology*, *54*, 83–89. https://doi.org/10.1016/j.conb.2018.09.003

Patz, S., Grabert, J., Gorba, T., Wirth, M. J., & Wahle, P. (2004). Parvalbumin expression in visual cortical interneurons depends on neuronal activity and TrkB ligands during an Early period of postnatal development. *Cerebral Cortex*, *14*(3), 342–351. https://doi.org/10.1093/cercor/bhg132

Paul, A., Crow, M., Raudales, R., He, M., Gillis, J., & Huang, Z. J. (2017). Transcriptional architecture of synaptic communication delineates GABAergic neuron identity. *Cell*, *171*(3), 522-539.e20. https://doi.org/10.1016/j.cell.2017.08.032

Pedrosa, L. R. R., Coimbra, G. D. S., Corrêa, M. G., Dias, I. A., & Bahia, C. P. (2022). Time window of the critical period for neuroplasticity in S1, V1, and A1 sensory areas of small rodents: A systematic review. *Frontiers in Neuroanatomy*, *16*, 763245. https://doi.org/10.3389/fnana.2022.763245

Phillips, J. M., Fish, L. R., Kambi, N. A., Redinbaugh, M. J., Mohanta, S., Kecskemeti, S. R., & Saalmann, Y. B. (2019). Topographic organization of connections between prefrontal cortex and mediodorsal thalamus: Evidence for a general principle of indirect thalamic pathways between directly connected cortical areas. *Neuroimage*, *189*, 832–846. https://doi.org/10.1016/j.neuroimage.2019.01.078

Pizzorusso, T., Medini, P., Berardi, N., Chierzi, S., Fawcett, J. W., & Maffei, L. (2002). Reactivation of ocular dominance plasticity in the adult visual cortex. *Science*, *298*(5596), 1248–1251. https://doi.org/10.1126/science.1072699

Pluta, S. R., Telian, G. I., Naka, A., & Adesnik, H. (2019). Superficial Layers Suppress the Deep Layers to Fine-tune Cortical Coding. *The Journal of Neuroscience*, *39*(11), 2052–2064. https://doi.org/10.1523/JNEUROSCI.1459-18.2018

Podsypanina, K., Ellenson, L. H., Nemes, A., Gu, J., Tamura, M., Yamada, K. M., Cordon-Cardo, C., Catoretti, G., Fisher, P. E., & Parsons, R. (1999). Mutation of Pten/Mmac1 in mice causes neoplasia in multiple organ systems. *Proceedings of the National Academy of Sciences of the United States of America*, *96*(4), 1563–1568. https://doi.org/10.1073/pnas.96.4.1563

Pouchelon, G., Dwivedi, D., Bollmann, Y., Agba, C. K., Xu, Q., Mirow, A. M. C., Kim, S., Qiu, Y., Sevier, E., Ritola, K. D., Cossart, R., & Fishell, G. (2021). The organization and development of cortical interneuron presynaptic circuits are area specific. *Cell Reports*, *37*(6), 109993. https://doi.org/10.1016/j.celrep.2021.109993

Price, D. J., Aslam, S., Tasker, L., & Gillies, K. (1997). Fates of the earliest generated cells in the developing murine neocortex. *Journal of Comparative Neurology*.

Privat, A. (1975). Postnatal gliogenesis in the mammalian brain. *International Review of Cytology*, *40*, 281–323. https://doi.org/10.1016/s0074-7696(08)60955-9

Priya, R., Paredes, M. F., Karayannis, T., Yusuf, N., Liu, X., Jaglin, X., Graef, I., Alvarez-Buylla, A., & Fishell, G. (2018). Activity Regulates Cell Death within Cortical Interneurons through a Calcineurin-Dependent Mechanism. *Cell Reports*, *22*(7), 1695–1709. https://doi.org/10.1016/j.celrep.2018.01.007

Quiquempoix, M., Fayad, S. L., Boutourlinsky, K., Leresche, N., Lambert, R. C., & Bessaih, T. (2018). Layer 2/3 pyramidal neurons control the gain of cortical output. *Cell Reports*, *24*(11), 2799-2807.e4. https://doi.org/10.1016/j.celrep.2018.08.038

Raber, J., Mehta, P. P., Kreifeldt, M., Parsons, L. H., Weiss, F., Bloom, F. E., & Wilson, M. C. (1997). Coloboma hyperactive mutant mice exhibit regional and transmitter-specific deficits in neurotransmission. *Journal of Neurochemistry*, *68*(1), 176–186. https://doi.org/10.1046/j.1471-4159.1997.68010176.x

Rakic, P. (1972). Mode of cell migration to the superficial layers of fetal monkey neocortex. *The Journal of Comparative Neurology*, *145*(1), 61–83. https://doi.org/10.1002/cne.901450105

Raptis, A., Torrejón-Escribano, B., Gómez de Aranda, I., & Blasi, J. (2005). Distribution of synaptobrevin/VAMP 1 and 2 in rat brain. *Journal of Chemical Neuroanatomy*, *30*(4), 201–211. https://doi.org/10.1016/j.jchemneu.2005.08.002

Rouiller, E. M., & Welker, E. (2000). A comparative analysis of the morphology of corticothalamic projections in mammals. *Brain Research Bulletin*, *53*(6), 727–741. https://doi.org/10.1016/S0361-9230(00)00364-6

Roux, C., Aligny, C., Lesueur, C., Girault, V., Brunel, V., Ramdani, Y., Genty, D., Driouich, A., Laquerrière, A., Marret, S., Brasse-Lagnel, C., Gonzalez, B. J., & Bekri, S. (2015). NMDA receptor blockade in the developing cortex induces autophagy-mediated death of immature cortical GABAergic interneurons: An ex vivo and in vivo study in Gad67-GFP mice. *Experimental Neurology*, *267*, 177–193. https://doi.org/10.1016/j.expneurol.2015.02.037

Rovó, Z., Ulbert, I., & Acsády, L. (2012). Drivers of the primate thalamus. *The Journal of Neuroscience*, *32*(49), 17894–17908. https://doi.org/10.1523/JNEUROSCI.2815-12.2012

Ruiz-Montasell, B., Aguado, F., Majó, G., Chapman, E. R., Canals, J. M., Marsal, J., & Blasi, J. (1996). Differential distribution of syntaxin isoforms 1A and 1B in the rat central nervous system. *The*

European Journal of Neuroscience, *8*(12), 2544–2552. https://doi.org/10.1111/j.1460-9568.1996.tb01548.x

Rymar, V. V., & Sadikot, A. F. (2007). Laminar fate of cortical GABAergic interneurons is dependent on both birthdate and phenotype. *The Journal of Comparative Neurology*, *501*(3), 369–380. https://doi.org/10.1002/cne.21250

Sakai, T., Oshima, A., Nozaki, Y., Ida, I., Haga, C., Akiyama, H., Nakazato, Y., & Mikuni, M. (2008). Changes in density of calcium-binding-protein-immunoreactive GABAergic neurons in prefrontal cortex in schizophrenia and bipolar disorder. *Neuropathology*, *28*(2), 143–150. https://doi.org/10.1111/j.1440-1789.2007.00867.x

Scarr, E., Gray, L., Keriakous, D., Robinson, P. J., & Dean, B. (2006). Increased levels of SNAP-25 and synaptophysin in the dorsolateral prefrontal cortex in bipolar I disorder. *Bipolar Disorders*, *8*(2), 133–143. https://doi.org/10.1111/j.1399-5618.2006.00300.x

Scheuer, K. S., Jansson, A. M., Zhao, X., & Jackson, M. B. (2024). Inter and intralaminar excitation of parvalbumin interneurons in mouse barrel cortex. *Plos One*, *19*(6), e0289901. https://doi.org/10.1371/journal.pone.0289901

Scheyltjens, I., & Arckens, L. (2016). The Current Status of Somatostatin-Interneurons in Inhibitory Control of Brain Function and Plasticity. *Neural Plasticity*, *2016*, 8723623. https://doi.org/10.1155/2016/8723623

Schoch, S., Deák, F., Königstorfer, A., Mozhayeva, M., Sara, Y., Südhof, T. C., & Kavalali, E. T. (2001). SNARE function analyzed in synaptobrevin/VAMP knockout mice. *Science*, *294*(5544), 1117–1122. https://doi.org/10.1126/science.1064335

Selten, M., Bernard, C., Hamid, F., Hanusz-Godoy, A., Oozeer, F., Zimmer, C., & Marín, O. (2023). Regulation of parvalbumin interneuron plasticity by neuropeptide-encoding genes. *BioRxiv*. https://doi.org/10.1101/2023.02.03.527010

Sempere-Ferràndez, A., Martínez, S., & Geijo-Barrientos, E. (2019). Synaptic mechanisms underlying the intense firing of neocortical layer 5B pyramidal neurons in response to cortico-cortical inputs. *Brain Structure & Function*, *224*(4), 1403–1416. https://doi.org/10.1007/s00429-019-01842-8

Shin, S., Santi, A., & Huang, S. (2021). Conditional Pten knockout in parvalbumin- or somatostatin-positive neurons sufficiently leads to autism-related behavioral phenotypes. *Molecular Brain*, *14*(1), 24. https://doi.org/10.1186/s13041-021-00731-8

Silva, C. G., Peyre, E., & Nguyen, L. (2019). Cell migration promotes dynamic cellular interactions to control cerebral cortex morphogenesis. *Nature Reviews. Neuroscience*, *20*(6), 318–329. https://doi.org/10.1038/s41583-019-0148-y

Sinclair, L. I., Tayler, H. M., & Love, S. (2015). Synaptic protein levels altered in vascular dementia. *Neuropathology and Applied Neurobiology*, *41*(4), 533–543. https://doi.org/10.1111/nan.12215

Skelton, P. D., Stan, R. V., & Luikart, B. W. (2020). The role of PTEN in neurodevelopment. *Molecular Neuropsychiatry*, *5*(Suppl 1), 60–71. https://doi.org/10.1159/000504782

Song, Y.-H., Yoon, J., & Lee, S.-H. (2021). The role of neuropeptide somatostatin in the brain and its application in treating neurological disorders. *Experimental & Molecular Medicine*, *53*(3), 328–338. https://doi.org/10.1038/s12276-021-00580-4

Southwell, D. G., Paredes, M. F., Galvao, R. P., Jones, D. L., Froemke, R. C., Sebe, J. Y., Alfaro-Cervello, C., Tang, Y., Garcia-Verdugo, J. M., Rubenstein, J. L., Baraban, S. C., & Alvarez-Buylla, A. (2012).

Intrinsically determined cell death of developing cortical interneurons. *Nature*, *491*(7422), 109–113. https://doi.org/10.1038/nature11523

Spencer, T. J., Biederman, J., & Mick, E. (2007). Attention-deficit/hyperactivity disorder: diagnosis, lifespan, comorbidities, and neurobiology. *Journal of Pediatric Psychology*, *32*(6), 631–642. https://doi.org/10.1093/jpepsy/jsm005

Sperow, M., Berry, R. B., Bayazitov, I. T., Zhu, G., Baker, S. J., & Zakharenko, S. S. (2012). Phosphatase and tensin homologue (PTEN) regulates synaptic plasticity independently of its effect on neuronal morphology and migration. *The Journal of Physiology*, *590*(4), 777–792. https://doi.org/10.1113/jphysiol.2011.220236

Spiegel, I., Mardinly, A. R., Gabel, H. W., Bazinet, J. E., Couch, C. H., Tzeng, C. P., Harmin, D. A., & Greenberg, M. E. (2014). Npas4 regulates excitatory-inhibitory balance within neural circuits through cell-type-specific gene programs. *Cell*, *157*(5), 1216–1229. https://doi.org/10.1016/j.cell.2014.03.058

Spreafico, R., Frassoni, C., Arcelli, P., Selvaggio, M., & De Biasi, S. (1995). In situ labeling of apoptotic cell death in the cerebral cortex and thalamus of rats during development. *The Journal of Comparative Neurology*, *363*(2), 281–295. https://doi.org/10.1002/cne.903630209

Sreenivasan, V., Serafeimidou-Pouliou, E., Exposito-Alonso, D., Bercsenyi, K., Bernard, C., Bae, S.-E., Oozeer, F., Hanusz-Godoy, A., Edwards, R. H., & Marín, O. (2022). Input-specific control of interneuron numbers in nascent striatal networks. *Proceedings of the National Academy of Sciences of the United States of America*, *119*(20), e2118430119. https://doi.org/10.1073/pnas.2118430119

Staiger, J. F., Zuschratter, W., Luhmann, H. J., & Schubert, D. (2009). Local circuits targeting parvalbumin-containing interneurons in layer IV of rat barrel cortex. *Brain Structure & Function*, *214*(1), 1–13. https://doi.org/10.1007/s00429-009-0225-5

Stambolic, V., Suzuki, A., de la Pompa, J. L., Brothers, G. M., Mirtsos, C., Sasaki, T., Ruland, J., Penninger, J. M., Siderovski, D. P., & Mak, T. W. (1998). Negative regulation of PKB/Akt-dependent cell survival by the tumor suppressor PTEN. *Cell*, *95*(1), 29–39. https://doi.org/10.1016/s0092-8674(00)81780-8

Steffensen, S. C., Henriksen, S. J., & Wilson, M. C. (1999). Transgenic rescue of SNAP-25 restores dopamine-modulated synaptic transmission in the coloboma mutant. *Brain Research*, *847*(2), 186–195. https://doi.org/10.1016/s0006-8993(99)02023-5

Stogsdill, J. A., Kim, K., Binan, L., Farhi, S. L., Levin, J. Z., & Arlotta, P. (2022). Pyramidal neuron subtype diversity governs microglia states in the neocortex. *Nature*, *608*(7924), 750–756. https://doi.org/10.1038/s41586-022-05056-7

Südhof, T. C. (2013). Neurotransmitter release: the last millisecond in the life of a synaptic vesicle. *Neuron*, *80*(3), 675–690. https://doi.org/10.1016/j.neuron.2013.10.022

Sultan, K. T., Brown, K. N., & Shi, S.-H. (2013). Production and organization of neocortical interneurons. *Frontiers in Cellular Neuroscience*, *7*, 221. https://doi.org/10.3389/fncel.2013.00221

Sun, W., Kim, H., & Moon, Y. (2010). Control of neuronal migration through rostral migration stream in mice. *Anatomy & Cell Biology*, *43*(4), 269–279. https://doi.org/10.5115/acb.2010.43.4.269

Sun, X., & Lin, Y. (2016). Npas4: linking neuronal activity to memory. *Trends in Neurosciences*, *39*(4), 264–275. https://doi.org/10.1016/j.tins.2016.02.003

Sussel, L., Marin, O., Kimura, S., & Rubenstein, J. L. (1999). Loss of Nkx2.1 homeobox gene function results in a ventral to dorsal molecular respecification within the basal telencephalon: evidence for a transformation of the pallidum into the striatum. *Development*, *126*(15), 3359–3370. https://doi.org/10.1242/dev.126.15.3359

Suzuki, A., de la Pompa, J. L., Stambolic, V., Elia, A. J., Sasaki, T., del Barco Barrantes, I., Ho, A., Wakeham, A., Itie, A., Khoo, W., Fukumoto, M., & Mak, T. W. (1998). High cancer susceptibility and embryonic lethality associated with mutation of the PTEN tumor suppressor gene in mice. *Current Biology*, *8*(21), 1169–1178. https://doi.org/10.1016/s0960-9822(07)00488-5

Takahashi, T., Nowakowski, R. S., & Caviness, V. S. (1995). The cell cycle of the pseudostratified ventricular epithelium of the embryonic murine cerebral wall. *The Journal of Neuroscience*, *15*(9), 6046–6057. https://doi.org/10.1523/JNEUROSCI.15-09-06046.1995

Takeuchi, K., Gertner, M. J., Zhou, J., Parada, L. F., Bennett, M. V. L., & Zukin, R. S. (2013). Dysregulation of synaptic plasticity precedes appearance of morphological defects in a Pten conditional knockout mouse model of autism. *Proceedings of the National Academy of Sciences of the United States of America*, *110*(12), 4738–4743. https://doi.org/10.1073/pnas.1222803110

Tamamaki, N., Fujimori, K. E., & Takauji, R. (1997). Origin and route of tangentially migrating neurons in the developing neocortical intermediate zone. *The Journal of Neuroscience*, *17*(21), 8313–8323. https://doi.org/10.1523/JNEUROSCI.17-21-08313.1997

Tanahira, C., Higo, S., Watanabe, K., Tomioka, R., Ebihara, S., Kaneko, T., & Tamamaki, N. (2009). Parvalbumin neurons in the forebrain as revealed by parvalbumin-Cre transgenic mice. *Neuroscience Research*, *63*(3), 213–223. https://doi.org/10.1016/j.neures.2008.12.007

Taniguchi, H., He, M., Wu, P., Kim, S., Paik, R., Sugino, K., Kvitsiani, D., Fu, Y., Lu, J., Lin, Y., Miyoshi, G., Shima, Y., Fishell, G., Nelson, S. B., & Huang, Z. J. (2011). A resource of Cre driver lines for genetic targeting of GABAergic neurons in cerebral cortex. *Neuron*, *71*(6), 995–1013. https://doi.org/10.1016/j.neuron.2011.07.026

Tarabykin, V., Stoykova, A., Usman, N., & Gruss, P. (2001). Cortical upper layer neurons derive from the subventricular zone as indicated by Svet1 gene expression. *Development*, *128*(11), 1983–1993. https://doi.org/10.1242/dev.128.11.1983

Thapar, A., O'Donovan, M., & Owen, M. J. (2005). The genetics of attention deficit hyperactivity disorder. *Human Molecular Genetics*, *14 Spec No. 2*, R275-82. https://doi.org/10.1093/hmg/ddi263

Thompson, P. M., Egbufoama, S., & Vawter, M. P. (2003). SNAP-25 reduction in the hippocampus of patients with schizophrenia. *Progress in Neuro-Psychopharmacology & Biological Psychiatry*, *27*(3), 411–417. https://doi.org/10.1016/S0278-5846(03)00027-7

Torigoe, M., Yamauchi, K., Kimura, T., Uemura, Y., & Murakami, F. (2016). Evidence That the Laminar Fate of LGE/CGE-Derived Neocortical Interneurons Is Dependent on Their Progenitor Domains. *The Journal of Neuroscience*, *36*(6), 2044–2056. https://doi.org/10.1523/JNEUROSCI.3550-15.2016

Tóth, K., & Maglóczky, Z. (2014). The vulnerability of calretinin-containing hippocampal interneurons to temporal lobe epilepsy. *Frontiers in Neuroanatomy*, *8*, 100. https://doi.org/10.3389/fnana.2014.00100

Tran, T., Sundaram, C. P., Bahler, C. D., Eble, J. N., Grignon, D. J., Monn, M. F., Simper, N. B., & Cheng, L. (2015). Correcting the Shrinkage Effects of Formalin Fixation and Tissue Processing for Renal

Tumors: toward Standardization of Pathological Reporting of Tumor Size. *Journal of Cancer*, *6*(8), 759–766. https://doi.org/10.7150/jca.12094

Tremblay, R., Lee, S., & Rudy, B. (2016). Gabaergic interneurons in the neocortex: from cellular properties to circuits. *Neuron*, *91*(2), 260–292. https://doi.org/10.1016/j.neuron.2016.06.033

Tuncdemir, S. N., Wamsley, B., Stam, F. J., Osakada, F., Goulding, M., Callaway, E. M., Rudy, B., & Fishell, G. (2016). Early somatostatin interneuron connectivity mediates the maturation of deep layer cortical circuits. *Neuron*, *89*(3), 521–535. https://doi.org/10.1016/j.neuron.2015.11.020

Urban-Ciecko, J., & Barth, A. L. (2016). Somatostatin-expressing neurons in cortical networks. *Nature Reviews. Neuroscience*, *17*(7), 401–409. https://doi.org/10.1038/nrn.2016.53

Valverde, F., López-Mascaraque, L., Santacana, M., & De Carlos, J. A. (1995). Persistence of early-generated neurons in the rodent subplate: assessment of cell death in neocortex during the early postnatal period. *The Journal of Neuroscience*, *15*(7 Pt 1), 5014–5024. https://doi.org/10.1523/JNEUROSCI.15-07-05014.1995

van Diepen, M. T., & Eickholt, B. J. (2008). Function of PTEN during the formation and maintenance of neuronal circuits in the brain. *Developmental Neuroscience*, *30*(1–3), 59–64. https://doi.org/10.1159/000109852

Vander Haar, E., Lee, S.-I., Bandhakavi, S., Griffin, T. J., & Kim, D.-H. (2007). Insulin signalling to mTOR mediated by the Akt/PKB substrate PRAS40. *Nature Cell Biology*, *9*(3), 316–323. https://doi.org/10.1038/ncb1547

Vanhaesebroeck, B., Guillermet-Guibert, J., Graupera, M., & Bilanges, B. (2010). The emerging mechanisms of isoform-specific PI3K signalling. *Nature Reviews. Molecular Cell Biology*, *11*(5), 329–341. https://doi.org/10.1038/nrm2882

Verhage, M., Maia, A. S., Plomp, J. J., Brussaard, A. B., Heeroma, J. H., Vermeer, H., Toonen, R. F., Hammer, R. E., van den Berg, T. K., Missler, M., Geuze, H. J., & Südhof, T. C. (2000). Synaptic assembly of the brain in the absence of neurotransmitter secretion. *Science*, *287*(5454), 864–869. https://doi.org/10.1126/science.287.5454.864

Viswanathan, S., Sheikh, A., Looger, L. L., & Kanold, P. O. (2017). Molecularly defined subplate neurons project both to thalamocortical recipient layers and thalamus. *Cerebral Cortex*, *27*(10), 4759–4768. https://doi.org/10.1093/cercor/bhw271

Vogt Weisenhorn, D. M., Celio, M. R., & Rickmann, M. (1998). The onset of parvalbumin-expression in interneurons of the rat parietal cortex depends upon extrinsic factor(s). *The European Journal of Neuroscience*, *10*(3), 1027–1036. https://doi.org/10.1046/j.1460-9568.1998.00120.x

Vogt, D., Cho, K. K. A., Lee, A. T., Sohal, V. S., & Rubenstein, J. L. R. (2015). The parvalbumin/somatostatin ratio is increased in Pten mutant mice and by human PTEN ASD alleles. *Cell Reports*, *11*(6), 944–956. https://doi.org/10.1016/j.celrep.2015.04.019

Wagner-Golbs, A., & Luhmann, H. J. (2012). Activity-dependent survival of developing neocortical neurons depends on PI3K signalling. *Journal of Neurochemistry*, *120*(4), 495–501. https://doi.org/10.1111/j.1471-4159.2011.07591.x

Wall, N. R., De La Parra, M., Sorokin, J. M., Taniguchi, H., Huang, Z. J., & Callaway, E. M. (2016). Brain-Wide Maps of Synaptic Input to Cortical Interneurons. *The Journal of Neuroscience*, *36*(14), 4000–4009. https://doi.org/10.1523/JNEUROSCI.3967-15.2016

Wang, Y. S., Qiu, T. Y., Fu, Q., Xiong, S. Q., Wang, Z. Z., Lu, M. F., Yang, J. H., & Hu, Z. Z. (2022). Unravelling biological roles and mechanisms of GABABR on addiction and depression through mood and memory disorders. *Biomedicine & Pharmacotherapy (Biomedecine & Pharmacotherapie)*, *155*, 113700. https://doi.org/10.1016/j.biopha.2022.113700

Washbourne, P., Thompson, P. M., Carta, M., Costa, E. T., Mathews, J. R., Lopez-Benditó, G., Molnár, Z., Becher, M. W., Valenzuela, C. F., Partridge, L. D., & Wilson, M. C. (2002). Genetic ablation of the t-SNARE SNAP-25 distinguishes mechanisms of neuroexocytosis. *Nature Neuroscience*, *5*(1), 19–26. https://doi.org/10.1038/nn783

Wen, Y., Li, W., Choudhury, G. R., He, R., Yang, T., Liu, R., Jin, K., & Yang, S.-H. (2013). Astroglial PTEN Loss Disrupts Neuronal Lamination by Dysregulating Radial Glia-guided Neuronal Migration. *Aging and Disease*, *4*(3), 113–126.

Wester, J. C., Mahadevan, V., Rhodes, C. T., Calvigioni, D., Venkatesh, S., Maric, D., Hunt, S., Yuan, X., Zhang, Y., Petros, T. J., & McBain, C. J. (2019). Neocortical Projection Neurons Instruct Inhibitory Interneuron Circuit Development in a Lineage-Dependent Manner. *Neuron*, *102*(5), 960-975.e6. https://doi.org/10.1016/j.neuron.2019.03.036

Whilden, C. M., Chevée, M., An, S. Y., & Brown, S. P. (2021). The synaptic inputs and thalamic projections of two classes of layer 6 corticothalamic neurons in primary somatosensory cortex of the mouse. *The Journal of Comparative Neurology*, *529*(17), 3751–3771. https://doi.org/10.1002/cne.25163

Willsey, A. J., Sanders, S. J., Li, M., Dong, S., Tebbenkamp, A. T., Muhle, R. A., Reilly, S. K., Lin, L., Fertuzinhos, S., Miller, J. A., Murtha, M. T., Bichsel, C., Niu, W., Cotney, J., Ercan-Sencicek, A. G., Gockley, J., Gupta, A. R., Han, W., He, X., … State, M. W. (2013). Coexpression networks implicate

human midfetal deep cortical projection neurons in the pathogenesis of autism. *Cell*, *155*(5), 997–1007. https://doi.org/10.1016/j.cell.2013.10.020

Wong, F. K., & Marín, O. (2019). Developmental cell death in the cerebral cortex. *Annual Review of Cell and Developmental Biology*, *35*, 523–542. https://doi.org/10.1146/annurev-cellbio-100818-125204

Wong, F. K., Bercsenyi, K., Sreenivasan, V., Portalés, A., Fernández-Otero, M., & Marín, O. (2018). Pyramidal cell regulation of interneuron survival sculpts cortical networks. *Nature*, *557*(7707), 668–673. https://doi.org/10.1038/s41586-018-0139-6

Wong, F. K., Selten, M., Rosés-Novella, C., Sreenivasan, V., Pallas-Bazarra, N., Serafeimidou-Pouliou, E., Hanusz-Godoy, A., Oozeer, F., Edwards, R., & Marín, O. (2022). Serotonergic regulation of bipolar cell survival in the developing cerebral cortex. *Cell Reports*, *40*(1), 111037. https://doi.org/10.1016/j.celrep.2022.111037

Wu, S. J., Dai, M., Yang, S.-P., McCann, C., Qiu, Y., Marrero, G. J., Stogsdill, J. A., Di Bella, D. J., Xu, Q., Farhi, S. L., Macosko, E. Z., Chen, F., & Fishell, G. (2024). Pyramidal neurons proportionately alter the identity and survival of specific cortical interneuron subtypes. *BioRxiv*. https://doi.org/10.1101/2024.07.20.604399

Wu, S. J., Dai, M., Yang, S.-P., McCann, C., Qiu, Y., Marrero, G. J., Stogsdill, J. A., Di Bella, D. J., Xu, Q., Farhi, S. L., Macosko, E. Z., Chen, F., & Fishell, G. (2024). Pyramidal neurons proportionately alter the identity and survival of specific cortical interneuron subtypes. *BioRxiv*. https://doi.org/10.1101/2024.07.20.604399

Wu, S.-X., Goebbels, S., Nakamura, K., Nakamura, K., Kometani, K., Minato, N., Kaneko, T., Nave, K.-A., & Tamamaki, N. (2005). Pyramidal neurons of upper cortical layers generated by NEX-positive

progenitor cells in the subventricular zone. *Proceedings of the National Academy of Sciences of the United States of America*, *102*(47), 17172–17177. https://doi.org/10.1073/pnas.0508560102

Xie, Y., Skinner, E., Landry, C., Handley, V., Schonmann, V., Jacobs, E., Fisher, R., & Campagnoni, A. (2002). Influence of the embryonic preplate on the organization of the cerebral cortex: a targeted ablation model. *The Journal of Neuroscience*, *22*(20), 8981–8991. https://doi.org/10.1523/JNEUROSCI.22-20-08981.2002

Xu, Q., Cobos, I., De La Cruz, E., Rubenstein, J. L., & Anderson, S. A. (2004). Origins of cortical interneuron subtypes. *The Journal of Neuroscience*, *24*(11), 2612–2622. https://doi.org/10.1523/JNEUROSCI.5667-03.2004

Xu, X., Roby, K. D., & Callaway, E. M. (2010). Immunochemical characterization of inhibitory mouse cortical neurons: three chemically distinct classes of inhibitory cells. *The Journal of Comparative Neurology*, *518*(3), 389–404. https://doi.org/10.1002/cne.22229

Xu, X., Sun, Y., Holmes, T. C., & López, A. J. (2016). Noncanonical connections between the subiculum and hippocampal CA1. *The Journal of Comparative Neurology*, *524*(17), 3666–3673. https://doi.org/10.1002/cne.24024

Yang, D., Qi, G., Ding, C., & Feldmeyer, D. (2022). Layer 6A Pyramidal Cell Subtypes Form Synaptic Microcircuits with Distinct Functional and Structural Properties. *Cerebral Cortex*, *32*(10), 2095–2111. https://doi.org/10.1093/cercor/bhab340

Yang, J., Nie, J., Ma, X., Wei, Y., Peng, Y., & Wei, X. (2019). Targeting PI3K in cancer: mechanisms and advances in clinical trials. *Molecular Cancer*, *18*(1), 26. https://doi.org/10.1186/s12943-019-0954-x

Ye, Z., Mostajo-Radji, M. A., Brown, J. R., Rouaux, C., Tomassy, G. S., Hensch, T. K., & Arlotta, P. (2015). Instructing perisomatic inhibition by direct lineage reprogramming of neocortical projection neurons. *Neuron*, *88*(3), 475–483. https://doi.org/10.1016/j.neuron.2015.10.006

Yetman, M. J., Washburn, E., Hyun, J. H., Osakada, F., Hayano, Y., Zeng, H., Callaway, E. M., Kwon, H.-B., & Taniguchi, H. (2019). Intersectional monosynaptic tracing for dissecting subtype-specific organization of GABAergic interneuron inputs. *Nature Neuroscience*, *22*(3), 492–502. https://doi.org/10.1038/s41593-018-0322-y

Yook, C., Kim, K., Kim, D., Kang, H., Kim, S.-G., Kim, E., & Kim, S. Y. (2019). A TBR1-K228E Mutation Induces Tbr1 Upregulation, Altered Cortical Distribution of Interneurons, Increased Inhibitory Synaptic Transmission, and Autistic-Like Behavioral Deficits in Mice. *Frontiers in Molecular Neuroscience*, *12*, 241. https://doi.org/10.3389/fnmol.2019.00241

Young, C. E., Arima, K., Xie, J., Hu, L., Beach, T. G., Falkai, P., & Honer, W. G. (1998). SNAP-25 deficit and hippocampal connectivity in schizophrenia. *Cerebral Cortex*, *8*(3), 261–268. https://doi.org/10.1093/cercor/8.3.261

Yozu, M., Tabata, H., & Nakajima, K. (2004). Birth-date dependent alignment of GABAergic neurons occurs in a different pattern from that of non-GABAergic neurons in the developing mouse visual cortex. *Neuroscience Research*, *49*(4), 395–403. https://doi.org/10.1016/j.neures.2004.05.005

Yozu, M., Tabata, H., & Nakajima, K. (2005). The caudal migratory stream: a novel migratory stream of interneurons derived from the caudal ganglionic eminence in the developing mouse forebrain. *The Journal of Neuroscience*, *25*(31), 7268–7277. https://doi.org/10.1523/JNEUROSCI.2072-05.2005

Yuan, M., Meyer, T., Benkowitz, C., Savanthrapadian, S., Ansel-Bollepalli, L., Foggetti, A., Wulff, P., Alcami, P., Elgueta, C., & Bartos, M. (2017). Somatostatin-positive interneurons in the dentate gyrus of mice provide local- and long-range septal synaptic inhibition. *ELife*, *6*. https://doi.org/10.7554/eLife.21105

Yun, K., Potter, S., & Rubenstein, J. L. (2001). Gsh2 and Pax6 play complementary roles in dorsoventral patterning of the mammalian telencephalon. *Development*, *128*(2), 193–205. https://doi.org/10.1242/dev.128.2.193

Zhang, H., Zhu, S., Zhu, Y., Chen, J., Zhang, G., & Chang, H. (2011). An association study between SNAP-25 gene and attention-deficit hyperactivity disorder. *European Journal of Paediatric Neurology*, *15*(1), 48–52. https://doi.org/10.1016/j.ejpn.2010.06.001

Zhou, J., & Parada, L. F. (2012). PTEN signaling in autism spectrum disorders. *Current Opinion in Neurobiology*, *22*(5), 873–879. https://doi.org/10.1016/j.conb.2012.05.004

Zikopoulos, B., & Barbas, H. (2006). Prefrontal projections to the thalamic reticular nucleus form a unique circuit for attentional mechanisms. *The Journal of Neuroscience*, *26*(28), 7348–7361. https://doi.org/10.1523/JNEUROSCI.5511-05.2006

Zolnik, Timothy A, Ledderose, J., Toumazou, M., Trimbuch, T., Oram, T., Rosenmund, C., Eickholt, B. J., Sachdev, R. N. S., & Larkum, M. E. (2020). Layer 6b Is Driven by Intracortical Long-Range Projection Neurons. *Cell Reports*, *30*(10), 3492-3505.e5. https://doi.org/10.1016/j.celrep.2020.02.044

Zolnik, Timothy Adam, Bronec, A., Ross, A., Staab, M., Sachdev, R. N. S., Molnár, Z., Eickholt, B. J., & Larkum, M. E. (2024). Layer 6b controls brain state via apical dendrites and the higher-order thalamocortical system. *Neuron*, *112*(5), 805-820.e4. https://doi.org/10.1016/j.neuron.2023.11.021